Storage conditions and dynamics of magma reservoirs feeding the major pumiceous eruptions of Dominica (Lesser Antilles Arc)

Clara Solaro

UNIVERSITÉ SORBONNE PARIS CITÉ

Université Sorbonne Paris Cité

Thèse préparée
à l'UNIVERSITÉ PARIS DIDEROT
École doctorale STEP'UP – ED N°560
IPGP- Equipe Systèmes Volcaniques

Storage conditions and dynamics of magma reservoirs feeding the major pumiceous eruptions of Dominica (Lesser Antilles Arc)

par

Clara Solaro-Müller

présentée et soutenue publiquement le

31 Janvier 2017

Thèse de doctorat de Sciences de la Terre et de l'environnement

dirigée par Georges Boudon

devant un jury composé de :

Bachmann Olivier Professeur (ETH,Zurich-Suisse)	Rapporteur
Druitt Timothy Professeur (Université Blaise Pascal, Clermont Ferrand)	Rapporteur
Kaminski Edouard Professeur (IPGP-Université Paris 7-France)	Examinateur
Parat Fleurice Maitre de Conférence (Université de Montpellier-France)	Examinatrice
Martel Caroline Directeur de Recherche CNRS (ISTO, Orléans)	Membre invité
Balcone-Boissard Hélène Maitre de conférence (ISTeP-UPMC-France)	Co-encadrante de thèse
Boudon Georges Physicien (IPGP-France)	Directeur de thèse

Remerciements

Je tiens tout d'abord à remercier les personnes qui m'ont aidé pendant l'élaboration de ma thèse et notamment mes directeurs et encadrants Georges Boudon, Hélène Balcone- Boissard et Caroline Martel. Je les remercie pour leur soutien et les nombreux conseils durant l'élaboration et rédaction de cette thèse. Merci aussi à Dan Morgan, qui m'a guidé dans le difficile «monde de la diffusion» et supporté dans les moments cruciaux de la rédaction.

Mes remerciements vont également à Olivier Bachmann et Tim Druitt pour avoir accepté d'être rapporteurs de ce travail de thèse ainsi qu'aux membres examinateurs du Jury.

Un grand merci aussi à tous les membres du laboratoire de « Systèmes Volcaniques » qui m'ont accueilli tout le long de ces trois dernières années, en apportant de nombreuses contributions et conseils. Les longues heures de travail de laboratoire derrière la loupe binoculaire ou les draps de polissage ont été aussi bien plus plaisantes en bonne compagnie.

Merci à la compagnie de Michel Fialin, Nicolas Rividi et Omar Boudouma pour les innombrables heures passées à la microsonde et au MEB. Entre deux points de mesure, j'ai beaucoup appris sur les chefs-d'œuvre de la musique classique et l'Opéra. Et oui Michel, je suis encore désolée pour les 100.000 points d'analyse en un week-end et le filament qui n'en pouvait plus.

Je remercie aussi les membres du laboratoire de pétrologie expérimentale de l'ISTO, pour l'atmosphère conviviale que leur groupe a su créer mais aussi pour leur aide lors de la préparation des échantillons, la mise en route et le suivi des manips à la presse. Un merci particulier à Rémi Champallier et Caroline Martel qui ont évité que je fasse exploser la salle des presses et m'ont appris beaucoup de choses, en gardant toujours la bonne humeur (les capsules ça fuit, les manips ça rate, les condensateurs peuvent créer une piscine dans le labo….on garde le sourire, la patience et on limite les dégâts!!). Et merci aussi au Gros Bleu, qui ne m'a pas fait de mauvaises surprises.
Merci à Pierangelo et Emanuela pour l'accueil chaleureux à chacun de mes passages à Orléans et les soirées siciliennes à base de « spaghetti al sugo » et « caponata » qui m'ont fait sentir à la maison.

De nombreux autres étudiants sont devenus au cours de ces trois ans de bons amis et je tiens à les remercier pour tous les moments que nous avons partagés entre bureaux et couloirs de laboratoire, autours d'un déjeuner, d'un café ou d'une bière. Merci à Lucie Grousset, Mariona Tarriago, Diane Bonnemains, Cédric O'Shaughnessy, Pierre Clouzet, Guillaume Boudoir.

Plus particulièrement je remercie le bureau 469 et « les filles » (Morgane Brunet, Géraldine Zdanowicz et Céline Vidal) pour avoir partagé de nombreux moments de joie, folie, rigolade et vrais fous rires!

Les mots les plus simples et riches en affection vont à ma famille et particulièrement à mes parents qui m'ont soutenu, écouté, guidé tout le long de cette « période parisienne » et davantage encore durant la thèse. Merci papa pour m'avoir fait connaître toute petite l'Etna, qui a suscité ma passion pour les volcans. Merci à vous d'être toujours là.

Puis le plus spécial des merci va à Mr. Ashman, qui a su me supporter (et j'espère continuera à le faire) pendant les meilleurs et les pires moments de cette thèse. Merci de m'avoir laissé

hurler contre mes données, la microsonde, mon ordinateur, Excel, Word et bien d'autres choses sans jamais perdre ta patience infinie et ton sourire. Merci pour ton aide et soutien quotidien et le confort que ton calme naturel apporte à mon tempérament un tantinet turbulent.

Et pour finir, mon plus grand merci va à la Dominique, qui m'a fait le plus beau des cadeaux et a changé ma vie à jamais.

Abstract

Large silicic eruptions (tens to hundreds of km^3 /eruption) have been a main subject of study for modern volcanology as they represent volcanic events of great impact on environment and human settlement on Earth. Petrologists have demonstrated that the crystal "cargo" of these eruptions can be used to unravel the pre-eruptive dynamic of their magmatic plumbing system and constrain timescales of the related magmatic processes. Specifically, several studies have proved that this "crystal cargo" can be remobilized and brought to eruption in short timescales of decades to centuries, making these systems more dynamic than previously believed.

Several ignimbritic eruptions with a volume of the order of ~10 km^3 have been recognized in Dominica (Lesser Antilles arc). On the basis of a detailed chronostratigraphy of the deposits, we present an integrated petrological study of the plinian fallout deposit of the latest three ignimbritic eruptions of Layou (~51kyrs cal BP), Roseau (~33kyrs cal BP) and Grand Fond (~24kyrs cal BP). We combine natural and experimental petrology to investigate the prevailing storage conditions within the reservoir that fed each eruption. Whole rocks are all dacites with crystal contents of ~30%, comprising plagioclase (An_{50-78}), orthopyroxene (En_{47-63}), clinopyroxene (Wo_{44-45}), amphibole (Mg# 0.52-0.60) and Fe-Ti oxide (Mag_{71-75} and Ilm_{86-87}) and rhyolitic residual melt. Pre-eruptive storage conditions of 850 (±5) °C, 400 MPa (16 km depth), ~ΔNNO+1 and melt water content of ~6-8wt% were determined for all studied eruptions through phase equilibria experiments.

Orthopyroxenes were used to investigate the architecture and pre-eruptive dynamics of the plumbing system through a crystal system analysis (CSA) combined to a Fe-Mg diffusion modelling. Textural and chemical features of analysed orthopyroxenes prove that for all eruptions ~80-85% of crystals are unzoned while 15-20% present clear normal, reverse and multiple zoning, with reverse zoning being prevalent. Unzoned crystals represent the main magmatic environment (ME) while reverse zoned ones suggest a pre-eruptive perturbation of the reservoir. 4 MEs are evidenced, with a main movement of crystals towards MEs of less evolved composition, linked with the observed reverse zoning. Nevertheless, major element composition of orthopyroxene-hosted melt inclusions shows that all MEs are in equilibrium with the same melt. Combining results on natural and experimental petrology we can define the reservoirs as a highly crystalline (~30%), moderately cold (850°C) and highly oxidized (~ΔNNO+1) environment with 80-85% of unzoned orthopyroxenes, and 15-20% of zoned orthopyroxenes recording a heating process of 25-30°C, possibly produced by an underplating hotter magma that is responsible of the rejuvenation of the reservoir. By modelling the diffusional relaxation of Fe-Mg chemical gradient on zoned orthopyroxenes, we argue that this heating occurs in short timescales of ~10 years prior to each eruption. This heating process develops, over the considered eruptive time, a plume heating geometry able to bring together, on the scale of the hand sample, crystals of different magmatic environments (MEs).

Résumé

Les grandes éruptions explosives (10 to 1000 km^3 /eruption) ont été l'un des sujets principaux d'étude de la volcanologie moderne car elles représentent des éruptions de grand impact sur la nature et sur les installations humaines sur Terre. Les pétrologues ont démontré que la proportion de cristaux dans les produits de ces éruptions peut être utilisée pour étudier les dynamiques pré-éruptives de la plomberie magmatique et contraindre les échelles de temps des processus magmatiques. Plus précisément, de nombreuses études ont prouvé que ces cristaux peuvent être remobilisés en des temps courts de 10 à 100 ans avant l'éruption, ce qui rend ces systèmes significativement dynamiques.

Plusieurs éruptions ignimbritiques d'un volume de l'ordre de la dizaine de km^3 ont été reconnues en Dominique (Arc des Petites Antilles). Nous présentons ici, sur la base d'une étude stratigraphique détaillée, une étude pétrologique des ponces de la phase plinienne qui débute les trois éruptions ponceuses majeures de la Dominique : Layou (~51kyrs cal BP), Roseau (~33kyrs cal BP) et Grand Fond (~24kyrs cal BP).

En combinant une étude pétrologique des produits naturels et des produits issus des travaux de pétrologie expérimentale, nous proposons un modèle complet des réservoirs à l'origine des trois éruptions. Les magmas sont des dacites à forte teneur en cristaux (~30%), comprenant plagioclases, orthopyroxènes, clinopyroxènes, amphiboles et oxides. Les expériences d'équilibre de phases sur ces dacites ont permis de contraindre les conditions de stockage à 850°C, 400 MPa (16 km), ~ΔNNO+1 et une teneur en eau pré-éruptive de ~6-8 wt % pour les trois éruptions.

Les orthopyroxènes ont été utilisés pour étudier les dynamiques pré-éruptives du système magmatique. Par une analyse systématique (« Crystal system analysis ») de leur zonation nous avons défini différents environnements magmatiques et leur connections.

Les échelles de temps des dynamiques pré-éruptives sont calculées par modélisation de l'interdiffusion Fe-Mg dans les orthopyroxènes. Les caractéristiques chimiques et texturales des orthopyroxènes montrent que ~80-85% des cristaux sont non-zonés, tandis que 15-20% présentent une zonation multiple, normale ou inverse, avec prévalence de cette dernière. Les cristaux non zonés représentent l'environnement magmatique principal, alors que les zonés suggèrent une perturbation pré-éruptive du réservoir. Le « crystal system analysis » appliqué à ces derniers suggère la présence de 4 environnements magmatiques (MEs), avec un mouvement principal des cristaux vers des MEs de compositions moins évoluées, lié à la zonation inverse des cristaux. Cependant, la composition des inclusions vitreuses des orthopyroxènes, montre que les différents MEs sont en équilibre avec un verre de même composition. Ces considérations, couplées aux résultats d'équilibres de phases, nous permettent de définir le réservoir comme un environnement fortement cristallisé (~30%), modérément froid (~850°C) et fortement oxydé (~ΔNNO+1) possédant 80-85% de cristaux non-zonés, remobilisé par un réchauffement de 25-30°C produit par l'injection d'un magma plus chaud sous-jacent. La modélisation de l'interdiffusion Fe-Mg dans les orthopyroxènes indique que le réchauffement s'est produit ~10 ans avant chaque éruption. Ce processus crée la zonation inverse retrouvée dans 15-20% des orthopyroxènes et développe un panache thermique interne au réservoir qui est responsable de l'hétérogénéité cristalline retrouvée dans les échantillons.

TABLE OF CONTENTS

INTRODUCTION

1. Subduction related volcanism

Subduction zones represent active tectonic boundaries of interaction in between two plates where one denser plate is subducting within the mantle creating a mechanism responsible of recycling of Earth oceanic crust and upper mantle into the deep mantle and more generally of chemical elements such as volatiles. This process is at the origin of a diversity of thermal, geochemical and petrological exchanges, playing a key role in the redistribution of elements in between the different Earth reservoirs (lithosphere, mantle, hydrosphere and atmosphere). Subduction zones are associated with significant deep and highly explosive volcanism, in which volcanoes are generally organized in arcs of islands or chains of mountains nearly parallel to the subduction margin. As a large number of volcanoes on Earth are located above a subduction zone, subduction can be considered as a "factory" for production of magma and continental crust.

Volcanism in subduction zones is known to be linked to the significant drop in solidus temperature of the mantle, a consequence of the presence of a significant amount of water-rich fluids originating from the subducting plate (Tatsumi, 1989; Peacock, 1990; Tatsumi and Eggings, 1995; Jarrard et al., 2003; Manning, 2004) (Fig. 1). This process of dehydration of the subducting plate (slab) - caused also by compaction of marine sediments and rocks such as amphibolites that contain water-bearing minerals - brings supercritical fluids into the overlying mantle wedge. As a consequence, the hydrated boundary layer of the mantle wedge crystallizes hydrous minerals (amphibole, serpentine and chlorite) whose composition is highly pressure dependent (Fig.1). This hydrated peridotite can be dragged down by convection and, by the breakdown of amphibole (~75-110 km, 22-30 kbar, Schmidt and Poli, 1998), receive water-rich fluids; in turn allowing peridotites to cross the hydrated solidus and promoting their partial melting (Tatsumi, 1989) (Fig.1). This first low-density magma pockets tend to move upward to region of low pressure / higher temperature and can evolve differently from one subduction zone to another. Because of the influence of various source components (subducted slab and its fluids, mantle wedge), a wide variety may be observed in the final magma composition, resulting in turn in the array of eruptive products typical of arc magmas, which range from tholeiite to rhyolite.

Despite this large range of potential compositions, arc magmas generally have some diagnostic features in common which distinguish them from mid-ocean ridge basalts (MORB)

or Ocean Island basalts (OIB) belonging to different geological contexts (Macdonald et al., 2000). Arc magmas exhibit relatively high water content, high oxidation states (Gill, 1981) and bear a particular geochemical signature with enrichment in LILE (large-ion lithophile elements: K, Sr, Ba, Rb) relative to HFSE (high-field strength elements: Zr, Th, U, REE), resulting from the fluid migration process at their origin (Fig.2).

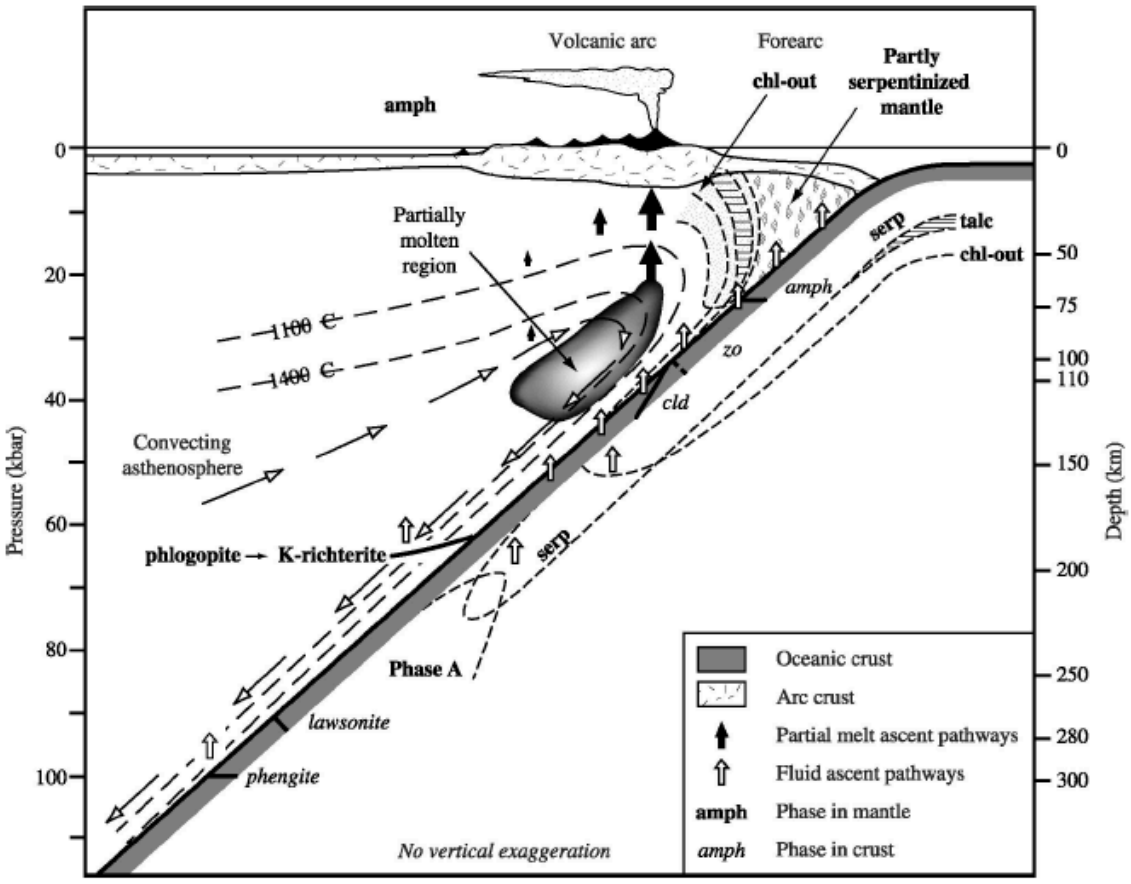

Figure 1: Simplified cross-section of a subduction zone*. Model of dehydration of subducted oceanic crust and peridotite (modified from Schmidt and Poli, 1998). The break-down of several water-rich minerals (amphibole, chlorite, zoisite) present in the subducting oceanic crust and the peridotite occurs until 150-200 km of depth and releases water into the overlying mantle wedge, thus lowering the solidus temperature and favouring melting. The partially molten region in the figure indicates the region where melting is expected to occur at a higher degree. Open arrows mark the release of fluids from the slab, solid arrows indicate rise of melts. Dashed lines outline stability fields of hydrous phases in peridotite. Amph : amphibole ; Cld : chloritoid ; Chl : chlorite ; Serp : serpentine; Zo : zoisite. (from Stern, 2002).*

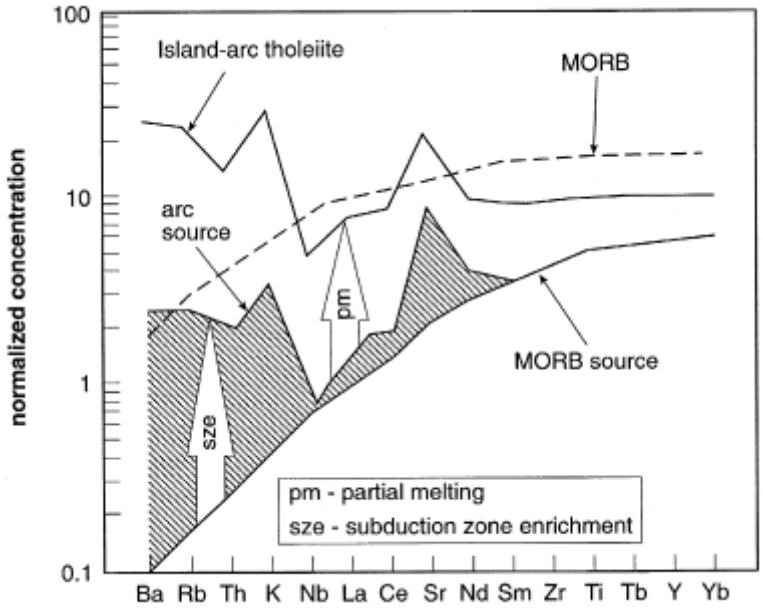

Figure 2: Trace elements characteristic of MORB and Island arc magmas*. Elements are arranged with decreasing incompatibility to the right and concentrations normalized to mantle composition. The enrichment in highly incompatible elements (Ba, Rb, Th, K) present in arc magmas can be produced by adding fluid-soluble elements (sze, dehydration of the slab) to a MORB source. The partial melting (pm) of this enriched source produces the island-arc thooleite. (from Macdonald et al., 2000).*

Subduction related volcanism in an island arc context is mainly characterized by the emission of relatively small volumes (~1 km^3 DRE, Dense Rock Equivalent) of andesitic to rhyolitic products. Nevertheless there are several geological and stratigraphic evidences of major eruptions occurring in subduction zones involving large erupted volumes (10-10^4 km^3 DRE). Examples are: 1) the 1600 BC Minoan eruption (Santorini, Greece) which emitted magma volumes of 40-60 km^3 (Heiken and McCoy, 1984; Druitt et al., 1992; Sigurdsson et al., 2006; Druitt et al. 2012); 2) the Taupo Volcanic Zone (TVZ, New Zealand), where intense silicic volcanism has created several large volume rhyolitic eruptions over the last 2 my (10000-20000 km^3 in at least 34 eruptions from the Central TVZ, Wilson et al., 1984; Houghton et al., 1995; Wilson et al., 1995; Wilson, 2001); 3) the Sunda arc region (Indonesia) where the 75 ka Toba eruption (2800 km^3 DRE of magma, Rose and Chestner, 1987), the ~30 and ~20 ka BP Batur eruptions (~13 km^3 DRE, Reubi and Nicholls, 2004, 2005), the 1815 Tambora eruption (Self et al., 1984) and the 1883 Krakatau eruption (18-21 km^3, Self and Rampino, 1981) produced large ignimbritic deposits; 4) the island of Dominica (Lesser Antilles arc), subject of this study, where several major pumiceous ignimbritic eruptions have been recognized (Sigurdsson, 1972; Carey and Sigurdsson, 1980; Lindsay et al., 2003; Lindsay et al., 2005a;

Smith et al;, 2013; Howe et al., 2014). Initial estimates of the volumes of the Dominica ignimbritic eruptions were ~58 km^3 (Roseau Tuff, Sigurdsson, 1972; Carey and Sigurdsson, 1980), which have been recently revised to several km^3 DRE/eruption (Smith et al., 2013). In any case, these still represent large magma volumes compared to the neighbouring island of the arc that mainly involved less than 1 km^3 of magma DRE/eruption.

Taken together, this evidence highlights that several large silicic systems are associated with subduction-related island arc environments. The issue remains to explain how—and over which timescales—such large volumes of magma can be generated, stored and preserved in the crust, and finally brought into eruption.

2. Large silicic eruptions

2.1. Formation and storage of large silicic magma volumes

Large silicic magma reservoirs, generally linked with caldera forming eruptions (Christiansen, 2001; Lindsay et al., 2001a, b; Lipman, 2007; Chesner, 2012), have for a long time been described as single long-lived magma chambers filled with largely molten material. The conventional concept of a large cauldron filled with magma would require an instantaneous and fast storage of large volumes of melt in the shallow crust. On the contrary, thermo-mechanical studies have demonstrated that magma emplacement does not occur as one unique event (which would raise several mechanical problems), but as a sequential multi-timescale emplacement of dikes and sills to form a complex plumbing system (Annen, 2009; Annen et al., 2015; Blundy and Annen, 2016). The construction of such large silicic systems by incremental growth requires long storage times (10^5- 10^6 years: Jellinek and de Paolo, 2003) and episodes of high magma fluxes (> 10^{-2} km^3/yr; Annen, 2009) characteristic of arcs in flare-up mode (Fig. 3). The flare-up mode, as opposed to the steady-state mode (Hildreth, 1981; de Silva and Gosnold, 2007; Hughes and Mahood, 2008), represents periods of extraordinary silica magma productivity with magma fluxes from the mantle reaching high values of 10^{-3} km^3 km^{-1} yr^{-1} (Fig.3, de Silva and Gosnold, 2007). The possibility of a further link with extensional tectonics, favouring the storage of large volumes of magma and their lateral extension, has been addressed by Jellinek and De Paolo, (2003).

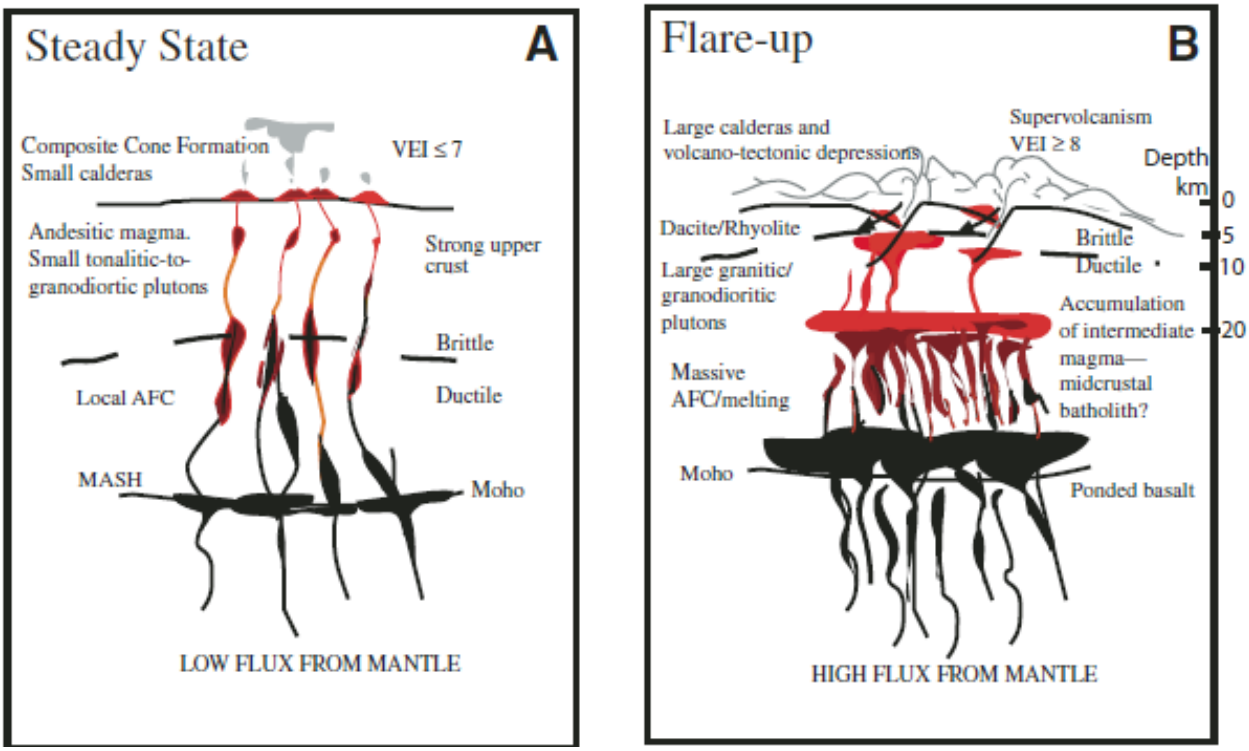

Figure 3: Distinction in between steady-state and flare-up mode in magmatic systems. *The steady state case (A) is characteristic of the long-term evolution of a volcanic region with low magma fluxes (10^{-4} km^3 km^{-1} yr^{-1}, Aleutians, Jicha et al., 2006) and occasional explosive eruptions of VEI <7. Steady-state level represents the "background flux" level. The Flare-up case (B) represents a transient event in the evolution of a volcanic region with higher magmatic fluxes and extraordinary input from the mantle. This results in the development of supervolcanoes with explosive eruptions of VEI >8. (from de Silva, 2008).*

2.1.1. The mush model

Advances in geophysical survey-monitoring and analytical techniques have proven that large melt provinces/pockets are present neither under continental volcanism nor under oceanic ridges (Dunn et al., 2000; De Gori et al., 2005). As a consequence, studies and observations provided a new view of magma chambers as a magma mush zone (crystals plus silicate liquid) in which several melt lenses are organized as sills or dikes (Marsh, 1996; Bachmann et al., 2003; Bachmann and Bergantz, 2008). These systems of melt lenses can exhibit very different degrees of crystallinity and can be formed by a mixture of various phases including fluids (dominated by H_2O-CO_2), melt and complex crystals phase assemblages as a function of each particular storage condition. As a consequence of this significant variability, dynamics and mobility of magma lenses constituting the system can differ and produce complex interactions, generally difficult to decipher in the final volcanic erupted products.

This new model of reservoir as a mush zone has thus brought new challenges in understanding: i) how the different parts of the magmatic plumbing system are defined (size, shape, volume); ii) what is their pre-eruptive composition and the related storage parameters (pressure/depth, temperature, redox conditions, volatile content); iii) how are they connected and iv), what are the main pre-eruptive dynamics.

There is much stratigraphic and geological evidence of multi-lens mush reservoirs at the origin of large (caldera forming) eruptions, particularly in extensional tectonic contexts. For the Taupo Volcanic Zone (TVZ, New Zealand), Bégué et al. (2014) studied the paired Mamaku and Ohakuri eruptions. Major differences in bulk rock compositions led Bégué et al. (2014) to argue for the presence of five separated magma ponds extracted from the same mush region, under different extraction conditions. These batches evolve separately until eruption without possibility of mixing or mingling (Bégué et al., 2014). Still in the Taupo Volcanic Zone, the Okareka eruption (Okataina volcanic center, NZ) has produced rhyolitic products with variable melt composition, crystallinity and volatile content. These changes in composition are consistent with rhyolites stored in three separate magma lenses inside a larger mush zone (Shane et al., 2008). Several other studies of Charlier et al. (2003), Gravley et al. (2007), Wilson and Charlier (2009) and Cooper et al. (2012) have contributed to the view of the TVZ as a large intermediate mush zone from which rhyolitic melt is incrementally extracted and forms different laterally extended magma batches that drive the regional volcanic activity. Moreover, the strong extensional tectonic setting of the area enhances lateral migration of magma and promotes the formation of sills and lenses.
For the Bishop Tuff (Long Valley caldera, USA), two different eruption-feeding melt lenses have been identified (Gualda and Ghiorso, 2013). The studies of Ellis and Wolff, (2012) and Ellis et al. (2013) on the Snake river Plain (Idaho, USA) have explained the heterogeneity in pyroxene crystal populations and glass composition as evidence for the existence of multiple batches of melt extracted from and preserved by the rigid network of the mush, then stored in proximity (Ellis et al., 2014). For the Colli Albani (Italy) volcanic system, variability in vesicularity and in whole rock and matrix glass composition suggest the presence of a complex system of melt lenses, horizontally and vertically dispersed within a wide crystal mush (Cashman and Giordano, 2014).
On the basis of these observations, the mush model has been increasingly used in modern volcanology to describe crustal reservoirs.

The mush is defined as a highly crystallized body made of "a mixture of crystals and silicate liquid whose mobility, and hence eruptability, is inhibited by a high fraction of solid particles" (Miller and Wark, 2008). The mush status implies crystallinities between 25 and 55% (Marsh, 1996; Bachmann and Bergantz, 2008; Fig. 4).

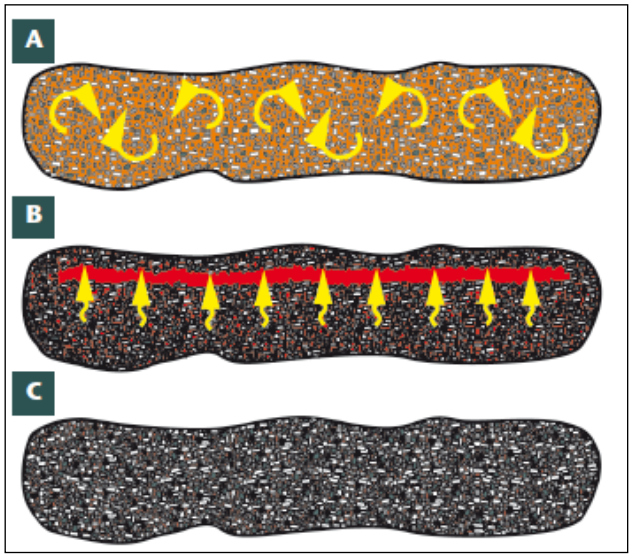

Figure 4: The mush model*. Schematic evolution of a mushy magma reservoir. (A) Crystallinity < 45 vol%: convective currents are present in the magma body and crystals are kept in suspension; (B) Crystallinity= 45-60 vol%: convection is hampered by the high amount of crystals forming a skeleton. Crystal-melt separation occurs by crystal compaction; this crystallinity range is the most efficient for crystal-melt separation; (C) Crystallinity> 60 vol%: the high crystallinity lowers the permeability and increases the viscosity of the melt; no extraction occurs. (From Bachmann and Bergantz, 2008)*

In these conditions the residual melt can be extracted by different mechanisms. For crystallinities < 50% (liquid-dominated systems), separation occurs by settling of the particles on the bottom of the magma chamber (Bachmann and Bergantz, 2004; Bachmann and Bergantz, 2008). At a crystal fraction of 45-60 vol% a mechanical rheological locking-point is reached and, by touching each other, crystals can form an interconnected network or a rigid skeleton. In this case convection is hindered so that the crystal-melt mixture cannot flow and is uneruptible (Marsh, 1996). As a consequence, for crystallinities > 50% (solid-dominated systems), the gravitational crystal-liquid separation occurs by compaction of crystals into their network (Fig. 4). Because of the high viscosities reached by high-crystallinity magma, these processes are very slow and require long storage periods.

2.1.2. Classification of large silicic eruptions

Products of large silicic eruptions, such as those listed above, can be divided in *Monotonous intermediates* (MI) crystal rich (≥35%) dacites and *Crystal poor rhyolites* (≤15%, CPR) as a function of their crystallinity and composition.

Both types of erupted products are inferred to have the same origin (Bachmann and Bergantz, 2004). The monotonous intermediate dacites represent remobilized and erupted mush with a homogeneous whole rock composition and high crystallinities (30 to 40 vol%). Eruption of such homogeneous voluminous products implies timescales sufficiently long enough for re-activation and re-homogenization of the reservoir by convection and stirring prior to eruption. It has been demonstrated that re-activation timescales are much greater (up to two order of magnitudes) than homogenization ones, meaning that crystal-rich monotonous intermediate (MI) dacites requiring a first re-activation stage are inevitably well-stirred in order to finally be uniform in composition (Huber et al., 2012). On the contrary, crystal poor rhyolites represent the uppermost cup of residual melt extracted from the mush by a crystal-liquid separation mechanism as crystal settling, or compaction and filter pressing of the mush (Bachmann and Bergantz, 2004; Bea, 2010; Dufek and Bachmann, 2010). Their eruption does not require any re-activation process as rhyolite magma batches are already rheologically eruptible (Huber et al., 2012).

The combination of CPR and MI creates three main categories of ignimbrites deposits (Bachmann and Bergantz, 2008): (i) ignimbrites showing a gradational zoning in composition and crystallinity with a CPR part at the base of the deposit and a MI part at its top. This type of ignimbrite is the most common and best studied (Bishop Tuff: Wilson and Hildreth, 1997; Hildreth et and Wilson, 2007; Gualda and Ghiorso, 2013; Huckelberry ridge Tuff: Wilson, 2008); (ii) ignimbrites showing no compositional gradient. These can be either a crystal-rich MI dacite (Fish Canyon: Lipman et al., 1997; Bachmann et al., 2002; Bachmann and Bergantz, 2003) or a CPR (Taupo Volcanic Zone, Oruaunui eruption: Wilson, 1995; Wilson et al., 2001, 2008); (iii) ignimbrites showing an abrupt zoning in between a lower CPR and an upper MI part. Eruptions start with a crystal-poor rhyolite and rapidly shift to a crystal-rich dacite with a significant compositional gap. An example of this kind of ignimbrite is the Crater Lake described by Bacon and Druitt (1988).

2.2. Rejuvenation and eruption

Large silicic eruptions can be triggered internally (from the chamber) or externally (from the roof). In the first case, the triggering process is linked with inner dynamics of the plumbing

system (e.g. injection of a less-evolved, hotter magma batch, magma mixing/mingling, or reheating), while in the second case, the triggering processes derives from the tectonic setting, the structure of the volcanic edifice (presence of fractures, dikes, flank instabilities) and the physico-mechanical characteristics of the magma chamber (shape, roof aspect ratio, wall-rock viscosity; Jellinek and DePaolo, 2003; Gudmundson, 2008).

Considering the internal triggers, in the last decades several mechanisms have been proposed to unlock and remobilize the mush to eruption: conductive heating and self-convection (Couch et al;, 2001), gas sparging (upward migration of a hot volatile phase originating from the underplating basaltic magma: Bachmann and Bergantz, 2003 and 2006), instability and overturning caused by density contrasts or thermal stratification (Sparks et al., 1984; Turner and Campbell, 1986; Ruprecht et al., 2008).

Monotonous ignimbrites showing no compositional or thermal gradients have prompted researchers to describe a process of heat transfer that involves limited mass transfer (Murphy et al., 2000; Couch et al., 2001; Bachmann and Bergantz, 2006).

Pure conduction can be considered as a primary heat transfer process. Nevertheless it has been demonstrated (Bachmann and Bergantz, 2006) that the efficiency of conduction is too low to allow re-heating of large volume eruptions, such as the Fish Canyon Tuff (~5000 km^3), under reasonable timescales (less than several million years), without including other heat transfer mechanisms.

The concepts of self-mixing and convection as remobilization processes have been developed by Murphy et al. (2000), Phillips and Woods (2002) and Couch et al. (2001). Murphy et al. (2000) and Couch et al. (2001) formulate the self-mixing idea to explain the whole-rock homogeneity vs. single crystal variability of Soufrière Hills (Montserrat) dacitic magmas. They suggest that a magma-mush body heated from below by an underplating magma can start a self-convection process when the interface between the mush and the mafic magma is destabilized (Rayleigh critical number). Self-mixing creates heat-plume geometries in the reservoir able to create a diversity of mineral textures in samples, bringing together—at the hand-sample scale—crystals having experienced different crystallization and thermal histories (Murphy et al., 2000). However the high crystallinity values found in monotonous ignimbrites (~35-40 vol%) indicates that during storage they have likely reached the threshold crystallinity level >50% in which they are locked, with no possible flow or melt convection. Therefore, a mechanism other than thermal convection (but still implying limited mass exchange) is needed to unlock the mush.

Gas sparging, the percolation of a low-density H_2O-CO_2 fluid phase through the mush skeleton, has been proposed by Bachmann and Bergantz (2003, 2006) as a mechanism to defrost the mush from its locked-state and rejuvenate it to eruption, with limited hybridization in between magmas. These authors have tested their multiphase flow model on the Fish Canyon Tuff and results show that the mechanism can produce significant reheating of the mush (>40°C in 150-200 kyrs) enabling it to defrost and, together with self-convection (Couch et al., 2001), remobilise it. Gas sparging can also create internal pressures in the mush, enhancing melt mobility and extraction by filter pressing. Nevertheless this mechanism cannot be considered as uniquely responsible for the formation of large volume rhyolitic cup, such as those known for example for the TVZ.

Revisiting the idea of Bachmann et al. (2002) and Bachmann and Bergantz (2006), Ruprecht et al. (2008) propose a gas-driven mixing event, in which the interaction between the underplating recharging magma and the hosting magma causes gas exsolution from the former, resulting in a density inversion and a subsequent overturn of the magmatic system. A stable stratified system is developed after the overturn. Significant heterogeneity in crystal compositions and textures found in many volcanic centres could be then explained by a single overturn of the system, bringing together crystals associated with different magmatic environments at the scale of the thin section.

External trigger mechanisms incorporate all processes arising from the volcanic edifice itself. Examples include the downward propagation of faults producing a roof collapse (Gregg et al., 2012), possible interactions with hydrothermal or metamorphic fluids favouring a weakening of wall rocks (Jellinek and DePaolo, 2003), destabilization of the flanks of the edifice (Pinel et Jaupart, 2000, 2003; Albino et al., 2010; Boudon et al., 2013), or other mechanisms particular to extensional tectonic settings (Jellinek and DePaolo, 2003).

2.3. Timescales of magma dynamics and rejuvenation

Assessing magma remobilization timescales of large silicic eruptions is a fundamental issue in modern volcanology due to the involvement of significant magma volumes, which has profound implications for hazard and risk management. Recent studies have used the crystal cargo of magma and the related textural-chemical record to unravel magma dynamics and timescales prior to eruption.

Kinetic modelling of diffusional relaxation of chemical-potential gradients in crystals has been widely used to obtain timescales on plumbing system pre-eruptive dynamics and to demonstrate that large melt volumes can be remobilized, assembled and brought to eruption

rapidly (Nakamura et al., 1995; Costa and Chakraborty, 2004; Tomiya and Takahashi, 2005; Morgan et al., 2004, 2006; Costa et al., 2010; Matthews et al., 2011; Charlier et al., 2012; Druitt et al., 2012; Ruprecht and Cooper, 2012 ; Allan et al., 2013; de Maisonneuve et al., 2015; Barker et al., 2016). These models prove that these systems can be much more dynamic than previously believed.

Costa and Chakraborty (2004) modelled Fe-Mg diffusion in olivines of San Pedro Volcano (Chilean Andes) andesites and obtained relatively short timescales of years to decades (1 to 50 years) prior to eruption for a basaltic andesite-dacite magma mixing.

In the study of Morgan et al. (2006) on Ba zoning in sanidine crystals of the 79 A.D. Vesuvius eruption, three different pre-eruptive recharge events are recognized and the timescales of the last recharge causing the zoning in crystals have been estimated at ~20 yr before eruption. The authors assess that the pre-plinian phonolitic system has been episodically recharged at the year to decade scale by the arrival of new phonolitic of tephriphonolitic magma. On the same volcano, Morgan et al. (2004) have performed a diffusion study on clinopyroxenes of the 1944 effusive eruption to obtain crystal residence times at magmatic temperature. They obtain timescales of 4.5 months up to 9 years before eruption and explain the pre-eruptive process as a continuous magma input from below and mixing characterizing the last period of intense and regular eruptive activity (1931-1944) prior to the final 1944 eruption.

Ruprecht and Cooper (2012) apply diffusion modelling to the eruptive products associated with the 1846-1847 eruption of the Quizapu volcano (Chilean Andes). In this study Mg diffusion in plagioclase crystals is used to assess timescales of pre-eruptive magma mixing. Results show that the mixing event occurred within days to weeks before eruption and likely acted as trigger for the final eruption.

Another studied explosive silicic eruption is the Santorini Minoan eruption of ~1600 BC. Timescale study of this eruption has been performed by Druitt et al. (2012). On the basis of the records of changes in the composition of feldspars, Druitt et al. (2012) showed that the transfer and assembly of magmas before the eruption took place over a relatively short time: centuries to months prior to the eruption. The main reservoir has been subject to several recharge events of large volumes of silicic magma. Considering the long rest period of about 18000 years prior the Minoan eruption, it is particularly interesting to realize how the magmatic system can get out of its rest period, become more dynamic and produce eruptible magma volumes in geologically very short timescales.

A complete and detailed study has been also performed on the Taupo Volcanic Zone (TVZ, New Zealand) for the Oruanui and the Wakamaru eruptions (Wilson, 1995; Wilson, 2001;

Allan et al., 2012; Matthews et al., 2012; Allan et al., 2013; Barker et al., 2016). Also in this specific case, diffusion modelling studies determine short timescales of pre-eruptive processes. For the Oruanui eruption (~26.5 ka, ~530 km^3), diffusion modelling of Fe-Mg interdiffusion in orthopyroxenes shows that a decompression event, representing the extraction of eruptible melt from the main mush body, had occurred at least 500 years before the eruption and produced the finally erupted crystal-poor (~10%) rhyolite (Allan et al., 2013). A peak in extraction ages at ~230 years before eruption has been recorded in the zoning pattern of modelled orthopyroxenes. For the same eruption, feldspars have shown that the major process of assemblage of the large volume of differentiated magma involved in the eruption had taken place in an open system, with many episodes of magma mixing affecting continued growth of the magma chamber, in contrast to the closed system model of evolution by fractional crystallization previously proposed (Charlier et al., 2008).

For the Wakamaru eruption (~340 ka, >1000 km^3), the study conducted by Matthews et al. (2012) on quartz zonation and diffusion modelling of Ti in quartz shows that timescales of the final recharge rejuvenating the mush reservoir are in the range of 10-60 years before the associated eruption.

All these studies demonstrate that large silicic systems in different geodynamical contexts, typically characterized by long rest periods, are usually made of a long-lived magma evolving for timescales of several 1000 years in the crust as a cold (<800°C) and highly crystalline mush region, locked to its rheological eruptability threshold. Nevertheless these systems can be in reality more dynamic than previously believed, as the final rejuvenation of the mush and assembly of the eruptive magma body (regardless its composition) can take place over relatively short timescales of years (for smaller volumes, 10-100 km^3) to decades or centuries (for larger volumes, 100-1000 km^3). This has important consequences for the evaluation and assessment of volcanic hazard: the time gap in between first precursory geophysical signals (seismicity, earthquakes, deformation of volcano, degassing) and eruptions can thus be short, and the characteristic unrest-rest cycle of a volcano can be interrupted fast by the occurrence of a large explosive eruption. Mechanisms and timescales of these events are thus important processes to be evaluated, especially in volcanic provinces where human settlement is highly developed.

3. Objectifs de la thèse

Ce travail de recherche a pour objectif de contraindre les conditions pré-éruptives de stockage, la dynamique et l'évolution du système d'alimentation magmatique à l'origine de

trois grandes éruptions ignimbritiques dans la zone centrale de la Dominique (Arc des Petites Antilles). Des études récentes (Lindsay et al., 2003, 2005 ; Smith et al., 2013 ; Howe et al., 2014) ont déterminé la présence sur l'île de plusieurs éruptions ponceuses dont certaines de gros volumes (dizaine de km^3). Ces éruptions, mettant en jeu un volume important, représentent une « anomalie » par rapport aux autres îles de l'arc (e.g. Martinique, Guadeloupe, Montserrat) dont les éruptions mettent en jeu de plus faibles volumes (généralement $\leq$ 1 km^3 DRE). Cette claire différence en termes de volume de magma mis en jeu a motivé ce projet de thèse centré sur le système de stockage magmatique qui alimente ces éruptions ignimbritiques.

La démarche que j'ai suivie se base sur une étude stratigraphique détaillée des dépôts. J'ai combiné une étude de pétrologie détaillée des produits (i) naturels et (ii) de ceux reproduits expérimentalement afin de déterminer les conditions de stockage de ces magmas. J'ai ensuite développé (iii) l'application de la démarche du « Crystal System Analysis » afin de préciser la géométrie et la dynamique du système d'alimentation de trois éruptions ignimbritiques choisies et j'ai effectué (iii) une modélisation de la diffusion intracristalline Fe-Mg dans des orthopyroxènes afin de contraindre temporellement la dynamique de ces magmas.

Cette étude se concentre sur les trois éruptions de Roseau, Layou et Grand Fond reconnues dans la partie centrale de la Dominique. Les corrélations pétro-géochimiques possibles avec d'autres ignimbrites majeures reconnues sur l'île (Grand Bay au sud et Grande Savane plus au nord) sont aussi discutées.

Nous focalisons ici l'étude sur les produits de retombées pliniennes situés à la base des dépôts des trois éruptions choisies, car les magmas émis en début d'éruption sont généralement stockés dans la partie sommitale du réservoir. De plus, ces produits, trempés au niveau de la fragmentation, sont rapidement refroidis dans le panache et ne souffrent pas de modifications post-fragmentation comme ce peut être le cas pour les volumineux écoulements qui restent à température élevée après dépôt ou même pour des produits résultant d'éruptions à dôme de lave qui peuvent subir des processus de modification ou contamination liées aux mécanismes de remontée dans les conduits.

(1) **Etude pétrologique des produits naturels.** La pétrologie naturelle des échantillons a été examinée en utilisant les techniques classiques d'analyse de roche totale et verre résiduel, la détermination du contenu en cristaux (compositions modales) et l'étude détaillée des phénocristaux avec une attention plus particulière pour les orthopyroxènes et plagioclases, cristaux majoritairement

présents. Ces derniers ont été étudiés en termes de texture et de composition, avec pour objectif de décrypter l'information sur la dynamique des réservoirs. Les textures des orthopyroxènes et plagioclases ont été obtenues par imagerie BSE haute-résolution et les variations de composition en éléments majeurs et mineurs par analyse à la microsonde électronique (EPMA). En parallèle, la composition en éléments majeurs, trace et les teneurs en H_2O, CO_2, F et Cl des inclusions vitreuses dans les orthopyroxènes et les plagioclases ont été obtenues (SIMS, University of Edimburgh, Balcone-Boissard et al. in prep). Les variations de textures et de composition dans les orthopyroxènes ont été modélisées en utilisant l'approche du « crystal system analysis », comme défini et utilisé par Kahl et al., (2011, 2013, 2015). Cette méthode permet d'obtenir un traitement statistique complet des variations de composition des cristaux. A partir de l'identification de certains groupes basés sur ces différences de composition, des environnements magmatiques ont été définis et leurs connections identifiées ; l'ensemble des données est ensuite rassemblé dans un modèle dynamique du système d'alimentation magmatique.

(2) **Etude par pétrologie expérimentale.** Les conditions de stockage magmatique ont été estimées en utilisant des expériences d'équilibre de phase dans des presses à chauffage interne (IHPV ; ISTO, Orléans). Les expériences ont été menées en conditions saturées ($xH_2O=1$) et sous-saturées ($xH_2O=0.8$) en H_2O, à différentes pressions et températures. Tous les produits expérimentaux ont été analysés par imagerie d'électrons rétrodiffusés (BSE) haute-résolution, pour caractériser l'assemblage de phases, et par microsonde électronique (EPMA), pour une analyse chimique quantitative des phases cristallines et des verres. La reproduction expérimentale de l'assemblage de phases naturelles et de ses proportions, ainsi que de la composition chimique des cristaux et des verres, nous a permis de déterminer les conditions pré-éruptives d'équilibre du réservoir. Conjointement, la diffusion dépendant de la température et de la fugacité d'oxygène, il était important de déterminer ces deux valeurs par pétrologie expérimentale afin de mieux contraindre les temps de diffusion obtenus sur les orthopyroxènes (volet 3).

(3) **Contraintes temporelles sur la dynamique des magmas en conditions pré-éruptives – diffusion intracristalline.** La modélisation des cinétiques de diffusion dans les cristaux d'orthopyroxènes nous a permis d'attribuer des échelles de temps aux dynamiques magmatiques pré-éruptives reconnues par le Crystal System

Analysis. Nous avons étudié l'interdiffusion Fe^{2+}-Mg le long de l'axe b d'orthopyroxènes zonés des éruptions de Layou, Roseau et Grand Fond en utilisant le coefficient de diffusion de Ganguly and Tazzoli (1994) et la méthode de Allan et al. (2013). La méthode est basée sur l'intercalibration d'analyses EPMA sur les valeurs d'échelle de gris d'images BSE haute-résolution, utilisées comme un proxy du Mg# (rapport Mg/Mg+Fe) de l'orthopyroxène. Cette technique nous a permis d'obtenir des histogrammes de distribution d'échelles de temps pour les éruptions de Layou et Roseau et des contraintes maximales sur les temps de résidence des cristaux de l'éruption de Grand Fond.

En combinant ces trois volets d'étude nous avons construit un modèle de réservoir pour les éruptions de la Dominique en termes de conditions de stockage, dynamique et échelles de temps des processus pré-éruptifs.

4. Plan du manuscrit

Le manuscrit s'organise en une introduction, deux parties principales et une synthèse

L'introduction situe le cadre de l'étude et permet de donner l'état de l'art sur les éruptions ignimbritiques et les zones de stockage de magmas correspondantes.

La première partie présente le contexte de l'étude, la démarche et les méthodes utilisées :

1- Dans le premier chapitre (« Geological Context ») on s'attachera à faire un bilan sur le contexte géologique de l'arc des Petites Antilles et plus particulièrement sur la géologie de l'île de la Dominique et son histoire éruptive récente.

2- Dans le deuxième chapitre (« Scientific approach, samples and analytical methods ») nous expliquons la sélection des échantillons, la démarche scientifique suivie pour ce travail et les différentes méthodes analytiques et expérimentales utilisées. Une large partie de ce chapitre est dédiée à l'explication des mécanismes de diffusion. Les bases théoriques-mathématiques et le principe de la méthode utilisée y sont traitées en détail.

La deuxième partie débute par la chronostratigraphie détaillées des éruptions ponceuses étudiées, puis se focalise sur les résultats obtenus en pétrologie sur les produits naturels, ainsi que ceux obtenus expérimentalement. Les résultats obtenus sur la dynamique du système d'alimentation, en particulier ceux de diffusion sont également présentés. Elle regroupe deux chapitres :

3- Dans le troisième chapitre (« Detailed stratigraphy of Dominica pumiceous eruptions ») nous présentons la stratigraphie détaillée des trois éruptions plus particulièrement étudiées au cours de ce travail de thèse : Layou, Roseau et Grand Fond. Cette stratigraphie est rédigée sous forme d'article qui sera soumis en début d'année 2017 au Bulletin of Volcanology.

4- Dans le quatrième chapitre (« Experimental determination of magma storage conditions ») nous présentons les résultats sur les conditions de stockage des magmas dacitiques de la Dominique obtenus d'une part par l'étude des produits naturels (composition du verre et des cristaux, geothermobaromètres naturels) et d'autre part via la réalisation d'expérience d'équilibres de phases sous presse (IHPV, ISTO). La discussion des résultats obtenus sur les trois éruptions cibles de cette étude est élargie aux autres éruptions ignimbritiques reconnues sur l'île. Ce chapitre est rédigé sous forme d'article qui doit être soumis en début d'année 2017 à Contribution to Mineralogy and Petrology.

5- Le cinquième chapitre (« The secret life of crystals: a record of pre-eruptive magma storage») est subdivisé en deux parties. La première partie présente une étude des textures et variations de composition reconnues dans les orthopyroxènes des échantillons choisis. L'application de la récente méthode de "crystal system analysis" nous a permis d'identifier les principales dynamiques pré-éruptives dans la plomberie magmatique et d'en suivre l'évolution sur la période considérée. Un modèle conceptuel de réservoirs magmatiques est présenté à la fin de cette première partie.

La deuxième partie se focalise sur la modélisation de l'interdiffusion Fe^{2+}-Mg sur des profils de composition reconnus dans les orthopyroxènes. La technique analytique et la méthode de modélisation (choix du coefficient de diffusion parmi les valeurs reportées dans la littérature, considération de l'effet de la fugacité d'oxygène et méthode d'intercalibration des profils) sont présentées en détail. Les résultats obtenus par cette méthode sont discutés dans le cadre d'un modèle de réactivation d'un réservoir de type mush.

Ces deux parties sont rédigées sous forme d'article et seront soumis conjointement en début d'année 2017.

La synthèse permet de rappeler les différentes avancées apportées par l'ensemble de ce travail de recherche et de présenter également les questions et ouvertures qui peuvent faire l'objet de travaux futurs.

CHAPTER I

GEOLOGICAL CONTEXT

Introduction

Dans ce premier chapitre nous présentons le contexte géologique de la zone d'étude, l'île de la Dominique dans les Petites Antilles. Le chapitre est subdivisé en deux parties.

Dans une première partie, nous présentons le contexte géologique et structural de l'arc des Petites Antilles, son histoire géologique, la composition générale et les conditions de stockage des magmas émis le long de l'arc.

Dans une deuxième partie, nous nous focalisons sur l'île de la Dominique. Nous en présentons le contexte structural et l'histoire éruptive et nous donnons un bref résumé des études antérieures. Les différents centres éruptifs actifs de l'île sont décrits, en termes de pétrologie des produits éruptifs et de possible future activité éruptive.

Les éruptions ignimbritiques majeures reconnues sur l'île (Roseau, Layou, Grand Fond, Grande Savane et Grand Bay) sont présentées plus en détail dans le chapitre III (« Detailed stratigraphy of Dominica pumiceous eruptions »).

I .1. Geological context of the Lesser Antilles arc

I.1.1. General tectonic and structural context

The Lesser Antilles arc (14°14’ 00’’ N, 16°21’00’’W, Fig.I.1) is an 850 km-long volcanic arc, extending north to south from the island of Saba to the island of Grenada, with a particular east-directed convexity. The arc is the result of the westward, oblique, slow subduction of the Atlantic lithosphere beneath the Caribbean Plate (average rate for the last 2 My estimated at 2 cm/yr; Wadge, 1984). This sudbuction has been active since Early-Eocene (Martin-Kaye, 1969; Nagle et al., 1976), but the rate of convergence of the two plates over the geological history of the arc has not remained constant: Macdonald and Holcombe (1978) have estimated a rate of 2 cm/yr for the period from 2.4 Ma to present, and a rate of 4 cm/yr for the period 8.3-2.4 Ma. These data demonstrate that the arc has been characterized by a low subduction rate, placing it at the lower limit of the arc spectrum (as a comparison, fast subducting arcs, such as Java, may reach convergence values of up to 8 cm/yr; Jarrard, 1986).

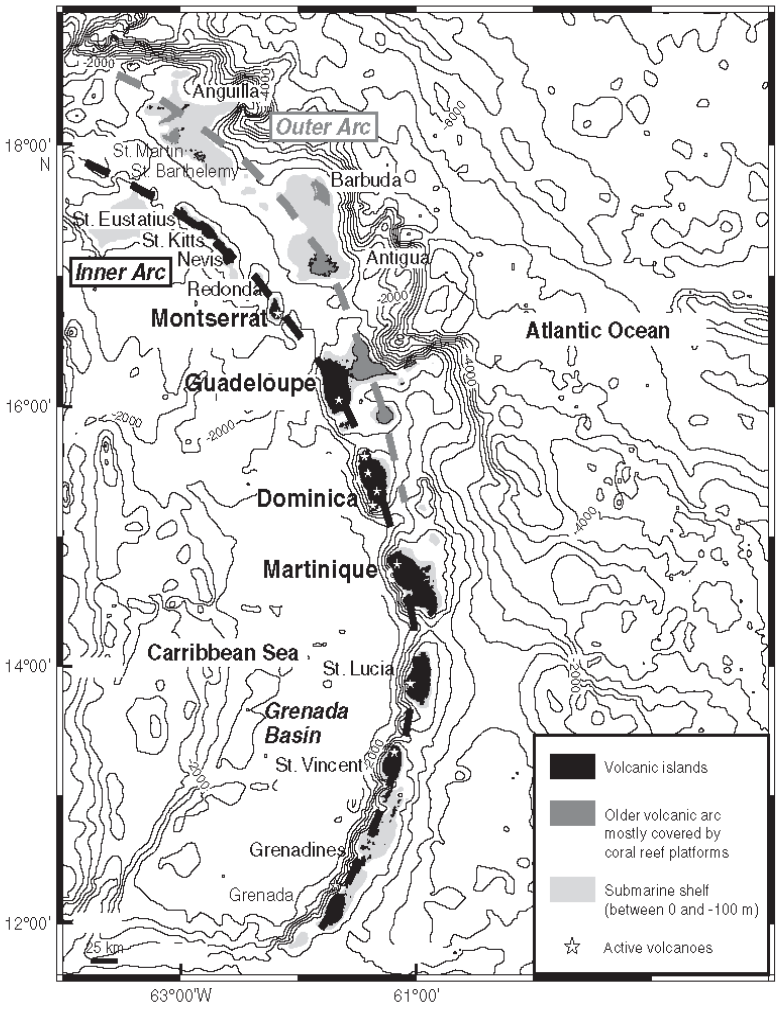

Figure I.1: The Lesser Antilles arc. *Predicted bathymetry from Smith and Sandwell (1997). Contour interval is 500 m and 2000 m; isolines are in bold.*
Black: volcanic islands; Dark grey: subaerial coral reef platforms. The 100 m depth submarine shelf is light grey. Active volcanoes are represented with white stars. (modified from Boudon et al., 2007)

Because of this low sudbuction rate the arc has been also characterized by low magma production rates over its history, ranging between 2-4*10^3 $km^3\,Ma^{-1}$ (Wadge, 1984; Macdonald et al., 2000).

On its west side the arc is bordered by the 140 km wide, 3 to 12 km deep and 600 km long Grenada back-arc Basin. The basin limits are the Lesser Antilles arc on the east side and the Aves Swell on the west side, a remnant arc (considered as a proto-Antilles arc) active since the beginning of late-Cretaceous (Bouysse, 1988). In its southern part—as far north as Dominica—the Grenada Basin has a mostly flat bathymetry with an average depth of 2900 m. In its northern part, on the other hand, the bathymetry becomes significantly rugged. Depths increase southward with values at 3-4 km west of Guadeloupe and reaching values of 12 km next to Grenadine (Bouysse, 1988). In recent decades, several studies on piston cores sampled in the basin (i.e. oceanographic mission GS7605, EN-20, CARAVAL, AGUADOMAR, JCR, Gwadaseis, IODP-340) have demonstrated that the basin acts as the collection area not only of hemipelagic sediments but also of volcanic tephra, turbiditic deposits, and debris avalanche deposits linked with the volcanic activity of the arc. Indeed, most of the associated volcanoes have undergone large flank-collapse events whereby debris avalanches flowed into the sea to different lateral extents (Boudon et al., 2007; Deplus et al., 2001; Le Friant et al., 2002, 2003a, 2015). On the basis of the geophysical and tephrochronological data obtained during these different expeditions, a better knowledge of the submarine extension of volcanic products has been obtained. For example, the results of the IODP 340 expedition (March-April 2012) highlight that chaotic deposits—previously understood to be debris avalanche deposits in the Grenada basin—are in fact sediments deformed by the weight of overlying debris avalanche deposits that came to rest at the base of the submarine flank of the volcano (Le Friant et al., 2013, 2015; Brunet et al., 2016). Many tephrochonological studies also afford improved knowledge of the history of some of the volcanoes (Boudon et al., 2013; Trofimovs et al., 2013; Cassidy et al., 2015; Solaro et al., in prep).

I.1.2. Arc structural segmentation

We can divide the Lesser Antilles arc in two parts. North of Dominica, the arc can be divided in two different sectors: the Outer arc, called also Older arc (Eocene to mid-Oligocene: Saint Martin, Antigua, Grande Terre de Guadeloupe, Marie Galante) and an Inner Arc, called also Recent arc (Miocene to Recent: Saba, St. Eustatius, St. Kitts, Nevis, Monserrat, Basse-Terre de Guadeloupe). The Older arc is linked with a first period of mainly sub-marine eruptive activity dating to the Eocene-Oligocene period (55-23 Ma, Westercamp, 1988; Bouysse et al.,

1990). This main volcanic basement is covered by limestone platforms, from Mid-Eocene to Pleistocene, and Pliocene coral reefs. From Eocene to Oligocene (~33 Ma), the eruptive activity of the arc changed from sub-marine to aerial; from Oligocene to Early-Miocene (~20Ma, Aquitanian), the arc records a quiescent period of 6-7 Ma (28-26 Ma to 20-18 Ma, Westercamp, 1988). This period of inactivity was due to the sudbuction of an aseismic ridge in the centre of the arc, which caused a rupture in the sudbuction plate and a displacement of volcanic activity to the west; in turn this created the second, internal segment of the Lesser Antilles arc (i.e. the Inner arc), active since the early-Miocene (~20 Ma, Bouysse and Westercamp, 1990). South of Dominica the two segments—Outer and Inner—merge into one, creating a single volcanic ridge which has been active since the Miocene epoch.

The recent activity of the arc (Pleistocene to Recent: <2.0 Ma) shows an important segmentation (Macdonald et al., 2000). Eruptions occur on three narrow segments of the arc, each less than 10 km wide (Fig.I.2): Saba-Montserrat, Guadeloupe-Martinique, and St Lucia-Grenada (Sigurdsson and Carey, 1981; Wadge and Shepherd, 1984). The segmentation of the arc is also recorded in seismicity and in the location of the Benioff plane, which changes its direction and dip from one segment to the other. For the Saba-Montserrat and Guadeloupe-Martinique segments the arc trends at 330° and the Benioff plane dips at 50-60°, while for St Lucia-Grenade segment the arc trends at 20° and the Benioff plane dips at 45-50° in the north and vertically in the south (Wadge and Shepherd, 1984), (Fig.I.2).

The segmentation of the arc is also reflected in the magma production rate. Over the last 0.1 ma of eruptive activity, the central segment of the arc has been characterized by the largest magma production rate, with Dominica reaching a peak ~40 km^3, and Martinique and Guadeloupe a volume of ~8 km^3. Contrastingly, the north and south segments of the arc have produced significantly smaller volumes of about 0-5 km^3 (Wadge, 1984; Macdonald et al., 2000). Moreover, the central segment of the arc encompasses the three largest islands of the archipelago: Martinique (with an areal extent of 1100 km^2), Dominica (790 km^2), and Basse-Terre of Guadeloupe (950 km^2). The currently active part of the arc (Inner arc: Saba to Grenada) hosts twelve active volcanoes: Mount Scenery (Saba), Mount Misery (St. Kitts), Soufrière Hills (Montserrat), Soufrière de Guadeloupe, Morne aux Diables, Morne Diablotins, Morne Trois Piton-Micotrin, Morne Plat Pays (Dominica), Montagne Pelée (Martinique), Soufrière of St. Lucia, Soufrière of St.Vincent, Kick'em Jenny (a submarine volcano on the northeastern submarine flank of Grenada). In the last 300 years, they have produced several historic explosive eruptions: i) magmatic eruptions at Montagne Pelée (1902-1905 and 1929-1932), Soufrière Hills (1995 to present), Soufrière of St. Vincent (1902, 1971, 1979-1980),

Kick'em Jenny (1939, 1943, 1953, 1965, 1966, 1972, 1974, 1990, 2001; ii) phreatic eruptions at Soufrière de Guadeloupe (1635, 1797-1798, 1822, 1965, 1976-1977), Soufrière of St. Lucia (1766), Desolation Valley in Dominica (1880, 1997).

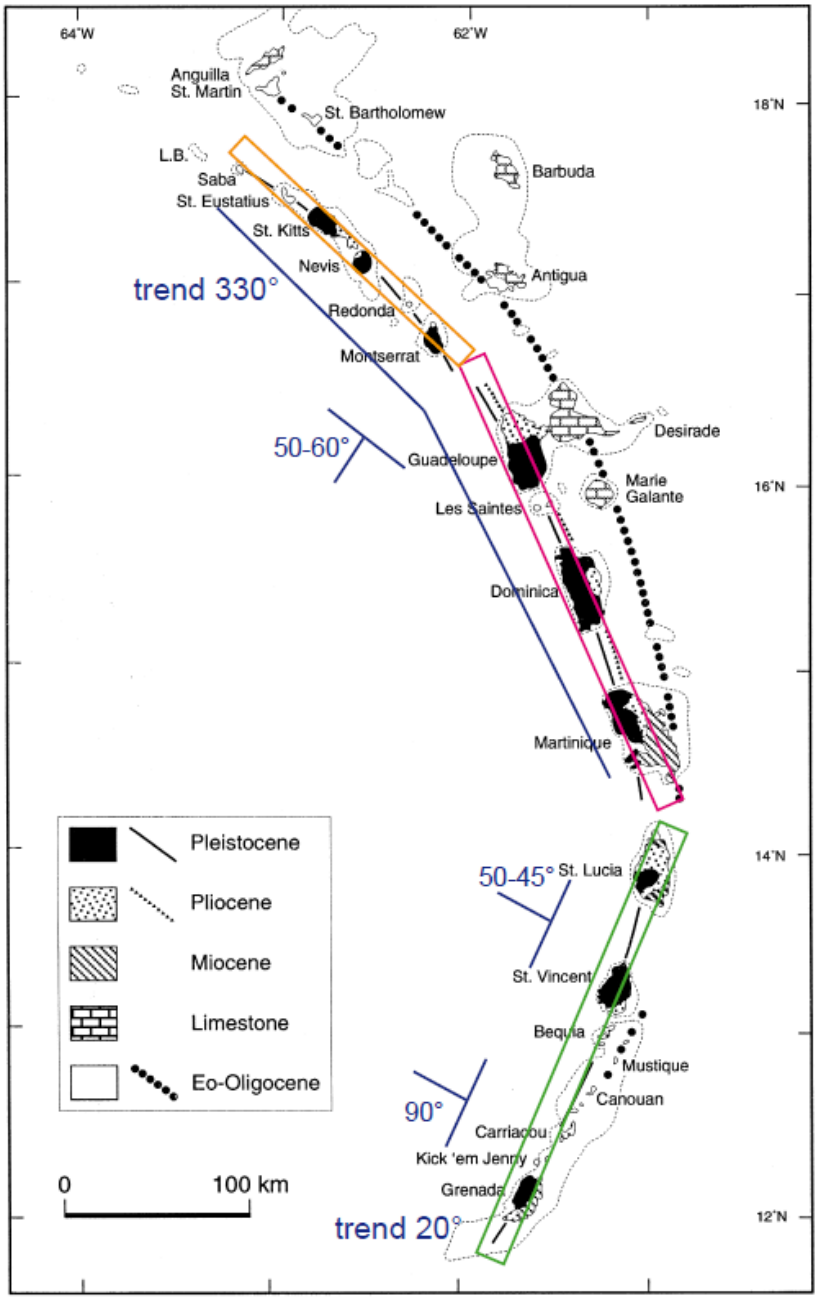

Figure I.2: Segmentation along the Lesser Antilles arc. *Three main segments can be recognized: Saba to Montserrat (orange square), Guadeloupe to Martinique (pink square) and St. Lucia to Grenada (green square). The segmentation of the arc is marked also by the trend and the dip of the Benioff plan (in blue in the figure). (modified from Macdonald et al., 2000).*

I.1.3. Composition of the magmas emitted along the Lesser Antilles arc

The structural segmentation of the arc is also reflected in the geology and distribution of the emitted magmas along the arc (Rea, 1982). Islands can be divided in three main groups:

(1) The north group Saba-Montserrat (Saba, Saint Eustache, Saint Kitts, Nevis, Montserrat) is mainly characterized by magmas of andesitic and basaltic composition. Rhyolites and dacites are rare but present in low proportion on Saint Kitts and Saint Eustache. Basalts are generally present as blocks included in the main andesitic pyroclasts, typically comprising a small volume fraction (about 3 to 10%: Macdonald et al., 2000).

(2) The central group Guadeloupe-St. Lucia (Guadeloupe, Dominique, Martinique and St.Lucia) has predominantly emitted magmas of andesitic to dacitic composition. Basalts and rhyolites are present but rare.

(3) The south group (Saint-Vincent to Grenada) is mainly marked by the presence of magmas of basaltic and basaltic andesite composition. The southern island of Grenada exhibits the less evolved type of basalts, with rare andesites and dacites (Devine, 1995).

I.1.4. Magma storage conditions along the Lesser Antilles arc

The main crustal magma storage region seems to be comparable for all the main islands of the arc. Several experimental petrology studies have been conducted to unravel the magma storage conditions (pressure, temperature, oxygen and water fugacity; Barclay et al., 1998; Martel et al., 1999; Pichavant et al., 2002; Poussineau, 2005; Pichavant and Macdonald, 2007).

Here we summarize different experimental results on magma storage conditions (mainly from phase equilibria crystallization experiments), obtained for different volcanoes of the Lesser Antilles arc, from the north to south islands (Table I.1).

Storage conditions of Soufrière Hills (Montserrat) magma have been investigated by Barclay et al., (1998). These authors argue that the phase assemblage of natural andesites of the January 1996 lava dome (amphibole, quartz, plagioclase, orthopyroxene, titanomagnetite and ilmenite) can be experimentally reproduced at a temperature of 840-875 °C, a pressure of 115-130 MPa (5-6 km depth for a water saturated magma, $xH_2O=1$) and an oxygen fugacity of ~NNO+1 (±0.5) (NNO= Nickel-Nickel oxide buffer).

For the Soufrière de Guadeloupe 1530 AD eruption (Boudon et al., 2008; Komorowski et al., 2008), Poussineau, (2005) defined, using phase equilibria experiments, pre-eruptive storage

conditions of 875-900°C, 150-175 MPa (6-7 km depth), an oxygen fugacity of ~NNO+0.8 and water content ranging in between 4.6 and 5.4 wt% H_2O.

For the Montagne Pelée (Martinique) recent eruptive products, Martel et al. (1998) obtained the same magma storage conditions for both recent Plinian and dome-forming eruptions, tapping magma at 875-900°C, 200 ± 50 MPa (~6 km in depth), an oxygen fugacity in the range ΔNNO= +0.4/-0.8 and 5.3-6.3 wt% H_2O in the final melt. Pichavant et al. (2002) refined the experimental determination of magma storage conditions by performing phase equilibria also on the basaltic andesite representative of the most mafic part of the plumbing system. Through this method, Pichavant et al. (2002) produce a model for a zoned elongated magma chamber in which the mafic underlying part can be reproduced at 950-1025°C, 4 kbar, NNO to NNO+4 and 8.3 to 2.6 wt% H_2O.

The Soufrière of St. Vincent magma storage conditions for the primitive basalt liquid (HMB= high-magnesia basalts) have been investigated by Pichavant and Macdonald (2007), who infer crystallization of these magmas at mid-crustal pressures (~10 kbar), temperature of ~1060-1160 °C, oxidized conditions of ΔNNO= +1.5-2.0 and water contents of ~5 Wt% H_2O. These conditions represent the early stage of differentiation of calc-alkaline magmas.

	Montserrat Soufrière Hills*	Guadeloupe Soufrière de Guadeloupe#	Martinique Montagne Pelée"	St. Vincent Soufrière de St. Vincent^
Sample-eruption	1996	1530 AD	P1, 1902,1929	HMB
Temperature (°C)	840-875	875-900	875-900	1060-1160
Pressure (MPa) / depth(km)	115-130 / 5-6	150-175 / 6-7	200 ± 50 / 6	1000
Oxygen fugacity (ΔNNO)	+1	+0.8	+0.4/ -0.8	+1.5/ +2.0
Water content (wt%)	~4.27 ± 0.54	4.6-5.4	5.3-6.3	~5

Table I.1: Magma storage conditions from phase equilibria experiments. **Barclay et al., (1998); #Poussineau, (2005); " Martel et al., (1998); ^ Pichavant and Macdonald (2007).*

Together, these studies demonstrate that andesitic to dacitic magmas of the north to central segment of the Lesser Antilles Arc (Montserrat, Guadeloupe, Martinique) share comparable storage conditions with temperatures in the range 840-900°C , mid-crustal storage depths of ~6-7 km and oxidized conditions (~NNO+1).

For Dominica Island, previous experimental determinations of magma storage conditions have not been performed. Some authors (Lindsay et al., 2005a; Gurenko et al., 2005; Halama

et al., 2006; Howe et al., 2015) have estimated storage pressure, temperature and oxygen fugacity conditions by the study of natural products and natural mineral-melt or mineral-mineral geothermobarometers (Table I.2). Thermobarometry results of Gurenko et al. (2005) on the products of the Cabrits lava dome (Plat Pays Volcanic Complex= PPVC) indicate an equilibration of the phenocrysts assemblage at 760-880°C, a pressure of ~200 MPa (5-6 km depth) and oxygen fugacity of 1-2 log units above FMQ (Fayalite-Magnetite-Quartz buffer). Results of Lindsay et al. (2005a) on magnetite-ilmenite, hornblende-plagioclase and two-pyroxene thermobarometers suggest a temperature of 800-890°C and a pressure of 200-300 MPa (similar to Gurenko et al., 2005) for andesite-dacite samples of Morne Anglais (PPVC). For dacitic magmas from the same complex, Halama et al. (2006) estimate equilibration conditions of 800-880°C, 110-230 MPa, oxygen fugacity of ~FMQ +1.5 and melt water content of ~5-6 wt%. Finally, Howe et al. (2015) suggest that Dominica andesites are the result of the interaction of a basaltic-andesitic long-lived mush zone at temperature of 750-890°C and an underplating hotter mafic intrusion (920-1030°C).

	Dominica Cabrits Dome*	Dominica Morne Anglais#	Dominica PPVC"	Dominica Central-South eruptive centres^
Temperature (°C)	760-880	800-890	800-880	750-890
Pressure (MPa) / depth(km)	200 / 5-6	200-300	110-230	80-150
Oxygen fugacity (ΔNNO)	0.5 /+1.5		+1	-0.25/ +0.67
Water content (wt%)			5-6	

Table I.2: Magma storage conditions of Dominica from natural geothermobarometry*. *Gurenko et al. (2005); #Lindsay et al, (2005a); " Halama et al. (2006); ^ Howe et al. (2015). Location of the different eruptive centres is reported in Fig. I.3.*

Results obtained using a natural petrology approach give a first order estimation of pre-eruptive storage conditions, albeit with large uncertainties on temperature and pressure values (Table I.2).

I.2. Dominica island

I.2.1. Structural context

Dominica Island (15° 25N, 61° 20W, Fig I.3) is located in the central part of the arc and has an area of 750 km². It has a highly rugged topography including two of the highest mountains of the arc: Morne Diablotins (1421 m) and Morne Trois Pitons (1394 m). Moreover,

Dominica has 9 major peaks over 1,000 m, each with its own radial drainage systems, comprising one of the largest river densities on Earth (Lindsay et al., 2005b).

A strong geothermal system is active under the island, as evidenced by the world's second largest hot spring—the Boiling Lake—a strongly hydrothermal active area located in the southern part of the island in the region named Valley of Desolation (Fig. I.5). This area is characterized by significant phreatic activity and has been source of two historical phreatic eruptions (in 1880 and 1997).

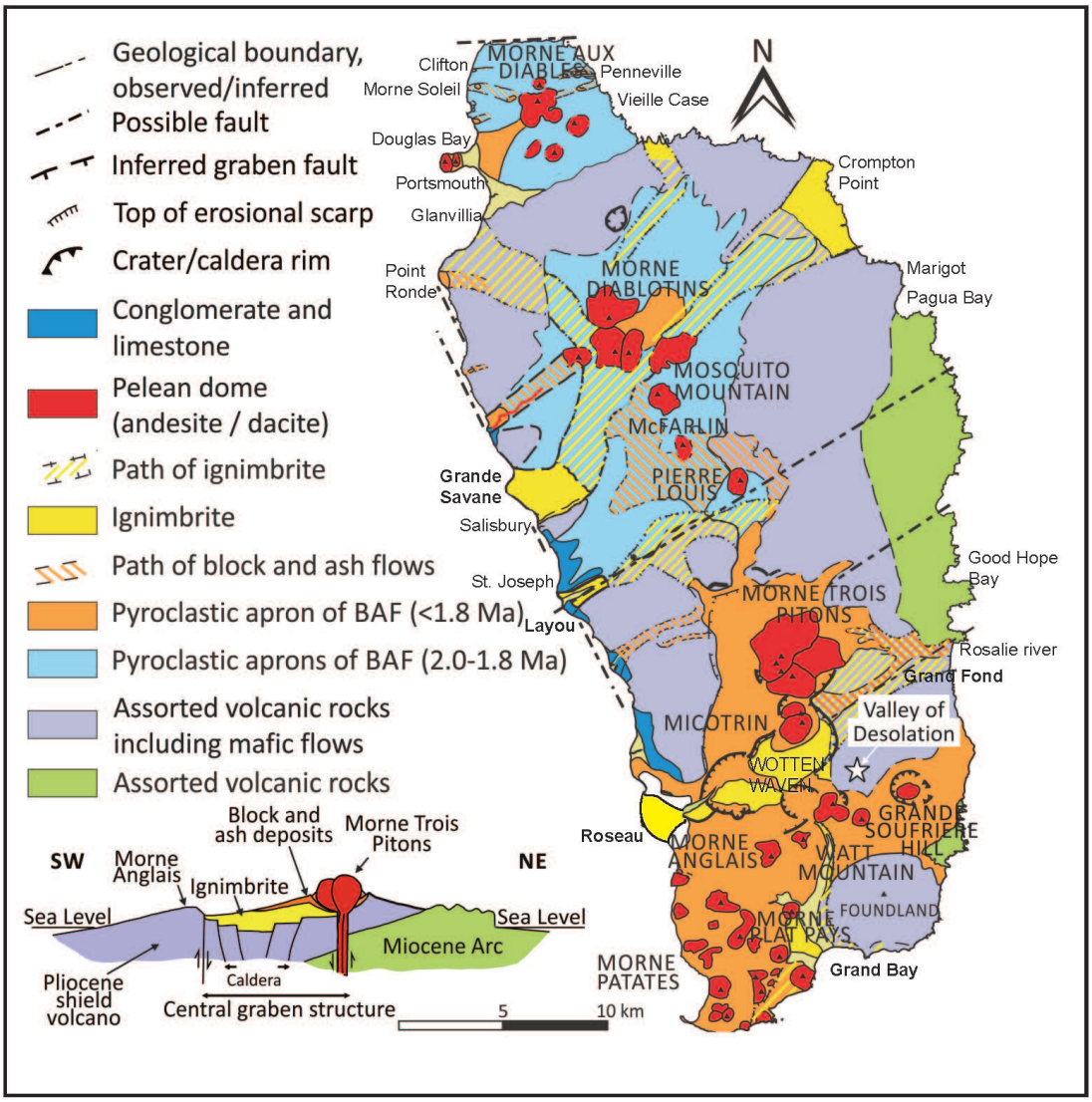

Fig.I.3: *Simplified geological map of Dominica (modified from Roobol and Smith, 2005; from Mayer et al. in review)*

The particularity of this island with respect to the rest of the arc is its active volcanic centre density and the volume of volcanic products emitted in the last period of activity (Pleistocene to Recent). Indeed, whereas all the other islands of the Lesser Antilles arc have only one active volcano, Dominica has four different potentially active volcanic centres, from north to

south: Morne aux Diables, Morne Diablotins, Morne Trois-Pitons / Micotrin and Plat Pays (Fig.I.3). These centres have all given manifestation of volcanic activity in the recent period. Small volcanic centres located in the southern part of Morne Trois Pitons - Micotrin volcanic centre have also been active in the recent period (Morne Anglais, Watt Montain, Grand Soufrière Hills).

Moreover, studies of eruptive products emitted over the last 100 kyr (Wadge, 1984) have demonstrated that Dominica bears evidence of eruptions at least one order of magnitude larger in volume than those characterizing the neighbouring islands of the arc (~40 km^3 compared to 5-8 km^3 of the neighbouring islands of Martinique and Guadeloupe: Wadge, 1984; Di Napoli et al., 2013).

Different hypotheses can be put forward to explain the particularity of Dominica's magma production rate and eruptive activity. The main idea relies on structural and tectonic considerations about the position of the island in respect to the subduction zone, and the presence and distribution of fault systems around the island. Indeed, Feuillet et al. (2010) recognised a complex system of faults cutting the Caribbean plate for several hundred km. Two specific systems of active faults are identified: 1) NE-SW oriented normal-oblique faults which create trench parallel extension and arc-perpendicular half-grabens that disrupt the fore-arc reef platforms of Guadeloupe, Antigua-Barbuda and St. Martins-St. Barthelemy (Feuillet et al., 2002; 2004); 2) a fault set arranged in a transtensional, right-stepping, *en echelon* array that follows the inner edge of the arc and accommodates a transtensional motion along the arc between Saba and Martinique. One of these transtensional faults is recognized in Dominica (Roseau fault, Bazin et al., 2010; Feuillet et al., 2011a,b). A significant change in the orientation-geometry of the subducting Atlantic plate is also observed at Dominica. The Benioff plane changes its direction and dip (330° and 50-60° north of Dominica and 20° and 45-50° south of Dominica). The fault geometry observed by Feuillet et al. (2010), associated with the change in subduction geometry (Wadge and Shepherd, 1984; Macdonald et al., 2000) could be responsible for the presence of a strong extensional component beneath Dominica, enabling and favouring the storage of large magma volumes at shallow crustal depths (Jellinek and DePaolo, 2003).

I.2.2. Geological history

Dominica's eruptive activity dates back to the Miocene, and can be divided in four main time units: Miocene, Pliocene, Older Pleistocene and Younger Pleistocene-Recent (Lindsay et al., 2005b).

During the Miocene period (7-5.3 Ma, from radiometric ages of Monjaret, 1985 and Bellon, 1988) the activity was characterised by basaltic lava flow concentrated in the eastern part of the island, on the Atlantic coast (Pagua Bay, Good Hope Bay, Fig. I.3).

The Pliocene period (3.7-2.0 Ma) is separated from the preceding one by a main unconformity (with a gap in radiometric ages from 5.3 to 3.7 Ma). Throughout the Pliocene period, activity was predominantly focalized in the northern part of the island in large basaltic to andesitic stratovolcanoes (Cochrane-Mahaut, Concord, Older Morne Diablotins, Foundland), whose structures are currently poor preserved because of weathering processes.

A saprolite-laterite layer overlies deposits from the Pliocene period and separates them from those of the following Older Pleistocene (2.0-1.8 Ma). The activity during Older Pleistocene period remained confined in the north of the island, with lava dome-forming eruptions and associated block-and-ash PDC deposits issuing from the volcanic centres of Morne aux Diables and Morne Diablotins. These two centres have been active from the Pleistocene up to the Holocene, showing signs of occasional shallow seismicity.

From Pleistocene to recent time, volcanic activity was displaced from north to the central-south part of the island. Six major andesitic/dacitic volcanic complexes were formed during the Younger Pleistocene to Recent period (<1.8 Ma): Morne Trois Pitons, Wotten-Waven Micotrin, Morne Watt, Grand Soufrière Hills, Morne Anglais and the Plat Pays Volcanic Complex. The central geothermal area of the island—the Valley of Desolation—has been active since this period and has been involved in the phreatic eruptions of the island in 1880 and 1997 (Lindsay et al., 2005b). Finally, the most recent activity has been concentrated in the south of the island at the Plat Pays Volcanic Complex (PPVC). This complex has produced a series of lava domes and associated block-and-ash PDC deposits, the last ones being Morne Crabier and Morne Patates (~450 yr BP for Morne Patates, Roobol et al., 1983; Lindsay et al., 2003), the last magmatic activity of the island. This volcanic complex was partly destroyed by a series of flank-collapse events of which the associated debris avalanches have flowed into the Caribbean Sea (Le Friant et al., 2002, Boudon et al., 2007). Several volcanological and magmatological works were undertaken to study this volcanic complex (Wadge, 1985; Le Friant et al., 2002; Lindsay et al., 2003; Gurenko et al., 2005; Lindsay et al., 2005b; Halama et al., 2006; Boudon et al. 2007).

I.2.3. Previous studies

Compared to the other islands of the arc, especially Martinique and Guadeloupe, Dominica has rarely been the object of comprehensive geological-petrological-geochemical study. This is largely because of poor outcrop preservation as a function of dense rainforest coverage. Until recent decades, the crustal storage system and the evolution of the magmatic plumbing system responsible for the major eruptions of the island were still poorly understood. The earliest descriptions of Dominica and its volcanic activity date back to 1880 (Bert, 1880; Daubrée, 1880a, b; Eldridge 1880; Endlich 1880; Nicholls 1880a, b; Watt, 1880) and were mainly focused on the description of the geothermal features and phreatic activity which characterized the Valley of Desolation phreatic eruption of January 1880.

Between 1970 and 1980, the first comprehensive volcanological studies of a late-Quaternary pumiceous pyroclastic density currents (PDC) were performed (Sigurdsson,1972; Carey and Sigurdsson, 1980; Sparks et al., 1980a, b; Wadge, 1985). Sigurdsson (1972) and Carey and Sigurdsson (1980) described the Roseau Tuff, a large pumiceous PDC deposit, recognized by on-land stratigraphy (Sigurdsson, 1972) and off-shore piston cores recovered in the western equatorial Atlantic and in the eastern Caribbean (Carey and Sigurdsson, 1980). Two more late-Quaternary PDCs were recognized on the island in the same period: the Grand Savane Ignimbrite (Sparks et al., 1980a, b) and the Grand Bay Ignimbrite (Wadge, 1985).

In the last decades of the 20th century, studies have also focused on the southern volcanic centres and other features of the island, in particular the Wotten Waven caldera and the Soufrière Depression (Wills, 1974; Roobol et al., 1983; Wadge, 1985; Demange et al. 1985). A more recent study on the Soufrière Depression has been conducted by Lindsay et al. (2003), which give a detailed stratigraphic study of the geology of the PPVC and the Grand Bay ignimbrite, as well as providing new radiogenic ages.

Deplus et al. (2001) and Le Friant et al. (2002) described several debris avalanche deposits recognized off-shore at the base of the Soufrière Depression, relating these to three major edifice flank-collapse events of Dominica's southern volcanic field. From the results of the Aguadomar marine survey carried in the Lesser Antilles Arc, Le Friant et al. (2002) argue that Dominica is likely at the origin of the most voluminous debris avalanche deposits known in the Caribbean arc. The more recent study of Brunet et al., (2016) mentioned above, proved that subsea deposits near Montagne Pelée (Martinique)—previously misinterpreted as debris avalanche flows—were in fact remobilized seafloor sediments deformed by overlying volcanic deposits. A similar interpretation may be possible for the large debris avalanche deposits so far recognized off the coast of Dominica.

I.2.4. Petrology

With the exception of conglomerates and raised limestones (in blue in Fig. I.3) present on the west coast between Roseau and Salisbury, Dominica is entirely made up of volcanic rocks and their weathering products, with a general andesitic-dacitic whole-rock composition. The only exception to these silicic compositions is Morne Anglais, which predominantly erupted basalts to basaltic andesites (Lindsay et al., 2005b).

These andesitic-dacitic rocks outcrop in the form of large volumes of ignimbrite deposits (Roseau, Grande Savane, Grand Bay, in yellow in Fig.I.3), lava dome complexes (in red in Fig.I.3) or dome collapse-related pyroclastic apron and block-and-ash PDC deposits (in orange in Fig.I.3).

From a geochemical-petrological point of view, very few studies have focused on Dominica rocks, the only well studied volcanic centre of the island being the PPVC, representing the largest concentration of lava domes and associated deposits. The rising interest in the PPVC derives from the occurrence in the period 1998-2000 of a major volcanic earthquake swarm spatially associated with the southern eruptive centres. Geochemical and petrological studies (Lindsay et al., 2003; Gurenko et al., 2005; Lindsay et al., 2005b; Halama et al., 2006; Smith et al., 2013; Howe et al., 2015) have attempted to characterize the magma reservoir in terms of storage, dynamics and pre-eruptive processes. Some of these studies show that a large part of the whole-rock andesitic composition of Dominica samples can be reproduced by fractional crystallization (>50%) from a basaltic andesite melt with no evidence of mafic recharge (Lindsay et al., 2005b). Indeed this high level of crystallization would imply that a large part of the magma injected under Dominica is uneruptible and remains stored in the crust for long periods (~200 ky) in a locked-mushy state (Marsh et al., 2000).

Moreover, despite being crystal-rich and exhibiting a relatively narrow range of bulk-rock compositions, Dominica andesite and dacite display a large array of crystal compositions and destabilization-disequilibrium features. This suggests that processes other than simple fractional crystallization may have occurred during the storage period, such as magma mingling or mixing, convective self-mixing or contamination.

Several models have been proposed to explain the dichotomy between the homogeneous whole-rock composition and the heterogeneous textures and compositions recognized in the mineral assemblage (Halama et al., 2006; Smith et al., 2013; Howe et al., 2015). Halama et al., (2006) proposed the existence of a long-lived highly-crystalline magma reservoir, periodically invaded by the intrusion of a more mafic and hotter (~1060°C) magma. Reiterating the mixing idea of Halama et al. (2006), Howe et al., (2015) suggest that

Dominica andesite may be explained by the interaction of three main magmatic components: i) a basaltic-andesitic highly-crystalline mush (representing the main magma body, having undergone protracted fractional crystallization and being locked above the rheological threshold of eruptability); ii) a rhyolitic interstitial melt, which, with fractional crystallization may have created some highly evolved and highly crystallized zones (likely to represent side-wall or roof-wall crystal concentrations); and, iii), an underplating basaltic melt, heating the main andesitic mush from below and producing the destabilization-disequilibrium features recognized in the crystal cargo.

The broad range of crystal textures and composition may indicate a mixture of crystal populations with differing thermal histories (Smith et al., 2013). Nevertheless, the similarity in bulk-rock composition and crystal content in samples from different eruptive centres suggests that their storage regions are possibly connected, signifying an island-wide batholith (Smith et al., 2013).

I.2.5. Active eruptive centres

In the following section we will present and describe the main active volcanic centres of the island (from south to north), discussing for each of them the most likely eruptive scenario and the hazard linked with eruption.

I.2.5.1 Plat Pays volcanism

The Plat Pays Volcanic Complex (Fig.I.4) is located on the southern part of the island. It is made of the Morne Plat Pays, the Soufrière Depression and series of 16 secondary lava domes (Morne Canot, Morne Vert, Morne Crabier, Morne Bois d'Inde, Morne Patates) located inside or outside the depression structure. The Soufrière Depression (Fig.I.4) truncates the south-western part of the Morne Plat Pays with a large horseshoe-shaped structure likely to be associated with a flank collapse event. It covers an area of 4.2 x 2.5 km with a vertical headwall of 900 m (Le Friant et al, 2002). The age of this flank-collapse event has been estimated between 6600 ± 50 and 2380 ± 75 yr BP (Le Friant et al, 2002).

The past eruptive activity of the Morne Plat Pays is primarily characterized by effusive lava dome-forming eruptions which are poorly constrained in terms of radiogenic dates. Only a PDC deposit out of the eastern edge of the Soufrière Depression has been dated by Lindsay et al. (2003) at 6.6-6.8 ka. With respect to the series of secondary lava domes punctuating the flank of the main Plat Pays stratovolcano, many are located outside the Soufrière Depression and so they must have formed before it. Moreover, they are covered by the more recent Grand Bay Ignimbrite, so they can be considered older than 38 ka BP (Lindsay et al., 2003). Some

lava domes are located within the Soufrière Depression (Morne Crabier, Morne Patates). Radiogenic dates for these domes from Monjaret (1985) indicate ages in between 39 ka and 450 years BP, with a last dome-forming eruption occurring 450-685 years BP (Roobol et al., 1983; Lindsay et al., 2003) and forming the dome of Morne Patates.

Besides Valley of Desolation and Boiling Lake, a second area of strong geothermal activity is located in the Plat Pays Volcanic Complex in the Soufrière Sulfur Springs site. This area is characterized by sulphur springs, hot fumaroles and steaming, with volatile and chemical composition suggesting that the hydrothermal system is dominated by meteoric water (Brown, 2002). Two other geothermal areas are located in the Plat Pays Volcanic Complex, respectively at the Galion field (in between the Morne Patates and Morne Crabier domes) and in Champagne, a zone of gas emission north of Pointe Guignard (black stars in Fig.I.4; Lindsay et al., 2003; Lindsay et al., 2005b). The Champagne fumaroles are located next to the beach and continue about 20 m offshore.

No historical eruptions are known for the Plat Pays Volcanic Complex; the only eruptive activity which could have been detected by humans is the last eruption of Morne Patates (450-685 years BP, Roobol et al., 1983; Lindsay et al., 2003), that occurred in a period corresponding to the earliest European arrival in the area.

The most likely eruptive scenario for the future eruptive activity of the PPVC is an effusive lava dome-forming eruption from either of the Morne Canot or Morne Patates lava domes. Recent studies have demonstrated that the seismic activity of the PPVC in the period 1998-2000 is of volcanic origin (Shepherd et al., 2000; Stasiuk et al., 2002), thus supporting the idea that the system is still linked to an active magma chamber and that a future lava dome-forming eruption is very likely to occur within the next 100 years. Moreover, seismic data indicate a depressurization of the system with seismic swarms becoming more energetic and shallower with time, the shallowest reaching depths of about 1 km. Nonetheless, because of the complexity of the PPVC region, a precise estimation of the vent location for future eruptions within the eruptive centre will be very difficult.

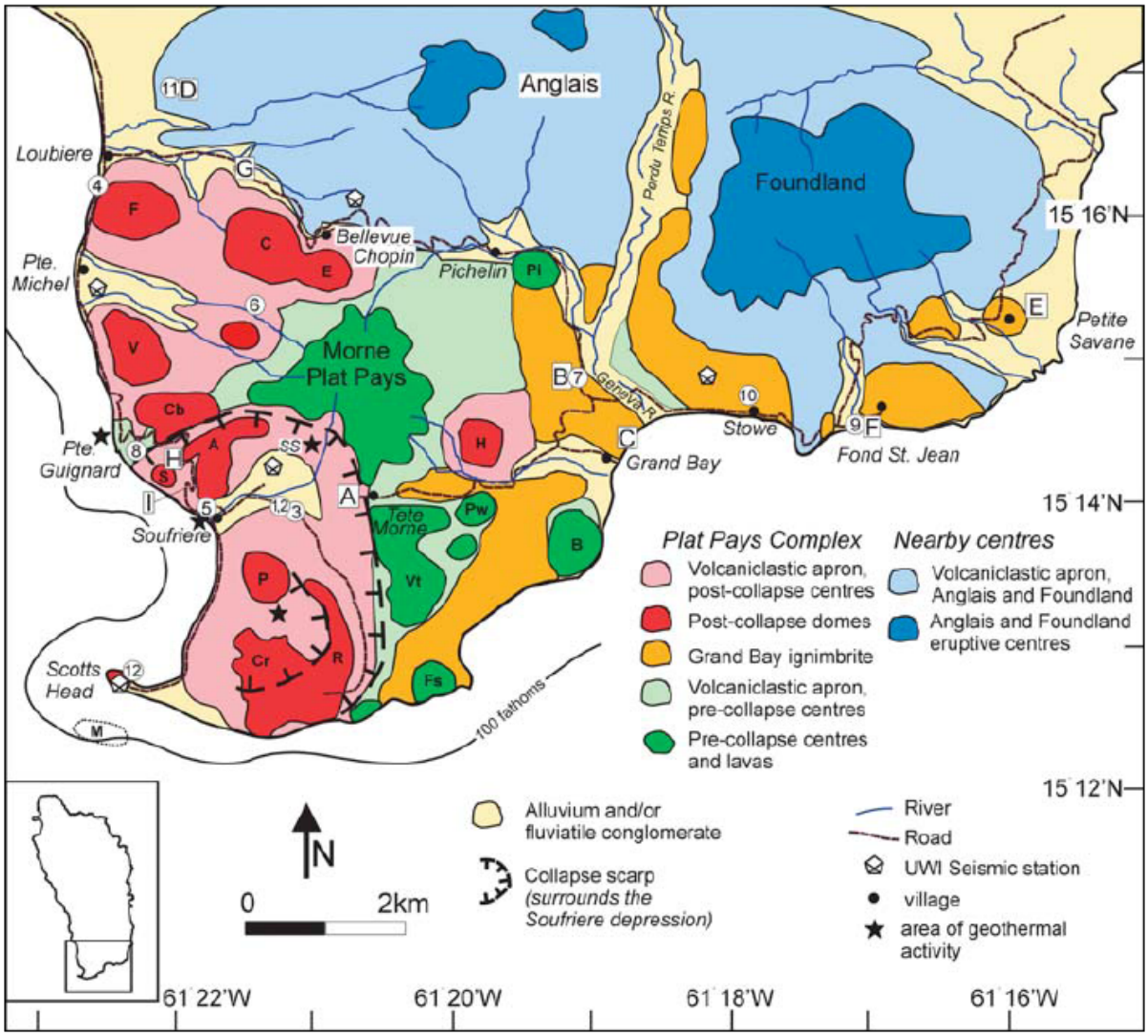

***Fig.I.4: Simplified geological map of the Plat Pays Volcanic Complex (PPVC)**. The Grand Bay ignimbrite is in yellow while volcanic lava domes are indicated in red (post-collapse) and green (pre-collapse). Letters on lava domes structures indicate their name as follows: F= La Falaise; C= Morne Canot; E= Morne Eloi; V= Morne la Vue; S= La Sorcière, A= Morne Acouma; P= Morne Patates; Cr= Morne Crabier; R= Morne Rouge; h=Hagley; P= Pichelin; Fs= Fous; M= Mountain top; B=Bois d'Inde;Pw= Powell; Vt= Morne Vert; Cb= Morne Cabrit; The horse-shoe shaped structure represents the Soufrière Depression. Black stars refer to geothermal areas (from Lindsay et al., 2003).*

I.2.5.2 Morne Trois Pitons –Wotten Waven/Micotrin- Valley of Desolation

This eruptive centre comprises the Morne Trois Pitons, the twin domes of Micotrin, the Wotten Waven caldera structure and the Valley of Desolation

Morne Trois Pitons

The Morne Trois Pitons structure was first described by Wills (1974) as the combination of three coalescent lava domes with a volume of approximately 1.5 km^3. Its eruptive activity can be divided in three different periods: material from the first phase are block-and-ash PDC deposits interbedded with conglomerates; deposits of the second phase are mainly made up of pumiceous ignimbrites (recognized in Pagua and Layou valleys) and represent a shift of volcanic activity from dome-forming eruptions to Plinian activity; deposits of third phase are again derived from block-and-ash PDC, representing the period of extrusion of the three current lava domes out of a 3.5 km-wide crater (Lindsay et al., 2005b). Radiocarbon dating of these deposits give ages of 17 240 years BP (Wadge, 1989) and 25 310 years BP (Roobol, 1983). With regard to the ignimbritic deposits of the second phase, stratigraphy and field relations have not yet clearly established whether they originated from an eruption from the Morne Trois Pitons or from the Micotrin area.

There has been no report of historical eruptions from the Morne Trois Pitons eruptive centre and the area is not characterized by significant geothermal activity. Moreover, no recent sign of strong seismic activity has been recorded in this centre, suggesting that it is less likely to erupt in the near future. Future eruptions of this centre may be either lava dome-forming or explosive Plinian eruptions.

Wotten Waven-Micotrin

Demange et al. (1985) describe for the first time the Wotten Waven structure as a "vast volcano tectonic depression", related to the eruption of the voluminous Roseau Tuff ignimbrite (Sigurdsson, 1972; Carey and Sigurdsson, 1980). The caldera has a size of 7 x 4.5 km and is elongated in the SW-NE direction. The Micotrin lava dome is located in the caldera, near the north-eastern margin.

The past eruptive activity of Wotten Waven-Micotrin area has been characterized by explosive Plinian eruptions and lava dome-forming eruptions. Plinian eruptions have produced small plinian fallout and large volumes of pumiceous pyroclastic density currents (similar to the Roseau Tuff) described and studied by Sigurdsson (1972) and Carey and Sigurdsson (1980). A more recent stratigraphic study of these PDCs has been performed by Howe et al. (2014). Despite the increasing interest in studying the Roseau Tuff, its vent source is currently not well known, as the outcrop conditions on the island make it difficult to map and trace deposits approaching the vent area. Sigurdsson (1972) inferred vents under the

Micotrin/Trois Pitons domes, whereas Demange et al. (1985) proposed that much of the ignimbrite originated from the Wotten Waven caldera.

The Wotten Waven caldera is also an important hydrothermally active area characterized by the presence of several fumaroles, pools and hot springs with temperatures reaching 90 to 99 °C. The largest bubbling pool of the area is the Yellow Pool, a 2 x 1.5 m basin adjacent to the River Blanc (a tributary of the Roseau river) and filled with water of very variable colour and temperature as a function of the weather conditions (milky colour and temperatures up to 87-93°C during the dry season, clear colour and temperatures of 71-74°C in the wet season).

There have been no reports of historical eruptions for the Wotten Waven-Micotrin eruptive centre. The most likely future eruption from this eruptive centre is a lava dome-forming eruption from Morne Micotrin, with associated block-andash-flow deposits, or a Plinian eruption from the Wotten Waven caldera. The likelihood of a future eruption from both these centres is increased in light of the recent seismicity recorded between 1997 and 2002.

In Morne Micotrin the lava dome-forming phase would be preceded by a phreatic activity phase and followed by the collapse of the lava dome with significant block-and ash-flow deposits, as for PPVC. Pyroclastic density currents could eventually reach the coast on both sides of the island and create deposits similar to those already recognized in Roseau and Grand Fond.

The significant geothermal activity still occurring in the Wotten Waven vent area and the shallow seismicity recorded in recent years, makes this centre likely to produce future plinian eruptions. A reactivation of this area would imply a large eruption affecting most of Dominica. In the Lesser Antilles arc, plinian columns usually reach heights of 20 to 30 km and a collapse of such a plinian column could create a first phase of ash- and pumice-fallout followed by a significant phase of PDCs reaching the west coast of Dominica from Mahaut to Roseau, and the east coast from Petite Soufrière to Petite Savanne. Given the absence of morphological barriers on the west side of the Wotten Waven caldera, pyroclastic density currents would easily follow topography and fill the main valleys of the region, as already observed in stratigraphic studies for the main ignimbritic deposits of Layou and Roseau (Lindsay et al., 2005b; Howe et al., 2014). In the hazard scenario evaluated by Lindsay et al. (2005b), a plinian eruption from Wotten Waven caldera would affect all the southern part of Dominica, south of a line connecting the two towns of Marigot and Salisbury. The north part of the island would be preserved by the presence of Morne Diablotins eruptive centre, which forms a topographical barrier for PDCs and surges.

Valley of Desolation

The Valley of Desolation (Fig. I.5) is located to the south of Morne Micotrin, in the Morne Trois Pitons National Park. The area is a concentration of several phreatomagmatic explosion craters, hot springs, fumaroles and bubbling springs linked with strong hydrothermal activity. This eruptive centre was one of the first on the island to be studied, after the eruption in 1880 (Bert, 1880; Daubrée, 1880a, b; Eldridge 1880; Endlich 1880; Nicholls 1880a,b, Watt, 1880). The area is the source of three prehistoric eruptions (Wadge, 1985) and two main historical eruptions: the phreatic eruptions of January 1880 and July 1997. Both eruptions had their vent in the same area, but the earlier eruption had a greater impact on surrounding regions, with formation of airfall of ash and accretionary lapilli over Roseau and few lahars.

The Boiling Lake, the second largest hot spring in the world, is part of the Valley of Desolation. The lake, first described by Watt and Nicholls (1870) is approximately 85 to 75 m across (Lindsay et al., 2000) and its volumes, water level and temperature fluctuate regularly with the hydrothermal activity. The average depth is about 10-15 m, while temperatures range between 80° and 90°C (Sapper 1903; Robson and Willmore, 1955; Brown, 2002). Recent phreatic activity has been monitored at the lake in the period December 2004 to April 2005, causing a variation of the water level of about 10 m below the high level mark.

The most likely eruption from this eruptive centre is a phreatic eruption from the Boiling Lake or from one of the other explosion craters present in the Valley of Desolation area (Lindsay et al., 2000). As experienced in previous eruptions, the direct effect of these eruptions would affect only areas surrounding the Valley of Desolation, no more than 1-2 km from the vent. Nevertheless, ash and ballistic fragments can reach greater distances and affect areas on the west coast of the island (as occurred during the 1880 eruptions). Generally, this kind of eruptions represents a hazard only for people staying near to the vent area at the time of eruption.

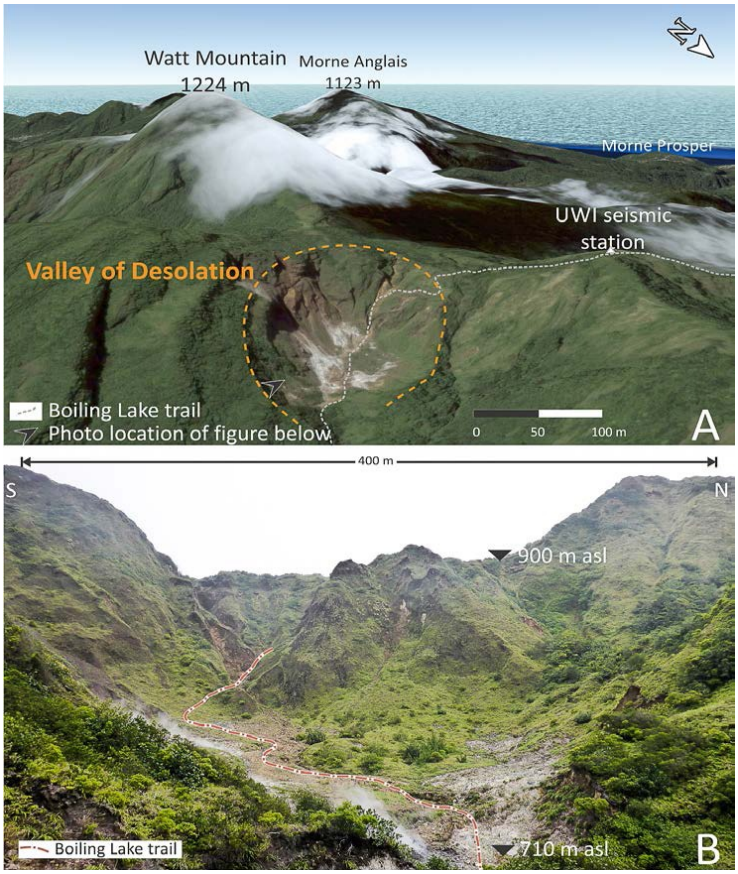

Figure I. 5: Valley of Desolation. *A) Google Earth image of the Valley of Desolation (orange dashed line); B) Photograph of the Valley of Desolation with the Boiling Lake trail (red dashed-dotted line). (from Mayer et al. in review).*

I.2.5.3 Morne Diablotins

This eruptive centre is active since the Pliocene - Older Pleistocene period and is placed on the laterite-saprolite surface developed over the Pliocene volcanic rocks. These rocks, forming the basement of the whole eruptive centre, can be divided in two stages, a submarine one and a subaerial one, with ages going from 3.7 to 2.2 Ma BP (Bellon, 1988). The eruptive centre is made up of lava flows, lava domes and block-and-ash-flow deposits, dating from the protracted Pliocene/Older-Pleistocene dome-forming activity (Martin and Kaye, 1960; Wadge, 1989). Pyroclastic density currents of this period have ages ranging from 0.72 Ma (Monjaret, 1985) to >46,620 years BP (Smith and Roobol, 2013).

Subsequent recent activity has been characterized by plinian eruptions producing significant pumiceous fallout deposits and pumiceous pyroclastic density current, dated at >22,200 to >40,000 years BP (Sparks et al. 1980a, b; Wadge 1989). The large PDC deposits linked with this phase spread radially as three main tongues in the direction of Crompton Point, Point Ronde and by some authors (Fig. I.3, Sparks et al., 1980a).

The summit area of the volcano is now covered by a complex of lava domes similar to the one present on the Morne Trois Pitons-Micotrin volcanic centre. The five main lava domes cover an area of 6 x 4 km^2 and are dated at ~0.7 Ma, from a K-Ar determination by Wadge (1989).
Minor geothermal activity has been reported on the western flank of the Morne Diablotins. There has been no report of historical eruptions from the Morne Diablotins eruptive centre. Present information on seismic and geothermal activity does not clarify the possibility of a future eruption from this volcanic centre.

I.2.5.4 -Morne aux Diables

This eruptive centre is a 7 x 7 km stratovolcano forming a peninsula in northern Dominica. Its active phase began in the Older-Pleistocene period (1.68, 1.72 and 2.01 Ma, Monjaret 1985; Bellon 1988). Nevertheless, the presence of three unconsolidated block-and-ash PDC deposits in Pennville, Morne Soleil and Douglas Bay (Fig.I.3, believed to be younger than 70 ka) indicate that the centre has also been active in the Recent-Holocene period.
As with the eruptive centres of Morne Trois Pitons and the Morne Diablotins, the Morne aux Diables summit area is composed of a lava dome complex (five main lava domes can be recognized), while its flanks are made up of several consolidated block-and-ash PDC deposits related to the dome-forming activity of the centre. Some plinian eruptions but also phreatomagmatic activity has also characterized this eruptive centre, as demonstrated by the occurrence of pumiceous fallout and surge deposits.
Geothermal activity is highly present directly to the south of the eruptive centre near Portsmouth and Glanvilla, with a series of geothermal hot-springs and fumaroles. A large part of this geothermal area is immerged into shallow waters in the Prince Rupert Bay. In the bay, several large solitary springs and diffuse degassing zones can be found at depths of over 20 m beneath the sea. Minor cold fumarolic activity has been recorded also at the “Penville cold Soufrière” area, on the western flank of Morne aux Diables (Robson and Tomblin, 1966), where milky-bubbling pools and springs reach temperatures of 23-29°C and pH of 1-2 (Joseph and Lindsay, 2002; Joseph and Robertson, 2003).
No historical eruptions are recorded for this eruptive centre, but recent seismicity and earthquakes swarms (1841, 1893, 2000-2003) make this centre one of the most likely to erupt in the future. In particular, the last significant earthquake swarms of April 2003 (500 earthquakes in less than a week) suggest the possibility of a future eruption. The most likely eruption to occur from Morne aux Diables is an effusive lava dome-forming eruption

(Lindsay et al., 2005b), as for the PPVC. An initial phase of phreatomagmatic activity would be followed by a dome-building phase from a central or a parasitic vent, and the occurrence of pyroclastic density currents spreading radially from the volcanic centre (Portsmouth and Clifton in the west and Pennville and Vieille Case to the east). This eruptive scenario would have strong impact only around the northern peninsula of Dominica.

I.2.6. Large silicic pumiceous eruptions

Voluminous ignimbritic deposits are present in the main valley of the central part of Dominica (including Morne Diablotins and Morne Trois Piton-Micotrin volcanic centres). These deposits were attributed in a first time to a large pumiceous eruption producing 58 km^3 of magma (Sigurdsson, 1972, Carey and Sigurdsson, 1980) and by more recent works to several less voluminous eruptions (Lindsay et al., 2005b; Smith et al., 2013; Howe et al., 2014). The detailed description of these deposits and of the evolution of the interpretation in the previous works is given in the chapter III on the new chronostratigraphy.

CHAPTER II:

SCIENTIFIC APPROACH, SAMPLES AND ANALYTICAL METHODS

Introduction

Dans ce chapitre nous présentons une description détaillée de l'approche scientifique et des différentes techniques analytiques utilisées dans cette étude.

Dans un premier temps nous présentons les échantillons et la démarche d'échantillonnage adoptée. Les ponces utilisées dans cette étude appartiennent à trois éruptions ignimbritiques majeures reconnues sur l'île de la Dominique : Layou (51 kyrs cal BP), Roseau (33 kyrs cal BP) et Grand Fond (24 kyrs cal BP). Elles ont été échantillonnées dans le dépôt de retombées pliniennes correspondant aux premiers produits émis pour chaque éruption. Ce choix s'explique par la nécessité de traiter des échantillons représentatifs des conditions de stockage pré-éruptives et donc trempés et non modifiés par des processus secondaires (par exemple pouvant intervenir dans des dépôts d'écoulements soudés et donc restant à température élevée pendant un certain temps).

Ces ponces ont ensuite été traitées selon un protocole de laboratoire bien défini, concassées pour obtenir des granulats libres d'impuretés utilisées différemment pour les analyses de roche totale (après broyage fin), de verre résiduel et pour la sélection des cristaux étudiés. Pour obtenir des cristaux séparés, les granulats ont été tamisées selon différentes granulométries et les cristaux prélevés à la main dans les granulométries comprises entre 315 µm et 1 mm.

Tous les cristaux séparés ont été observés au microscope électronique à balayage (MEB) afin d'identifier la présence de zonation. Sur les cristaux sélectionnés, des images MEB haute résolution ont été effectuées. Des analyses à la microsonde électronique (EPMA) ont été ensuite réalisées sur les cristaux sélectionnés. Des profils d'analyse bordure-cœur ou bordure-bordure avec espacement constant des points de mesure ont été effectués sur les orthopyroxènes zonés ainsi que sur certains plagioclases, tandis que des analyses ponctuelles ont été réalisées au cœur les cristaux d'orthopyroxènes non zonés, d'amphiboles et d'oxydes.

La partie expérimentale de cette étude a consisté à la réalisation d'expériences d'équilibre de phase en presse à chauffage interne (IHPV, ISTO-Orléans). En reproduisant expérimentalement les produits naturels (assemblage et composition des phases cristallines), ces expériences ont eu pour objectif de contraindre les conditions pré-éruptives de stockage des produits naturels. La poudre de roche totale utilisée comme produit de départ a été obtenue par successifs broyages et fusions des produits naturels de Roseau et Layou, puis chargé dans des capsules en Au avec différentes quantités d'H_2O et d'oxalate d'argent (source de CO_2), selon les conditions de saturation ($XH_2O=1$) et sous-saturation ($XH_2O=0.8$) en eau testées dans cette étude. Le poids de chaque charge expérimentale a été contrôlé tout au long

de leur préparation. La technique des sensors nous a permis de vérifier les valeurs de fugacité d'oxygène atteintes lors des expériences.

Les équilibres de phase ont été réalisés dans la gamme de pression 150-400 MPa, 800-900°C en température et à une fugacité d'oxygène fixée pour toutes les expériences à ~ΔNNO+1. La durée de chaque expérience a varié de 7 à 10 jours en fonction des conditions P-T (pression-température) et a visé à garantir une cristallisation à l'équilibre. Deux thermocouples ont permis le contrôle régulier des possibles variations de température le long de chaque expérience.

Toutes les expériences ont été terminées par trempe isobarique. Après contrôle de la cohérence des poids des capsules avant et après expérience, les charges expérimentales ont été imagées par MEB et analysées par microsonde électronique.

La deuxième partie de ce chapitre est dédiée à la description théorique des processus de diffusion et a leur application dans l'étude des dynamiques de réservoirs. Nous décrivons dans un premier temps le processus de diffusion d'un point de vue microscopique en précisant tous les mécanismes d'échange qui peuvent se produire au sein de la maille cristalline et favoriser le déplacement d'éléments. Dans un deuxième temps nous présentons une description macroscopique de la diffusion, donnant les équations (Lois de Fick) qui décrivent la diffusion dans l'espace et dans le temps et les solutions principales utilisées en mathématique pour résoudre ces équations. Dans le cas d'application aux cristaux, différents paramètres influent sur la diffusion : température, pression, fugacité d'oxygène, composition et anisotropie cristalline. L'influence ainsi que le degré d'importance de chaque paramètre sont discutés dans cette deuxième partie du chapitre.

Nous présentons par la suite une synthèse des travaux antérieurs sur différents couples diffusifs élément-minéral, avec un point plus détaillé sur les études concernant les orthopyroxenes.

Pour terminer nous discutons de la méthode et des contraintes nécessaires à la modélisation de la diffusion dans les cristaux et plus précisément de la méthode utilisée dans cette étude pour modéliser l'interdiffusion Fe-Mg dans les orthopyroxenes.

II.1. Sampling methodology

The main outcrops of the three eruptions are for the most part constituted of a basal Plinian fallout layer (< 1m thick) covered by thick, possibly partially welded pumiceous pyroclastic density current deposits (ignimbrites), reaching thicknesses up to 100 m in the main valleys (see description of the stratigraphic section in chapter III). During fieldwork, at least 100 pumice clasts and samples of the ash matrix were collected from the different units identified in the Plinian fallout deposits of each eruption. Some pumice clasts were also sampled in the overlying ignimbritic deposit. For the main part of the work, as we aim to constrain the pre-eruptive reservoir storage conditions and dynamics, particular care has been taken to select samples belonging exclusively to the basal Plinian fallout phase of each eruption. These samples consist of early-erupted and rapidly-quenched products, preserving information on reservoir conditions and processes as well as ascent conditions. Moreover, sampling from the Plinian fallout deposits ensures a good physical and chemical preservation of pumice clasts and their crystal content, avoiding possible contamination by post-eruptive entrainment of lithics and external material (such contamination may occur during the emplacement of pyroclastic density currents). The use of well-quenched and preserved samples is particularly important as we perform interdiffusion modelling in crystals to deal with timescales of reservoir dynamics. This ensures that the diffusion profiles are quenched on eruption and do not record gradual diffusive processes (progressive cooling) which may occur during pyroclastic emplacement.

II.2. Sample preparation

To ensure that sampled pumice clasts were representative of the magma emitted during each eruptive phase, between six and ten samples were selected that exhibited the modal density from populations of $\geq$100 clasts from the Plinian fallout deposit of each eruption (Layou: DOM41a3, Roseau: DOM60d1a, Grand Fond: DOM43b; see Chapter III, Fig. III.1). Sample diameter was from 2 to 6 cm.

II.2.1 Whole-rock and matrix glass analyses

After acid attack of powders, whole-rock samples were analyzed as “bulk rock” for major elements at the Centre de Recherches Pétrographiques et Géochimiques in Nancy (CRPG, France), using Inductively Coupled Plasma Optical Emission Spectroscopy (ICP-OES).

Major element compositions of the matrix glasses of pumice were determined using the SX-Five CAMECA electron microprobe (Service Camparis, Paris, France), at 15kV high voltage

and with counting time on peak varying from 10 to 25s depending on the element. To avoid Na loss, we used a 4 nA beam current, and Na and Si were counted first and simultaneously.

II.2.2 Single crystals

As a first step, pumice were cleaned by washing and scrubbing to remove any adherent matrix and oven-dried at 80 °C for ~ 48 h. In order to liberate isolated crystals for each sample, pumices were gently crushed into powder using a small hammer for big pumices (6 cm across) and a jaw crusher for fine particles (2-3 cm across). Particles were then sieved into different crystal size fractions using the geometric set 2-1-0.750-0.500-0.315-0.250-0.125 mm. Each fraction was then cleaned by washing, sieved under deionized water, passed through an ultrasound bath to remove fine adhering particles, and oven-dried a second time at 80 °C for ~ 24 to 48h.

After complete drying of samples, the larger particle size fractions (0.315-0.500 mm, 0.500-0.750 mm and 0.750-1mm) were subsequently recovered and used to sample isolated crystals. These fractions are the most useful as they allow crystals to be handled and visible to the unaided eye.

For crystal-specific investigation, crystals of plagioclase, amphibole, orthopyroxene, clinopyroxene and Fe-Ti oxide were handpicked under a binocular microscope. In total, 618 plagioclases, 83 amphiboles, 2581 orthopyroxenes, 42 clinopyroxenes and 147 Fe-Ti oxides were picked for the three eruptions. Crystals of each type were then mounted in epoxy resin (at room temperature and under ambient pressure conditions), then dried under an extractor hood for about 9 hours. Mounts were polished (from 22 μm to 0.3 μm) to bring crystals to the surface of the mount and obtain a perfectly smooth, mirror-like, flat surface. The quality of polishing and the resulting mount surface were regularly checked under the binocular microscope during polishing.

A summary of the sample preparation method is presented in Figure II.1.

Particular care has been taken in (1) filling mounts with crystals of comparable size and thickness, (2) arranging crystals so that they all present a similar orientation in the mount and (3) arranging crystals in fixed lines in order to facilitate their tracking and identification during scanning electron microscope (SEM) and electron probe microanalyser (EPMA) investigations. As they have been used for intracrystalline diffusion modelling, particular care was taken in the mounting of orthopyroxene crystals: all crystals were mounted with c-axis in North-South direction, and crystals of the same mount were specifically selected to have

comparable thickness and size (in order to enable polishing up to the central part of orthopyroxenes).

Before SEM or EPMA investigations, selected mounts were all carbon-coated. Carbon coating of samples, based on thermal evaporation of carbon, is required for both analytical methods as it creates a thin conductive layer of metal on the sample, inhibiting any possible charging effect when the electron beam is interacting with the sample surface. Moreover, coating of samples improves the secondary electron signal required for topographic examination at the SEM. For each analytical session samples were all coated simultaneously in order to ensure the same thickness of carbon, thus avoiding any potential influence on chemical analyses.

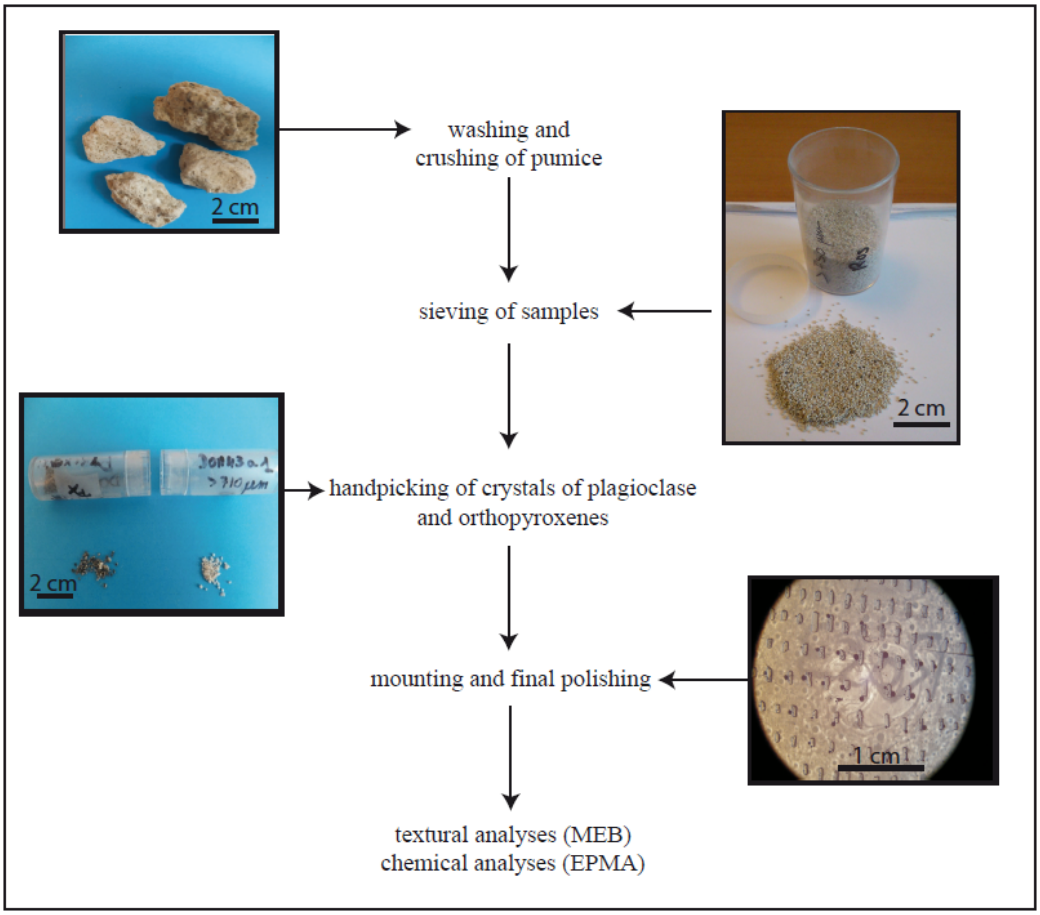

Figure II.1: Procedure for samples preparation from pumice to mounts. *a) Selected pumice samples from the Plinian fallout deposit of each eruption; b) samples after washing, crushing and sieving; c) example of handpicked orthopyroxenes (on the left) and plagioclases (on the right) from the crystal fraction > 500 µm; d) example of an orthopyroxene crystals mount, seen under binocular reflected light, after mounting of crystal with the c-axis in N-S direction and polishing.*

II.2.3 Experimental petrology starting material

The starting material for phase equilibria experiments has been selected on the basis of results obtained on natural whole-rock and matrix glass composition. Eruptions with comparable whole-rock composition can be considered as equivalent from a petrological point of view: under the same experimental conditions, they will crystallize the same type of crystal phase assemblage.

Results on whole-rock, matrix glass, and modal composition of natural products show that Roseau, Grand Fond and Grand Bay have comparable petrology, while Layou and Grande Savane can be distinguished by a more evolved dacitic composition and the presence of amphibole in the crystal assemblage.

On the basis of these results, Roseau is considered a good analogue of Grand Fond and Grand Bay, and Layou a good analogue of Grande Savane. As such, we performed phase equilibria crystallization experiments using only pumice from Layou and Roseau as starting samples.

We have selected five or six pumice of comparable size from the Plinian fallout phase of the Roseau and Layou eruptions. As the chemical composition of the starting material must represent pure reservoir conditions, pumice have to be cleaned from any adhering matrix and sawn with particular care to remove any external parts exhibiting alteration. Cleaned pumices were then oven-dried for ~48 h at about 80 °C and ground to <50 μm.

To obtain the experimental starting material (a compositionally homogeneous glass), the powder has to be (1) finely ground (down to <50 μm) and (2) fused at 1400 °C in a Pt crucible for 3 h under atmospheric conditions. In our case, samples have been subject to a double grinding and a double-fusion process, in order to finally obtain a homogeneous glass representative of the natural whole-rock composition and free of any crystal seeds.

Fragments of the final starting glass (Fig. II.2) have been mounted in epoxy resin, dried under an extractor hood for ~8-9 h and polished (from 22 μm to 0.3 μm). Homogeneity of the starting glass was checked by examining BSE images and performing 10 EPMA single-point analyses in different parts of the glass. Comparison of double-fused dry glass with natural bulk rock shows that they have a comparable composition and that no significant volatile loss has occurred during the double-fusion process (Table II.1).

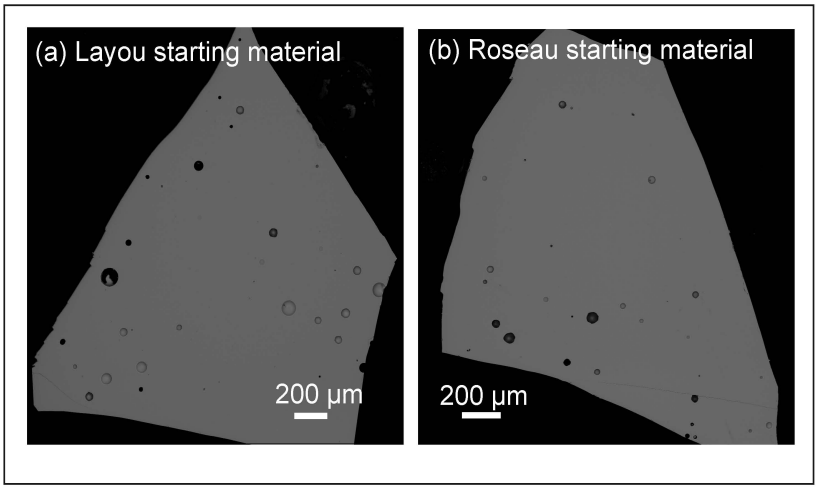

Figure II.2:BSE images of experimental starting material *.a) Fragment of starting glass obtained from Layou natural products; b) Fragment of starting glass obtained from Roseau natural products. Constant greyscale values indicate homogeneity in composition.*

	Layou					**Roseau**			
	Natural Whole Rock Dom 41a1-N2		Experimental Dry glass (n=6)			Natural Whole Rock DOM60d1a		Experimental Dry glass (n=6)	
wt%									
SiO2	66,20	*0,65*	65,43	*0,50*		63,50	*0,63*	64,08	*0,34*
TiO2	0,38	*0,02*	0,46	*0,06*		0,54	*0,03*	0,51	*0,07*
Al2O3	16,43	*0,16*	16,60	*0,23*		16,89	*0,16*	17,05	*0,14*
FeO tot	4,79	*0,11*	5,32	*0,26*		6,11	*0,13*	5,63	*0,28*
MnO	0,14	*0,01*	0,18	*0,05*		0,15	*0,01*	0,16	*0,04*
MgO	1,62	*0,08*	1,90	*0,06*		2,35	*0,12*	2,25	*0,12*
CaO	5,19	*0,10*	5,48	*0,12*		5,92	*0,12*	6,01	*0,12*
Na2O	3,48	*0,07*	3,41	*0,08*		2,93	*0,14*	2,98	*0,07*
K2O	1,67	*0,08*	1,65	*0,08*		1,50	*0,07*	1,57	*0,05*
P2O5	0,10	*0,01*	0,16	*0,05*		0,11	*0,01*	0,21	*0,03*
Total	100		100,00			100		100,54	
Na2O+K2O	*5,15*		5,05			*4,42*		4,55	
FeO+MgO	*6,41*		7,22			*8,46*		7,88	

Table II.1: Comparison of natural bulk rock with double-fused dry glass composition used as starting material for phase equilibria experiments. *Dry glass compositions represent an average of 6 single-point analyses.*

II.3. Experimental petrology approach

II.3.1. Internally heated pressure vessel (IHPV): description of the vessel and general working principle

All experiments of this study have been performed using the two IHPV (Internally Heated Pressure Vessel) of ISTO (Orléans), "Le Gros Bleu" and "Le Gros Vert" (Fig II.3a). They consist of a steel vessel in which samples and the oven are loaded horizontally. For each experiment, capsules of samples are mounted on a shutter (OK1 and OS1 shutters) on the top of two thermocouples (S or K) enabling the temperature at the top and the bottom part of the capsule region to be recorded with a precision of ±5 °C. This also allows a constant temperature to be maintained over the length of capsules (~30 mm). The oven is then mounted on the shutter and connected to it. Thermocouples and resistances pass through the shutter and then communicate with the computer system. Two different types of oven were used for our experiments: the kanthal and the molybdene oven. Once the shutter and the oven are connected and resistances are verified, the whole assemblage can be loaded into the vessel, sealed with a closure nut and connected to the computer system to allow a direct control on pressure and temperature conditions (Fig. II.3b).

Temperatures of 1400 °C and a pressure of ~400 MPa can be achieved with this experimental setup. High temperatures are reached using the resistance of the kanthal or molibdene cables, while high pressures are obtained by pressurizing a mixture of argon and hydrogen gas, the volume of which is a function of the specific redox conditions of each experiment.

Prior to pressurization, once the vessel was loaded with the sample assembly, the apparatus was completely flushed with Argon in order to ensure a perfect sealing of the vessel. Secondly, hydrogen was introduced (always before any heating of the experimental apparatus). The partial pressure of hydrogen has to be set as a function of the oxygen fugacity conditions the user wants to attain. Special attention must always be paid to the redox conditions of the preceding experiment, as the oven function includes a "memory effect" from one experiment to the next. In a third step argon was injected into the vessel until a pressure of 0.5 MPa (using a Maximator gas booster), then pressurized with a system of two hydraulic pumps (Basset Multiplier): a low pressure pump reaching 200 MPa, and a high pressure pump reaching 1000 MPa. Because of gas expansion and further pressurization during the subsequent heating procedure, pressurization was arrested at about 30-50 MPa below the final target pressure. The oven was then switched on to start the heating of the vessel until the intended temperature. Temperature was measured by the two thermocouples and regulated by a Eurotherm regulator. At the beginning of each experiment, temperature values recorded by

either thermocouple need to be accurately checked. The experimental charge zone must be isothermal (Fig.II.3b)—i.e. with no significant gradient—and, moreover, must exhibit no overturn in temperature values (i.e. where the upper values are cooler than the bottom values), which could create gas convection in the sample zone. Both pressure and temperature can be monitored during experiments with a precision of ±5 MPa and ±5 °C, respectively. They were regularly checked throughout the experimental duration (seven to ten days).

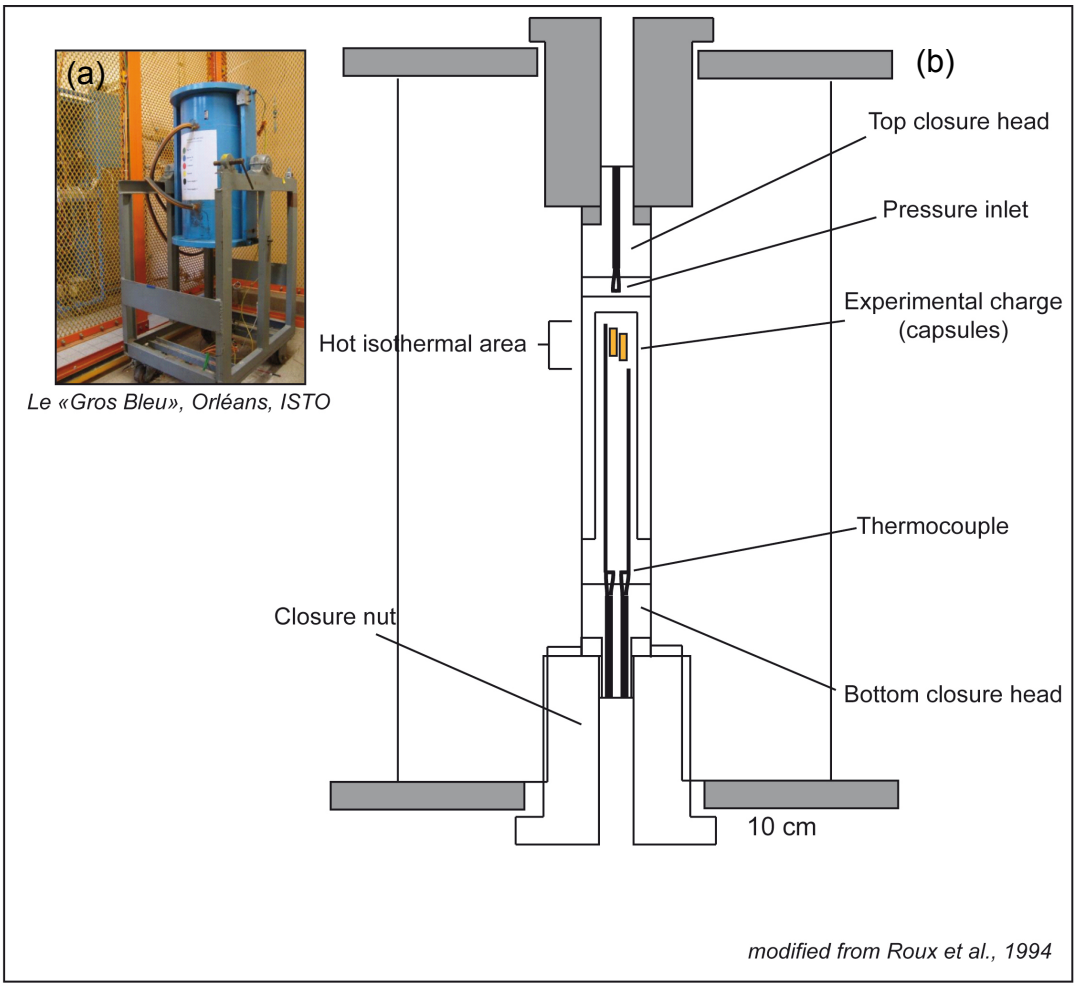

Figure II.3: The Internally Heated Pressure Vessel (IHPV). *a) Image of the IHPV "Le Gros Bleu" (ISTO, Orléans), representing one of the two vessels used in this study; b) Schema of the main components of an IHPV (modified from Roux et al., 1994). Yellow rectangles in the central part of the schema represent the capsules inserted for each run (experimental charges).*

The experiments were stopped using an isobaric quench of samples, whereby the decrease in temperature was performed whilst keeping the pressure constant (with variations in pressure smaller than ~1-2 MPa from the experimental fixed pressure). This allows volatiles (H_2O) to

be retained in samples as a dissolved phase. The pressure of gas in the vessel decreases as a consequence of decreasing the temperature, meaning that the use of the two hydraulic pumps was required to maintain the pressure at the experimental run value. For each quench the pressure was kept constant until a temperature lower than the glass transition temperature (Tg) of samples (~300 °C for the andesitic-dacitic samples of this study), in order to avoid decompression-induced formation of crystal phases. This type of isobaric quench needs 5-10 minutes to be performed with cooling rates of ~80 °C/min. Below Tg, pressure and temperature decrease in parallel. The vessel was then opened and the capsules recovered when the inner temperature reached values of ~20-30 °C. After each experiment, capsules were checked for their preservation and were carefully weighed to determine any possible volatile loss during the experiment and quench procedures.

Two different kinds of experiments can be performed to constrain pre-eruptive storage conditions using an IHPV: fusion experiments and crystallization experiments.
Fusions experiments start from a roughly ground natural sample (preserving natural crystals), and consists of fusing the sample so as to produce new crystals and crystal rims in equilibrium with a new matrix glass at the fixed experimental conditions. However, this kind of experiment would necessitate durations of years or more to achieve complete equilibrium conditions in samples. With typical run durations of 10 days to two weeks, only a local equilibrium can be reached. Moreover the differentiation in between inherited natural and new experimental crystals is particularly difficult in fusion experiments.
Crystallization experiments, on the other hand, start with a homogeneous glass powder free of natural crystal seeds. During experiments, new crystals form with a composition in equilibrium with the experimental glass (depending on the fixed physical conditions: pressure, temperature, oxygen fugacity, water fugacity). In this case the equilibrium conditions are ensured in the whole samples.

II.3.2. Capsules and experimental charges

Au 2.5/2.9 capsules (2.5 mm inner diameter, 2.9 mm outer diameter) were used to contain samples of each run. Au tubes of 1.7 cm in length were cut, cleaned twice in a mixture of deionized water and HCl for ~15 min at 250°C, annealed with a welding torch and welded on one side. Final Au capsules were then filled with ~30 mg of starting material (powder obtained after double fusion and grinding), with distilled water (for H_2O-saturated experiments) and distilled water plus silver oxalate ($Ag_2C_2O_4$) in different proportions (for

H_2O-undersaturated experiments), (Fig.II.4). Silver oxalate is used as a source of carbon dioxide vapor, enabling a homogeneous dissolution of H_2O during experiments. The ratio of fluid phase/glass powder has been kept constant at 10% for all experiments, to avoid changes of the silicate composition by incongruent dissolution in the fluid phase (Holtz et al., 1992).

We performed experiments with two initial water molar fractions: saturated conditions ($(XH_2Oin. = XH_2O/(XH_2O+XCO_2)=1$) and undersaturated conditions ($(XH_2Oin. = XH_2O/(XH_2O+XCO_2)= 0.8$). Saturated conditions have been selected on the basis of water content in natural orthopyroxene melt inclusions. They correspond to ~8 wt% H_2O at 3 kbar (Burham, 1979).

As water has a higher solubility in silicate than CO_2, its integration in the silicate phases during crystallization is favourable. Therefore, a small amount of water can contribute to the vapour phase. For this reason, after each experiment, final water content in residual glass has to be measured to assess water solubility.

After being filled with starting powder and H_2O+CO_2 in different proportions, capsules were closed and welded. To ensure no water loss during capsule preparation, all capsules used in this study have been weighed prior to welding, after welding, and after 8-12 h in the oven at ~250 °C before each experiment.

To have a direct control on the oxygen fugacity after each experiment, we used the H-solid sensors technique (Ni-Pd-NiO: Taylor et al., 1992; Pownceby et O'Neil, 1994). This technique is based on the principle that the composition of the binary alloy is sensitive to oxygen and hydrogen fugacity, following the equation:

$$Ni + \frac{1}{2}\ O_2 = NiO_2 \qquad \text{(II.1)}$$

All our runs contain a hand-made sensor capsule made by two Ni_x-Pd_{1-x}-NiO pellets (Ni_{15}-Pd_{85}-NiO and Ni_{85}-Pd_{15}-NiO), distilled water and Zr powder (to preserve isolation of the two pellets), loaded into a Pt capsule (2.5 cm long, 2.5 mm inner diameter, 2.9 mm outer diameter) sealed by arc-welding. By the calibration obtained by Taylor et al., (1992) we calculated the oxygen fugacity recorded by the sensor, and in turn, the fO_2 present in the vessel during experiments. Then, on the basis of the reaction of dissociation of pure water (using the fH_2O for pure water from Burnham et al., 1969 and the Kw from Robie et al., 1978), we calculated the fH_2 recorded in the vessel using the equation:

$$\log fH2 = \log fH2O^o - \frac{1}{2}\log fO2_{(sensor)} - \log K_W \qquad \text{(II. 2)}$$

Once the Kw and the fH_2 were obtained, and having calculated the fH_2O of each capsule as a function of the activity of water (aH_2O), we calculated the fO_2 of each capsule by the following equation:

$$\log fO2 = 2(\log fH2O - \log fH2 - \log K_W) \quad \text{(II. 3)}$$

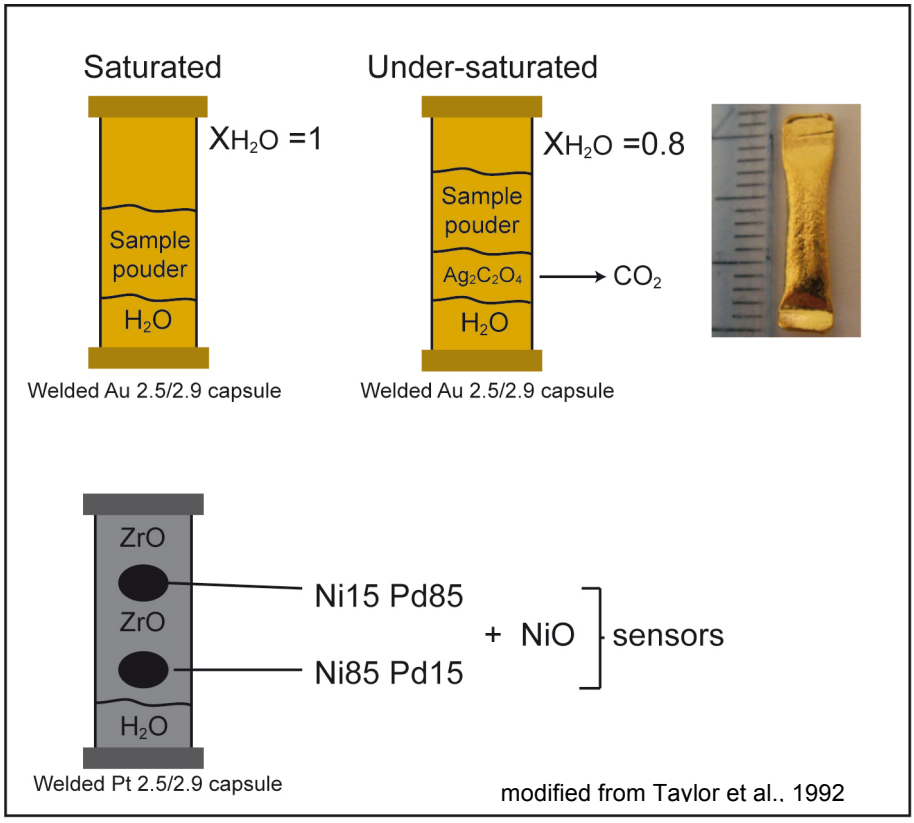

Figure II.4: Experimental capsules and sensors. *a) Capsule configuration used for experimental samples in saturated ($XH_2O=1$) and undersaturated ($XH_2O=0.8$) conditions; in undersaturated conditions $Ag_2C_2O_4$ (silver oxalate) powder is added as a source of CO_2; b) Sensor capsule configuration (modified from Taylor et al., 1992). The two pellets are represented by two black balls containing a Ni-Pd-NiO mixture. Isolation in between the two pellets is assured by ZrO powder.*

II.4. Analytical techniques

III.4.1. Scanning electron microscopy (SEM)

III.4.1.1. General operating principles

Backscattered scanning electron (BSE) images of crystals were acquired with a SEM Zeiss Supra 55VP (UMPC, ISTeP, Paris). The SEM principle is to scan the sample surface with a focused beam of electrons. These primary electrons interact with the atomic structure of the sample, in turn giving information on its topography. By the electron beam–sample interaction, atoms from the sample surface can be excited, resulting in the emission of several types of signals. These signals include secondary electrons (SE), backscattered electrons (BSE), X-rays, and cathodoluminescence (CL), (Fig. II.5)

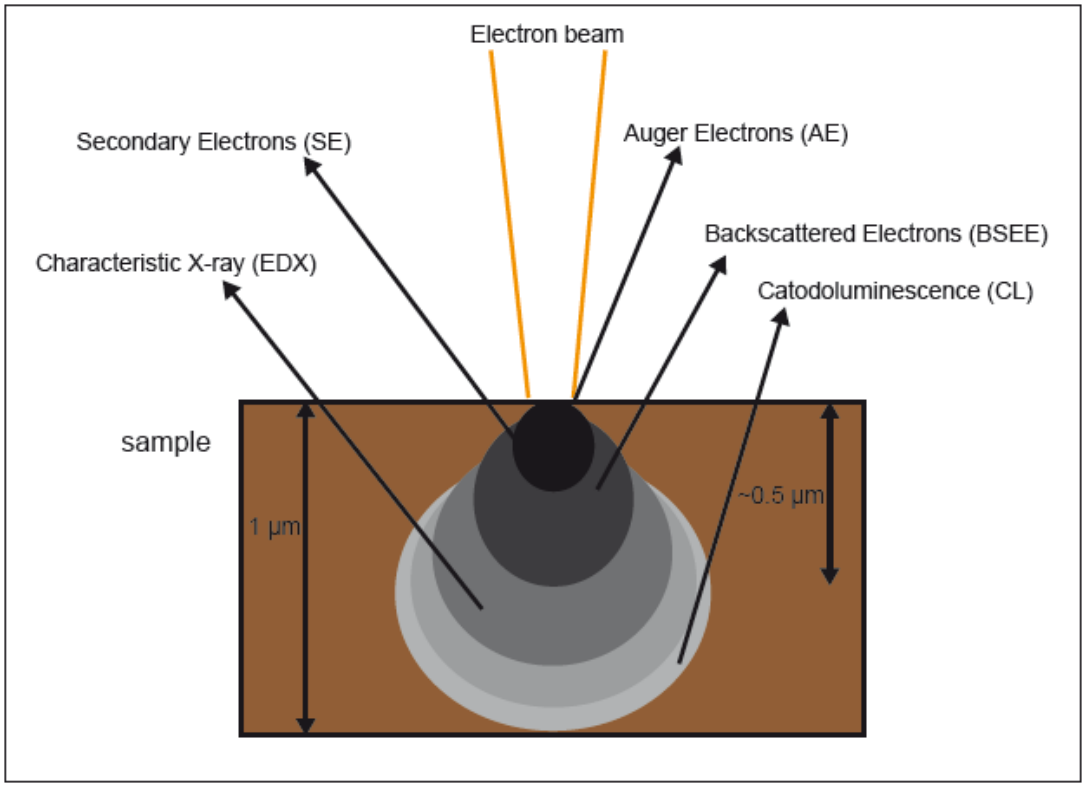

Figure II.5: General principle of primary electron–sample interaction in a SEM. *In scanning electron microscopy, the interaction of the primary electron beam with samples (interaction volume) produces emissions of different types of electrons (Auger, secondary, backscattered), which derive from different depths of the interaction volume.*

Secondary electrons result from emissions very close to the sample surface and consequently tend to yield images with a high quality and resolution (1 nm or less) allowing a check on the quality of sample surface. Backscattered electrons are produced by an elastic scattering of the

primary electron beam from the sample surface and derive from deeper regions of the sample. For this reason, BSE images have lower resolution than SE images. However, BSE are more often used for combined textural–chemical analyses because the BSE signal can be correlated to the atomic number (Z) of the constitutive elements of the sample: high atomic numbers (Ca, Fe, …) give higher greyscale values, while low atomic numbers give low greyscale values. This property is here used for studying plagioclase, amphibole, and orthopyroxene textures.

II.4.1.2. Characterization of samples textures

Natural samples

Backscattered scanning electron (BSE) images were acquired in different analytical sessions for plagioclases, orthopyroxenes, amphiboles and Fe-Ti oxide crystals, with an acceleration voltage of 20kV, a beam current of 8 nA and a crystal-dependent working distance of 7.4 to 8 mm (Fig. II.6a, b and c). To obtain high-resolution images, we used a scan speed of 7 and a rate of N = 8 passages per scan. Contrast and brightness were adapted to the sample type and size from one session to another. Images were acquired at different magnifications. For particular analysis of orthopyroxene textures, a first set of images was acquired for whole crystal description. A second set was acquired in order to investigate specific rim–core zoning patterns (subsequently used for intracrystalline diffusion modelling).

Melt inclusions in orthopyroxenes and plagioclases were also mapped and investigated using BSE images. Particular care was taken in selecting melt inclusions of sufficient size to be analysed by EPMA (>20 μm). Selected inclusions exhibited a typical rounded shape (unlikely to be affected by post-entrapment crystallization), and contained no bubbles (which would indicate degassing).

Experimental samples

High-resolution BSE images were also acquired for the analysis of the experimental starting glass and experimental runs resulting from phase equilibria crystallization experiments. Given the particularly small crystal size formed during these experiments (2 to 10 μm), it is extremely important to obtain high-resolution images of samples at different magnifications, so as to enable the operator to confidently locate and identify crystals during further EPMA chemical analyses. This is especially crucial for the analysis of plagioclase crystals, which

have a low grey-scale contrast, are particularly small in size, and exhibit poorly-preserved textures (Fig. II.6d, e and f).

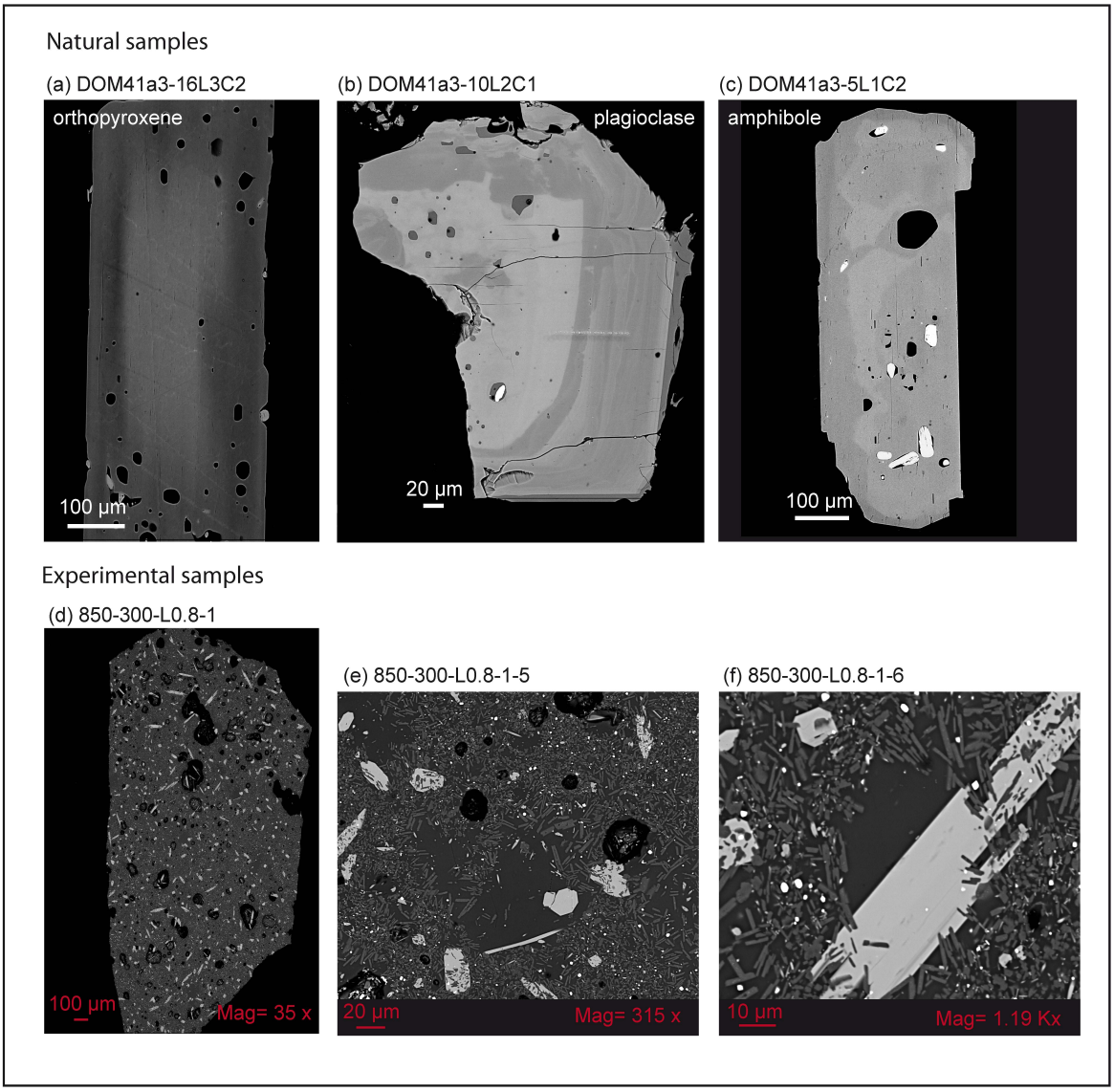

Figure II.6: Examples of high-resolution BSE images for natural and experimental samples*. For natural products: a) orthopyroxene; b) plagioclase and c) amphibole from Layou eruption; For Experimental samples: d) total image of fragment 1 of the run 850-300-L0.8 (T-P-XH_2Oin); e) more detailed image of a portion of the same fragment; f) detail of a Fe-Mg crystal and the adjacent matrix glass.*

BSE images of double-fused starting dry-glass and experimental samples were obtained with an acceleration voltage of 20 kV, a beam current of 10 nA, a working distance of 7 mm, a scanspeed of 7 and high counting time (N= 8) to decrease noise.

We first acquired images of each run fragment, before focussing on specific fragment portions at different magnifications in order to obtain a detailed map of the inner textures and crystal content of each experimental run. Calculation of total crystal content for each experimental run was then performed using BSE-images at different magnifications.

II.4.2. Electron probe microanalyser (EPMA)

II.4.2.1. General operating principles

Chemical analyses of natural crystals and experimental samples were performed with a SX-5 and SX-100 microprobe at the Service Camparis (Paris). Similar to the SEM principle outlined previously, the EPMA operating principle is based on the interaction of the sample with an electron beam. Samples are bombarded with an accelerated and focused electron beam. The ensuing interaction releases energy from the sample in the form of derivative electrons (Auger electrons, secondary electrons, and/or backscattered electrons) and X-rays. The latter are produced by inelastic collisions of the incident primary electrons with the inner atomic structure of the sample and correspond to ejections of sample electrons from one orbital layer. This causes a vacancy in the electron shell, so is followed by the replacement of the electron by a higher-shell electron, releasing energy as an X-ray. Each X-ray emission is characteristic of the energy-releasing element: elements with higher atomic numbers have higher emission energies. For quantitative analyses, only the X-ray emission is used.

The part of the sample reacting with the primary electron beam and producing X-rays corresponds to a specific sample volume (i.e. the interaction volume, Fig.II.5). Thus, when compositional traverses are performed with the electron probe microanalyser, particular care has to be taken in fixing the step in between single-point analyses to ensure that no convolution effect is occurring from one point to the other.

II.4.2.2. Analytical conditions and uncertainties linked with the method

Before analysis, the microprobe was calibrated using internal standards. Their composition is presented in Table II.2.

%	Albr	Phn9	Ortr	Apat	Vana	Fe2O3	Mnti
Si	32,13	25,68	30,06	-	-	-	-
Ti	-	-	-	-	-	-	31,76
Al	10,25	1,06	9,9	-	-	-	-
Fe	0,05	1,24	-	-	-	69,93	-
Mn	-	0,06	-	-	-	-	36,42
Mg	-	10,1	-	-	-	-	-
Ca	-	15,33	-	39,02	-	-	-
Na	8,75	1,03	0,8	-	-	-	-
K	0,02		12,4	-	-	-	-
O	48,82	44,38	46,14	38,92	13,1	30,07	31,82
Cr	-	1,08	-	-	-	-	-
Ni	-	0,04	-	-	-	-	-
Ba	-	-	0,7	-	-	-	-
P	-	-	-	18,31	-	-	-
Cl	-	-	-	0,35	2,62	-	-
F	-	-	-	3,4	-	-	-
V	-	-	-	-	10,42	-	-
Pb	-	-	-	-	73,8	-	-
TOT	100	100	100	100	100	100	100

Table II.2: Composition of internal standards used for calibration of EPMA.

All crystals (plagioclase, orthopyroxene, clinopyroxenes, Fe-Ti oxides, amphibole), melt inclusions and experimental samples have been analysed for their major element composition with the EPMA in several analytical sessions. Analytical settings (voltage, current, beam) have been changed as a function of the specific analysed crystal. Crystals have been analysed with single point analyses or with rim-to-rim and rim-to-core profiles as a function of their textures and structures**.**

For experimental samples two different beam sizes have to be selected: focused beam (2 μm) for crystal analyses and unfocused beam (10 μm) for glass analyses, in order to avoid alkali migration. Chemical analysis could not been performed on some samples where the crystals were too small to be rigorously analyzed (size <5μm). This problem was primarily encountered when analyzing plagioclase crystals (which tend to be difficult to identify on a BSE image and are usually too small, thin, or fractured) and Fe-Ti oxides. Undersaturated charges of low pressure experiments also yielded highly crystalline products, preventing the possibility of residual glass accurate analysis (Fig. II.7).

Analytical errors on major elements have been calculated at ~1 wt% for SiO_2, Al_2O_3 and CaO, 3 wt% for FeO, MgO and TiO_2, 5 wt% for MnO, Na_2O and K_2O, 500 ppm for Cl, and 200 ppm for P_2O_5.

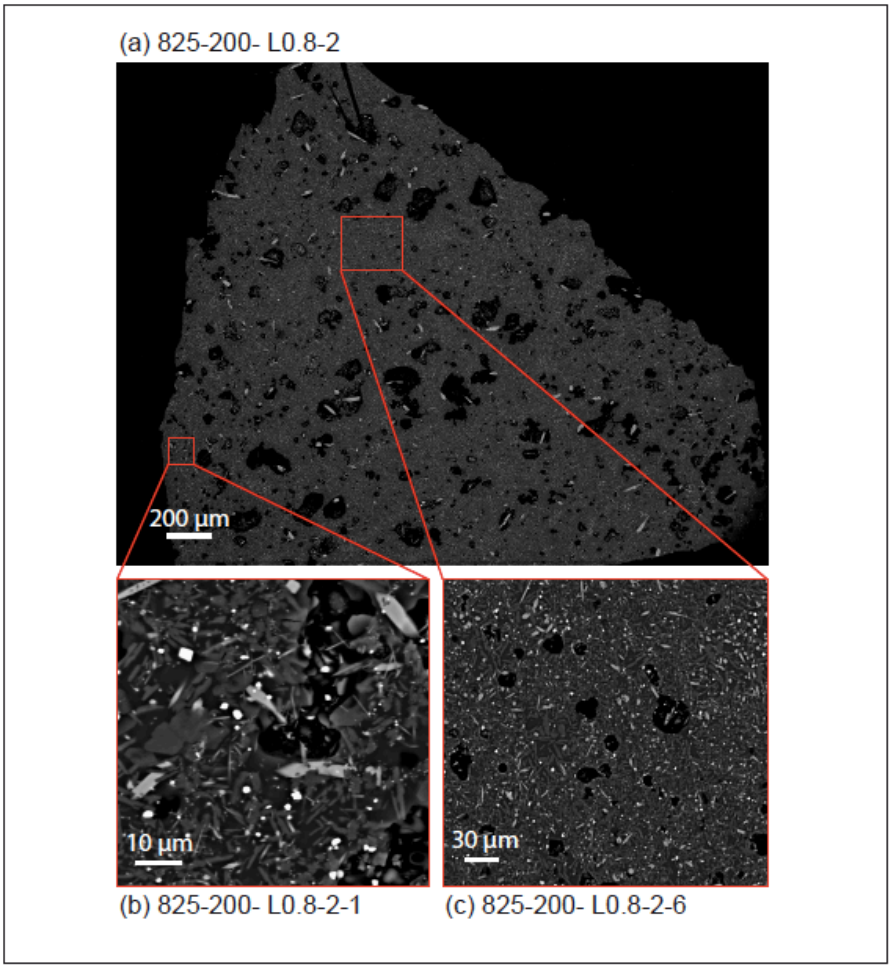

Figure II.7: High-resolution BSE images for the experimental run 825-200-L0.8. *a) total image of fragment 2 of the Layou undersaturated charge of the experiment at 825°C-200 MPa; b) and c) detail of the inner structure of the run demonstrating a high crystallinity (~40%), with few matrix glass portions larger than 10 µm (space necessary for glass analysis with unfocused beam using EPMA).*

Water content of experimental glasses was measured using the volatile-by-difference method (Devine et al., 1995). This procedure is not direct and requires the analysis of standard glasses with precisely known water contents, and a major element composition comparable to that of the natural samples. Natural products from Dominica typically exhibit high water content (6 to 8 wt% H_2O in orthopyroxenes and plagioclase-hosted melt inclusions). However, experimentally water-doped standard glass with water content higher than 4.7 wt% was not available for compositions analogous to Dominica dacites. For this reason, standards used in

this study are two orthopyroxene-hosted melt inclusions with known water contents of 6.57 and 7.43 wt% H_2O (Fig.II.8.a), previously obtained by secondary ion mass spectrometry (SIMS) analysis (University of Edinburgh; Balcone-Boissard et al., in prep). The volatile-by-difference method consists of calculating—for each standard—the difference of the total analysed major elements from 100%, then establishing a calibration line (diff 100%= f (water wt%)) in between this difference and the known water content (Fig.II.8.b). This calibration line then allows the calculation of water content for each experimental glass.

(a)

	STD-17-MIL1C4	STD-17-MIL4C5
SiO2	72,20	71,70
TiO2	0,21	0,23
Al2O3	12,35	12,61
FeO	1,97	1,70
MnO	0,04	0,04
MgO	0,19	0,19
CaO	1,86	2,03
Na2O	0,60	0,37
K2O	1,94	1,38
P2O5	0,02	0,00
F	0,02	0,03
Cl	0,22	0,24
S	0,00	0,00
TOT	91,61	90,49
H2O	6,57	7,43
Diff à 100%	8,39	9,51

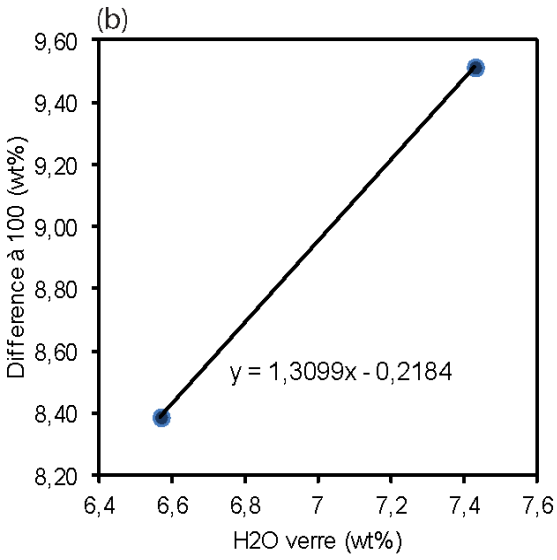

Figure II.8: Standards used for the volatile-by-difference method. *a) Table showing the major and minor elements composition of the two orthopyroxenes hosted melt inclusions used as standards to calculate water content of experimental glasses by the volatile-by-difference method; b) calibration line obtained from the standards melt composition.*

II.5. Diffusion chronometry

Modelling of diffusional relaxation of chemical gradients in crystals is a technique increasingly used to unravel timescales of pre-eruptive magma dynamics, as well as processes in other geodynamic contexts and geographic settings. Applications include—but are not limited to— the study of mid-ocean ridge volcanoes or subduction arc magmatism.

Here we use perform Fe-Mg interdiffusion modelling on orthopyroxenes to obtain timescales for a pre-eruptive reservoir rejuvenation mechanism, recognized for the three studied eruptions by a detailed analysis of crystals zoning patterns.

As diffusion modelling is a key feature of this study, we will here give a detailed overview about diffusion, starting with a physical description of laws governing diffusion, before discussion of the context and application of diffusion in crystals and, more in detail, to orthopyroxenes.

The parameters influencing diffusivities, together with the precise technical method used to perform diffusion modelling in orthopyroxenes are discussed in the following paragraphs.

II.5.1. Introduction

Diffusion chronometry is a technique increasingly used to constrain timescales of the evolution of magmatic plumbing systems under different geological and tectonic settings. In recent decades, several studies have demonstrated that the crystal cargo of magmas frequently shows textures (zoning patterns) which record changes and perturbations during magma storage. These textures can therefore be used as a powerful tool to assess magma chamber dynamics, changes in storage parameters, and movements of magma before eruption (Zellmer et al., 1999; Ruprech and Worner, 2000; Pan et al., 2002; Ginibre et al., 2002a, 2002b , 2004; Costa et al., 2003; Zellmer et al., 2003; Costa et al., 2004; Coombs and Gardner, 2004; Morgan et al., 2004; Shcherbakov et al.,2010; Kahl et al., 2011; Allan et al., 2013). Modelling diffusion relaxation of zoning patterns recognized in crystals provides timescales on these dynamics, with a number of new and important advantages (Costa et al., 2003; Morgan et al., 2004; Costa et al., 2005; Costa et al., 2008; Martin et al., 2008; Costa et al., 2010; Kahl et al., 2011; Matthews et al., 2011; Saunders et al.,2010; Saunders et al., 2012; Allan and Morgan, 2013; Kahl et al., 2015). Firstly, because of the different diffusivities of various elements in different crystals, this technique allows us to explore timescales ranging from millennia-centuries to hours-minutes. Moreover, diffusion modelling is performed in-situ on single crystals and can be performed in several parts of the same crystal, allowing a direct check on

internal efficiency and congruence of the method. This lends diffusion results a higher precision and accuracy.

The technique has been increasingly applied over the last 20 years of research on different kind of crystals, including plagioclases (Zellmer et al., 1999; Ruprecht and Wörner, 2000; Ginibre et al., 2002a, 2002b , 2004; Zellmer et al., 2003; Saunders et al., 2010; Shcherbakov et al.,2011; Druitt et al., 2012), olivines (Humler and Whitechurch, 1988; Costa et al., 2003, 2004; Martin et al., 2008; Kahl et al., 2011; Ruprecht and Plank, 2013; Rae et al., 2016), pyroxenes (Morgan et al., 2004, Allan et al., 2013; Barker et al., 2016), Fe-Ti oxides (Nakamura et al., 1995; Tomiya et al., 2013; Boudon et al., 2015), and quartz (Saunders et al., 2010; Matthews et al., 2011).

In this chapter, I will first give a detailed explanation of diffusion theory and the attendant mathematical formulations. Secondly I will give an overview of all parameters influencing and characterising diffusion. A review of previous studies and data on different diffusion coefficient will be presented, and we will finally describe how diffusion modelling can be applied to magmatic systems.

II.5.2. Theory and principles of diffusion

II.5.2.1. How to describe diffusion

Diffusion can be described as a thermally activated random movement of particles (atoms, molecules, ions) at the atomic scale. When a potential gradient exists in a material, this movement takes the form of a directed flux. Every kind of material can be affected by diffusion (gas, liquids, magmas, glasses, crystals). During their growth, crystals can be affected by sudden changes in the intensive storage parameters of the magma (pressure, temperature, oxygen fugacity, water fugacity). These changes are recorded as variably-strong zoning patterns with cores and rims of crystals exhibiting different compositions. As a consequence, crystals bear a chemical potential gradient which represent a disequilibrium condition inside their structures. Diffusion of atoms in the structure of crystals acts over time to chemically re-equilibrate crystals and restore a homogeneous composition from the core to the rim.

Diffusion mechanisms

In a crystal, diffusive transport is the sole mechanism enabling atoms to move from one crystal site to another. There are four different recognized displacement mechanisms in the crystal lattice: position, rotational, distortional and substitution disorders (Hazen and Navrotsky, 1996). Diffusion acts using the last of these mechanisms, deriving from changes in the crystallographic sites in between two or more atoms in the crystal lattice. While position, rotational and distortional disorders require small displacements of atoms (of the order of 0.2-0.5 Angstrom), substitution disorder implies larger movements of several Angstrom. For this reason the displacement of atoms from one crystallographic site to another needs to surpass a certain energetic threshold linked with the jumping distance in between the two sites.

The substitution disorder can act itself by way of different mechanisms: interatomic exchange, and/or the punctual default mechanism (Fig.II.9). The first mechanism can be described as a simple (two atoms) or a cyclic (three or more atoms) exchange in the crystal lattice where the repulsion energy in between atoms acts in a positive way, forcing atoms to move in a circular permutation (Fig.II.9.1 and 2). The punctual default mechanism (Fig.II.9.3, 4 and 5) involves migrations of atoms from one site to a neighbouring empty one (vacancy), and is the mechanism by which chemical gradient re-equilibration is realised.

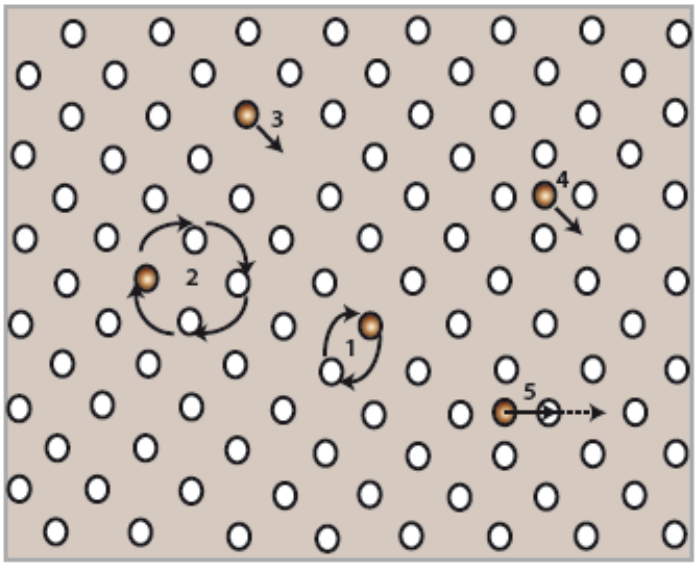

Figure II.9: Mechanisms of substitution disorder in the crystalline lattice.*1) Simple interatomic exchange; 2) cyclic interatomic exchange; 3) vacancy migration; 4) direct interstitial mechanism; 5) indirect interstitial mechanism; (modified from J. Philibert, Diffusion et transport de matière dans les solides; Monographie de Physique).*

Considering the total volume of a material, migrations of atoms from one site to another (punctual default mechanism) can occur by three main mechanisms: volume diffusion, grain boundary diffusion and surface diffusion.

Volume diffusion, the prevalent and most efficient mechanism, comprises all diffusive movements inside the crystal lattice from one atomic site to another. As a function of the crystallographic properties of the material, volume diffusion may be isotropic (magmas, glasses and isometric crystals) or anisotropic (un-isometric crystals such as pyroxenes and feldspars). Regardless of the crystal structure, volume diffusion requires the presence of crystal lattice defects (dislocations, point defects, vacancies, interstitial atoms) in order to operate. The most common diffusion mechanism involves vacancies (charge-balanced defects within the crystal where an ion is missing). Vacancies constitute an energetically favourable site for diffusion, as a jump to a vacancy requires less energy than an exchange of atoms in between two different crystal sites (Costa and Morgan, 2010).

Two main kinds of vacancies are present in crystals:

-intrinsic vacancies

-extrinsic vacancies

Intrinsic vacancies are prevalent at higher temperatures, as higher temperatures lower the free Gibbs energy and increase the configuration entropy of the crystal. Extrinsic vacancies are part of the proper crystal structure and are linked with substitution in the crystal lattice between ions with different ionic charge: for example the substitution $3Ca^{2+} \rightarrow 2Eu^{3+}$ in the structure of plagioclases, or the substitution $3Fe^{2+} \rightarrow 2Fe^{3+}$ in the structure of orthopyroxenes, creates a ionic vacancy and in turn promotes crystal lattice diffusion.

While the number of extrinsic vacancies is fixed by the composition (chemistry) and the structure of the crystal lattice, the number of intrinsic vacancies is dependent on temperature: increasing temperature fosters the formation of vacancies but also the jump of atoms into empty sites (Costa and Morgan, 2010). Accordingly, higher temperatures favour diffusion processes in crystals.

Grain boundary diffusion can be described as a diffusive movement along phase interfaces (crystal-crystal or crystal-melt interface). At low temperature, this is the prevalent mechanism and is helped by the defects widely present in the external structure of crystals.

Terminology

Diffusion in crystals can be distinguished also according to the specific diffusing element: i. Self diffusion; ii. Tracer diffusion; iii. Chemical diffusion (Costa and Chakraborty, 2008).
Self diffusion corresponds to the iso-chemical diffusion of an isotope, while tracer diffusion refers to diffusion of a trace element (<1 wt%) in a multi-component system with no chemical compositional gradient. Both these types of diffusion exclude the presence of a chemical or compositional potential gradient, meaning that the crystals can be considered a chemically homogeneous medium. However it has to be considered that self- and tracer- diffusion coefficients are usually dependent on composition (Chakraborty, 1997).
When a chemical potential gradient in major, minor, or trace elements is present in the mineral structure, chemical diffusion occurs to re-equilibrate the composition. In this case the movement of atoms takes the form of a flux (J). Chemical diffusion can be binary or multi-component. The case of binary diffusion, also called interdiffusion, includes diffusion in all systems that can be considered binary, such as Fe-Mg diffusion in olivines and orthopyroxenes. Most natural magmatic systems are multi-component (Cussler, 1976; Lasaga, 1979; Ghiorso, 1987; Trial and Spera 1994; Kress and Ghiorso, 1993, Liang et al., 1997; Mungall et al., 1998), but to ease processing and calculations they are usually treated as binary systems.

II.5.2.2. Macroscopic description of diffusion

Diffusion can be described using the Fick's laws (Adolf Fick, 1855). The presence of a driving force in the medium, such as a chemical potential gradient, will lead to a flow of atoms in a specific direction which can be described using the first Fick's law as:

$$J = -D\,\partial C/\partial x \qquad \text{(II.4)}$$

Where J is the flux (mol/m^{2}s), D is the diffusion coefficient (m^2/s), C is the concentration of the element considered in the medium (in kg/m^3 or in mol/m^3), x is the distance (m) and $\partial C/\partial x$ is the concentration gradient (Fig.II.10). The negative sign in the formula (II.4) indicates that the direction of the flux J is contrary to the direction of the chemical potential gradient. Here a one-dimensional flow (along x axis) is considered (Fig.II.10).
The diffusion coefficient is thus defined as the proportionality constant in between the flux (J) and the driving force (the concentration gradient $\partial C/\partial x$).

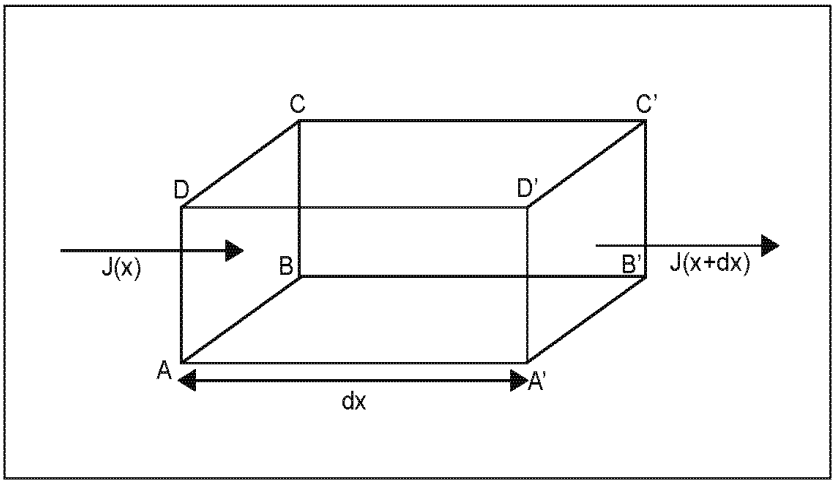

Figure II.10: Diffusion through the surface ABCD of an element of volume *(modified from Crank, 1975; The Mathematics of Diffusion).*

Nevertheless, Fick's first law does not take into consideration any time-dependence and is thus valid only in steady-state regimes, while most diffusion studies need to analyze evolution of diffusion profiles over time (in unsteady-state regimes).

In unsteady-state regimes, in order to consider flux evolution in both time and space, it is necessary to combine Fick's first law with a mass balance equation of the form:

$$\frac{\partial \mathrm{J}}{\partial \mathrm{x}} = - \frac{\partial \mathrm{C}}{\partial \mathrm{t}} \qquad \text{(II.5)}$$

Combining equations (II.4) and (II.5) we obtain the general diffusion equation:

$$\frac{\partial \mathrm{C(x,t)}}{\partial \mathrm{t}} = \frac{\partial}{\partial \mathrm{x}} * \left(D * \frac{\partial \mathrm{C(x,t)}}{\partial \mathrm{x}}\right) \qquad \text{(II.6)}$$

This equation describes how the concentration changes with time at any point of a concentration profile within a crystal. As it is a second-order partial derivative equation, equation (II.6) cannot be solved when D is dependent on concentration (so on both the parameters x and t). If we then consider the diffusion coefficient D to be constant with space (distance x), equation (II.6) can be written as follows:

$$\frac{\partial C(x,t)}{\partial t} = D * \frac{\partial^2 C(x,t)}{\partial x^2} \quad \text{(II.7)}$$

This equation, usually named Fick's second law, can be solved analytically for simple systems. The different solutions existing for this equation depend on the assumed initial and boundary conditions and can be expressed in the form of different diffusion profiles.
If generalized to a three dimensions flow, the two Fick's laws can be written as:

$$J = -D \text{ grad } C \quad \text{(II.8)}$$

$$\frac{\partial C(x,t)}{\partial t} = \text{div } (D \text{ grad } C) \quad \text{(II.9)}$$

II.5.2.3. Solutions of diffusion equation

Solutions of the diffusion equation (II.8) can be analytical or numerical. Analytical solutions (Crank, 1975) are generally in the form of an Erf (error function), a Bessel function or an exponential law, changing as a function of the specific medium considered (i.e. whether it is isotropic or anisotropic).
We will limit ourselves here to the description of three analytical solutions used to explain diffusion in the most common geological contexts (Philibert, 1985).

(1) Planar source- thin superficial layer (diffusion in a finite solid)

In this first case the diffusing species is deposited as a thin superficial layer at the surface of the sample, or in between two samples of identical chemical composition. The solution of diffusion equation in this case can be written in the form:

$$C(x,t) = M/(2\sqrt{\pi}Dt) \exp(-x^2/4Dt) \quad \text{(II.10)}$$

Where C is the concentration, M is the amount of diffusing material, D is the diffusion coefficient and x is the diffusion distance. The evolution over time of this kind of profile is represented in Figure II.11. The initial distribution is a Dirac distribution (infinite values when x=0 and zero value as $x \rightarrow \infty$) which evolves as a Gaussian distribution with the square root of time (Fig.II.11). This solution is valid only if the layer deposited on the surface of the sample is "thin", i.e. of a thickness negligible compared to the diffusion distance x.

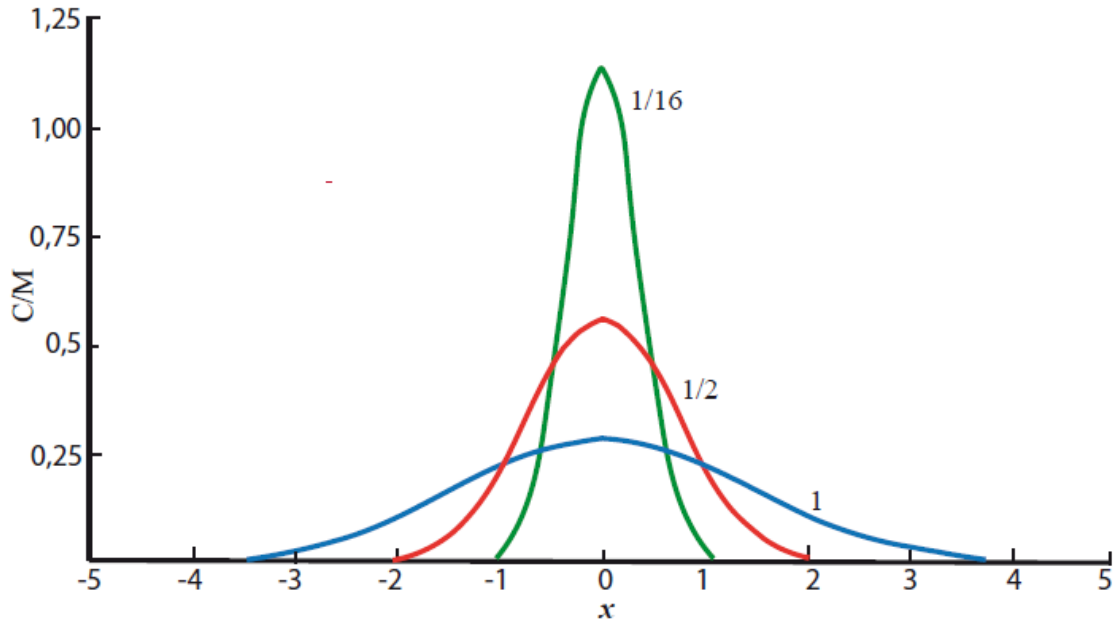

Figure II.11: Diffusion in a finite solid. Evolution of the concentration profile as a function of time*. C/M = concentration/amount of diffusing material. The evolution of concentration is shown for three values of Dt (1, 1/2 and 1/16). (modified from J. Philibert, 1985; Diffusion et transport de matière dans les solides; Monographie de Physique).*

(2) Planar source- Constant superficial concentration (diffusion in a semi-infinite medium)

In the case of a constant superficial concentration, the initial concentration at time t=0 is considered to be equal to $c(0,x)= c_0$ and boundary conditions are fixed in the way that for all $t>0$, $x=0$ and $c(0,t) = c_s$.

The solution can be written in the form:

$$(c-c_s)/(c_0-c_s) = \text{erf}\,(x/2\sqrt{Dt}) \qquad \text{(II.11)}$$

The temporal evolution of this kind of diffusion profile is presented in Figure II.12. The left part represents a desorption case and the right part an absorption case.

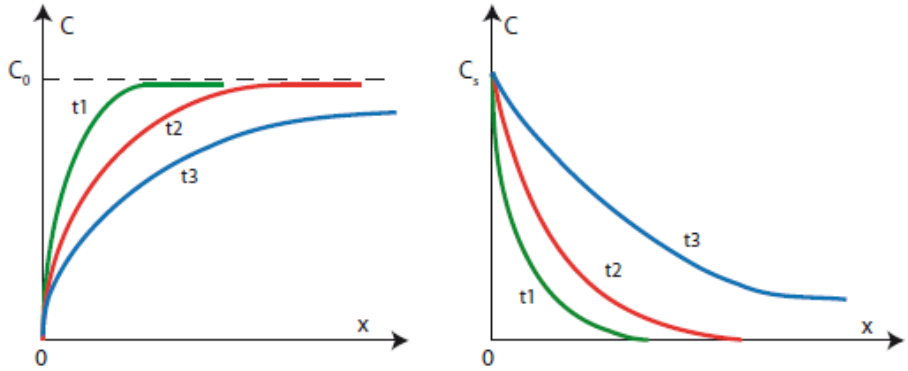

Figure II.12: Diffusion in a semi-infinite medium. *Evolution of the diffusion profile as a function of time (t1, t2 and t3) for desorption (left) and for absorption (right) ; (modified from J. Philibert, 1985; Diffusion et transport de matière dans les solides; Monographie de Physique)*

(3) Planar source : infinite initial distribution

In this third case a concentration of c1 in x>0 and c2 in x<0 are fixed as initial conditions. This describes an abrupt initial profile, symmetric and with concentration at the interface (x=0) equal to ½(c1 + c2). The solution of diffusion equation in this case is:

$$(c-c_1)/(c_2-c_1) = ½ \text{ erf } (x/2\sqrt{Dt}) \qquad \text{(II.12)}$$

The evolution of the profile with time is presented in Figure II.13. This analytical solution is used to solve interdiffusion problems in crystals and will be used here to solve 1D Fe-Mg interdiffusion modelling in orthopyroxene crystals. Starting from a simple step function (initial conditions), we model the evolution of the compositional profile in a sigmoid shape as a function of time.

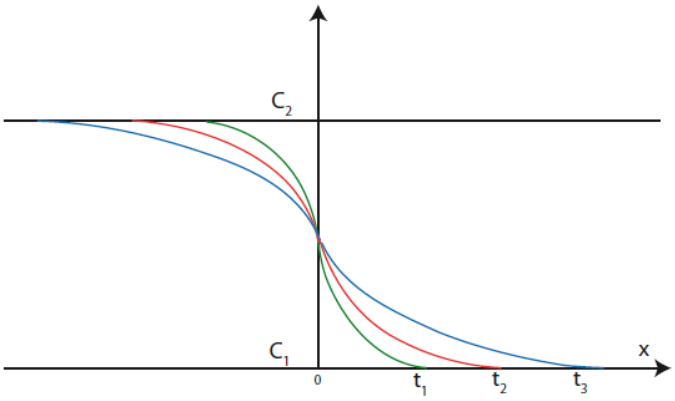

Figure II.13: Diffusion with an infinite initial distribution. *Evolution of the concentration profile as a function of time in the case of interdiffusion. The initial condition is a step function with fixed composition at the interface (x=0), (modified from J. Philibert, 1985)*

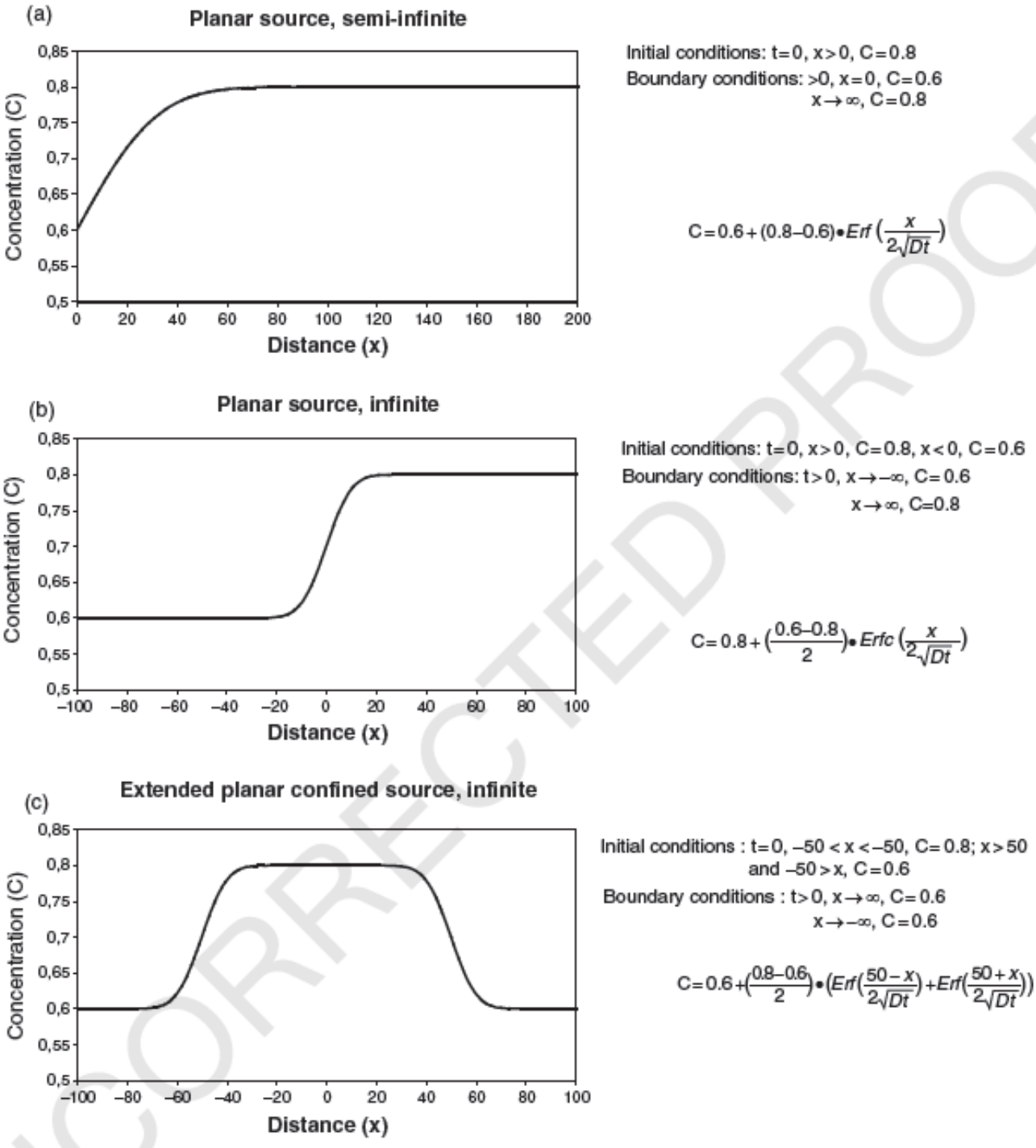

Figure II.14 : Three possible analytical solutions of diffusion equation *; (a) Semi-infinite planar source, applied for chemical homogeneous xenocrysts incorporated in a melt ; (b) infinite planar-source, applied for abrupt changes in crystals composition far from edges ; (c) infinite planar source, applied do model diffusion in the central portions of crystals. (from Costa and Morgan, 2010, solutions are from Crank, 1975).*

Figure II.14 summarizes three examples of analytical solutions for diffusion (Costa and Morgan, 2010): a) planar source in a semi-infinite medium, used to describe homogeneous crystals trapped in melt; b) planar source in an infinite medium, used to describe abrupt changes in crystal composition far from the edges; c) extended planar confined source in an infinite medium, used to model diffusion in the central parts of crystals. Nevertheless, the analytical solutions described here are nontrivial to apply in a practical geological context as a consequence of the variability of diffusivities and chemical potential gradients with initial chemical composition of minerals. In several crystals, the partition coefficient of many trace elements depends on the mineral composition itself, meaning that the concentration cannot be used as an automatic proxy for chemical potential gradient. Several numerical solutions are used to solve diffusion problems in geological contexts (Press et al., 2007). Those solutions can be adapted to all type of boundary and initial conditions but typically have the direct disadvantage of being computationally intensive.

II.5.2.4. Parameters influencing diffusion

Temperature

In a geological context, several parameters influence diffusion in solid media (temperature, pressure, crystal composition and crystallographic orientation, oxygen and water fugacity).

Temperature plays the major role; indeed, volume diffusion depends on changes of the thermal state of the system. As described in section II.5.2.1, increasing temperature will increase the energy of the system, favour vacancy formation within the crystal structure, and enhance diffusion processes. The dependence of diffusion on temperature can be described using the empirical Arrhenius relation (Arrhenius, 1889),

$$D = D_0 \exp(-E_a/RT) \quad \text{(II.13)}$$

Where D_0 is the pre-exponential factor ($m^2 \cdot s^{-1}$), E_a is the activation energy ($J \cdot mol^{-1}$), R is the gas constant (8,314 $J \cdot mol^{-1} \cdot K^{-1}$) and T is the temperature (K).

When the Arrhenius relation is expressed in its logarithmic form:

$$\text{Log } D = \text{Log } D_0 - E_a/RT \quad \text{(II.14)}$$

a linear relation exists between LogD and 1/T (Fig.II.15), with $LogD_0$ being the intercept and $-E_a/R$ the slope of the line.

When diffusion coefficients are measured, experiments are performed at a range of temperatures and D_0 (pre-exponential factor) and E_a (activation energy) are obtained from a plot of LogD= f(1/T) at a given pressure.

All other parameters (pressure, crystal composition, crystallographic orientation, oxygen and water fugacity) have a smaller effect on diffusion and are usually incorporated in the pre-exponential factor of the Arrhenius relation (Dohmen and Chakraborty 2007a, Costa and Chakraborty 2008). These are discussed here to obtain a complete overview of diffusion processes.

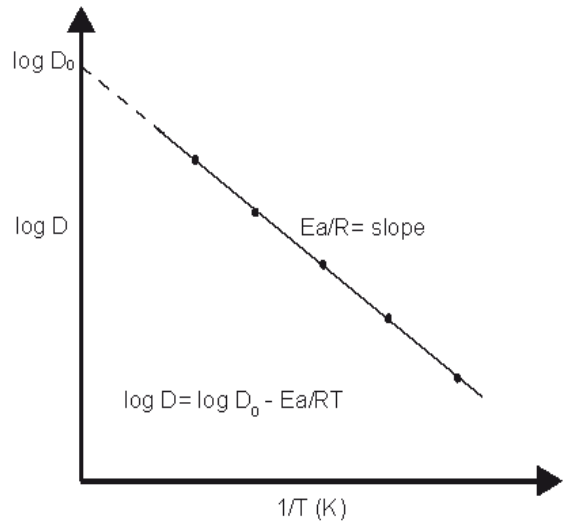

Figure II.15: Arrhenius relation in between the inverse of temperature and the logarithm of the diffusion coefficient *(modified from Freer, 1981).*

Pressure

It has been demonstrated by Mehrer (1996) that pressure plays a significant role in determining the volume of activation of diffusion (ΔV), corresponding to the isothermal change in volume inside the crystal when an atom jumps from one site to another in the crystal lattice. The activation volume generally has a positive value, meaning that at a fixed temperature, diffusivities decrease with increasing pressure. If we consider the atomistic description of diffusion, pressure can produce changes in the disorder volumes of crystals (defined as the difference in between the crystal volume in the disordered situation and the crystal volume in the ordered situation). As such, pressure can produce a major effect on order-disorder kinetics inside crystals, decrease cation mobility, and change the diffusion mechanism in the crystal lattice (Hazen and Navrotsky, 1996). For orthopyroxenes, where Fe is generally in the octahedral site M2, several studies have demonstrated that an increase in

the disorder level of the crystal structure (so of the number of Fe atoms in the site M1) produces an increase in the volume of the crystal cell (Domeneghetti et al., 1985; Domeneghetti et al., 1995 ; Hazen et al.,1993a). This suggests that an increase of pressure promotes a decrease in disorder volume, with a more ordered crystal structure.

The effect of pressure on diffusion is generally expressed as:

$$D_0 \alpha \exp (PV/RT) \quad \text{(II.15)}$$

where P is the pressure, V is the activation volume, R the constant of gas and T the temperature.

Activation volumes typically have low values (10^{-5}-10^{-6} m^3 mol^{-1}), and are generally too small to have significant consequences on diffusion at relevant crustal pressures (1 to 4 kbar).

Oxygen fugacity

Oxygen fugacity is a key parameter to be considered when the crystal structure may be influenced by changes in the oxidation state of the system. This is particularly important for minerals containing Fe (in both Fe^{2+} and Fe^{3+} oxidation states). Returning to the example of orthopyroxenes, for these crystals an increase in oxygen fugacity implies an increase in the amount of Fe^{3+} with respect to Fe^{2+} in the crystal structure. The substitution of Fe^{2+} with Fe^{3+} ($3Fe^{2+} \rightarrow 2Fe^{3+} + V$, where V denotes a vacancy) produces the formation of more vacancies in the crystal lattice, and so causes an increase of volume diffusion.

For all Fe-Mg silicate minerals, experimental studies have demonstrated that the dependence of diffusion from oxygen fugacity can be written of the form $D \boldsymbol{\alpha} fO_2^m$, where the exponent m is based on experimental results or on theoretical modelling of diffusion (Cherniak, 2001 for diffusion of Pb in pyroxenes; Chakraborty and Ganguly, 1991 for Fe-Mg interdiffusion in garnets; Buening and Buseck, 1973 for Fe-Mg interdiffusion in olivines; Ganguly and Tazzoli, 1994, Allan et al., 2013 and Dohmen et al., 2016 for Fe-Mg interdiffusion in orthopyroxenes). For the specific case of Fe-Mg interdiffusion in orthopyroxenes—on the basis of results obtained on olivine (Buening and Buseck, 1973) and garnet (Charkraborty and Ganguly, 1991)—Ganguly and Tazzoli (1994) have speculated a relation of the form:

$$D\alpha \left(\frac{fO2_{sample}}{fO2_{reference}}\right)^n \quad \text{(II.16)}$$

where n = 1/6.

In their study of Fe-Mg interdiffusion in orthopyroxenes of Oruanui eruption, Allan et al. (2013) considered this relation and derived from Ganguly and Tazzoli (1994) a more general expression of the form:

$$\log D_{Fe-Mg}\left[\frac{m^2}{s}\right] = -9.54 + 2.6\times X_{Fe} - \frac{12530}{T[K]} + \frac{1}{6}\times \log\frac{fO_2\,(sample,T)}{fO_2(IW,T)} \quad \text{(II.17)}$$

Where -9.54 is logDo [m^2/s], X_{Fe} is the crystal composition in terms of molar fraction of the ferrosilite component, T is the temperature in Kelvin, fO_2 (sample, T) and fO_2 (IW,T) are the oxygen fugacity of the sample and the iron-wustite buffer at a certain temperature.

The more recent study of Dohmen et al. (2016) re-opened the discussion about oxygen fugacity dependence in orthopyroxenes. They measured the Fe-Mg interdiffusion coefficient on two Mg-rich orthopyroxenes (Fs_1 and Fs_9) in the range 870-1100 °C for temperature and 10^{-11} and 10^{-7} Pa for oxygen fugacity. Different results were obtained for the two orthopyroxenes.

While for the less Fe-rich composition (Fs_1) a simple Arrhenius relation was obtained to describe diffusion, for the more Fe-rich composition (Fs_9) the authors identify a clear dependence of diffusivity on oxygen fugacity. Data for this orthopyroxene are fitted with the following equation:

$$logD^{c}{}_{Fe-Mg} = \log D_0 - \frac{Q}{\ln(10)RT} + n\,log\,fO_2 \quad \text{(II.18)}$$

where Q= 308 ± 23[kJ/mol], log (D_0 [m^2/s]) = 5.95 ± 0.83 and n= 0.053 ± 0.027.

Here the exponent *n* is equal to 1/20 (instead of the 1/6 used by Allan et al., 2013), arguing for a minor fO_2 dependence of the diffusion coefficient on oxygen fugacity.

When we compare equation II.17 (Ganguly and Tazzoli, 1994 with an applied oxygen fugacity correction; Allan et al., 2013) with equation III.18 (Dohmen et al., 2016), it appears that the speculated fO_2 correction applied by Allan et al. (2013) overestimates the fO_2 dependence, making calculated diffusivities about one order of magnitude higher than the measured values under common geological conditions (close to NNO buffer). On the contrary, when the two parameterizations are compared without including the oxygen fugacity correction, they appear to be very consistent with each other.

From the different studies it seems clear that the effect of oxygen fugacity on diffusivity is still at the centre of debate in diffusion modelling of Fe-bearing crystals (Ganguly and Tazzoli, 1994; Dimanov and Wiedenbeck, 2006; Allan et al., 2013; Mueller et al., 2013; Dohmen et al., 2016). Future experimental works may provide further advances in this topic.

Mineral composition and anisotropy

The composition of a crystal and its eventual anisotropy can also play an important role in the determination of its diffusion coefficient. It has been demonstrated for several silicates (plagioclases, pyroxenes, olivines) that the enthalpy of formation of vacancies—in turn, the diffusion coefficient of some major and trace elements—is strongly dependent on crystal composition.

This effect has been documented in plagioclases, where the diffusion coefficient of Mg, Sr, Ba, Pb is higher for Na-rich plagioclases (Albite) and lower for Ca-righ plagioclase (Anorthite) (Blundy and Wood, 1991; Van Orman et al., 2014). Fe-Mg crystals such as orthopyroxenes and olivines also bear evidence of dependence of diffusion on the molar fraction of X_{Fe}: crystals with a Fe-rich composition have more vacancies in their structure, as Fe can be present in its two oxidation states and facilitates charge balancing when a vacancy forms.

The effect of composition on diffusion can be expressed as:

$$D_0 \alpha \exp(\alpha X_i) \qquad \text{(II.19)}$$

Where α is constant and X is the molar fraction of the element constituting the mineral.

For the effect of composition on diffusion in orthopyroxene, Ganguly and Tazzoli, (1994) quantify a composition dependence of the form $\log D_{Fe\text{-}Mg} \alpha 2.6X_{Fe}$. Dohmen et al., (2016), however, do not obtain a quantitative constraint on the compositional dependence of $D_{Fe\text{-}Mg}$, suggesting a somewhat weaker dependence compared to that estimated by Ganguly and Tazzoli (1994).

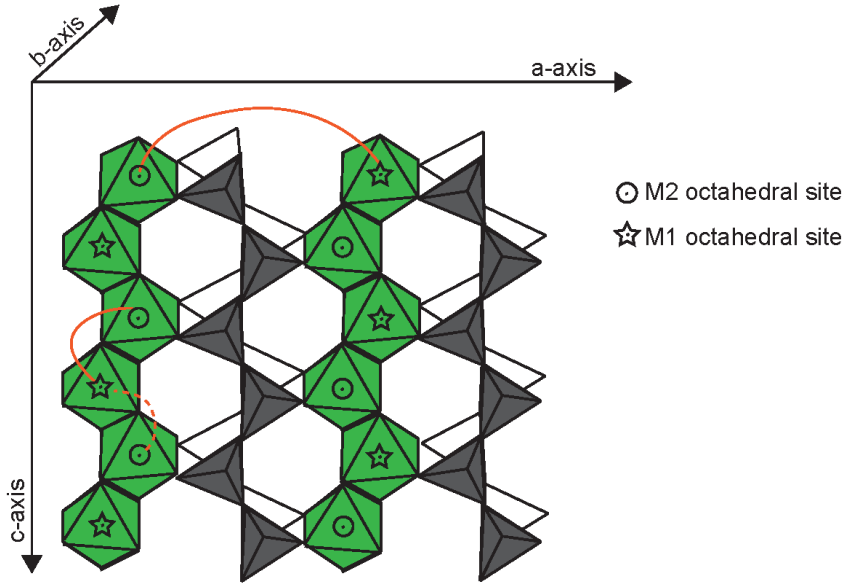

Figure II.16: Simplified orthopyroxene crystal structure. *Arrangement of octahedral (in green) and tetrahedral (in grey) sites along the a- and c-axes of orthopyroxenes: octahedral M1 sites are represented with stars while octahedral M2 sites with circles. Orange lines indicate the jump distance in between two octahedral sites along the different crystal directions. Jump distance along the a-axis is longer than along the c-axis.*

The effect of anisotropy depends directly on the inner structure of crystals, thus on the jump distance necessary for diffusion in the different directions (Fig.II.16). When the crystal structure is anisotropic, diffusion will operate faster in the crystal direction in which jump distances are shorter. For almost all tetragonal, trigonal, hexagonal and orthorhombic crystals, two or three different diffusion coefficients can be calculated as a function of the crystallographic direction. For monoclinic and triclinic crystals, diffusivities along the main crystal axes are less extensively studied (Brady and Cherniak, 2010; Zhang, 2010).

In crystals of orthopyroxene an important effect of crystal orientation has also been discussed. Orthopyroxenes belong to inosilicate groups, meaning the octahedral sites M1 and M2 (where Fe-Mg substitution occurs) are closer in the c-direction then on the a- and b- one (Fig.II.16). For this reason, diffusion in orthopyroxenes is considered anisotropic according to the following order: $D^{c}_{Fe\text{-}Mg} >> D^{b}_{Fe\text{-}Mg} >> D^{a}_{Fe\text{-}Mg}$ (Ganguly and Tazzoli, 1994), with $D^{c}_{Fe\text{-}Mg} \approx 3.5\ D^{a}_{Fe\text{-}Mg}$ (at 800-1100 °C, Dohmen et al., 2016).

An important anisotropy effect has been observed in the diffusion of oxygen. Having a large ionic radius, oxygen diffusion throughout the crystal lattice is highly dependent on ionic porosity of crystals (the percentage of ionic gap in the total volume of the crystal lattice), which can change significantly as a function of the considered direction in the lattice.

Specifically, the direction characterized by a higher ionic porosity also presents higher diffusivity. Nevertheless, whereas total ionic porosity has already been studied in several crystals (Sippel, 1963; Dowty, 1980; Connolly and Muehlenbacks,1988; Fortier and Giletti, 1989; Zheng and Fu, 1998), directed ionic porosity remains still to be constrained. To date, no detailed study is present in literature.

Final diffusion equation

If we now consider together all influencing parameters, the final equation for diffusivities can be written in the form:

$$D = D_0 \exp\left(\alpha X_i + \frac{-E_a + PV}{RT}\right) \times (fO_2)^m \times (fH_2O)^n \qquad \text{(II.20)}$$

However, for most of the diffusion coefficients determined in literature, only the temperature- and compositional-dependencies have been quantified. For several Fe-bearing minerals (orthopyroxenes, clinopyroxenes, garnets, olivines) the influence of oxygen fugacity on diffusion remains unclear. Particular care has to be taken when experimentally-determined diffusion data are selected from literature as the diffusion coefficient they report is valid only at the experimental conditions (P,T, fO_2) of the associated study and cannot be automatically extrapolated to other physical conditions.

II.5.2.5. Experimental determination of diffusion coefficient

Diffusion coefficients can be retrieved from experiments using different protocols as a function of the mineral-element couple and the conditions (T, P, fO_2) under consideration. Crystals used for these experiments are usually compositionally homogeneous gem quality crystals, without inclusions, imperfections, fractures, or deformations. An "artificial" chemical gradient is created in the crystal by doping it in a trace element or an isotope (immerging the crystal in a liquid or a powder with the same major element composition as the crystal but doped in trace element or isotope), or depositing on the crystal a thin layer of a different composition (for example a layer of olivine on a clinopyroxene). The diffusive couple is annealed (brought to the P,T, fO_2 condition required for the experiment) and kept under fixed conditions for a determined period of time. Ideally, only one parameter is modified during experiments while all the others are kept constant. However, strong interdependence of temperature and oxygen fugacities makes it difficult to change temperature at fixed oxygen fugacities. For this reason, experiments are usually conducted at different temperatures along a precise oxygen buffer (Costa and Morgan, 2010).

The final diffusion coefficient at each temperature can be calculated from the time of the experiment and the diffusion profile. When the experiment is repeated for several temperatures, the Arrhenius relation can be calculated and D_0 (the pre-exponential factor) and Ea (the activation energy) can be extracted (Fig. II.17).

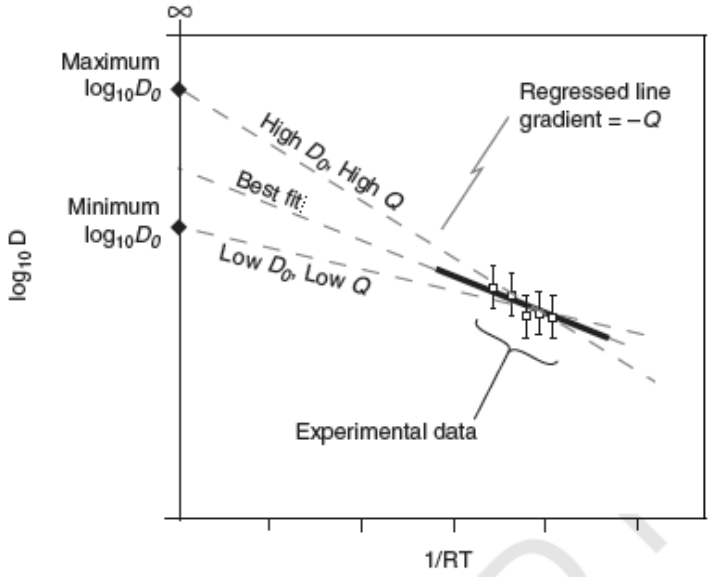

Figure II.17: Arrhenius plot of experimental data obtained at different temperatures*. The graph shows uncertainties on the pre-exponential factor and on the activation energy are not independent: high D_0 uncertainty should be processed with the high Q value to calculate one of the possible end-member diffusivities, and vice versa. (from Costa and Morgan, 2010).*

Uncertainties of experimental values strictly depend on the diffusive couple of interest and on the analytical techniques used to perform the study. The uncertainty at 1-sigma is usually in the range of 0.1-0.2 log unit, which reflects uncertainties of about 50% for D_0 and about 10% for Ea.

II.5.3. Previous studies

II.5.3.1. Diffusion in minerals

The study of diffusion in minerals started in the beginning of 20th century (Penrose, 1914; Van Orstrand, 1915; Reynolds, 1947; Garrels, 1949). However a real development of diffusion studies in minerals, magmas, and glasses, started with the refinement of analytical techniques such as the electron probe micro analyser (EPMA) and the secondary ion mass spectrometry (SIMS). These new techniques allowed the analysis of samples at a microscopic scale with much more detail and spatial resolution than previously attainable. The first experimental studies on diffusion coefficient calculation for different kind of minerals started in the 1960-70s. Diffusion studies have focused predominantly on silicates minerals, with more attention on feldspars (16%), followed by pyroxenes (14%), olivines (12%), and garnets

(8%). For non-silicate minerals, the best studied are phosphates (8%) and oxides (6%), followed by carbonates (4%) and sulphides (3%) (Fig. II.18.a).

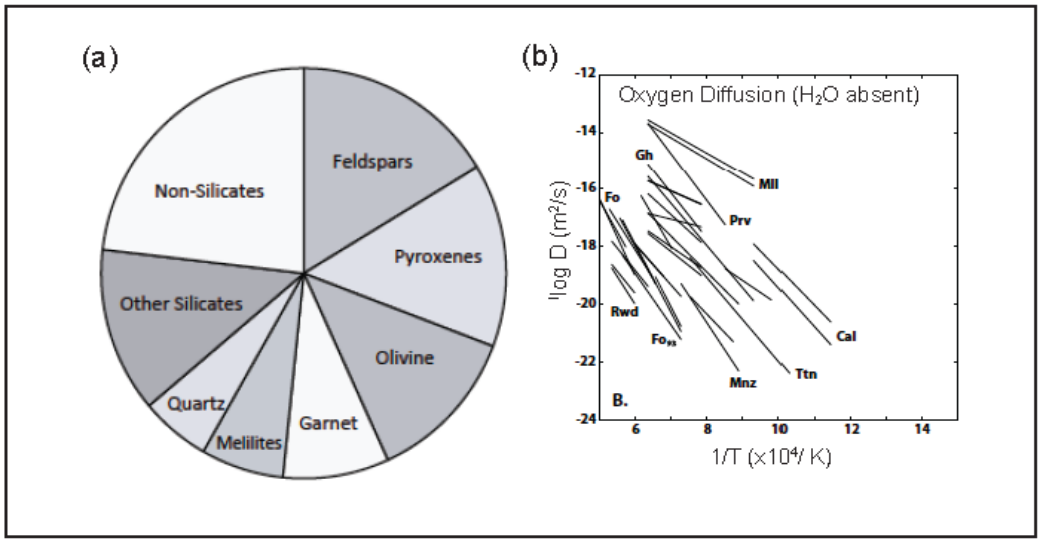

Figure II.18 : Diffusion in minerals *: a) graph of percentage of study of diffusion for different class of minerals: silicates are the most studied minerals (≈ 70 %) with feldspars, orthopyroxenes and olivine representing the largest part of studies currently known in literature; b) Arrhenius plot for the anhydrous (in absence of water vapor) self-diffusion of oxygen in different kind of minerals (Fo= forsterite ; Cal= calcite ; Rwd=Ringwoodite ; Ttn= titanite ; Gh= Gehlenite ; Mnz= Monazite ; Prv= Perovskite ; Mll= Melilite), (from Brady and Cherniak, 2010).*

To analyse and compare diffusion in different kinds of minerals, several types of relation can be used. The first of these is the Arrhenius relation, describing a linear relation between the logarithm of the diffusion coefficient and the inverse of temperature, where the intercept is the logarithm of the pre-exponential factor (D_0) and the slope is the ratio Ea/R (where Ea is the activation energy and R is the ideal gas constant). An example of Arrhenius diagram for comparing diffusion of oxygen in different minerals is presented in Figure II.18.b.

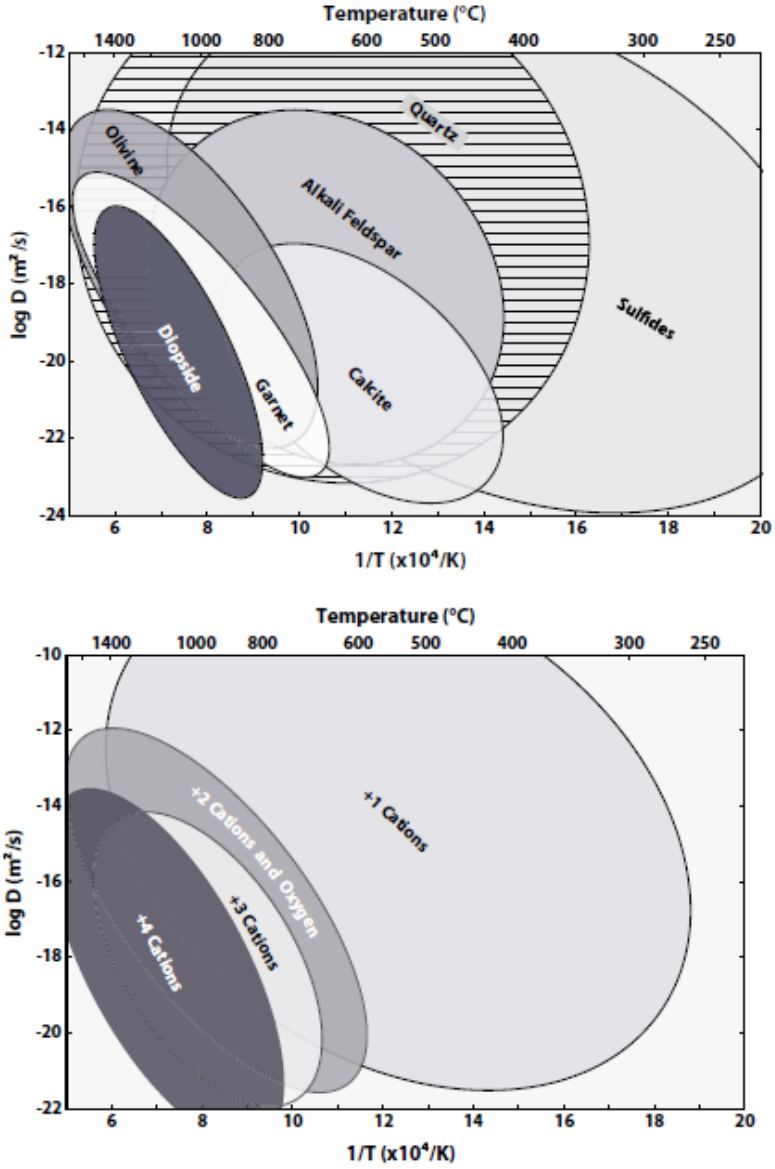

Figure II.19: Arrhenius plot of diffusion coefficient for all elements in different kind of minerals. *Top diagram: schematic Arrhenius diagram representing different diffusion domains measured for some silicate and non-silicate minerals typical of magmatic environment; bottom diagram: schematic Arrhenius diagram of different diffusion domains measured for several (monovalent, bivalent, trivalent and tetravalent) cations. It appears that, at the same temperature, a tetravalent element has lower diffusivity than a monovalent one (from Brady and Cherniak, 2010).*

Figure II.19 shows different diffusion coefficients measured for all elements (except H, He, Ar and Li) for silicates and non-silicates minerals. The graph shows that the diffusion coefficient is heavily dependent on the size and charge of the element under consideration: at

any given temperature, elements with a higher ionic charge have smaller diffusion coefficients and higher activation energies (Ea).

A second way to analyse diffusion in crystals is to look at the Meyer-Mendel effect, also known as the compensation effect. The Meyer-Mendel effect is a positive linear relation existing between the activation energy (Ea) and the logarithm of the pre-exponential factor (D_0) (Fig.II.20), known for diffusion in silicate glasses (Winchell, 1969; Winchell and Norman, 1969), diffusion of cations in basalts (Hofmann, 1980) and diffusion in silicates minerals (Hart, 1981). Indeed, it has been empirically demonstrated that, for a given mineral, in an Arrhenius diagram all the linear trends converge to one single point (so one single D_0) when the inverse of temperature (1/T) tends to zero, suggesting a relation in between Ea and D_0. If diffusion is ideally following the compensation relation, Arrhenius lines converge precisely to one point, which is defined as the isokinetic or the crossover temperature (i.e. the temperature at which all elements have the same diffusion coefficient in respect of the same mineral).

In the compensation effect diagrams elements can be distinguished by their charge: comparing bivalent, trivalent and tetravalent elements. With an increase in the element charge, a decrease in line slope is observed (Fig.II.20). This can be linked to a direct effect of the ionic charge on the mobility of the element itself: elements with a low ionic charge will be more mobile and will require lower activation energy than elements with a higher ionic charge (Brady and Cherniak, 2010; Fig.II.20).

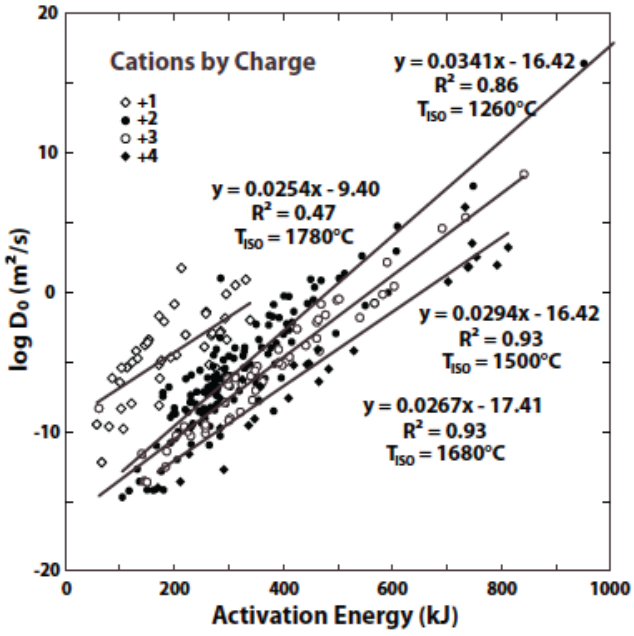

Figure II.20: Compensation diagram for diffusion of cations. *All minerals of the database of Brady and Cherniak (2010) are represented. Cations are arranged by charge; as charge increases from +1 to +4 a decrease of the compensation line slope can be observed; (from Brady and Cherniak, 2010).*

A third possibility to compare the diffusion coefficient of different elements relies on the estimation of the ionic porosity of a medium. The ionic porosity (Z) is a measure of the mean atomic density of a mineral (percentage of the volume of the crystal cell unoccupied by ions). Several studies (Dowty, 1980; Fortier and Giletti, 1989; Dahl, 1996; Zheng and Fu, 1998; Zhao and Zheng, 2007) have described and analysed the link between the inner structure of crystals (free sites in the lattice) and the mobility of different elements and chemical species, also in relation to their size and ionic charge. Indeed, it has been demonstrated that diffusivities and activation energies can depend on ionic porosity and that linear relations exist between the two parameters. However, Brady and Cherniak (2010) present a complete database of porosity-diffusivity trends showing only a low correlation between the two parameters (the best correlation being for oxygen).

II.5.3.2. Diffusion in pyroxenes

First studies

For pyroxenes, a large literature base of diffusion coefficient studies already exists. Several diffusion coefficients are already known for major, minor and trace elements. The study of cations diffusion in pyroxenes started in the 1970s, when more precise analytical techniques started developing (EPMA, SIMS, Laser ablation). The focus on pyroxene study derives from their wide presence in several geodynamical contexts; indeed they represent one of the major mineral phases in the lower crust and upper mantle, in terrestrial and extraterrestrial materials (Cherniak and Dimanov, 2010).

The importance of studying pyroxenes also stems from their particular crystal structure, which is able to adapt as a function of changes in temperature, pressure or oxygen fugacity. As a consequence, changes in these physical parameters affect the structure of crystals, in turn influencing diffusion exchanges inside the lattice.

Cherniak and Dimanov (2010) present a complete overview of all previous studies performed on diffusion in pyroxenes. The first studies addressing the interdiffusion of major divalent cations in pyroxenes were focused on extra-terrestrial material and on the difference in cooling rates and annealing rate between different extra-terrestrial assemblages. These studies examined lunar basalts, and performed diffusion modelling in olivine and orthopyroxene crystals on the basis of Fe-Mg interdiffusivity values calculated by Buening and Buseck, (1973), Huebner et al. (1975), Huebner (1976), Stanford and Huebner (1979) and Huebner and Nord (1981).

In the early 1980s, the first direct experiments to measure diffusion coefficient were undertaken, for example in diopside crystals (self diffusion of ^{45}Ca et ^{57}Fe, McCallister et al., 1979; interdiffusion Al-Fe and diffusion of ^{26}Mg and ^{43}Ca, Freer et al., 1982). However, these studies do not present consistent results on diffusion, but allowed the establishment of diffusivity boundary values for certain temperature, pressure, and major element ranges.
More detailed and consistent results were obtained by Brady and McCallister (1983) on cation interdiffusion in pyroxenes, starting from homogenization experiments at 2500 MPa and 1100-1250 °C on pigeonite lamellae deposited on diopside crystals. The results of Brady and McCallister (1983) are in agreement with the previous results of Freer et al. (1982), defining diffusivities values lower ($4x10^{-19}$ m^2/s at 1200 °C for Al and Fe and $7x10^{-19}$ m^2/s at 1250 °C for Ca and Mg) than those previously determined (McCallister et al., 1979 ; Sneeringer and Hart 1978 ; Seitz, 1973 ; Linder, 1955).
All studies performed prior to the 1980s have high level of uncertainties and are usually carried out at experimental conditions different from each other, making the data comparison quite difficult. Pressure (atmospheric for some studies and high pressure for others) and redox conditions are generally very different from one study to another and, moreover, the analytical technique used in this period did not have a sufficient spatial resolution to obtain well-defined diffusion profiles.

Recent studies

Only by the mid-1980s, with the ongoing development of microscopic analytical techniques (SIMS, RBS, NRA), were diffusivity measurements performed with a spatial and analytical resolution sufficient to allow the determination of diffusion profiles with a short diffusion length (x) and small compositional variations. In these years, diffusion modelling was increasingly employed to investigate the dependence of diffusion on the crystal composition, crystal lattice orientation, pressure, temperature and oxygen fugacity.

The first indirect estimation of the Fe-Mg diffusion coefficient in orthopyroxenes was performed by Ganguly and Tazzoli (1994). In this study, the Fe-Mg interdiffusion coefficient along the c- and b-axis of orthopyroxene was extracted from experimental data on intracrystalline exchange reactions, obtained by Besancon (1981), Anovitz et al. (1988) and Molin et al. (1991). These data included the disordering rate constant K+, the ordering rate constant K-, and the equilibrium distribution coefficient (K_D) of the Fe^{2+}- Mg fractionation

reaction between the M1 and M2 sites of orthopyroxene [Fe^{2+} (M2) + Mg (M1) ↔ Fe^{2+} (M1) + Mg (M2)]. Ganguly and Tazzoli (1994) interpret the constant of fractionation between the two sites (K_D) as a proxy of the diffusion coefficient for the intercrystalline Fe-Mg diffusion.

The final parameterization of Ganguly and Tazzoli (1994) is:

$$LogD(Fe\text{-}Mg)_{c\text{-}b}\ [cm^2/s] = -5.54 + 2.6\ X_{Fe} - 12530/T \qquad (II.21)$$

where XFe is the composition of crystal in terms of iron molar percent content and T is the temperature in Kelvin. This Ganguly and Tazzoli (1994) equation is valid for T= 500-800 °C, oxygen fugacity WI to WI+0.8 and XFe = 0.10-0.50.

These authors argue for diffusion anisotropy in orthopyroxenes, linked with the anisotropic structure of the crystals themselves, in which the octahedral sites (M1 and M2) are closer to each other in the c-axis direction and further apart in the a-axis direction. As a consequence diffusion anisotropy arises, with $D_c > D_b > D_a$.

The dependence of the diffusion coefficient on oxygen fugacity is briefly discussed by Ganguly and Tazzoli (1994). By analogy with results of Buening and Buseck (1973) on olivines and Chakraborty and Ganguly (1991) on garnet, they speculated that D(Fe-Mg) on orthopyroxenes varies approximately as $(fO2)^{1/6}$.

A further study of Klügel (2001) on iron-rich orthopyroxenes (in the temperature range 1050-1200°C and at QFM buffer) reports a diffusion coefficient of $D_{Fe\text{-}Mg} = 3 \times 10^{-19}$ m^2/s at T = 1130 °C. If extrapolated to higher temperatures and oxygen fugacities, the results of Ganguly and Tazzoli (1994) are in good agreement with those of Klügel (2001).

A recent experimental study has also been performed on clinopyroxenes by Müller et al., (2013), presenting results on the Fe-Mg interdiffusion coefficient along the c-axis of clinopyroxenes (Di93) under a range of experimental conditions (800-1200°C in temperature and 10^{-11} -10^{-17} bar in oxygen fugacity).

The final parameterization of Mueller et al. (2013) is:

$$D_{Fe\text{-}Mg} = 2.77(\pm 4.27 * 10^{-7}) \exp(-320.7 \pm 16.0\ kJ/mol/RT)\ [m^2/s] \qquad (II.22)$$

where D_0 =2.77± 4. 27* 10^{-7} [m^2/s] and Q (activation energy) = -320.7± 16.0 [kJ/mol/RT].

Mueller et al. (2013) use a simple Arrhenius equation to describe the effect of temperature on the diffusion coefficient. From their results, Mueller et al. (2013) do not argue for a dependence of diffusivities from oxygen fugacity in the range 10^{-11} to 10^{-17} bars.

These results are in contrast with those of Dimanov and Wiedenbeck, (2006), who found a dependence of the Fe-Mg interdiffusion coefficient on fO_2 (in the range $10^{-15} < fO_2 < 10^{-7}$). As the Fe content of starting samples from Dimanov and Wiedenbeck, (2006) and Mueller et al. (2013) is the same, Mueller et al. (2013) suggest that the observed difference could be related to the high Al content present in the crystal used for their study, preventing an efficient $3Fe^{2+} \rightarrow 2Fe^{3+}$ substitution in the crystal lattice.

More recently Dohmen et al., (2016) have performed a study on Fe-Mg interdiffusion in orthopyroxenes using olivine lamellae ($Fo_{30}Fa_{70}$) and Mg-rich orthopyroxene crystals (Fs_9 and Fs_1). Experiments were performed in the temperature range 800-1100 °C and the oxygen fugacity range between 10^{-16} and 10^{-12} bars. Final compositional profiles have been measured using RBS (Rutherford Backscattering Spectroscopy). In the more Mg-rich orthopyroxene a dependence of diffusion on oxygen fugacity has been detected and written in the following form:

$$logD^{c}{}_{Fe-Mg} = \log D_0 - \frac{Q}{\ln(10)RT} + n\ log\ fO_2 \qquad \text{(II.18)}$$

with the activation energy Q= 308 ± 23 [kJ/mol], log (D_0 [m^2/s]) = -5.95 ± 0.83 and n= 0.053 ± 0.027.

The oxygen fugacity exponent n= 1/20 is significantly lower than that speculated by Ganguly and Tazzoli (1994), (see paragraph III.5.2.4 for further discussion). A review of recent literature on diffusion (Buening and Buseck, 1973; Chakraborty and Ganguly, 1991; Ganguly and Tazzoli, 1994; Cherniak, 2001; Stimpfl et al., 2005; Dimanov and Wiedenbeck, 2006; Mueller et al., 2013; Dohmen et al., 2016) highlights that the influence of oxygen fugacity on diffusivity remains a source of debate and discussion.

II.5.4. Method for diffusion modelling

II.5.4.1. General Strategy

To model diffusion on crystals and solve the diffusion equation in each precise context we need to:

1- Obtain a diffusion profile from measurement (EPMA, LA-ICP-MS, SIMS, SEM);

2- Have a precise determination of the diffusion speed (know the values of the diffusion coefficient from literature);

3- Use an appropriate diffusion model (initial condition, boundary conditions);

4- Know the precise values for physical parameters of the system (temperature, fO_2, pressure) on which diffusion depends;

5- Know the specific process to which the diffusion timescale has to be assigned.

II.5.4.2. Initial conditions

Initial conditions correspond to the initial shape attributed to the compositional profile in the crystal before diffusion starts to operate to bring it back to equilibrium.

There are several models of initial conditions to be applied:

-Homogeneous initial condition

-Abrupt zoning

-Smooth zoning

-Oscillatory zoning

All four initial conditions are presented in Fig.II.21.

The simplest one is to imagine that the crystal has spent its time in a stable environment with no significant changes in any storage parameters (temperature, pressure, and oxygen or water fugacity). In this case the mineral grows constantly in equilibrium with the surrounding magma and its composition is constant from one edge to the other (Fig.II.21.a). A homogeneous composition can also be recorded in crystals which have experienced some major perturbation during their growth, but in which diffusion has had enough time to counteract and erase the compositional zoning created by the perturbation. Thus, homogeneous crystals can be generally be considered either as young crystals which have not recorded any variation in storage parameters, or as old crystals which have had a residence time in the main reservoir sufficiently long to allow re-equilibration in the event that compositional zoning was at some point present in its structure.

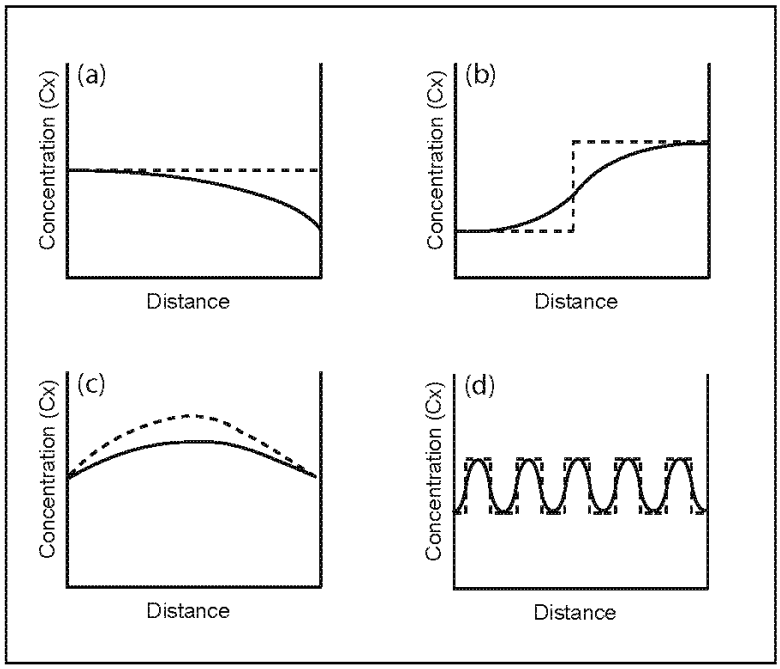

Fig.II.21: Initial conditions for diffusion modelling*. a) Homogeneous initial conditions; b) abrupt zoning; c) smooth zoning; d) oscillatory zoning. (modified from Costa et al., 2008).*

To be used for diffusion modelling, homogeneous initial conditions (homogeneous composition) must be altered during crystal growth by a change in an external physical-chemical storage parameter (by heating, decompression, and/or change in melt composition by injection). This will produce a chemical zoning in the crystal (i.e. disequilibrium). Diffusion will act then to erase this disequilibrium and bring the crystal back to a homogeneous composition. If diffusion stops early enough (for example by quenching of the crystal assemblage during eruption), part of the chemical gradient is still preserved and the diffusion profile is recorded in the crystals, so that timescale of the change in storage parameters can be assessed. Initially homogeneous profiles are usually used in modelling of olivines (Costa and Chakraborty 2004; Costa and Dungan, 2005).

A second initial condition is abrupt zoning, in which it is imagined that the crystal forms two or more different zones with radically different chemical composition following an abrupt change in crystal storage conditions, (Fig.II.21.b). This kind of initial condition assumes that the initial composition profile is a step function, slowly transformed into a sigmoid as diffusion acts to remove the chemical gradient. The step function in usually used to model diffusion for one-dimensional profiles. As in the previous case, diffusion must be stopped

early enough to preserve the initial composition of the profile on either side of the initial step profile.

The sharp initial step function is based on the fact that the change in storage conditions suffered by the crystal is faster than the growth rate of crystal. In this case, diffusion accounts for any and all deviations of the profile from the initial step geometry (Morgan et al. 2004, 2006). If, on the other hand, the change in storage conditions is slow, the initial shape of the profile is not sharp but already smoothed or gradual. In this case, distinguishing the real initial conditions from the effect of diffusion on a profile is not straightforward. A well-known method is to look at elements with very slow diffusivities. Their compositional profiles are not susceptible to modification by diffusion (e.g.: Al in orthopyroxenes or Na-Ca in plagioclases) and can thus be used as a proxy for initial conditions. This approach has been used for plagioclase (Costa et al., 2003), for sanidine (Morgan and Blake, 2006) and for olivines (Millman-Barris et al., 2008).

Other initial conditions are the smooth zoning and the oscillatory zoning scenarios. The first of these may be produced by magma fractionation during crystallization and would thus be linked with a pure closed-system process (Fig.II.21.c). The latter condition may be related to repeated, fast oscillations in crystal storage conditions (Fig.II.21.d).

In this study we use the sharp initial step function to model Fe-Mg interdiffusion in orthopyroxenes.

II.5.4.3. Boundary Conditions

The type of conditions established between the crystal and its surrounding medium are defined boundary conditions. They are mainly governed by the different kind of interchange present in between crystals and magma. Crystals can evolve in closed-boundary conditions (without exchange with the surrounding magma, concentration at the crystal boundary may vary) or in open-boundary conditions (with exchange with the surrounding magma, concentration at the crystal boundary is fixed).

When a crystal evolves in closed-boundary conditions, no matter or elements can flux from the crystal into the matrix glass or vice versa. When diffusion acts to re-equilibrate the chemical gradient present in the crystal, the re-equilibration has to be performed with only an internal flux and without loss of atoms from the edge of the crystal.

On the contrary, when a crystal evolves in open-boundary conditions, a flux of elements can take place in/out of the crystal, meaning that the diffusion re-equilibration of the initial chemical gradient takes longer. Thus, diffusion modelled with closed-boundary conditions

goes faster and gives shorter timescales than diffusion modelled with open-boundary conditions. The evolution of a crystal in open- or closed-boundary conditions depends on the element in consideration: if the diffusing element is not compatible or slowly diffusing in the external matrix glass, then the crystal will tend to evolve in a closed-boundary condition. Contrastingly, when the diffusing element is compatible and has high diffusivities in the matrix glass, then the crystal will exchange atoms of this element with the glass and evolve in open-boundary conditions. In typical magmatic systems, crystals are usually considered to evolve in open-boundary conditions.

II.5.4.4. Modelling method

(1) Here, Fe-Mg interdiffusion modelling of orthopyroxenes has been performed with the method presented by Allan et al. (2013). Using high-resolution microprobe data (EPMA), high-resolution BSE images of orthopyroxenes were calibrated for effective Mg number, in order to extract detailed zoning patterns (spatial resolution approaching 500 nm and analytical resolution close to 0.2 mol %).

High resolution BSE images were treated with the freely-available ImageJ image-processing program (http://rsb.info.nih.gov/ij/). This was accomplished by orienting BSE images so that the main rim-core boundary of interest for each crystal was oriented in North-South direction. From each image an East-West greyscale profile was extracted, averaging over a selected area. In effect, this averages together many individual pixel traverses across the image, necessary to reduce noise.

Our profiles were all performed across the *c*-axis, in the a- and *b*- crystal directions and away from the terminal faces of crystals. It has been noted by Allan et al. (2013) that traverses measured along the *c*-direction of orthopyroxenes can often return anomalous profiles, as the sectors oriented along the *c*-axis are vulnerable to recrystallization which can destroy the original zoning profile.

Profiles were extracted, and modelled, along the b-axis on zoned orthopyroxene crystals.

(2) Here we model Fe-Mg interdiffusion in crystals using the diffusion coefficient parameterization of Ganguly and Tazzoli (1994), (see equation II.21). Taking into account the relative agreement between the formulation of Ganguly and Tazzoli (1994) (extrapolated to the proper temperature range) and the experimental results of Dohmen et al. (2016), here we model Fe-Mg interdiffusion in crystals without correction for oxygen fugacity.

(3) The modelling was accomplished using 1-D modelling, acceptable procedure as the profiles are very short compared to the scale of the crystal, and diffusion is effectively normal to the long face with no additional components. As the diffusion coefficient of Ganguly and Tazzoli (1994) is composition-dependent, model profiles develop asymmetry that is more pronounced as the compositional contrast becomes greater. The modelling of profiles can be facilitated by exploiting the property that 1-D diffusion profiles proportionally share symmetry, such that if the compositional boundary conditions are the same, the difference between a profile at two different times is merely a stretch factor along the mean diffusion direction. This also holds true in the case of composition-dependent diffusion, where the curve shape is determined by the degree of compositional contrast, but the curve width is dependent on time. By using a library of profiles calculated for particular values of compositional contrast, the appropriate curve shape to apply to a natural crystal can be selected from the library based upon composition data, and then scaled in width to solve for time. The scaling factor needed is a simple expression of crystal composition, the diffusivity used for the library profiles, the diffusivity in the crystal, and the ratio of diffusion timescales in the library and the timescale of the crystal. As the scaling factor can be determined from data, the timescale for the crystal can be simply solved.

(4) The largest sources of uncertainty in diffusion modelling (and correspondingly the largest sources of uncertainty in diffusion timescales retrieved by this method) are temperature and oxygen fugacity values. For the case study of Oruanui eruptions, Allan et al. (2013) have already proved that a change of ±50°C in temperature, coupled with a change of ±1 in ΔNNO implies change of several decades—up to one order of magnitude—in the calculated timescales (Fig.II.22). On this basis we attempt to constrain the pre-eruptive temperature conditions with an uncertainty of ± 25°C, representing the current uncertainty values accepted for temperature in diffusion modelling. Results obtained by phase equilibria experiments suggest a temperature of 850 ± 25 °C and an oxygen fugacity at NNO+1.

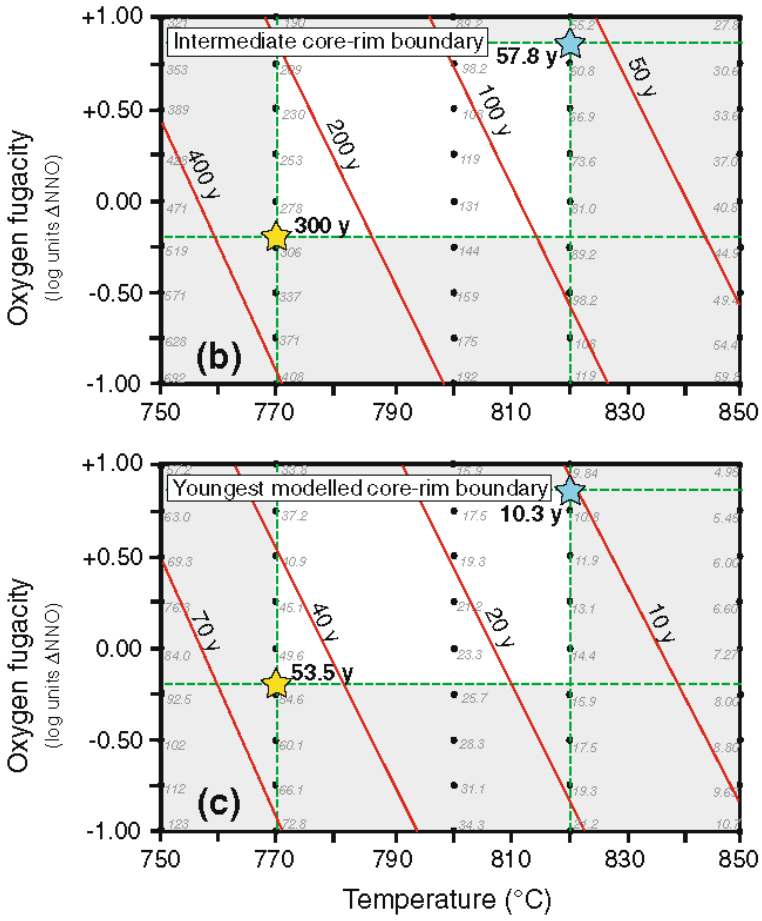

Fig.II.22: Effect of fO_2-T uncertainties on calculated timescales. *Temperature vs oxygen fugacity graphs showing the effect of variations of temperature and oxygen fugacity values on the modelled Fe-Mg interdiffusion timescales for intermediate and youngest core-rim boundaries of orthopyroxenes from Oruanui eruption. The blue and yellow stars indicate the upper (820°C/+0.8 NNO) and lower (770°C/-0.2 NNO) oxygen fugacity and temperature boundaries (770°C/-0.2 NNO). Timescales modelled at these different conditions show differences of several decades to one order of magnitude (from Allan et al., 2013).*

Therefore, we here adopt a temperature of 850± 25 °C for Fe-Mg diffusion modelling, neglecting the influence of oxygen fugacity as discussed.

(5) A detailed textural and compositional study of the zoning pattern recognized in orthopyroxenes of the three eruptions has been conducted to identify and count normal, reverse and multiple zoned crystals. A crystal system analysis approach enables recognition of several crystal groups (hereafter called “magmatic environments”) and some primary crystal pathways in between magmatic environments. With this tool we were able to identify and

characterize the main pre-eruptive dynamics prior to each eruption. Diffusion modelling was performed once the main event has been defined in each case.

II.5.4.5. Uncertainties in the timescales calculated by diffusion modelling

Diffusion coefficients and the resulting diffusion timescales generally have significant uncertainties. These derive mainly from uncertainties in temperature estimations, as this is the parameter with the chief influence on diffusivity. After temperature, several other sources of error and uncertainties have to be considered and coupled. These sources come on one hand from the precision of diffusion coefficient measurements (precision in determination of the regression line and D_0, Ea parameters), but also from the method used to perform diffusion modelling (BSE images and EPMA compositional profiles and intercalibration).

Therefore, for any diffusion modelling it is firstly important to have a precise constraint on the pre-eruptive storage temperature of natural samples. For this reason the current method requires detailed petrological studies on natural crystals in order to establish several mineral-mineral and/or mineral-melt geothermometers and in turn to obtain a temperature range with an acceptable level of uncertainty (±25 °C). Another possibility is to perform phase equilibria experiments (as has been done in this study) to improve upon the characteristically large uncertainties of ±40 °C offered by classical petrological analyses. Phase equilibria experiments allow the derivation of temperature values with higher precision (±10 °C to ±20 °C).

Uncertainties stem also from the method used to calibrate high-resolution BSE images for effective Mg-number using EMPA compositional profiles. The resolution on each BSE image used for modelling (pixel size, uncertainty on the pixel size, 1-sigma grey units in one crystal plateaux, number of lines in the image used) or the analytical precision of the microprobe EPMA profile (point spacing, uncertainty on point spacing, 1-sigma uncertainty on measurement) have to be considered and combined together in order to understand and assess uncertainties on timescales.

Here we use a Monte Carlo method to calculate the effect of all parameters on diffusion and to combine the effect of each parameter on the final diffusion timescales.

Uncertainties on temperature, D_0 and Ea each have a logarithmic effect on diffusion, so that uncertainties on final diffusion timescales do not scale linearly in time and are asymmetric with larger values on larger timescales than the low-time side (Costa and Morgan, 2010). Nonetheless, when expressed in log t uncertainties assume a quasi-Gaussian behaviour so that they can be propagated before being converted back into t (year) units.

When combining uncertainties arising from temperature, D_0, Ea and resolution of the analytical method, it has to be taken in consideration that the largest effect on final timescales uncertainties comes from temperature determination. Generally, the effect of quality and spatial resolution of images or EPMA analysis has an influence of ~1% on the final calculated timescales (Costa and Morgan, 2010).

CHAPTER III:

DETAILED STRATIGRAPHY OF DOMINICA PUMICEOUS ERUPTIONS

Introduction

Dans ce chapitre est abordée la chronostratigraphie des éruptions ponceuses de la partie centrale de la Dominique. Plusieurs études ont déjà été menées jusqu'à présent, regroupant au sein d'une même éruption une grande partie des dépôts ignimbritiques (Sigurdsson, 1972; Carey and Sigurdsson, 1980), ou les séparant en plusieurs éruptions (Howe et al., 2014 ; Smith et al., 2013). Toutefois les corrélations entre les différents dépôts n'ont jamais été précisément établies ne permettant pas ainsi d'avoir une chronostratigraphie précise. Trois campagnes de terrain ont été menées et ont permis une étude stratigraphique détaillée et un échantillonnage complet des différents dépôts observés.

Nous avons couplé à cette étude de terrain :

- Une chronologie basée sur des datations ^{14}C sur 14 bois carbonisés et 8 paléosols
- Une étude lithologique détaillée sur les échantillons de matrice prélevés systématiquement dans tous les dépôts de retombées ponceuses et d'écoulement. Cette lithologie basée sur la proportion des différentes phases minérales et pour certains dépôts des fragments accidentels (oxydés ou hydrothermalisés) a permis d'excellentes corrélations entre des dépôts ne présentant pas de caractéristiques différentes sur le terrain
- Une étude géochimique des éléments majeurs et traces des ponces des différents dépôts observés.

Sur la base de ces différentes études et des corrélations établies il a été possible de différencier 4 à 5 grandes éruptions ignimbritiques (Grande Savane, Layou, Roseau, Grand Fond et potentiellement Grand Bay), qui ont produit des volumes de magma DRE de l'ordre de plusieurs km^3 avec une proportion importante d'écoulements pyroclastiques (formant des falaises pouvant atteindre une centaine de mètres de hauteur) par rapport aux dépôts de retombées. Une grande partie de ces dépôts ont été dispersés en mer sous forme de retombées mais aussi de courants de turbidité lorsque ces écoulements se sont épanchés en mer.

A ces grandes éruptions se surajoutent un certain nombre d'éruptions pliniennes de plus faible volume dont on retrouve les dépôts principalement dans la vallée de Roseau mais aussi dans la partie sud de l'île.

Sur la base de la répartition de ces dépôts mais aussi des caractéristiques texturales, lithologiques, minéralogiques et géochimiques, nous avons pu définir la zone d'émission de

ces dépôts. Certaines éruptions se sont produites au niveau du centre volcanique du Morne Diablotins (Grande Savane, Layou) tandis que les autres proviennent du système Morne Trois Pitons-Micotrin (Roseau, Grand Fond, Grand Bay). L'absence de caldera de grande dimension peut être expliquée par la profondeur importante des zones de stockage (> 10 km). Nous abordons également le problème de l'origine de ces grandes éruptions et donc des grandes zones de stockage correspondantes et les comparaisons avec les îles avoisinantes.

A revised chronostratigraphy of recurrent ignimbritic eruptions in Dominica (Lesser Antilles Arc): Implications on the behavior of the magma plumbing system

G. Boudon[1], H. Balcone-Boissard[2], C. Solaro[1], C. Martel[3]

[1] *Institut de Physique du Globe de Paris, Sorbonne Paris Cité, Univ. Paris Diderot, CNRS, F-75005 Paris, (France)*

[2]*Sorbonne Universités, UPMC Univ. Paris 06, CNRS, UMR 7193, ISTeP, F-75005, Paris, (France)*

[3]*Institut des Sciences de la Terre d'Orléans (ISTO), UMR 7327 Université d'Orléans-CNRS-BRGM, Orléans, (France).*

Abstract

Even though large ignimbritic eruptions are not so commonly recognized, they represent catastrophic events due to the magma volume involved and the related consequences on Earth's environment in relation with the released gases and the tephra dispersal. Dominica (Lesser Antilles arc) has been recognized as hosting one of the major ignimbritic eruptions of the last 200 kyrs in the volcanic arc, called the Roseau Tuff. But more recent works have evidenced several pumiceous events instead of a single large one. Here we propose a revised chronostratigraphy of the explosive activity that occurred in the last 50 kyrs based on three field trips, new ^{14}C ages, detailed lithological and geochemical investigations, in particular a precise characterization of glass chemistry in trace elements. This eruptive history reconstruction is mainly based on outcrops along the coast and in the valley, since the luxury vegetation in the center of the island mostly precludes sections close to the central volcanic centers. We thus confirm that the Roseau event has been overestimated and that we may recognize four to five main ignimbritic events: Grande Savane, Layou (~51 kyrs), Roseau (~33 kyrs), Grand Fond (~24 kyrs) and Grand Bay. Grande Savane and Grand Bay eruptions are not well constrained in time. We discuss the possible volcanic center at their origin, in addition to correlations with some plinian events of lower magnitude that were identified in the Roseau valley and in the southern part of Dominica. This study help in better constrains the eruptive history of the most active volcanic islands of the Lesser Antilles arc, which has important implications on hazard mitigation.

Keywords: Dominica, ignimbrites, stratigraphy, ^{14}C dating, lithology, geochemistry

III.1. Introduction

Voluminous ignimbritic eruptions are not frequent in the world but when they occur they may have a dramatic effect not only due to the magma volume involved (order of magnitude of one to tens of km^3) but also because of their related consequences (tephra dispersal, climatic effect) on the Earth's environment across various temporal and space scales. Such large eruptions have occurred in the last thousand years. The Minoan eruption of Santorini volcano (Greece) (3 600 yrs BP) produced in the order of 40-60 km^3 of Dense Rock Equivalent (DRE) magma and was responsible of the disappearance of the Minoan civilization (Bond and Sparks, 1976; Druitt et al., 2012). In 1257 AD, the Samalas eruption on Lombok island (Indonesia) generated 40 km^3 of magma DRE and has been recently recognized as an important chronostratigraphic marker through a sulfate peak identified in the polar ice core (Lavigne et al., 2013;Vidal et al., 2016). More recently the Tambora eruption in 1815 (Indonesia) erupted about 50 km^3 of magma DRE, killed about 71 000 persons and significantly impacted the climat, in particular the following year "without summer" in the northern hemisphere (Self et al., 1984). Finally, the 1991 Pinatubo eruption (Philippines) was the largest eruption of the last decades with the emission of ~5 km^3 of magma DRE, involving a global temperature drop by about 0.5 °C in the years 1991-1993 (Self et al., 1993).

In the Lesser Antilles arc, the volume of magma involved in most of the eruptions along the volcanic arc is generally low (0.1 to 1 km^3) as evidenced in the volcanological history of most of the volcanoes (Lindsay et al., 2005a). It was the case for all the historical eruptions that produced less than 0.4-0.5 km^3 of magma. The lava dome-forming eruptions of 1902-1905 and 1929-1932 of Montagne Pelée (Martinique) erupted in the order of 0.2-0.3 km^3. The successive explosive and lava dome-forming eruptions of Soufrière of St Vincent in 1902-1903, 1971 and 1979, produced each less than 0.2 km^3, and the magma involved by each of the numerous submarine eruptions of Kick'em Jenny volcano is very low (less than 0.05-0.1 km^3). The recent and long lava dome-forming eruption of Soufrière Hills at Montserrat (1995-2010) is an exception as it produced in the order of 1 km^3 of magma (Wadge et al., 2010). But these volumes are low compared with the magma produced in Dominica during the last 50 kyrs.

The pioneer works recognized a voluminous pumiceous eruption called "the Roseau Tuff" (Carey and Sigurdsson, 1980; Sigurdsson, 1972). This eruption, dated between 50 and 30 ka, has been thought to be responsible of the emission of ~58 km^3 of magma DRE, leading to thick deposits of pumiceous pyroclastic density currents (PDC), welded for most of them, and

forming high cliffs (up to 100 m) in the main valleys. The emitted products extend further than Dominica itself as air-fall tephra identified offshore in piston cores several hundred kilometers from the island and within turbiditic deposits in the Grenada basin (Carey and Sigurdsson, 1980; Whitham, 1989; Boudon et al., 2008). Recent chronostratigraphical investigations have evidenced that these thick deposits belonged not to a unique event but to a series of 7 eruptions dated between 50 and 20 kyrs (Smith et al., 2013; Howe et al., 2014; Howe et al., 2015a). Although recognized as several eruptions and consequently with volume of the emitted products per eruption lower than previously proposed, the volume of magma produced by each eruption still contrasts with the common estimation along the Lesser Antilles arc. Dominica is thus characterized in the last 50 kyrs by infrequent large pumiceous eruptions whereas in the same period of time, several small pumiceous eruptions (generally < 0.5 km^3; Carazzo et al., 2012, Legendre, 2012) occurred on the neighboring islands of Guadeloupe and Martinique. In addition, whereas most islands of the Lesser Antilles arc only evidence one active volcano, Dominica exhibits the particularity of 4 large active volcanic centers and several others of lower volume (Lindsay et al., 2005b). Dominica and the neighboring islands of Guadeloupe and Martinique concentrate half of the active volcanoes of the arc within its central part, only accounting for 1/5 of its total length (Fig. 1a). Thus Dominica volcanism raises the question of the genesis, storage, and eruption of such large volume of magma in a short period of time (the last 50 kyrs).

To answer these questions, one key starting point is to clarify the spatial and temporal relationships between the different ignimbrites. We carried out three field trips in Dominica since 2011 to study the large pumiceous eruptions, focusing on those that occurred in the central part of the island. On the basis of these recent on-land investigations, together with new ^{14}C dating on charcoals and detailed petrological and geochemical data on pumice glass, we propose here a revised chronostratigraphy of the large ignimbritic eruptions. In the light of geochemical and lithological fingerprints, we propose new evidences on the relationships between the different eruptions such as the volcanic center at their respective origin and the chronology of the volcanic activity in Dominica in the last 50 kyrs. These data may help us to improve our knowledge of Dominica geology that has crucial implications in terms of volcanic risk mitigation in case of reactivation.

III.2. Geological setting

III.2.1. The Lesser Antilles arc

Dominica belongs to the Lesser Antilles Arc which extends from 12° to 18° N with a particular convexity to the East (Fig. III.1). Active since the late Miocene, the Lesser Antilles arc consists of 11 volcanic islands and marks the westward subduction of the oceanic North American Plate beneath the Caribbean Plate. Convergence is estimated at ~2 cm/year and is associated with a low magma production rate of ~3 km^3/Ma (Wadge, 1984), (Wadge and Shepherd, 1984). Due to the subduction of an aseismic ridge at the center of the arc, the arc is segmented, with Dominica being astride the southern and the northern segment. The northern part trend is at 330° whereas the southern part trend is at 020° (Bouysse and Westercamp, 1990). This north/south subdivision is coincident with a change in the slab-dip from 50–60° in the north to 60–90° in the south (Wadge and Shepherd, 1984). Dominica is thus located in a transitional area, where the subduction is the less oblique, which corresponds to the middle part of the arc.

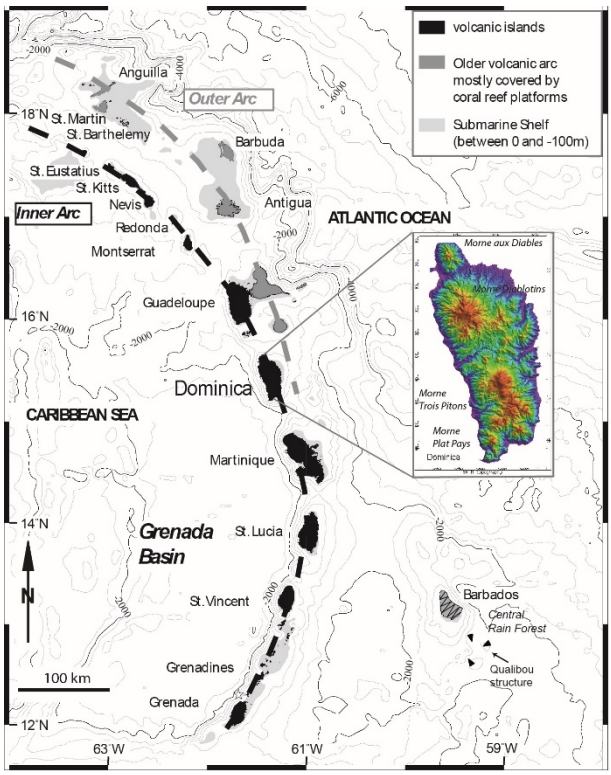

Figure III.1: ***The Lesser Antilles arc****. Predicted bathymetry is from Smith and Sandwell (1997). Contour interval 2000 m isolines is in bold. Volcanic islands are black, and subaerial coral reef platforms are dark gray. The 100 m depth submarine shelf is light gray. Dominica SRTM topographic radar map is highlighted (*Courtesy of Dr. Ian C.F.Stewart*).*

North of Dominica, the arc is divided into two groups of islands. In the eastern and older group, volcanoes are extinct and, on several islands, covered by a thick carbonate platform (Fig. III.1). Active volcanoes are located in the western group of islands and have been active since 20 Ma. From Dominica to the South, the two branches of the arc merge and deposits of the older arc underlie the recent one. This southern part of the arc is bordered to the west by the 3000 m deep back-arc Grenada Basin. Active volcanoes are located on the younger part of the arc (Saba, St Eustatius, Nevis, St. Kitts, Montserrat, Guadeloupe, Dominica, Martinique, St. Lucia, St. Vincent and Grenada). Dominica is the sole island of the arc that contains four large actives volcanic centers: from North to South, Morne aux Diables where a recent seismic crisis occurred in 2010, Morne Diablotins, Morne Trois Pitons - Micotrin and Plat Pays Volcanic Complex (PPVC) (Fig. III.2A). Small satellite centres are also present south of Trois Pitons-Micotrin volcanic centers (Watt Mountain, Morne Anglais, Grande Soufrière Hills). Dominica is thus the volcanically most productive as well as the potentially most hazardous volcanic island of the Lesser Antilles arc. Dominica is characterized by dominantly Pleistocene to recent volcanism. In the early Pleistocene (1.7–2 Ma), volcanism was constrained to the northern half of Dominica and led to the development of Morne Diablotins, a large stratovolcano, and Morne aux Diables, a smaller lava dome complex (Smith et al., 2013). During the late Pleistocene (0–1.1 Ma) Morne Trois Pitons - Micotrin and the Plat Pays Volcanic Complex (PPVC) developed; in parallel, three smaller volcanic centers in the southern flank of Morne Trois Pitons-Micotrin were also active, namely Watt Mountain, Morne Anglais and Grand Soufrière Hills. PPVC is the only well-studied volcanic center on the south-western part of the island (Wadge, 1985); (Le Friant et al., 2002), (Lindsay et al., 2003), (Lindsay et al., 2005a), (Gurenko et al., 2005), (Halama et al., 2006). Although this time period has been dominated by lava dome-forming eruptions, similar to the ongoing eruption of Soufrière Hills on Montserrat, large recent ignimbritic deposits (< 50 kyrs) outcrop across the island (Lindsay et al., 2005b); (Smith et al., 2013). The last magmatic activity occurred on the Plat Pays volcano with the building of the Morne Patate lava dome dated at 450 ±90 yrs. BP (M.J. Roobol et al., 1983). The Desolation valley within the Morne Trois Pitons - Micotrin volcanic center is the location of two historical phreatic eruption in 1880, and more recently in 1997 (Lindsay et al., 2005b); the Boiling lake area, characterized by an acid water lake, generally acts as a witness of the relation between surficial and seismic activity (Fournier et al., 2009).

III.2.2. Previous work on Dominica ignimbritic eruptions

During the last 50 000 years voluminous ignimbritic deposits were emitted in the central area of Dominica originated from Morne Trois Pitons-Micotrin and Morne Diablotins (Fig. III.1, III.2). A general study on the Dominica ignimbrite was carried out by Lindsay et al. (2005b), further completed by the works of Smith et al. (2013) and Howe et al. (2014, 2015a, b). These authors proposed detailed studies on the extent, mineralogy, and geochemistry of the deposits, as well as reconstructions of the possible volcanic emission centers. In particular, the voluminous ignimbritic deposits of Roseau, Layou, Grand Fond, Grand Bay and Grande Savane were studied stratigraphically and geochemically.

Roseau ignimbrite. The first fieldwork on these deposits was performed by Sigurdsson (1972) who identified an ignimbritic deposit (the "Roseau tuff" eruption), 3 km^3 in volume, welded in some parts, that filled the valley of Roseau. Sigurdsson (1972) identified in the Goodwill quarry of Roseau town, three PDC units and a summit pumice fallout unit separated by weathered horizon. The age proposed for the most voluminous deposits is between 28 400 ± 900 yrs. BP and 46 000 ± 4 500 yrs. BP (^{14}C dating). The second PDC has been dated at 28 400 ± 900 yrs. BP. Based on a tephrostratigraphic study on a series of piston core sampled off Dominica, Carey and Sigurdsson (1980) identified extensive and recent marine pumiceous deposits that they correlated with the Roseau tuff. The total volume of the deposits of the Roseau tuff was estimated at 58 km^3, divided into 3 km^3 identified on-land, 25 km^3 of tephra distributed to the Western Atlantic Ocean and 30 km^3 of subaqueous debris flows deposited to the west on the floor of the back-arc Grenada Basin. Witham (1989) carried a detailed study on the turbiditic deposits associated to the Roseau tuff in the Grenada Basin (to which he included the ignimbritic deposits that filled on-land the Layou valley).

Smith et al. (2013) suggested that the Roseau tuff deposit likely represents material from multiple Plinian eruptions from across the island: on the basis of ^{14}C ages the Roseau Tuff eruption can be subdivided into seven separate eruptive episodes (overlapping whole rock composition), showing clear time gaps between each other (>16 ka, from 30 to >46 ka cal yr. BP; with many ages not overlapping within uncertainty). The recent revised stratigraphic work on the basis of (U-Th)/He ages argue also for six or seven eruptions that occurred between 20 and 70 ka (Howe et al., 2014). The volcanic emission center of the Roseau Tuff has also been a matter of debate. Sigurdsson (1972) suggested the large dome complex of Micotrin volcano, as the source of the eruptive sequence. Carey and Sigurdsson (1980), however, noted that the calculated volume of the basal Roseau Tuff eruption was too large to

be contained into the Micotrin dome complex, which may indicate the existence of a caldera. Based on field mapping arguments, Demange et al. (1985) proposed a caldera at Wotten Waven, which is now mostly buried beneath Micotrin volcano. Therefore, Wotten Waven has considered to be the likely source of the Roseau Tuff eruption (Lindsay et al., 2005, Demange et al., 1985, Smith et al., 2013).

Grand Bay ignimbrite. The Grand Bay Ignimbrite is a laterally extended andesitic pumiceous PDC deposit that outcrops along the southern coast of Dominica (Lindsay et al., 2003). Originally mapped at Grand Bay Beach, the deposit was correlated by Lindsay et al. (2003) to PDC deposits at the Geneva quarry. ^{14}C ages on buried plant material taken from distal outcrops correlated to this ignimbrite indicate eruption ages of 27–42 kyrs cal BP. Yet, field mapping by Smith et al. (2013) indicates that these distal outcrops may not be lateral equivalents of the Grand Bay Ignimbrite, making the age of the Grand Bay Ignimbrite still unconstrained. Although Smith et al. (2013) suggested that the Grand Bay deposits were part of the Roseau Tuff Sequence based on overlapping whole rock geochemistry, Lindsay et al. (2003) ruled out such a correlation based on mineralogical and topographic constraints. Originally, the Plat Pays Volcanic Center was proposed as the source of the Grand Bay Ignimbrite (Lindsay et al., 2003), but more recent works implicated the Wotten Waven caldera as a possible eruptive center (Lindsay et al., 2005b, Smith et al., 2013).

Layou ignimbrite. The Layou PDC which outcrops within the confines of the Layou valley is thought to be sourced from the Morne Trois Pitons volcanic center (Sparks et al., 1980; Smith et al., 2013; Whitham, 1989).

Grande Savane ignimbrite. Sparks et al. (1980) showed that the Grande Savane fan is made of a series of block-and-ash flow deposits covered by ignimbritic deposits welded in their lower part, all these deposits originating from the Morne Diablotins volcanic center. The welded ignimbritic deposits forming high cliffs in the proximal valleys and a large submarine fan offshore indicate that a large part of the ignimbrite flowed under the sea. The unique age, obtained in a pumiceous surge deposit within the upper sequence, is >22 000 years (Sparks et al., 1980).

The Wesley/Londonderry ignimbrite. The Wesley/Londonberry PDC is located on the northeastern side of the island (Sparks et al., 1980). The pyroclastic flow deposits at Londonderry beach were recently re-mapped as the Wesley pyroclastic flow fan (Smith et al., 2013). The Wesley flow fan can be subdivided into two eruptive units separated by a thin

paleosol (Smith et al., 2013). Although the Wesley/Londonderry flow fan is sourced from Morne Diablotins volcano, based on topographical constraints, its eruption age is unknown and its relationship to the eastern Grande Savane Ignimbrite remains unclear (Smith et al., 2013).

Present lava domes. The summit parts of the volcanic centers of Morne Diablotins and Morne Trois Pitons – Micotrin, from which the ignimbrites probably originated, is now occupied by voluminous lava domes. The Morne Trois Pitons consists of a voluminous lava dome complex with associated block-and-ash flow deposits. Micotrin lava dome is less voluminous, located in the south of Morne Trois Pitons. Dating of block-and-ash flow deposits associated to these lava domes provide large time bracket between 877 ±108 and 28 844 ±1983 cal yrs BP (^{14}C dating, (Lindsay et al., 2005b). No chronological constrain exists on Morne Diablotins summit lava dome.

III.3. Methodology

Fieldwork. A series of three field trips were carried out in Dominica between 2011 and 2015 dedicated to the study of the ignimbritic eruptions (Fig.III.2). A detailed stratigraphy was established on the basis of field observations (textural and structural characteristics, thickness, grain size of the deposits…). Pumice rocks, matrix from the PDC and fallout deposits were systematically sampled for laboratory analysis. A particular care was taken to identify and sample in detail the fallout deposit at the base of the different eruptions. Considering the thickness of the PDC, samples (individual pumice and matrix) were picked within the base and the upper top of the accessible sequence, in addition to samples within different parts depending on the identified unit or degree of welding. Charcoals and paleosols were also sampled when present (Fig.III.2). Some scoriaceous deposits were also sampled for geochemical comparison with a basic endmember.

Lithology. Matrix samples from the different pumiceous PDC and fallout deposits were dried, weighted and sieved; different fractions were washed in an ultrasonic tank and quarted. Lithologic counting was made in three different fractions (0.5-1 mm; 0.250-0.5 mm; 0.125-0.250 mm) on a basis of a minimum of 500 clasts by fractions. Each component was identified and counted: crystals (plagioclases, orthopyroxenes, clinopyroxenes, amphiboles, quartz, oxides), pumice clasts, lava dome clasts or accidental (hydrothermal and oxidized clasts). The proportion of the different components in well-identified deposits serves as a criterion to correlate deposits that could not be correlated on a basis of field mapping.

Dating. Ages were determined on 14 charcoals and 8 paleosols using an accelerator mass spectrometry (AMS) at the LMC14 (Artemis, Laboratoire de Mesure du Carbone 14, CEA Saclay, France). The ages obtained were calibrated using the free software OxCal (OxCal 4.2,Bronk Ramsey, 2009) with the atmospheric IntCal13 calibration curve, recommended for the Northern Hemisphere (Reimer, 2013). OxCal is a program designed for the analysis of chronological information that we used to calculate the probable age range for each dated samples through radiocarbon calibration, and also more specifically here, to analyse groups of ages from stratigraphically-related deposits (i.e., the ages of stratigraphically-constrained samples of the same eruption are validated by using the R_Combine function and the χ^2 test prior to calibration (Ward and Wilson, 1978).

Geochemistry. Major elements on selected whole rocks were analyzed at CRPG by ICP-OES (Carignan et al., 2001). Major element (Si, Ti, Al, Fe, Mg, Mn, Ca, Na, K, P) and halogen (F, Cl) contents, on matrix glass were determined using electronic microprobe (EPMA, CAMECA SXFive, Camparis, France,) with an acceleration voltage of 15 kV, a beam current of 4nA for major elements and a counting time of 5s for Si and Na to limit Na loss and 10 s for the other elements. For halogen elements (F and Cl), analyses are realized with an acceleration voltage of 15kV, a beam current of 60nA and a dwell time of 180s. For inter-calibration of each EPMA session, three natural glass samples used as internal standard were analyzed (obsidians from Lipari, Eolian Island, Italy; Little Glass Mountain, California, United States; and Corbetti volcano, Ethiopia) (Balcone-Boissard et al., 2008).

Whole-rock, separated related matrix glass and separated minerals trace elements concentrations were measured using an Agilent 7900 ICP-QMS in low resolution mode (IPGP, France). Sample introduction was achieved with a micro-nebulizer (MicroMist, 0.2ml/min) through a Scott spray chamber. Except for lithium, elements below mass 80 were measured using a collision-reaction interface with helium gas (5ml/min) to remove isobaric interferences. A count to concentrations conversion was done using the BHVO-2 (basalt; Jochum et al., 2016), that was also used to assess the analytical derive of the ICP-MS.

III.4. Results

III.4.1. Stratigraphy

The fieldwork first aims at identifying the main ignimbritic deposits (Fig.III.2). The central part of the island, being covered by a dense rainy forest, only sea cliffs, large valleys, quarries and some roadsides offer the opportunity to study the pumiceous deposits. The different deposits are consequently disseminated in different sites (Fig.III.2). This work mainly focusses on the voluminous deposits filling the main valleys on the western and eastern coasts, but other pumiceous deposits from explosive eruptions of lower magnitude were also identified and will be discussed.

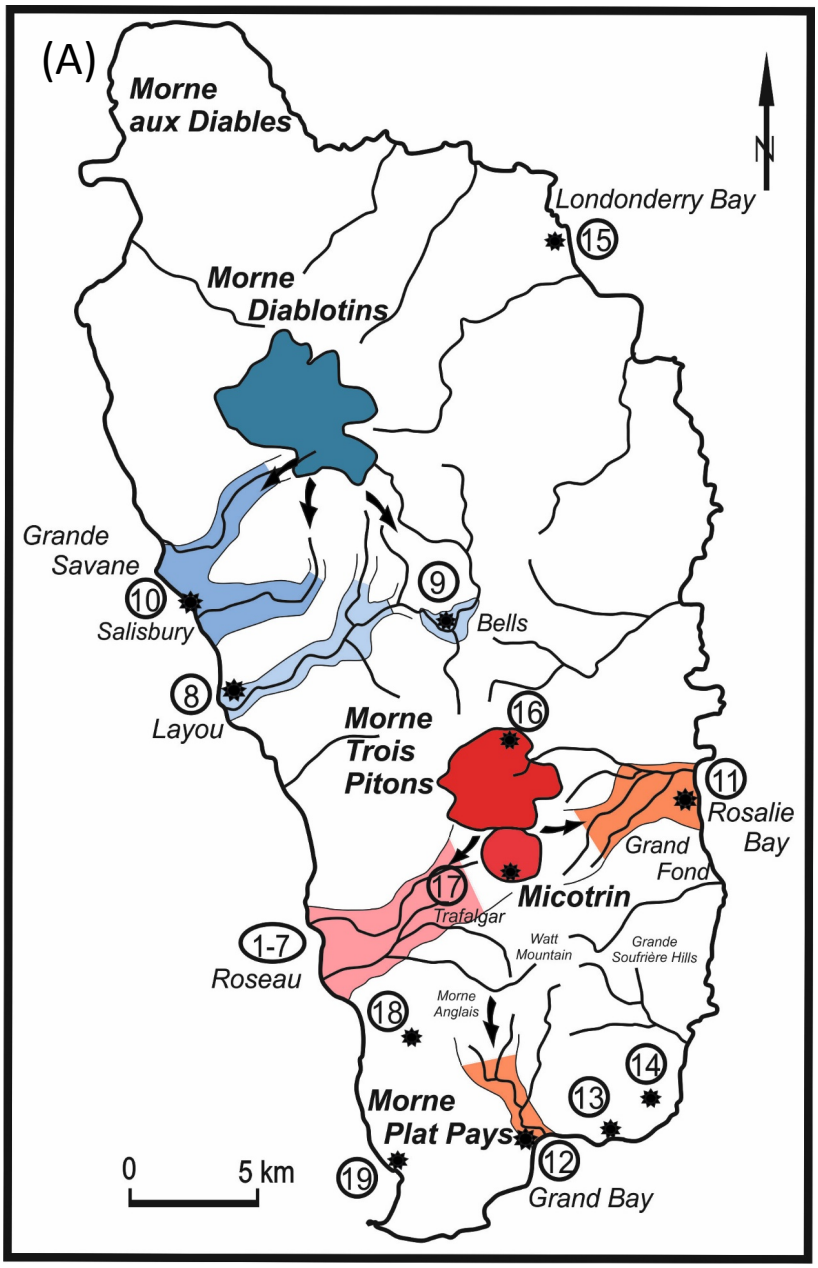

Figure III.2 (continued below)

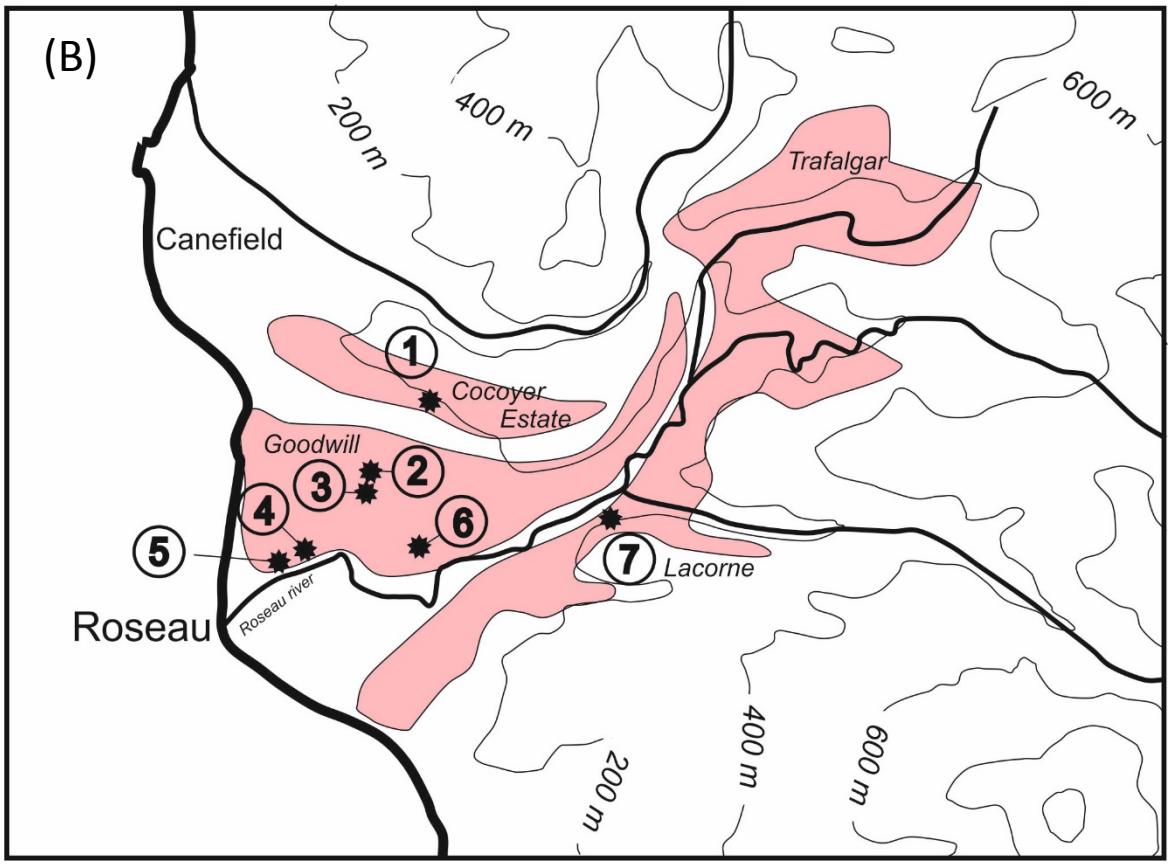

Figure III.2: Schematic map of the ignimbritic deposits and sampling location. *A- Dominica main ignimbrites highlighted in color from sea up to the valley, with the four main volcanic centers of Morne aux Diables, Morne Diablotins, Morne Trois Pitons – Micotrin and Morne Plat Pays. The numbers refer to the outcrop locations. Sampling comprises two scoria fallout deposits at Fond Baron-Beverly Hills (18, 15°16'26''N, 61°21'31''W) and Soufrière (19, 15°14'01''N, 61°21'46''W), the lava dome of Morne Trois Pitons (16, 15°23'21''N, 61°18'44''W; quarry on the northern side), and the lava dome of Micotrin (17, 15°20'08''N, 61°18'55''W; block and ash flow deposit near Freshwater lake for Micotrin). B- Detail of the outcrop locations within the Roseau valley.(1) Cocoyer Estate quarry, (2) Goodwill quarry, (3) Goodwill entrance, (4) Roseau right bank - roundabout, (5) Roseau right bank – Narakiel's inn, (6) Link road, and (7) Roseau left bank – Lacorne quarry. Pinkish domain: main fallout and PDC pumiceous deposits.*

The Roseau sections. In the lower part of the Roseau valley several outcrops and quarries allow to study pumiceous deposits; among them two main quarries give the opportunity to describe and sample a thick sequence of deposits: the "Goodwill" and the "Cocoyer Estate" quarries (Fig. 3a). The Goodwill quarry is the type locality historically described to refer to the "Roseau Tuff" eruption by Sigurdsson (1972).

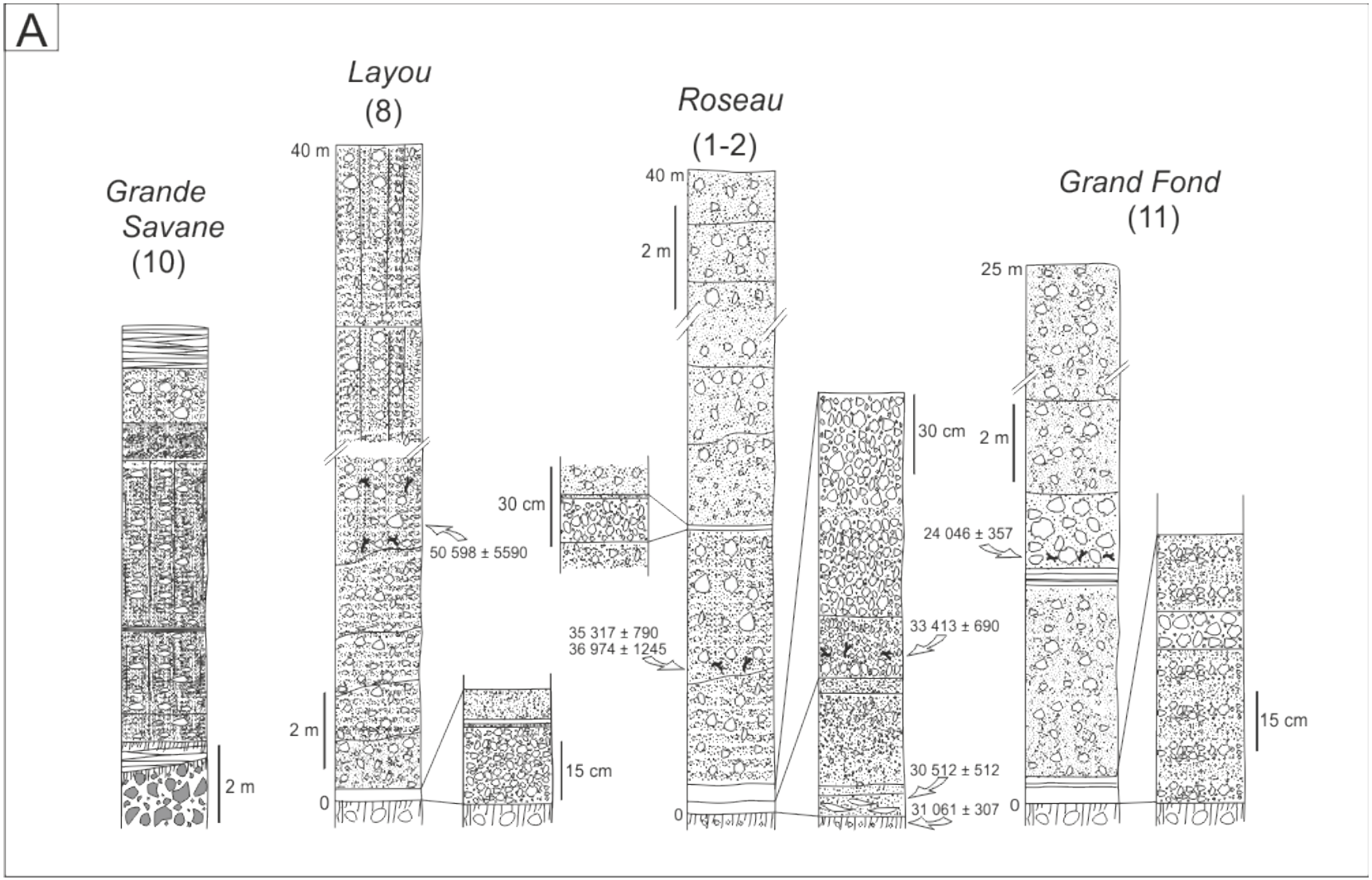

Figure III.3 (continued below)

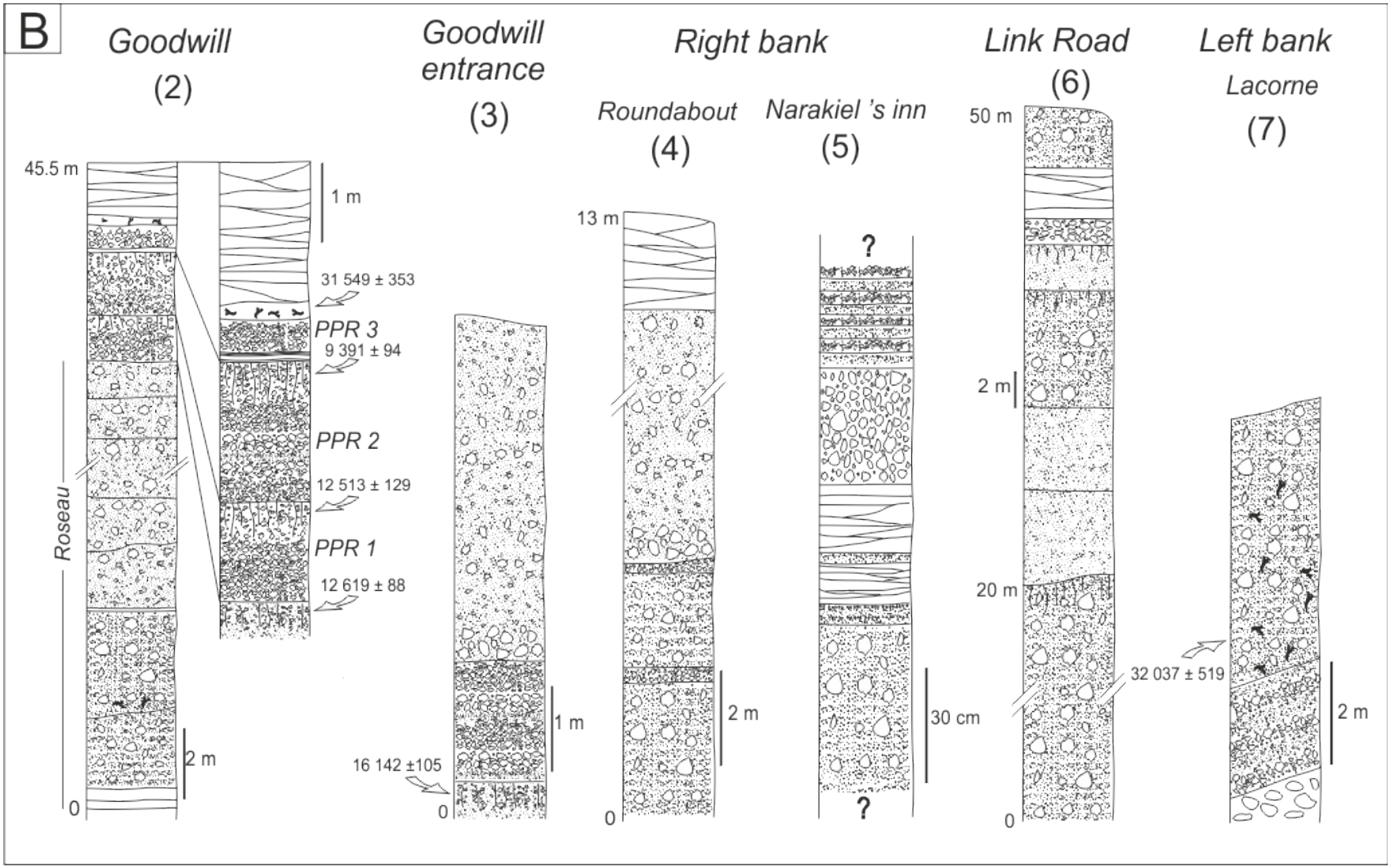

Figure III.3 (continued below)

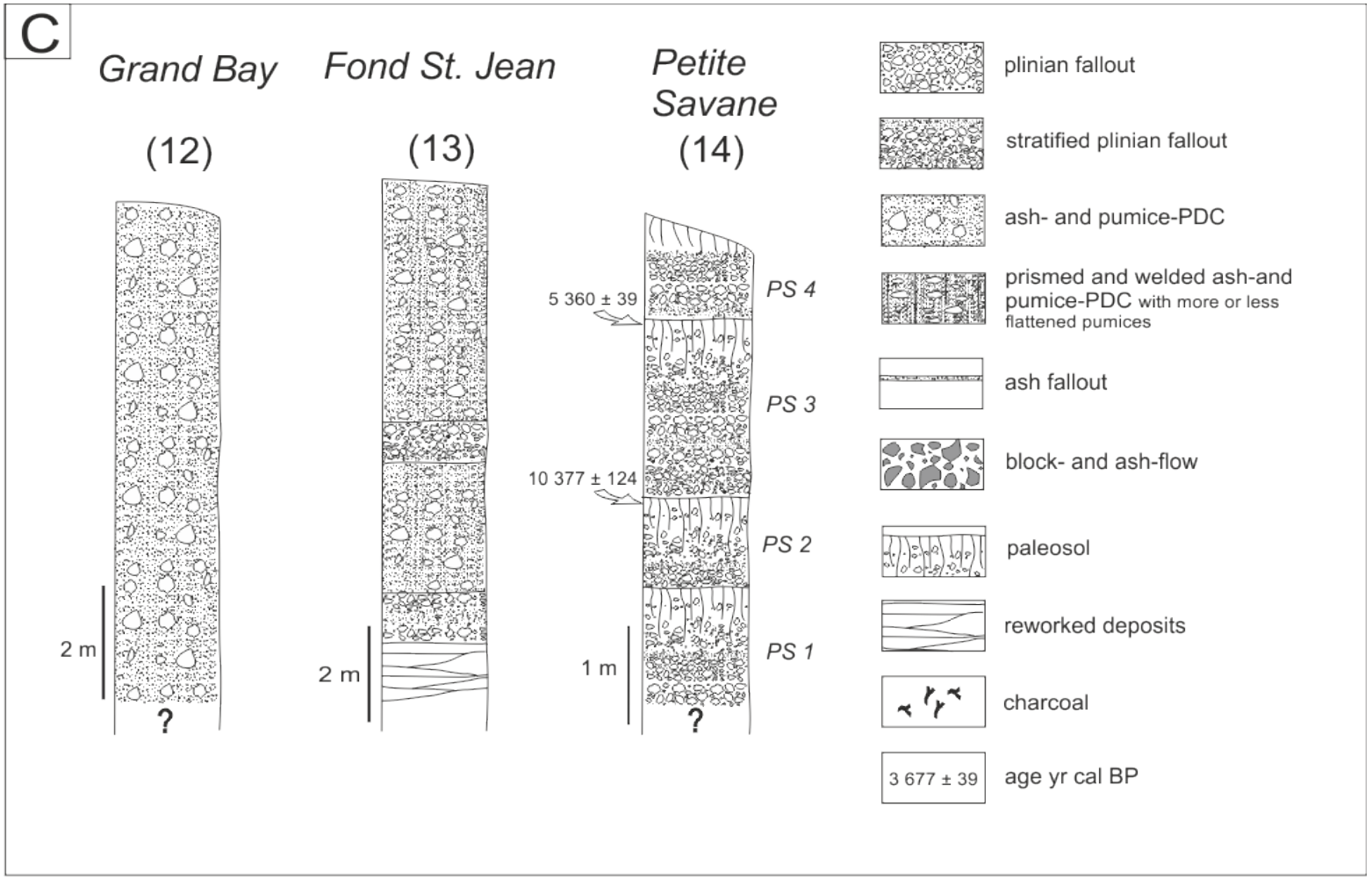

Figure III.3: Sections of the main Dominica ignimbrites. A- Layou, Roseau, Grand Fond and Grande Savane. *B- The "Roseau valley" sections, with Goodwill, Goodwill entrance, Roseau right bank (roundabout and Narakiel's inn), Link road and Roseau left bank, as referenced in Fig. II.2b. C- Grand Bay and laterally pumiceous deposits of Fond St. Jean and Petite Savane.* ^{14}C *ages given in cal yrs BP (Table 1 for details). .*

In the *"Cocoyer Estate" quarry (1, 15°18'40''N, 61°22'29''W;* Fig.III.2, 3, 4*)* a thick sequence of pumiceous deposits (>50 m) covers a paleosol formed in pebble-rich fluviatile deposits. The base of the volcanic deposit shows a fine-grained (ash and sand) fallout unit covered by a 30 cm thick pumice fallout deposit. This first sequence is covered by two 2 m thick ash- and pumice –PDC deposits, topped by a 15 cm thick plinian fallout deposit. Similar thin intercalated plinian fallout deposit is clearly visible in two other sites within the valley. Above this plinian deposit, there is a 40 m thick sequence of ash-and-pumice PDC deposits, finally covered by mature paleosoils and reworked deposits.

In the *Goodwill Quarry (2, 15°18'32''N, 61°23'02''W;* Fig. III.2, 3*)* a thick sequence of pumiceous deposits (several tens of meters) can be divided in four main stratigraphic units, separated by paleosols. The base of Unit 1 cannot be observed and the section begins here by a series of two ash- and pumice-PDC deposits with a dominant proportion of small pumices (< 10cm). It is overlain by a 15 cm thick plinian fallout deposit covered by several ash and pumice PDCs deposits, one of them being at least 20 m thick. The top of the last PDC deposit is covered by a low evolved paleosoil. Although the base is not visible this unit display characteristics similar to the one observed at Cocoyer quarry; hereafter we will consider both deposits as belonging to the same eruption. Unit 2 is a massive, 1.25 m thick plinian fallout deposit, hereafter referred as PPR1 (for 'Plinian Post-Roseau'); its upper part is modified by a thick paleosoil. Unit 3 is also a plinian fallout deposit, 1.75 cm thick, showing a succession of fine- and coarse-grained beds, hereafter referred as PPR2, topped by a thick paleosoil. Unit 4 is the last plinian fallout deposit, 47 cm thick, showing at its base a succession of fine-grained beds, hereafter referred as PPR3. This deposit is covered by a sequence of 2 m thick reworked deposits constituting the upper part of the quarry, hereafter referred as 'Goodwill reworked'. Few charcoals are present at their base.

Before the entrance of the Goodwill quarry *(3, 15°18'30''N, 61°23'03''W;* Fig.III. 2, 3*)*, a 135 cm thick, slightly stratified, pumice fallout deposit is covered by a few meter thick ash- and pumice-PDC deposit, hereafter referred as 'Goodwill entrance'. This plinian deposit covers a paleosol developped on the ash-and pumice-PDC of the unit 1 described inside the Goodwill quarry. On the right bank of the Roseau river, *(right bank, roundabout*: *4, 15°18'10''N, 61°23'11''W;* Fig. III.2, 3*)* two plinian fallout deposits (30 and 15 cm thick) are intercalated in a sequence of ash- and pumice-PDC deposits. The basal PDC deposit is rich in large pumice clasts (up to 80 cm in diameter) (Fig III.3b). Close to this outcrop (*Roseau river,*

right bank, Narakiel's Inn : 5, 15°18'09''N, 61°23'14''W; Fig. III.2, 3*)*, an ash- and pumice-PDC deposit is covered by a 40 cm thick sequence of stratified ash- and pumice-fallout beds, in which reworked volcanic material is intercalated; it is covered by a 30 cm thick lithic-rich plinian fallout deposit. The top of the outcrop is made of reworked ash and pumice-rich volcanic material. A small quarry, not totally vegetalized, on the left bank of the Roseau River (*Lacorne Quarry*: *7, 15°18'29''N, 61°21'48''W;* Fig. III.2, 3*)* shows the superposition of a stratified plinian fallout deposited on a strongly sloping basement (20° dip), followed by ash- and pumice-PCD deposits with abundant large pumice clasts and charcoals. The link road deposits *(6, 15°18'15''N, 61°22'34''W;* Fig. III.2, 3*)* along Santa Romet road have been studied in details by Howe et al. (2014). Three pumiceous PDCs are intercalated with ash flows, paleosols and a single fallout deposit. Here we focused our sampling on the fallout deposit (labelled 'link fall', in Howe et al., 2014) to link it to other deposits within Roseau and to the paleosol at its base. In the upper part of the Roseau valley, highly welded ignimbritic deposits form cliffs 50 to 100 high visible at Trafalgar falls *(15°19'34''N, 61°20'14''W;* Fig. III.2, 3, 4*)*. The deposits are prismed, highly indurated and pumices are highly flattened, generating fiammes.

The Layou sections *(8, sea cliff; 15°23'49''N, 61°25'35''W; 9, Bells, 15°25'32''N, 61°20'22''W;* Fig. III.2, 3, 4*)*. In the valley of Layou a thick sequence of ash-and pumice-PDC deposits is recognized in a large area including a sea cliff in continuity with a nearby large quarry. The sequence begins by a pumice-fall deposit covering a paleosol developed on a thick pebble-rich conglomerate. The pumice-fall deposit is 22 thick, massive, poorly sorted with small pumices. It is covered by an 8 cm thick accretionary lapilli-rich ash fallout deposit. A series of more than 40 m thick ash- and pumice-PDC deposit covers the fallout deposit. The thickness of the ash- and pumice-PDC deposits increases upward from few meters at the base to 10 meters at the top. The upper PDC are welded with prisms, but pumices are slightly to not flatten. Within the valley, large cliffs are visible in the landscape but not accessible for sampling. In the upper part of the Layou valley the ash- and pumice-PDC deposits outcrop along the road at Bells locality (*9, Bells, 15°25'32''N, 61°20'22''W;* Fig. III.2, 3).

Grande Savane – Salisbury sections *(10, 15°26'09''N, 61°26'21''W;* Fig. III.2, 3*)*. The Grande Savane deposits, north of Layou, near Salisbury, form a large fan on the west coast. The pumiceous sequence covers a thick sequence of block- and ash-flow deposits in some place replaced by pebble-rich conglomerate. This sequence can be divided in two stratigraphic units. Unit 1 (hereafter referred as Grande Savane 1) is composed of a series of

welded ash- and pumice-PDC deposits, rubefied for the first one. Unit 2 (hereafter referred as Grande Savane 2) is non-welded deposits that cover the Unit 1 welded deposits without intercalated soil formation. Unit 2 is composed of a fallout deposit made of a succession of ash- and pumice-beds, covered by a few meters thick ash-and pumice-PDC deposit. The top of unit 2 is composed of a succession of reworked stratified deposits with rounded pumices and a muddy matrix.

Grand Fond section *(11, 15°21'57''N, 61°15'16''W;* Fig. III.2, 3, 4*)*. As for the sequences described previously, the Grand Fond pumiceous deposits cover a paleosoil developed on a conglomerate. The sequence begins with a 70 cm thick stratified plinian fallout deposit composed of a succession of fine- and coarse-grained beds. This pumice fallout deposit is covered by a 5 m thick ash- and pumice-PDC deposit rich in large pumices (up to 40 cm in diameter), covered by a series of three surge deposits, all decimetric in thickness, ash- to sand-grained, normally graded, showing few laminations, and by a 2 m thick pumice PDC deposit containing very large pumices (up to 80 cm). These first emitted deposits are topped by a series of thick (~ 30 m in thickness) ash-and pumice-PDC deposits that can be followed in the valley. These deposits are not welded.

Grand Bay section *(12, Berekua, 15°14'34''N, 61°18'44''W*; Fig. III.2, 3*)*. In Berekua-Grand Bay, thick ash- and pumice-PDC deposits outcrop in a quarry near the sea. These deposits can be followed in the valley of Geneva where they form high cliffs in both sides of the valley. They are also present in a small quarry at Geneva estate where they are covered by a block-and ash-flow deposit associated to a lava dome originating from the Plat Pays volcanic complex.

Hereafter, we detail three additional outcrops that we studied for comparison with the ignimbritic eruptions. At Fond St. Jean *(13, 15°14'38''N, 61°16'58''W;* Fig. III.2, 3*)* along the south coast, a 1 m thick fallout deposit is covered by an ash-and pumice-PDC deposit forming a vertical cliff at the sea side. At Petite Savane, *(14, 15°15'12''N, 61°16'09''W;* Fig.III.2, 3*)* there is a series of four weathered plinian fallout deposits composed of small pumice clasts (less than 4 cm in diameter) and separated by thick mature paleosols. The upper two pumice fallout deposits are stratified. In the northwestern part of Dominica, north of Londonderry river near the Melville airport, *(15, 15°33'37''N, 61°17'50''W;* Fig.III.2, 3*)*, thick ash-and pumice-PDC deposits form a cliff at the sea side.

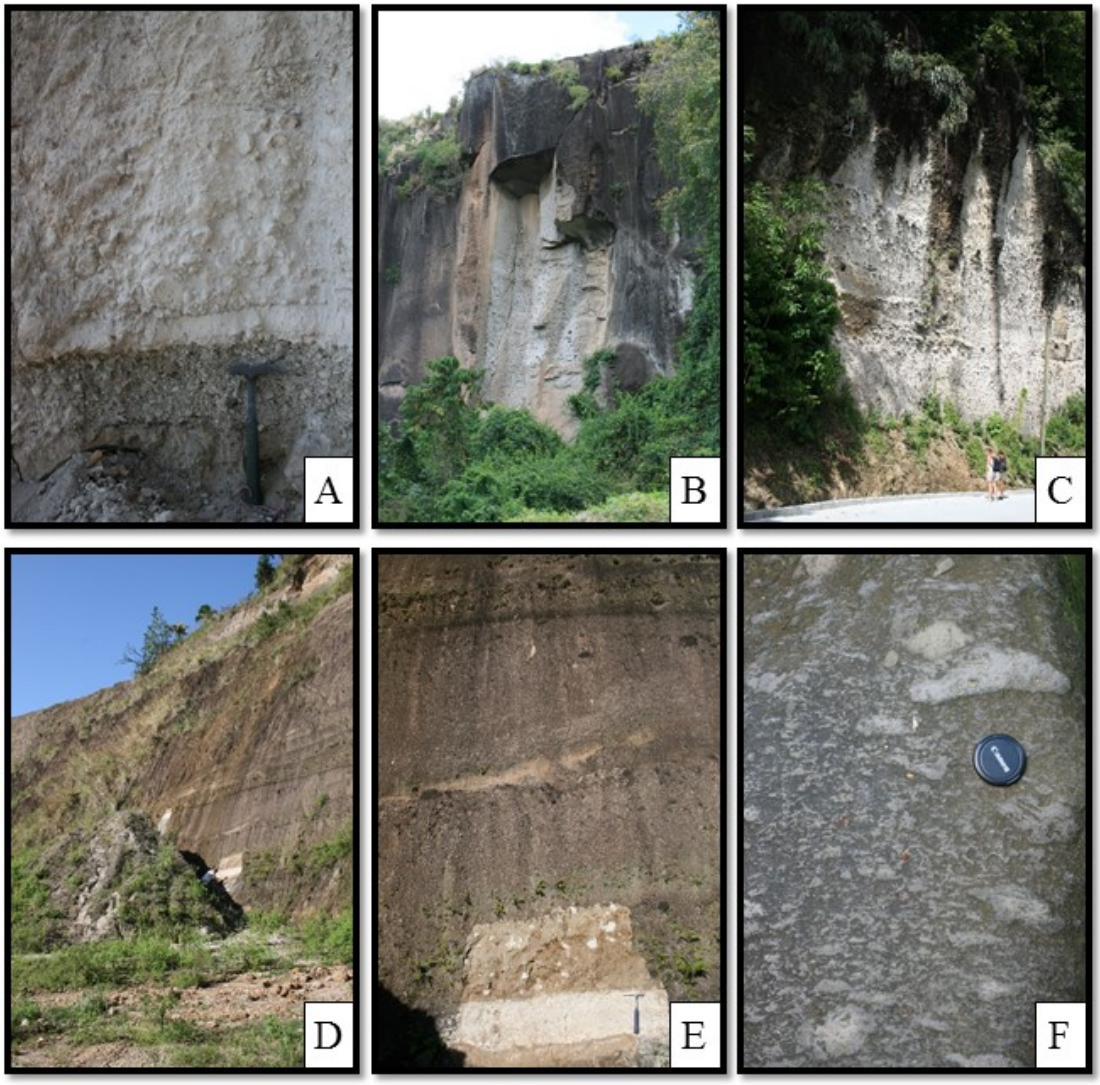

Figure III.4: ***Photos of the three main ignimbrites studied here: Layou, Roseau and Grand Fond****. A: Layou basal fallout deposit covered by a pyroclastic density current (PDC); B: Layou partially welded pumiceous PDC; C: Grand Fond PDC; D: Roseau outcrop at Cocoyer quarry showing a basal plinian fallout deposit (the white cleaned section on the outcrop) and overlain PDC deposits; E; Roseau basal pumice fallout (white part) and the first PDC; F: Roseau, welded PDC with fiammes at Trafalgar.*

III.4.2. ^{14}C ages

A series of charcoals and paleosols have been sampled in the different outcrops and quarries (see location in Fig. III.2). The results are reported in table III.1 and figure III.5.

Deposit	Location	Reference	Volcanic deposit type	Sample material	$\delta^{13}C$ (%)	Radiocarbon age year BP ±1 σ	Calendar age year (95.4%, 2σ) cal BC	Oxcal combined radiocarbon age uncal year BP ±1 σ	Calendar age year (95.4%, 2σ) cal BC	Calendar age year cal BP
Layou										
	8	DOM 46 a	fallout	charcoal	-27	49100 ±3300	62859 - 42173	48 788 ±2222	54235 - 43055	50 598 ±5590
	8	DOM 46 d	fallout	charcoal	-26	48500 ±3000				
	8	DOM 46 c	fallout	charcoal	-28	>47800				
Roseau										
	1	DOM 60 a0	fallout	paleosoil	-25	27010 ±250	29415 - 28801	29 137 ±141	31771 - 31007	33 342 ±382
	1	DOM 60 a1	fallout	organic matter	-26	26330 ±230	29071 - 28047			
	1	DOM 60 d1c	fallout	charcoal	-26	29300 ±330	32150 - 30770			
	2	DOM 48 g2-1	PDC	charcoal	-15	32670 ±460	36265 - 33776			
	2	DOM 48 g2-2	PDC	charcoal	-23	31310 ±400	34153 - 32574			
Grand Fond										
	11	DOM 43 b2	fallout	charcoal	-20	19990 ±140			22450 - 21736	24 046 ±357
other deposits										
Left bank	**7**	DOM 52 b1	PDC	charcoal	-28	28960 ±300	31868 - 30279	28 173 ±133	30603 - 29565	32 037 ±519
	7	DOM 52 b3	PDC	charcoal	-25	26350 ±220	29086 - 28119			
	7	DOM 52 b7	PDC	charcoal	-28	31830 ±400	34619 - 32918			
	7	DOM 52 b8	PDC	charcoal	-28	26400 ±210	29101 - 28268			
upper Goodwill	**2**	DOM 49 k1	reworked	charcoal	-22	27750 ±260		27 776 ±156	29948 - 29243	31549 ±353
	2	DOM 49 k2	reworked	charcoal	-18	27550 ±260				
	2	DOM 49 k3	reworked	charcoal	-27	27840 ±290				
Goodwill entrance	**3**	DOM 58	fallout	paleosoil	-30	14870 ±70			16347 - 15937	18 095 ±205
PPR1	**2**	DOM 55	fallout	paleosoil	-27	10615 ±45			10753 - 10578 (92,4%)	12 619 ±88
PPR2	**2**	DOM 56	fallout	paleosoil	-27	10510 ±45			10688 - 10431 (92,1%)	12 513 ±129
PPR3	**2**	DOM 57	fallout	paleosoil	-22	8370 ±40			7531 - 7344	9 391 ±94
Petite Savane PS3	**14**	DOM 75a	fallout	paleosoil	-27	9205 ±45			8547 - 8300	10 377 ±124
Petite Savane PS4	**14**	DOM 75c	fallout	paleosoil	-26	4900 ±30			3715 - 3638 (92,3%)	5 360 ±39

Table III.1: Radiocarbon ages and calendar age conversions. *Calibration uses the OxCal 4.2 program (Bronk Ramsey, 2009) and atmospheric data of the IntCal13 calibration curve (Reimer, 2013). The combined ages are radiocarbon ages. The calendar BP age is calculated on the basis of the range of cal BC ages obtained through OxCal, supposing a Gaussian repartition ofthe probability of occurrence of the age.*

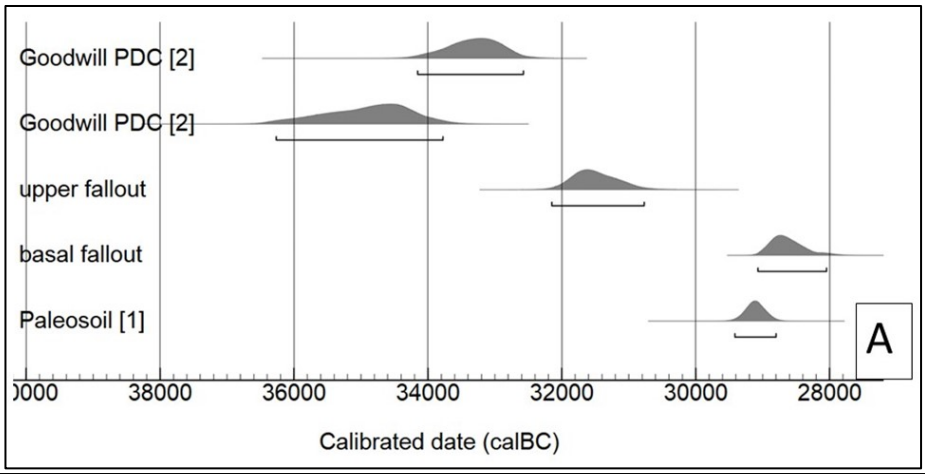
Goodwill PDC [2]
Goodwill PDC [2]
upper fallout
basal fallout
Paleosoil [1]
A
)000
38000
36000
34000
32000
30000
28000
Calibrated date (calBC)

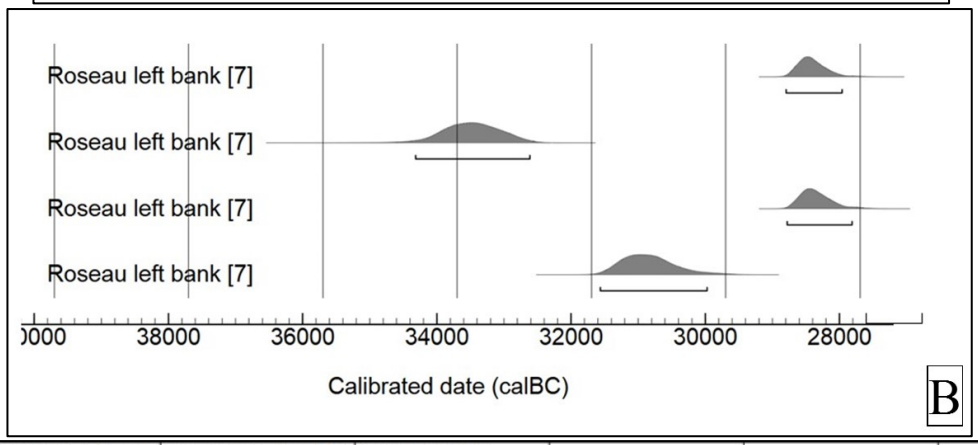
Roseau left bank [7]
Roseau left bank [7]
Roseau left bank [7]
Roseau left bank [7]
)000
38000
36000
34000
32000
30000
28000
Calibrated date (calBC)
B

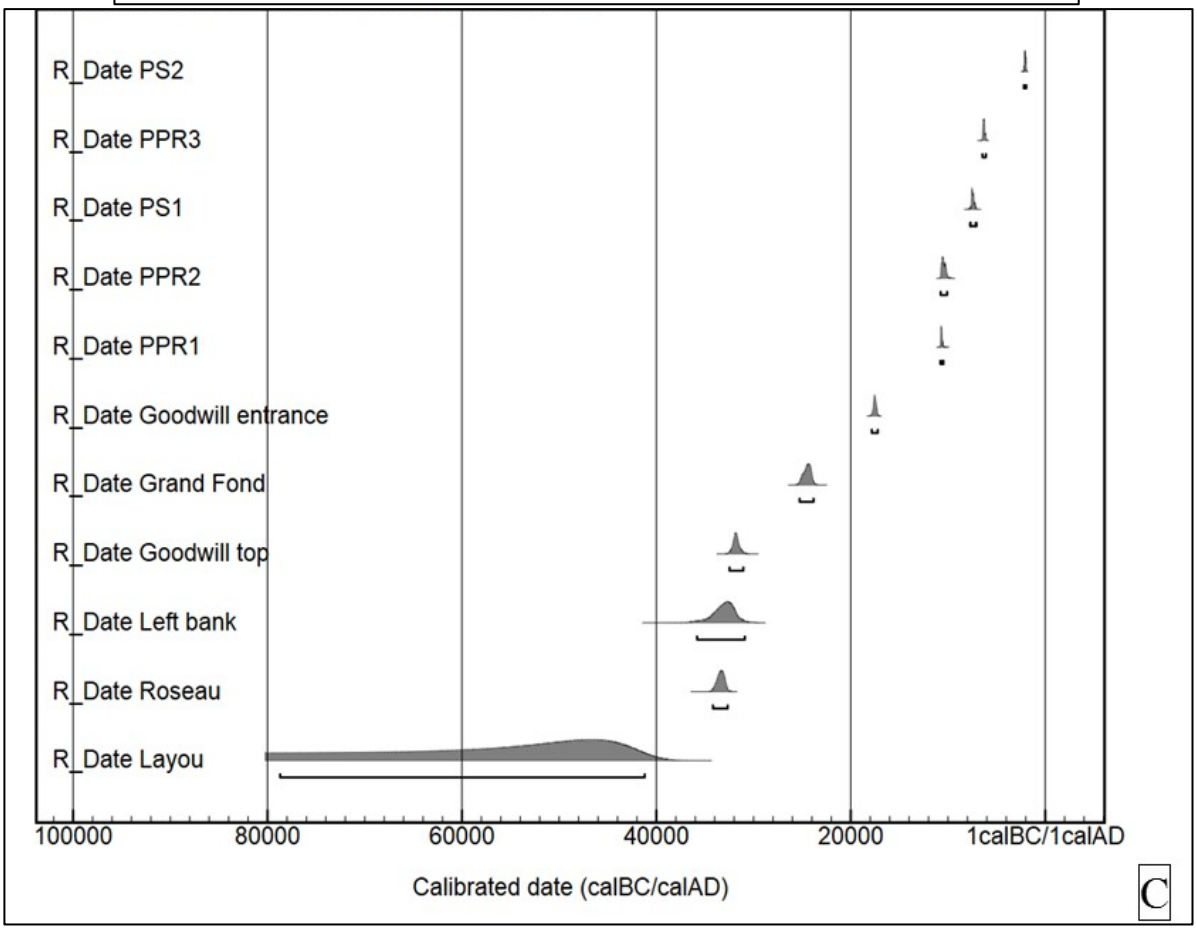
R_Date PS2
R_Date PPR3
R_Date PS1
R_Date PPR2
R_Date PPR1
R_Date Goodwill entrance
R_Date Grand Fond
R_Date Goodwill top
R_Date Left bank
R_Date Roseau
R_Date Layou
100000
80000
60000
40000
20000
1calBC/1calAD
Calibrated date (calBC/calAD)
C

Figure III.5: *Probability domain of calibrated ages (in cal BC) for (A) Roseau deposits (B) Roseau river left bank and (C) for Dominica. (A) Roseau deposits include the paleosol, the fallout and the pumiceous PDC deposits. (B) The four ages obtained for the left bank (quarry on the left bank of the Roseau river; location 7) come from charcoals that likely correspond to a "young" forest grown after the Roseau eruption. (B) Synthesis of the different ages obtained for Dominica: Layou, Roseau and Grand Fond. 'Goodwill top' represents the reworked material at the top of the Goodwill quarry. 'Goodwill entrance' is the fallout and pumiceous PDC deposit close to Goodwill quarry (location 3). PPR1 to 3 are the three fallout deposits at the top of the Goodwill quarry (location 2). PS1 and 2 are the fallout deposit at Petite Savane in the southeast of Dominica (location 14). Data are in Table 1.*

Charcoals sampled in the Layou ash- and pumice-PDC deposits give the oldest age, with 50 598 ± 5 590 yrs cal BP. The large uncertainty on the age is due to the fact that the age is at the resolution limit of the ^{14}C date; a third charcoal gives a radiocarbon age older than to 47 800 yrs BP. In the Roseau valley, the paleosol below the basal plinian fallout deposit in the Cocoyer Estate quarry and organic matter sampled within the first eruptive unit of the fallout deposit display similar age of 31 061 ± 307 and 30 512 ± 512 yrs cal BP. Two charcoals sampled in the ash- and pumice-PDC deposits in the Goodwill quarry, show a mean age of 33 413 ± 690 yrs cal BP. Four charcoals sampled in ash- and pumice-PDC in the Lacorne quarry (location 7, Fig. III.2) give a mean age of 32 037 ± 519 yrs cal BP. Three charcoals sampled in reworked deposits covering the last plinian fallout deposit of the Goodwill quarry have a mean age of 31 549 ± 353 yrs cal BP. A unique age of 24 046 ± 357 yrs cal BP has been obtained for the Grand Fond pumiceous deposit on a charcoal sampled in the first ash- and pumice-PDC deposit covering the plinian fallout deposit. No age has been obtained on the last two ignimbritic deposits of Grande Savane and Grand Bay.

A series of paleosol have been sampled at the base of different fallout deposits at the top of the Goodwill quarry (location 2, Fig. III.2), at the Goodwill entrance (location 5, Fig. III.2) and in the Petite Savane section (location 14, Fig. III.2). At Goodwill, the paleosols intercalated between the successive plinian fallout deposits give ages of 12 619 ± 88, 12 513 ± 129 and 9391 ± 94 yrs cal BP from the lower to the upper deposits. The paleosol at the base of Goodwill entrance fallout deposit provides an age 18 095 ± 105 yrs cal BP, intermediate between the last ignimbritic deposit of Grand Fond and the first deposit identified at the top of the Goodwill quarry. The two paleosols sampled at the base of two more recent fallout deposits at Petite Savane have an age of 10 377 ± 124 and 5360 ± 39 yrs cal BP.

III.4.3. Lithology

The lithology of matrix samples of 42 plinian fallout and PDC deposits has been carried out in three grain sizes: 0.125-0.250, 0.250-0.500, 0.500-1 mm. The results permit to distinguish different groups based on the proportion of orthopyroxenes, clinopyroxenes and amphiboles (Fig. III.6 and synthesis in Table III.2), the presence or not of quartz and also the abundance of xenolithic clasts (dominantly hydrothermally altered clasts) (Figure III.5).

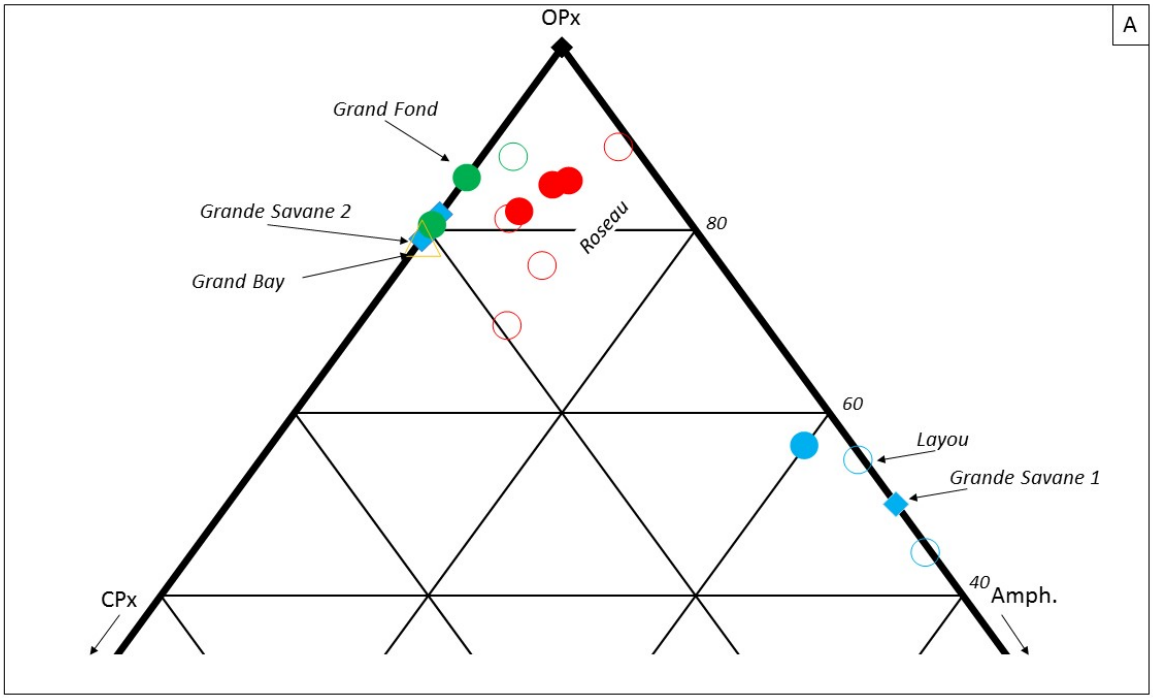

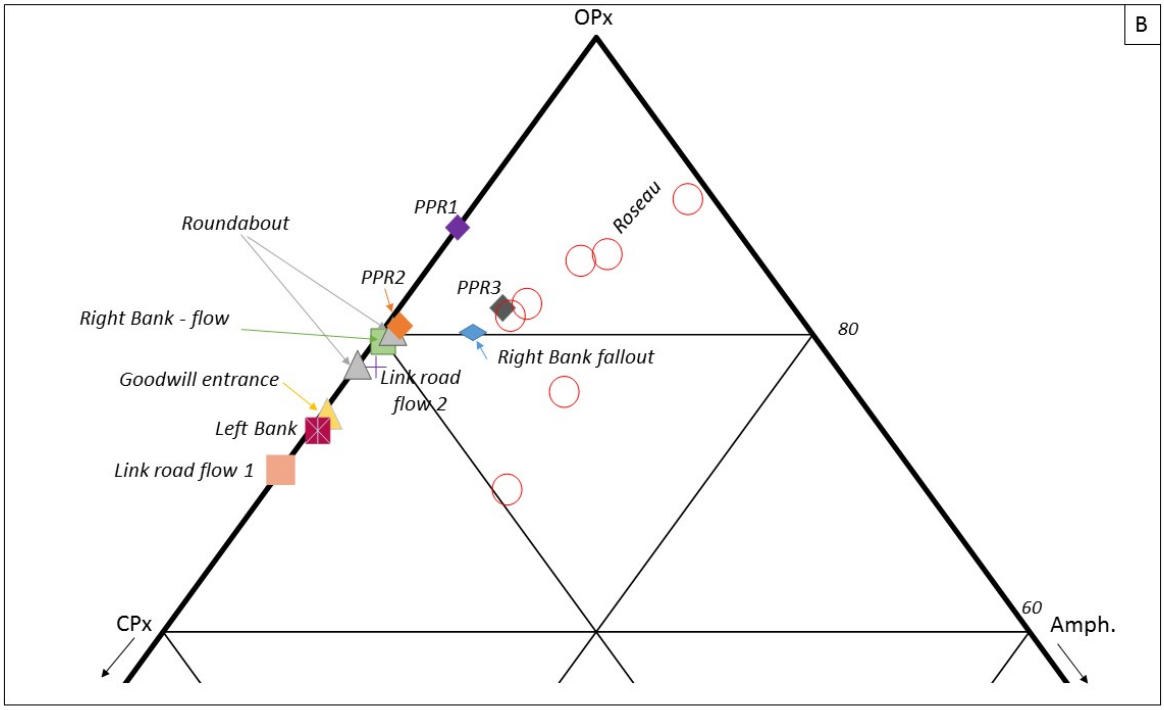

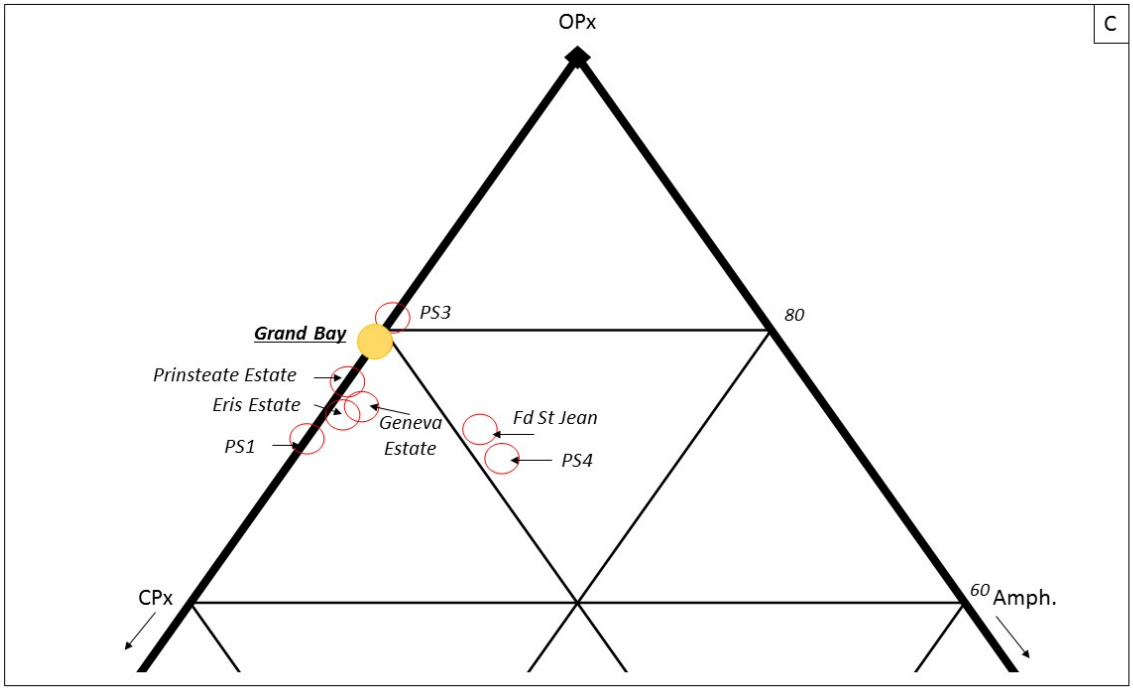

Figure III. 6: Pumice lithology in a orthopyroxene (OPx) - clinopyroxene (CPx) - amphibole (Amph) content ternary. *Solid symbols: fallout deposit samples. Open symbols: PDC deposit samples associated to the fallout deposit; blue circle for Layou, blue diamonds for Grande Savane, red circles for Roseau, green circle for Grand Fond, yellow for Grand Bay. A: the five ignimbritic deposits of Grande Savane (Unit 1 and Unit 2), Layou, Roseau, Grand Fond and Grand Bay. B: Details of the Roseau valley deposits. All the different outcrops located in the Roseau valley, as precised in Fig. 2, are detailed here. C: South Dominica: the Grand Bay ignimbritic deposit is compared to the other identified plinian and pumiceous PDC deposits in the southern Dominica (Fond St. Jean and Petite Savane).*

The comparison between the fallout and the pumiceous PDC deposit, when present within the same sequence, show that the plinian fallout deposits display more homogeneous lithological characteristics than their PDC counterpart (with the PDC domain overlapping the plinian one). This may be explained by the possible gravity segregation during transport within the flow compared to the fallout. Nevertheless, where the fallout is absent, the data obtained on the PDC may serve to discriminate between the different deposits, keeping in mind possible data dispersion.

The pumice fallout deposits from Layou depart from the other pumiceous deposits by containing a significant proportion of amphiboles (13%; Table III.2; Fig. III.6A) and few quartz (1-2%) – that are absent in the other deposits - but no or very few clinopyroxenes. The PDC deposit counterpart evidences similar proportion of amphibole as the fallout. The plinian

fallout deposits from Roseau contain a lower proportion of amphiboles than Layou (~ 2% with respect to 13%), slightly higher clinopyroxene content, for similar proportion of orthopyroxenes (~25%). The flow deposit counterpart shows a similar amphibole content but a more variable orthopyroxene/clinopyroxene ratio than the fallout. Grand Fond fallout deposit contains no amphibole, but similar proportions of pyroxenes (orthopyroxenes and clinopyroxenes) as Roseau. The flow deposit counterpart shows the same characteristics than the fallout. For Grande Savane, Unit 1 has the same signature as Layou, with a high proportion of amphibole (~10%) but without quartz, whereas Unit 2 shows completely different lithological proportions, with in particular no amphibole.

Within the Roseau valley numerous pumiceous deposits have been identified (location 3 to 7; Fig. III.2). The lithology evidences that only the PPR3 and the fallout deposit of the Roseau river right bank (Narakiel's inn) display similar signature as Roseau deposits. The others do not have amphibole and differ by the relative abundance of orthopyroxenes with respect to clinopyroxenes (Fig. III.6B). The PPR1 fallout deposits sampled in the Goodwill quarry show the highest proportion of orthopyroxenes. The two fallout deposits of the Roseau river right bank-roundabout show the same domain as the PPR2 fallout in the Goodwill quarry. The PDC deposits along the Roseau river right bank at Narakiel's inn and the unique fallout deposit identified along the Link Road (link fall) share the same characteristics. The Goodwill entrance fallout deposit, though close to Goodwill quarry, has a different signature with a higher proportion of clinopyroxenes; this is similar to the PDC deposits sampled in the left bank of Roseau river (location 7, Fig. III.2) and the bottom flow of the link road (location 6, Fig. III.2).

In the south of Dominica, we first focus on the Grand Bay ignimbrite, for which only PDC deposits can be identified, clearly on the beach but less easily along the different valleys. Three samples taken along the Geneva valley evidence the same signature as Grand Bay, with no amphibole and a orthopyroxene/clinopyroxene ratio similar to some deposits within the Roseau valley. The results obtained on five fallout deposits at Fond St. Jean and Petite Savane show either a composition close to those of Grand Bay (amphibole absent) or amphibole-present (the Fond St. Jean – fallout and the last plinian fallout of Petite Savane PS4) (Fig.III.6C).

Deposit	**Layou**				**Grande Savane**			
type	*Fallout*		*Flow*		*Flow - Unit 1*		*Flow - Unit 2*	
n	2		3		2		2	
	mean (%)	σ (%)	mean (%)	σ (%)	mean (%)	σ (%)	mean (%)	σ (%)
feldspar	57	7	72	1	78	2	79	3
orthopyroxene	23	6	11	2	10	2	15	2
clinopyroxene	1	1	0	0	0	2	4	1
amphibole	13	0	13	2	10	1	0	0
oxyde	5	1	2	1	1	1	3	0
quartz	2	0	1	0	0	0	0	0

Deposit	**Roseau**				**Grand Fond**				**Grand Bay**			
type	*Fallout*		*Flow*		*Fallout*		*Flow*		*Fallout*		*Flow*	
n	3		4		2		1				4	
	mean (%)	σ (%)	mean (%)	σ (%)	mean (%)	σ (%)	mean (%)	σ (%)	mean (%)	σ (%)	mean (%)	σ (%)
feldspar	67	2	78	3	65	3	72				68	8
orthopyroxene	25	1	16	0	26	3	23				21	5
clinopyroxene	3	1	2	2	5	1	3				7	2
amphibole	2	0	2	1	0	0	0				0	0
oxyde	4	1	2	1	3	2	3				2	0
quartz	0	0	0	0	0	0	0				2	3

Table III.2: Lithological signature of the Layou, Roseau, Grand Fond, Grande Savane and Grand Bay ignimbritic deposits*. Numbers are percentages calculated for crystal fraction.*

III.4.4. Magma composition

III.4.4.1. Major elements

All whole rocks are dacitic: Layou and Grande Savane deposits are clearly dacitic (SiO_2 >64 wt% for alkali content ~5 wt%) whereas Roseau, Grand Fond and Grand Bay are slightly less silia-rich (SiO_2 : 62-63 wt% for alkali content 4.5-5 wt%) (Fig. III.7A). The Morne Trois Pitons and the Micotrin lava domes are also dacite. The studied scorias are basaltic in composition, with SiO_2 between 49-51 wt% for alkali content between 2.5 – 4.5 wt%. All matrix glasses are rhyolitic in composition, with SiO_2 between 76.5-78 wt% for alkali content comprises 5.5-7 wt%.

We compare the composition of the five ignimbritic deposits with those of other stratigraphically correlated outcrops (Fig.III.7B). Londonderry shows the most andesitic composition (SiO_2 >61.5 wt% for alkali content ~4.5 wt%). The deposits in the Roseau valley are dacite too (SiO_2 >62.5-63.5 wt% for alkali content ~4.5-5.5 wt%). The Fond St. Jean is dacitic (SiO_2 :64 wt% for alkali content ~5 wt%). As for the major pumiceous eruptions, all matrix glassses are rhyolitic in composition, with SiO_2 between 75.5-78 wt% for alkali content comprises 5.5-6.5 wt%.

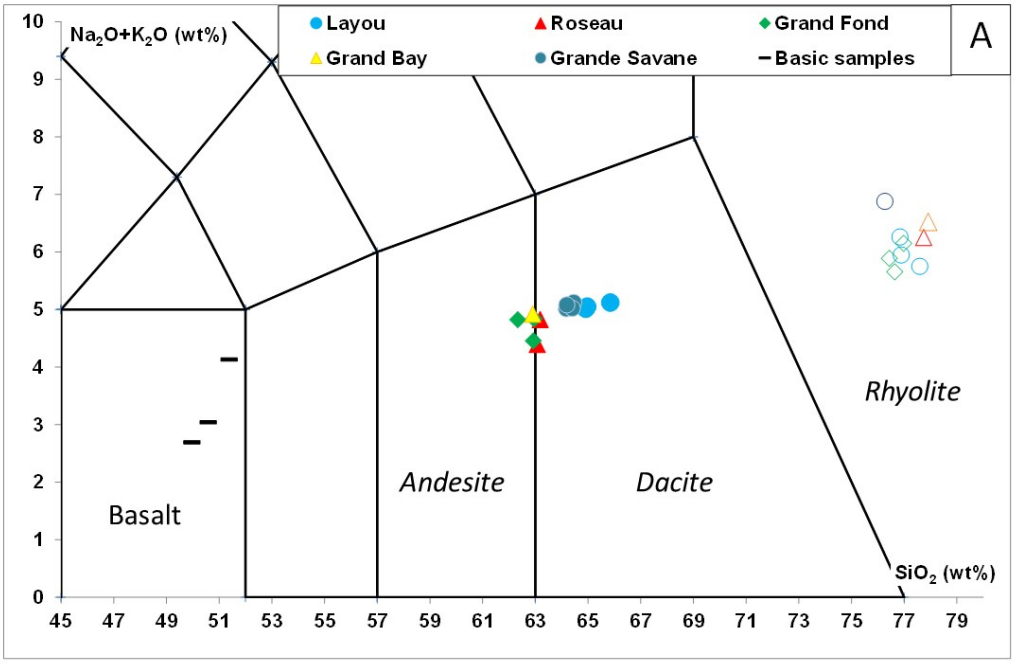

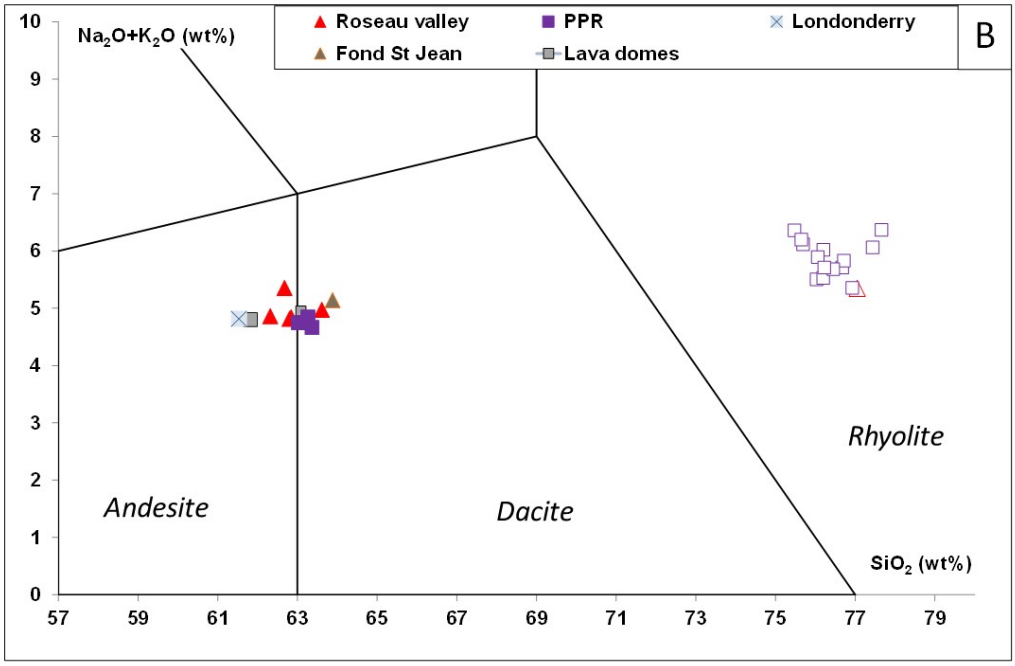

Figure III.7: Alkali-silica diagram for whole rocks (solid symbols) and matrix glass (open symbols). *A: the ignimbritic deposits of Layou, Roseau, Grand Fond, Grand Bay and Grande Savane and the basaltic scoria (locations 17 and 18, Fig. 2). B: the other studied deposits: the different outcrops in the Roseau valley (locations 3, 4, 5 , 7), the plinian eruptions that occur after the Roseau eruption (PPR1 to 3, location 2), the Londonderry ignimbritic deposit (location 15), the Fond St. Jean plinian deposit (location 13) and also the two lava domes of Morne Trois Pitons and Micotrin. Uncertainties: whole rocks : SiO_2 (<1%), Alkali (Na, K : <5%); matrix glass: each point represents a mean value of at least 5 analysis by EPMA (Camparis, France); SiO_2 (<0.7%), Alkali (Na, K : <5%).*

III.4.4.2. Trace element

Selected trace element correlation diagrams are presented in order to go in detail in the geochemical signature of the different eruptions (Fig.III.8). Whole rocks and matrix glasses describe a perfect linear correlation through origine between U and Th, both highly incompatible elements and used as a differentiation index. The results show that the correlation is similar for all studied deposits in Dominica. Such a positive U-Th correlation suggests that the whole rocks and the matrix glasses are related by a fractional crystallization process (Fig.III.8A, C). Sr generally behaves as a strong incompatible element ; but here the massive feldspar crystallization induces a compatible behaviour when plotting Sr as a function of K_2O in whole rocks and matrix glasses (Fig. III.8B, D).

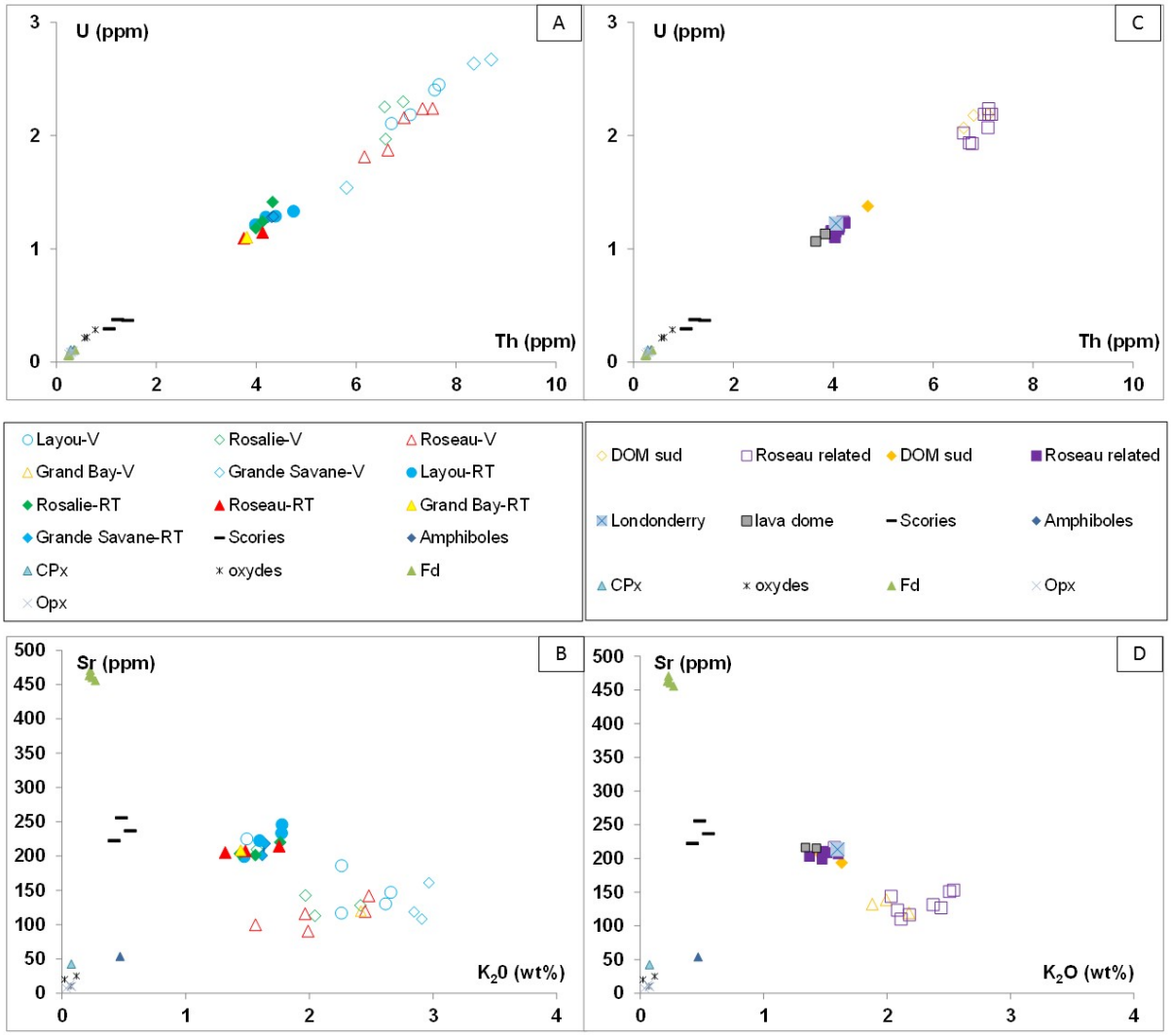

Figure III.8: Petrology of the eruptive products on the basis of U/Th and Sr/K_2O correlations for whole rocks (solid symbols) and matrix glasses (open symbols). *A, B: the ignimbritic deposits of Layou, Roseau, Grand Fond, Grand Bay, Grand Savane, the basaltic scoria (locations 17 and 18, Fig. 2), and the main minerals (feldspars, orthopyroxenes, clinopyroxenes, amphiboles and oxides). C, D: the different outcrops in the Roseau valley referred as 'Roseau related' including the deposits of the locations 2 (PPR1 to 3), 3 (Goodwill quarry), 4 (Roseau Roundabout), 5 (Roseau right bank) and 7 (Roseau left bank), the Londonderry ignimbritic deposit, the Fond St. Jean and Petite Savane plinian deposits (referred as DOM Sud) and also the two lava domes of Morne Trois Pitons and Micotrin. For each diagram the degree of melt differentiation increase from left to right. Data are obtained by ICP-MS on handpicked glass shards for matrix glass, powdered whole rocks and handpicked minerals. Uncertainties are reported in Tables III.S3 and Table III.S5 (supplementary material).*

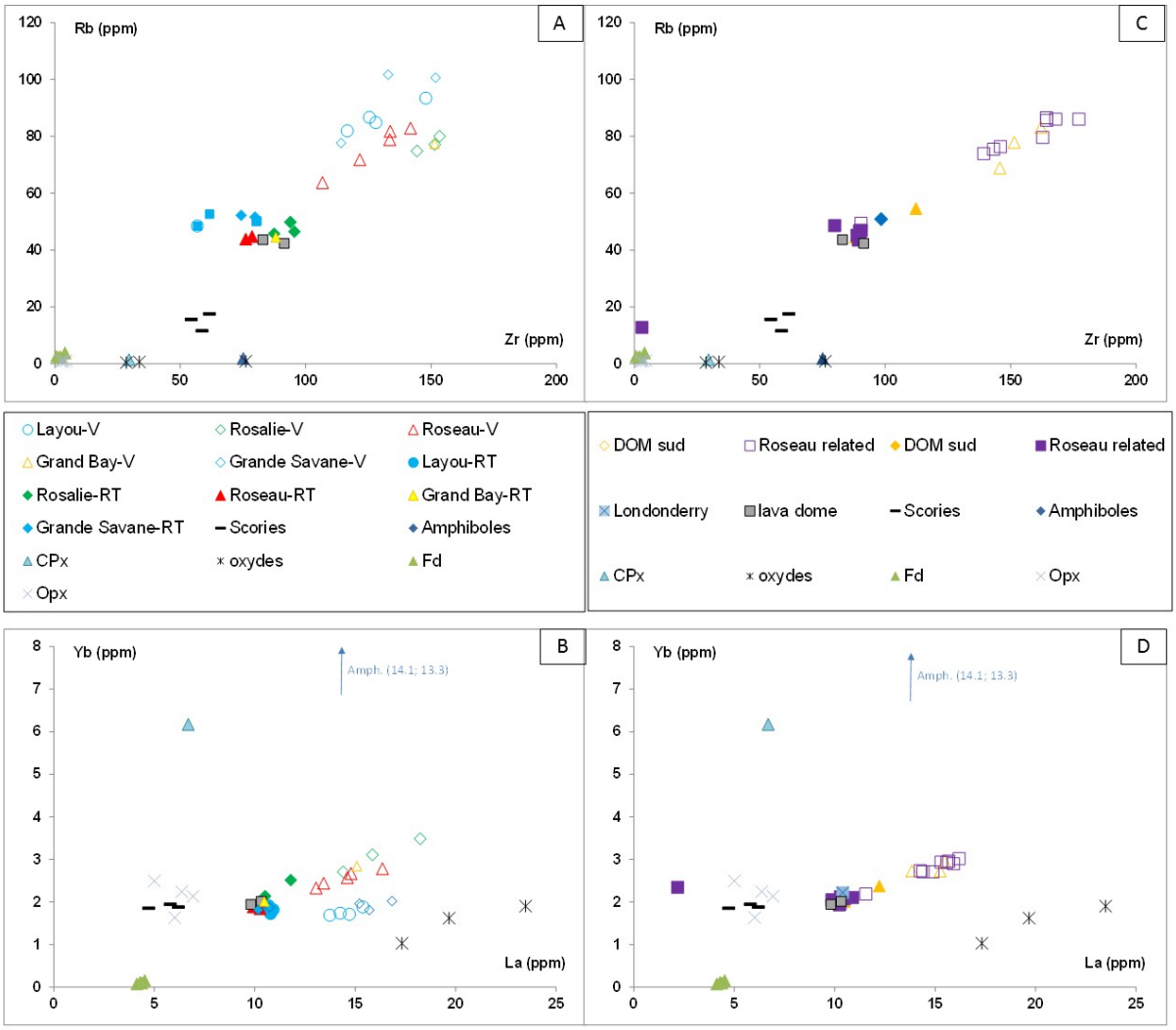

Figure III.9: Trace element signature on the basis of Rb/Zr and Yb/La correlations for whole rocks (solid symbols) and matrix glasses (open symbols). *(see legend Fig. III.8).*

Other trace element such as rare-earth elements (La, Yb), Rb or Zr are helpful to distinguish different trends within the three major pumiceous eruptions that may be used as a reference to correlate with other deposits (Fig. 9). In particular, Yb-La or Rb-Zr correlations, using La and Zr as incompatible element tracer of differentiation process, evidence two signatures : the Layou-Grande Savane trend, already present in whole rock but more precisely indentified using matrix glass, is dominated by the amphibole crystallization effect. Amphiboles induce a Yb impoverishment of the matrix glass with respect to whole rocks (similar to Y, not shown). Although the differentiation domain is similar to Roseau, Grand Bay and Grand Fond, amphibole provides a particular signature of the Layou-Grande Savane volcanic products. Unfortunately no systematic data has been obtained for Londonderry (only one whole rock). The three main crystals, orthopyroxenes-feldpars-oxydes are responsible for

the signature of Roseau, Grand Bay and Grand Fond magma. The volcanic products from the PPR and the southern part of Dominica (Fond St. Jean, Petite Savane) display geochemical signature which is similar in composition to the Roseau-Grand Fond-Grand Bay one.

III.5. Discussion

III.5.1. Toward a new stratigraphy of the ignimbritic deposits of Dominica

On the basis of the fieldwork (stratigraphy), ages (charcoals within volcanic deposits and paleosols), lithology and geochemical data (major and trace element signature on whole rock and matrix glass), we propose a revised chronostratigraphy of the ignimbritic deposits of Dominica of the last 50 kyrs. Following the first proposition of a unique and voluminous eruption, called the Roseau Tuff, (Sigurdsson, 1972, Carey and Sigurdsson, 1980), making this eruption the largest one of the last 200 ky in the Lesser Antilles, recent works have argued for several distinct events for the Roseau Tuff (Smith et al., 2013; Howe et al., 2014). Here we first focus on the four to five major ignimbritic deposits involving several to ten km^3 of magma, discussing their extent, their possible vent origin, and the relationships with typical plinian events of lower volume.

Roseau eruption: The Roseau sequence begins with a plinian fallout deposit (never described up to now since not visible in the Goodwill quarry), followed by a series of ash- and pumice-PDC deposits intercalated with one plinian fallout deposit. These deposits are observed principally in the Cocoyer Estate quarry (Fig.III.2, location 1; FigIII.3), in the lower part of the Goodwill quarry up to a first paleosol (Unit 1, Fig.III.2, location 2) and in several small sections in the Roseau town area that we correlated on the basis of similar lithology and geochemistry (Fig.III.2). Nevertheless, most of the deposits recognized in different sections in the bottom of the Roseau valley (Fig.III.2, locations 3-7) belong to more recent fallout and PDC eruptions, that were deposited in the valley dug by erosion after the Roseau event. In the higher part of the Roseau valley (e.g. at Trafalgar Falls), the Roseau deposits form also high cliffs (up to 100 m) of flattened pumice (generating fiammes) welded material (Fig.III.2, 4). Different ages were obtained for the deposits recognized in the Roseau valley (~28 000 to ~46 000 yr cal BP) by different authors (Lindsay et al., 2003 for a summary), but some of them probably belong to other eruptions, as we discuss hereafter. The ages that we obtain on a paleosoil at the base of the sequence, on a charcoal within the first pumice fallout deposit, and in the ash-and pumice-PDC deposits, bracket the Roseau eruption date between 28 000 and 36 000 yrs cal BP, with an average age of 33 342 ±382 yrs cal BP (Table 1; Fig.III.5).

The lithological and geochemical characteristics of the Roseau deposits, together with the new ages provided here, allowed correlating and deciphering the genetic origin of several sections that were originally attributed to the Roseau tuff eruption. The deposits of the Roseau eruption are typically characterized by a low proportion of amphibole (~10%) and clinopyroxenes (0-20%) compared to the high proportion of orthopyroxenes (70-90%); no quartz is present. The rhyolitic melt of Roseau dacitic magma may be explained by fractional crystallization, mainly dominated by feldspar crystallization, of a more mafic magma. The presence of a low proportion of amphiboles and clinopyroxenes do not influence the trace element signature, such as highlighted by the Rb-Zr or Yb-La correlations (Fig.III.8).

The distribution of the Roseau deposits argues for a vent localized on the summit area of Morne Trois Pitons- Micotrin volcanic center (Fig.III.2). The two voluminous lava domes of Morne Trois Pitons in the north and Micotrin in the south occupy the summit area. The similarity in the geochemical signature between these lava domes and the Roseau pumiceous deposits are in agreement with a common magma origin (Fig.III.8, 9). The ^{14}C dates on different block-and-ash flow deposits associated to these two lava domes provide a large range of time, between and 877 ±108 and 28 844 ±1983 cal yrs BP (Wadge, 1989, Roobol et al., 1983, Lindsay et al., 2005) which underlines the long and complex lava dome growth history that follows the Roseau eruption.

Grande Savane eruption: The related deposits that form the Grande Savane fan may be divided into two units with different lithological characteristics. The deposits of Grande Savane 1 are made of a succession of mainly highly welded PDC that can be followed in the valley reaching the Grande Savane fan (Fig. 2). No pumice fallout deposit is present at the base of the PDC deposits. Lithologically they are characterized by a high proportion of amphibole (10 %), but no clinopyroxene nor quartz. The non-welded deposits of Grande Savane 2 do not contain amphibole or quartz, but clinopyroxene (4 %), and higher proportion of orthopyroxenes. The unique age comes from the uppermost deposit of Grande Savane 2 and suggests > 22 000 yrs BP (Sparks et al., 1980). The geochemical signature of both units is clearly different from the other pumiceous deposits and is attributed to amphibole crystallization. Considering the location and distribution of Grande Savane 1 deposits within the different valleys leading to the sea, they clearly originate from Morne Diablotins volcanic center.

Layou eruption: The deposits that fill the Layou valley were first associated to the Roseau deposits (Carey and Sigurdsson, 1980), before becoming one independent ignimbritic eruption (Smith et al., 2013; Howe et al., 2014). The type deposit shows the succession of a plinian fallout deposit at the base and thick ash- and pumice-PDC deposits welded for some of them in the superior part (Fig.III.2). They are dated at 50 598 ±5530 yrs cal. BP (^{14}C dating); this age is the oldest obtained in this study and significantly differs from the other main ignimbrites . Lithologically, the Layou ignimbrite fingerprint is also different from the others, with a significant proportion of amphibole (13 %), automorphe quartz (1-2 %; the sole deposit to show them), and no clinopyroxene. The geochemical trend of Layou magma follows the one of Grande Savane 1 magma, although this latter do not have quartz and has a slightly lower differentiation degree. The lithological, geochemical, and age evidences thus validate Layou as an event independent from Roseau.

The origin of the Layou deposits is subjected to controversy. On the field, they can be followed in the higher part of the Layou valley up to the locality of Bells (9, Fig.III.2). In its higher part the Layou river results from the confluence of several rivers: most of them come from the Morne Diablotins volcanic center but some others originate from Morne Trois Pitons volcanic center. Unfortunately, the outcrop conditions in the upper part of the valleys preclude any clear identification of the origin of the Layou eruption. Yet, the geochemical signature of the magma (trace element correlation of glass) and the lithological data (the presence of amphibole) suggest that the magma at the origin of the Layou deposit share similar characteristics with the Grande Savane 1, whereas clearly differing from the other studied magmas, especially Roseau deposit. Thus we suggest that the vent at the origin of the Layou deposits is likely to be the Morne Diablotins volcanic center, as for the Grande Savane event.

Grand Fond eruption: The deposits that filled the valley of Rosalie and Grand Fond on the eastern coast of the island show first a succession of various pumice fallout and surges deposits followed by a thick sequence of pumiceous PDCs that form high cliffs in the different valleys reaching the Rosalie bay. The sole age obtained on a charcoal at the base of the first PDC overlying the fallout deposit is of 24 046 ± 357 yrs cal BP, which is slightly younger than the previous ages between 30 000 ± 1220 and 36 800 ± 8079 yrs cal BP (Carey and Sigurdsson, 1980). Taken into account the large uncertainty on these two ages and for comparison with the ages obtained in this study (by AMS), the age of 24 046 ± 357 yr cal BP for Grand Fond eruption is preferred. This makes this eruption more recent than Layou and

Roseau eruptions. The lithological data indicate a high proportion of orthopyroxenes, few clinopyroxenes but no amphibole and quartz, contrary to Roseau deposits that show some amphiboles and fewer clinopyroxenes. Although following the same geochemical signature as Roseau, Grand Fond and Roseau may be considered as two separate eruptions, based on their mineralogical and age differences. The Grand Fond deposits are located on the eastern flank of the Morne Trois Pitons - Micotrin volcanic center, which make it a probable eruptive center.

Grand Bay eruption: The outcrop conditions in the Grand Bay area precluded any identification of the base of the eruptive sequence: only thick ash- and pumice-flow deposits are observed in the Geneva valley down to Grand Bay. Geochemically, Grand Bay shares a common signature with Grand Fond and Roseau eruptions. The mineralogical composition of the deposits, with presence of clinopyroxene but no amphibole, is close to that of Grand Fond but clearly differs from Roseau. Different origins for Grand Bay eruption have been proposed. These deposits were originally related to the PPVC (Lindsay et al., 2003b), with no correlation with the Roseau eruption contrary to a more recent work that consider them as part of the Roseau sequence based on whole rock geochemistry (Smith et al., 2013). Because ages have been determined on deposits that are not clearly correlated to Grand Bay event (see discussion below for Fond St. Jean deposits), this leaves the age of the Grand Bay deposits still unclear. Taking into account the poor stratigraphic and age constraints on these deposits, we cannot rule out that Grand Bay could be contemporaneous to Grand Fond. We assume that Grand Bay deposits originate from Morne Trois Pitons – Micotrin volcanic center, the upper part of the Geneva valley doesn't allowing to follow clearly the cliffs due to the presence of younger lava domes (e.g. Watt Mountain or Morne Anglais dated to <10 000 yrs; Lindsay et al., 2005b).

Other pumiceous (plinian-type) eruptions

The post-Roseau plinian events

Several plinian and PDC eruptions occurred after the Roseau eruption, overlying the Roseau deposits at the top of the cliffs, in the Goodwill quarry (PPR 1 to 3; location 2; Fig.III.2, 3), or in the bottom of the Roseau valley (Goodwill entrance, location 3; right bank, location 4 to 6; left bank, location 7; Fig.III.2). Five eruptions can be distinguished. The first one, the deposits of which are located on the left bank of Roseau river, occurred probably soon after the Roseau eruption as indicating by the ages obtained on four charcoals sampled in the PDC

deposit, giving a mean age of 32 037 ± 519 yrs cal BP (Fig. III.2; location 7). Whereas this age is close to the Roseau event one, the two deposits differs in terms of presence of amphiboles (in the Roseau products but absent in this PDC deposit). The abundance of charcoals in the pumice PDC deposits indicates that the eruption occurred long enough after the Roseau event so that the forest had time to grow again (even if it does not take more that few centuries in a humid tropical climate). The four following eruptions are younger, based on ages obtained on different paleosoils at the base of the plinian deposits that cover the deposits of the Roseau eruption (i.e., Goodwill entrance: 18 095 ± 205 yrs cal BP, PPR1: 12 619 ± 88 yrs cal BP, PPR2 : 12 513 ± 129 yrs cal BP and PPR3: 9 391 ± 94 yrs cal BP). Although the magma compositions of these deposits are similar (andesite-dacite whole rocks and rhyolitic matrix glasses), there are some differences in terms of lithology with the presence of amphiboles in the more recent deposits of PPR3 and variations in the proportion of accidental clasts in the plinian fallout deposits. No age has been obtained on the Roseau right bank plinian deposit overlying the Roseau PDC, but this deposit is mineralogically close to PPR3. Therefore, these 5 post-Roseau plinian eruptions correspond to 5 distinct events. Interestingly, contrary to the large ignimbritic events, no voluminous PDCs followed, or were associated to, these plinian fallouts. All these plinian eruptions probably originate from Morne Trois Pitons-Micotrin volcanic center, as for the Roseau tuff.

Fond St. Jean – Petite Savane: Several plinian fallout deposits outcrop at Fond St. Jean and Petite Savane (Fig.III.2, 3) on the south-eastern part of Dominica. Four distinct fallout deposits separated by paleosol are present at Petite Savane. The two latest plinian eruptions are dated through their related paleosols and give ages of 10 377 ±124 and 5 360 ±39 yrs cal BP. Mineralogically they cannot be correlated to Fond St. Jean or Grand Bay deposits. They more likely correspond to an explosive activity that occurs during the recent period, possibly originated from vents such as Morne Anglais, Watt Mountain or Grande Soufrière Hill's (Fig. 1). Nevertheless ^{14}C datations of Fond St. Jean deposits provide ages of 41 012 ±939 yrs cal BP (Lindsay et al., 2005b), making it an older event, distinct from Grand Bay on the basis of mineralogy (amphibole present in Fond St. Jean whereas absent in Grand Bay). Therefore, Fond St. Jean may not be considered as the distal facies of Grand Bay ignimbrite, as previously proposed (Lindsay et al., 2005b; Smith et al., 2013). Mineralogically, Fond St. Jean resembles PS4, but linking both events would require ages younger than 5 360 ±39 yrs cal BP for Fond St Jean, which is not compatible with the age previously proposed (Lindsay et al., 2005b). Fond St Jean and PS4 are thus probably two distinct events.

We can consider that on the basis of these new data, four or five voluminous ignimbritic deposits (depending if we consider Grand Fond and Grand Bay deposits representing the same eruption or not) and between 6 to 9 smaller plinian eruptions occurred in the last 50 kyrs in the central part of Dominica. All these eruptions contributed to disperse ash- and pumice-fallout deposits offshore and for the voluminous ignimbritic eruptions turbiditic deposits when the large ash-and pumice-PDCs enter the sea. They contribute to the voluminous offshore deposits proposed previously to belong to a unique and large eruption (Carey and Sigurdsson; 1980; Witham, 1990).

III.5.2. Estimation of the erupted volume

The volume of the ignimbritic eruptions of Dominica is very difficult to estimate because of two major factors: i) the poor outcrop conditions on the island due to the dense rainforest, ii) the likely loss of PDC material into the sea, as highlighted by some piston cores analyses and pumiceous turbiditic deposits attributed to Dominica on lithological and geochemical basis. As for the on-land deposits, the attribution of the offshore deposits to a given ignimbritic episode is questioned. The pyroclastic material in the Grenada basin was first supposed to belong to the unique event of Roseau, but the following studies have shown that not only the Roseau eruption extended offshore in the Grenada basin, but nearly all the ignimbritic eruptions of Dominica. For instance, the Grande Savane ignimbrite show an offshore extension as a deep-sea fan (Sparks et al., 1980).

Recent works on cores obtained west of Martinique in the Grenada Basin during the IODP Expedition 340 also show that very thick pumiceous turbiditic deposits are present particularly in a cores located 90 km from the Martinique coast and 140 km from Dominica in the extension of the drainage areas of the western submarine flanks of Dominica (Le Friant, 2015). Thick sequence of pumiceous turbiditic deposits originating from Dominica, on the basis of lithological and geochemical data (unpublished data), are identified on a thickness in the order of 110 m. Some of the turbiditic deposits are more than 10 m thick. All these deposits belong to eruptions that cover the last 50 000 years but also older eruptions. Based on a series of piston cores, Carey and Sigurdsson (1980) and Witham (1989) estimated the offshore extension of the Roseau tuff eruption to cover a large area of $1.4\ 10^4$ km^2 in the Grenada basin, corresponding to a volume of 30 km^3., although these values originally given for a unique event must now be revised in the light of the recent stratigraphic constraints (i.e., several explosive events during the last 50 000 yrs).

As a consequence, the volume of the on-land deposits per ignimbritic eruption is probably in the order of 2-3 km^3 for the ash-and pumice-PDC deposits, 3-4 km^3 for the pumice fallout deposits (on-land and offshore) and probably a minimum of 5-6 km^3 for the offshore deposits (turbiditic deposits). A crude estimation of the volume of each of the largest eruptions is in the order of 10-13 km^3. The volume of the more recent plinian events is probably lower, of the order of the km^3.

III.5.3. The plinian versus pyroclastic flow volume ratio: characteristic of the ignimbritic eruptions in Dominica

One of the characteristics of the ignimbritic eruptions in Dominica is the low ratio between the volumes of the plinian fallout deposits and the ash- and pumice-PDC deposits. For the three eruptions of Layou, Roseau and Grand Fond, the thickness of the basal fallout deposits is 30 cm, 26 cm and 70 cm, respectively, for similar deposit distances from the emission vent of ~ 7-8 km. The thickness of the basal fallout deposit of Grand Fond is higher than for the other eruptions. Adding, however, a ~15 cm plinian fallout deposit intercalated between the first Roseau PDC deposits to the basal Plinian fallout makes the total thickness of fallout deposit of Roseau of 40 cm. The difference on the thickness of the basal fallout deposit of Roseau and Layou with respect to Grand Fond may also be explained by the geographical position of the studied sections. Indeed, for Layou and Roseau, the section thickness is measured on the leeward coast, whereas on the windward coast for Grand Fond, and the dispersion of the ash and pumice fallout in the Lesser Antilles is strongly dependent on the dominant wind in the high atmosphere. For plumes higher than 10 km the dispersion of the tephra is namely higher in the East than in the West, confirmed by distribution offshore of the ash-and pumice-fallout deposits dispersed to the East (Carey and Sigurdsson, 1980). This could better explain the difference in thickness of the fallout deposits of these eruptions than differences in the intensity of the beginning of the eruption.

In any case, the volume represented by the fallout deposits of each of the three ignimbritic eruptions is much lower than the volume of their ash-and pumice-PDC counterparts. Assuming an energetic transition between plinian columns and PDCs (that is, a plinian column collapses into PDCs when the column cannot be sustained energetically anymore), we can infer that these eruptions started with a small plinian phase with a column that did not reach very high altitudes followed by a total collapse of the column generating PDCs that

flows into the valleys. Yet, to account for the high volumes of the PDCs, one must invoke an eruptive dynamic of direct magma overflow from the vent. This is enhanced by the partly welded deposits in the proximal zones which indicate a high temperature of emplacement that cannot be reached by repetitive collapse of high plinian columns (Walker, 1983).

The other plinian eruptions of lower volume show a significantly higher thickness of deposits, with more than > 1m at the same distance on the leeward part of the island (as for PPR1 or 2), and comparatively lower volumes of ash- and pumice-PDC deposits. These eruptions are more typical of plinian eruptions, with a high eruptive column, leading to higher tephra dispersion, and a final column collapse that generates ash- and pumice-PDC of low volume and no trace of welding.

III.5.4. Summit lava domes and caldera(s)

The summit area of Morne Trois Pitons-Micotrin and Morne Diablotins volcanic centers is characterized by voluminous lava domes. The Morne Trois Pitons lava dome represents a very large volume of 2 km^3 and shows a complex lobe morphology that may result of either one long eruption or several eruptions. The Micotrin lava dome, located on the southern flank of Morne Trois Pitons, is less voluminous. Both lava domes have compositions similar to the Roseau and Grand Fond pumiceous deposits and may have grown from a degassed magma at the end of these eruptions or more recently since some block- and ash-flow deposits at the base of these lava domes give much younger ages of 877±108 yrs to ~28 843±1983 yrs cal BP (Wadge, 1989, Roobol et al., 1983, Lindsay et al., 2005b).

One striking field observation related to these eruptions is the absence of large caldera structures in the summit area of Morne Trois Pitons-Micotrin or Morne Diablotins (although some authors mentioned caldera rims in the summit area (Demange et al., 1985), but the structure has not be confirmed and probably does not exist). The absence of caldera associated with large-volume ignimbrite (in the order of 10-13 km^3 of products, equivalent to 4-5 km^3 DRE) is not common. Based on our recent experimental investigations, we propose an explanation related to the depth of the magma chambers below Dominica. Indeed, we estimate a magma storage around 400 MPa (~16 km) (Chapter IV), which reduces considerably the collapse effect at subsurface after the reservoir emptying (Jellinek and DePaolo, 2003). Possible small structures, however, could be filled at the end of the eruptions

or during more recent eruptions by the voluminous lava domes observed in the summit area, thus hiding them.

III.5.5. The high magma production of Dominica: an anomaly in the Lesser Antilles arc

The existence of 4-5 eruptions producing a large volume of magma in the last 50 kyrs is an anomaly in the Lesser Antilles arc compared to the volume of magma emitted by the eruptions on the other islands. At Montagne Pelée, in Martinique, the eruptions are frequent (more than 28 eruptions were identified in the last 15 kyrs; (Westercamp and Traineau, 1983, Boudon et al., 2013), but the volume of emitted magma for each eruption is low (< 0.3 km^3 DRE for the plinian eruptions (Carazzo et al., 2012) and less than 0.2 km^3 DRE for the lava dome forming eruptions) and we have no evidence of large volumes of deposits in the past. At Soufrière of Guadeloupe, the last large eruption occurred 42 000 years ago (Pintade eruption, Boudon et al., 1989) and produced an estimated volume of 2-3 km^3 of products (~1 km^3 DRE), which is still a lower volume than the eruptions of the central part of Dominica (4-5 km^3 DRE). The recurrence of ignimbritic eruptions in the central part of Dominica during the last 50 kyrs suggest an important magma production rate and voluminous magma storage, which has not been effective on the other volcanoes of Dominica (Morne aux Diables in the north and PPVC in the south) or on the neighboring islands. This raises the question of the origin of such a high magma production rate and the accumulation conditions of such large volumes of magma beneath the crust. One of the hypotheses may be the particular tectonic position of Dominica within the Lesser Antilles arc, i.e. south of a large arc-scale sinistral horse-tail structure that accommodates the oblique convergence between the American and Caribbean plates through slip-partitioning and bookshelf faulting (Feuillet et al., 2011). Between Dominica and St. Lucia, the stress regime changes: the trench parallel component of motion is smaller, and at the same time the deformation seems to be more diffuse and accommodated by smaller faults or fissures. The position of Dominica, astride two different stress and deformation regimes may thus partly favor higher magma production rate and crustal storage.

III.6. Conclusion

This study proposes a revised chronostratigraphy for the ignimbrite eruptions that occur in the 50 kyrs in Dominica. Thanks to a combined chronological, lithological and geochemical investigation we precise the volcanological history of this island. We may recognize five major ignimbritic eruptions involving several km^3 of magma DRE, namely Grande Savane and Layou eruptions that we infer coming from Morne Diablotins volcanic center and Roseau, Grand Fond and Grand Bay eruptions, that we infer coming from Morne Trois Pitons-Micotrin volcanic center. The presence of a caldera structure is not clearly established; we propose that the depth of magma storage is too deep to be responsible of a caldera at the surface. In addition to these ignimbritic eruptions we also identified several plinian eruptions, the last one occurred recently (in the last 5 kyrs). We propose some correlations of the different outcrops; in particular we emphasize that several pumiceous deposits located in the Roseau valley belong to distinct plinian eruptions. This work also emphasizes the importance to work on glass chemistry rather than whole rock data in order to correlate outcrops. This may be performed on sections identified on-land an in the case of island such as Dominica should also be correlated to cores within the basin that collect the sedimentation.

Acknowledgements

The authors began this work to a first financial support from IPGP before benefiting from INSU-Aléas support (2013). M. Fialin, N. Rividi are acknowledged for EPMA analyses, A. Michel and P. Bürckel for geochemical analyses and S. Hidalgo for sample preparations. J.-P. Dumoulin (LSCE) and the LMC14 team is acknowledged for ^{14}C dates.

Supplementary Material

	Roseau			*Roseau valley*						*Layou*				*Grande Savane*	
type	fallout	flow		fallout	flow	fallout	fallout	fallout		fallout	flow	flow	flow	flow	flow
Sample	DOM60d1a	DOM49a		DOM48c2	DOM48f	DOM50a2	DOM74c1	DOM52a		Dom 41a1	DOM41d2	DOM53c	DOM79a1	DOM40b	DOM69a
local name	*Cocoyer*	*Goodwill*		*Good. Entr.*	*Good. Entr.*	*roundabout*	*right bank*	*left bank*		*sea cliff*	*quarry*	*quarry*	*Bells*	*Salisbury*	*Salisbury*
location	1	2		3	3	*4*	*5*	*7*		8	8	8	9	10	10
n	1	1		2	1	1	1	1		1	2	1	1	2	1
SiO_2	61,39	60,95		61,11	62,32	60,98	60,37	61,81		63,82	62,79	64,13	62,78	63,02	62,75
TiO_2	0,52	0,47		0,50	0,49	0,51	0,50	0,52		0,37	0,44	0,40	0,41	0,44	0,44
Al_2O_3	16,33	16,62		16,38	16,12	16,48	15,74	16,34		15,84	15,81	16,18	16,05	15,99	16,04
Fe_2O_3	6,56	5,84		6,29	6,09	6,44	6,41	6,48		5,13	5,84	5,61	5,54	5,68	5,81
MnO	0,15	0,13		0,14	0,14	0,14	0,15	0,15		0,13	0,14	0,15	0,14	0,14	0,14
MgO	2,27	2,07		2,24	2,16	2,32	2,23	2,32		1,56	1,99	1,76	1,75	1,95	1,95
CaO	5,73	5,65		5,85	5,67	6,11	5,64	5,86		5,00	5,47	5,40	5,10	5,44	5,55
Na_2O	2,83	3,20		3,20	3,27	3,28	3,68	3,25		3,36	3,35	3,48	3,31	3,44	3,32
K_2O	1,45	1,45		1,49	1,61	1,48	1,48	1,51		1,61	1,54	1,50	1,54	1,57	1,64
P_2O_5	0,11	0,09		0,11	0,11	0,10	0,12	0,11		0,10	0,11	0,11	0,09	0,11	0,10
LOI	2,58	2,15		2,06	1,50	1,74	2,54	1,74		2,59	1,65	1,78	2,16	1,65	1,63
Total	99,91	98,61		99,36	99,45	99,59	98,85	100,09		99,51	99,14	100,49	98,86	99,42	99,38

	Grand Fond				*Grand Bay*
type	fallout	fallout	flow		flow
Sample	DOM43a2	DOM43b1	DOM43e		DOM31
local name	*Rosalie*	*Rosalie*	*Grand Fond*		*beach*
location	11	11	11		12
n	1	2	2		1
SiO_2	60,68	60,66	61,52		62,23
TiO_2	0,50	0,52	0,51		0,50
Al_2O_3	17,19	16,48	16,46		16,51
Fe_2O_3	6,24	6,57	6,32		6,39
MnO	0,14	0,15	0,14		0,15
MgO	2,05	2,35	2,17		2,21
CaO	5,25	5,79	5,77		5,97
Na_2O	2,85	3,22	3,22		3,34
K_2O	1,45	1,48	1,51		1,53
P_2O_5	0,09	0,11	0,10		0,11
LOI	3,59	1,63	1,96		1,64
Total	100,01	98,94	99,68		100,57

Table III.S1: Major element composition of whole rocks (wt%). *The sampling location is précised neamly and by reference to the numbering in Fig.III.1; n: mean value. The type of deposit is précised. Data are expressed with total Fe as Fe^{2+} with LOI detailed. Analyses were performed at CRPG (Nancy, France) by ICP-OES.*

	PPR			Fond St Jean	Londonderry	Morne Trois Pitons	Micotrin	Fond Baron		Soufrière
type	**fallout**	**fallout**	**fallout**	**fallout**	**flow**	**lava dome**	**lava dome**	**fallout**	**fallout**	**fallout**
Sample	DOM51b2	DOM49c2	DOM49i2	DOM61	DOM78a	DOM68	DOM66b	DOM64	DOM65	DOM73
local name	*PPR1*	*PPR2*	*PPR3*	*sea cliff*	*sea cliff*	*BAF*	*BAF*			
Position	2	2	2	13	15	16	17	18	18	19
n	2	2	2	1	1	1	1	1	1	1
SiO_2	60,66	61,19	61,40	61,60	59,05	61,19	63,16	49,35	49,68	48,78
TiO_2	0,48	0,50	0,48	0,45	0,54	0,54	0,51	0,92	1,03	0,90
Al_2O_3	16,68	15,96	16,09	17,06	16,71	16,62	16,45	19,29	18,43	19,71
Fe_2O_3	6,13	6,36	6,23	5,18	6,63	6,88	6,54	9,94	10,04	10,18
MnO	0,13	0,14	0,14	0,11	0,14	0,15	0,15	0,18	0,16	0,18
MgO	2,09	2,23	2,18	1,58	2,30	2,53	2,30	4,72	4,05	4,93
CaO	5,44	5,59	5,71	5,43	5,87	6,23	5,92	10,08	9,22	10,24
Na_2O	3,15	3,00	3,18	3,24	3,03	3,38	3,49	2,45	3,43	2,20
K_2O	1,42	1,51	1,52	1,72	1,59	1,37	1,47	0,52	0,56	0,43
P_2O_5	0,07	0,09	0,12	0,06	0,10	0,11	0,12	0,12	0,09	0,08
LOI	3,17	2,80	2,33	3,51	2,72	-0,08	-0,16	1,15	2,64	1,86
Total	99,41	99,36	99,38	99,95	98,68	98,91	99,95	98,71	99,34	99,49

Table III.S1 (continued)

Roseau		
locality	*Cocoyer*	*roundabout*
location	1	4
number	47b	Dom 50a2
type	fallout	fallout
n	10	9
SiO_2	76,82	77,05
TiO_2	0,26	0,22
Al_2O_3	13,22	13,17
Fe_2O_3	0,86	1,78
MnO	0,02	0,04
MgO	0,17	0,22
CaO	1,87	1,96
Na_2O	3,30	2,76
K_2O	2,73	2,59
P_2O_5	0,06	0,03
F (ppm)	205	230
Cl (ppm)	1357	2325

Layou		
sea cliff	*sea cliff*	*quarry*
8	8	8
Dom 41a3	41a1-77	41c1
fallout	fallout	flow
10	7	8
76,84	77,59	76,89
0,13	0,17	0,13
12,60	12,46	12,85
1,65	1,64	1,60
0,07	0,01	0,08
0,16	0,19	0,17
1,51	1,55	1,70
3,37	3,28	3,17
2,89	2,48	2,78
0,03	0,06	0,04
89	186	134
2705	2259	2231

Grand Fond		
Rosalie	*Rosalie*	*Grand fond*
11	11	11
43a1	43b1	43e
fallout	fallout	flow
10	10	7
76,65	76,98	76,44
0,23	0,17	0,19
13,00	12,53	12,54
1,93	1,68	1,45
0,06	0,08	0,04
0,25	0,22	0,17
1,90	1,80	1,53
3,08	3,55	3,38
2,57	2,60	2,51
0,03	0,04	0,04
426	96	23
2374	2331	1615

Grande Savanne	
locality	*Salisbury*
location	10
number	Dom 40b
type	fallout
n	10
SiO_2	76,27
TiO_2	0,16
Al_2O_3	12,65
Fe_2O_3	0,41
MnO	0,02
MgO	0,04
CaO	1,42
Na_2O	4,14
K_2O	2,74
P_2O_5	0,04
F (ppm)	132
Cl (ppm)	959

Roseau valley											
Goodwill	*Goodwill*	*Goodwill*	*Goodwill*	*Goodwill*	*Goodwill*	*Goodwill*	*Goodwill*	*Goodwill*	*Goodwill*	*Goodwill*	*Goodwill*
3	3	3	3	3	3	3	3	3	3	3	3
fallout	fallout	fallout	fallout	fallout	fallout	fallout	fallout	fallout	fallout	fallout	flow
48a2	48a2	48b2	48 c2	48c2	48c2	48c2	48 d2	48d2	48d2	48d2	48e
8	9	8	10	8	9	9	9	10	10	8	10
76,68	76,03	75,70	76,72	76,20	76,20	76,06	76,45	75,48	75,65	76,23	77,74
0,22	0,26	0,24	0,20	0,24	0,26	0,29	0,29	0,24	0,24	0,27	0,14
12,90	12,98	12,68	12,51	12,90	13,10	13,03	12,45	13,05	13,01	13,01	13,15
1,94	2,26	2,25	1,73	2,01	2,26	1,95	1,51	2,17	2,25	2,08	1,98
0,06	0,04	0,05	0,04	0,05	0,04	0,10	0,06	0,08	0,12	0,07	0,06
0,26	0,38	0,40	0,23	0,28	0,26	0,27	0,19	0,32	0,30	0,29	0,26
1,88	2,18	2,22	1,63	1,94	1,98	2,05	1,59	1,97	1,88	2,00	1,97
3,19	3,10	3,62	3,07	3,50	3,12	3,48	2,94	3,48	3,95	3,20	3,59
2,52	2,40	2,49	2,76	2,52	2,41	2,41	2,75	2,88	2,25	2,51	2,67
0,04	0,06	0,03	0,03	0,04	0,06	0,04	0,04	0,04	0,07	0,01	0,05
378	292	555	422	443	352	391	239	420	413	406	313
2467	2521	2495	2277	2534	2487	2484	1829	2285	2199	2612	2526

Plinian Post Roseau		
PPR1	PPR2	PPR3
2	2	2
Dom 51b2	Dom 49c2	Dom 49i2
fallout	fallout	fallout
10	9	10
76,93	77,66	77,44
0,18	0,26	0,22
12,92	12,81	12,85
1,92	2,06	2,01
0,04	0,06	0,06
0,23	0,28	0,32
1,86	1,84	1,83
2,77	3,59	3,41
2,59	2,78	2,65
0,02	0,05	0,04
312	392	315
2584	2487	2355

Table III.S2: Major element composition of residual glass. *Analyses are mean values (n: number of analyses). Data are from EPMA (Camparis, France).*

	Roseau		Roseau valley												Layou							
locality	*Cocoyer*		*Goodwill*		*Goodwill*		*Goodwill*		*roundabout*		*right bank*		*left bank*		*sea cliff*		*sea cliff*		*quarry*		*Bells*	
location	1		2		3		3		4		5		7		8		8		8		9	
number	Dom 60d1a		Dom 49a		Dom 48c2		Dom 48f		Dom 50a2		Dom 74c1		Dom 52a		Dom 41a1		Dom 41d2		Dom 53c		Dom 79a1	
type	fallout	S.D.	flow	S.D.	fallout	S.D.	flow	S.D.	fallout	S.D.	fallout	S.D.	fallout	S.D.	fallout	S.D.	flow	S.D.	flow	S.D.	flow	S.D.
Li	11,7	0,9	20,2	1,5	17,2	1,3	21,0	2,6	18,5	2,3	15,8	1,2	19,4	1,4	16,0	1,2	21,5	2,6	21,9	2,7	21,7	1,6
K (%)	1,38	0,02	1,43	0,02	1,51	0,02	1,60	0,28	1,48	0,25	1,48	0,01	1,48	0,01	1,62	0,01	1,61	0,28	1,49	0,26	1,53	0,02
Sc	15,2	0,5	14,5	0,3	16,4	0,5	15,6	2,1	17,8	2,4	14,9	0,5	16,6	0,3	10,4	0,2	14,2	1,9	11,1	1,5	12,3	0,6
Ti	0,5	0,0	0,5	0,0	0,5	0,0	0,5	0,1	0,5	0,1	0,5	0,0	0,5	0,0	0,4	0,0	0,4	0,1	0,4	0,1	0,4	0,0
V	114,1	1,23	100,6	1,08	108,1	1,28	103,6	13,10	116,7	14,74	101,2	1,33	113,6	1,22	66,0	0,77	101,0	12,76	70,8	8,94	82,3	0,89
Cr	3,9	0,101	4,6	0,141	2,7	0,141	3,9	0,484	2,5	0,319	2,7	0,112	3,1	0,099	2,7	0,066	7,7	0,964	2,5	0,309	3,3	0,076
Co	13,18	0,16	12,00	0,15	13,36	0,17	12,25	1,39	14,21	1,62	12,61	0,16	13,69	0,17	8,87	0,11	11,79	1,34	9,79	1,11	10,13	0,16
Ni	2,5	0,1	2,1	0,1	1,5	0,1	2,6	0,3	2,7	0,3	1,3	0,1	1,8	0,1	1,5	0,1	4,8	0,5	2,1	0,2	1,6	0,1
Cu	26,6	0,3	30,4	0,5	13,2	0,2	35,8	3,8	49,3	5,2	24,3	0,3	26,5	0,3	20,9	0,3	23,7	2,5	37,2	4,0	26,9	0,4
Zn	55,4	0,6	52,8	1,0	58,2	1,0	51,2	6,4	52,7	6,6	55,2	0,8	58,5	0,6	46,9	1,1	55,3	6,9	44,7	5,6	51,1	0,9
Rb	44,8	0,5	43,9	0,5	46,0	0,6	48,6	3,8	45,2	3,6	46,8	0,6	47,0	0,5	52,6	0,6	50,2	3,9	48,5	3,8	50,0	0,6
Sr	204,52	1,74	210,56	1,68	208,39	1,66	206,65	15,51	210,41	15,79	208,15	1,66	209,20	2,07	205,70	1,97	223,56	16,77	224,87	16,87	217,23	2,44
Y	17,40	0,22	16,10	0,21	18,95	0,22	16,90	1,30	19,76	1,52	17,78	0,20	18,30	0,24	15,46	0,17	16,85	1,30	16,14	1,24	16,03	0,20
Zr	78,63	0,68	76,11	0,69	89,88	1,03	79,88	6,21	88,76	6,91	89,81	0,73	90,44	0,82	61,67	0,63	80,65	6,27	56,85	4,42	80,30	0,91
Nb	2,69	0,03	2,73	0,04	2,92	0,05	2,79	0,23	2,80	0,23	2,97	0,05	2,91	0,04	2,84	0,04	2,74	0,22	2,62	0,21	2,72	0,03
Mo	0,7	0,1	0,7	0,1	0,8	0,1	1,2	0,1	1,1	0,1	0,8	0,1	0,7	0,1	0,8	0,1	1,3	0,1	1,1	0,1	0,7	0,1
Cd	0,10	0,03	0,14	0,05	0,09	0,04	0,14	0,05	0,18	0,06	0,09	0,03	0,09	0,03	0,08	0,03	0,12	0,04	0,07	0,02	0,09	0,03
Cs	2,1	0,1	1,7	0,1	1,8	0,1	1,9	0,3	1,8	0,3	2,4	0,1	1,7	0,1	2,0	0,1	2,1	0,4	2,1	0,4	2,4	0,1
Ba	251	3,68	268	3,03	267	3,01	269	14,42	264	14,19	255	2,88	266	3,70	286	3,26	275	14,75	259	13,93	275	3,11
La	9,9	0,1	10,3	0,1	10,5	0,1	10,2	0,5	10,9	0,6	10,3	0,1	10,3	0,1	10,9	0,1	10,7	0,6	10,6	0,6	10,8	0,1
Ce	20,45	0,27	20,94	0,28	21,89	0,29	21,18	1,10	21,73	1,13	21,48	0,29	21,72	0,29	22,30	0,30	22,38	1,16	21,81	1,13	21,57	0,29
Pr	2,56	0,03	2,59	0,03	2,82	0,03	2,62	0,14	2,91	0,16	2,65	0,03	2,67	0,03	2,66	0,03	2,72	0,15	2,71	0,15	2,64	0,03
Nd	10,46	0,13	10,35	0,19	11,67	0,14	10,54	0,51	11,86	0,57	10,83	0,15	11,11	0,14	10,21	0,23	10,65	0,51	11,06	0,53	10,42	0,18
Sm	2,36	0,06	2,35	0,07	2,71	0,10	2,42	0,13	2,85	0,15	2,48	0,07	2,56	0,08	2,20	0,05	2,38	0,13	2,39	0,13	2,22	0,05
Eu	0,77	0,01	0,76	0,02	0,84	0,01	0,77	0,04	0,89	0,05	0,76	0,01	0,80	0,01	0,77	0,01	0,78	0,04	0,78	0,04	0,76	0,01
Gd	2,61	0,06	2,54	0,05	2,97	0,06	2,53	0,11	2,98	0,13	2,59	0,06	2,79	0,06	2,41	0,10	2,56	0,11	2,49	0,11	2,39	0,05
Tb	0,42	0,01	0,41	0,01	0,47	0,01	0,43	0,02	0,48	0,02	0,43	0,01	0,45	0,01	0,38	0,01	0,40	0,02	0,40	0,02	0,39	0,01
Dy	2,70	0,07	2,61	0,07	3,05	0,08	2,63	0,12	3,03	0,14	2,76	0,07	2,92	0,07	2,40	0,06	2,61	0,12	2,55	0,11	2,38	0,06
Ho	0,59	0,02	0,55	0,02	0,65	0,02	0,58	0,04	0,65	0,03	0,59	0,02	0,62	0,02	0,53	0,02	0,56	0,03	0,56	0,03	0,53	0,02
Er	1,75	0,05	1,67	0,05	1,94	0,05	1,71	0,09	1,93	0,10	1,76	0,05	1,86	0,05	1,62	0,04	1,71	0,09	1,63	0,08	1,56	0,04
Tm	0,28	0,01	0,26	0,01	0,31	0,01	0,27	0,01	0,31	0,02	0,28	0,01	0,30	0,01	0,26	0,01	0,27	0,01	0,26	0,01	0,25	0,01
Yb	1,89	0,05	1,84	0,05	2,07	0,08	1,93	0,08	2,10	0,09	1,95	0,05	2,12	0,06	1,82	0,05	1,91	0,08	1,89	0,08	1,73	0,05
Lu	0,30	0,01	0,29	0,01	0,33	0,01	0,30	0,02	0,33	0,02	0,31	0,01	0,32	0,01	0,30	0,01	0,30	0,02	0,30	0,02	0,26	0,01
Hf	2,25	0,06	2,29	0,06	2,59	0,07	2,38	0,10	2,55	0,11	2,53	0,07	2,64	0,07	2,04	0,06	2,34	0,10	1,90	0,08	2,30	0,07
Ta	0,21	0,02	0,23	0,02	0,24	0,02	0,22	0,01	0,22	0,01	0,22	0,02	0,24	0,02	0,24	0,02	0,23	0,01	0,22	0,01	0,21	0,02
Pb	7,02	0,25	7,01	0,25	7,23	0,26	4,61	0,19	6,02	0,25	7,10	0,25	7,48	0,27	8,27	0,30	6,39	0,27	5,01	0,21	6,94	0,25
Th	3,75	0,16	4,13	0,18	4,11	0,18	4,23	0,17	3,96	0,16	3,96	0,17	4,12	0,18	4,75	0,20	4,39	0,18	3,99	0,16	4,19	0,18
U	1,09	0,09	1,15	0,10	1,17	0,10	1,23	0,11	1,16	0,10	1,15	0,10	1,20	0,10	1,33	0,12	1,29	0,11	1,21	0,10	1,28	0,11

Table III.S3: Trace element composition of whole rocks *(in ppm, except K in %). The sampling localization is précised, byreference to Fig.III.1. The deposit type is also provided: fallout, block-and-ash flow (BAF).*

	Grande Savane					Grand Fond						Grand Bay			Plinian Post Roseau							Fond St Jean	
locality	*Salisbury*		*Salisbury*			*Rosalie*		*Rosalie*		*Grand fond*			*beach*			PPR1		PPR2		PPR3			*sea cliff*	
location	10		10			11		11		11			12			2		2		2			13	
number	Dom 40b		Dom 69a			Dom 43a2		Dom 43b1		Dom 43e			Dom 31			Dom 51b2		Dom 49c2		Dom 49i2			Dom 61	
type	fallout	S.D.	flow	S.D.		fallout	S.D.	fallout	S.D.	flow	S.D.		flow	S.D.		fallout	S.D.	fallout	S.D.	fallout	S.D.		fallout	S.D.
Li	21,8	2,7	19,0	2,3		16,6	1,2	20,6	1,5	20,3	2,5		15,7	1,2		21,1	1,6	16,6	1,2	13,03	2,4		15,0	1,1
K (%)	1,64	0,28	1,62	0,28		1,42	0,01	1,49	0,01	1,58	0,27		1,45	0,02		1,37	0,01	1,48	0,03	49,4	0,27		1,63	0,02
Sc	14,3	1,9	13,3	1,8		17,5	0,3	17,2	0,3	18,3	2,5		14,8	0,4		15,7	0,6	16,4	0,7	20,15	2,1		14,7	0,4
Ti	0,4	0,1	0,4	0,1		0,5	0,0	0,5	0,0	0,5	0,1		0,5	0,0		0,5	0,0	0,5	0,0	90,40	0,1		0,4	0,0
V	92,4	11,67	94,6	11,95		105,1	1,34	113,7	1,23	120,5	15,22		105,3	1,64		104,0	1,12	112,2	1,46	3,06	12,81		93,5	1,04
Cr	4,9	0,620	1,7	0,218		2,5	0,061	3,9	0,063	3,4	0,421		3,0	0,130		3,8	0,118	3,5	0,086	1,1	0,257		1,5	0,094
Co	11,53	1,31	11,32	1,29		12,84	0,16	13,88	0,17	13,86	1,58		12,52	0,16		13,34	0,21	13,20	0,16	270	1,48		9,82	0,12
Ni	3,1	0,3	1,9	0,2		1,7	0,1	2,4	0,1	3,0	0,3		1,8	0,2		2,3	0,1	1,9	0,1	11,6	0,3		0,9	0,1
Cu	21,3	2,3	28,9	3,1		64,9	0,8	56,1	0,7	42,1	4,5		42,7	0,6		41,4	0,5	35,8	0,5	22,82	1,6		65,5	0,9
Zn	52,6	6,6	51,0	6,4		60,9	0,6	56,8	0,6	50,1	6,3		49,0	0,6		58,7	0,9	64,4	1,2	3,13	7,2		58,3	0,8
Rb	51,6	4,1	52,2	4,1		46,5	0,6	45,8	0,5	49,8	3,9		44,5	0,5		43,5	0,6	46,7	0,5	12,81	3,9		54,6	0,6
Sr	218,28	16,38	200,89	15,07		192,72	1,53	205,41	1,64	209,66	15,73		208,42	3,24		203,07	3,71	198,82	1,58	2,89	16,22		193,65	1,54
Y	16,53	1,27	16,15	1,24		21,69	0,25	18,71	0,20	20,59	1,58		18,16	0,22		17,03	0,22	18,20	0,21	0,88	1,55		22,92	0,25
Zr	79,86	6,21	74,26	5,78		95,55	0,85	87,44	0,77	93,91	7,31		88,07	0,88		89,33	0,81	90,40	0,97	3,07	7,03		112,23	0,90
Nb	2,81	0,23	2,63	0,21		2,97	0,05	2,75	0,04	2,95	0,24		2,96	0,04		2,92	0,04	2,87	0,04	0,51	0,25		2,79	0,03
Mo	1,2	0,1	1,2	0,1		0,7	0,1	0,8	0,1	1,2	0,1		0,8	0,1		0,7	0,1	0,8	0,1	3,22	0,1		0,8	0,1
Cd	0,75	0,25	0,08	0,03		0,11	0,04	0,22	0,07	0,14	0,05		0,08	0,03		0,09	0,03	0,11	0,04	0,69	0,04		0,10	0,04
Cs	2,0	0,4	2,2	0,4		2,4	0,1	1,8	0,1	2,1	0,4		1,8	0,1		1,6	0,1	1,9	0,1	2,01	0,4		2,8	0,1
Ba	273	14,64	266	14,28		270	3,05	258	3,61	278	14,92		257	3,31		261	3,49	281	3,17	0,33	14,50		281	3,17
La	10,7	0,6	10,2	0,5		11,8	0,1	10,5	0,1	10,7	0,6		10,5	0,1		9,9	0,1	10,2	0,1	2,19	0,6		12,2	0,2
Ce	22,17	1,15	20,86	1,08		22,96	0,30	21,50	0,29	22,35	1,16		21,43	0,28		21,48	0,29	21,82	0,29	0,34	1,19		22,99	0,31
Pr	2,68	0,14	2,55	0,14		3,45	0,04	2,81	0,05	2,83	0,15		2,78	0,05		2,54	0,04	2,67	0,04	2,65	0,17		3,30	0,04
Nd	10,57	0,51	10,12	0,49		14,13	0,21	11,47	0,14	11,85	0,57		11,38	0,17		10,32	0,13	10,75	0,21	0,26	0,62		13,53	0,20
Sm	2,39	0,13	2,26	0,12		3,37	0,08	2,73	0,09	2,75	0,14		2,60	0,06		2,41	0,11	2,49	0,06	6,16	0,15		3,28	0,07
Eu	0,78	0,04	0,74	0,04		0,94	0,02	0,82	0,01	0,87	0,05		0,84	0,01		0,77	0,02	0,75	0,01	4,19	0,05		0,93	0,02
Gd	2,50	0,11	2,38	0,10		3,44	0,07	2,89	0,07	2,97	0,13		2,88	0,06		2,59	0,08	2,73	0,06	1,24	0,13		3,52	0,08
Tb	0,41	0,02	0,38	0,02		0,59	0,02	0,46	0,01	0,47	0,02		0,47	0,01		0,42	0,01	0,45	0,01	0,54	0,02		0,57	0,02
Dy	2,53	0,11	2,43	0,11		3,74	0,10	3,00	0,08	3,17	0,14		2,89	0,07		2,70	0,07	2,84	0,07	3,42	0,15		3,57	0,09
Ho	0,54	0,03	0,54	0,03		0,80	0,03	0,64	0,02	0,68	0,03		0,62	0,02		0,58	0,02	0,62	0,02	0,75	0,03		0,79	0,02
Er	1,69	0,09	1,60	0,08		2,35	0,07	1,93	0,05	2,08	0,11		1,86	0,05		1,78	0,05	1,87	0,05	2,16	0,10		2,31	0,06
Tm	0,26	0,01	0,26	0,02		0,37	0,01	0,30	0,01	0,32	0,02		0,29	0,01		0,28	0,01	0,30	0,01	0,35	0,02		0,36	0,01
Yb	1,87	0,08	1,82	0,08		2,51	0,09	2,14	0,06	2,27	0,10		2,01	0,06		2,05	0,06	2,02	0,08	2,34	0,09		2,38	0,07
Lu	0,28	0,02	0,28	0,02		0,38	0,01	0,32	0,02	0,37	0,02		0,32	0,01		0,31	0,02	0,32	0,01	0,36	0,02		0,36	0,01
Hf	2,24	0,10	2,24	0,10		2,77	0,08	2,53	0,07	2,77	0,12		2,53	0,08		2,58	0,07	2,62	0,14	2,71	0,12		3,17	0,09
Ta	0,22	0,01	0,22	0,01		0,23	0,02	0,23	0,02	0,23	0,01		0,22	0,02		0,24	0,02	0,22	0,02	0,26	0,01		0,22	0,02
Pb	6,28	0,26	5,12	0,21		7,87	0,28	4,80	0,17	5,82	0,24		6,31	0,23		7,49	0,27	8,85	0,32	5,86	0,26		8,42	0,30
Th	4,31	0,17	4,35	0,18		4,33	0,18	4,00	0,17	4,12	0,17		3,81	0,16		4,03	0,17	4,05	0,17	4,07	0,17		4,69	0,20
U	1,28	0,11	1,28	0,12		1,41	0,12	1,18	0,10	1,24	0,11		1,10	0,09		1,10	0,09	1,15	0,10	1,21	0,11		1,38	0,12

	Londonderry			Morne Trois Pitons			Micotrin			Fond Baron					Soufrière	
locality	*sea cliff*			*quarry*			*quarry*									
location	15			16			17			18		18			19	
number	Dom 78a			Dom 68			Dom 66b			Dom 64		Dom 73			Dom 65	
type	flow	S.D.		BAF	S.D.		BAF	S.D.		fallout	S.D.	fallout	S.D.		fallout	S.D.
Li	11,9	0,9		22,0	1,3		17,0	1,6		8,3	0,6	8,4	0,6		9,0	0,7
K (%)	1,60	0,02		1,43	0,02		1,34	0,01		0,42	0,00	0,48	0,01		0,55	0,01
Sc	19,4	0,5		15,1	0,3		17,6	0,4		35,7	1,0	36,1	0,8		42,9	0,6
Ti	0,5	0,0		0,5	0,0		0,5	0,0		0,9	0,0	0,9	0,0		1,0	0,0
V	130,9	1,41		101,5	1,36		121,9	1,17		273,5	3,11	317,3	3,42		383,4	4,28
Cr	2,2	0,090		3,3	0,150		4,3	0,134		4,8	0,122	26,3	0,449		7,9	0,127
Co	14,90	0,28		12,95	0,24		14,78	0,16		31,90	0,40	31,17	0,39		26,37	0,38
Ni	1,8	0,2		1,6	0,1		2,3	0,1		8,7	0,3	15,5	0,2		6,5	0,2
Cu	29,5	0,5		33,5	0,9		71,3	0,4		86,1	1,1	1769,0	23,2		68,9	0,9
Zn	56,9	0,7		52,8	0,7		58,8	1,2		71,6	0,9	584,8	5,8		69,1	1,0
Rb	50,9	0,8		43,7	0,5		42,4	0,6		15,6	0,2	11,6	0,1		17,6	0,3
Sr	213,41	1,84		215,33	1,72		216,42	1,71		222,37	3,22	255,90	3,53		236,91	2,81
Y	20,99	0,28		18,35	0,26		18,35	0,21		18,93	0,28	20,23	0,29		19,39	0,22
Zr	98,37	1,05		82,93	0,72		91,43	0,66		54,41	0,56	58,69	0,50		61,64	0,49
Nb	2,69	0,05		3,01	0,03		2,80	0,05		1,67	0,02	1,67	0,04		1,81	0,03
Mo	0,9	0,1		0,6	0,1		0,7	0,1		0,2	0,1	0,4	0,1		0,2	0,1
Cd	0,11	0,05		0,07	0,03		0,09	0,03		0,10	0,04	0,12	0,04		0,19	0,06
Cs	2,2	0,1		1,5	0,1		1,4	0,1		0,6	0,0	0,5	0,0		15,9	0,6
Ba	263	2,97		261	2,93		247	2,94		91	1,03	102	1,15		87	0,99
La	10,4	0,1		10,3	0,1		9,8	0,1		4,7	0,1	6,2	0,1		5,8	0,1
Ce	22,84	0,30		21,53	0,28		20,72	0,29		11,58	0,15	14,37	0,19		13,65	0,18
Pr	2,89	0,05		2,74	0,03		2,60	0,03		1,66	0,02	2,09	0,02		2,01	0,02
Nd	11,90	0,17		11,05	0,16		10,51	0,16		7,93	0,15	9,59	0,25		9,26	0,13
Sm	2,87	0,09		2,62	0,09		2,49	0,10		2,32	0,05	2,57	0,06		2,60	0,06
Eu	0,87	0,02		0,83	0,01		0,83	0,01		0,83	0,01	0,90	0,02		0,89	0,03
Gd	3,14	0,07		2,78	0,08		2,69	0,06		2,73	0,06	2,94	0,06		2,93	0,06
Tb	0,52	0,02		0,45	0,01		0,45	0,01		0,48	0,01	0,49	0,01		0,49	0,01
Dy	3,30	0,08		2,83	0,07		2,83	0,07		3,10	0,08	3,16	0,08		3,25	0,08
Ho	0,70	0,02		0,62	0,02		0,62	0,02		0,68	0,02	0,69	0,02		0,71	0,02
Er	2,10	0,06		1,87	0,05		1,82	0,05		1,96	0,05	1,97	0,05		1,98	0,06
Tm	0,33	0,01		0,30	0,01		0,29	0,01		0,29	0,01	0,30	0,01		0,30	0,01
Yb	2,22	0,06		2,01	0,05		1,94	0,06		1,85	0,06	1,88	0,05		1,95	0,08
Lu	0,33	0,01		0,32	0,01		0,32	0,01		0,29	0,01	0,30	0,01		0,30	0,01
Hf	2,83	0,08		2,42	0,07		2,63	0,07		1,58	0,04	1,61	0,04		1,85	0,05
Ta	0,21	0,02		0,23	0,02		0,22	0,02		0,17	0,01	0,13	0,01		0,14	0,01
Pb	7,52	0,27		5,65	0,23		6,41	0,20		2,77	0,10	4,13	0,15		2,49	0,09
Th	4,06	0,17		3,84	0,16		3,65	0,16		1,23	0,05	1,06	0,05		1,43	0,06
U	1,22	0,10		1,13	0,09		1,07	0,10		0,38	0,03	0,29	0,03		0,37	0,03

	Roseau						Roseau valley													
locality	*Cocoyer*		*Cocoyer*		*Cocoyer*		*Goodwill*		*Goodwill*		*Goodwill*		*Goodwill*		*roundabout*		*roundabout*		*right bank*		*left bank*	
location	1		1		1		2		3		3		3		4		4		5		7	
number	Dom 60d1a		47b		47c1		Dom 49a		48c1		48e		Dom 48f		Dom 50a2		50c2		Dom 74c1		Dom 52a	
type	fallout	S.D.	fallout	S.D.	flow	S.D.	flow	S.D.	fallout	S.D.	flow	S.D.	flow	S.D.	fallout	S.D.	fallout	S.D.	fallout	S.D.	fallout	S.D.
Li	14,4	6,4	21,6	9,5	14,0	1,7	17,8	2,2	19,4	2,4	18,1	8,0	18,2	2,2	20,2	2,5	18,4	8,1	16,5	7,2	23,7	2,9
Sc	8,2	1,5	9,8	1,7	6,9	0,9	6,6	0,9	6,5	0,9	8,2	1,5	7,1	1,0	6,4	0,9	7,0	1,2	6,8	1,2	8,6	1,2
V	12,6	1,64	13,1	1,71	11,8	1,49	13,9	1,76	11,6	1,47	18,2	2,37	7,7	0,97	14,0	1,77	11,6	1,51	15,3	1,99	11,6	1,47
Cr	1,249	0,152	0,996	0,173	2,018	0,253	3,058	0,384	2,256	0,283	1,190	0,145	1,424	0,179	2,316	0,291	0,652	0,080	0,927	0,113	1,658	0,208
Co	2,94	0,29	2,67	0,26	1,92	0,22	2,52	0,29	2,15	0,24	2,58	0,25	2,13	0,24	2,16	0,25	2,20	0,22	2,85	0,28	2,83	0,32
Ni	<BLK		<BLK		0,9	0,1	1,0	0,2	0,8	0,2	0,3	0,1	0,7	0,1	1,1	0,2	<BLK		<BLK		0,6	0,1
Cu	65,8	7,7	88,3	10,4	45,8	4,9	34,2	3,6	182,0	19,4	<BLK		57,1	6,1	73,5	7,8	99,1	11,7	2,0	1,0	52,0	5,5
Zn	59,3	6,1	27,5	2,8	20,4	2,6	18,8	2,4	113,7	14,3	34,7	3,6	32,7	4,1	25,2	3,2	54,1	5,6	31,7	3,3	38,3	4,8
Rb	81,8	4,5	82,9	4,5	63,7	5,0	71,8	5,6	76,3	6,0	86,5	4,7	78,8	6,2	73,9	5,8	86,1	4,7	75,4	4,1	85,6	6,7
Sr	142,32	6,10	119,61	5,12	99,86	7,49	90,59	6,80	116,35	8,73	150,75	6,46	115,96	8,70	109,98	8,25	131,19	5,62	143,61	6,15	153,19	11,49
Y	22,83	1,07	25,15	1,18	19,48	1,50	20,95	1,61	25,10	1,93	27,25	1,28	22,79	1,75	24,10	1,85	28,42	1,34	23,36	1,10	26,37	2,03
Zr	133,69	6,74	141,80	7,14	106,67	8,30	121,60	9,46	145,95	11,36	164,29	8,28	133,51	10,39	139,32	10,84	168,02	8,47	143,21	7,22	164,44	12,79
Nb	4,24	0,23	4,45	0,24	3,24	0,26	3,55	0,29	4,12	0,34	4,54	0,25	4,14	0,34	3,69	0,30	4,73	0,26	4,07	0,22	4,49	0,37
Mo	1,3	0,1	1,4	0,1	1,4	0,1	1,7	0,1	1,8	0,2	1,6	0,1	1,8	0,2	1,6	0,1	1,4	0,1	1,3	0,1	1,9	0,2
Cd	0,14	0,05	0,08	0,03	0,14	0,07	0,12	0,05	0,13	0,05	0,11	0,04	0,08	0,03	0,18	0,06	0,13	0,04	0,11	0,04	0,13	0,05
Cs	4,6	0,3	4,7	0,3	2,4	0,4	2,6	0,5	2,2	0,4	4,7	0,3	3,0	0,5	2,5	0,5	4,7	0,3	5,1	0,4	3,0	0,6
Ba	406	15,96	431	16,97	344	18,48	384	20,63	395	21,18	436	17,17	418	22,45	398	21,39	430	16,91	386	15,17	432	23,21
La	14,6	0,6	16,4	0,7	13,1	0,7	13,4	0,7	14,3	0,8	15,9	0,7	14,8	0,8	14,9	0,8	16,2	0,7	14,4	0,6	15,6	0,8
Ce	29,81	1,24	32,22	1,34	25,47	1,32	27,39	1,42	29,82	1,55	33,81	1,40	30,50	1,58	29,57	1,54	33,02	1,37	30,29	1,26	32,87	1,71
Pr	3,61	0,15	4,23	0,17	3,37	0,18	3,47	0,19	3,73	0,20	4,14	0,17	3,76	0,20	3,89	0,21	4,18	0,17	3,70	0,15	4,00	0,22
Nd	14,09	0,58	16,70	0,68	13,69	0,66	13,71	0,66	14,91	0,72	16,59	0,68	14,80	0,71	15,42	0,74	16,46	0,67	14,43	0,59	16,00	0,77
Sm	3,04	0,09	3,66	0,18	3,09	0,16	3,15	0,27	3,52	0,18	3,77	0,09	3,30	0,17	3,54	0,19	3,81	0,09	3,27	0,08	3,59	0,19
Eu	0,71	0,03	0,79	0,03	0,71	0,04	0,57	0,03	0,76	0,04	0,87	0,04	0,76	0,04	0,76	0,04	0,81	0,03	0,71	0,03	0,83	0,05
Gd	3,25	0,12	3,88	0,15	3,20	0,19	3,22	0,14	3,58	0,15	3,97	0,15	3,56	0,15	3,75	0,16	4,15	0,16	3,48	0,13	3,75	0,16
Tb	0,54	0,02	0,61	0,03	0,53	0,02	0,53	0,02	0,62	0,03	0,65	0,02	0,59	0,03	0,61	0,03	0,67	0,03	0,56	0,02	0,63	0,03
Dy	3,43	0,11	3,75	0,12	3,23	0,15	3,29	0,15	3,99	0,18	4,18	0,14	3,70	0,17	3,86	0,17	4,23	0,14	3,58	0,12	3,91	0,18
Ho	0,76	0,03	0,86	0,04	0,73	0,04	0,73	0,04	0,85	0,04	0,91	0,04	0,83	0,04	0,82	0,04	0,92	0,04	0,80	0,03	0,87	0,04
Er	2,29	0,07	2,54	0,08	2,17	0,11	2,24	0,11	2,56	0,13	2,79	0,09	2,49	0,13	2,48	0,13	2,80	0,13	2,43	0,08	2,62	0,13
Tm	0,37	0,02	0,39	0,02	0,34	0,02	0,34	0,03	0,40	0,02	0,43	0,01	0,39	0,02	0,40	0,02	0,44	0,01	0,38	0,01	0,43	0,02
Yb	2,57	0,10	2,78	0,10	2,33	0,10	2,44	0,10	2,73	0,14	2,90	0,10	2,67	0,11	2,71	0,12	3,02	0,10	2,71	0,09	2,93	0,12
Lu	0,40	0,01	0,44	0,01	0,38	0,03	0,39	0,02	0,43	0,03	0,47	0,01	0,43	0,03	0,43	0,03	0,48	0,02	0,42	0,01	0,46	0,03
Hf	3,85	0,14	4,11	0,15	3,42	0,15	3,79	0,16	4,22	0,18	4,60	0,17	4,19	0,18	4,19	0,18	4,67	0,17	4,07	0,15	4,60	0,20
Ta	0,29	0,05	0,27	0,05	0,26	0,01	0,28	0,01	0,32	0,01	0,25	0,04	0,33	0,01	0,32	0,01	0,23	0,04	0,24	0,04	0,33	0,02
Pb	20,50	1,04	14,44	0,73	7,26	0,30	8,47	0,35	15,64	0,66	14,56	0,74	7,7	0,3	9,8	0,4	13,73	0,69	12,95	0,65	10,16	0,43
Th	6,96	0,27	7,33	0,28	6,16	0,25	6,64	0,27	6,72	0,27	7,11	0,27	7,5	0,3	6,8	0,3	7,12	0,27	6,61	0,25	7,10	0,29
U	2,16	0,19	2,24	0,20	1,81	0,16	1,87	0,18	1,94	0,17	2,24	0,20	2,2	0,2	1,9	0,2	2,19	0,19	2,02	0,17	2,07	0,18

Table III.S4: Trace element composition of the matrix glass *(in ppm). The sampling localization is précised, byreference to Fig.III.1. The deposit type is also provided: fallout, flow.*

	Layou									
locality	*sea cliff*		*sea cliff*		*quarry*		*quarry*		*Bells*	
location	8		8		8		8		9	
number	Dom 41a3		Dom 41d2		53a (17)		Dom 53c		Dom 79a1	
type	fallout	S.D.	flow	S.D.	flow	S.D.	flow	S.D.	flow	S.D.
Li	22,2	9,8	19,6	8,6	23,8	10,5	21,9	3,1	28,1	12,4
Sc	3,6	0,6	3,7	0,7	5,2	0,9	11,1	0,3	2,5	0,4
V	6,4	0,83	6,4	0,83	11,4	1,48	70,8	0,53	3,1	0,40
Cr	1,156	0,141	3,119	0,379	1,875	0,230	2,459	0,149	0,618	0,075
Co	1,86	0,18	1,82	0,18	2,20	0,22	9,79	0,08	0,54	0,05
Ni	<BLK		0,0	0,2	<BLK		2,1	0,1	<BLK	
Cu	82,8	9,7	2,5	0,9	0,5	1,1	37,2	3,8	19,4	2,3
Zn	66,4	6,9	45,3	4,7	25,0	2,6	44,7	2,3	25,9	2,7
Rb	81,9	4,5	93,5	5,1	84,9	4,6	48,5	6,6	86,7	4,7
Sr	130,22	5,58	147,01	6,30	185,92	7,97	224,87	8,72	116,71	5,00
Y	13,17	0,62	15,00	0,70	14,84	0,70	16,14	1,04	13,52	0,63
Zr	116,61	5,88	147,90	7,45	127,99	6,45	56,85	7,64	125,44	6,32
Nb	3,86	0,21	5,01	0,27	4,78	0,26	2,62	0,35	3,53	0,19
Mo	1,4	0,2	1,5	0,1	1,4	0,2	1,1	0,1	1,4	0,1
Cd	0,08	0,04	0,11	0,04	0,10	0,04	0,07	0,03	0,10	0,04
Cs	5,0	0,4	5,3	0,4	5,0	0,4	2,1	0,5	5,6	0,4
Ba	395	15,55	449	17,66	414	16,29	259	22,54	431	16,97
La	13,7	0,6	15,4	0,6	14,3	0,6	10,6	0,8	14,7	0,6
Ce	26,70	1,11	29,83	1,24	28,42	1,18	21,81	1,45	28,10	1,17
Pr	2,97	0,12	3,24	0,13	3,15	0,13	2,71	0,17	3,17	0,13
Nd	10,38	0,42	11,59	0,47	11,21	0,46	11,06	0,53	11,17	0,46
Sm	1,86	0,17	2,12	0,11	2,12	0,05	2,39	0,11	2,07	0,08
Eu	0,51	0,02	0,63	0,03	0,70	0,03	0,78	0,03	0,54	0,02
Gd	1,91	0,13	2,18	0,08	2,24	0,08	2,49	0,09	2,06	0,08
Tb	0,30	0,01	0,33	0,02	0,34	0,01	0,40	0,01	0,31	0,01
Dy	1,80	0,06	2,05	0,07	2,13	0,08	2,55	0,09	1,89	0,06
Ho	0,41	0,02	0,47	0,02	0,46	0,02	0,56	0,02	0,43	0,02
Er	1,32	0,04	1,46	0,07	1,51	0,05	1,63	0,07	1,35	0,04
Tm	0,23	0,01	0,25	0,01	0,24	0,01	0,26	0,01	0,24	0,01
Yb	1,69	0,08	1,88	0,09	1,73	0,06	1,89	0,08	1,71	0,06
Lu	0,28	0,01	0,32	0,02	0,30	0,01	0,30	0,02	0,30	0,01
Hf	3,43	0,12	4,07	0,15	3,50	0,13	1,90	0,14	3,73	0,13
Ta	0,26	0,04	0,23	0,04	0,25	0,04	0,22	0,02	0,25	0,04
Pb	16,42	0,83	14,66	0,74	11,99	0,61	5,01	0,32	12,75	0,64
Th	7,08	0,27	7,66	0,29	6,71	0,26	3,99	0,31	7,57	0,29
U	2,18	0,19	2,45	0,21	2,11	0,19	1,21	0,19	2,40	0,21

	Grande Savanne					
Salisbury		*Salisbury*		*Salisbury*	
10		10		10	
Dom 40b		Dom 69a		70a	
fallout	S.D.	flow	S.D.	flow	S.D.
26,2	11,5	20,3	8,9	9,9	4,4
5,2	0,9	3,7	0,7	6,2	1,1
10,0	1,30	7,4	0,97	13,5	1,75
0,862	0,105	1,338	0,163	0,513	0,078
2,28	0,23	1,36	0,13	2,25	0,22
2,4	0,2	0,0	0,2	<BLK	
76,5	9,0	12,8	1,5	144,9	17,0
71,8	7,4	40,0	4,1	17,4	1,8
100,6	5,5	101,7	5,5	77,6	4,2
161,13	6,90	108,13	4,63	118,64	5,08
16,82	0,79	15,15	0,71	19,01	0,89
151,76	7,65	132,87	6,69	114,15	5,75
4,54	0,25	4,43	0,24	4,73	0,26
1,8	0,1	1,6	0,1	0,8	0,1
0,12	0,04	0,07	0,04	0,14	0,05
5,9	0,4	6,0	0,4	3,8	0,3
483	19,01	468	18,43	383	15,06
16,8	0,7	15,2	0,6	15,7	0,7
33,17	1,38	29,73	1,23	31,66	1,31
3,63	0,15	3,22	0,13	4,31	0,17
13,01	0,53	11,34	0,46	17,05	0,70
2,50	0,12	2,08	0,05	3,73	0,11
0,70	0,03	0,56	0,02	0,82	0,03
2,53	0,10	2,22	0,15	3,71	0,14
0,39	0,01	0,35	0,02	0,55	0,02
2,43	0,08	2,09	0,07	3,18	0,10
0,54	0,02	0,49	0,02	0,65	0,03
1,72	0,05	1,52	0,07	1,84	0,08
0,29	0,01	0,27	0,01	0,27	0,01
2,02	0,07	1,96	0,11	1,81	0,06
0,35	0,01	0,32	0,01	0,27	0,01
4,19	0,15	3,91	0,14	3,35	0,12
0,27	0,05	0,31	0,05	0,31	0,05
16,91	0,85	12,32	0,62	14,57	0,74
8,35	0,32	8,70	0,33	5,81	0,22
2,64	0,23	2,67	0,23	1,54	0,13

	Petite Savane			
14		14		
75b1		75d1		
fallout	S.D.	fallout	S.D.	
20,3	9,0	19,7	8,7	
6,9	1,2	6,8	1,2	
8,6	1,11	9,6	1,25	
0,274	0,058	0,911	0,144	
2,23	0,22	2,10	0,21	
<BLK		<BLK		
8,8	1,0	1,6	0,6	
29,6	3,1	35,5	3,7	
68,9	3,8	77,9	4,2	
132,29	5,67	138,70	5,94	
24,03	1,13	24,34	1,14	
145,73	7,34	151,41	7,63	
3,99	0,22	4,68	0,25	
1,2	0,1	1,2	0,1	
0,14	0,05	0,12	0,04	
4,0	0,3	4,4	0,3	
372	14,64	414	16,29	
13,8	0,6	15,2	0,6	
29,01	1,20	30,93	1,28	
3,56	0,14	3,89	0,16	
14,03	0,57	15,34	0,63	
3,23	0,08	3,52	0,09	
0,72	0,03	0,74	0,04	
3,53	0,13	3,68	0,14	
0,57	0,02	0,58	0,02	
3,68	0,12	3,75	0,12	
0,81	0,03	0,82	0,03	
2,54	0,08	2,54	0,08	
0,40	0,01	0,40	0,02	
2,73	0,09	2,73	0,09	
0,43	0,01	0,43	0,01	
4,22	0,15	4,30	0,16	
0,26	0,05	0,22	0,04	
13,08	0,66	13,46	0,68	
6,61	0,25	6,81	0,26	
2,07	0,18	2,18	0,19	

Table III.S4 (continued below)

	Grand Fond								Grand Bay		Plinian Post Roseau						Fond St Jean	
locality	*Rosalie*		*Rosalie*		*Rosalie*		*Grand fond*		*beach*		PPR1		PPR2		PPR3		*sea cliff*	
location	11		11		11		11		12		2		2		2		13	
number	43a1		43b1		43a2		43e		Dom 31		Dom 51b2		Dom 49c2		Dom 49i2		Dom 61	
type	fallout	S.D.	fallout	S.D.	fallout	S.D.	flow	S.D.	flow	S.D.	fallout	S.D.	fallout	S.D.	fallout	S.D.	fallout	S.D.
Li ppm	18,4	8,1	20,8	2,6	15,6	6,9	20,3	2,4	23,0	2,8	20,6	9,1	20,2	8,9	19,9	2,2	13,7	6,0
Sc ppm	9,4	1,7	5,6	0,7	7,4	1,3	18,3	0,8	6,5	0,9	5,7	1,0	7,7	1,4	15,8	0,9	6,6	1,2
V ppm	14,0	1,83	8,1	1,03	9,3	1,21	120,5	1,51	10,6	1,34	8,4	1,10	10,3	1,34	101,4	2,25	8,8	1,14
Cr ppm	2,208	0,268	0,965	0,121	0,491	0,080	3,351	0,247	1,527	0,192	0,877	0,107	0,662	0,134	2,047	0,263	0,573	0,070
Co ppm	2,30	0,23	1,33	0,15	2,16	0,21	13,86	0,11	1,45	0,17	2,06	0,20	2,25	0,22	13,03	0,32	2,28	0,23
Ni ppm	0,2	0,1	0,5	0,1	<BLK		3,0	0,1	0,8	0,1	<BLK		<BLK		2,3	0,2	<BLK	
Cu ppm	96,1	11,3	48,8	5,2	30,5	3,6	42,1	4,5	178,8	19,0	8,0	0,9	57,6	6,8	15,3	3,9	7,4	0,9
Zn ppm	58,7	6,1	39,5	5,0	37,0	3,8	50,1	1,4	90,8	11,4	35,4	3,7	73,1	7,6	57,2	3,3	37,0	3,8
Rb ppm	77,1	4,2	74,8	5,9	80,0	4,4	49,8	5,9	77,4	6,1	79,6	4,3	86,0	4,7	49,4	5,2	83,2	4,5
Sr ppm	128,22	5,49	142,73	10,71	112,95	4,84	209,66	8,03	120,03	9,01	123,43	5,29	126,72	5,43	216,18	9,35	119,49	5,12
Y ppm	32,27	1,52	23,48	1,81	27,01	1,27	20,59	1,84	24,87	1,91	25,53	1,20	27,23	1,28	20,15	1,72	26,23	1,23
Zr ppm	151,44	7,63	144,36	11,23	153,42	7,73	93,91	10,69	151,41	11,78	162,84	8,20	177,25	8,93	90,40	9,57	162,07	8,17
Nb ppm	4,33	0,23	4,25	0,35	4,21	0,23	2,95	0,31	4,06	0,33	4,54	0,25	5,98	0,32	3,06	0,29	4,12	0,22
Mo ppm	1,2	0,1	1,7	0,2	1,3	0,1	1,2	0,1	1,8	0,2	1,4	0,1	1,4	0,1	1,1	0,1	1,4	0,1
Cd ppm	0,13	0,05	0,16	0,06	0,11	0,04	0,14	0,04	0,11	0,05	0,12	0,04	0,14	0,06	0,11	0,04	0,15	0,05
Cs ppm	4,8	0,4	2,9	0,5	4,8	0,4	2,1	0,5	2,2	0,4	4,4	0,3	4,6	0,3	2,1	0,4	4,8	0,4
Ba ppm	395	15,52	393	21,11	401	15,78	278	21,09	403	21,64	415	16,34	526	20,71	270	19,11	391	15,40
La ppm	18,2	0,8	14,4	0,8	15,9	0,7	10,7	0,7	15,1	0,8	15,3	0,6	15,7	0,7	11,6	0,8	15,5	0,7
Ce ppm	30,31	1,26	29,39	1,53	30,79	1,28	22,35	1,48	30,02	1,56	32,42	1,35	33,66	1,40	22,82	1,42	30,29	1,26
Pr ppm	5,40	0,22	3,71	0,20	4,36	0,18	2,83	0,19	3,87	0,21	3,91	0,16	4,06	0,16	3,13	0,20	4,05	0,16
Nd ppm	22,63	0,93	14,47	0,69	17,25	0,71	11,85	0,70	15,29	0,73	15,69	0,64	16,15	0,66	12,81	0,70	16,27	0,67
Sm ppm	5,04	0,14	3,40	0,18	3,90	0,10	2,75	0,22	3,57	0,19	3,48	0,09	3,70	0,09	2,89	0,18	3,60	0,09
Eu ppm	1,03	0,04	0,79	0,04	0,82	0,03	0,87	0,04	0,75	0,04	0,71	0,03	0,73	0,04	0,88	0,05	0,82	0,03
Gd ppm	5,20	0,20	3,53	0,15	4,08	0,15	2,97	0,16	3,84	0,16	3,68	0,14	3,87	0,15	3,07	0,16	3,85	0,15
Tb ppm	0,84	0,03	0,57	0,03	0,68	0,03	0,47	0,03	0,61	0,03	0,61	0,02	0,63	0,02	0,51	0,03	0,64	0,02
Dy ppm	5,23	0,17	3,70	0,17	4,40	0,14	3,17	0,17	3,93	0,18	3,86	0,13	4,15	0,14	3,22	0,17	3,98	0,13
Ho ppm	1,13	0,05	0,81	0,04	0,95	0,04	0,68	0,04	0,84	0,04	0,85	0,04	0,90	0,04	0,69	0,04	0,88	0,04
Er ppm	3,27	0,10	2,47	0,12	2,86	0,09	2,08	0,13	2,59	0,13	2,61	0,08	2,83	0,09	2,01	0,12	2,69	0,08
Tm ppm	0,50	0,02	0,39	0,02	0,45	0,01	0,32	0,02	0,41	0,02	0,41	0,02	0,44	0,02	0,33	0,02	0,43	0,01
Yb ppm	3,48	0,12	2,71	0,12	3,11	0,15	2,27	0,12	2,84	0,18	2,93	0,10	2,96	0,10	2,19	0,11	2,96	0,10
Lu ppm	0,53	0,02	0,43	0,02	0,48	0,01	0,37	0,03	0,45	0,03	0,46	0,01	0,47	0,02	0,34	0,02	0,45	0,01
Hf ppm	4,43	0,16	4,23	0,18	4,38	0,16	2,77	0,19	4,33	0,19	4,60	0,17	4,85	0,18	2,65	0,16	4,58	0,17
Ta ppm	0,29	0,05	0,32	0,01	0,23	0,04	0,23	0,02	0,32	0,01	0,23	0,04	0,25	0,04	0,26	0,01	0,24	0,04
Pb ppm	17,11	0,86	6,27	0,26	13,34	0,67	5,82	0,36	12,91	0,54	13,91	0,70	14,94	0,75	6,16	0,36	14,21	0,72
Th ppm	6,57	0,25	6,59	0,27	6,94	0,27	4,12	0,27	6,86	0,28	7,02	0,27	7,17	0,27	4,19	0,25	7,10	0,27
U ppm	2,25	0,20	1,97	0,17	2,30	0,20	1,24	0,18	1,95	0,17	2,19	0,19	2,19	0,19	1,24	0,15	2,19	0,19

Table III.S4 (continued)

	Feldspar							
eruption	L		R				GF	
local name	*sea cliff*		*Cocoyer*				*Rosalie*	
location	*8*	*S.D.*	*1*	*S.D.*	*1*	*S.D.*	*11*	*S.D.*
Li	10,7	2,4	13,4	3,0	19,3	4,4	14,4	3,3
Sc	0,2	0,1	0,2	0,1	0,3	0,1	0,3	0,2
Ti	0,0	0,0	0,0	0,0	0,0	0,0	0,0	0,0
V	2,4	0,56	1,5	0,36	1,7	0,39	1,4	0,33
Cr	1,4	0,316	4,6	1,067	11,0	2,578	1,1	0,250
Co	0,32	0,07	0,35	0,07	0,49	0,10	0,34	0,07
Ni	3,1	0,6	3,6	0,7	4,9	1,0	5,3	1,1
Cu	3,8	0,7	3,4	0,7	2,8	0,6	2,8	0,6
Zn	6,5	1,4	7,0	1,5	8,3	1,8	9,2	2,0
Rb	2,4	0,4	2,6	0,4	3,8	0,6	2,4	0,4
Sr	463	68,04	461	67,67	456	66,99	471	69,17
Y	0,80	0,12	1,01	0,15	1,43	0,22	1,22	0,19
Zr	1,96	0,31	0,72	0,11	4,05	0,63	2,22	0,35
Nb	1,38	0,21	0,90	0,14	0,98	0,15	0,98	0,15
Mo	0,2	0,0	0,0	0,0	0,1	0,0	0,2	0,0
Cd	0,01	0,01	0,01	0,01	0,03	0,01	0,02	0,01
Cs	0,1	0,0	0,1	0,0	0,2	0,0	0,1	0,0
Ba	109	12,00	116	12,80	119	13,11	109	12,04
La	4,1	0,5	4,4	0,5	4,5	0,5	4,3	0,5
Ce	6,31	0,69	6,72	0,74	7,09	0,78	6,57	0,72
Pr	0,60	0,06	0,65	0,07	0,71	0,07	0,66	0,07
Nd	1,88	0,20	2,10	0,22	2,32	0,25	2,22	0,23
Sm								
Eu	0,98	0,11	1,03	0,12	1,03	0,12	1,12	0,13
Gd	0,23	0,02	0,29	0,04	0,36	0,04	0,32	0,03
Tb	0,03	0,00	0,03	0,01	0,05	0,01	0,04	0,00
Dy	0,14	0,01	0,18	0,02	0,25	0,03	0,21	0,02
Ho	0,03	0,00	0,04	0,00	0,05	0,00	0,04	0,00
Er	0,08	0,01	0,10	0,01	0,15	0,01	0,12	0,01
Tm	0,01	0,00	0,02	0,00	0,02	0,00	0,02	0,00
Yb	0,07	0,01	0,10	0,01	0,16	0,02	0,11	0,01
Lu	0,01	0,00	0,02	0,00	0,02	0,00	0,02	0,00
Hf	<BLK		<BLK		<BLK		<BLK	
Ta	0,46	0,21	0,36	0,17	0,33	0,15	0,31	0,14
Pb	4,52	0,51	4,11	0,46	4,72	0,53	3,71	0,42
Th	0,25	0,02	0,27	0,02	0,37	0,03	0,23	0,02
U	0,06	0,01	0,06	0,01	0,11	0,01	0,06	0,01

	Orthopyroxene							
	L		R				GF	
	sea cliff		*Cocoyer*				*Rosalie*	
	8	*S.D.*	*1*	*S.D.*	*1*	*S.D.*	*11*	*S.D.*
	5,3	1,2	8,7	2,0	9,1	2,1	7,6	1,7
	29,5	7,9	46,9	12,5	50,1	13,4	62	16
	0,6	0,2	0,7	0,2	0,9	0,2	0,6	0,2
	134	32	189	45	182	43	158	37
	4,8	1,134	6,5	1,527	6,0	1,400	4,0	0,938
	69,6	14,56	98,0	20,5	99,0	20,7	101,5	21,2
	10,7	2,2	17,0	3,5	17,2	3,6	18,1	3,7
	5,2	1,0	9,0	1,8	9,1	1,8	8,9	1,8
	289,8	62,4	375,0	80,7	381,7	82,2	356,7	76,8
	0,8	0,1	1,1	0,2	1,1	0,2	1,0	0,2
	7,54	1,11	9,71	1,43	10,26	1,51	12,76	1,88
	10,39	1,59	14,68	2,25	15,68	2,41	16,65	2,56
	2,31	0,36	2,88	0,45	4,59	0,72	3,31	0,52
	2,16	0,32	2,19	0,33	2,82	0,42	1,85	0,28
	0,2	0,0	0,2	0,0	0,1	0,0	0,1	0,0
	0,13	0,05	0,16	0,05	0,16	0,06	0,16	0,07
	0,0	0,0	0,1	0,0	0,1	0,0	0,1	0,0
	4,8	0,53	6,9	0,76	7,9	0,87	7,5	0,82
	6,0	0,7	6,9	0,8	6,4	0,7	5,0	0,6
	14,28	1,56	16,61	1,82	15,60	1,71	11,83	1,30
	1,89	0,20	2,21	0,23	2,17	0,23	1,79	0,19
	7,87	0,83	9,80	1,04	9,55	1,01	8,13	0,86
	0,23	0,03	0,28	0,03	0,29	0,03	0,28	0,03
	1,69	0,17	2,21	0,23	2,31	0,24	2,25	0,23
	0,26	0,03	0,33	0,04	0,35	0,04	0,36	0,04
	1,63	0,17	2,19	0,23	2,36	0,25	2,42	0,26
	0,37	0,03	0,51	0,04	0,53	0,05	0,58	0,05
	1,21	0,11	1,56	0,15	1,71	0,16	1,86	0,17
	0,21	0,02	0,27	0,03	0,29	0,03	0,32	0,04
	1,63	0,16	2,13	0,21	2,24	0,22	2,49	0,24
	0,29	0,03	0,37	0,04	0,40	0,04	0,44	0,05
	<BLK		<BLK		<BLK		<BLK	
	0,32	0,15	0,55	0,25	0,56	0,26	0,47	0,21
	<BLK		0,10	0,03	0,49	0,05	0,07	0,02
	0,28	0,02	0,34	0,03	0,31	0,03	0,25	0,02
	0,09	0,01	0,10	0,01	0,09	0,01	0,07	0,01

	Amphibole	
	L	
	sea cliff	
	8	*S.D.*
	6,3	1,4
	187	50
	2,4	0,6
	525	124
	8,3	1,9
	78	16
	27,2	5,6
	7,6	1,5
	190,8	41,1
	1,9	0,3
	53,71	7,89
	146	22
	75,08	11,71
	10,01	1,51
	0,2	0,1
	0,28	0,10
	0,1	0,0
	48,7	5,37
	14,1	1,6
	53,85	5,90
	10,02	1,04
	54,35	5,75
	2,76	0,31
	20,38	2,10
	3,57	0,38
	23,54	2,48
	5,02	0,44
	14,31	1,34
	2,14	0,24
	13,34	1,30
	1,94	0,21
	2,19	1,24
	0,50	0,23
	1,20	0,13
	0,35	0,03
	0,11	0,02

	Clinopyroxene	
	GF	
	Rosalie	
	11	*S.D.*
	9,3	2,1
	240	64
	1,2	0,3
	329	78
	9,0	2,1
	56	12
	22,8	4,7
	11,7	2,3
	131,2	28,2
	1,4	0,2
	42,63	6,26
	63,64	9,76
	29,59	4,61
	3,26	0,49
	0,1	0,0
	0,41	0,14
	0,1	0,0
	14,7	1,62
	6,7	0,8
	20,39	2,23
	4,04	0,42
	21,94	2,32
	1,17	0,13
	9,40	0,97
	1,70	0,18
	11,30	1,19
	2,39	0,21
	6,62	0,62
	0,96	0,11
	6,17	0,60
	0,94	0,10
	0,03	0,07
	0,45	0,21
	0,80	0,09
	0,29	0,02
	0,11	0,01

	Oxyde					
	L		R			
	sea cliff		*Cocoyer*			
	8	*S.D.*	*1*	*S.D.*	*1*	*S.D.*
	3,6	0,8	3,5	0,8	3,2	0,7
	22,3	5,9	61,5	16,4	38,6	10,3
	16,9	4,5	19,8	5,2	12,7	3,3
	6030	1425	8500	2009	5793	1369
	165	39	236	55	132	31
	182	38	260	54	206	43
	51,3	10,6	84,1	17,4	125,3	26,0
	31,8	6,3	41,9	8,3	58,0	11,5
	884	190,3	1027	221,2	891	191,8
	0,4	0,1	0,7	0,1	0,9	0,1
	10,51	1,54	25,21	3,70	20,18	2,97
	17,03	2,61	30,66	4,70	30,52	4,68
	28,53	4,45	33,70	5,25	76,14	11,87
	10,50	1,58	11,31	1,70	18,55	2,79
	5,0	0,8	4,6	0,8	5,7	0,9
	0,11	0,04	0,10	0,05	0,17	0,07
	0,0	0,0	0,0	0,0	0,1	0,0
	2,6	0,28	5,2	0,58	7,5	0,83
	17,3	2,0	19,7	2,2	23,5	2,7
	40,78	4,47	47,04	5,15	56,19	6,16
	5,21	0,54	6,34	0,66	7,58	0,79
	21,86	2,31	28,50	3,01	33,19	3,51
	0,50	0,06	0,70	0,08	0,81	0,09
	4,00	0,41	6,62	0,68	7,39	0,76
	0,52	0,06	0,92	0,10	1,02	0,11
	2,77	0,29	5,01	0,53	5,69	0,60
	0,53	0,05	0,98	0,08	1,13	0,10
	1,36	0,13	2,46	0,23	2,86	0,27
	0,18	0,02	0,29	0,03	0,34	0,04
	1,03	0,10	1,62	0,16	1,90	0,19
	0,15	0,02	0,23	0,02	0,27	0,03
	8,59	4,85	10,90	6,15	1,79	1,01
	<BLK		<BLK		0,67	0,31
	<BLK		0,05	0,04	1,42	0,16
	0,56	0,05	0,61	0,05	0,78	0,06
	0,21	0,02	0,22	0,02	0,28	0,03

Table III.S5: Trace elements mineral composition (ppm)

CHAPTER IV:

EXPERIMENTAL DETERMINATION OF MAGMA STORAGE CONDITIONS

Introduction

Dans ce chapitre nous présentons les travaux de pétrologie expérimentale réalisés au cours de cette thèse. L'étude fera l'objet d'un article scientifique et est ainsi présentée sous forme d'article en préparation.

Cette étude a pour objectif de contraindre les conditions de stockage des magmas de la Dominique à partir des estimations obtenues par les méthodes de geo-oxythermobarométrie naturelle et par des expériences d'équilibre de phases.

Dans une première partie nous présentons une brève description du contexte géologique de la Dominique et des dépôts d'écoulement pyroclastiques cibles de cette étude. Nous détaillons par la suite la stratégie d'échantillonnage adoptée, la préparation des échantillons, la méthode expérimentale utilisée pour la réalisation des expériences d'équilibre de phase et les techniques d'analyse des échantillons expérimentaux et naturels. Les expériences d'équilibre de phase ont été réalisées avec des autoclaves à chauffage interne (IHPV : Internally Heated Pressure Vessels) à l'ISTO (Orléans) dans la gamme 800-900 °C, 150-400 MPa et à une fugacité d'oxygène fixée à ~ΔNNO+1. Cette gamme expérimentale a été choisie sur la base des premières estimations de pression, température et fugacité d'oxygène obtenues par l'étude des produits naturels. Sur la base des compositions en roche totale et modales des produits naturels de Layou, Roseau et Grand Fond, nous avons utilisé deux produits de départ (Roseau et Layou) et testé les deux conditions saturées ($xH_2O=1$) et sous-saturées ($xH_2O=0.8$) en H_2O. Les composants expérimentaux (produit de départ, eau et oxalate d'argent) ont été insérés dans des capsules en Or.

Pour chaque expérience, une série de quatre charges expérimentales et un sensor (utilisé pour vérifier la valeur de fugacité d'oxygène) a été montée dans l'autoclave. La durée des expériences varie de 7 à 10 jours en fonction des conditions de température choisies et vise à garantir l'atteinte des conditions de cristallisation à l'équilibre. La stabilité du point chaud dans l'autoclave ainsi que la valeur de température et pression ont été contrôlées régulièrement le long de chaque expérience. Toutes les expériences ont été terminées par une trempe isobarique.

Les produits expérimentaux, ainsi que les produits naturels, ont été analysés par microscopie électronique à balayage (MEB) et microsonde électronique (EMP). La réalisation d'images BSE (Back-Scattered Electrons) à haute résolution est particulièrement importante lors de l'analyse chimique des produits expérimentaux : la petite taille (généralement inférieure à 30

μm) des phases cristallines expérimentales nécessite une première phase d'identification par imagerie, facilitant le repérage lors de l'analyse chimique par microsonde électronique.

Les résultats obtenus sont présentés en deux volets. Un premier détaille la pétrologie des produits naturels, la composition des différentes phases cristallines et les premières estimations des conditions de stockage magmatique obtenues par les différents geothermobaromètres naturels (e.g. orthopyroxène-liquide, amphibole, titanomagnétite-ilmenite).
Cette première estimation présente des limites et doit être affinée en utilisant les résultats expérimentaux. Ces derniers (relation, proportion et composition des différentes phases cristallines et vitreuses) sont présentés dans le deuxième volet.
La comparaison des assemblages cristallins naturels et expérimentaux nous a ainsi permis de contraindre les conditions de stockage des magmas des éruptions de Layou et Roseau.

Dans une dernière partie, nous discutons des conditions de stockages des éruptions de Roseau et Layou, cibles de cette étude, et de la possibilité d'appliquer ces résultats aux autres éruptions ignimbritiques majeures de la Dominique (Grand Fond, Grand Savane et Grand Bay).
La particularité des conditions de stockage des magmas de la Dominique par rapport à ceux, moins volumineux, des autres îles de la portion centrale de l'arc (Guadeloupe, Martinique, Montserrat) sera aussi discutée.

Petrological and experimental constraints on the magma storage conditions of the large pumiceous eruptions in Dominica island (Lesser Antilles)

[a]***Solaro C.,*** [b]***Martel C.,*** [b]***Champallier R.,*** [a]***Boudon G.,*** [c]***Balcone-Boissard H.,*** [b]***Pichavant M.***

[a] Institut de Physique du Globe de Paris, Sorbonne Paris Cité, Univ. Paris Diderot, CNRS, F-75005 Paris, France

[b] Institut des Sciences de la Terre d'Orléans (ISTO), UMR 7327 Université d'Orléans-CNRS-BRGM, Orléans, France

[c] Sorbonne Universités, UPMC Univ. Paris 06, CNRS, UMR 7193, ISTEP, F-75005, Paris, France.

Abstract

Here we present a petrological and experimental study aimed at constraining the pre-eruptive conditions of the dacitic magma that lead to three major voluminous ignimbritic eruptions (plinian phase and pyroclastic flows; ~10 km^3 DRE) in Dominica (Lesser Antilles arc): Layou (51 kyrs cal BP), Roseau (33 kyrs cal BP), and Grand Fond (24 kyrs cal BP). All samples are dacitic (63-66 wt% SiO_2, ~4.5 wt% Na_2O+K_2O) and contain ~30 vol% of phenocrysts encompassing plagioclase (~21 vol%), orthopyroxene (~5 vol%), amphibole (0 to 5 vol%), and Fe-Ti oxides (<1 vol%), in a rhyolitic matrix glass (75-78 wt% SiO_2, ~6.0 wt% $Na2O+K_2O$).

Crystallization experiments were performed starting from pumices of Layou and Roseau (66 and 63 wt% SiO_2, respectively) at temperature from 800 to 900 °C, pressure from 150 to 400 MPa, oxygen fugacity ~ΔNNO +1, water-saturated and water-undersaturated conditions. The natural mineral assemblage, proportion, and compositions were reproduced for both samples at ~850 °C, ~400 MPa (~16 km deep), and 6-7 wt% melt H_2O for Roseau and 7-8 wt% H_2O for Layou (in agreement with the contents measured in orthopyroxene- and plagioclase-hosted melt inclusions). These results have been used to assess magma storage conditions for the ignimbrites of Grand Fond, Grand Bay and Grande Savane. Interestingly, the Dominica eruptive products were stored much deeper than those from the small-volume (< 1 km^3) eruptions of the neighbouring islands of Martinique, Guadeloupe, and Montserrat (≤ 200 MPa), likely related to a more extensive tectonic setting favouring accumulation of large magma volumes in the deep crust. Such a great depth of magma storage may also be the reason for the absence of clearly identified caldera in Dominica.

Keywords: Dominica; ignimbrite; dacite; phase equilibria; storage conditions

IV.1. Introduction

Island arc subduction related magmatism is known to mostly produce andesitic to dacitic eruptions of small to moderate volumes (1 to 5 km^3 DRE/eruption; DRE: dense rock equivalent). Nevertheless rare systems did produce large-volume silicic eruptions (10 to several 100 km^3 DRE/eruption), associated with caldera collapse and having thus important consequences in term of hazard assessment and risk management (Self and Rampino, 1981; Self et al., 1984; Heiken & McCoy, 1984; Druitt et al., 1989; Allen, 2001; Wilson, 2001; Reubi and Nicholls, 2005; Wilson et al., 2006). This raises several questions about the genesis, storage, and eruption of such large magma volumes. Using thermo-mechanical modelling of heat transfer, Annen and Sparks (2002) calculated that intrusion rates of at least $5x10^{-4}$ m/yr are necessary to generate large scale magma bodies in the crust by a process of sill accretion. Such flare-up periods of high magma production rates could result from high magmatic fluxes from the mantle (at least 10^{-2} km^3/yr; Annen, 2009), as evidenced for large plutonic batholith bodies (de Silva, 2008; de Silva and Gosnold, 2007; Lipman, 2007).

Jellinek and De Paolo (2003) suggest that the production of large magma volumes linked with caldera-forming eruptions derives from long periods (10^5-10^6 years) of magma supply in large magma chambers (> 10^2 km^3, larger volume compared to the volume of injections) having warm visco-elastic walls that prevent the creation of the overpressure needed for eruption. Such kind of storage regime can be enhanced in extensional tectonic contexts.

To trigger an eruption from these large volumes of magma, a critical overpressure must be reached by i) magma inputs (10^{-2} to 10^{-1} km^3/yr; de Silva, 2008) that largely exceed the long-term magma supply and/or ii) a chamber flattened in the vertical direction which would then favour dike generation, magma propagation and eruption (Jellinek and De Paolo, 2003).

Beyond the issues on the generation and the ability to keep eruptible large-scale magma bodies at crust level, one of the basic questions that need to be addressed is whether the storage conditions of such magmas are different, especially in terms of depth and temperature, from those of small-volume magma chambers. Several studies based on phase-equilibrium experiments have been conducted on small-volume magma chambers from subduction zones, suggesting temperatures from 820 to 900 °C and pressures from 100 to 200 MPa (e.g. for andesitic-dacitic magmas: Luhr et al., 1990; Gardner et al., 1995; Barclay et al., 1998; Martel et al., 1998; Sato et al., 1999; Scaillet and Evans, 1999; Hammer et al., 2002; Costa et al., 2004; Holtz et al., 2005). There are very few studies that precisely give the storage conditions of large volume reservoirs, but they tend to suggest pressures of ~400 MPa (Parat et al., 2008; Andujar et al., 2015). In Dominica, the petrological study of the dome-forming products and

pumiceous ignimbrites of Howe et al. (2015a) suggest crystallization conditions at temperature of 800-990 °C and oxygen fugacities of ΔNNO -0.25 to +0.35, relying on the use of geothermobarometers.

Based on these studies, we present hereafter a study combining petrological and experimental data to determine the storage conditions of the Dominica magmas. There are several important issues we would like to address: i) the depth, temperature, and volatile content of these large silicic pumice eruptions, ii) the possible differences in storage conditions between small- and large-volume eruptions, and iii) the 'local' reasons why Dominica emitted large magma volumes while the two neighbouring islands (Martinique and Guadeloupe) were erupting small magma volumes.

IV.2. Geological setting

IV.2.1. Lesser Antilles Arc

The Lesser Antilles volcanic arc is related to the subduction of the Atlantic oceanic lithosphere below the Caribbean plate at an average velocity of ~2 cm/yr for the recent period of the arc activity (Wadge, 1984). This subduction has been active since the early Eocene (Nagle et al., 1976). Built up by 11 main islands, the arc is 800 km long, with a particular convexity toward the East and is bordered on the West by the back-arc deep sedimentary basin of Grenada (Fig.IV.1). From Dominica Island, the arc can be divided into a South part (Grenada to Dominica) made by a unique segment of active volcanic islands and a North part (Dominica to Anguilla) made by two different segments of islands (Bouysse and Westercamp, 1990). The external segment (Marie Galante to Anguilla) consists of limestone platforms overlying a volcanic basement dating of the Eocene-Oligocene period (Westercamp, 1988), when volcanic activity was mainly submarine. From the Miocene (Aquitanian), the arc experienced a 6-7 Ma period of unrest linked with a major change in the geodynamics of the region: the subduction of an aseismic ridge in the center of the arc caused a rupture of the subduction plate and a displacement of the volcanic activity to the West, creating the second, internal segment (Bouysse and Westercamp, 1990). The internal segment (Dominica to Saba) and the South part of the arc are currently characterized by 12 active volcanoes that have been producing several explosive and effusive eruptions in the last 300 years.

IV.2.2. Dominica island

Dominica Island (15° 25N, 61° 20W; Fig IV.1) is located at the centre of the Lesser Antilles arc between Martinique and Guadeloupe. From North to South, four main active volcanic centres are present on the island: Morne aux Diables, Morne Diablotins, Morne Trois-Pitons-Micotrin and Plat Pays (Fig.IV.1).

The volcanic activity of the island is characterized by dome-forming eruptions, large explosive eruptions producing voluminous pyroclastic density currents, and also by phreatic eruptions of smaller impact mainly coming from the Boiling Lake, in the Valley of Desolation area.

From Pleistocene to recent time, the volcanic activity moved from North to South of the island. The oldest activity (late Pleistocene) was concentrated in the North with the formation of Morne Diablotins stratovolcano and Morne Aux Diables.

In the younger Pleistocene, the volcanic activity moved towards the central part of the island, forming the volcanoes of Morne Trois Pitons, Wotten-Waven Micotrin, and the minor centres of Foundland, Morne Watt and Morne Anglais. The central geothermal area of the island, the Valley of Desolation, is active since this period and has been involved in the phreatic eruptions in 1880 and 1997 (Lindsay et al., 2005b). Finally, the recent activity concentrates in the South of the island at the Plat Pays Volcanic complex (PPVC), made of the large Play Pays dome surrounded by several smaller and younger domes (e.g. Morne Crabier, Morne Patates). This has been so far the most studied area of Dominica (Wadge, 1985; Lindsay et al., 2003; Gurenko et al., 2005; Lindsay et al., 2005b; Halama et al., 2006).

Figure IV.1: Dominica Island. *Simplified version of Dominica geological map showing the extension of the major pyroclastic density currents, as reported by Sigurdsson (1972) and Lindsay et al. (2003). Quaternary pyroclastic density currents are mapped in clear yellow. The orange triangles indicate the major eruptive centres and the green stars show the sampling sites. (modified from Howe et al., 2014)*

IV.2.3. Main large ignimbritic eruptions

Even if the recent activity of Dominica has been more characterized by dome-forming eruptions and phreatic activity, in the 1980-1990 period, scientific attention has been focused on the study of the pumiceous pyroclastic density currents (PDC) that extensively outcrop in the central part of the island. In particular, the Pleistocene Roseau Tuff has been fully described (Sidgursson, 1972; Carey and Sidgursson, 1980). Based on analyses and correlation of tephra layers recovered in piston core from the Grenada basin and the West Atlantic, Carey and Sidgursson (1980) considered the Roseau eruption (~30 ky) as the only major eruption of

the island during the last 200 ky, producing a volume of 58 km^3/DRE of tephra from which ~ 33 km^3 of PDC descended the West flank of the Morne Trois-Pitons volcanic complex, i.e. towards the Roseau valley and spread in the Grenada Basin. The authors assessed that only ~3 km^3 of the total amount of the PDC are preserved onshore, whereas ~30 km^3 had suffered subaqueous transport as turbidity currents in the back-arc Grenada basin (Picard et al., 2006; Whitham, 1989).

Yet, recent on-land stratigraphic and chronological studies have evidenced that the Roseau eruption was not one but several different eruptive events (Smith et al., 2013; Howe et al., 2014). Boudon et al. (in prep) (chapter III) recognize at least three major pumiceous explosive eruptions (volume ~10 km^3/DRE per eruption) in the last 50 ky of volcanic activity: Layou (51 kyrs cal BP), Roseau (33 kyrs cal BP), Grand Fond (24 kyrs cal BP). These eruptions consist of a plinian phase, producing a relatively thin basal plinian pumice fallout (20 to 70 cm, < 10% of total erupted volume), followed by up to 100-m thick pumiceous pyroclastic density currents filling valleys. A detailed stratigraphy of these three eruptions is presented in chapter III.

Two others pumiceous PDC deposits have been recognized on the island: Grande Savane and Grand Bay. The Grande Savane ignimbrite is outcropping on the West coast, near the village of Salisbury. It has been described by Smith et al. (2013) as a lower ignimbritic sequence overlain by an upper pumiceous surge sequence. The deposit has been dated at ~22 ka from ^{14}C dating on organic material belonging to the upper sequence (Spark et al., 1980). The volume and the stratigraphic extension of this deposit are still not constrained. Mapping of Smith et al., (2013) suggests that the eruptive centre at the origin of this ignimbrite is the Morne Diablotins dome complex.

The Grand Bay ignimbrite is outcropping at the South coast near the village of Berekua and has been described in Lindsay et al. (2003) and Howe et al. (2014). In particular, the typical outcrop that forms the cliffs at Grand Bay beach has been described by Lindsay et al. (2003) as a massive, pumice- and lithic-rich PDC deposit. Some material from distal outcrops has been dated at 27-42 ka and correlated with the main Grand Bay outcrop by Lindsay et al. (2003). Nevertheless, this correlation has been recently questioned by Smith et al. (2013), thus letting the age of the Grand Bay ignimbrite still unconstrained. Also the volume and the eruptive centre of this ignimbrite are still matter of debate. Indeed, whereas Lindsay et al. (2003) suggested the PPVC as a possible eruptive centre, further works of Lindsay et al. (2005b) and Smith et al. (2013) proposed the Wotten Waven caldera.

In light of these eruptions, Dominica can be considered as an anomaly in the general eruptive behaviour of the central segment of the arc. Indeed, while the neighbouring islands of Martinique and Guadeloupe have only one active volcanic centre producing small volume (<1 km^3 DRE/eruption) plinian and dome-forming eruptions, Dominica recent activity has been characterized by five major pumiceous ignimbritic eruptions. Moreover it has been recently demonstrated that the last event triggering eruption from the reservoir occurred in relatively short timescales of decades prior to eruption (chapter V-Part II this volume), with respect to the preceding repose period of the system. These peculiarities raise the question of how and why such large magma volumes are stored and emplaced under Dominica.

IV.3. Petrological background

IV.3.1. Bulk-rock, modal proportion, and phase composition

Howe et al., (2014) and Boudon et al. (in prep.) (chapter III) performed a geochemical study on pumices from ignimbrites across the island (Grand Bay, Roseau, Layou, Grand Fond, Grande Savane, Londonderry). All analysed pumice clasts have calc-alcaline andesitic to dacitic whole-rock composition (61-66 wt% SiO_2). Layou and Grande Savane are dacitic, with 64-66 wt% SiO_2 and ~5 wt% Na_2O+K_2O, whereas Roseau and Grand Fond have less evolved compositions showing 62-63 wt% SiO_2 and ~4.5-5 wt% Na_2O+K_2O (recalculated with total iron as FeO and without the loss of ignition (LOI)). With bulk SiO_2 content increasing from 61 to 66 wt% SiO_2, FeO decreases from 6.5 to 5.1 wt%, whereas the other major elements remain constant (within analytical error). The pumice samples from the ignimbrites contain 25-30 vol% phenocrysts, encompassing plagioclase (15-24 vol%), orthopyroxene (0-5.5 vol%), clinopyroxene (0-3 vol%) and Fe-Ti oxides (0-4 vol%) (Howe et al., 2014). Amphiboles are only found in Layou and Grande Savane deposits. Compositions of these crystals are reported in Howe et al. (2014).

The groundmass glass is microlite free and rhyolitic in composition (76-78 wt% SiO_2, ~5.5-7 wt% Na_2O+K_2O) with a very narrow compositional range (Howe et al., 2014; Boudon et al., in prep-chapter III).

Howe et al. (2015) performed a petrologic study on products linked with dome-forming eruptions (block-and-ash flows and lavas) across the island. This study confirms that dome-related samples have also an andesitic to dacitic whole-rock composition, with a mineral assemblage similar to that of the pumice samples in ignimbrites. However, crystallinity is higher, about 40-55 vol%, and the samples all contain basalt to basaltic-andesite enclaves that are absent from the pumice samples.

IV.3.2. Melt inclusions

The composition of glass inclusions hosted in orthopyroxenes and plagioclases, as well as the speciation and content of their dissolved volatiles, have been studied by Balcone-Boissard et al. (in prep.), for which we summarize here the main results (see also chapter V).

The glass inclusions in orthopyroxene and plagioclase phenocrysts of Layou, Roseau, and Grand Fond pumiceous deposits show rhyolitic compositions (76-80 wt% SiO_2), but different Na_2O+K_2O content of ~5-6 wt% and ~2-5 wt% when hosted in plagioclase and orthopyroxene, respectively. Lower alkali contents in the plagioclase-hosted glass inclusions with respect to the bulk-rock (4-6 wt%) is contradictory with a magma differentiation process, thus raising the question of possible post-entrapment modification in plagioclase.

The volatile content of the melt inclusions have been measured by secondary ion mass spectrometry (SIMS; Edimburgh University, UK). The melt inclusions trapped in orthopyroxene phenocrysts display high H_2O content of 6.6-7.5$_{\pm 0.-3}$ wt% in Layou pumice, and 4.5-6.5$_{\pm 0.2}$ wt% in Roseau and Grand Fond pumice. Plagioclase-hosted melt inclusions show H_2O contents (4.7-6.8$_{\pm 0.3}$ wt%) similar to those hosted in the orthopyroxenes for Roseau and Grand Fond samples. For Layou, however, the H_2O contents are lower by 0.5-1.0 wt% where analysed in glass inclusions hosted in the plagioclases (6.2-6.5 wt% H_2O) with respect to those in the orthopyroxenes, a difference for which we do not have any explanation so far.

The inclusions also contain some CO_2, with concentrations ranging from 43 to 392$_{\pm 27}$ ppm in orthopyroxene-hosted melt inclusions and 81 to 422$_{\pm 20}$ ppm in plagioclase-hosted ones. There is no significant variation in CO_2 content from one eruption to the other (except for one single melt inclusion hosted in an orthopyroxene of Layou sample showing a suspicious high CO_2 content of 840$_{\pm 27}$ ppm). Fluorine reaches concentrations of ~600 and ~500 ppm in orthopyroxene- and plagioclase-hosted melt inclusions, respectively. Chlorine ranges between 2000 and 3100 ppm and 1500-2200 ppm in orthopyroxene- and plagioclase-hosted inclusions, respectively.

IV.4. Selection and preparation of the natural samples

The samples of this study have been collected from the basal plinian fallout deposit of each eruption, except for Grand Bay and Grande Savane, for which a basal plinian fallout phase has not been found and samples have been collected from the main pyroclastic flow unit (see chapter III). With the aim of determining the pre-eruptive conditions of the Dominica magmas, such pumice samples from the basal fallout deposits present several advantages: i) the base of the outcrop represents the early erupted products, therefore the top part of the

reservoir that is likely less affected by potential magma reinjections from below and magma mixing processes, ii) pumice textures evidence fast quenching during the eruption, which mostly prevents from post-eruptive modifications such as cooling-induced crystallization, and iii) pumice from fallouts are not transported on the ground across long distances, thus mitigating post-eruptive chemical and mechanical contamination (entrapment of non-juvenile material, welding, deformation). Therefore, we think that the pumice samples from the basal Plinian fallout are the best representatives of the magma composition in the reservoir just prior to eruption.

During the field campaign, thirty to forty andesitic-dacitic pumices (2 to 6 cm in diameter) were collected from the basal plinian fallout deposit of the eruptive sequence of Layou (DOM41a3), Roseau (DOM60d1a), Grand Fond (DOM43b), and from the main pumice flow deposit of Grande Savane (DOM40b) and Grand Bay (DOM31). For the specific purpose of this study, six to ten pumices were collected from the single mode of the density distributions (Boudon et al., in prep.-chapter III this volume).Pumices were cleaned and oven-dried at 80 °C for ~ 48 h. Some of the pumice clasts were mounted in epoxy resins, and polished for further textural and chemical analyses. However, since the number of crystals is extremely low in a clast section, some other pumice were gently crushed and sieved (size fractions from 315 μm to 1 mm) to allow handpicking of the different phenocryst populations under a binocular microscope. These isolated phenocrysts (orthopyroxenes, plagioclases, amphiboles, clinopyroxenes and magnetites) were also mounted in epoxy resins for chemical analyses on a statistically more relevant population.

IV.5. Experimental and analytical method

IV.5.1. Experimental methods

Starting material

The experiments were mainly performed starting from the pumice samples of Layou and Roseau eruptions. One experiment used Grande Savane and Grand Bay pumices as the starting material. Nevertheless, given their close similarities in bulk-rock compositions and crystal content (Table IV.1), the Layou products may be used to assess the storage conditions of Grande Savane magmas, whereas the Roseau products may be used for Grand Fond and Grand Bay storage conditions.

For the four eruptions (Layou, Roseau, Grande Savane, and Grand Bay), five to six pumices of 1-3 cm have been cleaned, carefully sawed to remove potential altered external parts (although no visible evidence for alteration), oven-dried for ~48 h, and ground to <50 µm.
To obtain the starting dry glass material, the pumice powder has been fused in a Pt crucible at 1400 °C and 1 atm for 3 h, water-quenched and ground in an automatic mortar down to <50 µm. The fusion-grinding cycle has been repeated twice to ensure chemical homogeneity of the starting glasses.

Equipment and run procedure

All experiments are crystallization runs (starting from a pure melt) performed using vertically-working internally-heated pressure vessels (IHPV; ISTO-Orléans).
In Au capsules (2 cm long, 2.5 mm inner diameter, 2.9 mm outer diameter), about 30 mg of the glass powder were inserted, with enough deionized water to achieve saturation at the target P-T of each experiment for the water-saturated conditions (XH_2Oin = initial $XH_2O/(XH_2O+XCO_2)$ = 1) and with deionized water plus different proportions of silver oxalate ($Ag_2C_2O_4$) as the source of CO_2 for the water under-saturated conditions (XH_2Oin = ~ 0.9 and 0.8). The fluid /silicate ratio has been kept constant at 10 wt% for all experiments, to avoid changes of the silicate composition by incongruent dissolution in the fluid phase (Holtz et al., 1992). The capsules were then arc-welded and stored at ~250 °C for 8-12 h to ensure H_2O vapour homogenization in the charge before experiment.
To check for possible water loss during capsule preparation and experiments, all capsules have been weighted prior and after welding, after storage at ~250 °C, and after experiment. Capsule weights that did not agree within 0.0004 g (balance analytical precision) before and after experiments were discarded.
To have a measurement of the oxygen fugacity prevailing during experiments, we used the H_2-solid sensors technique consisting of hand-pressed Ni-Pd-NiO pellets (Taylor et al., 1992; Pownceby et O'Neil, 1994) loaded with deionized water and Zr powder in a Pt capsule (2.5 cm long, 2.5 mm inner diameter, 2.9 mm outer diameter).
The pressurizing medium of the vessel was an Ar+H_2 mixture. About 0.1 MPa of H_2 has been loaded cold into the vessel for all experiments, in order to set the oxygen fugacity at a value close to one log unit above the Nickel-Nickel-Oxide (NNO) buffer (Huebner et Sato, 1970). Temperature was regulated by a Eurotherm controller and continuously measured during experiments using K or S-type thermocouples, with a precision of ±5°C. Control on

steadiness of temperature and pressure values along experimental duration has been done regularly, showing temperature variation of ±5°C and daily pressure variations of ±30 MPa.

We conducted 8 experiments in the range 150-400 MPa, 800-900 °C, and ~ΔNNO +1 to +2, with durations from 7 to 10 days (depending on temperature) to ensure crystallization at chemical equilibrium. For each run, four capsules (H_2O-saturated and H_2O-undersaturated samples of Layou and Roseau) and one redox sensor were loaded together in the vessel, except a single run (150 MPa, 800 °C) using Grande Savane and Grand Bay as starting materials, both H_2O-saturated, and without any redox sensor.

The runs were stopped by isobaric quenching of the samples, i.e. by switching off the furnace power and let the temperature drop down to ~300 °C (at an average of ~100°C/min) while maintaining pressure constant. No quench phases have been identified in the samples.

The fO_2 recorded by each charge has been then calculated by using the fO_2 value of the Ni-Pd-NiO sensor (retrieved from the formulation of Taylor et al., 1992), the constant of water dissociation (Kw, Robie et al., 1978) and the water fugacity (fH_2O) at the conditions of each experiment (knowing the fugacity of pure water, f^0H_2O, at the relevant P-T and water activity in each capsule). The fO_2 calculation suggests ~ΔNNO +1 for all experiments, except the one without sensor for which the Fe-Ti oxide compositions suggest ~ΔNNO +2.

IV.5.2. Analytical methods

Phase identification

As for the natural samples, fragments of the starting dry glass and fragments from each experimental charge were mounted in epoxy resin and polished (from 22 µm down to 0.3 µm). Both, experimental and natural samples, were further analysed by scanning electron microscope (SEM, ZEISS-Supra 55, ISTeP, UPMC, Paris; EDAX-Pegasus, BRGM-CNRS, Orléans) to produce the first mineralogical and textural observations. In particular, major crystal phases, proportions, and check for homogeneity in crystal distribution were performed in the experimental charges. Although some samples show heterogeneous crystal distribution with possible aggregates, the chemical analyses attested that these differences in textures did not affect phase composition.

Major elements

The chemical composition of the natural and experimental samples has been determined using a CAMECA-SX Five and a CAMECA-SX100 EMP (Service CAMPARIS, Paris) and a CAMECA-SX Five EMP (BRGM-CNRS, Orléans).

The natural and experimental crystals were analysed with an acceleration voltage of 15 kV, a beam current of 10 nA, and a focused beam (spot size < 2 µm). Peak and background counting times were set at 10 s for all elements. Glasses have been analysed with a beam current of 6 nA and a beam size of 10 by 10 µm, in order to minimize alkali migration during analysis.

Analytical errors on major elements have been calculated at ~1 wt% for SiO_2, Al_2O_3 and CaO, 3 wt% for FeO, MgO and TiO_2, 5 wt% for MnO, Na_2O and K_2O, 500 ppm for Cl and 200 ppm for P_2O_5.

In some experimental charges, some crystals or glass areas were too small to be analysed. This problem has been encountered especially in analysing plagioclase or magnetite, as well as and residual glass in the highly crystallised charges.

Sensor composition has been analysed for S, Fe, Co, Ni, Pd, Pt and Au with the CAMECA-SX Five electron microprobe (BRGM-CNRS, Orléans) with an acceleration voltage of 15 kV, a beam current of 20 nA and a focused beam. For all elements, the peak counting times were set at 10 s, while background counting times were at 5 s. Metallic elements and pyrite (for Fe and S) have been used as standards.

Water content of experimental glasses

The water content of the residual glass of each experimental charge has been determined by the 100-wt% difference method using the EMP (Devine et al., 1995). As H_2O standards, we used two melt inclusions of ~50 µm hosted in orthopyroxenes from Layou pumices, the water content of which has been determined by SIMS to be of 6.6 and 7.4 wt% (Balcone-Boissard et al., in prep). The advantages of using these glass standards are a composition (rhyolite) and H_2O contents close to those of the experimental glasses. H_2O content in the experimental glasses is given with an uncertainty of ±0.5 wt%.

Phase proportions

The area proportions of the different phenocrysts (> 200 μm) and matrix (bubble-free residual glass) in the natural samples were obtained by both, point counting on thin sections and mass balance calculation based on major and trace elements compositions (see chapter III).

Because the experimental products are commonly too small (5-10 μm) to allow phase determination by point counting using an optical microscope, the relative proportion of crystals (without distinction between the different mineral phases) and residual glass has been determined by image analysis using the SEM pictures. To obtain a value representative of the whole sample (discarding local heterogeneities), we treated 3 images per sample with different magnifications. The error on this method has been estimated at ±10%. The relative phase proportions (in wt%) of the different minerals in each experimental sample were determined by mass balance calculation (Stormer and Nicholls, 1978) using the EMP chemical composition. The method could not be applied to the samples that were lacking some crystal or glass chemical analysis. Some mass balance calculations reported residuals which were sometimes too high for Na_2O, probably reflecting the error relative to alkali analysis during EMP analysis of glasses.

IV.6. Results

IV.6.1. Petrology and geochemistry of Dominica dacites

IV.6.1.1 Phase assemblage and chemical composition

Bulk-rock compositions

The bulk-rock compositions of the main ignimbrites from Dominica are reported in Table IV.1.

Oxides (wt%)	Layou-like compositional group				Roseau-like compositional group				
	Layou	Layou	Grande Savane	Grande Savane	Roseau	Roseau	Grand Bay	Grand Bay	Grand Fond
	Exp	Nat	Exp	Nat	Exp	Nat	Exp	Nat	Nat
	LAY	Dom41a1	SAL	DOM40b	ROS	DOM60d1a	GB	DOM31	DOM43b1
SiO_2	65,43	66,20	65,65	64,83	64,08	63,50	63,02	63,31	62,76
TiO_2	0,46	0,38	0,37	0,45	0,51	0,54	0,63	0,51	0,54
Al_2O_3	16,60	16,43	17,51	16,45	17,05	16,89	16,92	16,80	17,05
FeO_{tot}	5,32	4,79	4,18	5,26	5,63	6,11	6,13	5,86	6,11
MnO	0,18	0,14	0,14	0,14	0,16	0,15	0,15	0,15	0,15
MgO	1,90	1,62	1,35	2,00	2,25	2,35	2,12	2,25	2,43
CaO	5,48	5,19	5,54	5,60	6,01	5,92	6,26	6,07	5,99
Na_2O	3,41	3,48	3,51	3,54	2,98	2,93	3,21	3,39	3,33
K_2O	1,65	1,67	1,76	1,62	1,57	1,50	1,52	1,56	1,53
P_2O_5	0,16	0,10	-	0,11	0,21	0,11	-	0,11	0,11
Total	100	100	100	100	100	100	100	100	100
Na_2O+K_2O	*5,05*	*5,15*	*5,27*	*5,15*	*4,55*	*4,42*	*4,73*	*4,95*	*4,86*
$FeO+MgO$	*7,22*	*6,41*	*5,53*	*7,26*	*7,88*	*8,46*	*8,27*	*8,10*	*8,54*

Table IV.1: Bulk-rock compositions of the main ignimbrites from Dominica: *Layou, Grande Savane, Roseau, Grand Fond, and Grand Bay . The total iron is recalculated as FeO_{tot} and the LOI (loss of ignition) has been removed. 'Exp' for experimental starting glass composition and 'Nat' for natural composition (wet chemistry analysis; from Boudon et al., in prep.), with the line below giving the sample number.*

Phenocryst assemblage and proportions

Whatever the considered eruption, the modal proportion is $30_{\pm5}$% total phenocrysts of plagioclase (~22%), orthopyroxene (~1-5%), clinopyroxenes (~1%), titanomagnetites-ilmenites (1-3%), and amphibole. Yet, Layou samples (as well as Grande Savane) contain up to 5% amphibole whereas practically absent (<1%) in Roseau and as traces in Grand Fond and Grand Bay.

From a textural point of view, it has to be noted that the plagioclases often exhibit strong signs of resorption in their core and important oscillatory zoning. Some orthopyroxenes show

also significant zoning textures (reverse, normal or multiple zonings; chapter V-Part I). These populations of zoned plagioclases or orthopyroxenes may bias the modal proportions determination by introducing crystal bits that are not in equilibrium with the residual glass (and thus do not reflect the pre-eruptive conditions). However, these zoned crystals represent a minor portion of the crystal budget (e.g. ~80% of the total amount of orthopyroxenes are chemically unzoned; chapter V-Part I).

Composition of the natural phenocrysts and glasses

Selected composition of the natural phenocrysts and glasses are reported in Table IV.2.

Plagioclases

Complete core to rim compositional traverses were obtained for about 40 crystals of the different eruptions, which some of them are presented in Fig. IV.2. Statistically speaking, three main compositional peaks can be identified (Fig. IV.3): An_{53-55} (An: anorthite molar%) present in both crystal core and rim, An_{70-75} usually present as short wavelength peaks in the oscillatory zoning part of the crystals, and An_{80-90} present mostly in cores of some crystals. Since we aim at defining the pre-eruptive conditions just prior to eruption, only the crystal rim composition in equilibrium with the residual glass is of relevance. Therefore, a close look at all traverses suggests that plagioclase rims have compositions of An_{50-55}, whatever the eruption considered (which also correlates with the main peak of the frequency histograms).

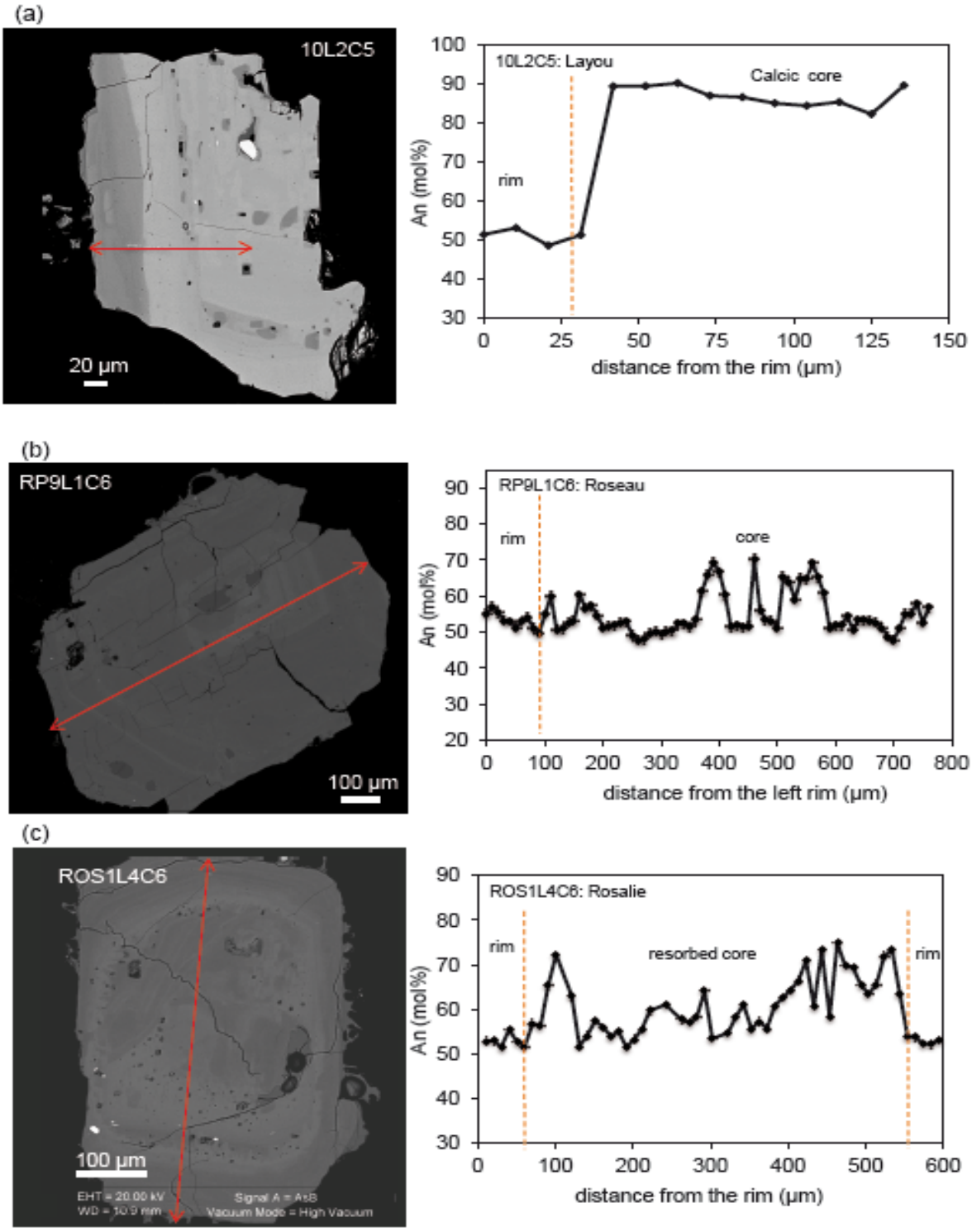

*(**Figure IV.2**: continued below)*

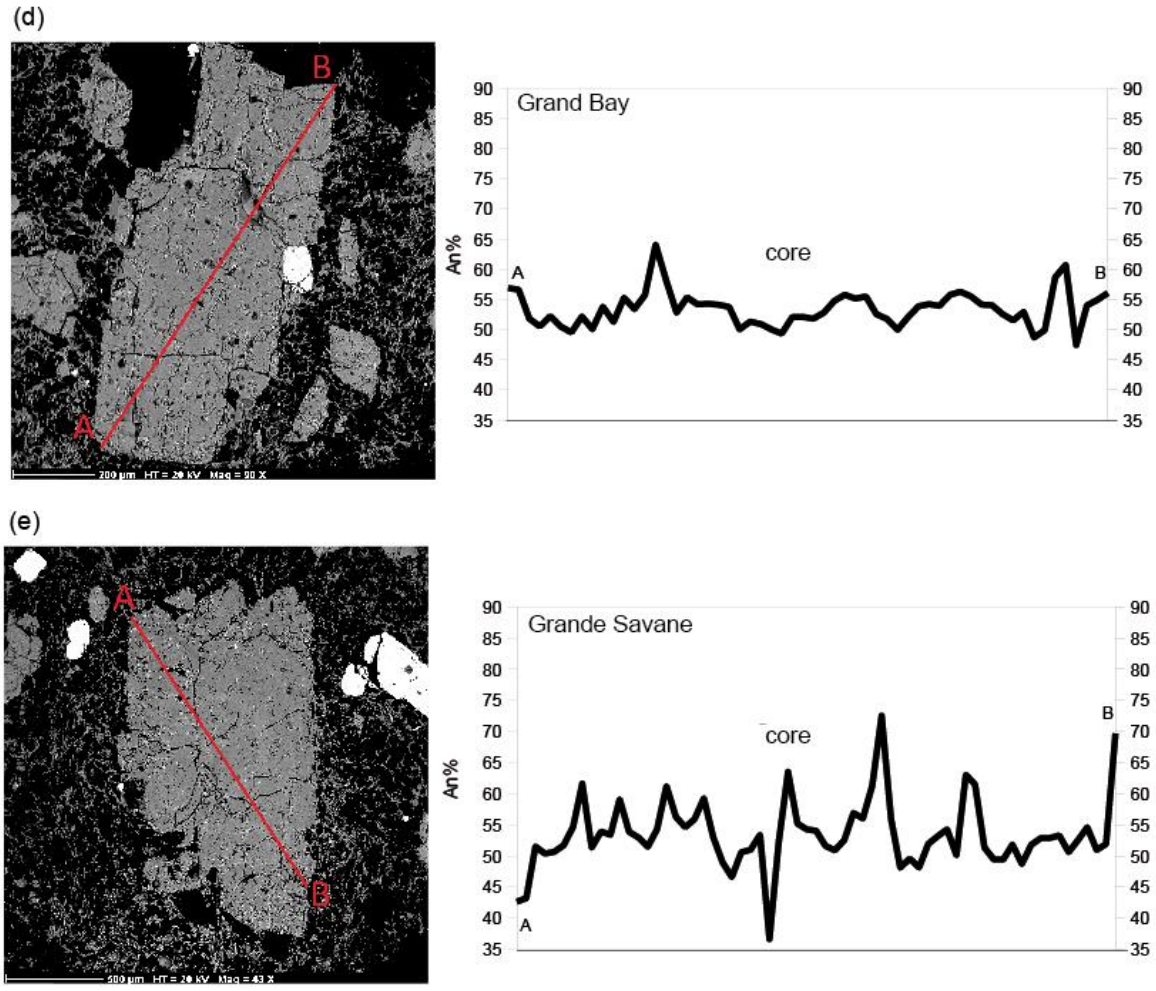

Figure IV.2: Selected plagioclase profiles *for (a) Layou, (b) Roseau, (c) Grand Fond, (d) Grand Bay, and (e) Grande Savane. The position of the analysed profile is indicated by the red line-arrow in each BSE images on the left. On the right, concentrations profiles are given in Anorthite (An) mol% as a function of the profile length (µm). Core and rim portions of crystals are identified.*

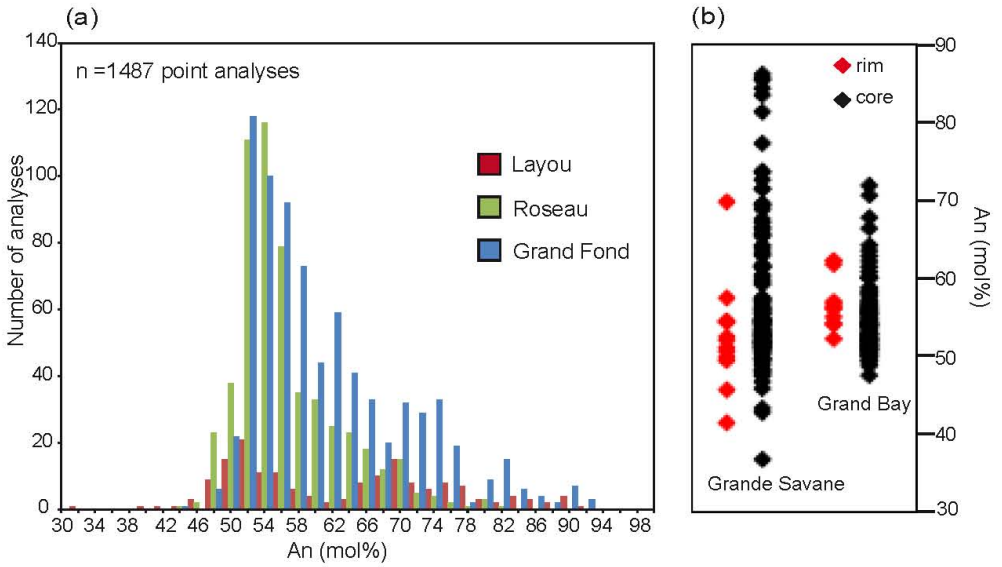

Fig. IV.3: Natural plagioclase compositions. *(a) Frequency histogram of chemical profiles (anorthite content in mol%) of natural plagioclases in Layou, Roseau, and Grand Fond eruptions. Roseau (in green) and Grand Fond (in blue) crystals show a unimodal distribution (peak at An53-55) while Layou (in red) crystals have a bimodal distribution (peaks at An50-55 and An68-70); (b) Composition of core (black) and rim (red) for the Grand Bay and Grande Savane crystals. Note that both eruptions exhibit a concentration of rim compositions at An50-55.*

Orthopyroxenes

The present orthopyroxene analyses, together with those presented in chapter V- Part I, suggest that orthopyroxenes share a comparable large compositional range between En_{47} and En_{63} (En: Enstatite content in mol %), with ~80-85% being unzoned and considered as representative of the pre-eruptive conditions in the reservoir (see chapter V- Part I). Yet, these unzoned crystals have slightly different compositions depending on the eruption considered, i.e. En_{52-53} for Layou, Roseau, and Grand Bay, En_{54-56} for Grand Fond, and En_{49-50} for Grande Savane samples.

Amphiboles

The rare amphiboles in Roseau samples are anhedral and show evidence of disequilibrium through important resorption boundaries and reactions rims. In contrast, the amphiboles in Layou and Grande Savane samples are euhedral and large in size (> 315 µm). Amphiboles of the three eruptions are ferri-magnesio-hornblendes after the classification of Leake et al. (1997), showing a very constant Al_2O_3 content of 6-8 wt% (Table IV.2) and Mg# ($MgO/(MgO+FeO_{TOT})$ values ranging from 0.52 to 0.57 for Layou, 0.54-0.60 for Roseau and from 0.59 to 0.64 for Grande Savane.

Layou	No.	SiO2		TiO2		Al2O3		FeO		MnO		MgO		CaO		Na2O		K2O		Total	Calc.
Plg (rim)	25	55,97	*0,57*	0,02	*0,02*	27,86	*0,36*	0,25	*0,03*	0,02	*0,02*	0,00	*0,00*	10,06	*0,37*	5,71	0,22	0,20	*0,01*	100,00	An50
Opx	19	49,93	*0,45*	0,09	*0,04*	0,57	*0,22*	27,96	*0,65*	1,19	*0,10*	17,09	*0,60*	0,97	*0,06*	0,01	*0,01*	0,01	*0,01*	97,84	En52
Amph	13	45,47	*0,53*	1,38	*0,15*	7,21	*0,46*	17,10	*0,47*	0,36	*0,06*	11,66	*0,39*	10,14	*0,19*	1,25	*0,09*	*0,34*	*0,04*	94,94	Mg#0.55
Mt	17	0,05	*0,03*	8,97	*0,17*	2,01	*0,63*	80,45	*0,72*	0,50	*0,05*	0,72	*0,06*	0,02	*0,03*	0,01	*0,01*	0,01	*0,01*	92,76	Mag73
#Ilm	2	0,06	*0,03*	41,27	*0,79*	0,11	*0,06*	47,15	*0,11*	0,565	*0,08*	1,725	*0,08*	0,005	*0,01*	0	*0,00*	0	*0*	90,89	Ilm85
Cpx	3	51,93	*0,47*	0,21	*0,04*	0,96	*0,04*	10,86	*0,14*	0,38	*0,02*	12,12	*0,22*	20,78	*0,15*	0,27	*0,03*	0,01	*0,01*	97,52	Wo45
RG	3	77,53	*0,38*	0,15	*0,03*	12,70	*0,20*	1,47	*0,02*	0,05	*0,04*	0,18	*0,02*	1,59	*0,10*	3,29	*0,10*	2,73	*0,22*	100,00	
MI(opx)	10	79,05	*0,74*	0,15	*0,07*	12,95	*0,43*	2,07	*0,25*	0,08	*0,05*	0,20	*0,03*	1,86	*0,18*	0,86	*0,44*	2,46	*0,51*	100,00	
MI(plg)	3	78,22	*0,54*	0,21	*0,06*	12,72	*0,35*	1,43	*0,15*	0,05	*0,03*	0,22	*0,03*	1,65	*0,06*	2,30	*0,26*	3,13	*0,13*	100,00	
STD-MI1	1	72,2	/	0,21	/	12,35	/	1,97	/	0,04	/	0,19	/	1,86	/	0,6	/	1,94	/	91,36	H2O~6
STD-MI2	1	71,7	/	0,23	/	12,61	/	1,7	/	0,04	/	0,19	/	2,03	/	0,37	/	1,38	/	90,25	H2O~7
Roseau																					
Plg (rim)	20	54,42	*0,37*	0,01	*0,02*	28,69	*0,24*	0,27	*0,04*	0,01	*0,02*	0,00	*0,00*	10,97	*0,19*	5,36	*0,13*	0,20	*0,02*	99,94	An52
Opx	30	50,03	*0,31*	0,10	*0,05*	0,50	*0,11*	27,58	*0,55*	1,13	*0,09*	17,47	*0,39*	0,98	*0,07*	0,01	*0,01*	0,01	*0,01*	97,81	En53
Amph	32	45,14	*0,57*	1,39	*0,13*	7,15	*0,37*	16,75	*0,48*	0,36	*0,05*	11,90	*0,37*	10,14	*0,16*	1,32	*0,08*	0,34	*0,04*	94,53	Mg#0.56
Mt	16	0,06	*0,02*	8,73	*0,29*	1,78	*0,12*	79,92	*0,60*	0,38	*0,06*	0,95	*0,04*	0,01	*0,01*	0,02	*0,02*	0,00	*0,01*	91,87	Mag73
Ilm	4	0,00	*0,01*	42,68	*0,62*	0,01	*0,01*	48,33	*0,32*	0,63	*0,05*	1,91	*0,02*	0,01	*0,01*	0,01	*0,01*	0,00	*0,00*	93,59	Ilm86
Cpx	4	52,51	*0,36*	0,14	*0,07*	0,95	*0,17*	11,12	*0,53*	0,47	0,05	13,04	*0,36*	21,07	*0,11*	0,22	*0,02*	0,01	*0,01*	99,07	Wo44
RG	12	76,46	*0,63*	0,24	*0,04*	12,93	*0,17*	1,83	*0,21*	0,07	*0,03*	0,29	*0,06*	1,95	*0,18*	3,36	*0,28*	2,55	*0,19*	100,00	
MI(opx)	9	78,86	*0,76*	0,12	*0,07*	12,61	*0,43*	2,15	*0,29*	0,09	*0,05*	0,21	*0,03*	1,58	*0,12*	1,19	*0,39*	2,87	*0,23*	100,00	
MI(plg)	6	78,35	*0,79*	0,11	*0,07*	12,58	*0,46*	1,30	*0,15*	0,05	*0,06*	0,19	*0,02*	1,51	*0,07*	2,63	*0,15*	3,26	*0,23*	100,00	
Grand Fond																					
Plg (rim)	18	55,30	*0,48*	0,02	*0,02*	28,36	*0,30*	0,31	*0,05*	0,01	*0,01*	0,00	*0,00*	10,63	*0,20*	5,37	*0,15*	0,18	*0,02*	100,18	An52
Opx	29	49,99	*0,94*	0,10	*0,04*	0,57	*0,17*	26,93	*0,95*	1,03	*0,11*	17,92	*0,53*	1,12	*0,74*	0,01	*0,02*	0,01	*0,01*	97,67	En54
Mt	4	0,10	*0,02*	9,62	*0,36*	2,04	*0,07*	78,87	*1,67*	0,42	*0,05*	1,01	*0,06*	0,03	*0,03*	0,01	*0,02*	0,00	*0,00*	92,09	Mag71
Ilm	12	0,18	*0,37*	42,67	*0,63*	0,02	*0,05*	49,08	*0,29*	0,60	*0,04*	1,93	*0,03*	0,04	*0,03*	0,02	*0,03*	0,01	*0,01*	94,56	Ilm85

RG	2	77,00	0,27	0,20	0,04	12,80	0,32	1,63	0,16	0,07	0,01	0,23	0,02	1,86	0,07	3,33	0,33	2,59	0,02	100,00	
MI(opx)	11	78,36	*0,86*	0,19	*0,06*	12,96	*0,34*	2,41	*0,23*	0,08	*0,05*	0,25	*0,05*	1,87	*0,10*	0,93	*0,42*	2,60	*0,22*	100,00	
MI(plg)	4	77,55	*0,17*	0,21	*0,08*	12,82	*0,26*	1,65	*0,11*	0,07	*0,03*	0,25	*0,02*	1,83	*0,03*	2,72	*0,29*	2,86	*0,11*	100,00	
Grande Savane	No.	SiO2		TiO2		Al2O3		FeO		MnO		MgO		CaO		Na2O		K2O		Total	Calc.
Plg (rim)	11	55,51	*0,74*	0,01	*0,02*	25,99	*0,42*	0,14	*0,08*	0,02	*0,03*	0,01	*0,01*	10,69	*0,35*	5,43	*0,26*	0,18	*0,03*	97,98	An52
Opx	3	51,55	*0,38*	0,01	*0,02*	0,38	*0,07*	26,94	*0,24*	0,97	*0,06*	16,02	*0,26*	0,97	*0,03*	0,03	*0,05*	0,00	*0,00*	96,87	En49
Amph	7	46,32	*1,03*	1,43	*0,18*	6,71	*0,66*	16,17	*0,35*	0,32	*0,08*	11,04	*0,35*	10,50	*0,15*	1,34	*0,11*	0,26	*0,04*	94,09	Mg# 0.63
Mt	3	0,05	*0,02*	8,89	*0,24*	1,59	*0,03*	75,80	*0,59*	0,32	*0,07*	0,76	*0,07*	0,05	*0,04*	0,00	*0,00*	0,03	*0,02*	87,48	Mag72
RG	2	77,36	*0,94*	0,23	*0,00*	12,78	*0,16*	1,85	*0,26*	0,06	*0,08*	0,27	*0,02*	1,90	*0,02*	2,87	*0,50*	2,68	*0,07*	100,00	
MI	6	76,86	*0,59*	0,16	*0,16*	12,32	*0,26*	2,22	*0,65*	0,04	*0,06*	0,55	*0,4*	1,62	*0,32*	2,89	*0,19*	3,34	*0,57*	100,00	
Grand Bay																					
Plg (rim)	9	53,88	*0,68*	0,02	*0,02*	27,23	*0,50*	0,28	*0,08*	0,03	*0,05*	0,01	*0,02*	10,83	*0,33*	5,36	*0,20*	0,15	*0,03*	97,78	An52
Opx	4	51,79	*0,13*	0,09	*0,04*	0,52	*0,14*	25,62	*0,49*	0,90	*0,09*	17,37	*0,34*	1,56	*1,08*	0,04	*0,04*	0,01	*0,02*	97,9	En52
Mt	9	0,19	*0,40*	9,31	*0,51*	1,60	*0,11*	76,21	*3,70*	0,36	*0,09*	0,79	*0,07*	0,07	*0,06*	0,02	*0,02*	0,01	*0,01*	88,55	Mag71
Ilm	1	0,00	/	41,35	/	0,15	/	47,69	/	0,51	/	1,73	/	0,00	/	0,00	/	0,00	/	91,43	Ilm83
Cpx	2	51,49	*0,31*	0,11	*0,03*	0,89	*0,07*	10,93	*0,36*	0,46	*0,13*	12,57	*0,04*	20,90	*0,22*	0,26	*0,04*	0,00	*0,00*	97,59	Wo44
RG	1	77,50	/	0,25	/	13,10	/	0,76	/	0,02	/	0,09	/	1,80	/	3,68	/	2,81	/	100,00	
MI(opx)	2	79,36	*1,09*	0,02	*0*	12,48	*0,47*	0,42	*0,03*	0,03	*0,04*	0,01	*0,01*	1,31	*0,42*	3,18	*0,35*	3,2	*0,07*	100,00	

Table IV.2: Average compositions of the natural crystals, glasses and melt inclusions for Layou *(DOM41a3)****, Roseau*** *(DOM60d1a)****, Grand Fond*** *(DOM43b1)****, Grande Savane (****DOM40b),* ***and Grand Bay (****DOM31)* ***deposits.*** *All oxides are in wt%; No. indicates the number of analyses on which the composition has been averaged. Numbers in italic character represent the calculated standard deviation on each element; Plg: plagioclase; Opx: orthopyroxene; amph: amphibole; Mt: titanomagnetite; Ilm: ilmenite; RG: residual glass; MI: melt inclusion An: Anorthite content (mol%); En: Enstatite content (mol%); Mg#: Magnesium number; Mag: Magnetite content (mol%); Ilm: Ilmenite content (mol%). #Ilm represent a composition averaged on two ilmenites of the Layou ignimbrite (pyroclastic density current) overlying the plinian fallout deposit.*

Clinopyroxenes

Clinopyroxenes in Roseau, Layou, and Grand Bay samples are all diopsides, with Wo_{44-45}, En_{37-38} and Fs_{18-19} (wollastonite, enstatite, and ferrosilite in mol%, respectively) whatever the eruption considered (Table IV.2). Samples show Mg# between 0.61 and 0.71, with a broad peak at 0.68.

Although present, clinopyroxenes have not been analysed for Grand Fond and Grande Savane eruptions.

Fe-Ti oxides

Fe-Ti oxides in the five eruptions are titanomagnetites and ilmenites. Titanomagnetites show constant compositions from one eruption to the other, exhibiting ~75-80 wt% FeO_{tot} and ~10 wt% TiO_2, with magnetite molar content of 71-75 % on the magnetite-ulvospinel join (Mag_{71-75}). Ilmenites display ~48 wt% FeO_{tot} and ~45 wt% TiO_2, with ilmenite molar content of 86-87 % on the ilmenite-hematite join (Ilm_{86-87}). Both Fe-Ti oxides formula were calculated following Sauerzapf et al. (2008).

One ilmenite has been analysed for Grand Bay eruption, showing ~47 wt% FeO_{tot} and ~41 wt% TiO_2, with ilmenite molar content of 83% (Ilm_{83}).

IV.6.1.2. Results and limitations of the estimates of the dacites magma storage conditions

The results and limitations of using natural geo-oxythermobarometers to constrain pre-eruptive crystallization conditions are presented in detail to allow further comparison with the experimental results.

Temperature and fO_2

The presence of both titanomagnetites and ilmenites as phenocrysts in pumice of the three eruptions can be used to constrain the T-fO_2 pre-eruptive crystallization conditions, using the oxythermometer of Ghiorso and Evans (2008). The oxythermometer could not be tested on our experimental charges because of the lacking analyses of both crystal phases in the same charge. Nevertheless the oxythermometer of Ghiorso and Evans (2008) has been intrinsically calibrated on silicic magmas very close to our dacitic compositions. Two touching titanomagnetite-ilmenite pairs in the pumice of Grand Fond, which pass the test for chemical equilibrium using the regression line of Bacon and Hirschmann (1988), give T of ~850-860 °C and fO_2 of ΔNNO +0.60 to +0.65 (see Table IV.S1 in the Supplementary material).

Crystallization temperature may also be retrieved from amphibole composition using the formulation of Ridolfi and Renzulli (2012), not requiring equilibrium with any other mineral phases, based on amphibole composition (recalculated on a basis of 13 cations), and calibrated for basaltic to dacitic composition. Tested on our amphibole-bearing run products (825°C-300 MPa), the formulation shows that the calculated and experimental temperatures agree within an acceptable uncertainty of ±30 °C and oxygen fugacity within ΔNNO ±0.2. Using the formulation for the natural amphiboles of Layou and Roseau eruptions suggests T from 776 to 801 ±22 °C, which is lower by ~50-80 °C in comparison to the T estimated from the Fe-Ti oxides pairs (Table IV.S2 in the Supplementary Material). For both Layou and Roseau eruptions, the calculated fO_2 suggests ΔNNO +1.

A third mean of estimating crystallization temperature is to use the orthopyroxene-melt geothermometer of Putirka (2008), based on the Fe-Mg partition coefficient between orthopyroxene and melt ($K_D(Fe\text{-}Mg)^{opx\text{-}melt} = (X_{Fe}^{opx} X_{Mg}^{melt})/(X_{Mg}^{opx} X_{Fe}^{melt})$). Couples of orthopyroxenes and melt inclusions in equilibrium conditions (Kd= 0.29 ± 0.06; Putirka et al., 2008; see also chapter V-PartI) give T in the range of 850-870 °C (after the equation 28b of Putirka et al., 2008), in agreement with those obtained using the Fe-Ti oxides pairs (Table IV.S3 in the Supplementary material).

Pressure

Pressure may be retrieved from amphibole composition using the formulation of Ridolfi and Renzulli (2012). The test on the experimental amphiboles shows that calculated pressures are usually underestimated of ~100 MPa (Table S2), which is not satisfactory enough to be used on the natural amphiboles. In particular, both experimental and natural Dominica amphiboles show low Al_2O_3 contents (7-8 wt%) which invariably leads to low P after the formulation of Ridolfi and Renzulli (2012), whereas parameters other than P may influence the amphibole Al content (e.g. T, melt composition, as demonstrated by Erdmann et al., 2014).

Pressure may be retrieved directly from the volatile content of the melt inclusions trapped in phenocrysts, assuming that these melt inclusions formed in the magma chamber and did not suffer any post-entrapment modification (e.g. crystallization of the host mineral or fracturing that may be responsible of volatile loss). In the absence of evidence of such post-entrapment modifications, we consider the 6.5-7.5 wt% H_2O and 200 ppm CO_2 measured in orthopyroxene-hosted melt inclusions of Layou (Balcone-Boissard et al., in prep) as representative of the pre-eruptive concentrations for this eruption. From Roseau and Grand

Fond orthopyroxene hosted melt inclusions, we consider a pre-eruptive volatile content at ~6 wt% H_2O and 200 ppm CO_2 (Balcone-Boissard et al., in prep). Using the H_2O-CO_2 solubility model of Newman and Lowenstern (2002), this constraints a minimum storage pressure of ~300-350 MPa for Layou and 150-250 MPa for Roseau and Grand Fond.

Another method to obtain pre-eruptive water contents is to use the plagioclase-liquid geohygrometer of Water and Lange (2015), giving H_2O contents of 4.2 to 4.7 wt% at 850°C and 300 MPa for Layou eruption. Water contents calculated by this method seem to underestimate those obtained by SIMS analysis (i.e. 6.5-7.5 wt%).

Pre-eruptive conditions deduced from the natural products

In summary, the pre-eruptive storage conditions estimated from the petrological study of the dacites gives (1) T of either 760-800 °C (amphiboles) or 850-870 °C (Fe-Ti oxides and orthopyroxene-liquid) for all studied eruptions, (2) fO_2 of ~ΔNNO +0.6 to +1.0 (Fe-Ti oxides and amphibole) and (3) water contents from ~4.5 wt% (plagioclase-liquid) to 6.5-7.5 wt% (melt inclusions) for Layou and 4.5-6.0 wt% for Roseau and Grand Fond (melt inclusions) (4) P from 300 to 350 MPa for Layou and from 150 to 250 MPa for Roseau and Grand Fond (H_2O-CO_2 solubility model).

As a result, the petrology study of the natural phase assemblage shows two possible ranges of T and poorly-constrained P (between ~150 and 350 MPa) mostly resulting from a large range of volatile concentrations. In order to refine these broad conditions of magma storage, phase-equilibrium crystallization experiments have been performed under conditions that bracket these results.

IV.6.2. Experimental phase equilibria

Phase-equilibrium crystallization experiments were performed in the T range of 800-900 °C, P of 150-400 MPa, at a fixed fO_2 of ΔNNO +1, and XH_2Oin varying from 0.8 to 1 (H_2O-undersaturated to saturated conditions). The experimental conditions for each run are listed in Table IV.3.

What we aim to reproduce experimentally is $30_{\pm5}$ wt% crystals consisting of $An_{50\text{-}55}$, $En_{52\text{-}53}$, amphibole with 7-8 wt% of Al_2O_3 (Al7-8), $Mag_{71\text{-}74}$, and $Ilm_{85\text{-}86}$ in a 77 wt% SiO_2 glass (Liq77) for the Layou sample and $30_{\pm5}$ wt% crystals consisting of $An_{53\text{-}55}$, $En_{52\text{-}53}$, $Mag_{72\text{-}75}$, and Ilm_{85} in a 76 wt% SiO_2 glass for the Roseau sample. In this latter case, we do not consider amphiboles as in equilibrium with the other phases of the assemblage given their important signs of resorption processes.

IV.6.2.1. Phase relations

H_2O-saturated charges

For both Layou and Roseau compositions, Fe-Ti oxides are the liquidus phases, crystallizing at T > 900 °C and stable over the entire range of investigated P-T conditions (Fig. IV.4.a, c).
For both starting compositions, Plg appears around 875 °C between 300 and 400 MPa. Opx is stable at lower P-T conditions, i.e. P < 200-300 MPa and T < 850-875 °C, with opx present at 300 MPa for Roseau (Fig. IV.4-c) whereas absent under these conditions for Layou (Fig. IV.4-a). Amphibole is unstable in the low-P high-T field, i.e. below 300 MPa – 900 °C and 200 MPa – 825 °C. Amphibole is stable at 150 MPa – 800 °C for Layou (Fig. IV.4.a) whereas absent under these conditions for Roseau (Fig. IV.4.c).

H_2O-undersaturated charges

For XH_2Oin ~ 0.8, both Layou and Roseau compositions (Fig. IV.4.b, d) have ubiquitous Fe-Ti oxides, Plg and opx in the investigated range of P-T conditions. The only difference comes from amphibole that is stable in Layou for P > 300 MPa (Fig. IV.4.b) whereas absent in Roseau (Fig. IV.4.d).
For XH_2Oin ~0.9 only investigated at 850 °C and 250 MPa, both Layou and Roseau compositions present the same crystal phase assemblage of plg, opx and Fe-Ti oxides.

Table IV.3: Experimental conditions and results

Run #	Sample	XH2Oin	Major phases (proportions in wt%)	$\sum R^2$	Gl/cryst (vol%)	$H2O_{melt}$ (wt%)
Run 1, 274 MPa, 850 °C, ~ΔNNO +1, 240 h						
850-300-R1	ROS	1	Gl(75) + Plg(11)+ Amph(11) + Mt(3)	2,36	74/26	9,5
850-300-R0.8	ROS	0,78	Gl(54) + Plg(36) + Opx(10) + Mt(1)	0,67	66/34	6,7
850-300-L1	LAY	1	Gl(73) + Plg(12) + Amph(13) + Mt(2)	1,12	77/23	8,9
850-300-L0.8	LAY	0,78	Gl(53) + Plg(36) + Opx(10) + Mt(1)	0,3	60/40	6,2
Run 2, 192 MPa, 850 °C, ~ΔNNO +1, 208 h						
850-200-R1	ROS	1	Gl(72) + Plg(18) + Opx(7) + Mt(3)	0,99	62/38	9,3
850-200-R0.8	ROS	0,81	Gl(46) + Plg(47) + Opx(7) + Mt(2)	0,67	57/43	6,2
850-200-L1	LAY	1	Gl(73) + Plg(17) + Opx(7) + Mt(3)	0,98	71/29	8,7
850-200-L0.8	LAY	0,76	Gl + Plg + Opx + Mt		72/28	6,4
Run 3, 283 MPa, 825 °C, ~ΔNNO +1, 172 h						
825-300-R1	ROS	1	Gl(69) + Plg(17) + Opx(2) + Amph(9) + Mt(3)	3,85	73/27	9,1
825-300-R0.8	ROS	0,79	Gl(59) + Plg(30) + Opx(10) + Mt(1)	1,56	56/44	*6,7
825-300-L1	LAY	1	Gl(73) + Plg(14) + Amph(10) + Mt(3)	2,5	78/22	8,4
825-300 -L0.8	LAY	0,8	Gl(32) + Plg(58) + Opx(10) + Mt(<1)	0,98	69/31	*6,2
Run 4, 195 MPa, 825 °C, ~ΔNNO +1, 242 h						
825-200-R1	ROS	1	Gl + Plg + Opx + Mt		63/37	8,7
825-200-R0.8	ROS	0,78	Gl + Plg + Opx + Mt		74/26	*6,2
825-200-L1	LAY	1	Gl + Plg + Opx + Mt		71/29	9,6
825-200-L0.8	LAY	0,82	Gl(54) + Plg(36) + Opx(8) + Mt(1) + Ilm(<1)	1,11	60/40	*6,4
Run 5, 395 MPa, 850 °C, ~ΔNNO +1, 162 h						
850-400-R1	ROS	1	Gl(73) + Plg(10) + Amph(13) + Mt(3)	5,22	79/21	9,2
850-400-R0.8	ROS	0,79	Gl(58) + Plg(30) + Opx(10) + Mt(1) + Ilm(<1)	2,06	67/33	8,2
850-400-L1	LAY	1	Gl(74) + Plg(9) + Amph(14) + Mt(3)	3,4	78/22	9,8
850-400-L0.8	LAY	0,78	Gl(62) + Plg(25) + Amph(7) + Opx(5) + Mt(1)	0,43	68/32	7,9
Run 6, 238 MPa, 850 °C, ~ΔNNO +1, 190 h						
850-250-R1	ROS	1	Gl(73) + Plg(15) + Opx(5) + Amph(5) + Mt(2)	2,22	76/24	8,7
850-250-R0.9	ROS	0,89	Gl(61) + Plg(30) + Opx(8) + Mt(1)	1,19	72/28	#7,8
850-250-R0.8	ROS	0,8	Gl(62) + Plg(28) + Opx(9) + Mt(1)	1,12	67/33	#6,9
850-250-L1	LAY	1	Gl(76) + Plg(11) + Opx(2) + Amph(13) + Mt(2)	1,75	70/30	8,6
850-250-L0.9	LAY	0,89	Gl(64) + Plg(27) + Opx(8) + Mt(1)	0,62	64/36	#7,7
850-250-L0.8	LAY	0,81	Gl(57) + Plg(32) + Opx(9) + Mt(1)	0,26	65/35	5,7
Run 7, 299 MPa, 900 °C, ~ΔNNO +1, 190 h						
900-300 -R1	ROS	1	Gl(90) + Opx(7) + Mt(3)	2,66		*9,5
900-300 -R0,8	ROS	0,82	Gl(71) + Plg(19) + Opx(7) + Mt(3)	2,2	70/30	*6,7
900-300 -L1	LAY	1	Gl(90) + Amph(6) + Mt(4)	4,39		*8,9
900-300 -L0,8	LAY	0,8	Gl(70) + Plg(20) + Opx(8) + Mag(2)	1,22	69/31	*6,2
Run 8, 150 MPa, 800 °C, ~ΔNNO +2, 120 h						
800-150-SAV1	SAL	1	Gl + Plg + Amph + Mt (+Opx?)		50/50	
800-150-BAY1	GB	1	Gl + Plg (+Opx?)		50/50	

Table IV.3: Experimental conditions and results *XH_2Oin= initial $XH_2O/(XH_2O+XCO_2)$; phase proportion calculated using mass balance calculation (Gl: glass; Plg: plagioclase; Opx: orthopyroxene; Amph: amphibole; Mg: titanomagnetite; Ilm: ilmenite). ΣR^2= mean square deviation resulting from mass balance calculations. Gl/cryst (vol%)= glass to crystal proportion determined by image analysis. H_2O_{melt} (wt%)= Water content in the melt determined by the EPM by-difference method, with * denoting H_2O content estimation from other charges at the same pressure and XH_2Oin and # denoting H2O content estimation from other charges of the same run.*

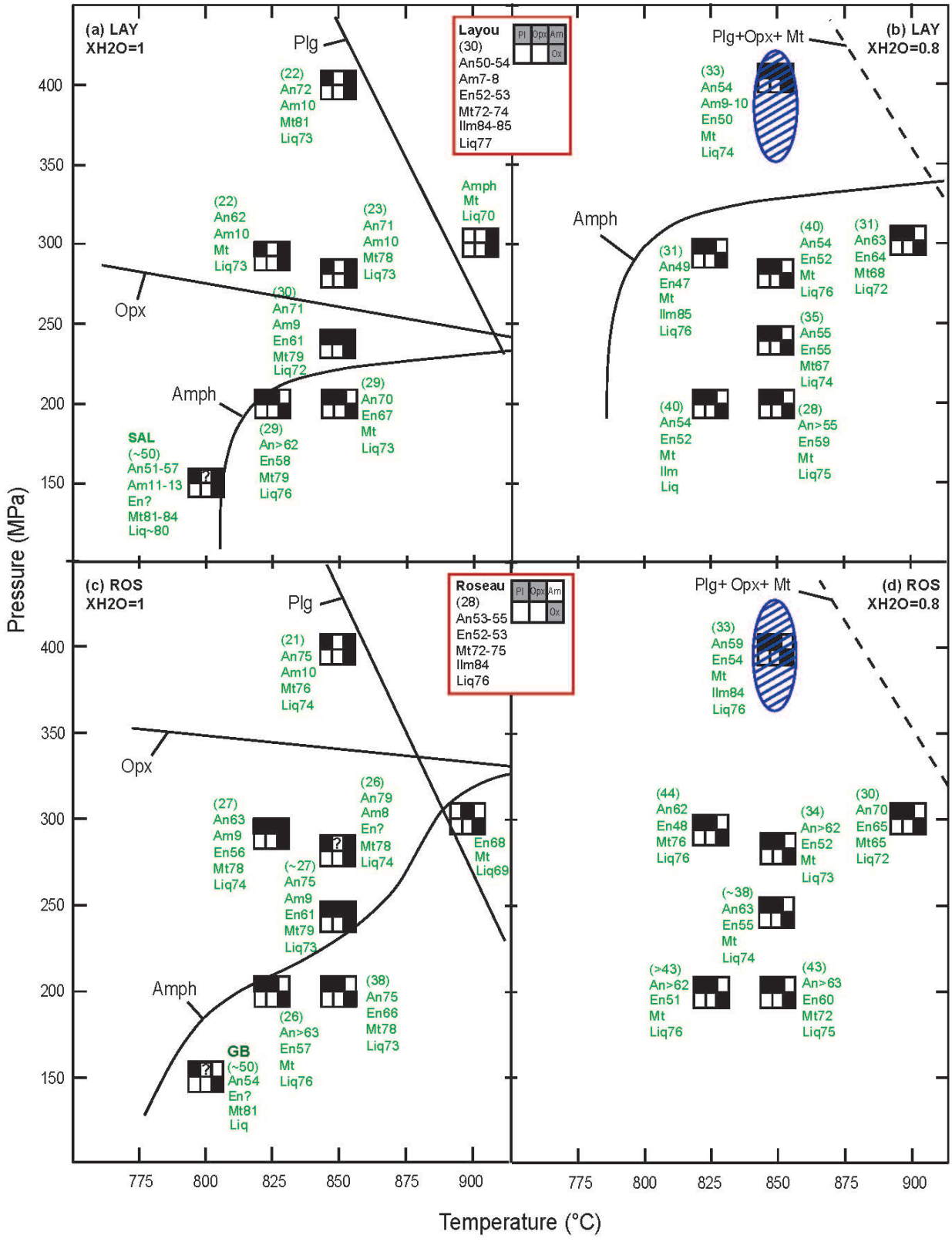

Figure IV.4: Phase relations for the Layou (a and b) and Roseau (c and d) dacites *for H_2O-saturated (a and c) and undersaturated (b and d) conditions. All experiments are performed at ~ΔNNO +1. The central red box gives the natural phase assemblage: total crystallinity (in brackets; ±5 wt%), phase assemblage in the six squares, and a listing of the phase compositions). Phase abbreviations as in Table IV.2. For each run, black filled squares represent the experimental phase assemblage, with volume proportions given in brackets and phase composition listed in green. Question marks for non-determined. The continuous lines-curves delimit the phase stability fields (dashed line for unconstrained). The blue shaded areas correspond to the P-T conditions for which the natural and the experimental phase assemblage and proportions are similar.*

IV. 6.2.2. Phase proportions

The phase proportions determined by mass balance using the major-element compositions of the experimental glasses and crystals are reported in Table IV.3. Where the composition of some phases was not available, we have used the composition of the same mineral in the charge performed at the closest conditions. Total crystallinity ranges from ~10 wt% in the H2O-saturated and high T (900 °C) charges to ~50 wt% in the H_2O-undersaturated, low T (800 °C) and low P (150 MPa) charges, and may differ by less than 12% from the values calculated by image analysis.

IV.6.2.3. Phase compositions

The compositions of the experimental crystals and glasses are reported in Tables IV.4 to IV.8 and in Figures IV.5 to IV.9.Oxydes (titanomagnetites and ilmenites) present small size, generally <5 µm, making EMP analysis often impossible.

Composition of experimental titanomagnetite in H_2O-saturated charges covers two different ranges: Mt_{78} to Mt_{80} in LAY and Mt_{76} to Mt_{77} in ROS (Table IV.7 and Fig.IV.5). In the run at 150 MPa and 800 °C, the titanomagnetites of SAL and GB have higher Mt content of Mt_{81} and Mt_{83}. In H_2O-undersaturated charges the composition ranges from Mt_{65} to Mt_{70} for both ROS and LAY. Ti (atoms p.f.u.) ranges from 0.16-0.22 for H_2O-saturated charges to 0.27-0.32 for H_2O-undersaturated ones. Two ilmenites have been analysed in LAY and ROS charges showing compositions of Ilm_{84-85} (runs 850-4-R0.8 and 825-2-L0.8).

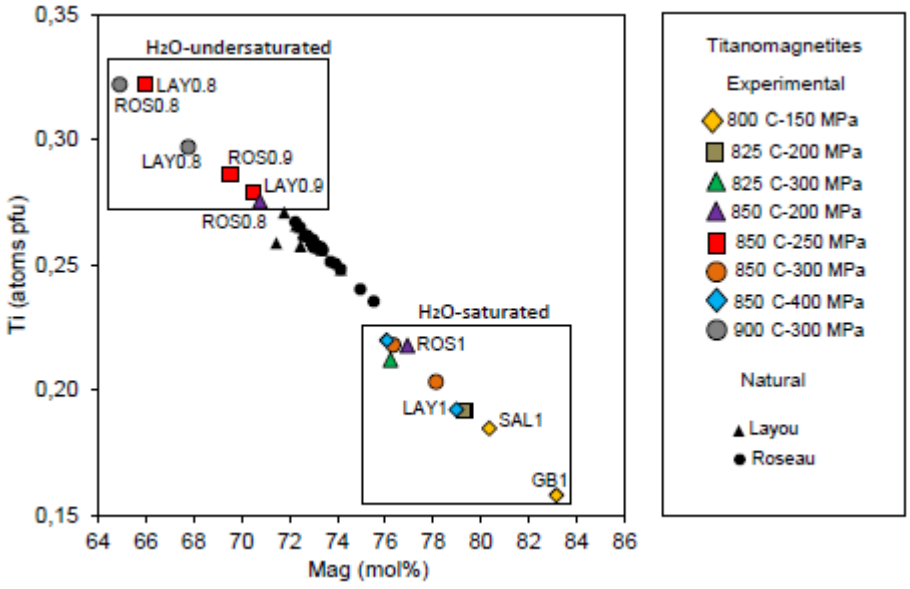

Figure IV.5: Natural and experimental titanomagnetite compositions. *Ti (atoms pfu) vs Mag (mol%), as calculated following Sauerzapf et al. (2008). Data labels correspond to the starting glass composition (LAY, ROS, SAL, GB, as in Table IV.3) with XH_2Oin (1, 0.9 or 0.8).*

Plagioclase crystals present usually thin lath shapes and sizes <10 µm, which made them difficult to analyse, especially for H_2O-undersaturated conditions. Plagioclase compositions (Table IV.5 and Figure IV.6) cover a wide range from ~An_{79} for H_2O-saturated and high-T conditions to An_{49} for H_2O-undersaturated and low-T conditions, confirming previous conclusions of the strong influence of H_2O content and T on plagioclase composition (e.g. Martel et al., 1998).

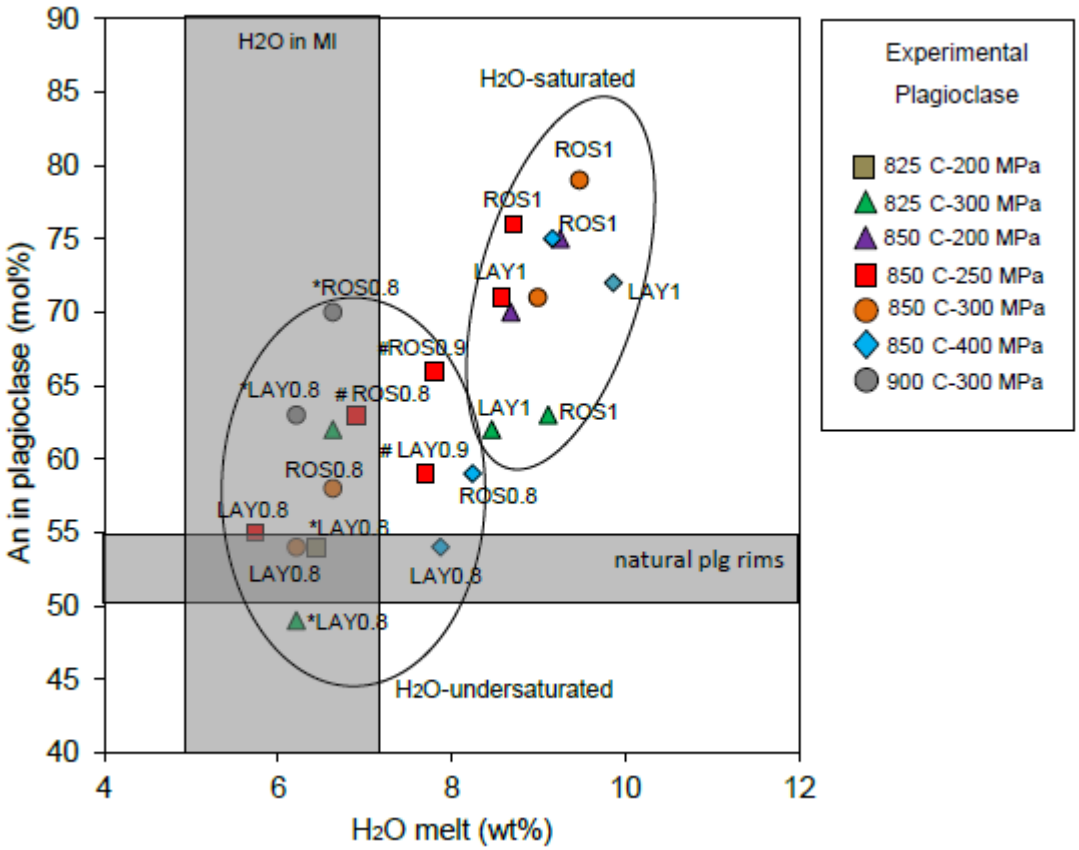

Figure IV.6: Natural and experimental plagioclase compositions. *Composition of experimental plagioclase is presented as the Anortite content (An in mol%) of the plagioclase as a function of the H_2O content (wt%) of the residual glass. For comparison, the An content of the natural plagioclase rims and the H_2O content (wt%) measured in melt inclusions (MI; both plagioclase- and orthopyroxene-hosted; from Balcone-Boissard et al., in prep.) are represented by the horizontal and vertical grey shaded boxes, respectively. Data labels as in Fig. IV.5, * indicating charges for which the H_2O content has been estimated from that of another charge performed at comparable pressure and XH_2Oin and # denoting charges for which the the H_2O content has been estimated from other charge of the same run.*

Ferromagnesian crystals (orthopyroxenes and amphiboles) have euhedral shapes and relatively large sizes (~40 to 60 µm).

Amphiboles in both LAY and ROS show 8-12 wt% Al_2O_3, ~10 wt% CaO, 11-16 wt% FeO, and 12-15 wt% MgO. After the classification of Leake et al. (1997), they are magnesiohornblendes at 850 °C - 400 MPa (with Mg# ranging from 0.55 to 0.69) and ferri-magnesiohornblendes (with higher Mg# of 0.62- 0.70) in all the other charges (Table IV.6 and Fig. IV.7).

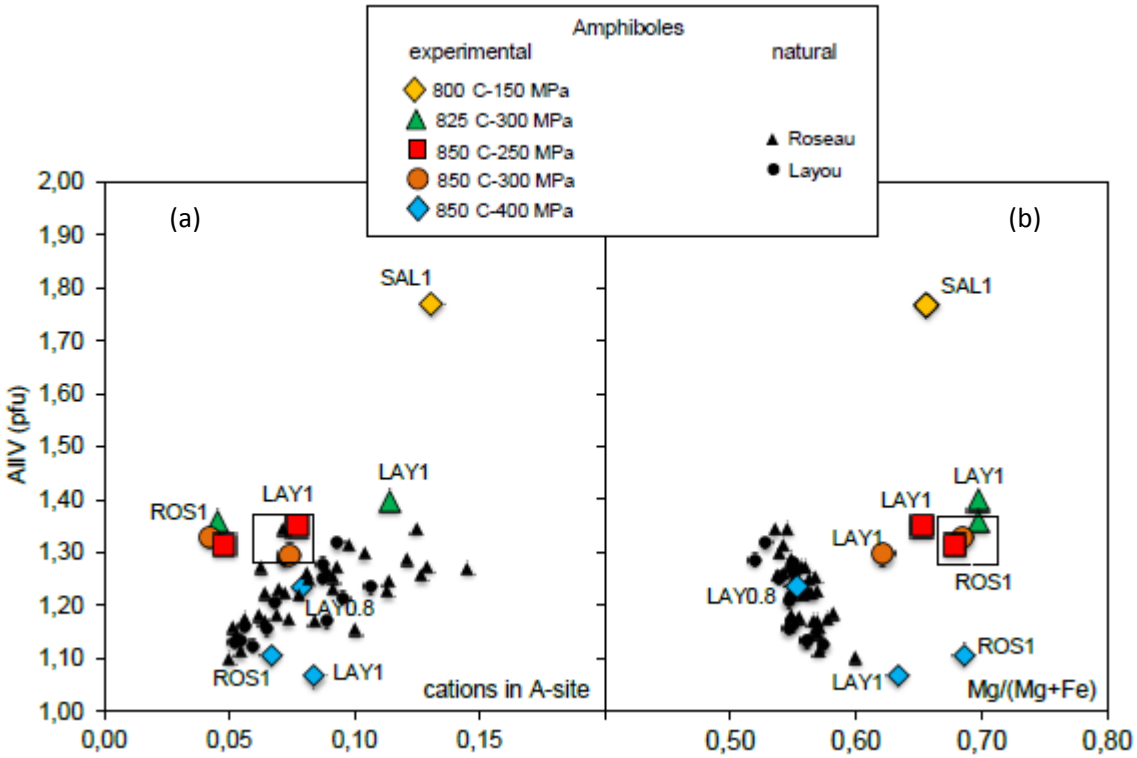

Figure IV.7 *:* ***Natural and experimental amphibole composition.*** *Compositions are calculated after Leake et al. (1997). (a) Al^{IV} vs number of cations in the A-site; (b) Al^{IV} vs Mg# =Mg/(Mg+Fe_{TOT}). Data labels as in Figure IV.5.*

The experimental orthopyroxenes show a wide compositional range from En_{67} in the H_2O-saturated charges at 850 °C and 200 MPa to En_{47} in the H_2O-undersaturated ones at 825 °C and 300 MPa (Table IV.4 and Fig. IV.8). Orthopyroxene is known to be mostly dependent on fO_2 (e.g. Martel et al., 1998), but since we kept fO_2 constant in our experiments, the compositional differences are attributed to changes in the P-T-H_2O conditions. For instance, a T increase from 825 to 850 °C at constant P of 200 MPa (H_2O-saturated) produces an increase in En content from ~En_{57} to ~En_{67} for both LAY and ROS (Fig. IV.4. and Fig. IV.8b). At P of 300 MPa and XH_2Oin = 0.8, a T increase from 825 to 850 and 900 °C produces orthopyroxene compositions varying from ~En_{48}, En_{52} and ~En_{65} for ROS and LAY (Fig.IV.4).

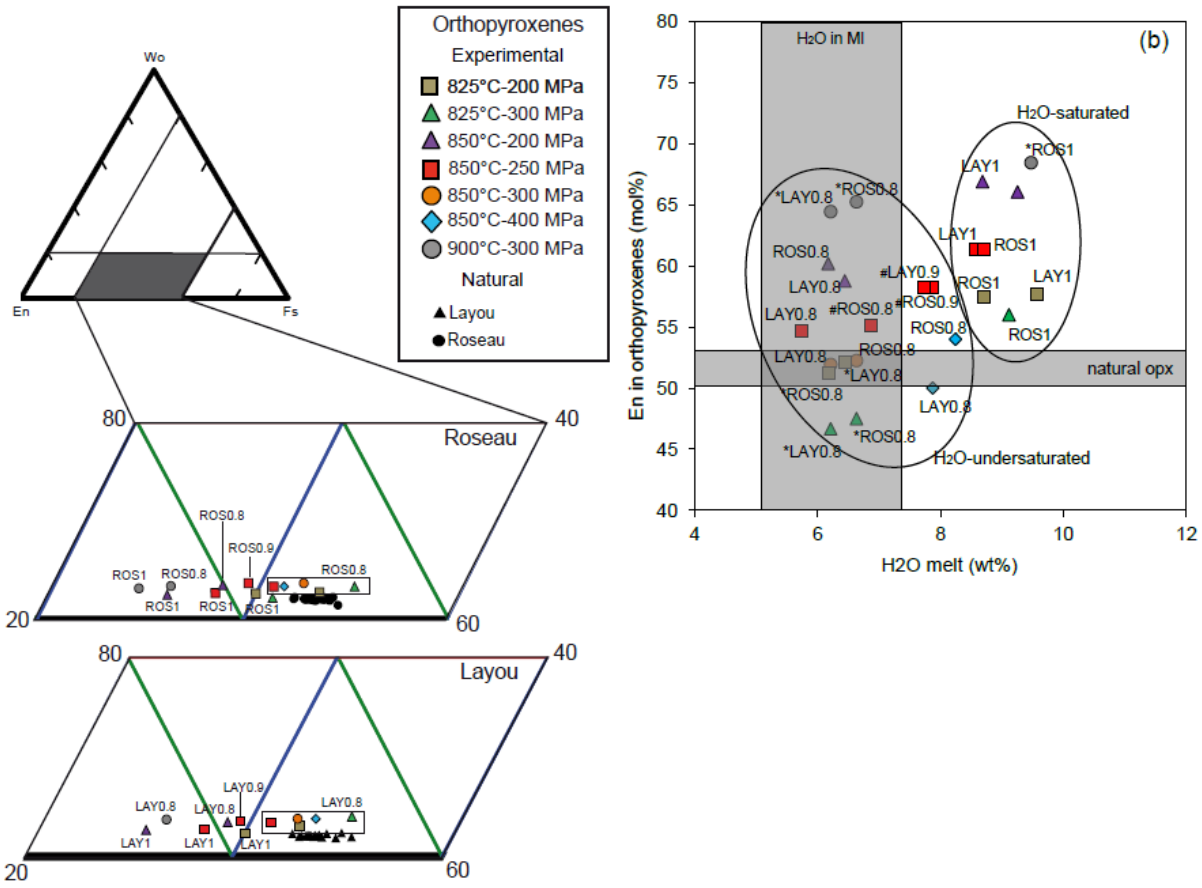

Figure IV.8: Natural and experimental orthopyroxene composition. *a) Orthopyroxene composition in the En-Fe-Wo diagram, with enlargement for ROS (upper diagram) and LAY (lower diagram); b) melt H_2O content (wt%) of the residual glass vs En (mol%) of the orthopyroxene. For comparison, the En content of the natural orthopyroxenes (80% unzoned, Solaro et al., in prep) and the H_2O content (wt%) measured in melt inclusions (MI; both plagioclase- and orthopyroxene-hosted; from Balcone-Boissard et al., in prep.) are represented by the horizontal and vertical grey shaded boxes, respectively. Data labels as in Fig. IV.6 with * indicating charges for which the H_2O content has been estimated from another charge performed at comparable pressure and XH_2Oin and # denoting charges for which the the H_2O content has been estimated from other charge of the same run.*

The experimental residual glasses are dacitic to rhyolitic in all charges, with 69 to 77 wt% SiO_2, 13 to 18 wt% Al_2O_3, 2-4 wt% CaO and 1 to 3 wt% K_2O (Table IV.8 and Figure IV.9). The H_2O content of the experimental residual glasses ranges from 5.7 wt% at 200 MPa to 9.9 wt% at 400 MPa.

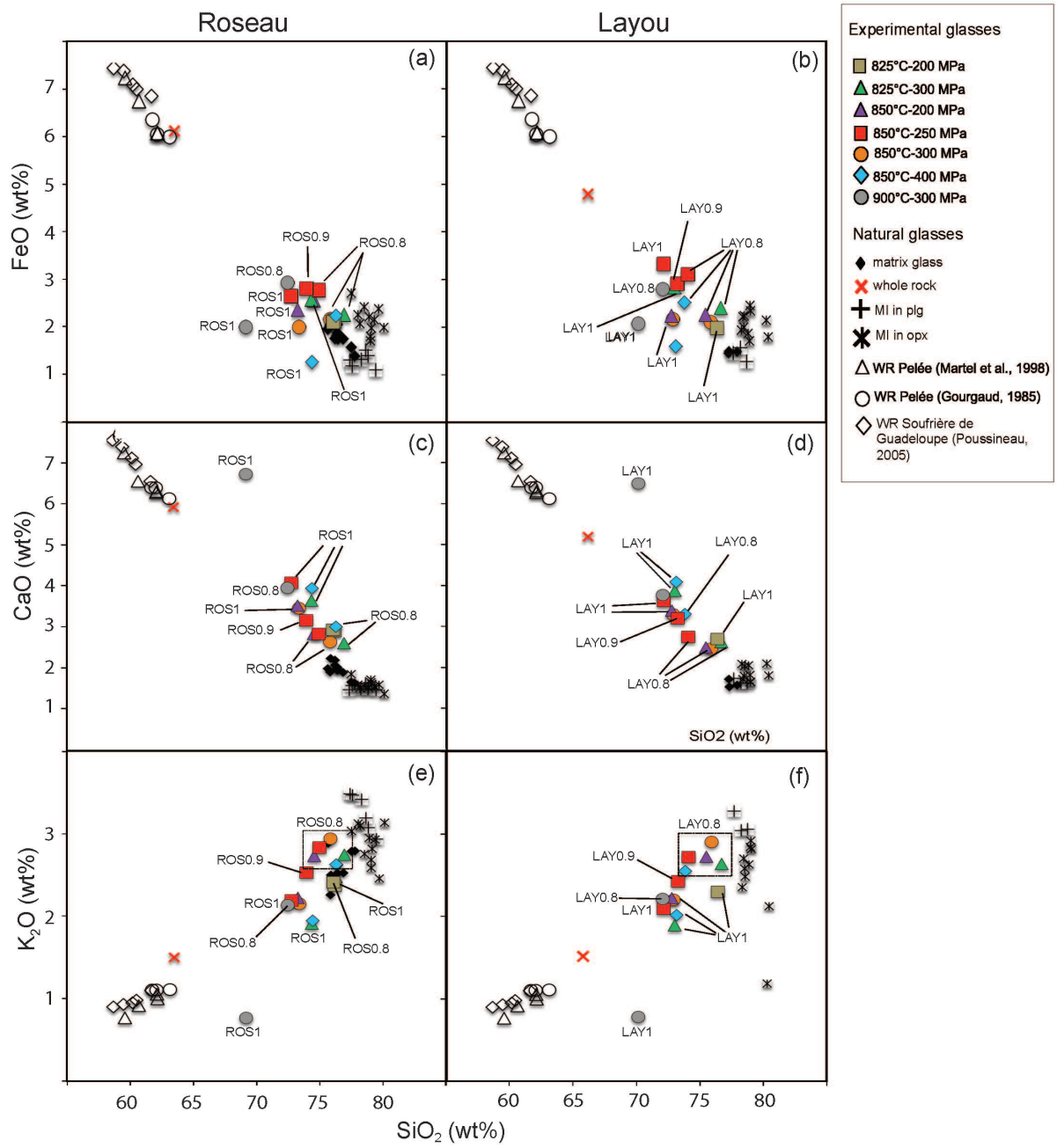

Figure IV.9 : Natural and experimental glass composition *of Roseau (left) and Layou samples (right), as a function of SiO2 (wt%) vs FeO (a, b),CaO (c, d), and K_2O (e, f)). The coloured symboles are the experimental residual glasses. For comparison, the natural matrix glasses and the melt inclusions are shown. The natural whole rock compositions are also presented, together with those of Montagne Pelée, Martinique (Martel et al., 1998;Gourgaud, 1985) and La Soufrière, Guadeloupe (Poussineau, 2005).*

Table IV.4

Run	n	SiO2		TiO2		Al2O3		Cr2O3		FeO		MnO		MgO		CaO		Na2O		K2O		Total	En	Fs	Wo
850-300-R0.8	9	50,33	*0,43*	0,24	*0,04*	1,59	*0,17*	0,00	*0,00*	27,36	*0,32*	0,85	*0,04*	17,41	*0,33*	1,71	*0,20*	0,02	*0,02*	0,02	*0,02*	99,52	52	44	4
850-300-L0.8	5	50,30	*0,39*	0,26	*0,05*	1,51	*0,17*	0,00	*0,00*	27,58	*0,25*	0,93	*0,07*	17,25	*0,30*	1,74	*0,30*	0,03	*0,02*	0,03	*0,02*	99,63	52	44	4
850-200-R1	4	51,92	*0,36*	0,13	*0,05*	1,98	*0,59*	0,00	*0,00*	20,78	*0,43*	0,97	*0,06*	22,63	*0,34*	1,20	*0,20*	0,02	*0,01*	0,02	*0,02*	99,64	66	31	3
850-200-R0.8	5	51,41	*0,53*	0,25	*0,04*	1,50	*0,22*	0,00	*0,00*	23,13	*0,15*	0,88	*0,08*	20,45	*0,26*	1,65	*0,16*	0,03	*0,02*	0,03	*0,03*	99,33	60	36	3
850-200-L1	2	51,68	*0,27*	0,17	*0,12*	1,88	*0,33*	0,00	*0,00*	20,96	*0,04*	1,18	*0,08*	22,76	*0,02*	1,25	*0,18*	0,02	*0,02*	0,01	*0,01*	99,92	67	30	3
850-200-L0.8	4	51,09	*0,14*	0,18	*0,03*	1,60	*0,17*	0,00	*0,00*	24,17	*0,38*	0,94	*0,02*	19,82	*0,17*	1,61	*0,13*	0,02	*0,02*	0,03	*0,00*	99,46	59	38	3
825-300-R1	1	49,70		0,15		2,64		0,00		25,63		0,98		18,41		1,01		0,00		0,00		98,51	56	42	2
825-300-R0.8	2	50,20	*0,48*	0,32	*0,25*	1,70	*0,33*	0,01	*0,02*	28,70	*0,69*	0,72	*0,05*	15,83	*0,39*	1,55	*0,05*	0,01	*0,02*	0,03	*0,03*	99,08	48	49	3
825-300-L0.8	7	50,02	*0,46*	0,22	*0,07*	1,62	*0,23*	0,02	*0,01*	28,99	*0,15*	0,82	*0,08*	15,46	*0,10*	1,84	*0,33*	0,01	*0,01*	0,02	*0,02*	99,02	47	49	4
825-200-R1	6	51,74	*0,57*	0,20	*0,04*	1,83	*0,47*	0,02	*0,02*	23,65	*0,42*	1,01	*0,08*	19,61	*0,19*	1,25	*0,14*	0,03	*0,01*	0,01	*0,01*	99,35	57	40	3
825-200-R0.8	3	51,41	*1,05*	0,16	*0,05*	1,66	*0,11*	0,01	*0,02*	26,65	*0,13*	0,84	*0,08*	17,42	*0,08*	1,31	*0,10*	0,01	*0,02*	0,01	*0,02*	99,49	51	46	3
825-200-L1	8	51,48	*0,37*	0,18	*0,07*	2,09	*0,28*	0,01	*0,02*	23,52	*0,28*	1,24	*0,11*	19,54	*0,30*	1,08	*0,12*	0,01	*0,02*	0,02	*0,02*	99,16	58	40	2
825-200-L0.8	5	51,56	*0,31*	0,19	*0,07*	1,30	*0,05*	0,02	*0,02*	26,18	*0,31*	0,92	*0,04*	17,78	*0,34*	1,45	*0,12*	0,01	*0,01*	0,02	*0,01*	99,42	52	45	3
850-400-R0.8	1	50,10		0,12		2,31		0,06		25,63		0,84		18,03		1,55		0,00		0,00		98,64	54	42	4
850-400-L0.8	4	50,14	*0,20*	0,21	*0,06*	1,91	*0,29*	0,00	*0,00*	28,29	*1,37*	0,99	*0,07*	16,59	*0,12*	1,73	*0,24*	0,04	*0,03*	0,02	*0,02*	99,92	50	46	4
850-250-R1	4	51,09	*0,64*	0,19	*0,06*	2,22	*0,78*	0,00	*0,00*	24,48	*0,23*	0,88	*0,07*	20,72	*0,10*	1,27	*0,23*	0,03	*0,02*	0,00	*0,01*	100,88	61	36	3
850-250-R0.9	6	51,46	*0,49*	0,24	*0,07*	1,92	*0,23*	0,00	*0,00*	25,14	*0,33*	0,80	*0,07*	19,59	*0,43*	1,75	*0,06*	0,04	*0,04*	0,04	*0,05*	100,98	58	39	4
850-250-R0.8	7	50,56	*0,41*	0,27	*0,04*	1,55	*0,18*	0,00	*0,00*	27,57	*0,31*	0,86	*0,08*	18,52	*0,28*	1,56	*0,19*	0,02	*0,02*	0,01	*0,01*	100,92	55	41	3
850-250-L1	2	51,52	*0,21*	0,11	*0,03*	1,99	*0,23*	0,00	*0,00*	24,54	*0,42*	1,03	*0,00*	20,80	*0,04*	1,29	*0,08*	0,03	*0,00*	0,03	*0,03*	101,33	61	36	3
850-250-L0.9	6	51,31	*0,40*	0,21	*0,05*	1,71	*0,10*	0,00	*0,00*	25,92	*0,57*	0,93	*0,09*	19,50	*0,32*	1,66	*0,29*	0,02	*0,01*	0,02	*0,02*	101,28	58	39	4
850-250-L0.8	6	51,22	*0,34*	0,20	*0,04*	1,37	*0,41*	0,00	*0,00*	27,63	*0,35*	0,91	*0,05*	18,52	*0,21*	1,59	*0,14*	0,02	*0,02*	0,01	*0,01*	101,47	55	42	3
900-300-R1	8	52,58	*0,49*	0,20	*0,04*	2,43	*0,46*	0,00	*0,00*	18,46	*0,31*	0,53	*0,07*	23,98	*0,46*	1,54	*0,20*	0,01	*0,01*	0,01	*0,02*	100,00	68	28	3
900-300-R0,8	5	51,97	*0,29*	0,23	*0,07*	2,68	*0,36*	0,00	*0,00*	19,62	*0,77*	0,79	*0,21*	22,46	*0,46*	1,63	*0,17*	0,02	*0,03*	0,03	*0,02*	99,00	65	31	3
900-300-L0,8	5	52,02	*0,64*	0,17	*0,01*	2,49	*0,22*	0,00	*0,00*	20,25	*2,01*	0,77	*0,19*	22,15	*1,43*	1,77	*0,24*	0,05	*0,02*	0,04	*0,01*	100,00	64	32	4

Table IV.4: Composition of the experimental orthopyroxenes. *All oxides and total are given in wt%. Numbers in italic give the statistical error on the preceding value. En, Fs and Wo are the mole % of Enstatite, Ferrosillite and Wollastonite respectively.*

Table IV.5

Run	n	SiO2		TiO2		Al2O3		FeO		MnO		MgO		CaO		Na2O		K2O		P2O5		Total	Or%	Ab%	An%
850-300-R1	4	48,26	*0,58*	0,04	*0,03*	32,39	*0,93*	0,67	*0,02*	0,02	*0,02*	0,00	*0,00*	15,76	*0,60*	2,21	*0,13*	0,13	*0,09*	0,23	*0,03*	100	1	20	79
850-300-L1	2	50,91	*0,00*	0,01	*0,00*	30,68	*0,68*	0,67	*0,03*	0,07	*0,02*	0,00	*0,00*	13,90	*0,23*	3,07	*0,00*	0,19	*0,04*	0,19	*0,03*	100	1	28	71
850-300-L0.8	1	56,05		0,06		26,75		1,24		0,04		0,25		10,34		4,60		0,43		0,14		100	3	43	54
850-200-R1	3	49,50	*0,60*	0,02	*0,02*	31,97	*0,82*	0,91	*0,03*	0,04	*0,02*	0,00	*0,00*	15,11	*0,62*	2,64	*0,17*	0,14	*0,04*	0,21	*0,02*	101	1	24	75
850-200-R0.8	1	57,43		0,22		21,90		1,10		0,05		0,20		8,45		2,94		0,88		0,19		93	7	36	57
850-200-L1	2	50,51	*0,53*	0,09	*0,08*	31,14	*0,07*	1,00	*0,34*	0,02	*0,02*	0,00	*0,00*	14,10	*0,12*	3,28	*0,04*	0,15	*0,02*	0,23	*0,01*	101	1	29	70
825-300-R1	2	52,94	*0,55*	0,01	*0,01*	29,85	*0,34*	0,54	*0,10*	0,01	*0,01*	0,05	*0,02*	12,75	*0,58*	4,08	*0,28*	0,12	*0,01*	0,04	*0,02*	100	1	36	63
825-300-R0.8	1	54,37		0,08		27,06		1,82		0,02		0,37		11,80		3,73		0,34		0,04		100	2	36	62
825-300-L1	8	52,82	*0,65*	0,03	*0,04*	29,60	*0,54*	0,62	*0,19*	0,02	*0,03*	0,03	*0,02*	12,66	*0,49*	4,18	*0,26*	0,12	*0,02*	0,04	*0,02*	100	1	37	62
825-200-L0.8	1	55,03		0,11		26,61		1,61		0,07		0,33		10,47		4,69		0,31		0,09		99	2	44	54
850-400-R1	3	50,64	*1,28*	0,10	*0,05*	30,41	*1,04*	0,94	*0,30*	0,04	*0,04*	0,12	*0,16*	14,20	*0,82*	2,29	*0,14*	0,27	*0,04*	0,15	*0,04*	99	2	22	76
850-400-R0.8	3	54,18	*0,29*	0,11	*0,01*	27,35	*1,04*	1,69	*0,56*	-0,01	*0,05*	0,05	*0,02*	11,19	*0,60*	3,99	*0,26*	0,37	*0,03*	0,09	*0,06*	99	2	38	59
850-400-L1	2	50,70	*0,77*	0,03	*0,03*	30,91	*1,11*	0,95	*0,35*	0,08	*0,03*	-0,03	*0,01*	14,19	*0,72*	2,84	*0,15*	0,22	*0,02*	0,29	*0,09*	100	2	27	71
850-400-L0.8	2	54,54	*0,02*	0,11	*0,00*	26,78	*0,05*	2,51	*0,20*	0,05	*0,04*	0,24	*0,10*	10,37	*0,03*	4,70	*0,28*	0,36	*0,08*	0,13	*0,00*	100	2	44	54
850-250-R1	4	49,44	*1,13*	0,03	*0,06*	31,04	*0,79*	0,96	*0,10*	-0,01	*0,02*	-0,01	*0,01*	14,81	*0,80*	2,59	*0,25*	0,20	*0,03*	0,20	*0,02*	99	1	24	75
850-250-R0.9	4	54,91	*3,37*	0,13	*0,07*	26,64	*2,25*	1,59	*0,63*	0,02	*0,02*	0,09	*0,07*	11,45	*1,35*	3,10	*0,46*	0,51	*0,28*	0,16	*0,03*	99	4	32	65
850-250-R0.8	2	53,92	*1,79*	0,05	*0,07*	27,91	*0,85*	1,70	*0,01*	0,02	*0,05*	0,11	*0,04*	12,01	*0,71*	3,70	*0,28*	0,38	*0,12*	0,17	*0,00*	100	2	35	63
850-250-L1	2	50,44	*0,02*	0,02	*0,02*	31,12	*0,74*	0,77	*0,03*	0,05	*0,01*	-0,04	*0,06*	14,28	*0,37*	3,14	*0,13*	0,14	*0,01*	0,16	*0,02*	100	1	28	71
850-250-L0.9	2	53,20	*1,72*	0,10	*0,09*	27,23	*1,04*	2,24	*0,68*	0,02	*0,02*	0,17	*0,12*	11,31	*0,71*	4,08	*0,30*	0,29	*0,14*	0,17	*0,03*	99	2	39	59
850-250--L0.8	2	55,38	*0,21*	0,09	*0,04*	26,83	*0,77*	1,80	*0,91*	0,04	*0,02*	0,10	*0,03*	10,49	*0,15*	4,59	*0,22*	0,34	*0,16*	0,14	*0,04*	100	2	43	55
800-150-Sal1	3	54,61	*0,54*	0,03	*0,02*	27,91	*1,02*	0,61	*0,02*	0,003	*0,01*	0,05	*0,02*	10,9	*0,7*	4,99	*0,32*	0,25	*0,07*			100	1	44	54
800-150-GB1	1	53,58		0,3		25,95		4,06		0,05		0,62		10,14		4,65		0,29				100	2	45	54
900-300-R0,8	2	52,42	*0,46*	0,10	*0,01*	29,57	*0,08*	1,12	*0,04*	0,05	*0,14*	0,08	*0,00*	13,24	*0,25*	2,91	*0,28*	0,35	*0,03*	0,03	*0,00*	100	2	28	70
900-300-L0,8	2	54,32	*0,68*	0,06	*0,00*	28,85	*0,76*	0,86	*0,14*	-0,02	*0,06*	0,08	*0,04*	11,91	*0,82*	3,67	*0,63*	0,25	*0,02*	0,06	*0,00*	100	2	35	63

Table IV.5: Composition of the experimental plagioclases. *All oxides and total are given in wt%. Numbers in italic give the statistical error on the preceding value. Or, Ab and An are the mole % of Orthoclase, Albite and Anorthite respectively.*

Table IV.6

Run	n	SiO2		TiO2		Al2O3		FeO		MnO		MgO		CaO		Na2O		K2O		Total	Mg#
850-300-R1	6	46,93	*1,07*	1,11	*0,25*	8,52	*0,67*	12,49	*1,64*	0,56	*0,12*	15,23	*1,15*	10,55	*0,32*	1,08	*0,20*	0,23	*0,03*	96,71	0,68
850-300-L1	4	46,37	*1,22*	0,98	*0,19*	10,08	*0,56*	13,81	*1,39*	0,48	*0,07*	12,72	*0,64*	10,20	*0,91*	1,38	*0,02*	0,40	*0,08*	96,43	0,62
825-300-R1	5	46,17	*0,95*	0,93	*0,15*	9,56	*0,66*	11,57	*2,38*	0,35	*0,09*	14,95	*3,16*	10,17	*1,12*	1,19	*0,13*	0,25	*0,06*	95,28	0,70
825-300-L1	6	46,13	*0,57*	0,85	*0,26*	10,07	*1,00*	11,55	*1,58*	0,33	*0,04*	14,93	*1,48*	10,89	*0,71*	1,39	*0,15*	0,32	*0,06*	96,65	0,70
850-400-R1	2	47,76	*0,90*	0,97	*0,10*	10,18	*1,53*	10,93	*1,64*	0,52	*0,06*	13,40	*1,06*	10,35	*0,60*	1,08	*0,02*	0,36	*0,11*	95,75	0,69
850-400-L1	4	48,73	*1,87*	0,88	*0,15*	10,28	*0,51*	12,94	*0,70*	0,41	*0,03*	12,54	*1,09*	10,06	*0,75*	1,26	*0,05*	0,46	*0,12*	97,56	0,63
850-400-L0.8	5	47,64	*0,94*	1,44	*0,16*	9,66	*0,43*	16,63	*0,32*	0,38	*0,07*	11,53	*1,27*	9,60	*0,31*	1,42	*0,08*	0,44	*0,12*	98,73	0,55
850-250-R1	1	47,59		1,06		9,53		12,53		0,37		14,84		10,43		1,34		0,27		97,97	0,68
850-250-L1	8	46,87	*1,10*	1,16	*0,12*	9,75	*0,66*	13,31	*0,47*	0,38	*0,05*	14,04	*0,79*	10,63	*0,41*	1,48	*0,04*	0,30	*0,07*	97,92	0,65
800-150-Sal1	3	43,25	*1,64*	1,01	*0,39*	12,20	*1,16*	12,92	*0,53*	0,51	*0,01*	13,82	*2,15*	10,95	*0,58*	1,33	*0,13*	0,37	*0,15*	96,36	0,66

Table IV.6: Composition of the experimental amphiboles. *All oxides and total are given in wt%. Numbers in italic give the statistical error on the preceding value. Mg# = $MgO/(MgO+FeO_{tot})$*

Table IV.7

Run	n	SiO2		TiO2		Al2O3		Cr2O3	FeO		MnO		MgO		CaO		Na2O		K2O		P2O5		Total	Usp	Mag
850-300-R1	4	0,36	*0,15*	7,67	*0,17*	3,57	*0,08*	0,00	80,11	*0,30*	0,47	*0,04*	1,41	*0,02*	0,16	*0,04*	0,03	*0,02*	0,05	*0,01*	0,04	*0,03*	93,90	22	78
850-300-L1	3	0,42	*0,18*	7,14	*0,35*	3,21	*0,11*	0,00	81,19	*0,60*	0,52	*0,05*	1,21	*0,05*	0,14	*0,03*	0,01	*0,01*	0,04	*0,01*	0,01	*0,01*	93,90	22	78
850-200-R1	2	0,31	*0,06*	7,56	*0,47*	2,52	*0,01*	0,00	79,96	*0,44*	0,48	*0,00*	1,65	*0,03*	0,20	*0,04*	0,01	*0,01*	0,04	*0,02*	0,01	*0,01*	92,76	22	78
850-200-R0.8	1	0,17		9,54		2,59		0,00	78,05		0,47		1,53		0,16		0,00		0,02		0,00		92,64	28	72
825-300-R1	1	1,30		6,73		4,40		6,13	70,68		0,31		1,34		0,29		0,02		0,08		0,00		91,34	22	78
825-200-L1	1	2,77		6,07		2,97		0,00	73,28		0,45		1,11		0,13		0,14		0,10		0,02		87,14	21	79
850-400-R1	3	0,61	*0,22*	8,06	*0,24*	3,84	*0,08*	0,00	83,75	*0,14*	0,39	*0,06*	1,22	*0,11*	0,23	*0,01*	0,03	*0,03*	0,05	*0,01*	-0,18	*0,03*	98,00	24	76
850-400-L1	3	1,29	*1,86*	6,81	*0,73*	3,93	*0,46*	0,00	81,36	*3,23*	0,42	*0,03*	1,27	*0,17*	0,17	*0,04*	0,07	*0,07*	0,09	*0,11*	-0,19	*0,03*	95,23	19	81
850-250-R0.9	3	0,45	*0,36*	10,10	*0,47*	2,73	*0,16*	0,00	79,47	*0,86*	0,36	*0,04*	1,36	*0,04*	0,18	*0,04*	0,03	*0,07*	0,04	*0,00*	-0,17	*0,05*	94,55	31	69
850-250-L1	3	0,46	*0,18*	7,01	*0,12*	3,23	*0,22*	0,00	84,68	*0,70*	0,42	*0,08*	1,48	*0,04*	0,13	*0,06*	0,01	*0,05*	0,04	*0,00*	-0,17	*0,06*	97,32	21	79
850-250-L0.9	1	0,25		10,14		2,59		0,00	82,33		0,51		1,39		0,17		0,01		0,03		-0,18		97,24	29	71
850-250-L0.8	2	0,85	*0,27*	11,51	*0,54*	2,53	*0,04*	0,00	79,75	*0,19*	0,52	*0,01*	1,29	*0,02*	0,22	*0,08*	0,00	*0,01*	0,05	*0,01*	-0,16	*0,01*	96,56	33	67
800-150-Sal1	1	1,67		5,4		2,76		0,00	81,02		0,47		1,15		0,24		0,05		0,07		0		92,82	84	16
800-150-GB1	1	3,21		6,36		2,69		0,00	80,40		0,69		1,34		0,40		0,04		0,06		0		95,19	81	19
900-300-R0,8	1	0,32		10,83		3,56		0,00	72,35		0,47		1,81		0,15		0,01		0,00		-0,04		89,46	35	65
900-300-L0,8	1	0,19		9,99		3,39		0,00	73,78		0,17		1,71		0,08		-0,01		0,05		0,00		89,33	32	68
																								Ilm	Hem
850-400-R0.8	1	1,05		43,64		0,59		0,00	51,28		0,47		1,76		0,27		0,07		0,08		-0,12		99,09	84	16
825-200-L0.8	1	0,63		42,00		0,29		0,00	47,55		0,66		1,50		0,13		0,11		0,05		0,00		92,91	85	15

Table IV.7: Composition of the experimental Fe-Ti oxides. *All oxides and total are given in wt%. Numbers in italic give the statistical error on the preceding value. Usp and Mag represent the Ulvospinel and the Magnetite molar % on calculated after the formulation of Sauerzapf et al. (2008)*

Table IV.8

Run	n	SiO_2		TiO_2		Al_2O_3		FeO		MnO		MgO		CaO		Na_2O		K_2O		P_2O_5		Mg#	Na_2O+K_2O
850-300-R1	8	73,36	*0,54*	0,26	*0,07*	16,06	*0,17*	2,00	*0,22*	0,09	*0,05*	0,33	*0,06*	3,45	*0,12*	2,01	*0,23*	2,15	*0,08*	0,20	*0,03*	0,14	4,17
850-300-R0.8	8	75,84	*0,33*	0,23	*0,07*	13,33	*0,16*	2,16	*0,09*	0,10	*0,06*	0,30	*0,06*	2,63	*0,09*	2,32	*0,20*	2,95	*0,10*	0,07	*0,04*	0,12	5,26
850-300-L1	14	72,93	*0,66*	0,22	*0,09*	15,94	*0,24*	2,16	*0,43*	0,12	*0,06*	0,37	*0,17*	3,30	*0,11*	2,47	*0,22*	2,20	*0,10*	0,16	*0,03*	0,15	4,67
850-300-L0.8	6	75,91	*0,17*	0,24	*0,05*	13,21	*0,13*	2,10	*0,17*	0,08	*0,05*	0,31	*0,05*	2,45	*0,11*	2,63	*0,12*	2,91	*0,07*	0,08	*0,05*	0,13	5,54
850-200-R1	5	73,27	*0,65*	0,35	*0,07*	14,72	*0,21*	2,35	*0,34*	0,09	*0,08*	0,52	*0,15*	3,52	*0,11*	2,68	*0,27*	2,22	*0,09*	0,13	*0,08*	0,18	4,90
850-200-R0.8	6	74,56	*0,38*	0,44	*0,04*	13,49	*0,21*	2,55	*0,07*	0,11	*0,06*	0,49	*0,04*	2,82	*0,02*	2,64	*0,26*	2,73	*0,10*	0,11	*0,04*	0,16	5,37
850-200-L1	6	72,81	*0,43*	0,25	*0,09*	15,48	*0,20*	2,24	*0,31*	0,13	*0,05*	0,50	*0,14*	3,38	*0,16*	2,77	*0,25*	2,22	*0,08*	0,17	*0,05*	0,18	4,99
850-200-L0.8	5	75,50	*0,27*	0,29	*0,08*	13,17	*0,17*	2,26	*0,12*	0,08	*0,07*	0,48	*0,10*	2,48	*0,10*	2,89	*0,18*	2,72	*0,08*	0,08	*0,04*	0,18	5,61
825-300-R1	6	74,34	*0,24*	0,18	*0,08*	15,55	*0,15*	2,58	*0,22*	0,12	*0,03*	0,41	*0,11*	3,65	*0,14*	1,02	*0,14*	1,91	*0,08*	0,14	*0,06*	0,14	2,93
825-300-R0.8	2	76,94	*0,22*	0,25	*0,00*	12,95	*0,01*	2,26	*0,10*	0,07	*0,02*	0,29	*0,01*	2,59	*0,10*	1,70	*0,05*	2,75	*0,08*	0,06	*0,02*	0,11	4,45
825-300-L1	5	73,03	*0,22*	0,25	*0,04*	15,71	*0,18*	2,84	*0,24*	0,13	*0,02*	0,49	*0,13*	3,87	*0,13*	1,54	*0,14*	1,89	*0,05*	0,14	*0,04*	0,15	3,44
825-300-L0.8	4	76,71	*0,28*	0,26	*0,06*	13,43	*0,17*	2,40	*0,07*	0,12	*0,02*	0,28	*0,02*	2,62	*0,13*	1,36	*0,37*	2,64	*0,04*	0,04	*0,06*	0,10	3,99
825-200-R1	3	76,18	*0,61*	0,32	*0,10*	14,08	*0,01*	2,12	*0,50*	0,06	*0,05*	0,48	*0,23*	2,90	*0,01*	1,31	*0,08*	2,37	*0,02*	0,09	*0,03*	0,18	3,68
825-200-R0.8	3	76,04	*0,69*	0,32	*0,05*	14,12	*0,09*	2,10	*0,17*	0,05	*0,04*	0,38	*0,06*	2,93	*0,10*	1,47	*0,23*	2,41	*0,15*	0,08	*0,03*	0,15	3,88
825-200-L1	6	76,41	*0,20*	0,20	*0,07*	14,37	*0,20*	1,98	*0,13*	0,11	*0,04*	0,38	*0,06*	2,69	*0,14*	1,34	*0,16*	2,30	*0,11*	0,08	*0,03*	0,16	3,64
850-400-R1	4	74,41	*0,37*	0,23	*0,05*	16,64	*0,28*	1,26	*0,09*	0,12	*0,05*	0,14	*0,03*	3,94	*0,05*	1,05	*0,13*	1,94	*0,09*	0,15	*0,03*	0,10	2,99
850-400-R0.8	3	76,29	*0,53*	0,28	*0,04*	13,90	*0,10*	2,23	*0,15*	0,02	*0,01*	0,30	*0,06*	3,00	*0,10*	1,17	*0,18*	2,63	*0,10*	0,09	*0,02*	0,12	3,80
850-400-L1	6	73,15	*0,51*	0,23	*0,06*	16,99	*0,15*	1,59	*0,43*	0,10	*0,05*	0,14	*0,06*	4,09	*0,08*	1,55	*0,16*	2,02	*0,05*	0,14	*0,02*	0,08	3,57
850-400-L0.8	5	73,84	*0,44*	0,25	*0,09*	14,60	*0,39*	2,52	*0,12*	0,09	*0,03*	0,38	*0,04*	3,30	*0,20*	2,39	*0,21*	2,55	*0,07*	0,09	*0,04*	0,13	5,14
850-250-R1	4	72,75	*0,66*	0,36	*0,07*	15,36	*0,09*	2,65	*0,41*	0,09	*0,04*	0,30	*0,10*	4,08	*0,15*	2,05	*0,19*	2,19	*0,07*	0,17	*0,04*	0,10	4,24
850-250-R0.9	7	73,95	*0,52*	0,38	*0,07*	14,24	*0,41*	2,81	*0,26*	0,07	*0,02*	0,43	*0,13*	3,16	*0,05*	2,31	*0,26*	2,53	*0,04*	0,12	*0,04*	0,13	4,85
850-250-R0.8	5	74,94	*0,21*	0,34	*0,03*	13,36	*0,10*	2,77	*0,04*	0,06	*0,02*	0,43	*0,09*	2,83	*0,07*	2,36	*0,25*	2,84	*0,09*	0,08	*0,07*	0,14	5,20
850-250-L1	3	72,17	*0,80*	0,27	*0,05*	15,58	*0,11*	3,32	*0,54*	0,10	*0,01*	0,65	*0,31*	3,62	*0,36*	2,06	*0,54*	2,09	*0,12*	0,13	*0,05*	0,16	4,16
850-250-L0.9	6	73,27	*0,39*	0,34	*0,04*	14,62	*0,13*	2,91	*0,15*	0,09	*0,05*	0,45	*0,06*	3,20	*0,06*	2,52	*0,42*	2,43	*0,09*	0,17	*0,04*	0,13	4,95
850-250-L0.8	5	74,10	*0,58*	0,36	*0,06*	13,59	*0,30*	3,11	*0,48*	0,07	*0,06*	0,46	*0,20*	2,74	*0,06*	2,74	*0,08*	2,72	*0,05*	0,12	*0,04*	0,13	5,46
800-150-Sal1	3	78,09	*0,34*	0,18	*0,01*	12,79	*0,12*	1,62	*0,05*	0,08	*0,05*	0,42	*0,14*	2,02	*0,11*	2,00	*0,16*	2,79	*0,04*			0,21	4,79

Table IV.8

Run	n	SiO_2		TiO_2		Al_2O_3		FeO		MnO		MgO		CaO		Na_2O		K_2O		P_2O_5		Mg#	Na_2O+K_2O
900-300-R1	4	69,16	*0,63*	0,32	*0,01*	18,08	*0,31*	2,00	*0,20*	0,07	*0,02*	0,11	*0,04*	6,72	*0,24*	2,62	*0,15*	0,76	*0,08*	0,16	*0,07*	0,05	3,38
900-300-R0,8	5	72,47	*0,17*	0,56	*0,02*	15,41	*0,17*	2,92	*0,21*	0,11	*0,08*	0,33	*0,06*	3,95	*0,12*	1,99	*0,30*	2,14	*0,09*	0,11	*0,06*	0,10	4,13
900-300-L1	5	70,16	*0,51*	0,34	*0,02*	17,17	*0,09*	2,07	*0,22*	0,23	*0,13*	0,06	*0,02*	6,50	*0,32*	2,57	*0,16*	0,78	*0,08*	0,12	*0,01*	0,03	3,35
900-300-L0,8	7	72,09	*0,89*	0,48	*0,05*	15,66	*0,54*	2,79	*0,68*	0,05	*0,12*	0,35	*0,19*	3,77	*0,17*	2,43	*0,45*	2,21	*0,15*	0,15	*0,09*	0,11	4,65

Table IV.8: Composition of the experimental residual glasses. *All oxides and total are given in wt%. Numbers in italic give the statistical error on the preceding value; Mg# = MgO/(MgO+FeO).*

IV.7. Discussion

IV.7.1. Pre-eruptive storage conditions of Dominica ignimbritic eruptions.

Layou

The natural phase assemblage of Layou consists of plagioclase, amphibole, orthopyroxene, Fe-Ti oxides, which is experimentally reproduced in H_2O-under-saturated conditions for pressure > 300 MPa (for which amphibole is stable; Fig. IV.4b) and in H_2O-saturated conditions at P < 300 MPa (for which orthopyroxene is stable) and T < 850 °C for which amphibole is stable (Fig. IV.4c). For H_2O-saturated conditions, low P-T conditions of 800 °C and 150 MPa can be ruled out because of the total crystal proportion (~50 wt%) notably higher than in the natural products (~30 wt%). Conditions of 250 MPa and 850 °C reproduce the required crystallinity of ~30 wt%, but both An content in plagioclase and En content in orthopyroxene are much higher than for the natural crystals. These different mismatches between experimental and natural phase assemblage, proportions, and compositions, compromise H_2O-saturated conditions as acceptable ones for the Dominica ignimbritic magmas. For H_2O-undersaturated conditions, the run performed at 850 °C and 400 MPa reproduces the natural phase assemblage, proportions, and very close compositions. Indeed, this experiment shows crystallization of plagioclase (25 wt%, An_{54}), amphibole (7 wt%, 9-10 wt% Al_2O_3), orthopyroxene (5 wt%, En50), and titanomagnetite (<1 wt%; not analysed). The experimental amphibole have slightly higher Al_2O_3 content (9-10 wt%) than the natural ones (7-8 wt%), but comparable Al_{IV}, cations in A-site, and Mg-number values (Fig.IV.5). Although the experimental residual glass (74 SiO_2 wt%) lacks 3 wt% SiO_2 with respect to the natural ones, the other similarities validate conditions close to 850 °C, 400 MPa (equivalent to ~16 km, considering a rock density of 2.45 g/cm^3), ΔNNO +1, and 7-8 wt% H_2O dissolved in the melt (XH2Oin ~ 0.8; in agreement with the H2O contents measured in Layou melt inclusions) for the magma storage prior to Layou eruption.

Roseau

The natural phase assemblage of Roseau consists of plagioclase, orthopyroxene and Fe-Ti oxides, experimentally reproduced in H_2O-undersaturated conditions for the whole P-T range investigated in this study (200-400 MPa, 825-900°C; Fig. IV.4d) and in H_2O-saturated conditions for pressures ≤ 200 MPa (Fig. IV.4c). The H_2O-saturated conditions can be ruled out as representing the natural ones, because of either too high crystallinities (e.g. 800 °C - 150 MPa and 850 °C –200 MPa) or mismatching crystal compositions (e.g. An >63, En >57). For H_2O-undersaturated conditions, experiments at P < 300 MPa and 300 MPa and 825 °C

have crystallinities higher than the ~30 wt% measured in the natural pumice. At 300 MPa, the An content in plagioclase (between An_{62} and An_{70}) is much higher than the An_{53-55} natural crystal rims. At 400 MPa and 850 °C, crystallinity and compositions of the orthopyroxene, Fe-Ti oxides, and residual glass are comparable within error to the natural ones. Plagioclase is however a bit too calcic (An_{59}), which could be reduced to compositions closer to An_{53-55} by slightly reducing either T or melt H_2O content. Decreasing T would however increase crystallinity, which would not fit the natural samples anymore. Reducing H_2O content from ~8 wt% (measured in the run at 400 MPa, 850 °C, XH2Oin ~ 0.8; Table IV.3) would indeed better fit the ~7.0 wt% H_2O measured in Roseau melt inclusions.

Therefore, in absence of additional runs to refine plagioclase composition, we here consider 400 MPa (about 16 km in depth), 850 °C, ΔNNO +1, and ~7 wt% H_2O in the melt, as possible pre-eruptive conditions for the Roseau andesitic magmas.

Grand Fond, Grande Savane and Grand Bay

In terms of source origin of the ignimbrite deposits, the recent results of Boudon et al. (in prep) (chapter III) suggest that Grande Savane and Layou ignimbrites would both be linked to the eruptive centre of Morne Diablotins, thus rejecting the previous idea of Roobol and Smith (2004) and Lindsay et al. (2005) that Layou ignimbrites originate from Morne Trois Pitons-Micotrin, In terms of geochemistry, Grande Savane and Layou share comparable compositions in major elements (i.e. 65-66 wt% SiO_2, ~5 wt% Na_2O+K_2O; Table IV.1) and trace elements (see chapter III). The crystal phase assemblage of Layou and Grande Savane are similar, both exhibiting the presence of significant amount of amphibole (~5 %). Finally, phase compositions are also similar, possibly with orthopyroxenes slightly depleted in magnesium (En_{49-50} against En_{52-53}; Table IV.2). We do not have any data on melt H_2O content. Therefore, the pre-eruptive conditions determined for Layou magmas below Morne Diablotins may also be relevant for the small and younger eruption of Grande Savane, i.e. close to 850 °C, 400 MPa, ΔNNO +1, and ~7-8 wt% H_2O.

Grand Fond and Roseau ignimbrites have been recognized as the East- and West-side pyroclastic flows of a common eruptive centre: Morne Trois Pitons-Micotrin (chapter III this volume). The origin of Grand Bay ignimbrite is still debated, but may come from Wotten Waven or the Plays Pays complex. However, Grand Fond, Grand Bay, and Roseau show comparable compositions in major elements (i.e. 63-64 wt% SiO_2, ~4.5 wt% Na_2O+K_2O; Table IV.1), trace elements (chapter III this volume), crystal phase assemblage (no stable

amphibole), and phase compositions (Table IV.2). Therefore, the ROS starting material may be used as an analogue for Grand Fond and Grand Bay magmas, suggesting similar pre-eruptive conditions close to 850 °C, 400 MPa, ΔNNO +1, and ~6-7 wt% H_2O.

Accordingly, we propose here that the main Dominica ignimbrites tap two reservoirs, both located at ~16 km deep (400 MPa) and ~850 °C, with pre-eruptive H_2O content of 7-8 wt% for Morne Diablotins, favouring the crystallization of amphibole in Layou and Grande Savane magmas, and 6-7 wt% for Morne Trois Pitons-Micotrin, outside the amphibole stability field of Roseau, Grand Fond, and Grand Bay magmas. Both types of magma probably come from the same magma source, but at a stage slightly more differentiated for Layou with respect to Roseau.

Kopp et al. (2011) acquired seismic data across the volcanic arc North of Dominica (where the Tiburon Ridge subducts obliquely beneath the forearc) and, by a tomographic inversion, obtained a model of the crust beneath the arc, divided in three distinct layers: a three kilometer thick upper crust of volcanogenic sedimentary rocks and volcaniclastics, underlain by an intermediate to felsic middle crust and a plutonic mafic (gabbros) lower crust. Under Dominica, the middle-lower crust limit is placed at ~16 km, close to the reservoir depth deduced from our experimental study (FigIV.10a), implying that Dominica magmas could be preferentially stored at a structural level where the density contrast between the felsic and mafic components may favors storage and ponding of magma.

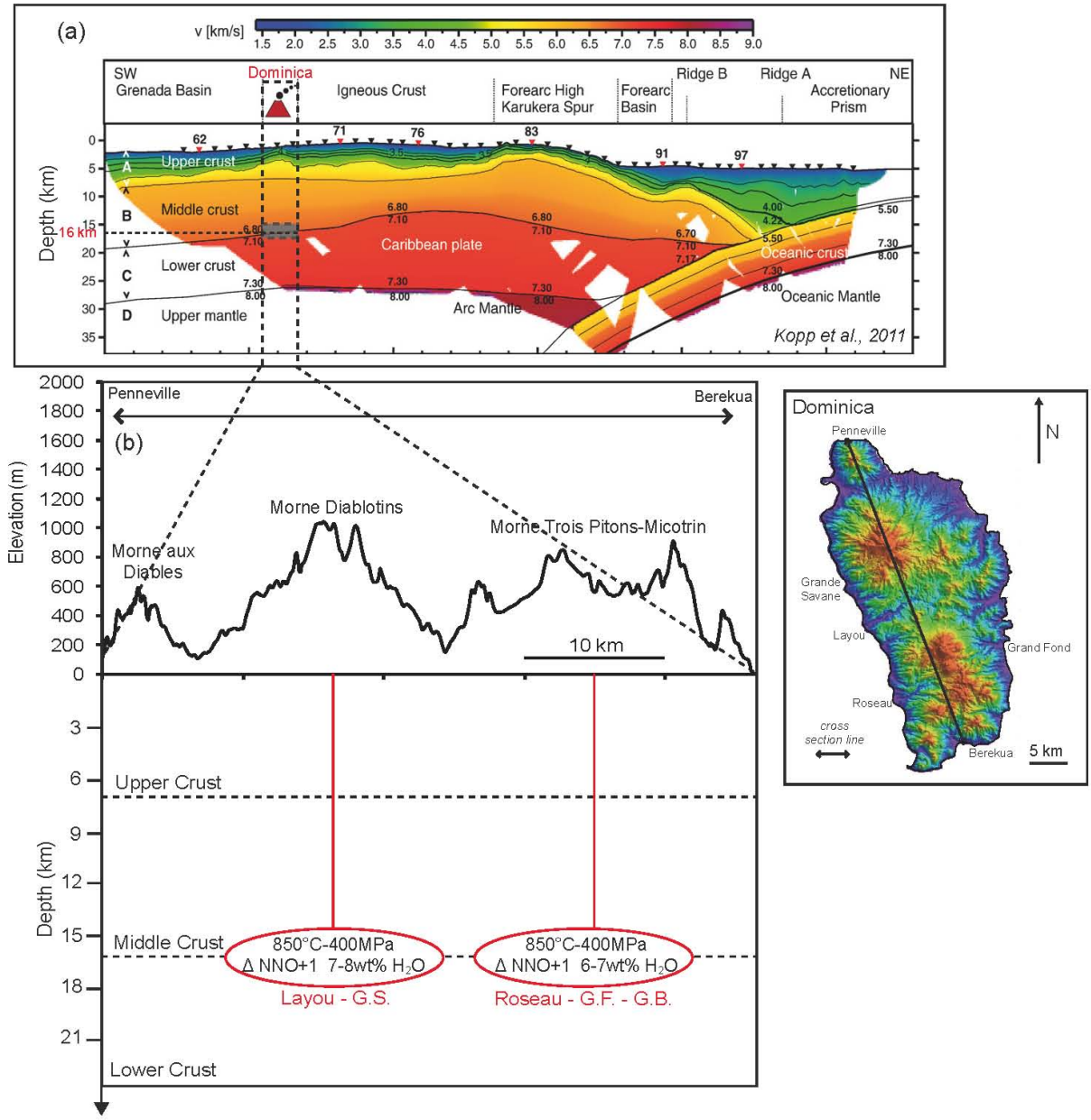

Figure IV.10: Schematic section of the crust along the Lesser Antilles Arc*. (a) Three dimensions velocity model of the crust and upper mantle along the Lesser Antilles arc (modified from Kopp et al., 2011). A: Upper crust of sediments and volcanoclastic rocks; B: Middle crust of felsic to intermediate compositions; C: Lower crust of gabbroic plutons; D: Upper Mantle. Below Dominica, the lower-middle crust discontinuity is located at ~16-18 km in depth, where the ignimbritic reservoirs have been experimentally located (grey box). (b) Detail of the structure of the crust below Dominica. The reported topographic profile corresponds to the cross-section line Penneville-Berekua indicated on the Dominica radar map on the right. The red ovals indicate the dacitic reservoirs with precised storage conditions. G.S.=Grande Savane; G.F.= Grand Fond; G.B.= Grand Bay.*

IV.7.2. Comparison with the magma storage conditions on the neighbouring islands of the arc

The neighbouring islands of the Lesser Antilles arc are characterized by a single active eruptive centre (at least during the recent period of activity), small-volume eruptions (< 1 km^3), and more frequent eruptions. The magma storage conditions for the recent eruptions on these islands have been determined experimentally via phase-equilibrium studies.

In Montserrat, the magma of the on-going eruption of Soufriere Hills has been found to be stored at 820-840 °C, low pressure of ~130 MPa (< 5 km deep), ~ΔNNO +1, and $4.3_{\pm 0.5}$ wt% H_2O in the melt (Barclay et al., 1998).

In Guadeloupe, the magma (~60 wt% SiO_2) from the 1350 AD sub-plinian eruption of La Soufrière suggests storage at 875-900°C, ~175 MPa, ~ΔNNO +0.5 to 1, and ~5.5 wt% H_2O in the melt (Poussineau, 2005 ; Pichavant et al., in prep.).

In Martinique, the historical eruptions of Mt Pelée, either plinian fallout or dome-forming eruptions, have been found to be fed by a magma (~61 wt% SiO_2) stored at 875-900°C, ~200 MPa (~6 km deep), ~ΔNNO + 0.4 to 0.8, and ~6 wt% H_2O in the melt(Martel et al., 1998).

These studies show that these andesitic small-volume eruptions were fed by magmas stored at comparable conditions, with temperatures of 850-900 °C, pressure of 175-200 MPa, redox conditions ~ΔNNO +1, and melt H2O contents close to H2O-saturation. In comparison, Dominica magmas constitute an anomaly in the sense of erupting (i) large magma volumes (>10 km^3 DRE/eruption; chapter III this volume), (ii) more evolved compositions (dacite against andesite), and (iii) magma that was stored at much deeper conditions (~16 km against 6-7 km), which also implies higher melt H_2O contents (7-8 wt% against < 6.5 wt%).

Although Kopp et al. (2011) suggest a middle-lower crust limit at ~16 km, previous seismic refraction studies suggested significant differences in the depth of the middle-lower crust limit from one island to another, with variations from 2 to 20 km (Boyton et al., 1979; Macdonald et al., 2000). Although we do not have conclusive evidence, it is possible that this structural limit at ~16 km below Dominica moves to only ~7-8 km below Martinique, Guadeloupe, and Montserrat. Such deep magma storage conditions could explain the absence of any evident caldera structure on the eruptive centres of the island (Geyer et al., 2006; Boudon et al., in prep-chapter III), in contrary to several other systems where voluminous ignimbritic eruptions are associated with a reservoir collapse after emptying and resultant caldera structures.

With regard to the difference in erupted magma volumes, the structure of the arc and the presence of different fault systems could be the cause of Dominica particularity. Firstly, as the Lesser Antilles arc is segmented, the local component of convergence normal to the front decreases away from a maximum (~35 km/Ma) in the central segment of the arc (Sykes et al., 1982; Wadge et al., 1986). Secondly, a complex system of faults cutting the Caribbean plate in different directions has been recognized by Feuillet et al. (2010). Two specific systems of active faults are identified: (i) NE-SW oriented normal-oblique faults creating trench parallel extension and arc-perpendicular half-grabens that disrupt the fore-arc reef platforms of Guadeloupe, Antigua-Barbuda and St. Martins - St. Barthelemy (Feuillet et al., 2002; 2004); (ii) a fault set arranged in a transtensional, right-stepping, *en echelon* array that follows the inner edge of the arc and accommodates a transtensional motion along the arc between Saba and Martinique. The Roseau Fault (Bazin et al., 2010; Feuillet et al., 2011a,b) is part of this second fault set.

The coupling of the segmentation of the arc structure and the change in subduction geometry (Wadge and Shepherd, 1984; Macdonald et al., 2000) with the observed system of faults (Feuillet et al., 2010) can potentially create a geodynamical context with a strong extensional component beneath Dominica, fostering the lateral expansion of reservoirs and the storage of larger magma volumes.

IV.8. Conclusions

The large ignimbritic eruptions observed on Dominica island raises two main questions: 1) how and where are these large magma volumes stored; 2) why is Dominica characterized by larger erupted volumes than the neighbouring islands of the arc.

Combining a petrological study of basal plinian deposits of the main eruptions in Dominica with phase-equilibrium experiments we show that the dacitic ignimbrites in Dominica were supplied by two main reservoirs that differ by their composition (bulk-rock, phase assemblage and composition) and volatile contents (~7-8 wt% H_2O for Layou and Grande Savane magmas, and ~6-7 wt% H_2O for Roseau, Grand Fond and Grand Bay magmas). Yet, both reservoirs are located at the same pressure of ~400 MPa (~16 km deep), temperature of ~850 °C, and fO_2 of ~ΔNNO +1. In contrast, the present eruptive centres in Martinique, Guadeloupe, and Montserrat have much shallower reservoirs ($\leq$ 200 MPa).

In the light of seismic crustal model across the Lesser Antilles arc and under Dominica (Kopp et al., 2011), we interpret the location of these reservoirs to be linked with the middle-lower crust boundary under Dominica. The larger volumes of erupted material in Dominica with

respect to the neighbouring islands may result from a geodynamic context with more extensive components (Feuillet et al., 2002, 2004, 2010) that may promote magma accumulation around Dominica. Dominica magmas are thus stored deeper in the middle-lower crust boundary than those of the neighbouring islands, in a geodynamical context that promote magma accumulation through extension components. The deep storage probably gives few opportunities for the magma to reach the surface, more time to differentiate to dacitic compositions, but large volumes when eventually erupted. In contrast, the shallower magma storage conditions below the neighbouring islands lead to more frequent eruptions, smaller volumes, and andesitic magmas.

Acknowledgement

We would like to thank Michel Fialin and Nicolas Rividi (service CAMPARIS) for assistance during microprobe analyses and Omar Boudouma (SEM, UPMC) for help during SEM imaging.

We thank Vincent Christmann who started the study during his master 2 thesis in 2012 (Orléans).

Supplementary Material

Table IV.S1: Fe-Ti oxide thermometry. *Results on temperature and oxygen fugacity obtained on two touching ilmenite-titanomagnetite pairs of Grand Fond eruption using the model of Ghiorso and Evans (2008).*

Grand Fond	Ros6-L1C2	Ros6-L1C2	Ros6-L2C6	Ros6-L2C6
	titanomag	ilmenite	titanomag	ilmenite
SiO2	0,22	0,18	0,28	0,04
TiO2	9,41	42,67	9,45	42,46
Al2O3	1,97	0,02	1,92	0,00
FeO	78,92	49,08	79,45	49,46
MnO	0,42	0,60	0,43	0,57
MgO	1,09	1,93	0,95	1,86
CaO	0,25	0,04	0,04	0,03
Na2O	0,01	0,02	0,01	0,00
K2O	0,01	0,01	0,02	0,01
P2O5	0,21	0,01	0,02	0,00
Cr2O3	0,03	0,01	0,02	0,03
Total	92,58	94,62	92,61	94,51
log (Mg/Mn)	0,662	0,752	0,586	0,756
Ghiorso and Evans (2008)				
T°C (Fe-Ti exchange)	856		860	
logfO_2 (relative to NNO)	0,63		0,65	

Table IV.S2: Amphibole thermobarometry. *Results on temperature, pressure and oxygen fugacity obtained using the model of Ridolfi and Renzulli (2012).*

	Sample	Specie	T (°C)	uncertanty (σest)	P (MPa)	uncertanty (Max error)	ΔNNO	logfO$_2$	uncertanty (σ_{est})
Layou	Lay-Amph-1	Mg-Hbl	783	22	119	13	1,0	-13,3	0,4
	Lay-Amph-2	Mg-Hbl	792	22	132	14	0,8	-13,2	0,4
	Lay-Amph-3	Mg-Hbl	777	22	109	12	1,0	-13,3	0,4
	Lay-Amph-4	Mg-Hbl	788	22	117	13	1,1	-13,0	0,4
	Lay-Amph-5	Mg-Hbl	801	22	142	35	0,8	-13,0	0,4
	Lay-Amph-6	Mg-Hbl	793	22	129	14	0,8	-13,2	0,4
	Lay-Amph-7	Mg-Hbl	776	22	114	13	0,9	-13,4	0,4
	Lay-Amph-8	Mg-Hbl	793	22	127	14	1,0	-13,0	0,4
	Lay-Amph-9	Mg-Hbl	798	22	132	15	1,0	-12,9	0,4
	Lay-Amph-10	Mg-Hbl	797	22	137	15	0,9	-13,0	0,4
	Lay-Amph-11	Mg-Hbl	776	22	98	11	1,3	-13,1	0,4
	Lay-Amph-12	Mg-Hbl	777	22	101	11	1,2	-13,1	0,4
	Lay-Amph-13	Mg-Hbl	779	22	105	12	1,1	-13,2	0,4
Roseau	Ros-Amph-1	Mg-Hbl	793	22	118	13	1,1	-12,9	0,4
	Ros-Amph-2	Mg-Hbl	774	22	101	11	1,3	-13,1	0,4
	Ros-Amph-3	Mg-Hbl	788	22	122	13	1,0	-13,1	0,4
	Ros-Amph-4	Mg-Hbl	797	22	127	14	0,9	-13,0	0,4
	Ros-Amph-5	Mg-Hbl	779	22	109	12	1,2	-13,1	0,4
	Ros-Amph-6	Mg-Hbl	784	22	108	12	1,2	-13,0	0,4
	Ros-Amph-7	Mg-Hbl	777	22	107	12	1,1	-13,2	0,4
	Ros-Amph-8	Mg-Hbl	781	22	108	12	1,3	-13,0	0,4
	Ros-Amph-9	Mg-Hbl	799	22	126	14	0,9	-12,9	0,4
	Ros-Amph-10	Mg-Hbl	798	22	128	14	1,0	-12,9	0,4
	Ros-Amph-11	Mg-Hbl	778	22	103	11	1,2	-13,1	0,4
	Ros-Amph-12	Mg-Hbl	781	22	105	12	1,2	-13,1	0,4
	Ros-Amph-13	Mg-Hbl	805	22	143	16	1,1	-12,6	0,4
	Ros-Amph-14	Mg-Hbl	786	22	113	12	1,2	-13,0	0,4
	Ros-Amph-15	Mg-Hbl	789	22	120	13	1,1	-12,9	0,4
	Ros-Amph-16	Mg-Hbl	794	22	123	14	0,9	-13,1	0,4
	Ros-Amph-17	Mg-Hbl	796	22	129	14	1,1	-12,9	0,4
	Ros-Amph-18	Mg-Hbl	795	22	120	13	1,1	-12,9	0,4

	Sample	Specie	T (°C)	uncertanty (σest)	P (MPa)	uncertanty (Max error)	ΔNNO	logfO$_2$	uncertanty (σ_{est})
	Ros-Amph-19	Mg-Hbl	774	22	100	11	1,4	-13,0	0,4
	Ros-Amph-20	Mg-Hbl	793	22	123	14	1,0	-13,0	0,4
	Ros-Amph-21	Mg-Hbl	794	22	121	13	1,1	-12,9	0,4
	Ros-Amph-22	Mg-Hbl	779	22	112	12	1,2	-13,1	0,4
	Ros-Amph-23	Mg-Hbl	789	22	118	13	1,1	-13,0	0,4
	Ros-Amph-24	Mg-Hbl	777	22	109	12	1,2	-13,2	0,4
	Ros-Amph-25	Mg-Hbl	799	22	126	14	1,0	-12,9	0,4
	Ros-Amph-26	Mg-Hbl	780	22	106	12	1,1	-13,2	0,4
	Ros-Amph-27	Mg-Hbl	797	22	130	14	0,9	-13,0	0,4
	Ros-Amph-28	Mg-Hbl	809	22	144	16	0,9	-12,7	0,4
	Ros-Amph-29	Mg-Hbl	787	22	116	13	1,1	-13,0	0,4
	Ros-Amph-30	Mg-Hbl	793	22	118	13	1,2	-12,8	0,4
	Ros-Amph-31	Mg-Hbl	793	22	130	14	0,9	-13,1	0,4

Table IV.S2(continued)

Table IV.S3: Orthopyroxene-melt thermometry. *Results on temperature estimation obtained on orthopyroxenes-melt inclusions couples using the parameterization of Putirka (2008).*

	Layou		Roseau			Grand Fond					
melt inclusion	17-l3c2-MI1	16-l5c11-MI2	RP3-l2c9-MI1	RP4-l3c15-MI1	RP4-l8c11-MI2	Ros2-l2c1-MI5	Ros10-l3c4-MI2	Ros10-l4c10-MI1	Ros13-l2c13-MI2	Ros13-l1c10-MI2	Ros13-l3c1-MI3
SiO2	71,6659	69,7467	71,2219	70,1593	71,9132	70,3988	70,4153	70,2339	69,5024	67,0831	69,7378
TiO2	0,1443	0,1807	0,2184	0,2202	0,1961	0,1154	0,2599	0,1432	0,1508	0,2074	0,1358
Al2O3	11,4816	11,5653	11,4304	11,8847	10,9749	11,2155	12,1092	11,5585	11,1847	11,6662	11,2015
FeO	2,6723	3,0175	3,0615	3,2043	2,8135	3,1958	3,0242	3,2122	3,1838	3,5402	3,0985
MnO	0,0702	0,1649	0,1421	0,0647	0,1056	0,18	0,1055	0,0654	0,1402	0,0971	0,0438
MgO	0,3603	0,4388	0,6194	0,5872	0,5776	0,6449	0,4867	0,622	0,5801	0,9279	0,5966
CaO	1,4015	1,6262	1,6558	1,8611	1,3935	1,5384	1,6918	1,7481	1,7092	1,7515	1,6757
Na2O	1,8005	2,6407	2,6132	2,8893	2,8419	2,7483	2,7223	2,7839	2,7849	2,8268	2,7168
K2O	3,0347	2,7386	2,5395	2,3912	2,5856	2,9065	2,5948	2,587	2,3597	2,576	2,9435
P2O5	0,0499	-0,0663	-0,0237	0,0191	0,0736	0,0068	0,0341	0,0563	0,12	0,0201	-0,0075
Total	92,6814	92,0531	93,4788	93,2811	93,4754	92,9506	93,4438	93,0105	91,7157	90,6963	92,1425
Na2O+K2O	4,8352	5,3793	5,1527	5,2805	5,4275	5,6548	5,3171	5,3709	5,1446	5,4028	5,6603
hosting orthopyroxene											
En	0,485	0,494	0,525	0,512	0,520	0,522	0,530	0,530	0,520	0,570	0,513
Fs	0,497	0,485	0,451	0,469	0,462	0,457	0,449	0,448	0,458	0,408	0,467
Wo	0,018	0,021	0,024	0,019	0,018	0,021	0,021	0,022	0,022	0,022	0,020
Kd (Fe-Mg)	0,25	0,25	0,31	0,30	0,33	0,31	0,24	0,29	0,29	0,33	0,31
molar Fe/Mg opx	1,025	0,982	0,860	0,915	0,888	0,875	0,848	0,844	0,881	0,716	0,910
molar Fe/Mg liq	4,160	3,857	2,772	3,061	2,732	2,779	3,485	2,897	3,078	2,140	2,913
T°C (Putirka, 2008, eq.28b)	847	857	889	881	890	888	866	883	871	889	879
T°C (Putirka, 2008, eq.28a)	844	850	874	864	861	874	870	872	860	877	858
error (SSE)	26	26	26	26	26	26	26	26	26	26	26

CHAPTER V:

THE SECRET LIFE OF CRYSTALS,

A RECORD OF PRE-ERUPTIVE MAGMA STORAGE

Introduction

Les cristaux sont des témoins privilégiés de l'évolution des magmas avant une éruption. Leur composition dépend fortement des conditions de stockage du magma (température, pression, teneur en éléments volatils, fugacité d'oxygène). Tout changement entraîne une cristallisation aux bordures de composition différente, à l'origine de gradients de composition dans les cristaux. Plusieurs cristaux comme les olivines, les plagioclases, le quartz ou les orthopyroxènes présentent des zonations significatives attestant de changements des conditions pré-éruptives dans le système d'alimentation (Blundy et Shimizu, 1991; Ginibre et al., 2002a, b; 2004 et 2007, Tomiya et Takahashi, 2005; Humphreys et al., 2006; Ruprecht et Wörner, 2007; Wark et al., 2007). Ces changements peuvent être produits par un certain nombre de processus : les plus courants sont le mélange de magma, la décompression, le transfert de chaleur ou le gaz fluxing (Nelson et Montana, 1992; Murphy et al, 2000; Couch et al, 2001; Bachmann et Bergantz, 2003, 2006). **L'étude pétrologique fine de la composition des cristaux peut donc être utilisée pour déchiffrer la nature du/des processus pré-éruptif(s) affectant l'évolution du magma lors de son stockage dans la croûte.**

Dans ce chapitre, nous présentons les résultats obtenus sur les zonations des orthopyroxènes des trois éruptions de Layou, Roseau et Grand Fond, réalisés en combinant une approche de « Crystal System Analysis » avec une modélisation de l'interdiffusion Fe/Mg dans les orthopyroxènes. Les deux approches sont présentées sous la forme de deux parties séparées, mais complémentaires.

PARTIE I

La partie I présente les résultats détaillés sur la pétrologie des orthopyroxènes (cristaux et inclusions vitreuses) en suivant l'approche du « Crystal System Analysis ». Décrypter l'histoire individuelle des cristaux peut se révéler difficile; l'établissement de modèles de dynamique des systèmes d'alimentation en conditions pré-éruptives peut ainsi se révéler complexe. Par conséquent, une méthode permettant de traiter statistiquement un ensemble de données pétrologiques est nécessaire pour surmonter cette impasse. L'approche de la « Crystal System Analysis », présentée d'abord par Palm (2005), a été récemment appliquée par Kahl et al. (2011, 2013, 2015) sur les olivines de l'Etna sur la période éruptive entre 1991 et 2008. A

partir de l'enregistrement des variations de composition des cristaux, la méthode permet de définir les environnements magmatiques à l'équilibre avec ces compositions qui forment le système d'alimentation magmatique ainsi que leurs connexions. Ce travail permet d'établir un modèle dynamique du système d'alimentation des éruptions.

Nous avons appliqué cette approche à nos échantillons. Les textures et la composition des cristaux d'orthopyroxène ont été étudiées par des images BSE haute résolution et des analyses quantitatives le long de profils à la microsonde électronique (EPM).
Néanmoins, la « Crystal System Analysis » seule fournit peu d'informations sur la nature physique des environnements magmatiques. D'autres outils sont nécessaires pour déterminer quel paramètre a varié, provoquant ainsi l'apparition de différents environnements magmatiques (les perturbations dynamiques) et savoir si les environnements reconnus sont reliés spatialement ou non. Nous utilisons ici des analyses couplées orthopyroxene-inclusion vitreuse, des résultats de pétrologie expérimentale (voir le chapitre IV) et des observations de stratigraphie pour déterminer quel processus produit les différentes environnements reconnus dans nos échantillons.
Les résultats sur les orthopyroxènes et la composition des inclusions vitreuses, interprétés dans le sens de la « Crystal System Analysis », ont permis de présenter un premier modèle théorique de la structure pétrologique et dynamique des réservoirs alimentant les trois éruptions Layou, Roseau et Grand Fond.

PARTIE II

Une fois que la dynamique principale du système d'alimentation magmatique a été établie, la modélisation de l'interdiffusion Fe-Mg dans les orthopyroxènes permet de contraindre les échelles de temps de cette dynamique avant l'éruption. La zonation chimique créée dans les cristaux par le processus perturbateur dans le réservoir (réchauffement de la zone de stockage dans notre cas) tend à être lissée au cours du temps par la cinétique de diffusion, agissant pour rééquilibrer les gradients chimiques cristallins tant que les cristaux restent à haute température ($\geq$500°C). Lorsque des éruptions explosives se produisent, les cristaux sont trempés et amenés rapidement à basse température ; dans ce cas la diffusion n'agit plus. Le profil de diffusion dans chaque cristal est ainsi préservé et peut être utilisé pour déterminer le laps de temps entre le processus pré-éruptif perturbateur (chauffage dans notre cas) et l'éruption.

La partie II présente la méthode de modélisation de l'interdiffusion de Fe-Mg et les résultats obtenus sur les orthopyroxènes de la Dominique. Les échantillons et les cristaux sont exactement les mêmes que ceux de la partie I. La modélisation 1D de l'interdiffusion Fe-Mg a été réalisée parallèlement à l'axe b des cristaux en utilisant le coefficient de diffusion de Ganguly et Tazzoli (1994) sans tenir compte de l'effet de la fugacité d'oxygène (selon les résultats expérimentaux récents de Dohmen et al., 2016) et avec la méthode de modélisation d'Allan et al. (2013). Tous les profils sont modélisés à 850 (± 25)°C, d'après les résultats de pétrologie expérimentale (voir chapitre IV). La méthode donne des résultats d'échelles de temps satisfaisants de 3-10 ans avant les éruptions de Layou et Roseau, alors que pour Grand Fond, la forme des profils suggèrent l'action de processus autres que la diffusion pure qui, perturbant les profils de diffusion, empêchant d'effectuer une modélisation précise.
Compte tenu des échelles de temps courtes obtenues pour Layou et Roseau, comparables à celles obtenues sur d'autres grandes éruptions (Martin et al., 2008, Druitt et al, 2012, Matthews et al., 2012, Bouvet de Maisonneuve et al., 2015, Barker et al. , 2016), on peut supposer que les réservoirs de la Dominique montrent aussi des signes de remobilisation rapide de grands volumes de magma avant l'éruption. Ceci caractérise le système comme étant très dynamique, ce qui est important à prendre en compte dans la gestion du risque volcanique de l'île.

Un résumé final présente un modèle pétrologique incluant, la dynamique et l'évolution du système d'alimentation magmatique obtenu en combinant les résultats sur la pétrologie naturelle et expérimentale (chapitre IV), l'analyse en « Crystal System Analysis » des orthopyroxènes et la modélisation de la diffusion (chapitre V).

PART I:

CRYSTAL SYSTEM ANALYSIS

Structure and evolution of the magmatic plumbing system at the origin of silicic pumiceous eruptions at Dominica (Lesser Antilles Arc): a crystal system analysis approach.

Solaro C. [a]***, Boudon G.*** [a]***, Balcone-Boissard H.*** [b]***, Morgan D.J.*** [c]***, Martel C.*** [d]

[a] Institut de Physique du Globe de Paris, Sorbonne Paris Cité, Univ. Paris Diderot, CNRS, F-75005 Paris, (France) ; solaro@ipgp.fr

[b]Sorbonne Universités, UPMC Univ. Paris 06, CNRS, UMR 7193, ISTEP, F-75005, Paris, (France)

[c]School of Environmental Sciences, University of Leeds, Leeds (UK)

[d] Institut des Sciences de la Terre d'Orléans (ISTO), Orléans, (France).

Abstract

Modern volcanology studies have demonstrated that the crystal "cargo" of magmas and recorded zoning patterns can be used to unravel the dynamics of magmatic plumbing systems. Here we present a petrological study of three major pumiceous dacitic eruptions produced on Dominica (Lesser Antilles Arc) in the last 50ky: Layou (~51kyrs cal BP), Roseau (~33kyrs cal BP) and Grand Fond (~24kyrs cal BP). We perform textural and chemical analyses of orthopyroxenes and relative melt inclusions to use them with a systems analysis approach. This enables to decipher remobilization processes of crystals before each eruption, and to map the plumbing system evolution over time.

Textural analyses show that for each of the three eruptions about 80-85% of orthopyroxenes are unzoned, while about 15-20% exhibit normal, reverse and multiple zoning. Systems analysis of the zoned crystals reveals the presence of four different magmatic environments (ME): En_{46-51}(ME1), En_{52-53}(ME2), En_{54-58}(ME3) and En_{59-63}(ME4). During the eruptive history, the main magmatic environment, represented by the 80% of unzoned orthopyroxenes, moves from ME2 (for Layou and Roseau) to ME3 (for Grand Fond), indicating a shift of the system to less-evolved compositions. For all eruptions, a main crystal transfer pathway can be identified between ME2-ME3, describing a progressive sinking of crystals from the main environment En_{52-53}(ME2) to the less-evolved En_{54-58} (ME3), which receives crystals, and, by the Grand Fond eruption, becomes the volumetrically most significant magmatic environment. Occurrence of ME4 (En59-63) in the Roseau and Grand Fond eruptions further suggests a progression toward a less-evolved composition.

Composition of orthopyroxenes hosted melt inclusions, combined with stratigraphic and petrological considerations, suggest that ME3 and ME4 are caused by a pre-eruptive heating process.

In our model we propose that orthopyroxene crystals of ME2 (~80%, En_{52-53}) represent the main crystallized mush body in Layou and Roseau reservoir. Grand Fond shows a less evolved reservoir composition at En_{54-56}. The ME1 is considered as volumetrically less important wall-roof highly crystallized portions of main reservoirs, with lower En content. Finally this reservoir suffers from the intrusion of a less evolved magma that re-heats the system from below producing the predominant reverse zoning patterns in pyroxenes (ME3 and ME4: En_{54-56} and En_{58-63} rims).

Keywords: Dominica, orthopyroxenes, zoning patterns, crystal system analysis, magmatic environment

V.I.1. Introduction

Characterising magma storage regions in terms of their structural organization and their evolution is particularly important for hazard mitigation in volcanic areas of relevant human settlement. This becomes even more crucial for super-eruptions in which the large volume of erupted products (10 to 1000 km^3) can spread out on the form of pyroclastic density currents over long distances (10-100 km) or tephra dispersal, and have a significant impact on human society over long timescales (Chester et al., 2000; Cutter, 2003; Self, 2006; Cashmann and Giordano, 2008; Oppenheimer, 2011; Reide, 2016).

For these reasons magma storage regions have been studied from petrological, mechanical, thermal and geophysical (seismic, tomography, ground deformation) point of view. Mechanical and thermal considerations about formation and accumulation of large eruptible magma body (Annen and Sparks, 2002; Jellinek and DePaolo, 2003; Annen, 2009, 2011; Schöpa and Annen, 2013; Annen et al., 2014; de Silva and Gregg, 2014), combined with tomography and seismic analysis, brought a significant change in the scientific vision of storage regions. The "standard model" of a unique, large magma chamber filled with highly molten material has been replaced by a more realistic vision in which the storage region is constituted as a mush zone (Marsh, 1996; Bachmann and Bergantz, 2004, 2008) with multiple melt lenses (interconnected sills and dikes) or a single tabular storage region formed by stacking of smaller sheet intrusions (Annen et al., 2014). These regions made of crystals, interstitial melt and fluids can have various degrees of crystallinity and different melt compositions.

When different (coeval or asynchronous) melt lenses feed the same eruption, their interaction becomes an important parameter to be constrained in order to understand magma dynamics. The storage location, shape, size, longevity, composition of each melt lenses and the connections between them need to be characterized to precisely define the storage system structure and its dynamic prior to eruption. Interactions between melts in chemically open-systems (injection, convection, mixing or mingling, reheating from an underplating magma) has been recognized as a critical process to sustain eruptive activity of many volcanic centres and as an important eruption trigger (Nakamura et al., 1995; Murphy et al., 1998; Murphy et al., 2000; Bachmann et al., 2002; Leonard et al., 2002; Nakagawa et al., 2002; Kent et al., 2010; Druitt et al., 2012; Tomiya et al., 2013). These interactions, or any movement of melt in the magmatic plumbing system, produce also interactions of their respective crystal cargos, which can suffer changes in chemical composition.

In this context, the crystal cargo of magmas can be considered as a precious archive of magma evolution (Tepley et al., 2000; Ginibre et al., 2002; Wallace and Bergantz, 2002, 2004, 2005; Humphreys et al., 2006; Ginibre et al., 2007; Ruprecht and Wörner, 2007) and represents a robust tool to map the inner organization-connection of a magmatic plumbing-system (Kahl et al., 2011, 2013 and 2015). Crystals as plagioclases, olivines or orthopyroxenes generally present a strong zoning pattern (changes in crystal compositions), which manifest the occurrence of variable regimes in the system during crystal growth. When this zoning pattern is preserved after eruption, it can be used to map the system and unravel how many magmatic components are present in the magma plumbing system, how they are differentiated, what is their spatial storage organization and how are they connected. Kahl et al. (2011, 2013 and 2015) use a System Analysis (Palm, 2005) of the 1991-2008 eruptive period olivine crystal cargo of Mt. Etna to distinguish the different magmatic environments (MEs) constituting the plumbing system and their interactions.

System analysis is a method based upon analysing the zoning texture of single crystals (e.g. olivines) and their associated chemical compositional variation, along assigned rim to rim or rim to core traverses. When profiles show compositional plateaus, the latter are interpreted as crystal growth under a constant set of thermodynamic variables, defining a precise magmatic environment (ME). Assuming sequential crystal growth from core to rim, connections in between MEs are investigated following crystals plateaus from core to rim. When repeated on a statistically consistent amount of crystals, the method enables to obtain information about the direction of transfer pathways that populations of crystals and their carrier liquids took on their way to the surface (Kahl et al., 2015).

Here we focus on three major pumiceous ignimbritic eruptions of Dominica (Lesser Antilles Arc): Layou (~51 kyrs cal BP), Roseau (~33 kyrs cal BP) and Grand Fond (~24 kyrs cal BP), having eruptive volumes of several km^3 DRE/eruption (DRE= dense rock equivalent volume). We present results on the zoning patterns of orthopyroxenes belonging to the basal plinian fallout phase of the three eruptions and apply the Crystal System Analysis approach to obtain a full statistical treatment of their compositional data and investigate the meaning of the zoning patterns in terms of magmatic dynamics and interactions. To know how these environments are produced and whether they are spatially separated or part of the same reservoir we have analysed melt inclusions hosted in a range of orthopyroxenes representative of all MEs. Results on major element composition of orthopyroxene-melt inclusion pairs, coupled with consideration about samples stratigraphy and results of phase equilibria

experiments (Martel et al., 1998; chapter IV), allow to build a complete geochemical model of the reservoirs feeding the three considered eruptions and interpret the crystal pathways.

V.I.2. Geological Setting

The Lesser Antilles arc (14°14' 00'' N, 16°21'00''W, Fig.V.I.1) consists of 11 volcanic islands and is the result of the westward oblique subduction of Atlantic oceanic lithosphere beneath the Caribbean plate at an average rate of about 2cm/yrs (Wadge, 1984). The arc extends North to South from the island of Saba to the island of Grenada with a particular convexity towards the East.

Dominica Island (Fig.V.I.1) is the sole island of the arc that contains several active volcanic centres (from North to South: Morne Aux Diables, Morne Diablotins, Morne Trois Pitons-Micotrin and Plat Pays Volcanic Complex). Morne Trois Pitons-Micotrin volcano located in the central part of the island (Fig. V.I.1) has produced in the past voluminous pumiceous eruptions that generated on-land large volume of pumiceous pyroclastic density currents represented in marine settings as voluminous, turbiditic, density current deposits (Carey and Sigurdsson, 1980). Previous studies (e.g. Sigurdsson,1972; Carey and Sigurdsson, 1980) considered that significant volumes of evolved magma emitted in the last 50 ky, could be linked to a unique major eruption of the Morne Trois Pitons-Micotrin volcanic centre: the Roseau Tuff eruption, that produced a volume of ~58 km^3, making this eruption the largest explosive eruption of the last 200 ky in the Lesser Antilles Arc. More recent works (Lindsay et al., 2005; Smith et al., 2013; Howe et al., 2014, 2015; Boudon et al., in prep-chapter III this volume) have reinterpreted the pumiceous deposits and considered that they belong to several eruptions produced in the last 50 ka. Five ignimbritic eruptions may be recognized (chapter III this volume); among them the three well dated event of Layou at (~51 kyrs cal BP), Roseau (~33 kyrs cal BP) and Grand Fond (~24 kyrs cal BP) (Fig.V.I.1). Each of them represents erupted magma volumes of the order of several km^3/DRE. Stratigraphic relations and geochemistry of erupted products (chapter III this volume) suggest that Layou eruption is linked with the Morne Diablotins eruptive centres while Roseau and Grand Fond are linked with the Morne Trois Pitons.

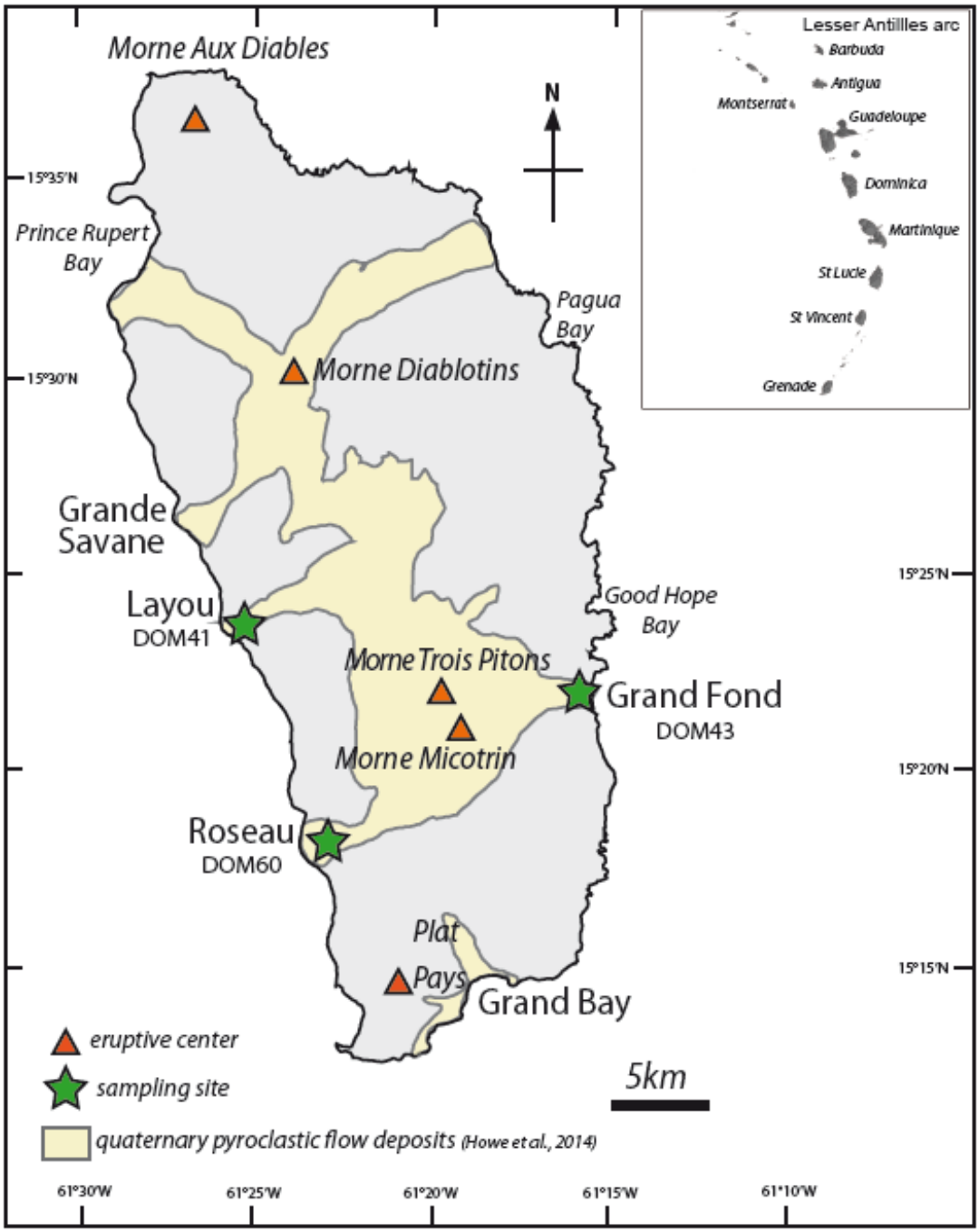

Figure V.I.1: Dominica island (Lesser Antilles Arc): geodynamic setting and volcanic centres. *Simplified map of Dominica. Orange triangle: active volcanic centres; brownish domain: major quaternary pumiceous pyroclastic flow deposits; green stars: sampling sites of the three major eruptions of Layou (DOM41), Roseau (DOM60) and Grand Fond (DOM41). (modified from Howe et al., 2014)*

V.I.3. Samples, method and analytical techniques.

V.I.3.1. Sampling

Our study focuses on the three major eruptions of Layou (DOM41), Roseau (DOM60) and Grand Fond (DOM43) (Fig.V.I.1). Samples for this study were collected from the basal plinian fallout of each eruption; the fallout deposit represents the early-erupted products likely corresponding to the uppermost levels of the magma reservoir. Due to the nature of air fall deposits, such samples represent a rapidly-quenched set of products, representative of reservoir conditions and not suffering of post-eruptive processes linked with deposit emplacement (as lava dome or pyroclastic density current products).

V.I.3.2. Sample preparation

On the basis of a density distribution obtained on at least 100 pumice clasts collected in different layers from the basal plinian fallout deposit of each eruption, six to ten pumice clasts were taken from the density distribution mode, in order to ensure a representative sampling of the main reservoir conditions.

Pumice clasts were cleaned by washing and scrubbing, dried at 80 °C for ~ 48h and gently crushed to obtain isolated crystals for each sample. Crushed samples were then sieved in different size fractions (1-0.750, 0.750-0.500, 0.500- 0.315, 0.315-0.250, 0.250-0.125 mm). Each fraction was finally cleaned by washing, sieved under deionized water, treated in an ultrasonic bath to remove fine adhering particles, and finally oven dried at 80 °C for ~ 24 to 48h. Orthopyroxene were handpicked under a binocular microscope from size fractions ranging from 315 microns to 1 mm. Orthopyroxenes were picked, mounted in epoxy resin and polished sequentially with diamond grit to a final 0.3 μm polish grade. As our study focuses on their textural-compositional analysis, particular care has been taken in the mounting process: all crystals were mounted with c-axis in a North-South direction and crystals of the same mount were specifically selected to have comparable thickness and size, in order to enable consistent polishing to the central part of orthopyroxenes. This enabled easy comparison of crystals within and between different mounts and, for further diffusion modelling (see next Part II), the easiest image treatment and highest chances of success.

V.I.3.3. Method for identification of textural patterns in orthopyroxenes

High resolution back-scattered images of orthopyroxene crystals (BSE images) were acquired to investigate crystal texture (possibly zonation) and point out the location of the different rim to core or rim to rim profiles, then measured using electron microprobe. Imaging was performed with a Scanning Electron Microscope ZEISS-Supra 55 (UPMC, Paris), with 20 kV

acceleration voltage, a beam current of 8nA and high counting time (N=8, 8 integrations on each line of the image to reduce noise impact).

Before using images, it has been checked that the variations in greyscale values present in each BSE image reflect only variations in Fe-Mg content of crystals, without effect of Ca on the recorded signal. For this, the Ca content of orthopyroxenes and its possible variations along each compositional profile has been checked. The Wo (Wollastonite, mol%) content of orthopyroxene from the three eruptions does not show significant changes along single crystals profile and from one crystal to another, with mean Wo content of ~2-3 % for both rims and cores of crystals (Table V.I.S1 in Supplementary Material). In general, less than 3% of observed BSE greyscale variation can be attributed to Ca fluctuations, leaving the Mg number as the dominant control. This establishes that the zoning patterns recognized in orthopyroxenes are a reflection of changes in the Fe-Mg content of crystals from core to rim. Crystals of each eruption were classified into normal-zoned crystals (having Mg-rich core and Fe-rich rims), reverse-zoned crystals (having Fe-rich core and Mg-rich rims) and multiple-zoned crystals (defined here as crystals with two or more reversals in their enstatite content). Furthermore, each crystal has been carefully analysed for major and minor elements composition on rim-to-rim or rim-to-core profiles (see next section 3.4) in order to identify on each crystal specific core and rim compositional plateaus and, based on core composition of crystals, creating different crystals groups for each eruption.

V.I.3.4. Analytical method for compositional analysis of crystals and melt inclusions.

Chemical composition of crystals has been measured using a CAMECA- SX5 and a CAMECA-SX100 electron microprobe in several analytical sessions (Service CAMPARIS, Paris). Orthopyroxene composition (major and minor elements: Si, Na, Ti, Al, Ca, K, Fe, Mg, Mn, P,Cl) was measured with an acceleration voltage of 15 kV, a beam current of 10 nA and a focused beam (beam size < 2 μm). Counting time on peak and background was set at 10s for all elements. Two different kinds of analysis have been performed: crystal core single-point analyses for unzoned crystals, and 2 μm step rim-to-rim or rim-to-core traverses for zoned crystals. The analysis step is maintained constant at 2 μm for all crystals, regardless their size of structures.

For the three eruptions a set of 50 melt inclusions hosted in orthopyroxenes with various enstatite contents (En, mol%) were analysed by EPMA (Service Camparis) for major and minor elements. We used run conditions of 15 kV, 10 nA with an unfocused (~10μm wide)

beam for glasses to limit Na, K loss. The beam was focused for host crystal analysis. Counting times of 10 s on peak and background were used for all major and minor elements (Na, Mg, Si, Al, K, Ca, Fe, Mn, Ti, P). One, single-point analysis has been measured in each melt inclusion, while host crystals have been analysed with two single point analyses at a distance of ~10 μm from the edge of melt inclusions and in the same zone as the inclusion (North-South direction following crystal mounting).

After EPMA analysis, equilibrium conditions of melt inclusions with the hosting crystal have been verified. As for olivine, the Rhodes' diagram (Roeder and Emslie, 1970) can be used to test for equilibrium for orthopyroxenes, using the $K_D(Fe\text{-}Mg)^{opx\text{-}melt} = (X_{Fe}^{opx} X_{Mg}^{melt})/(X_{Mg}^{opx} X_{Fe}^{melt})$. The test conducted by Putirka (2008) on 785 experimental data, yields to $K_D(Fe\text{-}Mg)^{opx\text{-}melt} = 0.29 \pm 0.06$ in equilibrium conditions. Full set of compositional data and test for equilibrium is presented in Table V.I.S2 and Table V.I.S3 of Supplementary Material).

V.I.3.5. Evolution of the magmatic plumbing system: the crystal system analysis method

Crystal populations in magma have previously been studied by method such as the crystal size distribution, crystal shape or spatial distribution patterns (Mangan, 1990; Higgins, 1996; Marsh, 1998; Wallace and Bergantz, 2002; Morgan and Jerram, 2006; Morgan et al., 2007; Jerram and Martin, 2008; Salisbury et al., 2008). Nevertheless, in the last years a new technique allowing to track crystals movements and stories has been developed by Kahl et al. (2011, 2013 and 2015). The authors use a "system analysis" approach on the study of zoning patterns of crystals to map the components and the evolution of a magmatic plumbing system. The system analysis has been described and presented for the first time by Palm et al. (2005) as a method to study how the connections between the elements influence the overall behaviour of a system. When applied on crystals, the system analysis method allows defining from the compositional zoning of crystals the main magmatic environments present in a plumbing system and their connections (Fig. V.I.2). The principle of the method is to study composition of zoned single crystals along rim to rim or rim to core traverses in order to identify some compositional plateaus (Fig. V.I.2a and b; zone of the crystal with a constant composition; e.g. En (enstatite) for orthopyroxenes). Compositional plateaus have been here defined as regions of the profiles with a minimum length of 10 μm on which the enstatite content [En (mol%)] of the crystal show a constant value, with accepted variability of ± 0.5 En (mol%).

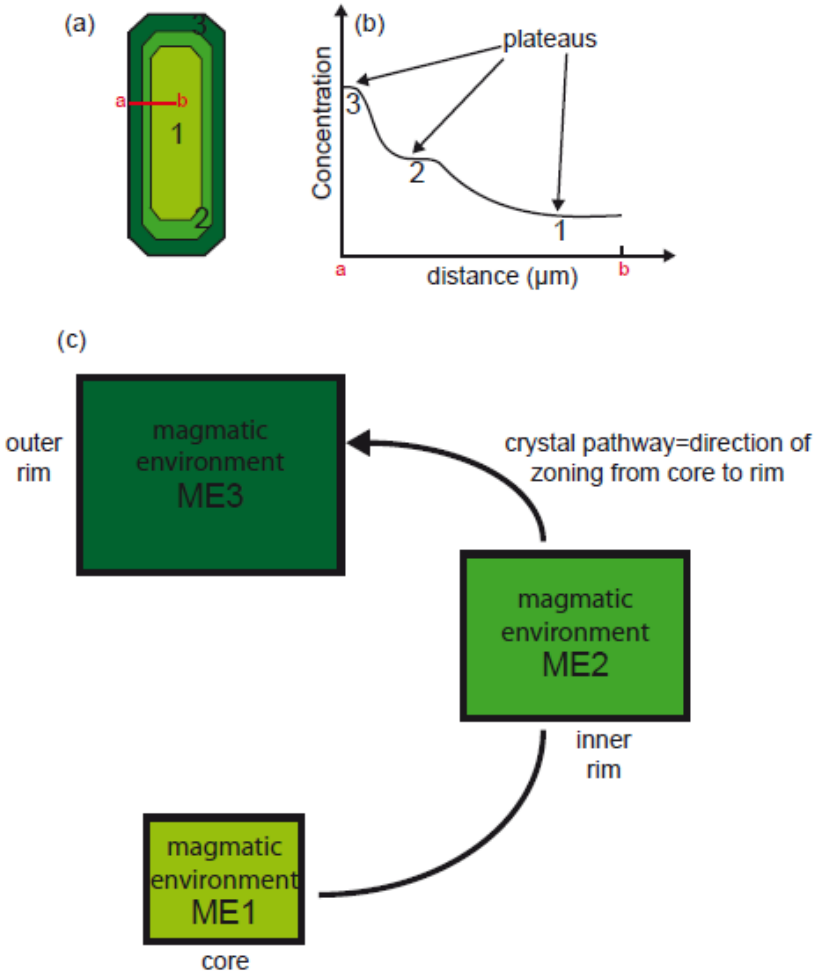

Figure V.I.2: Schematic illustration of the crystal system analysis principles. *(a) Orthopyroxene zoned crystal presenting three different sectors (1 to 3); (b) compositional profile of the same crystal along the a-b line (in red in the figure) revealing the presence of three compositional plateaus associated to the zoning; (c) system analysis plot resulting from the crystal zoning: each compositional plateau correspond to a particular magmatic environment (characterized by specific P,T, fO_2, fH_2O); the black arrow indicate the direction of the zoning pattern from core to rim.*

The composition of each plateau is then calculated as an average of all values defining the plateau. The occurrence of plateaus can be interpreted as a result of crystal growth in different magmatic environments (Fig. V.I.2b and c), with permanency timescales in each environment long enough to be recorded by crystals growth but also short enough that the compositional gradient is not erased by diffusional equilibration. Thus, each plateau corresponds to a crystallization period in a particular environment and their repetitive occurrence indicates that compositional zoning observed in crystal has not been merely produced by pure fractionation during growth but by subsequent and fast changes during crystal growth of the crystallization conditions within the 'magmatic environment' defined by pressure, temperature, oxygen

fugacity and water fugacity values. Nevertheless, for the plateau to be formed and preserved, the effect of local magma dynamics has to be averaged out during the timescale of growth of the relative zone of the crystal (Kahl et al., 2015). For these reasons we can here argue that each compositional plateau found in orthopyroxene crystal corresponds to a migration of crystal (and its carrying melt) into a new crystallization environment for timescales of interest for constrains of pre-eruptive magma movement in the magmatic plumbing system.

In this way, assuming that crystal growth occurred consequently from core to rim, cores represent the first environment recorded by crystals while rims represent the last one (Fig. V.I.2c). Analysis of compositional plateaus from core to rim allows in this way to track the history of movement of crystals and the carrying melt in between different environments through the plumbing system until eruption (Fig.V.I.2c). This work has to be repeated on all analysed crystals in order to define crystal populations, their proportions and crystal pathways. In Crystal System Analysis diagrams each magmatic environment is represented as a box, with box sizes proportional to the relative importance of each environment (i.e. numbers of crystals) in the constitution of the whole plumbing system (Fig.V.I.2c). The connection arrows in between them represent the transfer pathway of crystals (and the carrying melt) from one environment to another, from core to rim, while the thickness of each arrow is proportional to the number of crystals moving in between two environments (Fig. V.I.2c). This method allows overpassing the difficulty of combining and interpreting diverse and complicated zoning patterns in between crystals of the same sample.

To summarize, using Crystal System Analysis, we obtain for each eruption the definition and number of magmatic environments, their respective size and the direction of crystal-melt movements in between them.

V.I.4. General petrology and mineral chemistry – previous work

Whole rock, matrix glass composition (major, minor and trace elements) and crystal content of natural products of Layou, Roseau and Grand Fond eruptions are presented in chapter III and IV of this volume. Magmas of the Layou eruption show a dacitic whole rock composition (64-66 wt% SiO_2, ~5 wt% Na_2O+K_2O) whereas for Roseau and Grand Fond the composition is astride Andesite and Dacite (62-63 wt% SiO_2, ~4.5-5 wt% Na_2O+K_2O). For all, the matrix glass is rhyolitic in composition (76-78 wt% SiO_2, 5.5-7 wt% Na_2O+K_2O).

Samples are porphyritic with ~30-35% of crystals (after a vesicle-free estimation by point counting on thin sections), with comparable phenocryst assemblage of plagioclase, orthopyroxene, amphibole, clinopyroxene, Ti-magnetite and ilmenite embedded in a microlite-free matrix glass (chapter IV this volume). Modal composition of the magma of each eruption evidences that plagioclase represents the most abundant phenocryst (70%), followed by orthopyroxene (15-17%), amphibole (1 to 17%) and, in lesser proportions, clinopyroxene and Fe-Ti oxides. Layou, presenting a slightly more evolved bulk composition (~66 wt% SiO_2), has ~17% of amphiboles, while they are less abundant in the products of Roseau and absent in those of Grand Fond (< 1%). Regarding differences in chemical signature and phase assemblage, (chapter III) suggest that Layou eruption would belong to a magmatic system linked with the Morne Diablotins volcanic centre, while Roseau and Grand Fond would be linked with the Morne Trois Pitons-Micotrin volcanic centre.

Composition of crystals is presented in chapter IV of this volume. Plagioclase crystals show significant zoning patterns and resorption textures, with anorthite content (An, expressed in mol%) spanning a broad range between An_{42} to An_{90}. Nevertheless, for the three magmas a dominant compositional peak can be recognized at $An_{50\text{-}55}$, representing the most common composition of plagioclase rims (chapter IV). Amphiboles are ferri-magnesiohornblende (following the classification of Leake et al., 1997) with a very constant Al_2O_3 content fixed at 6-8 wt% and Mg-number (Mg#= $Mg/Mg+Fe_{TOT}$) values ranging from 0.52 to 0.60. Clinopyroxenes are augitic around Wo_{44} En_{38} Fs_{18} (Wo= Wollastonite; En= Enstatite; Fs= Ferrosilite, expressed in mol%), with Mg# ranging from 0.61 to 0.71 and a broad peak around Mg# 0.68. Fe-Ti oxide compositions are constant from one eruption to the other with titanomagnetite fixed at $Mag_{71\text{-}75}$ $Usp_{29\text{-}25}$ (Mag= magnetite, mol%; Usp= ulvospinel, mol%), and ilmenite at Ilm_{87} Hem_{13} (Ilm= ilmenite, mol%; Hem= hematite, mol%), (chapter IV). The orthopyroxene composition, focus of this study, is presented in section 5.

V.I.5. Results

V.I.5.1. Orthopyroxene zoning and chemistry

A total of 2266 orthopyroxenes for the three eruptions (751 for Layou, 701 for Roseau and 814 for Grand Fond) have been investigated for their texture and chemical composition. Complete rim and core composition of each orthopyroxene are presented in Table S1 (Supplementary Material). Textural analysis by high-resolution BSE images shows that, for the three eruptions, 15-20% of orthopyroxenes present clear and visible zonation, whilst 80-85% of crystals are unzoned, with a strong dependence of their texture on the size of crystals. Orthopyroxenes belonging to larger size classes (750 μm to 1 mm) are usually unzoned and present a more massive structure while smaller size classes (250-315 μm and 315-500 μm) present clear zonation. This difference could result either from a long period of stable equilibrium conditions allowing growth of large unzoned crystals or from a diffusional re-equilibration of any previous chemical gradient.

BSE images and EPMA chemical traverses of characteristic zoned orthopyroxenes for the three eruptions are presented in Figure V.I.3. Crystals can exhibit normal (Fig. V.I.3a), reverse (Fig. V.I.3b) or multiple (Fig. V.I.3c) zoning. The frequency of occurrence of each crystal population is presented in Table V.I.1. Prevalence in reverse zonation is clear for all the three eruptions (44% in Layou, 76 % in Roseau and 71% in Grand Fond).

Even if orthopyroxene crystals seem to share a comparable compositional range (En_{47}- En_{63}), compositional peaks can be distinguished in their Enstatite contents (Fig. V.I.4). Unzoned crystal of Layou and Roseau show a compositional peak at En_{52-53}, while crystals of Grand Fond move to slightly less evolved compositions at En_{53-55} (Fig. V.I.4a, c and e). 60 % of Layou zoned crystals (Fig. V.I.4b) have core compositions centred at En_{52-53} while rims shows a bimodality with two different compositions centred at En_{47-51} and En_{53-58}. Roseau reverse-zoned (Fig. V.I.4d) crystals show cores centred at En_{52-53} and rims at En_{54} to En_{60}, with a clear peak at En_{56-58}. Finally, Grand Fond zoned orthopyroxenes (Fig. V.I.4f) display a wider compositional range with core compositions going from En_{49} to En_{56} and rim compositions from En_{50} to En_{57}. 10% of crystals present significantly higher En content at En_{63} (Fig. V.I.4f). Compositions of unzoned orthopyroxenes and zoned orthopyroxene cores and rims for the three eruptions are summarized in Table V.I.2.

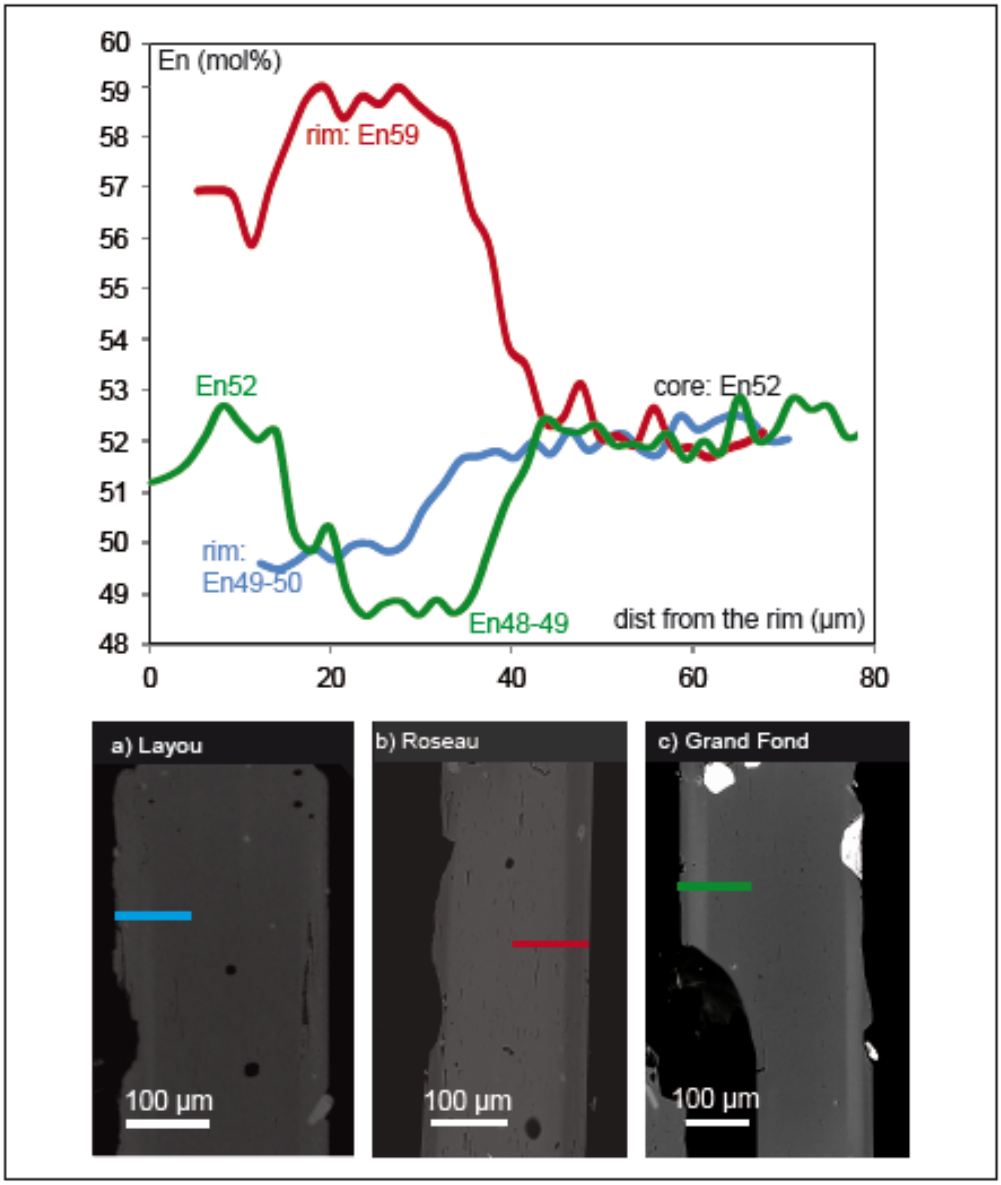

Figure V.I.3: Examples of high resolution BSE images and corresponding rim to core EPMA traverses in orthopyroxenes for Layou, Roseau and Grand Fond. *BSE images and compositional profiles for normal (a), reverse (b) and multiple (c) zoning. Reverse zoned crystals present darker rim (higher En content) while normal zoned crystals present clearer rim (lower En content). Lines in the BSE image: position of EPMA traverse. EPMA traverses are expressed in terms of En content variations (En mol%) as a function of distance from the rim of the crystal expressed in µm. Rim and core compositions of crystals are identified by analysis of crystal compositional plateau.*

Eruption	**Layou (51 kyrs cal BP)**			
Total crystal number	751			
Type of crystal	unzoned opx	zoned opx		
Number of crystals	601	150		
Type of zoning		reverse	normal	multiple
% zoned crystals		44%	28%	28%
Eruption	**Roseau (33 kyrs cal BP)**			
Total crystal number	701			
Type of crystal	unzoned opx	zoned opx		
Number of crystals	596	105		
Type of zoning		reverse	normal	multiple
% zoned crystals		76%	8%	16%
Eruption	**Grand Fond (24 kyrs cal BP)**			
Total crystal number	814			
Type of crystal	unzoned opx	zoned opx		
Number of crystals	692	122		
Type of zoning		reverse	normal	multiple
% zoned crystals		71%	10%	19%

***Table V.I.1**: **Percentage of occurrence of each type of orthopyroxene in the three eruptions**, for a total number of counted crystals of 751 for Layou, 701 for Roseau and 814 for Grand Fond.*

Layou		
unzoned opx	zoned opx	
80%	20%	
En%	En% core	En% rim
52-53	46-53	47-51
		53-58
Roseau		
unzoned opx	zoned opx	
85%	15%	
En%	En% core	En% rim
52-53	52-53	54-60
Grand Fond		
unzoned opx	zoned opx	
85%	15%	
En%	En% core	En% rim
53-55	49-56	50-63

Table V.I.2: Composition in term of En content (mol%) of unzoned and zoned (cores and rims) orthopyroxenes.

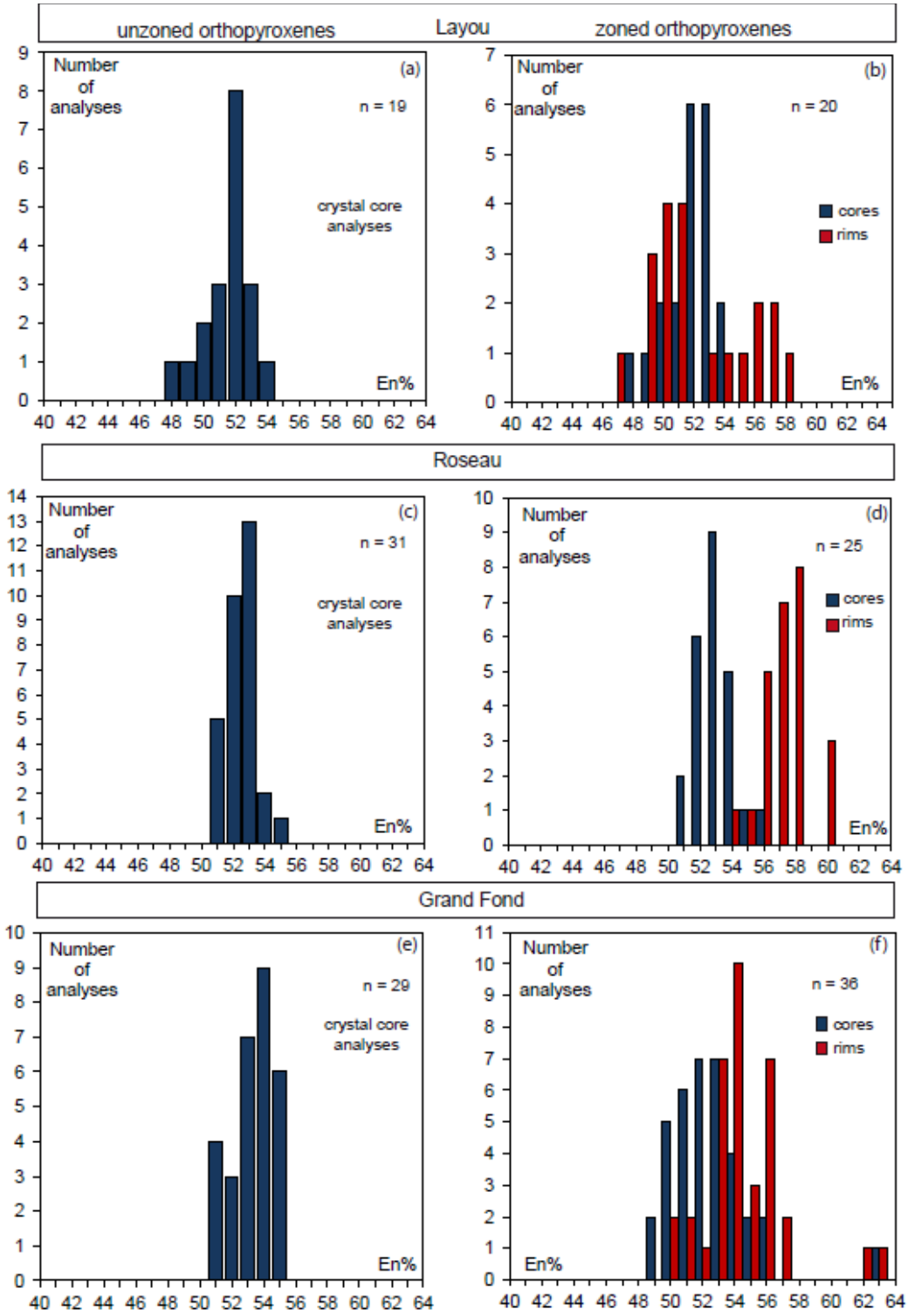

Figure V.I.4: Frequency histograms of orthopyroxene compositions. *Composition of unzoned orthopyroxenes of Layou (a), Roseau (c) and Grand Fond (e) expressed in terms of En (mol%). Composition of zoned orthopyroxenes of Layou (b), Roseau (d) and Grand Fond (f). Unzoned orthopyroxene analyses are single point analyses in the core of crystals while core and rim composition of zoned crystals represents averaged plateaus compositions. n: number of analysed orthopyroxenes.*

V.I.5.2. Orthopyroxene-melt equilibrium pairs

After EPM analysis, the 50 melt inclusion-orthopyroxene pairs have been tested for equilibrium on the basis of the $K_D(Fe\text{-}Mg)^{opx\text{-}melt}$ (Putirka, 2008).

Test for equilibrium shows that 80% (39 on the 50 inclusions) of analysed melt inclusions (MI) have suffered either post-entrapment crystallization (PEC) at their boundary ($K_D(Fe\text{-}Mg)^{opx\text{-}melt}$ lower than equilibrium value; 31 MI), or re-equilibration with the host orthopyroxene ($K_D(Fe\text{-}Mg)^{opx\text{-}melt}$ higher than the equilibrium value; 8 MI). 11 melt inclusions, being hosted in orthopyroxenes of En_{47} to En_{53}, demonstrated equilibrium with the hosting orthopyroxene (Fig. V.I.5a). These inclusions do not allow us to investigate the whole of the observed orthopyroxene compositional range (En_{54} to En_{60} not being represented).

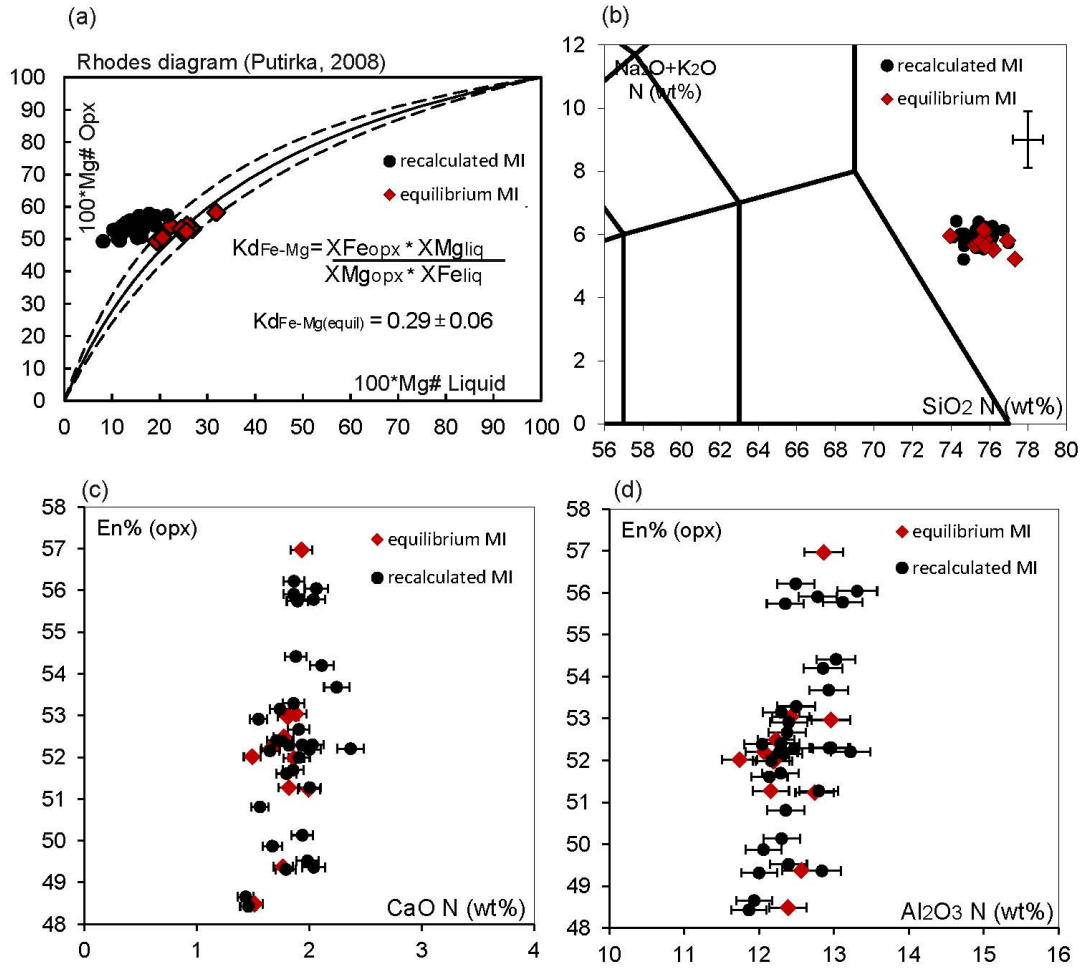

Figure V.I.5: Melt inclusion compositions. *(a) Equilibrium orthopyroxene-melt inclusions criteria in a Rhodes diagram based on the partition coefficient K_D (Fe-Mg) (Putirka, 2008). Red rhombs: 11 melt inclusions showing equilibrium values; black circles: 31 melt inclusions showing Kd lower than equilibrium values; (b) TAS diagram of equilibrium (red rhombus) and recalculated (black circles) melt inclusions; (c) and (d) Ca and Al content (normalized wt%) of melt inclusions (equilibrium and recalculated) as a function of the En content (mol%) of their hosting orthopyroxenes.*

Assuming that PEC is a closed-system process in which the melt inclusion crystallizes a thin border of orthopyroxene at its edge, so that its final composition is depleted in elements particularly compatible with orthopyroxene (such as Fe and Mg), PEC can be numerically corrected (Sisson and Layne, 1993). After correction of PEC, which only represents between 1 and 2% of MI in volume, we obtain a total of 42 melt inclusions (11 in equilibrium and 31 corrected from PEC; Table S2 and S3 of Supplementary Material).

As a conclusion, regardless of the orthopyroxene composition, melt inclusions have the same major elemental composition (Fig. V.I.5b to d and Table V.I.S2, V.I.S3 of Supplementary Material).

V.I.6. Discussion

V.I.6.1. Occurrence of compositional plateaus

A detailed analysis of rim to rim and rim to core EPMA profiles has allowed to recognize compositional plateaus in the core and rim parts of several orthopyroxenes and define some main groups. Plateaus never being present as core and rim part of the same crystal have been considered as belonging to the same group. On this basis we have distinguished four main, separated compositional plateau groups at En_{47-50}, En_{51-53}, En_{54-58} and En_{59-63} (Fig.V.I.6).

Based on core composition, in Layou eruption 2 different crystal groups can be recognized with two main core compositions (En_{46-50} and En_{51-53}). Three main rim compositions are associated to these cores: En_{46-50}, En_{51-53} and En_{54-58}. Roseau eruption shows 1 main group, with cores having a composition of En_{51-53} associated with two types of rim at En_{54-58} and En_{59-63}. Grand Fond, the last eruption in time, presents the most complex system, with 4 crystal groups (cores at En_{46-50}, En_{51-53}, En_{54-58} and En_{59-63}) associated to rims covering the whole compositional range (Fig.V.I.6).

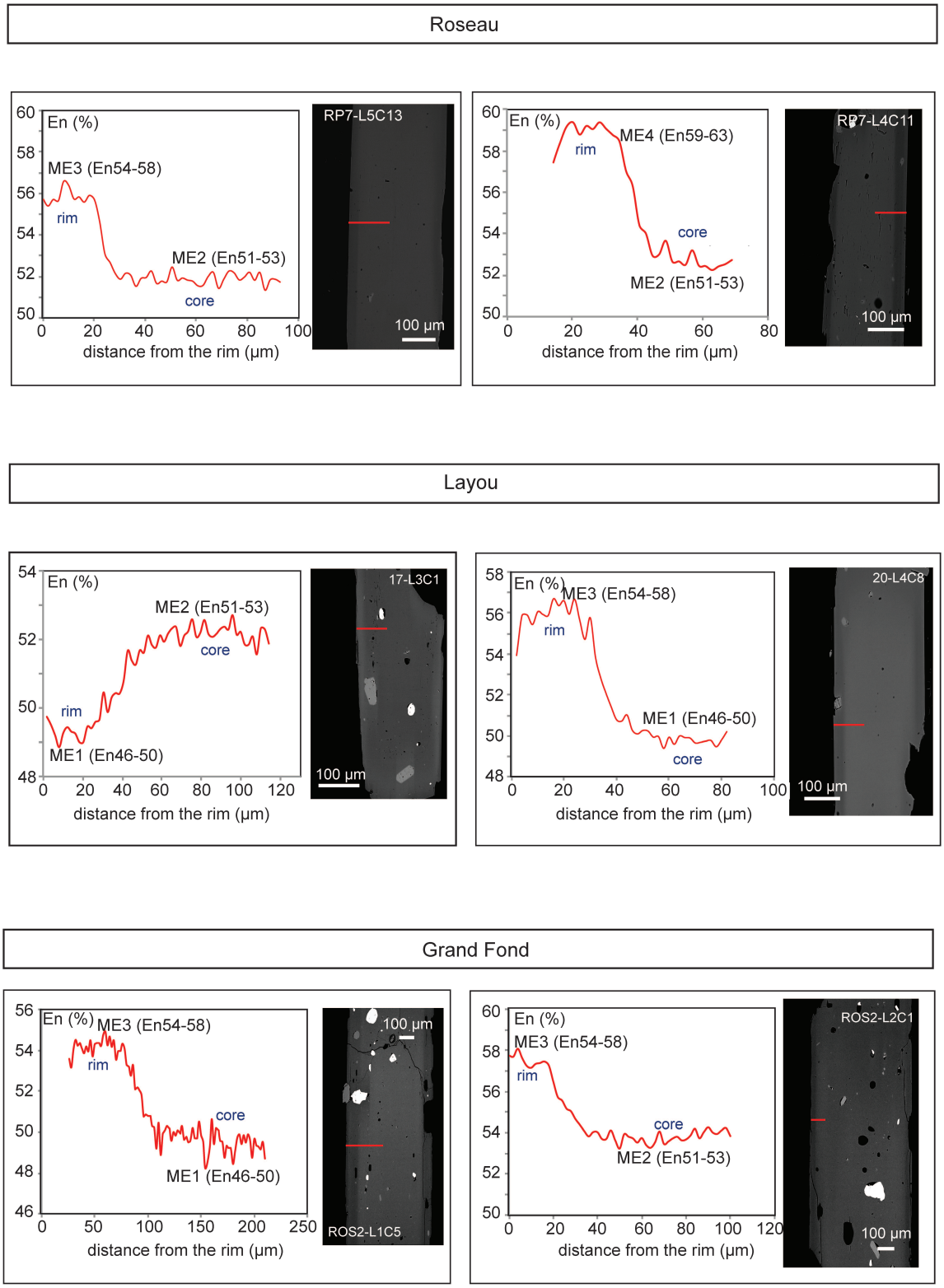

Figure V.I.6: Examples of compositional plateaus*. High resolution BSE-images and electron microprobe profiles for orthopyroxenes of Layou, Roseau and Grand Fond eruptions. Crystals representative of each recognized crystals group are presented for each eruption. Red lines on the BSE image correspond to the electron microprobe profile. EPMA profiles are expressed in En (mol%) and magmatic environments are named as in the text ME1 to ME4.*

V.I.6.2. Definition of magmatic environments

On the basis of the 'plateau' groups recognized in each eruption we define four main magmatic environments that account for the overall orthopyroxenes diversity in composition: ME1 (En_{47-50}), ME2 (En_{51-53}), ME3 (En_{54-58}) and ME4 (En_{59-63}). Statistical counting of core and rim compositions had been performed to weight the occurrence of each environment in each eruption. A total of 22 orthopyroxenes for Layou, 25 for Roseau and 36 for Grand Fond have been analysed and counted (Fig.V.I.7). In case of multiple zoning of orthopyroxenes, rims1 indicates the composition of inner rims and rims2 indicates the composition of outer rims.

Layou eruption shows the occurrence of environments ME1 to ME3 (Fig.V.I.7a), with 36% of cores in environment ME1 and 64% of cores in ME2, while rims are mainly in environments ME1 and ME3 (Fig.V.I.7a, 45% in ME1 and 55% in ME3). Roseau eruption shows the occurrence of environments ME2 to ME4 (Fig.V.I.7b). Cores are all in ME2, while rims show higher enstatite contents in environments ME3 (78% of rims) and ME4 (22% of rims). Grand Fond shows the occurrence of all environments (Fig. V.I.7c), with crystals cores and rims showing a broad range of composition: cores are mainly in environments ME1 (39% of cores) and ME2 (47% of cores), whilst rims are mainly in ME3 (22 inner rims on the total of 36 crystals), then in environments ME2 (7 inner rims; 2 outer rims), ME1 (4 inner rims) and ME4 (3 inner rims). In Figure V.I.7 the composition of unzoned orthopyroxenes shows a shift from ME2 for Layou and Roseau eruptions to ME3 in Grand Fond.

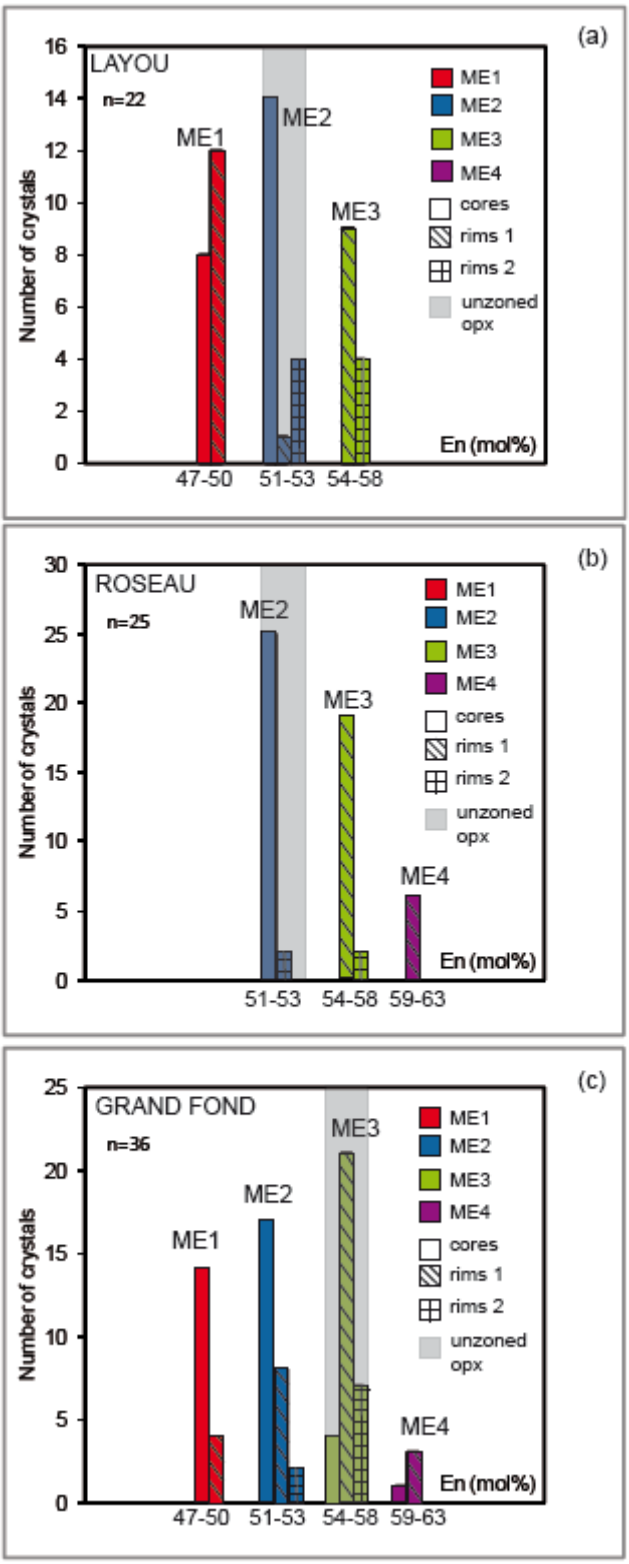

Figure V.I.7: Histograms of orthopyroxenes core, inner rim (rim1) and outer rim (rim2) composition *(expressed as En (mol%) according to the defined magmatic environments (ME). Colours define each environment (ME1=red, ME2= blue, ME3= green, ME4= purple), while hatching defines rims compositions. Unzoned orthopyroxenes composition is represented as a grey box.*

V.I.6.3. Definition of crystal pathways

To illustrate the zoning record of the studied orthopyroxenes we use a schematic Crystal System Analysis representation (Fig. V.I.8).

For Layou eruption, unzoned crystals, representing the 80% of total orthopyroxenes, have a composition centred at En_{52-53} in ME2 (Fig.V.I.8a). Two main crystals pathways can then be recognized: ME1-ME3 (7 crystals on 22) and ME2-ME1 (6 crystals on 22). Four crystals display a cyclic movement ME2-ME1-ME3, while minor pathways (2 crystals) are represented by ME2-ME1-ME2 and ME2-ME3 (Fig.V.I.8a). The composition of unzoned crystal of Roseau eruption is still fixed at En_{52-53} (ME2) (Fig. V.I.8b). Results shows a progression of the system to less evolved compositions, losing the connection with ME1 and gaining the environment ME4 of higher enstatite contents (En_{59-63}), (Fig.VI.8b). All zoned crystals have their core in ME2 (see also Fig. V.I.7) and one main crystal pathway has been identified in between ME2 and ME3, counting 17 crystals on 25. Two crystals show a cyclic movement in between ME2 and ME3 and the other 6 crystals show also a general movement to the higher enstatite contents of ME4 (En_{59-63}). Finally Grand Fond eruption displays a shift of the volumetrically largest environment represented by the unzoned orthopyroxenes toward environment ME3 (En_{54-58}) (Fig.V.I.8c). A more complex pathway system may be evidenced, with the presence of all four environments and two main crystals pathways: ME1-ME3 and ME2-ME3. On 36 analysed crystals 18 show these pathways (8 crystals show ME1-ME3 and 10 ME2-ME3). Other more complicated and less abundant pathways (2-3 crystals per pathway) are ME2-ME1-ME3 and ME1-ME2-ME3 (Fig.V.I.8c).

It has to be noted that the environment ME3 (En_{54-58}) is generally located at the end of crystals pathways for all studied eruptions, representing a rim composition for the largest amount of zoned crystals.

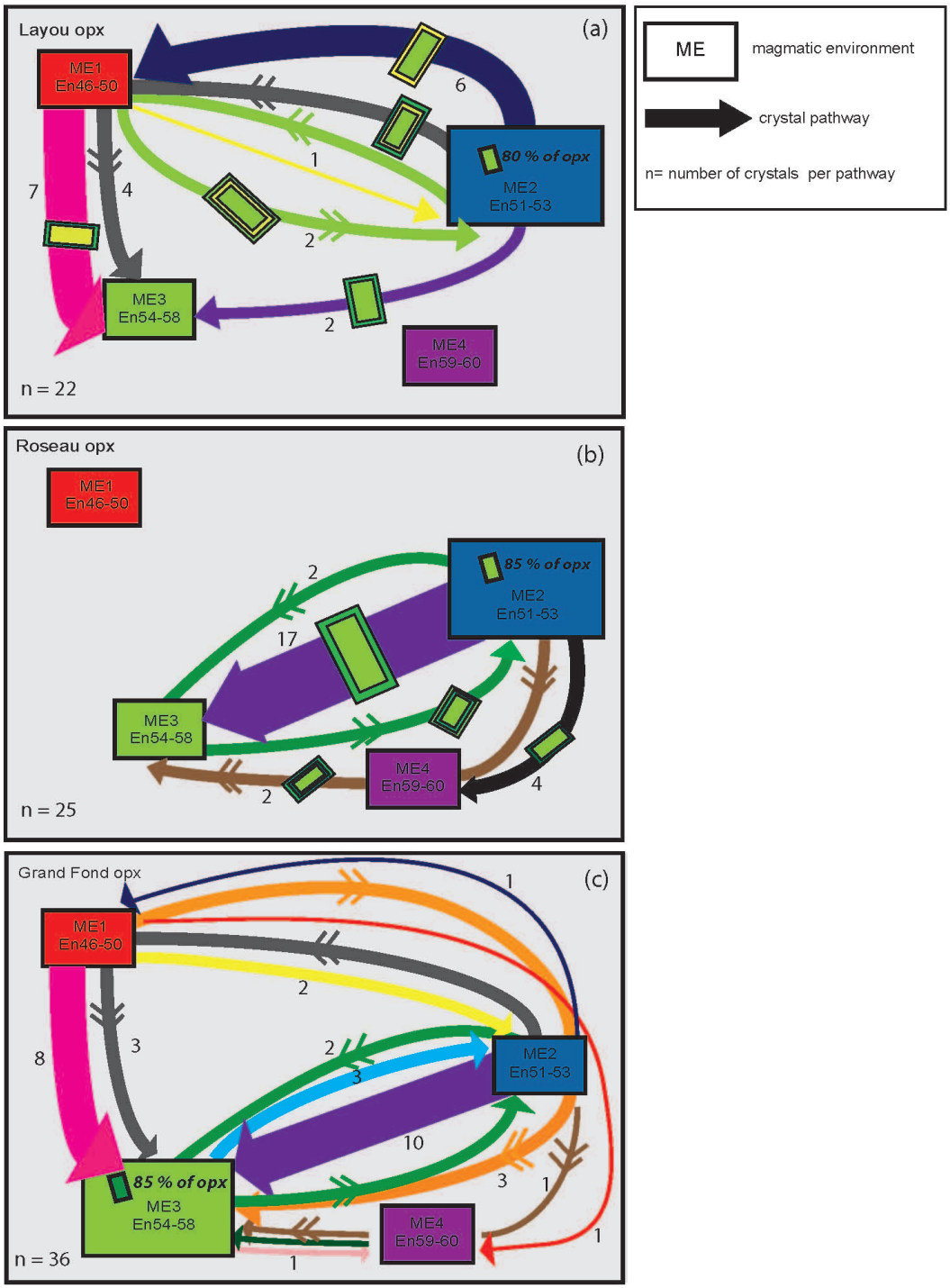

Figure V.I.8: Crystal system analysis diagram of orthopyroxene compositions *for Layou (a), Roseau (b) and Grand Fond (c) eruptions. Each box represents a magmatic environment identified by the zoning patterns analysis. Boxes size is proportional to the abundance of crystals insides them. The largest box indicates the environment occupied by unzoned crystals. Each arrow indicates the zoning pattern recognized in single orthopyroxene crystals beginning at the ME recorded by the core, passing through all the ME recorded from core to rim and ending at the ME recorded by the final rim composition. Their thickness is proportional to the number of crystals showing that pathway. Multiple connectivities are highlighted by double arrowheads.*

V.I.6.4. Main structure of the magmatic plumbing system

The crystal system analysis reveals that, even if the initial system can display a high level of complexity, some crystals compositional groups can be recognized and some prevalent melt-crystals pathways identified. This allows us to define a primary block-structure of the plumbing system feeding the three eruptions (Fig. V.I.9).

Firstly, unzoned crystals have core composition located in ME2 (En_{52-53}) in Layou and Roseau eruptions (Fig. V.I.9a and b), while Grand Fond shows a shift of unzoned crystal compositions to ME3 (En_{54-58}) (Fig. V.I.9c). Given their abundance (80-85%), they represent the main environment and the volumetrically most important part of each magmatic plumbing system. They represent the equilibrium crystallization conditions, existing prior to the perturbation producing the observed zoning textures in the other 15-20% of crystals. Furthermore, the shift of unzoned crystals composition from ME2 in Roseau to ME3 in Grand Fond (Fig.V.I.9c) suggests a long term perturbation of magma storage conditions producing a shift to less evolved crystals compositions over the eruptive time in between the two eruptions (~10 kyr). In the three eruptions, zoned crystals show two dominant crystals pathways: ME1-ME3 and ME2-ME3. Both pathways indicate a movement of crystals towards less evolved compositions (higher En values). ME2-ME3 is recognized in both Roseau and Grand Fond eruptions and presents the highest amount of crystals [~44%, Fig.V.I.9b and c]. It can be described as a progressive sinking of crystals from the main environment En_{52-53} (ME2) to the less-evolved En_{54-58} (ME3), which receives crystals, and, by the Grand Fond eruption, becomes the volumetrically most significant magmatic environment (Fig. V.I.9c). Moreover, the occurrence of the environment ME4 (En_{59-63}) in the Roseau and Grand Fond eruptions further suggests a progression toward a less-evolved composition.

To summarize, a shift of crystal to higher enstatite content is present in all eruptions. For Layou eruption the ME2-ME1 and the ME1-ME3 can be considered as the major connections in the plumbing system. For Roseau and Grand Fond eruptions, the ME2-ME3 connection is defined as the main dynamic occurring in the plumbing system (~44% of zoned crystals).

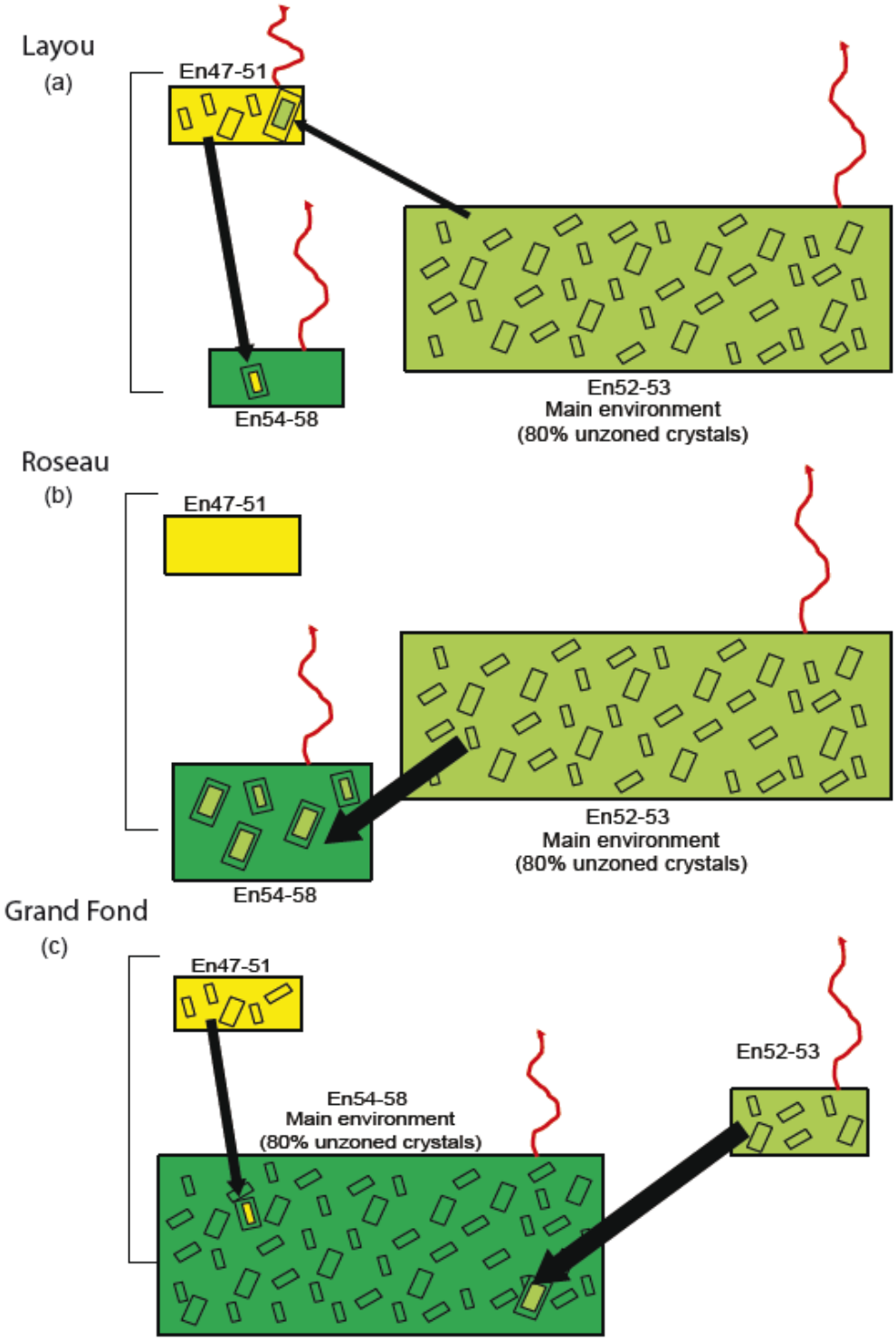

Figure V.I.9: Schematic structure of the plumbing system feeding the three eruptions *of Layou (a), Roseau (b) and Grand Fond (c). Yellow box: ME1, light green box: ME2, dark green box: ME3. ME4 is not represented as it does not participate to the main recognized interconnections. The main magmatic environment (80-85% unzoned crystals) is highlighted by larger size. Black arrows indicate the main recognized interconnections ME1-ME3 (15 crystals) and ME2-ME3 (27 crystals), with thickness proportional to crystal numbers. Red curvilinear arrows indicate connection of each environment with eruption.*

V.I.6.5. Physical nature of magma environments and their connections

The presence in a plumbing system of different magmatic environments can be produced by a change in any of the main intensive thermodynamic parameters characterizing a magmatic system: (i) melt composition (injection of a new magma batch having a significant different composition), (ii) pressure conditions (a pre-eruptive decompression of the system, magma ponding and re-equilibration at shallow crustal level) or (iii) temperature conditions (an increase of temperature, heating).

A change in one or more of these parameters can be caused by a large variety of processes like the injection of new magma in the reservoir and further mixing or by a decompression of the system. Furthermore, movements of crystals from one environment to another, does not necessary imply an effective spatial movement: two magmatic environments (MEs) can be chemically different but spatially included in the same physical magma body/reservoir. Thus, to explain the possible mechanism creating the different magmatic environments and depict the final geometry of the plumbing system feeding the three eruptions (whether there is one main zoned reservoir or different interlinked magma pockets), we need a tool to discriminate the physical nature of these environments (Kahl et al., 2015).

For testing the possibility of a change in melt composition here we have analysed melt inclusions-orthopyroxenes couples (see section 5.2). The constant major element composition of melt inclusions hosted in cores and rims of orthopyroxenes having different enstatite content (En_{47} to En_{60}) have proved that all magmatic environments are in equilibrium with the same melt composition, ruling out the possibility that they would be linked with the existence of different, separated magma batches of different melt composition, or with the mixing in between a felsic and a mafic magma. Ruled out the possibility of change in melt composition, a change in pressure, temperature, and oxygen fugacity still need to be tested.

Significant changes in magma storage pressure, for instance based upon vertical stratification, can also be ruled out by going back to consideration of the field relations, the sampling strategy and the textures of hand-samples and crystals. Pumices were sampled from the plinian fallout phase of each eruption, recognized here as the early-erupted products from the uppermost portion of the reservoir. Moreover, the chemistry of orthopyroxenes belonging to the main magma body shows crystal core compositions centred around En_{52-53} for Layou and Roseau and around En_{54-55} for Grand Fond. If a pre-eruptive decompression event has occurred, it would have created a new set of crystals with lower core Enstatite content (more

Fe rich), (Tomiya and Takahashi, 2005; Allan et al., 2013), not recorded in our samples. A new set of unzoned crystals is indeed recognized in the latest Grand Fond eruption, but having higher En content (En_{54-55}) incompatible with a decompression process. Thus, decompression could not have produced the prevalent reverse zoning going to En_{54-60} recognized in orthopyroxenes. These considerations allow us to reject the possibility of significant (± 100 MPa) pressure changes during storage of our samples.

A modification in temperature conditions is then the final parameter to consider as the origin of the presence of different environments. Various phase equilibria crystallization experiments show that, at fixed melt composition, fixed pressure (e.g. 300 MPa) and oxygen fugacity conditions of ΔNNO+1, the Enstatite content of experimental orthopyroxenes can be moved from En_{50} to En_{55} with an increase of ~25°C in temperature (e.g. Martel et al., 1998; Solaro et al. in prep, chapter IV of this volume). Orthopyroxene compositions belonging to ME3 and ME4 are then likely to be linked with a heating of the reservoir. The presence of significant resorption sieve textures and trapped melt inclusions in plagioclase also reinforce the idea of injection of a hotter magma, producing dissolution of crystals (Couch et al., 2001; Stewart and Fowler, 2001; de Silva et al., 2008). The possibility of dissolution by decompression (Nelson and Montana, 1992) can be discarded going back to considerations about orthopyroxenes normal vs reverse zoning discussed in the previous paragraph.

In has to be noted that the homogeneous whole rock composition and phase assemblage inside each eruption suggest a heating with no significant mass exchange in between the main magma body and the injected one. Few crystal cores have composition higher than En_{54}, they mainly seem to belong to the main crystallization conditions (ME2). Crystals of a second group in equilibrium with the injecting magma body are not found in selected samples, ruling out possibility of mingling/mixing in between the two magma bodies. This means that the hotter magma is probably injected and underplating the main host magma in a short timescale before eruption.

V.I.6.6. A conceptual model for reservoirs structure and dynamics

Results of Crystal System Analysis allowed to draw a petrological schematic model of the reservoirs feeding the three ignimbritic eruptions of Layou, Roseau and Grand Fond.

To understand the following reservoir model it must be noted that the work of Boudon et al. (in prep.), (chapter III this volume) suggests that the Layou eruption is linked with the Morne Diablotins eruptive centre, while Roseau and Grand Fond eruptions are likely originating from the Morne Trois Pitons-Micotrin eruptive centre. These considerations, coupled with

phase equilibria experimental results (chapter IV this volume), imply that Layou eruption would be fed by a separated magma body while Roseau and Grand Fond are potentially sharing the same.

Giving their spatial proximity and their relative similarity in composition, we suggest that they both belong to a unique horizontally developed mush present in the middle-upper crust of Dominica (Fig. V.I.10). The presence of a single large crustal batholith source under Dominica, feeding all eruptive centres, has been already suggested by Smith et al. (2013). Both Layou and Roseau-Grand Fond systems are stored at ~400 MPa (~16 km depth), 850°C and ΔNNO+1 (see chapter IV). Following the crustal model under Dominica (Kopp et al., 2011) this reservoirs are located near to the middle crust- lower crust limit (Fig. V.I.10). In each reservoir we have identified four magmatic environments (MEs). We propose that in each eruption all magmatic environments are in reality not spatially individualized but belong to different portions of the same reservoir, characterized by different crystal/melt rations and/or by different temperatures. For Layou eruption the environment ME2 (En_{51-53}) is presented here as the dominant one, where 80% of unzoned crystals resides (Fig. V.I.10). This environment is likely to represent the main reservoir with equilibrium crystallization conditions at 850°C, 400 MPa, ΔNNO+1 and 7-8 wt% H_2O (after experimental results, chapter IV). The environment ME1 (En_{47-51}) is volumetrically less important but still plays an important role in reservoir dynamics, with strong ME1-ME3 connections (Fig. V.I.8 and V.I.9). As its presence is mainly in crystals cores, we suggest that this environment is also part of the main reservoir and can be depicted as roof- or wall- sections of more evolved crystallization (Fig. V.I.10). The normal zoning recognized in crystals of this eruption (ex: En_{52-53} in the crystal core to En_{47-48} in the crystal rim, ~28% of total zoned crystals) is then considered as a proper feature of the main magma body, deriving from possible migrations of crystals through the highly crystallized (~30%) but still dynamic mushy reservoir. The environment ME3 (En_{54-58}), receiving crystals from the two others (ME1-ME3 and ME2-ME3, represents the heating process (~25°C) by the underplating magma, producing the reverse zoning pattern recognized in ~44% of zoned crystals.

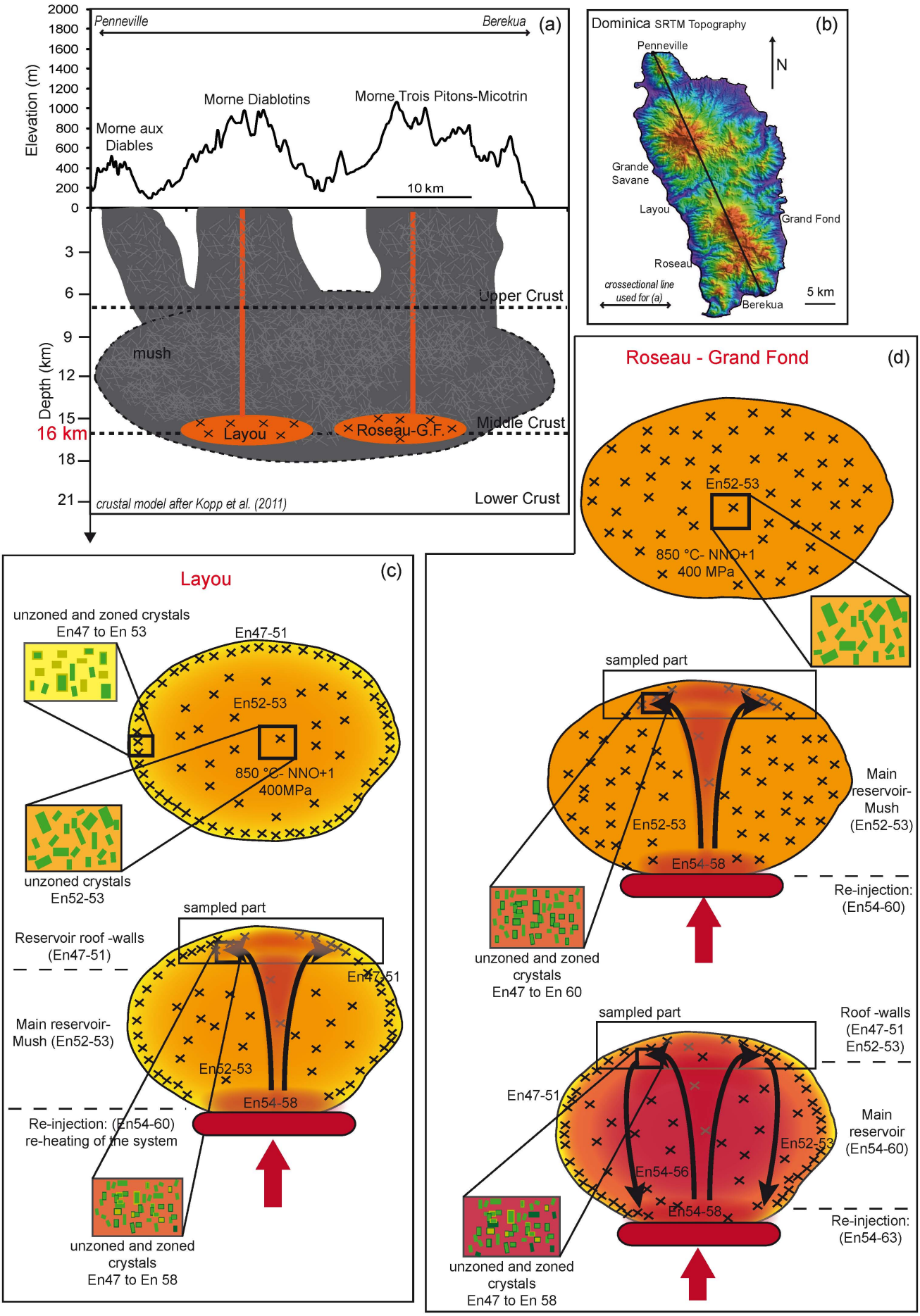
(a)
Penneville
Berekua
Elevation (m)
Morne aux Diables
Morne Diablotins
Morne Trois Pitons-Micotrin
10 km
Depth (km)
Upper Crust
mush
Layou
Roseau-G.F.
Middle Crust
16 km
Lower Crust
crustal model after Kopp et al. (2011)
(b)
Dominica SRTM Topography
Penneville
N
Grande Savane
Layou
Grand Fond
Roseau
crossectional line used for (a)
Berekua
5 km
(c)
Layou
unzoned and zoned crystals En47 to En 53
En47-51
En52-53
850 °C- NNO+1
400MPa
unzoned crystals En52-53
sampled part
Reservoir roof -walls (En47-51)
Main reservoir-Mush (En52-53)
En54-58
Re-injection: (En54-60) re-heating of the system
unzoned and zoned crystals En47 to En 58
(d)
Roseau - Grand Fond
En52-53
850 °C- NNO+1
400 MPa
sampled part
Main reservoir-Mush (En52-53)
En54-58
Re-injection: (En54-60)
unzoned and zoned crystals En47 to En 60
Roof -walls (En47-51 En52-53)
En47-51
Main reservoir (En54-60)
En54-56
Re-injection: (En54-63)
unzoned and zoned crystals En47 to En 58

Figure V.I.10: Conceptual model for the plumbing system for the Layou, Roseau and Grand Fond eruptions. *(a) topography of Dominica with underlying of magma chambers crustal setting (after Solaro et al. in prep; chapter IV this volume); (b) Dominica topography map with the cross-section line used for the topography profile in (a); (c) schematic illustration of dynamics and MEs in Layou reservoir before and after the heating event: the main magma body is at ME2, his roof-wall parts at ME1 and the underplating magma creates the reverse zoning and the introduction of ME3 in the system; (d) schematic illustration of dynamics and evolution of the Roseau-Grand Fond reservoir before and after the heating event: the main homogeneous magma body is at ME2 and the heating from the underplating magma creates the ME3. The heating process assumes a larger scale developing a plume geometry and bringing the composition of the whole system to ME3 by the Grand Fond eruption. Crosses represent crystals; magmatic environments are defined as in the text; the underplating magma is schematically represented by a red box.*

Roseau represents a simplified case in which the environment ME1 is not recognized, indicating that the reservoir is more homogeneous than the Layou one (Fig. V.I.10). Indeed, all crystals (unzoned and cores of zoned one) belong to the ME2 (En_{51-53}), being again the main reservoir with equilibrium conditions at 850°C, 400 MPa and ~NNO+1 (but probably lower water content of 6-7 wt% H_2O, see chapter IV). The ME2-ME3 connection is here more marked (19 crystals on 25) suggesting that a stronger heating event is recorded by the reservoir, producing the ~69% on reverse zoned crystals. The appearance of the ME4 (En_{59-63}) suggests also a stronger heating process than in the Layou case.

Grand Fond eruption presents some main features similar to the Roseau eruption but with a higher level of complexity in crystal zoning and connectivity. At first, the shift of the main environment to the higher En content (ME3, En_{54-58}) indicates that the heating process started in Roseau is likely subsisting over longer timescales so to affect the whole reservoir and move its equilibrium composition to En_{54-56} and temperature to ~875-880°C. The environment ME3, now volumetrically dominant, still receives crystals from the less evolved ME1 and ME2 (Fig.V.I.10). The heating process is thus still responsible of the ~71% of reverse zoned crystal found in this eruption. The presence of crystals compositions in ME1 in Grand Fond implicates that the reservoir presents portions with higher crystallinities where orthopyroxenes exhibit more evolved compositions.

V .I.7.Conclusions

To summarize, we explain the final structure of the reservoirs feeding the three ignimbritic eruptions of Layou, Roseau and Grand Fond as two different highly crystallized (≥30%) dacitic magma bodies having an equilibrium temperature about 850°C (for Layou and Roseau) and 875°C (for Grand Fond). In both magma bodies 80-85% of orthopyroxenes crystals have a fixed composition while 15-20% of orthopyroxenes present normal, reverse or multiple zoning. The normal zoning recognized in crystals (ex: En_{52-53} in the crystal core to En_{47-48} in the crystal rim) is then considered as a proper feature of the main magma body, deriving from its inner structure so characterized by roof- or wall-sections of more evolved crystallization (Fig. V.I.10). On the other hand, the abundance (up to 71% of zoned crystals) of reverse zoning is attributed to a hotter underplating magma causing a ~25-30°C heating able to remobilize the system and, for Grand Fond eruption, to bring the whole system to a new equilibrium composition (En54-56) and a higher temperature (~875-880°C). Crystallinity being likely under the ~50% mobility threshold (Marsh, 1996; Bachmann and Bergantz, 2008), self convection (Couch et al., 2001) can act in the reservoir and develop a heating plume geometry able to bring together samples with different crystallization histories and progressively shift the main composition of the reservoir.

The absence in analysed samples of two spatially separated crystal groups showing different core En content (Tomiya and Takahashi, 2005) combined with the very homogeneous whole rock and residual glass composition, enable us to rule out the possibility of significant mixing (mass transfer) between the resident magma and the underplating one.

At the present state of the study, the chemical composition of the injecting magma cannot be assessed, as the natural products we have sampled are chemically homogeneous and do not present any evidence of a chemically distinct magma. This implies that the underplating recharge event rejuvenating the main reservoir is likely not brought into the eruption.

Supplementary material

Table V.I.S1: Major elements composition of cores and rims of orthopyroxenes for the three eruptions. *Each composition represents an average over a compositional plateau identified over a selected area of the crystal across the c-axis. The code name of each sample (ex: 17l3c1) corresponds to the mount number (17) followed by the crystal line (l3) and the crystal position into each line (c1).*

	Layou-DOM41a3												
Cores	17-l3c1	17-l3c2	17-l3c4	17-l6c2	19-l1c2	16-L1C5	16-L2C3	19-l6c4	19-l7c3	22-l2c1	20-l5c5	17-l1c1	19-l3c8
SiO2	52,61	51,65	52,00	52,37	51,26	51,70	51,21	51,71	51,99	51,62	50,42	52,37	52,08
Al2O3	0,57	0,43	0,55	0,54	0,53	0,53	0,53	0,62	0,49	0,55	0,59	0,46	0,48
FeO	28,44	29,14	28,27	28,93	27,36	28,21	28,83	27,97	28,51	27,57	27,74	29,17	28,63
MnO	1,59	1,43	1,10	1,33	1,07	0,00	0,00	1,13	1,22	0,04	0,00	1,18	1,62
MgO	17,62	17,16	17,49	17,06	17,32	17,77	17,65	16,97	18,00	17,59	17,22	16,30	16,64
CaO	1,04	0,98	0,95	1,04	1,03	1,01	0,88	0,93	1,07	0,97	0,96	1,15	0,92
Total	102	101	100	101	99	99	99	99	101	98	97	101	100
Wo%	2	2	2	2	2	2	2	2	2	2	2	2	2
En%	51	50	51	50	52	52	51	51	52	52	51	49	50
Fs%	46	48	47	48	46	46	47	47	46	46	47	49	48
Mg#	0,525	0,512	0,524	0,51	0,530	0,529	0,522	0,520	0,529	0,532	0,525	0,499	0,509
Rims													
SiO2	52,50	51,92	51,89	51,00	50,77	50,63	48,96	52,59	50,70	49,96	50,36	51,97	51,76
Al2O3	0,51	0,52	0,52	1,01	0,52	0,73	1,36	0,46	1,40	1,15	1,07	0,59	0,51
FeO	29,56	29,54	29,79	29,82	29,25	30,21	31,56	29,50	29,44	29,89	30,06	27,48	29,38
MnO	1,42	1,43	1,49	1,48	1,47	1,43	1,40	1,38	1,44	1,41	1,35	1,15	1,46
MgO	16,12	16,33	16,60	16,00	16,42	15,93	15,30	16,78	16,62	16,25	15,84	18,02	16,79
CaO	0,87	0,86	0,77	1,03	1,64	0,92	0,91	0,90	0,95	0,99	0,90	1,15	0,91
Total	101	101	101	100	100	100	99	102	101	100	100	100	101
Wo%	2	2	2	2	3	2	2	2	2	2	2	2	2
En%	48	49	49	48	48	47	45	49	49	48	47	53	49
Fs%	50	49	49	50	48	51	53	49	49	50	51	45	49
Mg#	0,493	0,496	0,498	0,489	0,500	0,484	0,463	0,503	0,502	0,492	0,484	0,539	0,505

Table V.I.S1 (continued)

Cores	16-L4C1	16-L7C3	19-l7c5	22-L6C1	20-L2C2	20-L4C8	20-L6C1
SiO2	51,11	50,77	52,78	51,45	50,86	50,85	51,11
Al2O3	0,42	0,47	0,52	0,48	0,42	0,41	0,49
FeO	31,40	29,41	30,24	29,81	29,34	30,47	29,00
MnO	0,00	0,01	1,45	0,00	0,04	0,00	0,00
MgO	16,10	16,85	16,07	17,61	17,15	16,97	17,55
CaO	0,67	0,92	1,12	0,96	0,95	0,76	0,95
Total	100	98	102	100	99	99	99
Wo%	1	2	2	2	2	2	2
En%	47	50	47	50	50	49	51
Fs%	52	49	50	48	48	49	47
Mg#	0,477	0,505	0,486	0,513	0,510	0,498	0,519
Rims							
SiO2	50,95	52,03	51,80	50,41	53,16	51,08	50,69
Al2O3	0,62	0,70	0,62	0,55	0,87	0,64	0,68
FeO	27,21	25,12	26,94	27,14	27,12	26,81	26,39
MnO	1,22	1,05	1,13	1,18	1,27	1,12	1,09
MgO	18,65	19,40	18,80	19,67	17,46	19,12	19,36
CaO	1,11	1,33	1,17	1,06	1,09	1,10	1,16
Total	100	100	100	100	101	100	99
Wo%	2	3	2	2	2	2	2
En%	54	56	54	55	52	55	55
Fs%	44	41	44	43	45	43	42
Mg#	0,550	0,579	0,554	0,564	0,534	0,560	0,567

Table V.I.S1 (continued)

	Roseau-DOM60d1a												
Cores	RP6-L2C7	RP6-L4C2	RP6-L8C5	RP6-L9C4	RP3-L2C4	RP3-L4C12	RP3-L8C9	RP7-l1c4	RP7-l1c7	RP7-l3c6	RP7-l3c16	RP7-l4c11	RP7-l5c13
SiO2	51,34	49,70	50,48	50,81	51,40	51,46	51,30	52,03	52,30	52,07	52,66	52,39	51,92
Al2O3	0,59	0,92	0,46	0,48	0,64	0,45	0,53	0,59	0,52	0,49	0,46	0,61	1,30
FeO	28,62	31,02	28,88	29,03	29,01	27,41	28,31	28,08	27,66	28,08	27,68	28,67	29,44
MnO	1,12	1,55	1,40	1,21	1,35	1,20	1,31	1,36	1,29	1,27	1,04	1,21	1,43
MgO	18,23	15,68	17,55	17,41	17,08	17,89	17,90	17,73	17,76	17,61	17,86	17,49	17,01
CaO	0,97	0,78	1,03	0,97	0,90	1,09	1,09	1,02	0,96	1,02	1,15	0,92	0,75
Total	101	100	100	100	100	99	100	101	100	101	101	101	102
Wo%	2	2	2	2	2	2	2	2	2	2	2	2	2
En%	52	47	51	51	50	53	52	52	52	52	52	51	50
Fs%	46	52	47	47	48	45	46	46	46	46	45	47	48
Mg#	0,532	0,474	0,520	0,517	0,512	0,538	0,530	0,529	0,534	0,528	0,535	0,521	0,507
Rims													
SiO2	50,57	51,76	50,41	51,66	51,17	50,75	50,84	53,28	53,12	52,57	52,55	53,00	53,68
Al2O3	0,52	0,54	0,93	0,60	0,64	1,14	0,69	1,04	0,55	1,32	0,49	0,88	0,52
FeO	26,56	26,17	25,79	26,24	25,98	25,45	25,68	24,09	26,50	23,88	26,66	24,78	26,31
MnO	0,98	0,94	0,94	1,09	0,97	0,94	0,98	0,83	0,99	0,91	1,00	0,87	0,99
MgO	19,98	18,97	19,66	18,80	19,65	19,53	19,72	20,22	18,31	19,87	18,93	20,10	18,67
CaO	1,04	1,07	1,39	1,08	1,19	1,37	1,14	1,33	1,08	1,20	1,09	1,19	1,06
Total	100	99	99	99	100	99	99	101	101	100	101	101	101
Wo%	2	2	3	2	2	3	2	3	2	3	2	2	2
En%	56	55	56	55	56	56	56	58	54	58	55	58	55
Fs%	42	43	41	43	42	41	41	39	44	39	43	40	43
Mg#	0,573	0,564	0,576	0,561	0,574	0,578	0,578	0,599	0,552	0,597	0,558	0,591	0,558

Table V.I.S1 (continued)

Cores	RP7-l7c2	RP7-l7c4	RP7-l7c5	RP7-l8c10	RP4-l3c15	RP4-l5c1	RP4-l6c4	RP4-l7c5	RP4-l8c11	RP4-l9c6	RP2-l2c7	RP2-l5c5
SiO2	52,60	52,48	52,67	52,27	51,56	51,74	52,22	52,16	51,83	52,52	52,62	51,89
Al2O3	0,47	0,61	0,54	0,95	0,54	0,53	0,54	0,46	0,55	0,64	0,58	0,38
FeO	28,76	27,08	27,60	28,06	28,76	28,38	28,17	28,08	28,97	28,52	26,89	29,43
MnO	1,47	1,00	1,26	1,20	1,47	1,46	1,53	1,20	1,21	1,29	1,29	1,30
MgO	17,01	18,38	18,06	17,08	17,57	17,62	17,48	17,69	16,96	17,33	18,85	17,16
CaO	0,88	0,98	0,98	0,88	0,85	0,95	1,03	1,06	0,90	1,08	0,99	0,66
Total	101	101	101	100	101	101	101	101	100	101	101	101
Wo%	2	2	2	2	2	2	2	2	2	2	2	1
En%	50	54	53	51	51	51	51	52	50	51	54	50
Fs%	48	44	45	47	47	47	46	46	48	47	44	48
Mg#	0,513	0,547	0,538	0,520	0,521	0,525	0,525	0,529	0,510	0,520	0,555	0,510
Rims												
SiO2	51,61	53,57	54,13	53,80	52,48	52,73	53,25	52,78	53,11	53,46	52,70	53,36
Al2O3	1,02	0,90	0,84	1,23	0,58	1,01	0,79	0,58	0,70	0,51	0,55	0,52
FeO	25,19	25,35	25,38	24,78	27,87	25,09	25,60	26,29	26,40	26,38	26,36	26,04
MnO	0,96	1,04	0,98	0,94	1,24	0,96	0,96	1,04	0,96	0,97	0,98	0,97
MgO	19,16	18,89	18,32	17,93	17,66	18,97	18,70	18,75	18,07	18,47	19,44	18,63
CaO	1,23	1,24	1,18	1,87	0,89	1,43	1,25	1,12	1,16	1,05	1,10	1,08
Total	99	101	101	101	101	100	101	101	100	101	101	101
Wo%	3	3	3	4	2	3	3	2	2	2	2	2
En%	56	56	55	54	52	56	55	55	54	54	56	55
Fs%	41	42	43	42	46	41	42	43	44	44	42	43
Mg#	0,575	0,570	0,563	0,563	0,530	0,574	0,565	0,560	0,549	0,555	0,568	0,560

Table V.I.S1 (continued)

	Grand Fond-DOM43a1												
Cores	ROS2-l1c5	ROS2-l1c5	ROS2-l1c8	ROS2-l2c1	ROS2-l3c11	ROS2-l4c8	ROS2-l6c8	ROS7-l3c2	ROS7-l5c1	ROS7-l6c6	ROS10-l3c6	ROS10-l4c8	ROS10-l4c11
SiO2	50,06	49,86	49,83	50,68	51,29	50,67	50,57	50,58	50,85	51,22	51,26	50,75	51,21
Al2O3	0,59	0,51	0,55	0,50	0,58	0,54	0,53	0,50	0,53	0,60	0,62	0,66	0,58
FeO	29,43	27,21	28,67	27,09	26,19	27,65	28,53	28,60	28,62	26,92	28,03	29,53	28,42
MnO	1,36	1,10	1,26	1,04	0,98	1,06	1,25	1,23	1,27	1,03	1,11	1,31	1,25
MgO	16,69	18,26	17,25	18,39	19,06	18,20	17,28	17,31	17,43	18,78	17,83	16,76	17,64
CaO	1,24	1,09	0,89	1,11	1,13	1,00	0,95	1,08	1,01	1,11	1,08	0,97	0,95
Total	99	98	98	99	99	99	99	99	100	100	100	100	100
Wo%	3	2	2	2	2	2	2	2	2	2	2	2	2
En%	49	53	51	53	55	53	51	51	51	54	52	49	51
Fs%	48	44	47	44	42	45	47	47	47	44	46	49	47
Mg#	0,503	0,545	0,517	0,547	0,565	0,540	0,519	0,519	0,520	0,554	0,531	0,503	0,525
Rims													
SiO2	50,88	49,43	49,69	50,36	51,00	50,49	51,56	50,73	52,37	50,90	51,93	50,37	51,24
Al2O3	0,66	0,56	0,53	0,92	0,49	0,73	0,64	0,65	0,59	0,57	0,57	0,68	0,65
FeO	27,53	28,69	29,75	25,39	27,60	26,26	26,70	26,54	26,26	28,06	26,93	26,70	26,75
MnO	1,04	1,18	1,37	0,85	1,05	0,93	0,96	0,93	0,97	1,08	1,00	0,92	0,99
MgO	18,36	17,09	16,39	19,92	18,27	19,34	18,39	19,40	18,39	18,32	18,55	19,44	19,15
CaO	1,20	1,06	0,91	1,18	1,08	1,12	1,10	1,11	1,08	1,08	1,10	1,13	1,10
Total	100	98	99	99	99	99	99	99	100	100	100	99	100
Wo%	2	2	2	2	2	2	2	2	2	2	2	2	2
En%	53	50	49	57	53	55	54	55	54	53	54	55	55
Fs%	45	47	49	41	45	42	44	42	43	45	44	43	43
Mg#	0,543	0,515	0,495	0,583	0,541	0,568	0,551	0,566	0,555	0,538	0,551	0,565	0,561

Table V.I.S1 (continued)

Cores	ROS10-I5c11	ROS10-I6c6	ROS12-I2c9	ROS12-I3c8	ROS12-I3c8	ROS12-I3c12	ROS12-I4c8	ROS12-I5c13	ROS12-I6c7	ROS13-I1c10	ROS13-I1c10	ROS13-I2c10	ROS13-I3c1
SiO2	51,29	51,33	51,11	51,35	51,77	52,25	51,19	51,61	51,56	51,72	51,73	51,28	51,46
Al2O3	0,65	0,61	0,53	0,58	0,61	1,46	0,78	0,57	0,54	0,73	0,70	0,52	0,56
FeO	27,42	27,70	28,96	26,62	26,54	22,06	27,23	27,35	27,82	25,93	26,08	28,38	28,44
MnO	1,07	1,10	1,26	0,98	1,00	0,73	0,99	1,16	1,13	0,91	0,97	1,32	1,16
MgO	18,26	18,13	17,26	19,08	19,00	21,65	18,46	18,52	18,17	19,53	19,26	17,73	17,93
CaO	1,07	1,09	1,03	1,11	1,19	1,53	1,03	0,99	0,96	1,20	1,19	0,91	1,04
Total	100	100	100	100	100	100	100	100	100	100	100	100	101
Wo%	2	2	2	2	2	3	2	2	2	2	2	2	2
En%	53	53	50	55	55	62	54	54	53	56	55	52	52
Fs%	45	45	47	43	43	35	44	44	45	42	42	46	46
Mg#	0,543	0,538	0,515	0,561	0,561	0,636	0,547	0,547	0,538	0,573	0,568	0,527	0,529
Rims													
SiO2	51,03	50,91	52,15	50,72	51,58	51,39	51,05	51,41	52,18	50,87	53,09	51,03	50,97
Al2O3	0,51	0,63	0,64	0,55	0,60	0,63	0,55	1,06	0,64	1,52	0,62	0,56	0,68
FeO	28,43	26,83	26,80	28,89	28,71	26,90	28,92	26,19	26,38	23,12	23,97	26,78	26,32
MnO	1,19	0,97	0,96	1,22	1,14	1,01	1,21	0,93	0,95	0,75	0,90	0,98	0,96
MgO	17,58	19,54	18,58	17,82	17,26	18,85	17,06	18,62	18,67	21,80	20,38	19,22	19,85
CaO	1,09	1,08	1,09	1,01	0,97	1,15	1,00	1,44	1,11	1,39	1,14	1,08	1,12
Total	100	100	100	100	100	100	100	100	100	99	100	100	100
Wo%	2	2	2	2	2	2	2	3	2	3	2	2	2
En%	51	55	54	51	51	54	50	54	54	61	59	55	56
Fs%	46	43	44	47	47	43	48	43	43	36	39	43	42
Mg#	0,524	0,565	0,553	0,524	0,517	0,555	0,513	0,559	0,558	0,627	0,602	0,561	0,573

Table V.I.S1 (continued)

Cores	ROS13-l4c3	ROS13-l6c8	ROS13-l8c16	ROS14-l1c3	ROS14-l5c17
SiO2	51,38	51,50	51,19	51,31	51,68
Al2O3	0,51	0,51	0,52	0,91	0,54
FeO	29,57	28,72	29,46	29,04	28,55
MnO	1,33	1,33	1,35	1,29	1,27
MgO	16,99	17,44	16,98	17,36	17,49
CaO	0,89	0,85	0,85	0,76	0,90
Total	101	100	100	101	100
Wo%	2	2	2	2	2
En%	50	51	50	51	51
Fs%	48	47	48	48	47
Mg#	0,506	0,520	0,507	0,516	0,522
Rims					
SiO2	52,42	52,28	52,11	52,95	51,82
Al2O3	0,46	0,65	0,69	0,62	1,50
FeO	27,38	26,70	26,77	26,98	21,96
MnO	1,05	0,98	1,01	1,04	0,68
MgO	17,85	18,53	18,50	18,04	21,77
CaO	1,12	1,16	1,09	1,16	2,03
Total	100	100	100	101	100
Wo%	2	2	2	2	4
En%	52	54	54	53	61
Fs%	45	44	44	45	35
Mg#	0,538	0,553	0,552	0,544	0,639

Table V.I.S2: Major elements composition of equilibrium melt inclusions and their hosting orthopyroxenes. *The code name of each sample (ex: RP4L8C11-MI1) corresponds to the mount number (RP4), followed by the crystal line (L8), the crystal position into each line (C11) and the number of the analysed melt inclusion in the crystal (MI1).*

	Layou-DOM41a3		Roseau-DOM60d1a			Grand Fond-DOM43a1					
Glass	17-l3c2-MI1	6-l5c11-MI2	RP3-l2c9-MI1	RP4-l3c15-MI1	RP4-l8c11-MI2	Ros2-l2c1-MI5	Ros10-l3c4-MI2	Ros10-l4c10-MI1	Ros13-l2c13-MI2	Ros13-l1c10-MI2	Ros13-l3c1-MI3
SiO2	77,33	75,77	76,19	75,21	76,93	75,74	75,36	75,51	75,78	73,96	75,68
TiO2	0,16	0,20	0,23	0,24	0,21	0,12	0,28	0,15	0,16	0,23	0,15
Al2O3	12,39	12,56	12,23	12,74	11,74	12,07	12,96	12,43	12,19	12,86	12,16
FeOtot	2,88	3,28	3,28	3,44	3,01	3,44	3,24	3,45	3,47	3,90	3,36
MnO	0,08	0,18	0,15	0,07	0,11	0,19	0,11	0,07	0,15	0,11	0,05
MgO	0,39	0,48	0,66	0,63	0,62	0,69	0,52	0,67	0,63	1,02	0,65
CaO	1,51	1,77	1,77	2,00	1,49	1,66	1,81	1,88	1,86	1,93	1,82
Na2O	1,94	2,87	2,80	3,10	3,04	2,96	2,91	2,99	3,04	3,12	2,95
K2O	3,27	2,98	2,72	2,56	2,77	3,13	2,78	2,78	2,57	2,84	3,19
P2O5	0,05	-0,07	-0,03	0,02	0,08	0,01	0,04	0,06	0,13	0,02	-0,01
Na2O+K2O	5,22	5,84	5,51	5,66	5,81	6,08	5,69	5,77	5,61	5,96	6,14
Total	100	100	100	100	100	100	100	100	100	100	100
Hosting orthopyroxene											
SiO2	51,00	51,07	51,49	51,46	51,23	51,39	52,06	51,62	51,03	51,61	51,27
Al2O3	0,35	0,46	0,80	0,50	0,49	0,40	0,48	0,49	0,55	0,61	0,47
FeO	30,93	30,91	28,63	29,83	29,39	28,98	28,48	28,52	29,10	26,31	29,90
MnO	1,37	1,21	1,07	1,13	1,21	1,13	0,95	1,00	1,10	0,83	1,24
MgO	16,92	17,66	18,68	18,28	18,55	18,59	18,85	18,96	18,53	20,60	18,42
CaO	0,88	1,07	1,17	0,93	0,88	1,05	1,06	1,09	1,10	1,12	1,02
Total	101,45	102,37	101,84	102,13	101,76	101,56	101,87	101,68	101,40	101,08	102,32
Wo%	2	2	2	2	2	2	2	2	2	2	2
En%	48	49	52	51	52	52	53	53	52	57	51
Fs%	50	48	45	47	46	46	45	45	46	41	47
Kd(Fe-Mg)	0,25	0,25	0,31	0,30	0,33	0,31	0,24	0,29	0,29	0,33	0,31

Table V.I.S3: Major elements composition of recalculated melt inclusions and their hosting orthopyroxenes. *The code name of each sample follows the same structure as in Table V.I.S2.*

	Layou-DOM41a3			Roseau-DOM60d1a						
Recalculated glass	17-l3c2-MI3	16-l5c11-MI4	22-l2c1-MI2	RP4-l8c11-MI1	RP6-l2c7-MI1	RP6-l6c5-MI1	RP6-l6c5-MI2	RP6-l9c4-MI1	RP6-l9c4-MI3	RP8-l5c8-MI1
SiO2	76,72	74,66	75,74	75,37	76,10	75,16	76,17	76,16	76,98	75,65
TiO2	0,07	0,21	0,27	0,25	0,15	0,21	0,05	0,19	0,19	0,30
Al2O3	11,93	12,39	12,36	12,84	12,29	12,80	12,47	12,06	12,00	12,49
FeOtot	3,01	4,68	3,07	3,13	3,03	3,22	3,25	3,27	2,77	2,92
MnO	0,14	0,11	0,15	0,14	0,05	0,08	0,02	0,14	0,03	0,13
MgO	0,54	0,80	0,57	0,54	0,54	0,64	0,62	0,56	0,43	0,71
CaO	1,43	1,98	1,56	2,04	1,86	2,00	1,82	1,67	1,79	1,86
Na2O	2,88	2,61	2,91	3,37	2,86	3,33	3,09	2,89	2,81	3,08
K2O	3,25	2,60	3,33	2,33	3,05	2,54	2,46	3,04	2,92	2,83
P2O5	0,03	-0,04	0,05	0,00	0,08	0,02	0,05	0,02	0,07	0,03
Na2O+K2O	6,13	5,21	6,24	5,70	5,91	5,87	5,55	5,93	5,73	5,91
Total	100	100	100	100	100	100	100	100	100	100
Hosting opx										
SiO2	51,22	51,72	50,87	50,96	51,34	51,41	51,40	51,17	50,90	51,80
Al2O3	0,38	0,46	0,52	0,55	0,56	0,51	0,50	0,54	0,51	0,88
FeO	31,18	30,35	29,54	30,44	29,53	29,78	29,12	30,51	30,59	26,06
MnO	1,34	1,29	1,20	1,30	1,19	1,15	1,17	1,30	1,23	0,93
MgO	17,22	17,45	17,89	17,29	18,50	18,35	18,67	17,71	17,42	19,95
CaO	0,93	1,06	1,02	0,91	0,99	1,01	0,97	0,95	1,03	1,26
Total	102,27	102,33	101,04	101,44	102,10	102,21	101,83	102,19	101,68	100,88
Wo%	2	2	2	2	2	2	2	2	2	3
En%	49	50	51	49	52	51	52	50	49	56
Fs%	49	48	47	49	46	47	46	48	49	41
Recalculated Kd (Fe-Mg)	0,32	0,30	0,31	0,30	0,29	0,32	0,30	0,30	0,27	0,32

Table V.I.S3 (continued)

	Grand Fond-DOM43a1											
Recalculated glass	Ros2-l2c1-MI2	Ros2-l1c6-MI1	Ros2-l1c6-MI2	Ros2-l1c6-MI3	Ros2-l1c6-MI4	Ros2-l4c8-MI1	Ros2-l4c8-MI3	Ros2-l6c4-MI1	Ros10-l4c10-MI2	Ros10-l4c3-MI1	Ros10-l4c3-MI2	Ros10-l5c11-MI1
SiO2	74,69	74,67	74,49	75,44	74,68	75,68	75,80	76,04	75,31	75,42	74,90	75,88
TiO2	0,29	0,32	0,29	0,20	0,09	0,21	0,06	0,19	0,26	0,12	0,26	0,27
Al2O3	12,93	13,12	13,31	12,78	12,85	12,27	12,30	11,86	12,16	12,93	12,96	12,04
FeOtot	3,24	3,04	3,07	2,67	3,65	3,48	3,42	3,69	3,92	2,82	3,42	3,22
MnO	0,09	0,05	0,07	0,09	0,14	0,11	0,11	0,16	0,14	0,11	0,14	0,05
MgO	0,62	0,71	0,64	0,53	0,70	0,69	0,61	0,59	0,76	0,55	0,64	0,61
CaO	2,24	2,04	2,06	1,86	2,11	2,00	1,74	1,46	1,91	1,93	2,03	1,76
Na2O	3,36	3,15	3,17	3,06	3,06	2,89	2,99	2,97	3,09	3,49	3,07	3,18
K2O	2,44	2,87	2,84	3,34	2,58	2,65	2,97	3,03	2,49	2,48	2,67	2,83
P2O5	0,09	0,03	0,06	0,03	0,12	0,00	0,00	0,01	-0,02	0,13	-0,08	0,16
Na2O+K2O	5,80	6,03	6,01	6,40	5,65	5,54	5,97	6,00	5,57	5,98	5,75	6,01
Total	100	100	100	100	100	100	100	100	100	100	100	100
Hosting orthopyroxenes												
SiO2	51,70	51,76	51,90	51,57	51,40	51,43	51,61	50,70	51,31	51,50	51,25	51,78
Al2O3	0,58	0,83	0,70	0,62	0,61	0,56	0,43	0,42	0,52	0,57	0,51	0,41
FeO	28,05	26,96	26,80	26,97	27,92	29,01	28,22	31,10	29,21	28,90	28,84	28,93
MnO	0,92	0,96	0,96	0,97	1,02	1,10	1,07	1,38	1,04	0,98	1,07	1,04
MgO	19,19	20,03	20,13	20,08	19,45	18,65	18,77	16,96	18,57	18,64	18,60	18,72
CaO	1,14	1,04	1,03	0,98	1,07	1,12	0,98	0,85	1,04	1,09	1,09	1,08
Total	101,59	101,57	101,52	101,18	101,47	101,88	101,10	101,41	101,70	101,69	101,36	101,96
Wo%	2	2	2	2	2	2	2	2	2	2	2	2
En%	54	56	56	56	54	52	53	48	52	52	52	52
Fs%	44	42	42	42	44	46	45	50	46	46	45	45
Recalculated Kd(Fe-Mg)	0,28	0,31	0,28	0,27	0,27	0,31	0,27	0,29	0,30	0,30	0,29	0,29

Table V.I.S3 (continued)

Recalculated glass	Ros10-l5c11-MI5	Ros12-l3c8-MI1	Ros12-l3c8-MI3	Ros12-l4c8-MI2	Ros12-l2c9-MI2	Ros12-l6c7-MI4	Ros12-l6c7-MI2	Ros13-l2c13-MI3	Ros13-l1c12-MI1	Ros13-l1c12-MI1
SiO2	74,09	75,09	74,28	75,75	75,75	75,29	76,12	75,79	76,15	75,16
TiO2	0,23	0,24	0,19	0,23	0,19	0,21	0,12	0,24	0,13	0,29
Al2O3	13,22	12,35	13,03	12,49	12,30	12,33	12,29	12,14	12,40	12,37
FeOtot	3,34	3,73	3,32	2,95	3,18	3,55	3,15	3,44	2,91	3,68
MnO	0,17	0,10	0,12	0,02	0,12	0,13	0,23	0,14	0,04	0,12
MgO	0,63	0,84	0,66	0,55	0,56	0,70	0,57	0,65	0,54	0,72
CaO	2,37	1,89	1,88	1,86	1,94	1,65	1,71	1,80	1,55	1,91
Na2O	3,29	2,84	3,15	3,12	3,13	3,27	2,84	3,03	3,34	3,15
K2O	2,62	2,99	3,27	2,87	2,74	2,87	3,03	2,77	2,92	2,60
P2O5	0,05	-0,08	0,11	0,14	0,09	0,00	-0,06	0,02	0,03	0,01
Na2O+K2O	5,91	5,83	6,42	6,00	5,87	6,14	5,87	5,80	6,26	5,74
Total	100	100	100	100	100	100	100	100	100	100
Hosting orthopyroxenes										
SiO2	51,51	52,04	51,65	51,69	51,39	51,58	51,77	51,31	51,46	51,29
Al2O3	0,39	0,63	0,62	0,52	0,51	0,43	0,44	0,45	0,46	0,52
FeO	29,07	27,23	27,79	28,28	29,94	29,08	28,74	29,38	28,72	28,91
MnO	1,07	0,87	0,95	1,08	1,17	1,08	1,20	1,17	1,03	1,14
MgO	18,67	20,30	19,62	18,92	17,65	18,60	18,54	18,40	18,87	18,95
CaO	1,09	1,16	1,16	0,99	1,04	1,03	0,98	1,07	0,94	1,12
Total	101,80	102,23	101,79	101,48	101,70	101,79	101,67	101,78	101,49	101,93
Wo%	2	2	2	2	2	2	2	2	2	2
En%	52	56	54	53	50	52	52	52	53	53
Fs%	46	42	43	45	48	46	46	46	45	45
Recalculated Kd(Fe-Mg)	0,29	0,30	0,28	0,28	0,30	0,31	0,28	0,30	0,28	0,30

PART II:

TIMESCALES FROM DIFFUSION MODELLING

Timescales of pre-eruptive reheating recorded in orthopyroxenes from sequential eruptions in Dominica (Lesser Antilles Arc)

Solaro C. [a]***, Balcone-Boissard H.*** [b]***, Morgan D.J.*** [c]***, Boudon G.*** [a]***, Martel C.*** [d]

[a] Institut de Physique du Globe de Paris, Sorbonne Paris Cité, Univ. Paris Diderot, CNRS, F-75005 Paris, (France) ; solaro@ipgp.fr

[b]Sorbonne Universités, UPMC Univ. Paris 06, CNRS, UMR 7193, ISTEP, F-75005, Paris, (France)

[c]School of Environmental Sciences, University of Leeds, Leeds (UK)

[d] Institut des Sciences de la Terre d'Orléans (ISTO), Orléans, (France)

Abstract

Recent studies demonstrate that the perturbations in magma storage conditions can be investigated using the compositions of the crystal cargo of the magma, and the timescales determined by modelling the diffusive relaxation of crystal chemical gradients. Studies focusing on large, silicic eruptions (10 to 1000 km^3 DRE/eruption) show that rheologically-locked crystal populations can be re-mobilized over timescales of decades to centuries prior to eruption, making these systems more dynamic than previously suspected.
Using diffusion modelling on orthopyroxenes, here we quantify timescales of a pre-eruptive heating event characterizing three major, ignimbritic eruptions of Dominica (Lesser Antilles Arc): Layou (~51kyrs cal BP), Roseau (~33kyrs cal BP) and Grand Fond (~24kyrs cal BP).
Diffusion modelling has been applied along the b-axis of 66 zoned orthopyroxene recognised in the three eruptions, at a magmatic temperature of 850°C (±25) and without correction for oxygen fugacity.
Regardless of the orthopyroxene zoning pattern, timescales for Layou (24 opx) and Roseau (21 opx) show that the heating occurred tens of years prior to eruption. For the Grand Fond eruption (21 opx), complexities of growth superimposed upon diffusion profiles prevented us from estimating timescales via this method.
In the light of these results we propose that the two magma reservoirs are rejuvenated and heated by 25-30 °C about 10 yrs prior to eruption by the injection of hotter magma, creating the reverse zoning patterns of erupted orthopyroxenes.

Keywords: Dominica eruptions, ignimbrite, Orthopyroxenes Fe-Mg interdiffusion, rejuvenation, heating

V.II.1. Introduction

Unravelling the dynamics and timescales of magma reservoir processes (e.g. mixing-mingling, decompression, heating) prior to eruption is key to understanding how volcanic systems behave, for instance how large explosive eruptions can be triggered. It has been recently demonstrated that for several large volumes eruptions magma can be re-mobilised, assembled and brought into eruptions in short timescales of decades to centuries, significantly shorter than the long rest periods (several thousand years) characterizing these volcanic systems (Costa et al., 2004; Charlier et al., 2012; Druitt et al., 2012; Allan et al., 2013; Chamberlain et al., 2014; Bouvet de Maisonneuve et al., 2015). These results underscore the importance of the temporal component in the description of such systems, especially for volcanic areas characterised by dense human settlement where better planning and more appropriate hazard mitigation can be crucial to minimise socio-economic impact of eruptions (Self, 2006).

In the last decades the method of intracrystalline diffusion modelling has been increasingly utilised to study timescales of pre-eruptive processes. Because of the differential diffusivities (m^2/s) of different elements in crystals, this technique allows investigation of timescales spanning hours to thousands of years and, being applicable to single crystals, it can yield timescales of singular processes. Several minerals have been studied, including olivine (Humler and Whitechurch, 1988; Costa et al., 2003, 2004; Costa and Dungan, 2005; Costa et al., 2010; Kahl et al., 2011, 2015; Ruprecht and Plank, 2013; Rae et al., 2016), plagioclase (Zellmer et al., 1999; Ruprecht and Wörner, 2000; Ginibre et al., 2002a, 2002b , 2004; Zellmer et al., 2003; Saunders et al., 2010; Shcherbakov et al.,2011; Druitt et al., 2012; Bouvet de Maisonneuve et al., 2015), pyroxenes (Morgan et al., 2004; Saunders et al., 2012; Allan et al., 2013; Barker et al., 2016) or magnetites (Nakamura et al., 1995; Boudon et al., 2015).

Several studies have already been conducted on different systems, from mid ocean ridge volcanism (Humler and Whitechurch, 1988; Costa et al., 2010) to arc magmatism (Nakamura et al., 1995; Costa and Chakraborty, 2004; Tomiya and Takahashi, 2005; Charlier et al., 2012; Matthews et al., 2012; Druitt et al., 2012; Allan et al., 2013; Barker et al., 2016), involving different compositions of magmas and eruptive dynamics and using different crystal-element couples. For example, on the basis of the records of changes in the composition of feldspars, Druitt et al. (2012) showed that the transfer and assembly of magmas before the major Minoan caldera-forming eruption of Santorini volcano (40-60 km^3) took place over relatively short time, between centuries to months prior to the eruption. The Fe-Mg interdiffusion in

orthopyroxenes of the Oruanui eruption of Taupo volcano (New Zealand), involving a volume of 530 km^3, helped to constrain the timing of decompression events occurring in the centuries before the eruption (Allan et al., 2013). Fe-Mg interdiffusion in orthopyroxenes is also applied by Barker et al. (2016) to assess timescales of priming and accumulation of magma prior to the three youngest eruptions (<2.15 ka) of the same volcanic centre. Their results indicate that the rapid heating and priming of the mush from which the final melt-dominant magma body is extracted occurred in < 120 years prior to eruption. Still in the Taupo Volcanic Zone, the study conducted by Matthews et al. (2011) for the Whakamaru eruption (~340 ka, >1000 km^3) on quartz zonation and diffusion modelling of Ti in quartz, shows that timescales of the final recharge rejuvenating the mush reservoir are in the range of 10-60 years before eruption. These studies show that eruptible melt volumes characterising large silicic eruptions may be assembled rapidly, over timescales which are geologically very short – decades to centuries before eruption – especially when compared with the preceding repose period of the system.

We here present a study on timescales of pre-eruptive dynamics relating to three large ignimbritic eruptions of Dominica (Lesser Antilles arc) that occurred between 50 and 20 ka BP. These repetitive, voluminous eruptions of Dominica raise questions about how magma is stored (see Chapter IV) and evolves (see Chapter V-Part I) prior to eruptions, and how fast magma can be remobilised into an eruptible body in the Lesser Antilles arc environment. We assess these questions through examination of compositionally-zoned orthopyroxene crystals that preserve a record of pre-eruptive reservoir processes and retain timescale information, on the basis of the BSE-EPMA intercalibration method developed by Allan et al. (2013).

Our work is based on the detailed analysis of orthopyroxene compositional zoning and on the reservoirs model presented in the previous Part I. The Crystal System Analysis applied on orthopyroxenes, enabled to define the reservoirs as highly crystalline dacitic mush bodies suffering of a pre-eruptive heating process of ~25-30°C caused by an underplating magma, of a composition likely similar to the resident one.

Here we use modelling of diffusional modification of orthopyroxene compositional zoning patterns recognised in Part I to constrain the pre-eruptive timescales of this heating process. In the following pages we will report details about the diffusion modelling method including the choice of appropriate diffusion coefficient, the effect of oxygen fugacity considerations on calculations and the detail of intercalibration method (Allan et al., 2013) used to fit profiles. Following that introduction, we will present timescales results obtained on the three eruptions

of Layou, Roseau and Grand Fond and discuss then the implication of these timescales on the dynamics and the rejuvenation of the reservoirs before eruption.

V.II.2. Geological context

Dominica island is located in the central part of the Lesser Antilles arc (14°14' 00'' N, 16°21'00''W, Fig.V.II.1). The arc itself is the expression of the westward subduction of the North-South American Plates under the Caribbean one at an average rate of 2 cm/yr (Wadge, 1984). North of Dominica the arc presents a bifurcation with two groups of islands: the eastern-older group of extinct volcanoes (Limestone Caribees: Anguilla to Marie Galante) and the western-younger group of active volcanoes (Volcanic Caribbees: Saba to Basse Terre). South of Dominica the two segments merge and one main group of islands is recognized (Dominica to Grenada). The arc is also physically segmented with a North segment trending at 330° and a South segment trending at 20° (Macdonald et al., 2000). Located at the junction of the two segments where the arc has its maximum curvature, Dominica is characterised by four potentially active volcanic centres (Morne aux Diables, Morne Diablotins, Morne Trois Pitons-Micotrin and Plat Pays, Lindsay et al., 2005; Fig.V.II.1), high volcanic production rates (up to ~40 km^3 in the last 100 000 yr, Wadge, 1984), presence of voluminous, partially-welded pyroclastic flow deposits recognised on both coastlines of the island (Smith et al., 2013; Howe et al.,2014).

Five main ignimbritic pyroclastic flow deposits are currently recognised on the island: the Grand Bay, the Roseau, the Grand Fond, the Layou and the Grande Savane ignimbrites (Lindsay et al., 2003; Smith et al., 2013; Howe et al., 2014; Boudon et al.,in prep; chapter III Fig.V.II.1). These deposits have been recently mapped, analysed and dated by Boudon et al. (in prep; chapter III this volume). The authors provide new ^{14}C ages for the Layou, Roseau and Grand Fond ignimbrites respectively at ~49 ka, ~30 ka and ~22 ka, each of them representing erupted magma volumes of the order of several km^3/DRE (Dense Rock Equivalent). The precise eruptive center at the origin of each eruption is still a matter of debate. Current study (Smith et al., 2013; Howe et al., 2014; Howe et al., 2015) consider the Roseau and Grand Fond ignimbrite to both originate from the Micotrin eruptive centre, while the closely spaced Layou deposit is likely to be sourced from Morne Trois Pitons. On the basis of a different geochemical signature in Layou products, the recent study of Boudon et al. (in prep. chapter III) suggests instead that Layou, is likely to be linked with the Morne Diablotins eruptive centre.

A detailed stratigraphic description of Roseau, Layou and Grand Fond outcrops is presented in chapter III. Generally, each deposit is subdivided in a basal plinian fallout part (representing <10% of total erupted volumes), covered by thick (up to 100 m) pumiceous pyroclastic density current deposits with variability in grain size and distribution (see chapter III for more details).

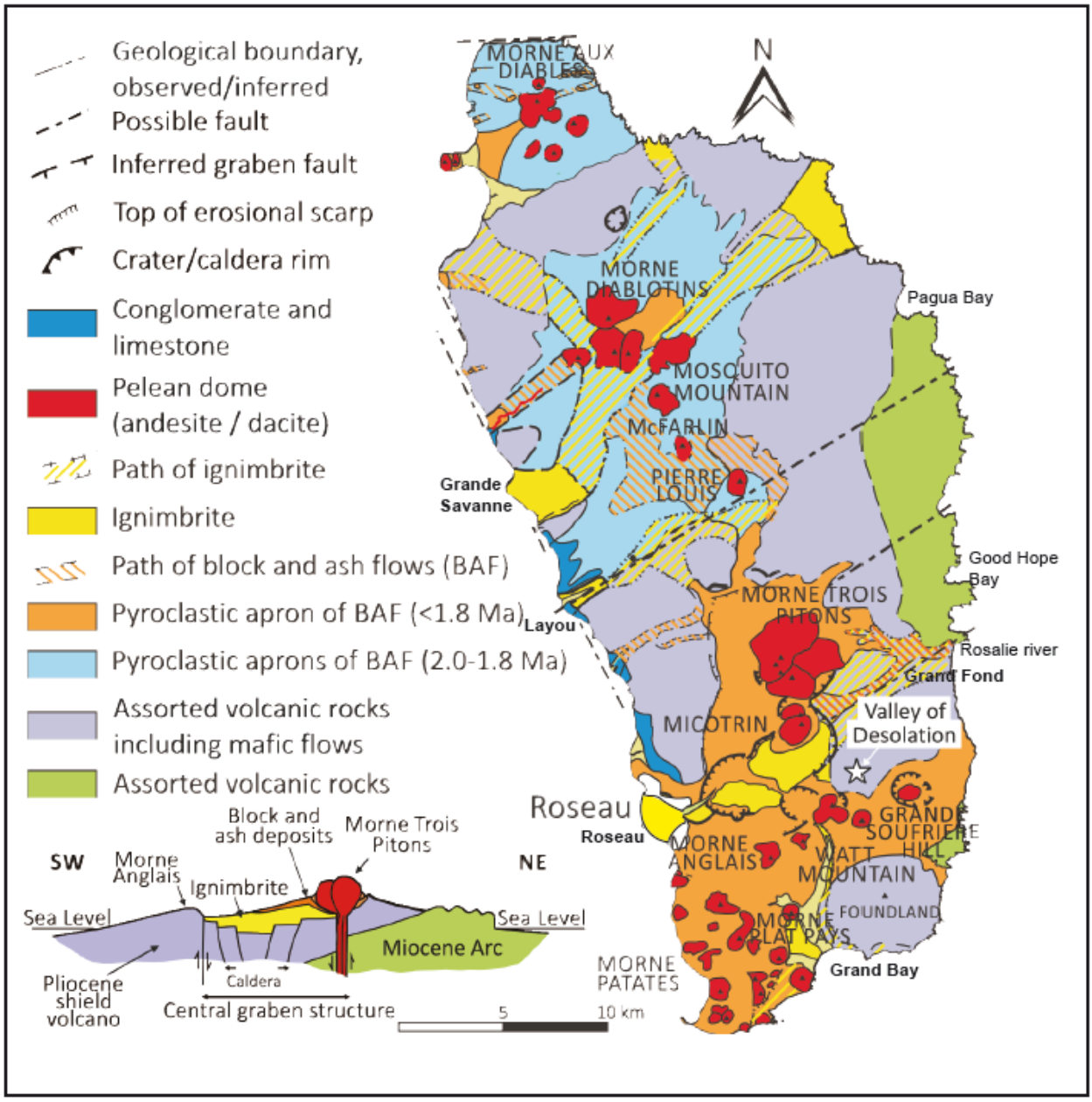

Figure V.II.1: Simplified geological map of Dominica island *(modified from Mayer, 2016 and simplified from Roobol and Smith, 2005). The main eruptive centres are marked in red while the ignimbritic deposits are marked in yellow.*

V.II.3. Method

V.II.3.1. Samples and analytical techniques

Pumices and orthopyroxenes mounts used in this study correspond to those reported in Part I. They are white, homogeneous pumices collected from the basal plinian fallout part of Layou (51 kyrs cal BP), Roseau (33 kyrs cal BP) and Grand Fond (24 kyrs cal BP) outcrops. They have been carefully treated in order to obtain isolated crystals ready to be analysed for their texture and chemical composition. Detailed methods used for pumice treatment and sample preparation are reported in the previous Part I. Here we summarise the orthopyroxene sample preparation and method used for diffusion modelling.

Orthopyroxene single crystals were mounted in epoxy resin in order to obtain crystal b-c sections needed for diffusion modelling along the b-axis of crystals. All crystals have been imaged by SEM (UPMC, Paris) and analysed for major elements by electron microprobe (Cameca SX-Five and SX-100, Service Camparis, Paris). Further details of analytical settings, strategy and method for identification of zoning patterns can be found in the Method section of the previous Part I.

V.II.3.2. Diffusion modelling

In this section we will give a short overview of the recent studies concerning diffusion modelling in orthopyroxenes and specify which diffusion coefficient formulation and modelling technique is used in this study.

V.II.3.2.1 Diffusion coefficient

A complete review of the state of the art about diffusion in minerals is given by Costa et al. (2008), Chakraborty (2008), Cherniak and Dimanov (2010), Costa and Morgan (2010). First approaches on experimental determination of cation diffusion coefficient in pyroxenes crystals date back to 1980 (^{45}Ca et ^{57}Fe self-diffusion in diopside, McCallister et al., 1979; interdiffusion Al-Fe and ^{26}Mg and ^{43}Ca self-diffusion in diopside, Freer et al., 1982; Brady and McCallister 1983).

With the development of techniques of high spatial and analytical resolution in the late 80's and 90's, new, detailed studies have been performed. A first indirect estimation of the Fe-Mg interdiffusion coefficient in orthopyroxenes was performed by Ganguly and Tazzoli (1994). In this study, the Fe-Mg interdiffusion coefficient along the c- and b-axis of orthopyroxenes is derived from estimates of order-disorder kinetics and cations ordering over M1 and M2 sites of orthopyroxenes [Fe^{2+} (M2) + Mg (M1) ↔ Fe^{2+} (M1) + Mg (M2)], obtained by Besançon (1981), Anovitz et al. (1988) and Molin et al. (1991).

The final parameterization of Ganguly and Tazzoli (1994) is:

$$LogD(Fe-Mg)_{c-b} = -5.54 + 2.6\ X_{Fe} - \frac{12530}{T} \qquad \text{(Eq. 1)}$$

where D is the interdiffusivity, D_0= -5,54 [cm^2/s]) is the pre-exponential factor, X_{Fe} is the molar fraction of the ferrosilite component and T is the temperature in Kelvin. Ganguly and Tazzoli (1994) equation is formulated for T= 500-800°C, oxygen fugacity WI to WI+0.8 (WI= Iron-Wüstite buffer) and X_{Fe} = 0.10-0.50. In their paper, Ganguly and Tazzoli conjectured that the oxygen fugacity dependence could follow the same form as that for olivine, with an exponent of 1/6, assuming the same mechanism of vacancy generation through iron oxidation.

A further study of Klugel (2001) in iron rich orthopyroxenes (in the temperature range 1050-1200°C and at QFM [quartz-fayalite-magnetite] oxygen buffer) reports a diffusion coefficient of $D_{Fe\text{-}Mg} = 3 \times 10^{-19}$ [m^2s^{-1}] at T = 1130 °C. If extrapolated to higher temperatures and oxygen fugacity, results of Ganguly and Tazzoli (1994) are in good agreement with those of Klugel (2001).

A more recent experimental study about Fe-Mg interdiffusion coefficient in mafic minerals is from Mueller et al. (2013), presenting results on Fe-Mg interdiffusion coefficient along the c-axis of clinopyroxenes (Di_{93}, Diopside in mol%) on a range of experimental conditions of 800-1200°C in temperature and 10^{-11} -10^{-17} bar in oxygen fugacity (±0.1 log units), closer to Dominica storage parameters compared to Ganguly and Tazzoli (1994) parameterization.

The final parameterization of Mueller et al. (2013) uses a simple Arrhenius equation to describe the effect of temperature on diffusion coefficient as following:

$$D_{Fe-Mg} = 2.77\ (\pm 4.27) \times 10^{-7} \times \exp((-320.7\ \pm 16.0)\ /RT) \qquad \text{(Eq.2)}$$

Were D_0 =2.77 (± 4. 27) * 10^{-7} [m^2/s] and Q (activation energy) = -320.7± 16.0 [kJ/mol].

A final, and recent, experimental study has been conducted by Dohmen et al. (2016) on Fe-Mg interdiffusion in orthopyroxenes (Fs_9 and Fs_1, Fs= Ferrosilite in mol%) parallel to the three main crystallographic axes at experimental conditions fixed in the range 870 – 1100 °C, atmospheric pressure and oxygen fugacity between 10^{-11} and 10^{-7} Pa. For the less Fe-rich composition (Fs_1) a simple Arrhenius relation is obtained to describe diffusion with log(D_0 [m^2/s])= -3.78 ± 1.26 and Q= 377 ± 30 kJ/mol.

Contrariwise, for the more Fe-rich composition (Fs_9) authors obtain a clear , though weak, dependence of diffusivity on oxygen fugacity and data for this orthopyroxene are fitted with the following parameterisation:

$$logD^{c}_{Fe-Mg} = \log D_0 - \frac{Q}{\ln(10)RT} + n\, log\, fO_2 \qquad \text{(Eq.3)}$$

Where Q= 308 ± 23 [kJ/mol], log (D_0 [m^2/s]) = 5.95 ± 0.83 and n= 0.053 ± 0.027.

Dohmen et al. (2016), attribute the difference in dependence on oxygen fugacity in between the two crystals to a change in diffusion mechanism from a fO_2-dependent TaMED mechanism (transition metal extrinsic diffusion) in Fs_9 to a fO_2-independent PED one (pure extrinsic diffusion) in Fs_1. As a consequence, besides the effect of oxygen fugacity on diffusion, the major and minor element composition (trivalent major and minor cations) of the orthopyroxene has a significant effect on diffusion rates. A positive dependence of diffusivity on X_{Fe} has been observed by these authors, even if not precisely quantified. This is somewhat in agreement with the calculations of Ganguly and Tazzoli (1994), which display a significant compositional control (the exponent 2.6 in equation 1). Similarly to what has been discussed by Ganguly and Tazzoli (1994), Dohmen et al. (2016) also observe a diffusion anisotropy in orthopyroxenes, with $D^{c}_{Fe-Mg} \geq D^{b}_{Fe-Mg} \geq D^{a}_{Fe-Mg}$, and $D^{c}_{Fe-Mg} = 3.5\ D^{a}_{Fe-Mg.}$ A summary of the parameterisations of the three studies presented here can be found in Table V.I.S1 (Supplementary Material).

V.II.3.2.2 Effect of oxygen fugacity

Given the presence of Fe (in both Fe^{2+} and Fe^{3+} oxidation states) in the mineral structure and composition of pyroxenes, diffusion dependence on oxygen fugacity has to be discussed in detail. For different mafic minerals it has been suggested that increasing oxygen fugacities would cause an increase in diffusion rates, as a direct consequence of more abundant crystal lattice vacancies due to $3Fe^{2+} \rightarrow 2Fe^{3+} + V^{\cdot}$ substitution, where $V^{\cdot}$ denotes a vacancy (Buening and Buseck, 1973; Chakraborty and Ganguly, 1991; Ganguly and Tazzoli, 1994; Cherniak, 2001; Stimpfl et al., 2005; Dimanov and Wiedenbeck, 2006; Ter Heere et al., 2006).

By analogy with diffusion results on olivine (Buening and Buseck, 1973) and garnet (Charkraborty and Ganguly, 1991), Ganguly and Tazzoli (1994) speculated an oxygen fugacity dependence of the form:

$$D\alpha\ \left(\frac{fO2_{sample}}{fO2_{reference}}\right)^{n} \qquad \text{(Eq.4)}$$

with n = 1/6; this was the parameterisation used in Allan et al., (2013).

The recent experimental results of Mueller et al. (2013) on clinopyroxenes at oxygen fugacities going from 1×10^{-11} 1×to 10^{-17} bar, show no significant diffusivity variations with fO_2, suggesting a simple Arrhenius equation. This result contrasts with that of Dimanov and Wiedenbeck (2006), who found a dependence of the Fe-Mg interdiffusion coefficient on fO_2 (in the range of fO_2 of $<1\times10^{-7}$ and $>1\times10^{-15}$ bar). As the Fe content of starting samples from Dimanov and Wiedenbeck, (2006) and Mueller et al. (2013) is the same, Mueller et al. (2013) propose that the difference could be related to the high Al content present in the crystal used for their study. The $3Mg^{2+} \rightarrow 2Al^{3+} + V^{\cdot}$ happens more readily than the $3Fe^{2+} \rightarrow 2Fe^{3+} + V^{\cdot}$ substitution, so that in crystals containing Al, vacancies may be created by Al exchange, which does not depend on oxygen fugacity.

The study of Dohmen et al. (2016) argues for a minor dependence of the diffusion coefficient on oxygen fugacity (n=1/20 instead of 1/6). When Dohmen et al. (2016) results are compared to the parameterisation of Ganguly and Tazzoli (1994) with applied oxygen fugacity correction (Allan et al. 2013), it appears that the speculated Ganguly and Tazzoli (1994) fO_2 correction would overestimate the fO_2 dependence, making calculated diffusivities about one order of magnitude higher than the measured ones at common geological conditions (close to NNO [Nickel- Nickel Oxide] buffer). On the contrary when the Ganguly and Tazzoli (1994) parameterisation is used without fO_2 correction, it appears to be very consistent with the Dohmen et al. (2016) experimental results.

From the different studies it appears evident that the dependence of diffusivities on oxygen fugacity is still a debatable parameter (Ganguly and Tazzoli, 1994; Dimanov and Wiedenbeck, 2006; Allan et al., 2013; Mueller et al., 2013; Dohmen et al., 2016). Taking into account the relative agreement in between Ganguly and Tazzoli (1994) calculation (extrapolated at the proper temperature range) and Dohmen et al. (2016) experimental results, here we model Fe-Mg interdiffusion in crystals using the equation of Ganguly and Tazzoli (1994) without correction for oxygen fugacity (as in Eq. 1), due to the high X_{Fe} of our samples which overlaps with the range studied by Ganguly and Tazzoli (1994) and which is notably more Fe rich than the compositions studied by Dohmen et al., (2016).

In the discussion section we will return to the effect of including fO_2 in our modelling and the results obtained with this correction, with Dohmen et al. (2016) equation (see Eq. 3).

V.II.3.2.3 Modelling method

Diffusion profiles have been all modelled at 850°C (with a nominal uncertainty of ±25°C), after the experimental results of Solaro et al. (in prep) (chapter IV). To constrain magma storage conditions, Solaro et al. (in prep) performed phase equilibria experiments on natural products of both Layou and Roseau eruptions in the range of 800-900 °C, 150-400 MPa and at a fixed oxygen fugacity of ≈ NNO +1 (NNO= Nickel- Nickel oxide buffer, as defined by Heubner and Sato, 1979). Both water saturated (XH_2Oin= 1) and water under-saturated (XH_2Oin= 0.8) conditions have been experimented. Results argue for storage at 300-400 MPa, 850°C and 6-8 wt% H_2O in the final melt.

Fe-Mg interdiffusion modelling has been performed with the method presented by Allan et al. (2013): using high-resolution microprobe data, high-resolution BSE images of orthopyroxenes were calibrated for effective Mg number, in order to extract detailed zoning patterns (spatial resolution approaching 500 nm and analytical resolution close to 0.2 mol%), (Fig.V.II.2).

High resolution BSE images were treated with the freely-available Image J image-processing program (http://rsb.info.nih.gov/ij/). This was accomplished by orienting BSE images so that the main rim-core boundary of interest for each crystal was oriented in North-South direction (Fig. V.II.2a). From each image an East-West greyscale profile was extracted (Fig. V.II.2c), averaging over a selected area. In effect, this averages together many individual pixel traverses across the image, necessary to reduce noise (Fig. V.II.2b).

Our profiles were all measured across the *c*-axis, in the *b*- crystal directions and away from the terminal faces of crystals (Fig.V.II.2a), as traverses measured along the *c*-direction of orthopyroxenes can often return anomalous profiles, since the sectors oriented along the *c*-axis are vulnerable to recrystallization, which can destroy the original zoning profile (Allan et al., 2013).

Profiles have been extracted, and modelled, for 66 selected zoned orthopyroxene (24 Layou, 21 Roseau and 21 Grand Fond), on both normal and reverse zoning for Layou and Grand Fond and only on reverse zoning for Roseau (given the abundance of reverse zoned crystals in this eruption). The internal consistency of timescales obtained by this modelling method is tested by modelling several profiles on the same core-rim boundary of the same crystal and verify for the acquisition of comparable timescales.

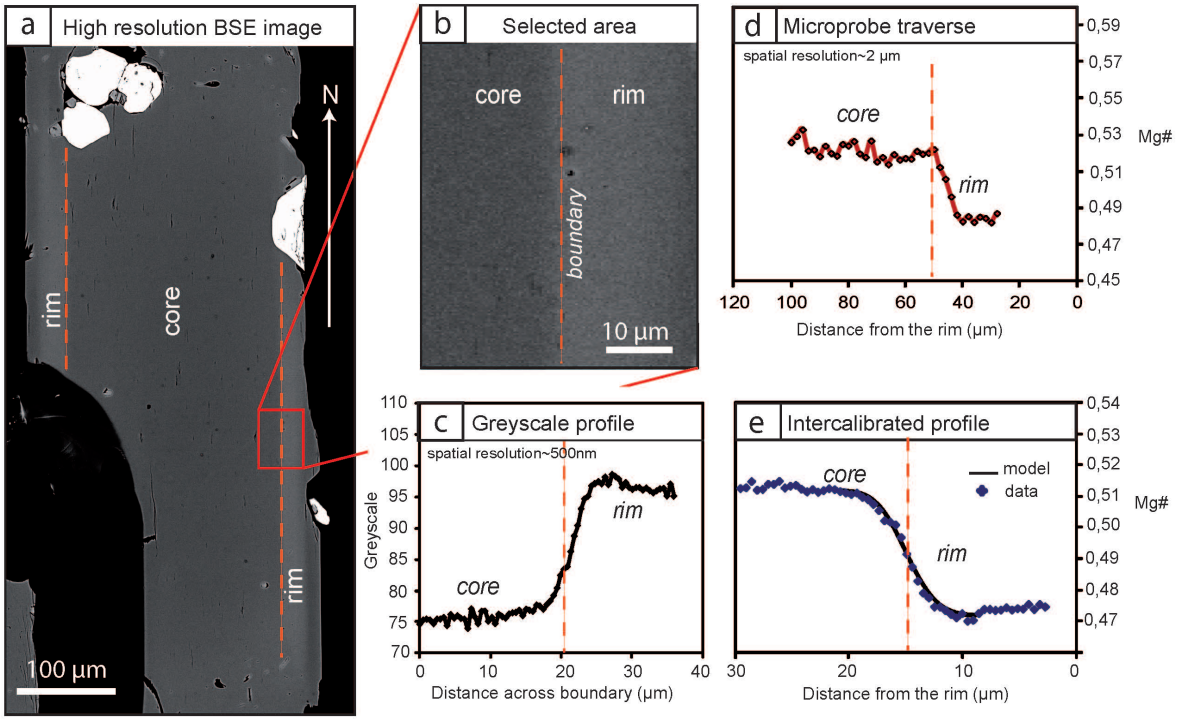

Figure V.II.2: From crystal to diffusion profile. *(a) High resolution backscattering image (BSE image) of an orthopyroxene oriented with the c- axis in N-S direction. The core and the rim parts of the crystal are identified; (b) Detailed BSE image of the main core-rim boundary; (c) Core to rim greyscale profile: averaged greyscale values over the selected area of the boundary in (b) using the free software ImageJ; (d) Microprobe Mg# (Mg# = Mg/(Mg+*Fe_{tot}*) rim to core traverse over the selected area of the crystal. Spatial resolution is of 2 µm; (e) Final modelled profile resulting from the intercalibration of BSE greyscale values on microprobe analyses.*

As we proceeded in modelling without correction for oxygen fugacity, the largest source of uncertainty in diffusion modelling, and hence in the diffusion timescales retrieved by this method, derive from the temperature. For the case study of Oruanui eruptions, Allan et al. (2013) have already proved that varying the input values of temperature of ±50°C in the Fe-Mg interdiffusion modelling for the same boundary implies change of several decades, up to one order of magnitude, in the calculated timescales.

Phase equilibria results (see chapter IV) allow to precisely constrain the pre-eruptive temperature at 850°C for the three eruptions, with an uncertainty of ± 25°C deriving from the spacing of experimental run conditions, being the current uncertainty values accepted for temperature in diffusion modelling.

The modelling was accomplished using 1-D modelling, an acceptable procedure as the profiles are very short compared to the scale of the crystal, and diffusion is effectively normal to the long face with no additional components. As the diffusion coefficient of Ganguly and

Tazzoli (1994) is composition-dependent, model profiles develop asymmetry that is more pronounced as the compositional contrast becomes greater. The modelling of such profiles can be eased by exploiting the property that 1-D diffusion profiles proportionally share symmetry, so that if the compositional boundary conditions are the same, the difference between a profile at two different times is merely a stretch factor along the mean diffusion direction. This also holds true in the case of composition-dependent diffusion, where the curve shape is determined by the degree of compositional contrast, but the curve width is dependent on time. By using a library of profiles calculated for particular values of compositional contrast, the appropriate curve shape to apply to a natural crystal can be selected from the library based upon composition data, and then scaled in width to solve for time, leading to very rapid processing. The scaling factor needed is a simple expression of crystal composition, the diffusivity used for the library profiles, the diffusivity in the crystal and the ratio of diffusion timescales in the library and the timescale of the crystal. As the scaling factor can be determined from data, the timescale for the crystal can be simply solved.

V.II.4. Petrology of natural products

The general petrology of natural products has been detailed in Part I. Here we summarise the main characteristics of samples used for the study. Pumice samples from the basal plinian fallout deposits can all be classified as homogeneous crystal rich (~30-35 vol%) andesites-dacites (63-66 wt% SiO_2, ~4.5-5 wt% Na_2O+K_2O), with the common crystal phase assemblage made of plagioclase, orthopyroxene, amphibole, clinopyroxenes and Fe-Ti oxides (ilmenite, titanomagnetite), (see chapter III and chapter IV).

Results of phase equilibria experiments performed on these samples (see chapter IV) enable us to constrain pre-eruptive magma storage conditions for the three eruptions at a temperature of 850°C, pressure of 400 MPa, oxygen fugacity of $fO_2 \sim \Delta NNO+1$ and with ~7-8 wt% H_2O in the melt for Layou and ~6-7 wt% H_2O in the melt for Roseau and Grand Fond.

Bulk-rock homogeneity of samples composition is contrasted by high level of heterogeneity in single crystals textures and chemical composition. Plagioclases and orthopyroxenes (see Part I), present zoning patterns suggesting the occurrence of variable regimes during the storage period (changes in temperature, pressure, oxygen fugacity).

Orthopyroxene zoning patterns and composition were detailed in the preceding Part I. Here we will limit the discussion to presenting the results about timescales obtained by modelling diffusional relaxation of crystal zoning.

V.II.5. Results

Fe-Mg interdiffusion has been modelled on 24 crystals of Layou, 21 crystals of Roseau and on 21 crystals of Grand Fond eruptions. All the modelling has been conducted at a fixed temperature of 850°C (±25°C), with no dependence of oxygen fugacity on the diffusion coefficient following the indications from Dohmen et al. (2016), that this is a weak effect.

We use the diffusion coefficient of Ganguly and Tazzoli (1994) (i.e. D dependent on crystal composition, with D ~10^{-20} [m^2 s^{-1}]). Initial condition is a step-wise profile (i.e. instantaneous growth followed by diffusional relaxation). Examples of modelled diffusion profiles for Layou and Roseau are shown in Figure V.II.3.

Results show a significant peak of Fe-Mg interdiffusion timescales at 3-10 years before eruption for both Layou and Roseau eruptions (Fig. V.II.4a and b).

Contrariwise, Grand Fond crystals have revealed important problems linked with particular profile shapes inconsistent with pure diffusive modification of an initial step-wise growth boundary (Fig. V.II.5). Indeed, Grand Fond profiles show the presence of high frequency bumps and peaks on the slope (Fig. V.II.5b) or/and on the rim side (Fig. V.II.5a and c) of the compositional profiles. As these profiles cannot be modelled with a simple 1D diffusive modification from an initial step-wise boundary, here we do not exploit timescales results obtained on this eruption.

Nevertheless, it can be stated that the bumps and peaks recorded in profiles are likely to be linked with the kinematics of rapid growth of crystals in changing environments shortly before the eruption, producing overlapping and complex signals when combined with diffusive relaxation of the initial chemical gradients. The short length-scale of the zonation patterns, together with their complexity, argues for a timescale comparable to or shorter than that found for the preceding Layou and Roseau eruptions.

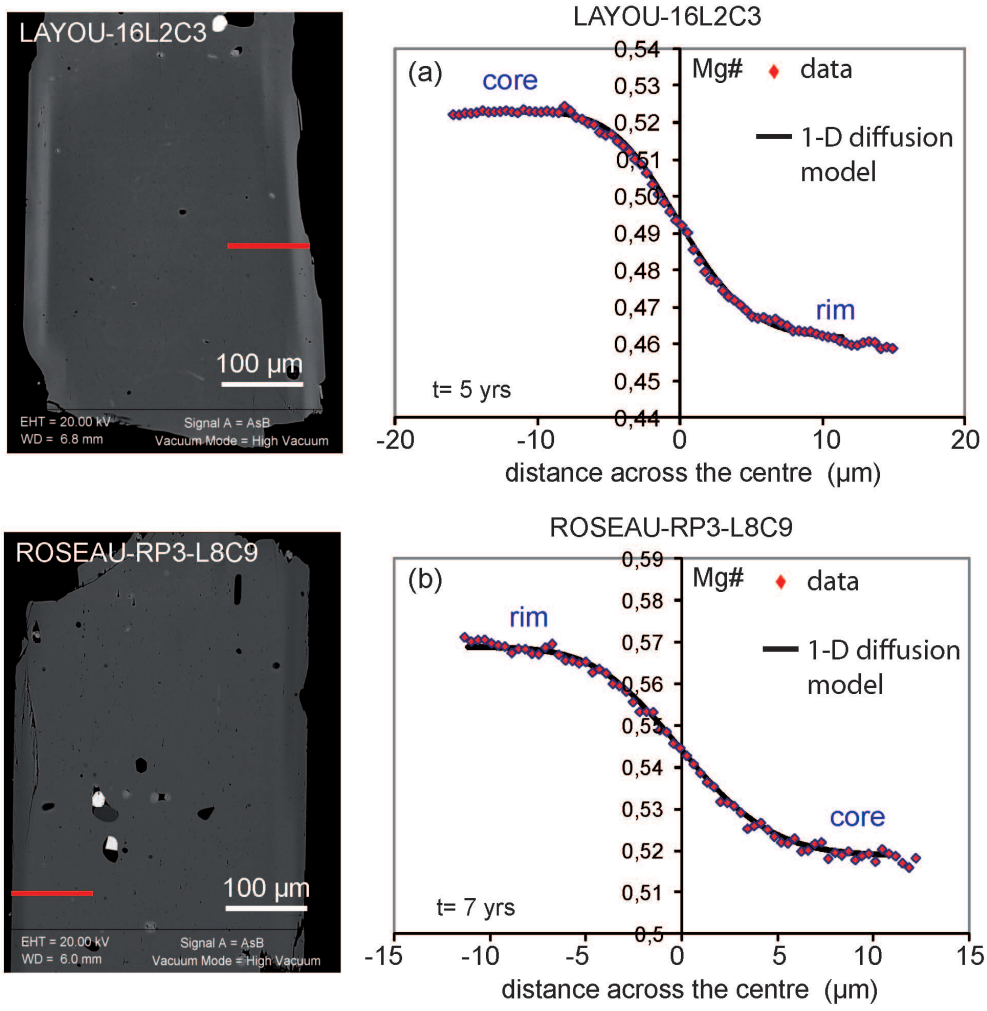

Figure V.II.3: Examples of two modelled diffusion profiles for Layou (a) and Roseau (b). *The red line on each BSE image (left) indicates the profile position (total EPMA profile) on the respective orthopyroxene. Diffusion profiles (right) are reported as Mg# [Mg#= Mg/(Mg + Fe_{tot})], as a function of the distance from the centre of the profile (in µm). Red rhombs: EPMA and BSE greyscale intercalibrated data; black line: diffusion model.*

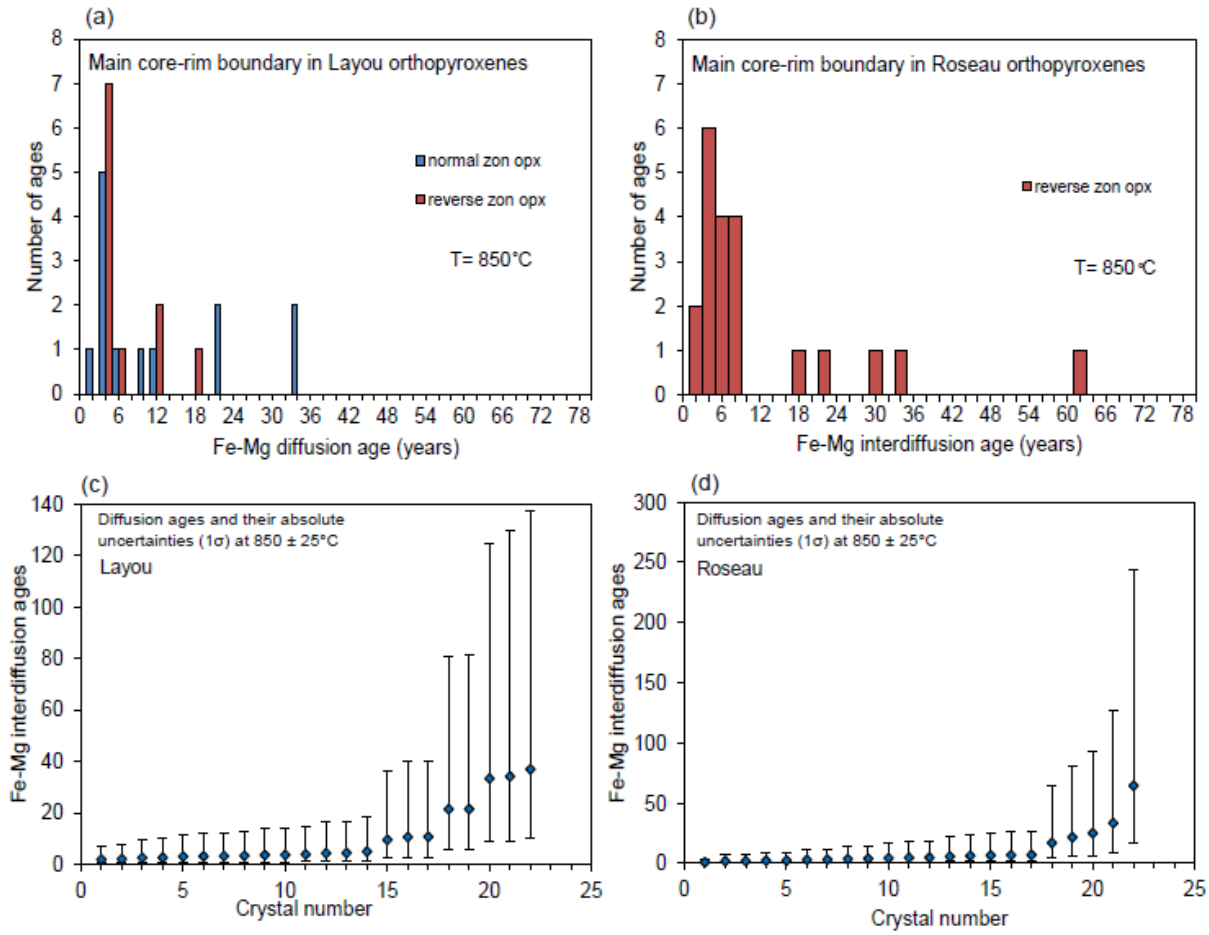

Figure V.II.4: Timescale estimate after Fe-Mg interdiffusion modelling in orthopyroxenes. *Frequency histogram of Fe-Mg interdiffusion timescales modelled at 850°C for the main core-rim boundary of Layou (a) and Roseau (b) orthopyroxene; (c) and (d) Individual ages and their absolute uncertainties based on the propagation of a temperature uncertainty of ± 25 °C for Layou (c) and Roseau (d).*

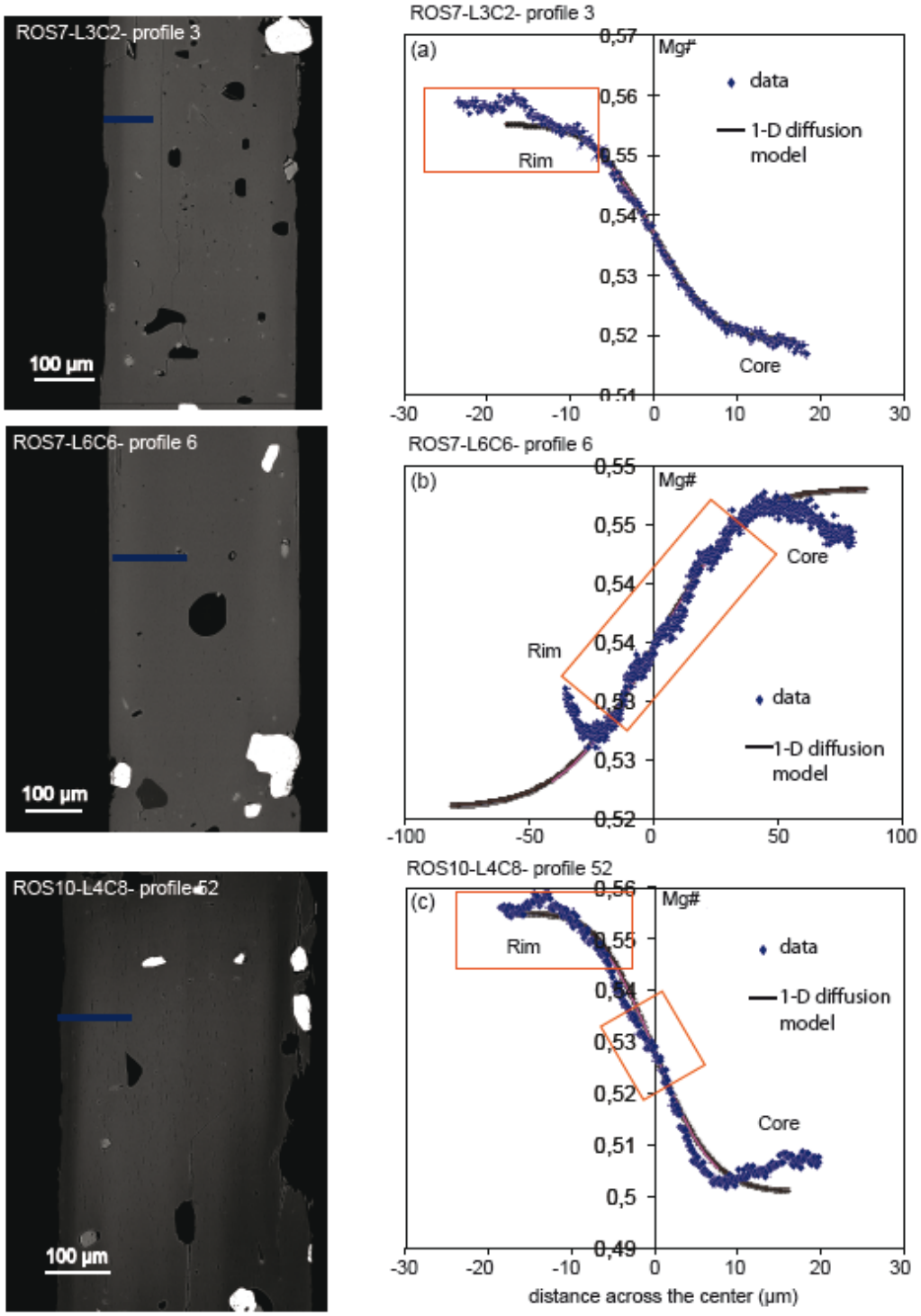

Figure V.II.5: BSE images and relative compositional profiles of Grand Fond orthopyroxenes*. Blue lines in the BSE images show the position of the EPMA compositional traverse for each crystal. Profiles are presented as Mg# [Mg#= Mg/(Mg + Fe_{tot})], as a function of the distance from the centre of the profile (in µm). Blue rhombs: EPMA and BSE greyscale intercalibrated data; black line: diffusion model. Orange boxes: part of the profile affected by presence of high frequency bumps and peaks on the rim side (a) on the slope part (b) or both parts (c) of the profile.*

Final uncertainties on timescales reported in our results (Fig. V.II.4c and d) arise from uncertainties in diffusion coefficient (D) calculations which derive in turn from (1) uncertainties in measurements of diffusion coefficients (D_0, Ea); (2) uncertainty in temperature (Arrhenius relation gives an inverse exponential dependence on diffusion); (3) considerations about the resolution of greyscale values of the BSE images used for profiles calibration (pixel size, 1σ uncertainty on pixel size, 1σ uncertainty on grey values defining a plateau). Even if resolution of BSE images has usually a small effect on final uncertainties (~1%; Costa and Morgan, 2010), the combined influence on timescales of all these parameters is here evaluated using a Monte Carlo method. Uncertainties on temperature, the pre-exponential factor (D_0) and the activation energy (Ea) have all a logarithmic effect on final calculated timescales so that the final uncertainties are not Gaussian in time but asymmetric, with larger error bar on the high-time side and smaller error bar on the low-time side. Resulting absolute uncertainties on Fe-Mg interdiffusion timescales for Layou and Roseau eruptions are reported in Figure V.II.4c and d. 15 crystals on 24 for Layou and 17 crystals on 21 for Roseau show positive absolute uncertainties of +25 years on the calculated timescales for our chosen diffusivity parameters.

V.II.6. Discussion

V.II.6.1. Decadal rejuvenation timescales

Modelling the diffusional relaxation of the chemical zoning within orthopyroxene crystals enables us to constrain at 3 to 10 years prior to eruption the timescales of the heating process (about 25°C) responsible for the perturbation of the reservoir from equilibrium storage conditions, for both Layou and Roseau eruptions.

When single crystal timescales are reported on each pathway (Fig.V.II.6), results show that, regardless of the considered crystal pathways, timescales of melt-crystals movement from one environment to another are comparable, with only few crystals (2 for Layou and 3 for Roseau) showing timescales higher than a decade.

By contrast, the Grand Fond eruption shows a diverse range in orthopyroxene compositions and zoning patterns, with seeming inheritance of chemical features from the previous (Roseau) eruption. Compositional profiles measured show evidence of significant deviation from purely diffusive behaviour. The bumps and peaks recorded in profiles are likely to be linked with the kinematics of rapid growth of crystals in changing environments shortly before the eruption, producing overlapping and complex signals when combined with

diffusive relaxation of the initial chemical gradients. The short length-scale of the zonation patterns, together with their complexity, argues for a timescale comparable to or shorter than that found for the preceding Layou and Roseau eruptions.

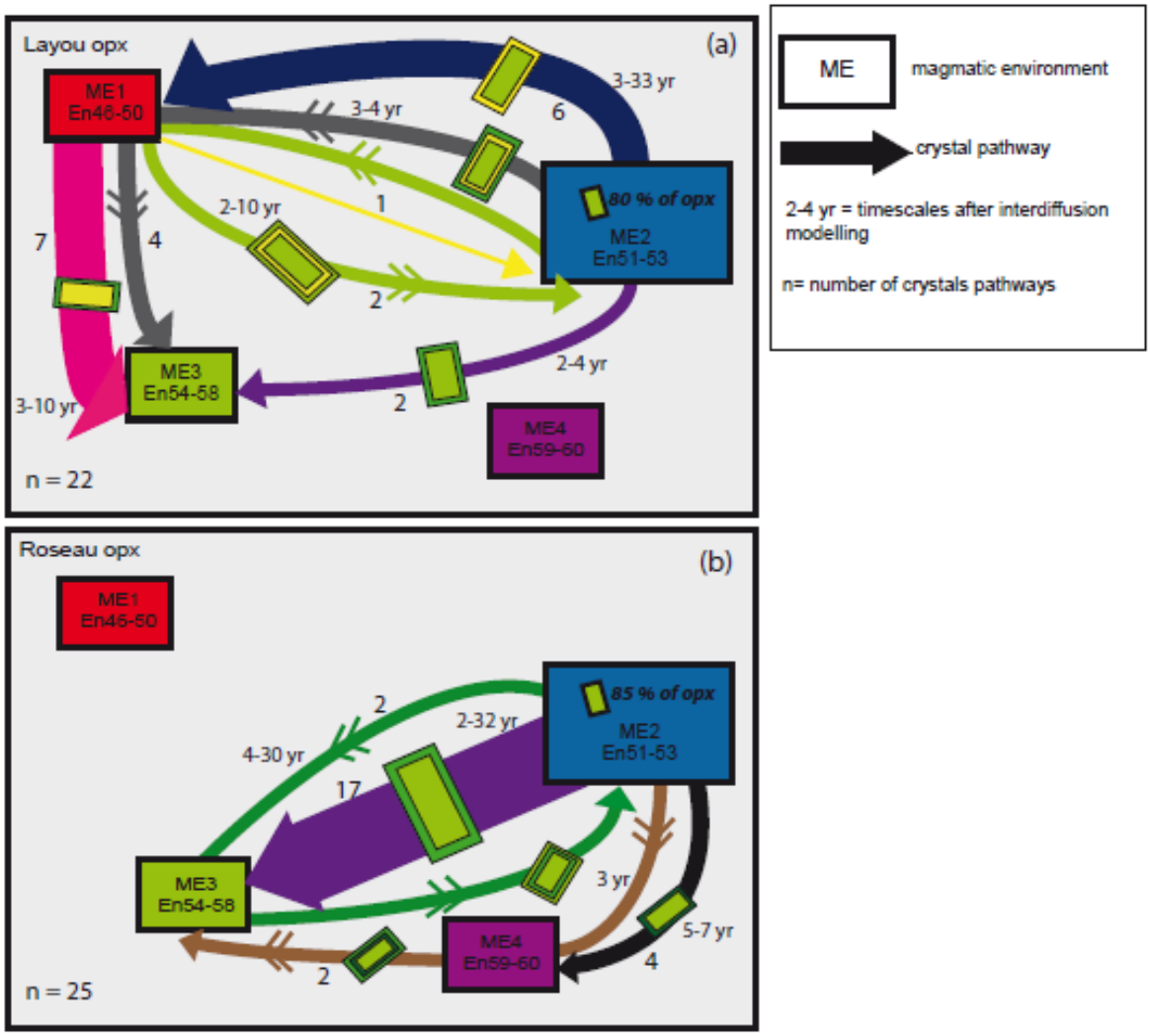

Figure V.II.6: Timescales of crystal pathways*. Crystal system analysis diagram (from Figure V.I.8 of Part I) for Layou (a) and Roseau (b) with reported calculated timescales (in years) for different crystal zoning pattern (crystal pathways).*

V.II.6.2. Effect of oxygen fugacity on diffusion timescales

Here we have modelled diffusion on compositional profiles without additional fO_2 correction. Nevertheless, as oxygen fugacity influence on diffusion is still a debatable issue (Ganguly and Tazzoli, 1994; Dimanov and Wiedenbeck, 2006; Allan et al., 2013; Mueller et al., 2013; Dohmen et al., 2016), it is important to us to discuss the possible effect of fO_2 correction on our timescales results.

The last experimental results on natural orthopyroxenes of Dohmen et al. (2016), conducted in a range of 870-1100 °C and 10^{-11} to 10^{-7} Pa, argues for a minor dependence of diffusion coefficient on oxygen fugacity, with an exponent n= 1/20, significantly smaller than the 1/6 speculated by Ganguly and Tazzoli (1994) from simplified point defect and order-disorder kinetics models in orthopyroxenes. As a consequence, the diffusion coefficient decreases by a factor of ~4 with decreasing oxygen fugacity from 10^{-12} to 10^{-16} bar, while the parameterization suggested by Ganguly and Tazzoli (1994) and used in Allan et al. (2013) would produce a decrease of the diffusion coefficient by an order of magnitude in the same oxygen fugacity range.

Dohmen et al. (2016) underlines that the estimate of Ganguly and Tazzoli (1994), when extrapolated to their experimental temperatures and used without considering the fO_2 dependence and a composition close to pure enstatite, is in good agreement with their experimental data. On that basis, we can argue that the diffusion coefficient we have used in our modelling is close to the new value proposed by Dohmen et al. (2016).

Utilising the diffusivity parameterisation of Dohmen et al. (2016) for compositions up to Fs_9 (where Fs= ferrosilite; considerably more Mg-rich than in this study), with an fO_2 exponent of 0.05 and fO_2 of NNO+1, diffusivity would be slower, and timescales longer, by a factor of ~9 compared to diffusivities calculated by Ganguly and Tazzoli (1994) for compositions of XFs = 0.4. This would push timescales into the range of decades to a century prior to eruption.

V.II.6.3. Implications of timescales in plumbing system dynamics

In the process of sequential accretion of sills by which large crustal magma reservoirs form (Annen, 2009; Blundy and Annen, 2016), the resident magma can cool and partially crystallise in between successive magma pulses to become a crystal mush (Marsh et al., 2006). Crystallinity stays in the 50-60% range and the solidus (100% crystals) is not reached quickly because of the release of latent heat during crystallisation (Marsh, 1981, 1989). This type of highly-crystallised crustal reservoirs raises questions regarding their mobility and on how they can be re-mobilised (rejuvenated) to eruptible magmas in reasonable geological timescales. Several mechanisms have been proposed as heat transfer for mush rejuvenation and possible melt extraction: self-mixing (Couch et al., 2001), addition of volatile by gas sparging (Bachmann and Bergantz, 2003 and 2006; Huber et al., 2010b; Pistone et al., 2013), convective overturn (Ruprecht et al., 2008), convective stirring (Huber et al., 2011). In any case, underplating mafic magmas bringing heat and volatiles are considered major players in the re-activation of mush. The transfer of heat and volatiles changes the rheological properties

of the mush (buoyancy, crystallinity), favouring its mobility (formation of melt connections, volatiles foams, Pistone et al., 2013). Numerical modelling has been performed and tested for several large silicic eruptions to assess which mechanism could be the most effective for rejuvenation in reasonable timescales and what mechanism would create the difference in between crystal rich monotonous dacites and crystal poor rhyolites.

Huber et al. (2012) conducted a numerical thermo-mechanical modelling study about reactivation and stirring of crystal mush, and defined a heating reactivation timescale not depending on crystal or magma injection sizes, being the time required to unlock the mush over the critical boundary layer thickness required to start convection. Results of Huber et al. (2012) show that the reactivation timescale is much greater than the following homogenisation one, so that crystal rich dacites, needing a first reactivation, would be inevitably well stirred. Results suggest that for small crystal mush (e.g. the 1991 Pinatubo eruption of about 5-7 km^3 DRE, Scott et al., 1996), the reactivation time is of about half a year, considering a reservoir thickness of a few hundred meters, close to the timescales of Pallister et al. (1992) inferred by seismicity and phreatic eruptions.

For eruptive volumes of these Dominica eruptions (several km^3 DRE/ eruption, see chapter III), which are of the same order of magnitude than those of Pinatubo eruption, our diffusion timescales of about 3 to 10 years before eruption (in case of diffusion modelling without oxygen fugacity correction), indicating a rapid re-heating of magma reservoir prior to eruption, are consistent with modelling results of Huber et al (2012), so that the main reservoir would have had a sufficient time for reactivation and subsequent homogenisation by self-convective stirring (5-10 overturns, Huber et al., 2009).

Nevertheless, it has to be noted that the efficiency of the heat transfer necessary to unlock a crystal mush highly depends not only on the size but also on the composition and temperature of the intruding magma body. In the case study of the Pinatubo eruption the intrusion has a basaltic composition, while we here suggest that the intrusion likely has a comparable composition (dacitic) with the resident mush. This implies that in our case the enthalpy carried by the intrusion could be lower than in the Pinatubo case, deriving from lower temperature. On the other hand the injection has likely a high volatile content (~7wt% H_2O in melt inclusions, Balcone-Boissard et al., in prep) which enhances the upward propagation of the melting front, favouring the defrosting and remobilisation of the mush (Huber et al., 2010b). For mush sizes of a few km^3, reactivation timescales in between some months and some years are a reasonable estimation (Huber et al., 2012).

Moreover, the pre-eruptive temperature before the heating of the system is 850 °C (phase equilibria results; see Chapter IV). This represents a relatively high temperature which would have likely not allowed the reservoir to be in rigid-locked conditions (>50 % of crystals; Marsh, 1989) prior to the heating event. As a consequence, the reactivation and following convective-stirring in the reservoir may have easily acted and needed shorter timescales of some months to one year.

Considering the long time gap between the two different eruptions of Roseau and Grand Fond (~10 ky), magma volumes involved require a long storage period of tens of thousands of years before rejuvenation into an eruptible magma body shortly prior to eruption. Such short rejuvenation timescales raise questions on the dynamics and behaviour of long-lived systems and imply that large magma volumes may be assembled and/or remobilised over short timescales of decades prior to eruption. This has already been evidenced for several systems of crystal-rich andesite-dacite and for crystal-poor rhyolite, both linked with arc volcanism. Studying plagioclase zoning patterns of the Minoan eruption (Santorini), Druitt et al. (2012) claim that the final assembly of the large silicic eruptible magma body (40-60 km^3) took place in decades to months before the eruption. Using compositional record of orthopyroxenes from Oruanui eruption (Taupo Volcanic Zone, New Zealand) Allan et al. (2013) assess that the erupted crystals-poor rhyolite magma body has been assembled in some centuries (with a peak at ~230 years) before eruption. On the Whakamaru eruption (Taupo Volcanic Zone) Matthews et al. (2011) suggested that the rejuvenation and final assembly of the eruptive magma body had occurred ~10-85 years prior to the caldera-forming eruption (from results of diffusion modelling on quartz zoning patterns). For the same eruption, Saunders et al. (2010) used diffusion modelling of the greyscale cathodoluminescence intensity of quartz to assess that the final pre-eruptive magma mixing occurred less than 300 years prior to eruption (with a peak at 50-70 years). For the eruption of the Bishop Tuff Chamberlain et al. (2014) infer short timescales for the rejuvenation of the lower part of the Bishop Tuff. Fe-Mg interdiffusion in orthopyroxene and Ti diffusion in quartz provides ages < 150 years before eruption for the formation of the final overgrowth rim in crystals, while Ba and Sr diffusion in plagioclase provides longer ages of 500 years. The authors explain the difference in timescales obtained via each diffusion chronometer by the possible different crystallization history experienced by each kind of crystals.

Thus, several systems characterised by long period of thousands years of volcanic rest, have demonstrated that times in between the formation and setting up of the main magma volume responsible for large silicic eruptions and the eruption itself can be of some centuries to only

decades or months. Regardless of their long rest and repose periods, these systems can be thus considered highly dynamic with short lead times prior to eruption.

V.II.7. Conclusions

Diffusion modelling on the chemical zoning recognised in orthopyroxenes of Layou and Roseau eruptions places onto the pre-eruptive re-heating a timescale of a year to a decade prior to eruption, significantly short when compared to the long rest period of each eruptive centre.

In the context of the Lesser Antilles arc, this represents one of the first complete studies on pre-eruptive dynamics and timescales of magma chamber processes obtained by crystal texture analysis and diffusion kinetic modelling.

Our study, the first evidence on the Lesser Antilles arc volcanic system of a rapid remobilisation of large volumes of magma before eruptions, shows that these magma volumes are rejuvenated from their long lived "dormant" state in a period of less than one decade and brings important constraints on the hazard management of the central part of Dominica.

Supplementary material

Table V.II.S1: *Diffusion modelling parameters following the parameterizations of Ganguly and Tazzoli (1994), Mueller et al., (2013) and Dohmen et al., (2016).*

	Ganguly and Tazzoli, 1994	Dohmen et al., 2016		Mueller et al., 2013
T (°C)	500-800	870-1100		800-1200
P	atm	atm		atm
fO_2 (bar)	IW to 0.8+IW	10^-11 to 10^-7		10^-11 to 10^-17
crystal type	opx	opx	opx	cpx
crystal composition	XFe = 0.10-.50	XFe = 0.01	XFe = 0.09	XDi= 0.93
log (D_0 [m^2/s])	-9.54	-3.78	-5.95	D_0= 2,77*10^-7
Q	57338 (cal/mol)	377 (kJ/mol)	308 (kJ/mol)	320.7 (kJ/mol)
fO_2 depend.	yes (from olivine)	no	yes	no
n	1/6		1/20	
composition depend.	yes (2.6)	not quantitative		no
Equations	logD=-5.54+2.6XFe-12530/T	logD=logD_0-Q/(RT)	logD=logD_0-Q/(RT)+n*log(fO2)	D=D_0*exp(Q/RT)
with Allan et al., 2013 fO_2 correction	logD=-5.54+2.6XFe-12530/T+1/6 *((fO2sample)/(fO2 IW))			

Concluding summary

The Crystal System Analysis allowed to perform a complete and statistical study of the pre-eruptive dynamics present in the plumbing system feeding the three eruptions studied here. Combining this tool with diffusion modelling on crystals we obtain a conceptual model of the plumbing system for Dominica major pumiceous ignimbritic eruptions.

We propose that for Layou and Roseau-Grand Fond reservoirs the main crystallized mush body is represented by ME2 (~80% of crystals, En_{52-53}). About 3-10 years before eruption this main reservoir suffers a perturbation from its equilibrium crystallization state because of the arrival of a new hotter underplating magma which provides heat to the reservoir from below, without significant physical mixing with the resident magma. This process, likely fostered by high amount of fluids coming from the underplating magma, re-heats the system and produces the reverse zoning patterns recognized in crystals of Layou and Roseau eruptions (rims at ME3 and ME4: En_{54-58} and En_{58-63}). Starting as a local process, the heating takes a larger scale in Grand Fond eruption, causing the shift of the main magmatic environment to less evolved compositions (orthopyroxenes at ME3: En_{54-56}). Before this eruption, the enduring heating has likely assumed a plume geometry over time, allowing interaction of crystals coming from different sections of the main reservoir. Thus, the heat plume can be considered as responsible for the high level of complexity recorded in orthopyroxenes of the Grand Fond eruption (more complex zoning and crystal pathways showing higher interconnectivity), the last in time over the considered eruptive period. We propose that this more complicate crystal patterns are the result of several magmatic self-convective heat-driven over-turns.

At the current state of the study, given the homogeneity in whole rock and residual glass composition coupled with the absence of two separated orthopyroxene core populations in the same eruption, we argue for a pure thermal interaction in between the hosting magma and the underplating one, with no significant mass exchange (mixing-mingling) in between them. Nevertheless, the sampled portion of the outcrop represents the upper part of the reservoir so that we cannot exclude the presence of enclaves or other mixing-mingling traces in portions of the upper pyroclastic density current deposit.

Acknowledgments

This study was partly founded by the program Tellus-Aleas of INSU (CNRS). DJM would like to thank IPGP for the award of a visiting lectureship which enabled this work to take place.

Michel Fialin, Nicolas Rividi and Omar Boudouma are thanked for assistance during EPMA and SEM analyses. We thank Olivier Bachmann, Christian Huber and Maren Kahl for discussions.

CONCLUSIONS AND FUTURE WORKS

1. Summary and Conclusions

1.1. Main issues of this study: storage and evolution of magma in large silicic crustal reservoirs

The study of large silicic eruptions has been one of the main focuses of modern volcanology, as a result of their hazard and environmental impact and the important socio-economic consequences they can have on human life for timescales up to decades (Lowenstern et al., 2006; Self, 2006). These eruptions are all characterized by the emission of significant magma volumes (from few 10 km^3 to several hundred to thousands km^3 per eruption), spreading over areas of several thousand km^2 wide (e.g. the 1600 B.C. Minoan eruption [40-60 km^3, Santorini, Greece]; the 186 AD Taupo eruption [65 km^3, Indonesia]; the 75 ka Toba eruption [2800 km^3, Indonesia]; the 1815 Tambora eruption [30-33 km^3, Indonesia]; the 1883 Krakatau eruption [18-21 km^3, Japan]; the 1991 Pinatubo eruption [5-6 km^3 Philippines]). In addition, large silicic volcanoes are usually characterized by long periods of rest making their eruptive behaviour difficult to estimate and predict. For their impact, the interest of volcanological communities on these eruptions has been growing in the last decades with several studies focusing on the analysis of the plumbing system of related volcanoes with different techniques, in order to answer to some key questions:

(1) what are the physico-mechanical-thermal conditions of magma storage prior to eruption and their preservation over long timescales;

(2) which are the structure (geometry) of the plumbing system organized at depth, so how many "storage regions" are present at depth and what are the pre-eruptive dynamics of these magmas (differentiation, mixing, mingling, assimilation);

(3) in which timescales prior to eruption these dynamics occur.

Magma storage : Studies of thermo-mechanical behaviour and numerical modelling of magmatic systems provided an answer to different questions related to the conditions for the formation of such large crustal silicic reservoirs, for their preservation over geologically relevant timescales and for their remobilization into eruptible melts (Annen et and Sparks, 2002; Annen, 2009; Blundy and Annen, 2016). Large silicic reservoirs form over long accumulation timescales (10^5-10^6 years, Jellinek and De Paolo, 2003) and are originated by repetitive sills or dikes injections (Annen, 2009) during flare-up periods of high magma flux from the mantle (de Silva, 2008). Once these large magma regions are created, their preservation over long timescales depends on the time lapse in between each sill injection and on their enthalpy. Because of cooling, magma will tend to crystallize but the latent heat of

crystallization will prevent it to quickly reach the solidus and a complete solidification. For this reason, the reservoir will tend to reach crystallinity values of 50-60% in which it consists of a highly crystallized, uneruptible mush (Marsh, 2006; Bachmann and Bergantz, 2008). A crystal mush could then be remobilised from its uneruptible state (and re-homogenised) by a variety of thermal processes (conduction and self-mixing, convective-stirring, gas sparging; Couch et al., 2001; Bachmann and Bergantz, 2003; Ruprecht et al., 2008; Huber et al., 2010b; Huber et al., 2012) all implying the arrival of a hotter mafic magma carrying the enthalpy necessary for "defrosting" the mush.
Beyond the thermo-mechanical considerations of mush formation, preservation and evolution, a method used to unravel the storage parameters of these reservoirs is experimental petrology. The conditions prevailing in a magma chamber prior to eruption can be reproduced by phase equilibria experiments.

Plumbing system and pre-eruptive magma dynamic: Several studies in the last decades have demonstrated that crystals are a valuable stratigraphic record of the "pre-eruptive history" of magmas (Ginibre et al., 2002a; 2002b; Ruprecht and Worner, 2007) and can be used to constrain the geometry of a magmatic plumbing system (Kahl et al., 2011; 2013; 2015). The compositional zoning of crystals like plagioclase, olivine and orthopyroxene, have been increasingly used to determine which processes magmas suffered during evolution (e.g. heating, decompression, mixing) and what has been their way up to the surface.

Timescales prior eruption: In the last decades, the timescales of pre-eruptive processes have been determined from diffusion modelling of the compositional zoning of crystal cargos in magma. Diffusion modelling in crystals enables to recover the time lapse between a significant change in the thermodynamics conditions of magma storage (P,T, fO_2) and the time the crystal passes across the closure temperature for diffusion (e.g. eruption). With the fast development of precise analytical techniques, diffusion modelling has been increasingly applied on a large variety of minerals (e.g. olivine, plagioclase, orthopyroxene, quartz). Several studies have focused on large silicic eruptions (Matthews et al., 2011; Druitt et al., 2012; Allan et al., 2013; Bouvet de Maisonneuve, 2015; Barker et al., 2016) and have proved that the assembly and remobilization of large magma volumes occurs in centuries to decades (or even years) prior to eruptions, making these systems more dynamic than previously believed and demonstrating how rapidly they can change their behaviour and

generate large eruptible magma bodies in timescales of direct relevance on humans and monitoring activity (Barker et al., 2016).

These three main issues have been treated and developed in this study by applying a natural and an experimental petrological approach on the eruptive products of three major ignimbritic eruptions recognized on Dominica (Lesser Antilles Arc).

1.2. Scientific approach

The study relies on a detailed fieldwork focused on the ignimbritic eruptions of Dominica. Samples used for natural and experimental petrology, Crystal System Analysis or diffusion modelling belong thus to a complete dataset. Here we have studied samples belonging to the basal plinian fallout phase from the Layou (~51 kyrs cal BP), Roseau (~33 kyrs cal BP) and Grand Fond (~24 kyrs cal BP) eruptions. They are dacitic (63-66 % SiO_2, 4.5-5 wt% Na_2O+K_2O) highly crystalline (~30% of phenocrysts) magmas, containing a crystal assemblage made of plagioclase, orthopyroxene, amphibole, clinopyroxene and Fe-Ti oxides, in a microlites-free rhyolitic (76-78 wt% SiO_2, 5.5-7 wt% Na_2O+K_2O) matrix glass.

(1) Starting from glasses representative of whole-rock natural composition, we have performed phase equilibria experiments in order to determine pre-eruptive magma storage conditions for the three eruptions, with a higher precision than common geothermobarometers estimations. Experiments have been conducted in the range of 800-900°C in temperature, 150-400 MPa in pressure and at constant fO_2 of ~ΔNNO+1. Both water-saturated ($xH_2O=1$) and undersaturated ($xH_2O=0.8$) conditions have been tested. In this sense, reproducing experimentally the natural equilibrium compositions enables to assess pre-eruptive T, P, fO_2 and fH_2O (see Chapter IV).

(2) The structure of the magmatic plumbing system and its pre-eruptive dynamics has been studied by focusing on natural orthopyroxene zoning textures and compositional variations. A “Crystal System Analysis” method (Kahl et al., 2011; Kahl et al., 2015) has been applied on orthopyroxenes. The use of this statistical method allow to analyze with much more accuracy the complex diversity of composition and zoning patterns recognized in these eruptives products in order to recognize the main magmatic environments (ME) present in the plumbing system and map crystals main pathways from one ME to another over the considered eruptive history. A statistical

treatment of these data, coupled with orthopyroxenes hosted melt-inclusions data and experimental petrology results, allowed us to constrain the general chemical structure of the reservoirs and recognize a perturbation of the system occurring in the late stage of its development (see Chapter V-Part I).

(3) Finally, using modelling of diffusion relaxation of Fe-Mg chemical gradient in orthopyroxenes, we finally assign pre-eruptive timescales on the recognized heating process (see Chapter V-Part II). Diffusion modelling has been performed at temperature conditions derived from phase equilibria experiments (~850°C). We have used the diffusion coefficient of Ganguly and Tazzoli (1994) (i.e. diffusivity dependent on crystal composition) without oxygen fugacity correction and initial step-wise conditions (i.e. instantaneous growth followed by diffusion re-equilibration).

1.3. Main results of this study

The main results of this study enable us to present a complete petrological model for magma storage conditions, pre-eruptive dynamics and timescales for the three investigated eruptions.
This work is based on a complete revised chronostratigraphy of the explosive activity that occurred in the last 50 kyrs in Dominica based on detailed field investigation, new ^{14}C ages dating, lithological and geochemical investigations (chapter III this volume). This work has allowed to confirm that the Roseau event has been overestimated. Fours to five main ignimbritic events can be recognized: Grande Savane, Layou (~51 kyrs), Roseau (~33 kyrs), Grand Fond (~24 kyrs) and Grand Bay. Further discussion about the eruptive centre at the origine of each eruption and their possible correlation is discussed (see chapter III) and brings new advances in the description of the recent eruptive history of Dominica..

1-Deep storage conditions

An extensive study of natural crystals, with particular detail for plagioclase and orthopyroxenes showing remarkable chemical zoning, has allowed, to distinguish the crystals compositions representative of reservoir pre-eruptive conditions, among the different compositional variations. These compositions have been used as a target to be reproduced in our phase equilibria experiments. Results on petrology of experimental runs (total crystal content, phase assemblage and phase compositions), compared with results on petrology of natural samples, has allowed to fix the pre-eruptive storage conditions for the three eruptions

at a temperature of ~850°C, a pressure of ~400 MPa (corresponding to a depth of about 16 km, considering a crust density of about 2450 kg/m^3), highly oxidized conditions (~ΔNNO+ 1) and a pre-eruptive glass water content of ~6-8 wt% H_2O.

These results highlight the particularity of Dominica storage system compared to the other islands of the Lesser Antilles Arc. At first, the reservoir is located at higher pressures and in a much deeper position. Secondly, these magmas have significant higher water content, suggesting a "wet" pre-eruptive environment. Previous studies have already demonstrated that the neighbouring volcanic systems are characterized by shallower storage localization and lower volatile contents. As an example, Martel et al. (1998) argue for a storage pressure of ~200 MPa and water content of ~5.3-6.3 wt% H_2O for the recent plinian and pelean eruptions of Montagne Pelée (Martinique; P1 eruption: 650 yr BP, 1902 and 1929 eruptions). Barclay et al. (1998) determines the pre-eruptive storage conditions for the andesitic magma erupted at Soufrière Hills (Montserrat) at pressure of 115-130 MPa (water saturated pressure), equivalent to a depth of 5-6 km, and ~4 wt% H_2O in pre-eruptive melt. For the Soufrière de Guadeloupe (Guadeloupe), Poussineau (2005) determines pre-eruptive magma storage conditions for the 1530 AD eruption at a pressure of 150 -175 MPa (depth of ~6-7 km) and about 4.6-5.4 wt% H_2O in pre-eruptive melt. Thus, typical eruptive centers of the Lesser Antilles arc are characterized by storage of relatively small volumes (< 1 km^3/eruption) of magma at shallow crustal depth (5-6 km), while Dominica shows evidence of deep crustal storage (~16 km) of large, water-rich magma volumes. Our data agree with the crustal model of Kopp et al. (2011) which locates the lower-intermediate crust limit under Dominica at ~16 km in depth. On this basis, here we have suggested that the lower-intermediate crust limit corresponds to a region of significant changes in physical-chemical parameters (composition and density, rheology of host rocks) in which the storage of large volumes of magma can be favored. The middle-lower crust limit is much shallower (5-6 km) below the other islands of the central segment of the arc (Guadeloupe, Martinique; Boyton et al., 1979), explaining the significant difference in storage depths of Dominica magmas.

2- A reservoir model: rejuvenation and heating recorded by orthopyroxenes

The detailed study of the crystal cargo of magmas through their composition and zoning profiles, melt inclusions composition and crystal system analysis enabled us to build a chemical model for the two main reservoirs feeding the Layou, Roseau and Grand Fond eruptions. Taking back to lithological and geochemical considerations of Boudon et al. (in prep, see Chapter III this volume) here we assumed that Layou has a separate reservoir

connected to the Morne Diablotins eruptive centre while Roseau and Grand Fond are fed by the same reservoir, connected with the Morne Trois Pitons eruptive centre and evolving with time from one eruption to the other.

The analysis of zoning texture and composition of orthopyroxenes shows that for all eruptions a large part of crystals (~80%) are unzoned while ~20% is zoned (with reverse, multiple and normal zoning). The 80% of unzoned crystals likely depict a long-lived magma body characterised by stable crystallisation conditions. The other 20% suggests a late perturbation of the reservoir, with prevailing reverse zoning.

A detailed Crystal System Analysis (Kahl et al., 2015) of these data allowed to recognize a magmatic plumbing system made of four different magmatic environments characterized by orthopyroxenes of different enstatite content (M1=En_{46-50}; ME2=En_{51-53}; ME3=En_{54-58} and ME4=En_{59-63}), but in equilibrium with the same melt composition (from results on melt inclusions, see Chapter V-Part I). This argues for spatially closed magma environments, likely part of the same reservoir. Unzoned orthopyroxenes indicate a shift to less evolved compositions in the time lapse (~10 kyr) in between the two eruptions of Roseau and Grand Fond.

Rounding out all these results, we suggest a conceptual reservoirs model for the three eruptions with two separated highly crystallized dacitic mush bodies belonging to a unique horizontally developed mush and having an equilibrium temperature about 850°C (for Layou and Roseau) and 875°C (for Grand Fond), (see Figure V.I.10). These magmas have experienced a long period of storage in relatively stable crystallization conditions (no significant changes in storage physic-chemical parameters), chemically represented by the large amount of unzoned crystals found in our samples. This indicates that if any previous perturbation of the system has occurred, it has been in timescales long enough for diffusion to erase the textural-chemical instability in crystals.

The normal zoning recognized in some crystals of Layou and Grand Fond eruptions is considered as a proper feature of the main magma body, deriving from its inner structure so characterized by roof- or wall-sections of more evolved crystallization. Contrariwise, the abundant reverse zoning is attributed to a late heating process of ~25-30°C coming from an underplating hotter magma, bringing sufficient enthalpy to remobilize the system and, for Grand Fond eruption, to bring the whole system to a new equilibrium composition that correspond to a higher temperature (~875°C against 850 °C). The absence of evident mafic enclaves and of two different orthopyroxene core populations in the same sample, tend to suggest a poor mixing in between the resident and the injecting magma. The latter acts as a

heating plate and releases high amount of fluids (H_2O+CO_2; gas sparging; Bachmann and Bergantz, 2003) enhancing the heat transfer, the propagation of the melting front and the remobilization of the mush. The strong concentration of H_2O in melt inclusions (up to ~8 wt% for Layou; Balcone-Boissard et al., in prep.) supports this idea. Crystallinity being likely under the ~50% mobility threshold (Marsh, 1996; Bachmann and Bergantz, 2008), self convection (Couch et al., 2001) can act in the reservoir to develop a heating plume geometry able to bring together at the scale of the hand-samples crystals with different histories and progressively shift the main composition of the reservoir.

3- Short magma remobilization timescales

Modelling of the diffusional relaxation of Fe-Mg chemical profiles on orthopyroxenes has revealed that the heating event suffered by both Layou and Roseau-Grand Fond reservoirs has occurred about a decade prior to each eruption.

Considering the long rest period characterizing these systems, it is remarkable to note how fast they can pass from rest to unrest with remobilization in only few years before eruption. This has already been evidenced for several large silicic eruptions, with rejuvenation timescales going from years to centuries (e.g. Santorini, Taupo Volcanic Zone, Bishop Tuff, Fish Canyon) and raises the attention of volcanologists also on hazard and risk management in the dense populated areas in the vicinity of these large volcanic systems.

In the context of the Lesser Antilles arc, this represents a first and unique estimation of pre-eruptive remobilization timescales for these large volume eruptions and implies new concerns in the risks management of the central part of Dominica. Main cities, for example the capital city of Roseau, are in the direct path of the pyroclastic density currents of these eruptions and would consequently be highly damaged or destroyed by the future occurrence of such large eruptions.

2. Remaining questions and future works on Dominica eruptions

This research work provides new highlights on pre-eruptive magma dynamics and reservoir processes of the three major ignimbritic eruptions of Layou, Roseau and Grand Fond of Dominica.

Using an experimental approach we constrain pre-eruptive magma storage conditions for these eruptions. By combining textural and compositional analysis of orthopyroxenes and Fe-Mg interdiffusion modelling of chemical gradient recognized in crystals, we propose a new model of the main magma storage region, with timescale estimates on pre-eruptive reservoir dynamics. Nevertheless, several remaining questions can be addressed from a stratigraphic and petrological point of view.

2.1. Stratigraphy

Improving volumes estimations

The particular attention of this study on the ignimbritic eruptions of Dominica derives from their remarkable volumes, one order of magnitude larger than the other eruptions characterizing the arc. On the Roseau, Grand Fond and Grande Savane ignimbrites volumes have been estimated by Carey and Sidgursson (1980), Linsday et al. (2003) and Boudon et al. (in prep.; chapter III). By correlation of deep-sea tephra layers with the deposits of the Goodwill Quarry, Carey and Sidgursson (1980) calculated a total tephra volume (on-land and off-shore) of ~58 km^3 for the Roseau Tuff, considering a single main eruption. Smith et al. (2013) proposed that the Roseau Tuff is constituted by 7 separate eruptive episodes of smaller volumes (~10-20 km^3). On the base of the recent stratigraphic constrains Boudon et al. (in prep) give a coarse estimation of the volumes of each main ignimbritic eruption at several km^3.

Nevertheless, the current volume estimations are not precise, and the agreement in between the different stratigraphic studies has not been reached yet. Due to poor exposure, limited outcrop access and easy reworking of the deposits produced by extreme weathering regimes characteristic of tropical environments (Rad et al., 2013), preservations of suitable outcrops is difficult and stratigraphic relations difficult to decipher by study of subaerial deposits. Given the particularity of Dominica eruptive volume at the scale of the arc, future research should focus of refining the estimations of erupted volumes. The possibility of further correlation of on-land and over-sea deposits (using deep sea cores and subaerial stratigraphy) would help in better constrains volumes of single eruptive events. As an example, the recent IODP-340

mission (Le Friant et al., 2015) has drilled a series of sites offshore Monteserrat, Martinique and Dominica. Among them, the core U1398, located at ~140km south from the coast of Dominica, record the presence of several thick pumiceous turbiditic deposits, likely to be linked with the eruptive activity of the central part of the island. Further correlation of tephra from this core with on-land data may bring new constrain on volumes estimations.

Post-Roseau events

This study focuses on the basal plinian fallout of each eruption, considered as the early erupted product at the beginning of each event. Nevertheless the stratigraphic study of Boudon et al. (in prep) (see Chapter III) has demonstrated that the Roseau and the Grand Fond eruptions are followed by several pumiceous eruptions of lower volume with a dominant plinian phase (higher proportion of fallout deposits). Are these eruptions belonging from the same deeper reservoir as the larger ignimbritic eruptions or from a shallower storage? Are their pre-eruptive dynamics similar to those of large ignimbritic eruptions?

A detailed study of whole rock, residual glass composition and phase assemblage has been performed on these eruptions by Boudon et al. (in prep) (see chapter III) but a precise study on their crystal cargo, in term of crystal composition and detailed zoning patterns needs still to be performed.

It would worth to apply a statistical approach, as used here for Layou, Roseau and Grand Fond, to check for the presence and nature of zoned crystals (with focus on plagioclase and orthopyroxenes) and count their abundance, in order to compare results with the basal fallout phase studied here. This could give further information on the possible evolution of the storage conditions during the eruptive story and its modification over time. Further diffusion modelling could be realized on orthopyroxenes with comparison with Fe-Mg interdiffusion timescales obtained here for Roseau and Grand Fond fallout.

2.2. Storage conditions parameters- Phase equilibria experiments

Concerning the experimental approach used here to investigate the pre-eruptive storage conditions of central Dominica magmas, a further study should consider the possibility to investigate a larger domain of P-T-fO_2 by performing a complete and longer experimental petrology study. No previous phase equilibria studies have been conducted on Dominica eruptive products and here, also for a reasons of time and specific strategy, experiments were performed at a constant oxygen fugacity of ~ΔNNO+1, a relatively small temperature range

(800-900°C) and with two main initial volatile content (XH_2O=1 and XH_2O=0.8). These specific range of tested parameters, derives from previous T, P, fO_2 constrains obtained analysing natural products petrology (natural geothermobarometers). Still, it would be worthwhile to run a new set of experiments with different oxygen fugacities (to study the effect of this variations on the composition of Fe-bearing crystal phases as orthopyroxenes and Fe-Ti oxides) and with and intermediate initial water of to XH_2O=0.9, here tried only for one experimental run (850°C-250 MPa). Indeed the composition of natural Fe-Ti oxides is here never experimentally reproduced. Intermediate water content would help in reproducing natural magnetite. Specifically, to better constrain magma storage conditions of Roseau, it would be worthwhile to test an experiment at 850°C-400 MPa and a initial water content of XH_2O=0.9 to decrease the natural Anorthite content of plagioclase (An_{59} in the run 850°C-400MPa-XH_2O=1) to match the natural An_{53-55}. Exploring a larger range in temperature and pressure would also allow better constraining the phase assemblage and determining the liquidus conditions for all crystal phases.

2.3. Magma dynamics and timescales of magmatic events

Crystals zoning textures

Here we have focused a large part of our study on orthopyroxenes single crystals, representing the second more abundant phase in the crystal assemblage. But plagioclase (~70 % of total phenocrysts) represents also an important phase to be considered and studied for compositional zoning. Because of their long crystallization histories, plagioclases present usually a complex structure-texture and highly developed compositional zoning patterns (normal, reverse or oscillatory zoning, resorption zones and patchy zoning) which can bring more information about magma dynamics and give much more proofs of the heating and partial re-melting of the reservoirs. Moreover a crystal system analysis method could be developed also on plagioclase and would allow to overpass the difficulty usually encountered in the statistical treatment of the complex zoning patterns of these crystals.

Diffusion modelling on other crystals

With diffusion modelling in orthopyroxenes we assessed a timescale on the last pre-eruptive magmatic event, likely the one acting as an eruption trigger. The power of diffusion is in its possibility to be performed using different element-crystal couples, so that, as a function of the elemental diffusion rate, the technique allows to investigate single crystal processes

spanning timescales going from centuries to days. To that end, in Layou, Roseau and Grand Fond pumice samples, diffusion modelling could be performed also on plagioclase (Charlier et al., 2012; Druitt et al., 2012) using the diffusion of Sr and Mg to attain timescales of centuries prior to eruption. This could enable to go further in the reservoir history and investigate remote processes and dynamics. As for orthopyroxenes, a detailed compositional zoning study has to be performed on these crystals to determine the process on which we want to put a timescales on.

2.4. General model for the Dominica crustal plumbing system

The lateral connection of the reservoirs feeding the different eruptive centres is still a matter of debate, since poor work has been realised to image the reservoir region (seismic tomography). Particular geochemical trends given by some eruptive products suggest that magmas are stored in different reservoirs each characterised by particular storage conditions. The current developed idea suggests the presence under Dominica of a main large batholith (Smith et al., 2013) with a “hot zone” made by different reservoirs (sills) originated from and belonging to a unique storage system. In this way all reservoirs are linked from a petrological point of view as their magma source would thus be the same but each reservoir could be stored at different conditions (e.g. P, T) and evolve and with variable dynamics. Nevertheless, more detailed geophysical investigation would be required to corroborate this idea and better define the structure of the magmatic system under Dominica.

BIBLIOGRAPHIE

A-B-C

Albino, F., Pinel, V., & Sigmundsson, F. (2010). Influence of surface load variations on eruption likelihood: application to two Icelandic subglacial volcanoes, Grímsvötn and Katla. Geophysical journal international, *181*(3), 1510-1524.

Allan, A. S. R., Morgan, D. J., Wilson, C. J. N., & Millet, M. A. (2013). From mush to eruption in centuries: Assembly of the super-sized Oruanui magma body. Contributions to Mineralogy and Petrology, 166(1), 143–164.

Allen, S. R. (2001). Reconstruction of a major caldera-forming eruption from pyroclastic deposit characteristics: Kos Plateau Tuff, eastern Aegean sea. Journal of Volcanology and Geothermal Research 105, 141–162.

Andújar, J., Scaillet, B., Pichavant, M., & Druitt, T. H. (2015). Differentiation conditions of a basaltic magma from Santorini, and its bearing on the production of andesite in arc settings. Journal of Petrology, 56(4), 765-794.

Annen, C. (2009). From plutons to magma chambers: Thermal constraints on the accumulation of eruptible silicic magma in the upper crust. Earth and Planetary Science Letters, 284(3–4), 409–416.

Annen, C. (2011). Implications of incremental emplacement of magma bodies for magma differentiation, thermal aureole dimensions and plutonism–volcanism relationships. Tectonophysics, 500(1), 3-10.

Annen, C., & Sparks, R. S. J. (2002). Effects of repetitive emplacement of basaltic intrusions on thermal evolution and melt generation in the crust. Earth and Planetary Science Letters, 203(3), 937-955.

Annen, C., Paulatto, M., Sparks, R. S. J., Minshull, T. A., & Kiddle, E. J. (2014). Quantification of the intrusive magma fluxes during magma chamber growth at Soufrière Hills Volcano (Montserrat, Lesser Antilles). Journal of Petrology, 55(3), 529-548.

Annen, C., Blundy, J. D., Leuthold, J., & Sparks, R. S. J. (2015). Construction and evolution of igneous bodies: Towards an integrated perspective of crustal magmatism. Lithos, 230, 206-221.

Anovitz LM, Essene EJ, Dunham WR (1988). Order-disorder experiments on orthopyroxenes: implications for the orthopyroxene geospeedometer. American Mineralogist 73: 1060-1073

Arrhenius, S. (1889). On the reaction velocity of the inversion of cane sugar by acids. Z. Phys. Chem. 4, 226.

Bachmann, O., & Bergantz, G. W. (2003). Rejuvenation of the Fish Canyon magma body: A window into the evolution of large-volume silicic magma systems. Geology, 31(9), 789–792.

Bachmann, O., & Bergantz, G. W. (2004). On the origin of crystal-poor rhyolites: Extracted from batholithic crystal mushes. Journal of Petrology, 45(8), 1565–1582.

Bachmann, O., & Bergantz, G. W. (2006). Gas percolation in upper-crustal silicic crystal mushes as a mechanism for upward heat advection and rejuvenation of near-solidus magma bodies. Journal of Volcanology and Geothermal Research, 149(1–2), 85–102.

Bachmann, O., & Bergantz, G. (2008). The magma reservoirs that feed supereruptions. Elements, 4(1), 17–21.

Bachmann, O., Dungan, M. A., & Lipman, P. W. (2002). The Fish Canyon magma body, San Juan volcanic field, Colorado: Rejuvenation and eruption of an upper-crustal batholith. Journal of Petrology, 43(8), 1469–1503.

Bachmann, O., Miller, C. F., & de Silva, S. L. (2007). The volcanic-plutonic connection as a stage for understanding crustal magmatism. Journal of Volcanology and Geothermal Research, 167(1–4), 1–23.

Bacon, C. R., & Druitt, T. H. (1988). Compositional evolution of the zoned calcalkaline magma chamber of Mount Mazama, Crater Lake, Oregon. Contributions to Mineralogy and Petrology, 98(2), 224-256.

Bacon, C. R., & Hirschmann, M. M. (1988). Mg/Mn partitioning as a test for equilibrium between coexisting Fe-Ti oxides. American Mineralogist, 73(1-2), 57-61.

Balcone-Boissard, H., Villemant, B., Boudon, G., & Michel, A. (2008). Non-volatile vs volatile behaviours of halogens during the AD 79 plinian eruption of Mt. Vesuvius, Italy. Earth and Planetary Science Letters, 269(1), 66-79.

Barclay, J., Rutherford, M.J., Carroll, M.R., Murphy, M.D., Devine, J.D., Gardner, J., Sparks, R.S.J., (1998). Experimental phase equilibria constraints on pre-eruptive storage conditions of the Soufriere Hills magma. Geophysical. Research Letters 25, 3437.

Barker, S. J., Wilson, C. J. N., Morgan, D. J., & Rowland, J. V. (2016). Rapid priming, accumulation, and recharge of magma driving recent eruptions at a hyperactive caldera volcano. Geology, G37382.1.

Bazin, S., Feuillet, N., Duclos, C., Crawford, W., Nercessian, A., Bengoubou-Valerius, M., Beauducel, F., Singh, S.C., (2010). The 2004-2005 Les Saintes (French West Indies) seismic aftershock sequence observed with ocean bottom seismometers. Tectonophysics 489, 91_103.

Bea, F. (2010). Crystallization dynamics of granite magma chambers in the absence of regional stress: multiphysics modeling with natural examples. Journal of Petrology 51 (7), 1541-1569.

Bégué, F., Deering, C. D., Gravley, D. M., Kennedy, B. M., Chambefort, I., Gualda, G. A. R., & Bachmann, O. (2014). Extraction, storage and eruption of multiple isolated magma batches in the paired Mamaku and Ohakuri eruption,Taupo volcanic zone, New Zealand. Journal of Petrology, 55(8), 1653–1684.

Bellon, H. (1988). Reconnaissance chronologique des deux premières phases d'activité volcanique en Dominique (Petites Antilles). Compte Rendus Académie des Sci. Paris 306, 1487–1492.

Bert, L. (1880). Eruption et chute de poussières volcaniques, le 4 janvier 1880, à la Dominique (Antilles anglaises). Compte Rendus Académie des Sci. Paris 90, 622–624.

Besancon, J. R. (1981). Rate of cation disordering in orthopyroxenes. American Mineralogist, 66(9-10), 965-973.

Bindeman, I. N., & Valley, J. W. (2001). Low-δ18O rhyolites from Yellowstone: Magmatic evolution based on analyses of zircons and individual phenocrysts. Journal of Petrology, 42(8), 1491-1517.

Bindeman, I. N., & Valley, J. W. (2003). Rapid generation of both high-and low-δ18O, large-volume silicic magmas at the Timber Mountain/Oasis Valley caldera complex, Nevada. Geological Society of America Bulletin, 115(5), 581-595.

Blundy, J. D., & Shimizu, N. (1991). Trace element evidence for plagioclase recycling in calc-alkaline magmas. Earth and Planetary Science Letters, 102(2), 178-197.

Blundy, J. D., & Wood, B. J. (1991). Crystal-chemical controls on the partitioning of Sr and Ba between plagioclase feldspar, silicate melts, and hydrothermal solutions. Geochimica et Cosmochimica Acta, 55(1), 193–209.

Blundy, J. D., & Annen, C. J. (2016). Crustal magmatic systems from the perspective of heat transfer. Elements, 12(2), 115–120.

Bond, A., Sparks, R.S.J. (1976). The Minoan eruption of Santorini, Greece. J. Geol. Soc. London. 132, 1–16.

Boudon, G., Semet, M.P., Vincent, P.M., 1989. The Evolution of La Grande Découverte (La Soufriére) Volcano, Guadeloupe (F.W.I.), in: Latter, J.H. (Ed.), Volcanic Hazards: Assessment and Monitoring. Springer Berlin Heidelberg, Berlin, Heidelberg, pp. 86–109.

Boudon, G., Le Friant, A., Komorowski, J.-C., Deplus, C., Semet, M.P., (2007). Volcano flank instability in the Lesser Antilles Arc: Diversity of scale, processes, and temporal recurrence. Journal Geophysical Research. Solid Earth 112.

Boudon, G., Komorowski, J.C., Villemant, B., Semet, M.P., (2008). A new scenario for the last magmatic eruption of La Soufrière of Guadeloupe (Lesser Antilles) in 1530 A.D. Evidence from stratigraphy radiocarbon dating and magmatic evolution of erupted products. Journal of Volcanology and Geothermal Research 178, 474490.

Boudon, G., Villemant, B., Friant, A. Le, Paterne, M., Cortijo, E., (2013). Role of large flank-collapse events on magma evolution of volcanoes. Insights from the Lesser Antilles Arc. Journal of Volcanology and Geothermal Research 263, 224–237.

Boudon, G., Balcone-Boissard, H., Villemant, B., & Morgan, D. J. (2015). What factors control superficial lava dome explosivity? Scientific Reports, 5, 14551.

Bouvet de Maisonneuve, C., Costa, F., Patia, H., & Huber, C. (2015). Mafic magma replenishment, unrest and eruption in a caldera setting: insights from the 2006 eruption of Rabaul (Papua New Guinea). Geological Society, London, Special Publications, 422(1), 17-39.

Bouysse, P., (1984). The Lesser Antilles Island-Arc-structure and geodynamic evolution. Initial Reports of the Deep Sea Drilling Project, 78(AUG), 83-103.

Bouysse, P., (1988). Opening of the Grenada back-arc Basin and evolution of the Caribbean plate during the Mesozoic and early Paleogene. Tectonophysics 149, 121–143.

Bouysse, P., Westercamp, D., (1990). Subduction of Atlantic aseismic ridges and Late Cenozoic evolution of the Lesser Antilles island arc. Tectonophysics 175.

Bowen, N.L. (1921). Diffusion in silicate melts. J. Geol. 29, 295-317.

Boynton, C. H., Westbrook, G. K., Bott, M. H. P., & Long, R. E. (1979). A seismic refraction investigation of crustal structure beneath the Lesser Antilles island arc. Geophysical Journal International, 58(2), 371-393.

Brady, J. B., & McCallister, R. H. (1983). Diffusion data for clinopyroxenes from homogenization and self-diffusion experiments. American Mineralogist 68, 95-105.

Brady, J. B., & Cherniak, D. J. (2010). Diffusion in Minerals: An Overview of Published Experimental Diffusion Data. Reviews in Mineralogy and Geochemistry, 72(1), 899–920.

Bronk Ramsey, C. (2009). Bayesian Analysis of Radiocarbon Dates. Radiocarbon 51, 337–360.

Brown, L., (2002). Gas Geochemistry of the Volcanic hydrothermal Systems of Dominica and St. Lucia, Lesser Antilles: implications for volcanic monitoring. University of New Mexico.

Brunet, M., Le Friant, A., Boudon, G., Lafuerza, S., Talling, P., Hornbach, M., Ishizuka, O., Lebas, E., Guyard, H., Party, I.E. 340 S., (2016). Composition, geometry, and emplacement dynamics of a large volcanic island landslide offshore Martinique: From volcano flank-collapse to seafloor sediment failure? Geochemistry, Geophys. Geosystems 17, 699–724.

Buening, D. K., & Buseck, P. R. (1973). Fe-Mg lattice diffusion in olivine. Journal of Geophysical Research 78, 6852-6862.

Burnham, C. W. (1979). The importance of volatile constituents. The evolution of the igneous rocks, 439, 82.

Burnham, C. W., Holloway, J. R., Davis, N. F. (1969). Thermodynamic properties of water to 1000°C and 10000 bars. Geol. Soc. Am. Spec. Paper 132:96.

Carazzo, G., Tait, S., Kaminski, E., Gardner, J.E. (2012). The recent Plinian explosive activity of Mt. Pelée volcano (Lesser Antilles): The P1 AD 1300 eruption. Bulletin of Volcanology 74, 2187–2203.

Carey, S.N., Sigurdsson, H., (1980). The roseau ash: Deep-sea tephra deposits from a major eruption on Dominica, lesser antilles arc. Journal of Volcanology and Geothermal Research 7, 67–86.

Carignan, J., Hild, P., Mevelle, G., Morel, J., Yeghicheyan, D. (2001). Routine Analyses of Trace Elements in Geological Samples using Flow Injection and Low Pressure On-Line Liquid Chromatography Coupled to ICP-MS: A Study of Geochemical Reference Materials BR, DR-N, UB-N, AN-G and GH. Geostand. Newsl. 25, 187–198.)

Cashman, K. V., & Giordano, G. (2008). Volcanoes and human history. Journal of Volcanology and Geothermal Research, 176(3), 325-329.

Cashman, K. V., & Giordano, G. (2014). Calderas and magma reservoirs. Journal of Volcanology and Geothermal Research, 288, 28–45.

Cassidy, M., Watt, S.F.L., Talling, P.J., Palmer, M.R., Edmonds, M., Jutzeler, M., Wall-Palmer, D., Manga, M., Coussens, M., Gernon, T., Taylor, R.N., Michalik, A., Inglis, E., Breitkreuz, C., Le Friant, A., Ishizuka, O., Boudon, G., McCanta, M.C., Adachi, T., Hornbach, M.J., Colas, S.L., Endo, D., Fujinawa, A., Kataoka, K.S., Maeno, F., Tamura, Y., Wang, F., (2015). Rapid onset of mafic magmatism facilitated by volcanic edifice collapse. Geophysical Research Letters. 42, 4778–4785.

Chakraborty, S. (1997). Rates and mechanisms of Fe-Mg interdiffusion in olivine at 980°C-1300°C. Journal of Geophysical Research 102, 12317-12331.

Chakraborty, S. (2008). Diffusion in solid silicates: a tool to track timescales of processes comes of age. Annu. Rev. Earth Planet. Sci., 36, 153-190.

Chakraborty, S., & Ganguly, J. (1991). Compositional zoning and cation diffusion in garnets. In: Ganguly, J., Ed. (1991). Diffusion, atomic ordering and mass transport. Springer-Verlag, 120-175

Chamberlain, K. J., Morgan, D. J., & Wilson, C. J. (2014). Timescales of mixing and mobilisation in the Bishop Tuff magma body: perspectives from diffusion chronometry. Contributions to Mineralogy and Petrology, 168(1), 1-24.

Charlier, B. L. A., Peate, D. W., Wilson, C. J. N., Lowenstern, J. B., Storey, M., Brown, S. J. A. (2003). Crystallisation ages in coeval silicic magma bodies: 238U-230Th disequilibrium evidence from the Rotoiti and earthquake flat eruption deposits, Taupo Volcanic Zone, New Zealand. Earth and Planetary Science Letters 206 (3-4), 441-457.

Charlier, B. L. A., Wilson, C. J. N., & Davidson, J. P. (2008). Rapid open-system assembly of a large silicic magma body: Time-resolved evidence from cored plagioclase crystals in the Oruanui eruption deposits, New Zealand. Contributions to Mineralogy and Petrology, 156(6), 799–813.

Charlier, B. L. A., Morgan, D. J., Wilson, C. J. N., Wooden, J. L., Allan, A. S. R., & Baker, J. A. (2012). Lithium concentration gradients in feldspar and quartz record the final minutes of magma ascent in an explosive supereruption. Earth and Planetary Science Letters, 319–320, 218–227.

Cherniak, D. J. (2001). Pb diffusion in Cr diopside, augite, and enstatite, and consideration of the dependence of cation diffusion in pyroxene on oxygen fugacity. Chemical Geology, 177(3), 381-397.

Cherniak, D. J., & Dimanov, A. (2010). Diffusion in Pyroxene, Mica and Amphibole. Reviews in Mineralogy and Geochemistry, 72(1), 641-690.

Chester, D. K., Degg, M., Duncan, A. M., & Guest, J. E. (2000). The increasing exposure of cities to the effects of volcanic eruptions: a global survey. Global Environmental Change Part B: Environmental Hazards, 2(3), 89-103.

Coombs, M. L., & Gardner, J. E. (2004). Reaction rim growth in silicic melts: Implications for magma mixing. American Mineralogist 89, 748-759.

Cooper, K. M., & Kent, A. J. R. (2014). Rapid remobilization of magmatic crystals kept in cold storage. Nature, 506(7489), 480–3.

Cooper, G. F., Wilson, C. J., Millet, M. A., Baker, J. A., & Smith, E. G. (2012). Systematic tapping of independent magma chambers during the 1Ma Kidnappers supereruption. Earth and Planetary Science Letters, 313, 23-33.

Costa, F., & Chakraborty, S. (2004). Decadal time gaps between mafic intrusion and silicic eruption obtained from chemical zoning patterns in olivine. Earth and Planetary Science Letters, 227(3–4), 517–530.

Costa, F., & Dungan, M. (2005). Short time scales of magmatic assimilation from diffusion modeling of multiple elements in olivine. Geology, 33(10), 837-840.

Costa, F., & Morgan, D. (2010). Time Constraints from Chemical Equilibration in Magmatic Crystals. Timescales of Magmatic Processes: From Core to Atmosphere. Whiley, Chichster, 125-159.

Costa, F., Chakraborty, S. (2008). The effect of water on Si and O diffusion rates in olivine and implications for transport properties and processes in the upper mantle. Phys. Earth Planet. Inter. 166, 11-29.

Costa, F., Chakraborty, S., & Dohmen, R. (2003). Diffusion coupling between major and trace elements and a model for the calculation of magma chamber residence times using plagioclase. Geochimica et Cosmochimica Acta, 67(12), 2189–2200.

Costa, F., Scaillet, B., Pichavant, M. (2004). Petrological and experimental constraints on the pre-eruption conditions of Holocene dacite from Volcan San Pedro (36 degree S, Chilean Andes) and the importance of sulphur in silicic subduction-related magmas. Journal of Petrology 45(4), 855-881.

Costa, F., Dohmen, R., & Chakraborty, S. (2008). Time scales of magmatic processes from modeling the zoning patterns of crystals. Reviews in Mineralogy and Geochemistry, 69(1), 545-594.

Costa, F., Coogan, L. A., & Chakraborty, S. (2010). The time scales of magma mixing and mingling involving primitive melts and melt-mush interaction at mid-ocean ridges. Contributions to Mineralogy and Petrology, 159(3), 371–387.

Couch, S., Sparks, R. S., & Carroll, M. R. (2001). Mineral disequilibrium in lavas explained by convective self-mixing in open magma chambers. Nature, 411(6841), 1037–1039.

Crank, J. (1975). The Mathematics of Diffusion. Oxford Sci. Publications, Oxford.

Cussler, E. L. (1976). Mu&component Diffusion. Chemical Engineering Monographs 3, Elsevier Scientific Publishing Co., New York.

Cutter S.L. (2003). The science of vulnerability and the vulnerability of science."Annals of the Association of American Geographers 93(1): 1-12

D-E-F

Dahl, P.S. (1996). The effects of composition on retentivity of argon and oxygen in hornblende and related amphiboles: A field-tested empirical model. Geochimica and Cosmochimica Acta 60, 3687-3700.

Daubrée, M., (1880a). Examen des poussières volcaniques tombées le 4 janvier 1880 à la Dominique et de l'eau quie les accompagnait. Compte Rendus Académie des Sci. Paris 90, 624–626.

Daubrée, M., (1880b). Produits solides et liquides qui continuaient à sortir, en avril 1880, d'un cratère de la Dominique (Antilles anglaises). Compte Rendus Académie des Sci. Paris 91, 949–950.

Davidson, J., Tepley, F. III., Palacz, Z., Meffan-Main, S. (2001). Magma recharge, contamination and residence times revealed by in situ laser ablation isotopic analysis of feldspar in volcanic rocks. Earth and Planetary Science Letters 184, 427-442.

De Gori, P., Chiarabba, C., & Patanè, D. (2005). Qp structure of Mount Etna: Constraints for the physics of the plumbing system. Journal of Geophysical Research: Solid Earth, 110(B5).

Demange, J., Leborne, H., Traineau, H., Westercamp, D. (1985). Histoire volcano- structurale de la Region sud de la Dominique.

de Silva, S. (2008). Arc magmatism, calderas, and supervolcanoes. Geology, 36(8), 671–672.

de Silva, S. L., & Gosnold, W. D. (2007). Episodic construction of batholiths: Insights from the spatiotemporal development of an ignimbrite flare-up. Journal of Volcanology and Geothermal Research, 167(1–4), 320–335.

de Silva, S., Salas, G., & Schubring, S. (2008). Triggering explosive eruptions—The case for silicic magma recharge at Huaynaputina, southern Peru. Geology, 36(5), 387-390.

de Silva, S. L., & Gregg, P. M. (2014). Thermomechanical feedbacks in magmatic systems: Implications for growth, longevity, and evolution of large caldera-forming magma reservoirs and their supereruptions. Journal of Volcanology and Geothermal Research, 282, 77-91.

Demange, J., Iundt, F., Puvilland, P., (1985). Geothermal field model of Wotten Waven Island of Dominica, Lesser Antilles. Trans. - Geotherm. Resour. Counc. 9, 409–415.

Deplus, C., Le Friant, A., Boudon, G., Komorowski, J.-C., Villemant, B., Harford, C., Ségoufin, J., Cheminée, J.-L., (2001). Submarine evidence for large-scale debris avalanches in the Lesser Antilles Arc. Earth and Planetary Science Letters 192, 145–157.

Devine, J. D., Gardner, J. E., Brack, H. P., Layne, G. D., & Rutherford, M. J. (1995). Comparison of microanalytical methods for estimating H2O contents of silicic volcanic glasses. American Mineralogist, 80(3–4), 319–328.

Di Napoli, R., Aiuppa, A., Allard, P., (2014). First Multi-GAS based characterisation of the Boiling Lake volcanic gas (Dominica, Lesser Antilles). Ann. Geophys.

Dimanov, A., & Wiedenbeck, M. (2006). (Fe, Mn)-Mg interdiffusion in natural diopside: effect of pO2. European Journal of Mineralogy, 18(6), 705-718.

Dohmen, R., & Chakraborty, S. (2007). Fe-Mg diffusion in olivine II: Point defect chemistry, change of diffusion mechanisms and a model for calculation of diffusion coefficients in natural olivine. Physics and Chemistry of Minerals, 34(6), 409–430.

Dohmen, R., Ter Heege, J. H., Becker, H. W., & Chakrabortrty, S. (2016). Fe-Mg interdiffusion in orthopyroxene. American Mineralogist, 101(10), 2210-2221.

Domeneghetti, M. C., Molin, G. M., & Tazzoli, V. (1985). Crystal-chemical implications of the Mg (super 2+)-Fe (super 2+) distribution in orthopyroxenes. American Mineralogist, 70(9-10), 987-995.

Domeneghetti, M. C., Molin, G. M., Stimpfl, M., & Tribaudino, M. (1995). Orthopyroxene from the Serra de Magé meteorite: structure refinement and estimation of C2/c pyroxene contributions to apparent Pbca diffraction violations. American Mineralogist, 80(9-10), 923-929.

Dowty, E. (1980). Crystal-chemical factors affecting the mobility of ions in minerals. American Mineralogist 65, 174-182.

Druitt, T. H., Mellors, R. A., Pyle, D. M. & Sparks, R. S. J. (1989). Explosive volcanism on Santorini, Greece. Geological Magazin 126(2), 95–126.

Druitt, T. H. (1992). Emplacement of the 18 May 1980 lateral blast deposit ENE of Mount St. Helens, Washington. Bulletin of Volcanology, 54(7), 554-572.

Druitt, T. H., Costa, F., Deloule, E., Dungan, M., & Scaillet, B. (2012). Decadal to monthly timescales of magma transfer and reservoir growth at a caldera volcano. Nature, 482(7383), 77–80.

Dufek, J., Bachmann, O. (2010). Quantum magmatism magmatic compositional gaps generated by melt-crystal dynamics. Geology 38 (8), 687-690.

Duffell, S. (1937). Diffusion and its relation to ore deposition. Economic Geology 32, 494-510.

Dunn, R. A., Toomey, D. R., & Solomon, S. C. (2000). Three-dimensional seismic structure and physical properties of the crust and shallow mantle beneath the East Pacific Rise at 9° 30'N. Journal of Geophysical Research: Solid Earth, 105(B10), 23537-23555.

Eldridge, (1880). Recent volcanic eruption at the grand Souffriere, in the island of Dominica. Procedings R. Geogr. Soc. 2, 363–366.

Ellis, B. S., & Wolff, J. A. (2012). Complex storage of rhyolite in the central Snake River Plain. Journal of Volcanology and Geothermal Research, 211–212(January), 1–11.

Ellis, B. S., Wolff, J. A., Boroughs, S., Mark, D. F., Starkel, W. A., & Bonnichsen, B. (2013). Rhyolitic volcanism of the central Snake River Plain: A review. Bulletin of Volcanology, 75(8), 1–19.

Ellis, B. S., Bachmann, O., & Wolff, J. A. (2014). Cumulate fragments in silicic ignimbrites: The case of the Snake River Plain. Geology, 42(5), 431–434.

Endlich, (1880). The island of Dominica. Am. Nat. 14, 761–772.

Erdmann S., Martel C., Pichavant M. & Kushnir A.R.L. (2014) Amphibole as an archivist of magmatic crystallization conditions: problems, potential, and implications for inferring magma storage prior to the paroxysmal 2010 eruption of Mount Merapi, Indonesia. Contribution to Mineralogy and Petrology 167, 1016.

Eskola, P. (1934). A note on diffusion and reactions in solids. Bull. Commiss. Geol. Finlande 104, 145-156.

Feuillet, N., Manighetti, I., Tapponnier, P., Jacques, E., (2002). Arc parallel extension and localization of volcanic complexes in Guadeloupe, Lesser Antilles. Journal of Geophysical Research: Solid Earth 107.

Feuillet, N., Tapponnier, P., Manighetti, I., Villemant, B., King, G.C.P., (2004). Differential uplift and tilt of Pleistocene reef platforms and Quaternary slip rate on the Morne-Piton normal fault (Guadeloupe, French West Indies). Journal of Geophysical Research: Solid Earth 109.

Feuillet, N., Leclerc, F., Tapponnier, P., Beauducel, F., Boudon, G., Le Friant, A., Deplus, C., Lebrun, J.-F., Nercessian, A., Saurel, J.-M., Clément, V., (2010). Active faulting induced by slip partitioning in Montserrat and link with volcanic activity: New insights from the 2009 GWADASEIS marine cruise data. Geophysical Research Letters 37.

Feuillet, N., Beauducel, F., Tapponnier, P., (2011a). Tectonic context of moderate to large historical earthquakes in the Lesser Antilles and mechanical coupling with volcanoes. Journal of Geophysial Research: Solid Earth 116, 1–26.

Feuillet, N., Beauducel, F., Jacques, E., Tapponnier, P., Delouis, B., Bazin, S., Vallée, M., King, G.C.P., (2011b). The Mw = 6.3, November 21, 2004, les Saintes earthquake (Guadeloupe): Tectonic setting, slip model and static stress changes. Journal of Geophysical Research: Solid Earth 116, 1–25.

Fick, A., (1855). On liquid diffusion. Phil. Mag. J. Sci. 10, 31-39.

Fortier, S.M., Giletti, B.J. (1989). An empirical model for predicting diffusion coefficients in silicate minerals. Science 245, 1481-1484.

Fournier, N., Witham, F., Moreau-Fournier, M., Bardou, L., 2009. Boiling lake of dominica, west indies: High-temperature volcanic crater lake dynamics. Journal of Geophysical Research Solid Earth.

Francis, P. W., Roobol, M. J., Walker, G. P. L., Cobbold, P. R., & Coward, M. (1974). The San Pedro and San Pablo volcanoes of northern Chile and their hot avalanche deposits. Geologische Rundschau, 63(1), 357-388.

Freer, R., Carpenter, M. A., Long, J. V. P., & Reed, S. J. B. (1982). "Null result" diffusion experiments with diopside: implications for pyroxene equilibria. Earth and Planetary Science Letters, 58(2), 285-292.

G-H-I-J

Ganguly, J., & Tazzoli, V. (1994). Fe2+-Mg interdiffusion in orthopyroxene: retrieval from the data on intracrystalline exchange reaction. American Mineralogist 79, 930-937.

Gardner, J. E., Rutherford, M., Carey, S. & Sigurdsson, H. (1995). Experimental constraints on pre-eruptive water contents and changing magma storage prior to explosive eruptions of Mount St. Helens volcano. Bulletin of Volcanology 57, 1-17.

Garrels, R. M. (1949). Diffusion of ions through intergranular spaces in water-saturated rocks. Geol. Soc. Am. Bull. 60, 1809-1828.

Geyer, A., Folch, A., & Marti, J. (2006). Relationship between caldera collapse and magma chamber withdrawal: an experimental approach. Journal of Volcanology and Geothermal Research, 157(4), 375-386.

Ghiorso, M. S. (1987). Chemical mass transfer in magmatic processes, III: crystal growth, chemical diffusion and thermal diffusion in multicomponent silicate melts. Contributions to Mineralogy and Petrology 96, 291-313.

Ghiorso, M. S., & Evans, B. W. (2008). Thermodynamics of rhombohedral oxide solid solutions and a revision of the Fe-Ti two-oxide geothermometer and oxygen-barometer. American Journal of science, 308(9), 957-1039.

Ginibre, C., Wörner, G., & Kronz, A. (2002a). Minor- and trace-element zoning in plagioclase: implications for magma chamber processes at Parinacota volcano, northern Chile. Contributions to Mineralogy and Petrology, 143(3), 300–315.

Ginibre, C., Kronz, A., & Worner, G. (2002b). High-resolution quantitative imaging of plagioclase composition using accumulated backscattered electron images: new constraints on oscillatory zoning. Contributions to Mineralogy And Petrology, 142(4), 436–448.

Ginibre, C., Wörner, G., & Kronz, A. (2004). Structure and dynamics of the Laacher See magma chamber (Eifel, Germany) from major and trace element zoning in sanidine: A cathodoluminescence and electron microprobe study. Journal of Petrology, 45(11), 2197–2223.

Ginibre, C., Wörner, G., & Kronz, A. (2007). Crystal zoning as an archive for magma evolution. Elements, 3(4), 261-266.

Gourgaud, A., & Bourdier, J. L. (1985). Les Depots des eruptions de 1902 et 1929 de la Montagne Pelee (Martinique): melange de magmas et declenchement des eruptions peleennes. Institut national d'astronomie et de geophysique.

Gravley, D. M., Wilson, C. J. N., Leonard, G. S., & Cole, J. W. (2007). Double trouble: Paired ignimbrite eruptions and collateral subsidence in the Taupo Volcanic Zone, New Zealand. Geological Society of America Bulletin, 119(1-2), 18-30.

Gregg, P. M., De Silva, S. L., Grosfils, E. B., & Parmigiani, J. P. (2012). Catastrophic caldera-forming eruptions: Thermomechanics and implications for eruption triggering and maximum caldera dimensions on Earth. Journal of Volcanology and Geothermal Research, 241–242, 1–12.

Gualda, G. A., & Ghiorso, M. S. (2013). The Bishop Tuff giant magma body: an alternative to the Standard Model. Contributions to Mineralogy and Petrology, 166(3), 755-775.

Gudmundsson, A. (2008). Magma-chamber geometry, fluid transport, local stresses and rock behaviour during collapse caldera formation. Dev. Volcanol. 10, 313-349.

Gurenko, A.A., Trumbull, R.B., Thomas, R., Lindsay, J.M., (2005). A melt inclusion record of volatiles, trace elements and Li-B isotope variations in a single magma system from the Plat Pays Volcanic Complex, Dominica, lesser antilles. Journal of Petrology. 46, 2495–2526.

Halama, R., Boudon, G., Villemant, B., Joron, J.L., Le Friant, A., Komorowski, J.C., (2006). Pre-eruptive crystallization conditions of mafic and silicic magmas at the Plat Pays volcanic complex, Dominica (Lesser Antilles). Journal of Volcanology and Geothermal Research 153, 200–220.

Hammer, J. E., & Rutherford, M. J. (2002). An experimental study of the kinetics of decompression-induced crystallization in silicic melt. Journal of Geophysical Research: Solid Earth, 107(B1).

Hart, S. R. (1981). Diffusion compensation in natural silicates. Geochimica et Cosmochimica Acta, 45(3), 279–291.

Hazen, R. M., & Navrotsky, A. (1996). Effects of pressure on order-disorder reactions. American Mineralogist, 81(9–10), 1021–1035.

Heiken, G., & McCoy, F. (1984). Caldera development during the Minoan eruption, Thira, Cyclades, Greece. Journal of Geophysical Research: Solid Earth, 89(B10), 8441-8462.

Higgins, M. D. (1996). Crystal size distributions and other quantitative textural measurements in lavas and tuff from Egmont volcano (Mt. Taranaki), New Zealand. Bulletin of Volcanology, 58(2-3), 194-204.

Hildreth, W. (1981). Gradients in silicic magma chambers: implications for lithospheric magmatism. Journal of Geophysical Research: Solid Earth, 86(B11), 10153-10192.

Hildreth, W., & Wilson, C. J. (2007). Compositional zoning of the Bishop Tuff. Journal of Petrology, 48(5), 951-999.

Hofmann, A. W. (1980). Diffusion in natural silicate melts: a critical review, to be published in Physics of Magmatic Processes. Bowen Volume II. Princeton University Press, in press.

Holtz, F., Pichavant, M., Barbey, P., Johannes, W. (1992). Effects of H2O on liquidus phase relations in the haplogranite system at 2 and 5 kbar: American Mineralogist 77, 1223-1241.

Holtz, F., Sato, H., Lewis, J., Behrens, H. et Nakada, S., (2005). Experimental petrology of the 1991-1995 Unzen dacite, Japan. Part I: phase relations, phase composition and preeruptive conditions. Journal of Petrology, 46(2), 319-337.

Houghton, B. F., Wilson, C. J. N., McWilliams, M. O., Lariphere, M. A., Weaver, S. D., Briggs, R. M., & Pringle, M. S. (1995). Chronology and dynamics of a large silicic magmatic system. Central Taupo volcanic zone, New Zealand. Geology, 23(1), 13–16.

Howe, T. M., Lindsay, J. M., Shane, P., Schmitt, A. K., & Stockli, D. F. (2014). Re-evaluation of the Roseau Tuff eruptive sequence and other ignimbrites in Dominica, Lesser Antilles. Journal of Quaternary Science, 29(6), 531-546.

Howe, T.M., Lindsay, J.M., Shane, P., (2015a). Evolution of young andesitic-dacitic magmatic systems beneath Dominica, Lesser Antilles. Journal of Volcanology and Geothermal Research 297, 69–88.

Howe, T. M., Schmitt, A. K., Lindsay, J. M., Shane, P., & Stockli, D. F. (2015b). Time scales of intra-oceanic arc magmatism from combined U-Th and (U-Th)/He zircon geochronology of Dominica, Lesser Antilles. Geochemistry, Geophysics, Geosystems, 16(2), 347-365.

Huber, C., Bachmann, O., & Manga, M. (2009). Homogenization processes in silicic magma chambers by stirring and mushification (latent heat buffering). Earth and Planetary Science Letters, 283(1), 38-47.

Huber, C., Bachmann, O., & Dufek, J. (2010a). The limitations of melting on the reactivation of silicic mushes. Journal of Volcanology and Geothermal Research, 195(2), 97-105.

Huber, C., Bachmann, O., & Manga, M. (2010b). Two competing effects of volatiles on heat transfer in crystal-rich magmas: thermal insulation vs defrosting. Journal of Petrology, egq003.

Huber, C., Bachmann, O., & Dufek, J. (2012). Crystal-poor versus crystal-rich ignimbrites: A competition between stirring and reactivation. Geology, 40(2), 115-118.

Huebner, J. S. (1976). Diffusively rimmed xenocrysts in 77115. Lunar Planet. Sci. Conf. 7, 396-398.

Huebner, J. S., & Sato, M. (1970). Oxygen fugacity-temperature relationships of manganese oxide and nickel oxide buffers. American Mineralogist, 55(5-6), 934.

Huebner, J. S., & Nord, G. L. (1981, March). Assessment of diffusion in pyroxenes: what we do and do not know. In Lunar and Planetary Science Conference (Vol. 12, pp. 479-481).

Huebner, J. S., Ross, M., & Hickling, N. (1975). Significance of exsolved pyroxenes from lunar breccia 77215. In Lunar and Planetary Science Conference Proceedings (Vol. 6, pp. 529-546).

Hughes, G. R., & Mahood, G. A. (2008). Tectonic controls on the nature of large silicic calderas in volcanic arcs. Geology, 36(8), 627–630.

Humler, E., & Whitechurch, H. (1988). Petrology of basalts from the Central Indian Ridge (lat. 25 23′ S, long. 70 04′ E): estimates of frequencies and fractional volumes of magma injections in a two-layered reservoir. Earth and Planetary Science Letters, 88(1), 169-181.

Humphreys, M. C., Blundy, J. D., & Sparks, R. S. J. (2006). Magma evolution and open-system processes at Shiveluch Volcano: insights from phenocryst zoning. Journal of Petrology, 47(12), 2303-2334.

Jarrard, R.D., (1986). Terrane motion by strike-slip faulting of forearc slivers. Geology 14 , 780–783.

Jarrard, R. D. (2003). Subduction fluxes of water, carbon dioxide, chlorine, and potassium. Geochemistry, Geophysics, Geosystems, 4(5).

Jellinek, A. M., & DePaolo, D. J. (2003). A model for the origin of large silicic magma chambers: Precursors of caldera-forming eruptions. Bulletin of Volcanology, 65(5), 363–381.

Jerram, D. A., & Martin, V. M. (2008). Understanding crystal populations and their significance through the magma plumbing system. Geological Society, London, Special Publications, 304(1), 133-148.

Jochum, K.P., Weis, U., Schwager, B., Stoll, B., Wilson, S.A., Haug, G.H., Andreae, M.O., Enzweiler, J., 2016. Reference Values Following ISO Guidelines for Frequently Requested Rock Reference Materials. Geostand. Geoanalytical Res. 40, 333–350.

Joseph, E., Lindsay, J., (2002). Sampling of geothermal features in Saint Lucie and Dominica 14th-20th November 2002. Intern. Report, Seism. Res. Unit, St. Augustine, Trinidad.

Joseph, E., Robertson, R., (2003). Sampling of geothermal features in Saint Lucia and Dominica, 3rd-9th November 2003. Intern. Report, Seism. Res. Unit, St. Augustine, Trinidad.

K-L-M

Kahl, M., Chakraborty, S., Costa, F., & Pompilio, M. (2011). Dynamic plumbing system beneath volcanoes revealed by kinetic modeling, and the connection to monitoring data: An example from Mt. Etna. Earth and Planetary Science Letters, 308(1–2), 11–22.

Kahl, M., Chakraborty, S., Costa, F., Pompilio, M., Liuzzo, M., & Viccaro, M. (2013). Compositionally zoned crystals and real-time degassing data reveal changes in magma transfer dynamics during the 2006 summit eruptive episodes of Mt. Etna. Bulletin of Volcanology, 75(2), 1-14.

Kahl, M., Chakraborty, S., Pompilio, M., Costa, F. (2015). Constraints on the nature and evolution of the magma plumbing system of Mt. Etna volcano (1991-2008) from a combined thermodynamic and kinetic modelling of the compositional record of minerals. Journal of Petrol.=ogy 56, 2025–2068.

Kent, A. J., Darr, C., Koleszar, A. M., Salisbury, M. J., & Cooper, K. M. (2010). Preferential eruption of andesitic magmas through recharge filtering. Nature Geoscience, 3(9), 631-636.

Klügel, A. (2001). Prolonged reactions between harzburgite xenoliths and silica-undersaturated melt: implications for dissolution and Fe-Mg interdiffusion rates of orthopyroxene. Contributions to Mineralogy and Petrology, 141(1), 1-14.

Komorowski, J.C., Legendre, Y., Caron, B., Boudon, G., (2008). Reconstruction and analysis of sub-plinian tephra dispersal during the 1530 A.D. Soufrière (Guadeloupe) eruption: Implications for scenario definition and hazards assessment. Journal of Volcanology and Geothermal Research 178, 491–515.

Kopp, H., Weinzierl, W., Becel, A., Charvis, P., Evain, M., Flueh, E. R., Klaeschen, D. (2011). Deep structure of the central Lesser Antilles Island Arc: relevance for the formation of continental crust. Earth and Planetary Science Letters, 304(1), 121-134.

Kress, V. C., Ghiorso, M. S. (1993). Multicomponent diffusion in mgO-Al2O3-SiO2 and CaO-MgO-Al2O3-SiO2 melts. Geochimica and Cosmochimica Acta 57, 4453-4466.

Lasaga, A. C. (1979). Multicomponent exchange and diffusion in silicates. Geochimica and Cosmochimica Acta 43, 455-469.

Lavigne, F., Degeai, J.-P., Komorowski, J.-C., Guillet, S., Robert, V., Lahitte, P., Oppenheimer, C., Stoffel, M., Vidal, C.M., Surono, Pratomo, I., Wassmer, P., Hajdas, I., Hadmoko, D.S., de Belizal, E. (2013). Source of the great A.D. 1257 mystery eruption unveiled, Samalas volcano, Rinjani Volcanic Complex, Indonesia. Proc. Natl. Acad. Sci. 110, 16742–16747.

Leake, B. E., Woolley, A. R., Arps, C. E. S., Birch, W. D., Gilbert, M. C., Grice, J. D., et al. (1997). Nomenclature of amphiboles: report of the Subcommittee on Amphiboles of the International Mineralogical Association, commission on new minerals and minerals names. American Mineralogist 82, 1019-1037.

Le Friant, A., Boudon, G., Komorowski, J.C., Deplus, C., (2002). L'île de la Dominique, à l'origine des avalanches de débris les plus volumineuses de l'arc des Petites Antilles. Comptes Rendus Geosci. 334, 235–243.

Le Friant, A., Boudon, G., Deplus, C., Villemant, B., (2003a). Large-scale flank collapse events during the activity of Montagne Pelée, Martinique, Lesser Antilles. Journal of Geophysical Research: Solid Earth 108.

Le Friant, A., O. Ishizuka, N. A. Stroncik, and the Expedition 340 Scientists (2013), Proceedings of Integrated Ocean Drilling Program, 340, Integrated Ocean Drill. Program Manage. Int. Inc., Tokyo.

Le Friant, A., Ishizuka, O., Boudon, G., Palmer, M.R., Talling, P.J., Villemant, B., Adachi, T., Aljahdali, M., Breitkreuz, C., Brunet, M., Caron, B., Coussens, M., Deplus, C., Endo, D., Feuillet, N., Fraas, A.J., Fujinawa, A., Hart, M.B., Hatfield, R.G., Hornbach, M., Jutzeler, M., Kataoka, K.S., Komorowski, J.-C., Lebas, E., Lafuerza, S., Maeno, F., Manga, M., Martínez-Colón, M., McCanta, M., Morgan, S., Saito, T., Slagle, A., Sparks, S., Stinton, A., Stroncik, N., Subramanyam, K.S. V, Tamura, Y., Trofimovs, J., Voight, B., Wall-Palmer, D., Wang, F., Watt, S.F.L., (2015). Submarine record of volcanic island construction and collapse in the Lesser

Antilles arc: First scientific drilling of submarine volcanic island landslides by IODPExpedition 340. Geochemistry, Geophysics, Geosystems 16, 420–442.

Legendre, Y. (2012). Reconstruction fine de l'histoire éruptive et scénarii éruptifs à la Soufrière de Guadeloupe: vers un modèle intégré de fonctionnement du volcan. IPGP.

Leonard, G. S., Cole, J. W., Nairn, I. A., & Self, S. (2002). Basalt triggering of the c. AD 1305 Kaharoa rhyolite eruption, Tarawera volcanic complex, New Zealand. Journal of Volcanology and Geothermal Research, 115(3), 461-486.

Liang, Y., Richter, F. M., Chaberlin, L. (1997). Diffusion in silicate melts: III. Empirical models for multicomponent diffusion. Geochimica and Cosmochimica Acta 61, 5295-5312.

Lindner, R. (1955). Studies on solid state reactions with radiotracers. The Journal of Chemical Physics, 23(2), 410-411.

Lindsay, J., Stasiuk, M., & Shepherd, J. (2003). Geological history and potential hazards of the late-Pleistocene to Recent Plat Pays volcanic complex, Dominica, Lesser Antilles. Bulletin of Volcanology, 65, 201–220.

Lindsay, J.M., Trumbull, R.B., Siebel, W., (2005a). Geochemistry and petrogenesis of late Pleistocene to Recent volcanism in Southern Dominica, Lesser Antilles. Journal of Volcanology and Geothermal Research 148, 253–294.

Lindsay J, Robertson R, Shepherd B, et al. editors. (2005b). Volcanic Hazard Atlas of the Lesser Antilles. Seismic Research Centre,Trinidad and IAVCEI: University of the West Indies.

Lipman, P., Dungan, M., & Bachmann, O. (1997). Comagmatic granophyric granite in the Fish Canyon Tuff, Colorado: Implications for magma-chamber processes during a large ash-flow eruption. Geology, 25(10), 915–918.

Lipman, P. W. (2007). Incremental assembly and prolonged consolidation of Cordilleran magma chambers: Evidence from the Southern Rocky Mountain volcanic field. Geosphere, 3(1), 42-70.

Luhr, J. (1990). Experimental phase relations of water and sulfursaturated arc magmas and the 1982 eruptions of El Chichon volcano. Journal of Petrology 31, 1071-1114.

Macdonald, K.C., Holcombe, T.L., (1978). Inversion of magnetic anomalies and sea-floor spreading in the Cayman Trough. Earth and Planetary Science Letters 40, 407–414.

Macdonald, R., Hawkesworth, C. J., & Heath, E. (2000). The Lesser Antilles volcanic chain: A study in arc magmatism. Earth Science Reviews, 49(1–4), 1–76.

Mangan, M. T. (1990). Crystal size distribution systematics and the determination of magma storage times: the 1959 eruption of Kilauea volcano, Hawaii. Journal of Volcanology and Geothermal Research, 44(3-4), 295-302.

Manning, C. E. (2004). The chemistry of subduction-zone fluids. Earth and Planetary Science Letters, 223(1), 1-16.

Marsh, B. D. (1981). On the crystallinity, probability of occurrence, and rheology of lava and magma. Contributions to Mineralogy and Petrology, 78(1), 85-98.

Marsh, B. D. (1989). Magma chambers. Annual Review of Earth and Planetary Sciences, 17, 439-474.

Marsh, B. D. (1996). Solidification fronts and magmatic evolution. Mineralogical Magazine, 60(1), 5-40.

Marsh, B. D. (1998). On the interpretation of crystal size distributions in magmatic systems. Journal of Petrology, 39(4), 553-599.

Marsh, B. D. (2000). Magma chambers. Encyclopedia of volcanoes, 1, 191-206.

Marsh, B. D. (2006). Dynamics of magmatic systems. Elements, 2(5), 287-292.

Martel, C., Pichavant, M., Bourdier, J. L., Traineau, H., Holtz, F., & Scaillet, B. (1998). Magma storage conditions and control of eruption regime in silicic volcanoes: experimental evidence from Mt. Pelée. Earth and Planetary Science Letters, 156(1), 89-99.

Martel, C., Pichavant, M., Holtz, F., Scaillet, B., Bourdier, J.-L., Traineau, H., (1999). Effects of fO2 and H2O on andesite phase relations between 2 and 4 kbar. Journal of Geophysical Research: Solid Earth 104, 29453–29470.

Martin, V. M., Morgan, D. J., Jerram, D. A., Caddick, M. J., Prior, D. J., & Davidson, J. P. (2008). Bang! Month-Scale Eruption Triggering at Santorini Volcano. Science, 321(5893), 1178–1178.

Martin-Kaye, P., (1960). Preliminary notes on the geological map of Dominica. Unpublished progress reports of the Government Geologist 1-12. Geological Survey, Windward Islands

Martin-Kaye, P., (1969). A summary of the geology of the Lesser Antilles. Overseas Geol. Mineal Resour. 10, 172–206.

Matthews, N. E., Pyle, D. M., Smith, V. C., Wilson, C. J. N., Huber, C., Hinsberg, V. (2011) Quartz zoning and the pre-eruptive evolution of the ~340-ka Whakamaru magma systems, New Zealand. Contributions to Mineralogy and Petrology 163, 87-107.

Matthews, N. E., Huber, C., Pyle, D. M., & Smith, V. C. (2012). Timescales of magma recharge and reactivation of large silicic systems from ti diffusion in quartz. Journal of Petrology, 53(7), 1385–1416.

McCallister, R. H., Brady, J. B., & Mysen, B. O. (1979). Self-diffusion of Ca in diopside. Carnegie Inst. Washington Yearb, 78, 574-577.

Mehrer, H. (1996). Diffusion in intermetallics. Materials transactions, JIM, 37(6), 1259-1280.

Miller, C.D., (1978). Holocene pyroclastic-flow deposits from Shastina and Black Butte, west of Mount Shasta, California. J. Res. U.S. Geol. Surv. 6, 611–623.

Miller, C. F., Wark, D. A. (2008). Supervolcanoes and their explosive supereruptions. Elements, 4(1), 11-15.

Milman-Barris, M. S., Beckett, J. R., Michael, M. B., Hofmann, A. E., Morgan, Z., Crowley, M. R., Vielzeuf, D., Stolper, E. (2008). Zoning of phosphorus in igneous olivine. Contributions to Mineralogy and Petrology 155, 739-765.

Molin, G., & Zanazzi, P. F., 1991. Intracrystalline Fe2+-Mg ordering in augite: experimental study and geothermometric applications. European Journal of Mineralogy, 3(5), 863-875.

Molin, G. M., Saxena, S. K., & Brizi, E. (1991). Iron-magnesium order-disorder in an orthopyroxene crystal from the Johnstown meteorite. Earth and Planetary Science Letters, 105(1-3), 260-265.

Monjaret, M.-C., (1985). Contribution à l'étude de l'arc des Petites Antilles. Le Volcanisme de la Dominique, Données chronologiques, minéralogiques et géochimiques. Unpublished Thesis, Université de Bretagne Occidentale, pp1-77

Morgan, D. J., & Blake, S. (2006). Magmatic residence times of zoned phenocrysts: Introduction and application of the binary element diffusion modelling (BEDM) technique. Contributions to Mineralogy and Petrology, 151(1), 58–70.

Morgan, D. J., & Jerram, D. A. (2006). On estimating crystal shape for crystal size distribution analysis. Journal of Volcanology and Geothermal Research, 154(1), 1-7.

Morgan, D. J., Blake, S., Rogers, N. W., DeVivo, B., Rolandi, G., Macdonald, R., & Hawkesworth, C. J. (2004). Time scales of crystal residence and magma chamber volume from modelling of diffusion profiles in phenocrysts: Vesuvius 1944. Earth and Planetary Science Letters, 222(3–4), 933–946.

Morgan, D. J., Blake, S., Rogers, N. M., De Vivo, B., Rolandi, G., & Davidson, J. P. (2006). Magma chamber recharge at Vesuvius in the century prior to the eruption of A.D. 79. Geology, 34(10), 845–848.

Morgan, D. J., Jerram, D. A., Chertkoff, D. G., Davidson, J. P., Pearson, D. G., Kronz, A., & Nowell, G. M. (2007). Combining CSD and isotopic microanalysis: magma supply and mixing processes at Stromboli Volcano, Aeolian Islands, Italy. Earth and Planetary Science Letters, 260(3), 419-431.

Mueller, T., Dohmen, R., Becker, H. W., ter Heege, J. H., & Chakraborty, S. (2013). Fe-Mg interdiffusion rates in clinopyroxene: Experimental data and implications for Fe-Mg exchange geothermometers. Contributions to Mineralogy and Petrology, 166(6), 1563–1576.

Mungall, J. E., Romano, C., & Dingwell, D. B. (1998). Multicomponent diffusion in the molten system K2O-Na2O-Al2O3-SiO2-H2O. American Mineralogist, 83(7-8), 685-699.

Murphy, M. D., Sparks, R. S. J., Barclay, J., Carroll, M. R., Lejeune, A. M., Brewer, T. S., ... & Young, S. (1998). The role of magma mixing in triggering the current eruption at the Soufriere Hills volcano, Montserrat, West Indies. Geophysical Research Letters, 25(18), 3433-3436.

Murphy, M. D., Sparks, R. S. J., Barclay, J., Carroll, M. R., & Brewer, T. S. (2000). Remobilization of andesite magma by intrusion of mafic magma at the Soufriere Hills Volcano, Montserrat, West Indies. Journal of petrology, 41(1), 21-42.

N-O-P-Q

Nagle, F., Stipp, J.J., Fisher, D.E., (1976). K-Ar geochronology of the Limestone Caribbees and Martinique, Lesser Antilles, West Indies. Earth and Planetary Science Letters 29, 401–412.

Nakamura, M. (1995). Continuous mixing of crystal mush and replenished magma in the ongoing Unzen eruption. Geology, 23(9), 807-810.

Nakagawa, M., Wada K., & Wood C. P. (2002). Mixed magmas, mush chambers and eruption triggers: evidence from zoned clinopyroxene phenocrysts in andesitic scoria from the 1995 eruptions of Ruapehu volcano, New Zealand. Journal of petrology, 43(12), 2279-2303.

Nelson, S. T., Montana A. (1992). Sieve-textured plagioclase in volcanic rocks produced by rapid decompression. American Mineralogist, 77, 1242-1249.

Newman, S., & Lowenstern, J. B. (2002). VolatileCalc: a silicate melt–H 2 O–CO 2 solution model written in Visual Basic for Excel. Computers & Geosciences, 28(5), 597-604.

Nicholls, H., (1880a). The volcanic eruption in Dominica. Nature 21, 372–373.

Nicholls, H., (1880b). Visit to the scene of the late volcanic eruption. Dominica.

Oppenheimer, C. (2011). Eruptions that shook the world. Cambridge University Press.

Pallister, J. S., Hoblitt, R. P., & Reyes, A. G. (1992). A basalt trigger for the 1991 eruptions of Pinatubo Volcano?. Nature, 356(6368), 426-428.

Palm, W. J. (2005). System dynamics. McGraw-Hill Higher Education.

Pan, Y., & Batiza, R. (2002). Mid-ocean ridge magma chamber processes: constraints from olivine zonation in lavas from the East Pacific Rise at 9°30'N and 10°30'N. Journal of Geophysical Research 107, 2022-2035.

Parat, F., Holtz, F., & Feig, S. (2008). Pre-eruptive conditions of the Huerto andesite (Fish canyon system, San Juan volcanic field, Colorado): influence of volatiles (C–O–H–S) on phase equilibria and mineral composition. Journal of Petrology, 49(5), 911-935.

Peacock, S. M. (1990). Fluid processes in subduction zones. Science, 248(4953), 329-337.

Penrose, R. A. F. Jr. (1914). Certain phases of superficial diffusion in ore deposits. Econ. Geol. 9, 20-24.

Perret, F.A., (1935). The eruption of Mt. Pelée, 1929-1932. Canergie Inst. Washington Publication.

Phillips, J. C., & Woods, A. W. (2002). Suppression of large-scale magma mixing by melt–volatile separation. Earth and Planetary Science Letters, 204(1), 47-60.

Picard, M., Schneider, J. L., & Boudon, G. (2006). Contrasting sedimentary processes along a convergent margin: the Lesser Antilles arc system. Geo-Marine Letters, 26(6), 397-410.

Pichavant, M., Macdonald, R., (2007). Crystallization of primitive basaltic magmas at crustal pressures and genesis of the calc-alkaline igneous suite: Experimental evidence from St Vincent, Lesser Antilles arc. Contributions to Mineralogy and Petrology 154, 535–558.

Pichavant, M., Martel, C., Bourdier, J.-L., Scaillet, B., (2002). Physical conditions, structure, and dynamics of a zoned magma chamber: Mount Pelée (Martinique, Lesser Antilles Arc). Journal of Geophysical Research 107, 2093.

Pinel, V., & Jaupart, C. (2000). The effect of edifice load on magma ascent beneath a volcano. Philosophical Transactions of the Royal Society of London A: Mathematical, Physical and Engineering Sciences, 358(1770), 1515-1532.

Pinel, V., & Jaupart, C. (2003). Magma chamber behavior beneath a volcanic edifice. Journal of Geophysical Research: Solid Earth, 108(B2).

Pistone, M., Caricchi, L., Ulmer, P., Reusser, E., & Ardia, P. (2013). Rheology of volatile-bearing crystal mushes: mobilization vs. viscous death. Chemical Geology, 345, 16-39.

Poussineau, S., (2005). Dynamique des magmas andésitiques: approche expérimentale et pétrostructurale; application à la Soufrière de Guadeloupe et à la Montagne Pelée (Thèse).

Pownceby, M. I., & O'Neil, H. (1994) Thermodynamic data from redox reactions at high temperature. III. Activity-composition relations in Ni-Pd alloys from EMF measurements at 850-1250 K, and calibration of the NiO-Ni-Pd assemblage as a redox sensor. Contribution to Mineralogy and Petrology 116, 327-339.

Press, W. H., Tekolsky, S. A., Vetterling, W. T., Flannery, B. P. (2007) Numerical Recipes. Cambridge University Press, Cambridge.

Putirka, K. D. (2008). Thermometers and barometers for volcanic systems. Reviews in Mineralogy and Geochemistry, 69(1), 61-120.

R-S-T-U

Rad, S., Rivé, K., Vittecoq, B., Cerdan, O., & Allègre, C. J. (2013). Chemical weathering and erosion rates in the Lesser Antilles: An overview in Guadeloupe, Martinique and Dominica. Journal of South American Earth Sciences, 45, 331-344.

Rae, A. S. P., Edmonds, M., Maclennan, J., Morgan, D., Houghton, B., Hartley, M. E., & Sides, I. (2016). Time scales of magma transport and mixing at Kilauea Volcano, Hawaii. Geology, 44(6), 463–466.

Reide, (2016). Volcanic activity and human society. Quaternary International, 394, 1-5.

Reimer, P. (2013). Selection and Treatment of Data for Radiocarbon Calibration: An Update to the International Calibration (IntCal) Criteria. Radiocarbon 55, 1923–1945.

Reubi, O., & Nicholls, I. A. (2004). Variability in eruptive dynamics associated with caldera collapse: An example from two successive eruptions at Batur volcanic field, Bali, Indonesia. Bulletin of Volcanology, 66(2), 134–148.

Reubi, O., & Nicholls, I. A. (2005). Structure and dynamics of a silicic magmatic system associated with caldera-forming eruptions at Batur volcanic field, Bali, Indonesia. Journal of Petrology, 46(7), 1367–1391.

Reynolds, D. L. (1947). The granite controversy. Geology Mag. 84, 209-223.

Ridolfi, F., & Renzulli, A. (2012). Calcic amphiboles in calc-alkaline and alkaline magmas: thermobarometric and chemometric empirical equations valid up to 1,130° C and 2.2 GPa. Contributions to Mineralogy and Petrology, 163(5), 877-895.

Robie, R., Hemingway, B., & Fisher, J. (1978). Thermodynamic Properties of Minerals and Related Substances at 298.15K and 1bar Pressure and at Higher Temperatures. US Geological Survey, 1452.

Robson, G.R., Willmore, P.L., (1955). Some heat measurements in West Indian Soufrières. Bulletin of Volcanology 17, 13–39.

Robson, G.R., Tomblin, J.F., (1966). Catalogue of the active volcanoes of the world including solfatara fields, part 20, the West Indies, in: International Association of Volcanologists. pp. 1–56.

Roeder, P. L., & Emslie, R. (1970). Olivine-liquid equilibrium. Contributions to Mineralogy and Petrology, 29(4), 275-289.

Roobol, M. J., & Smith, A. L. (2005). Geological Map of Dominica, scale 1: 100,000. Volcanic Hazard Atlas of the Lesser Antilles, University of the West Indies.

Roobol, M.J., Wright, J. V., Smith, A.L., (1983). Calderas or gravity-slide structures in the Lesser Antilles island arc? Journal of Volcanology and Geothermal Research 19, 121–134.

Rose, W. I., & Chesner, C. A. (1987). Dispersal of ash in the great Toba eruption, 75 ka. Geology, 15(10), 913-917.Schmidt, M. W., & Poli, S. (1998). Experimentally based water budgets for dehydrating slabs and consequences for arc magma generation. Earth and Planetary Science Letters 163 (1), 361-379.

Roux, J., Holtz, F., Lefevre, A. and Schulze, F. (1994). A reliable high temperature setup for internally heated pressure vessels - Applications to silicate melt studies. American Mineralogist, 79: 1145-l 149.

Ruprecht, P., & Cooper, K. M. (2012). Integrating the uranium-series and elemental diffusion geochronometers in mixed magmas from Volcan Quizapu, Central Chile. Journal of Petrology, 53(4), 841–871.

Ruprecht, P., & Wörner, G. (2007). Variable regimes in magma systems documented in plagioclase zoning patterns: El Misti stratovolcano and Andahua monogenetic cones. Journal of Volcanology and Geothermal Research, 165(3), 142-162.

Ruprecht, P., & Plank, T. (2013). Feeding andesitic eruptions with a high-speed connection from the mantle. Nature 500 (7460), 68-72.

Ruprecht, P., Bergantz, G. W., & Dufek, J. (2008). Modeling of gas-driven magmatic overturn: Tracking of phenocryst dispersal and gathering during magma mixing. Geochemistry, Geophysics, Geosystems, 9(7).

Rutherford, M. J., Sigurdsson, H. & Carey, S. (1985). The May 18, 1980, eruption of Mount St. Helens, 1. Melt compositions and experimental phase equilibria. Journal of Geophysical Research 90, 2929-2947.

Salisbury, M. J., Bohrson, W. A., Clynne, M. A., Ramos, F. C., & Hoskin, P. (2008). Multiple plagioclase crystal populations identified by crystal size distribution and in situ chemical data: implications for timescales of magma chamber processes associated with the 1915 eruption of Lassen Peak, CA. Journal of Petrology, 49(10), 1755-1780.

Sapper, K., (1903). Ein Besuch von Dominica. Zentralblatt für Mineral. Geol. Paleontol. 305–314.

Sato, H., Nakada, S., Fujii, T., Nakamura, M. & Suzuki-Kamata, K. (1999). Groundmass pargasite in the 1991-1995 dacite of Unzen volcano: phase stability experiments and volcanological implications. Journal of Volcanology and Geothermal Research 89, 197-212.

Sauerzapf, U., Lattard, D., Burchard, M., & Engelmann, R. (2008). The titanomagnetite–ilmenite equilibrium: new experimental data and thermo-oxybarometric application to the crystallization of basic to intermediate rocks. Journal of Petrology, 49(6), 1161-1185.

Saunders, K. E., Morgan, D. J., Baker, J. A., & Wysoczanski, R. J. (2010). The magmatic evolution of the Whakamaru supereruption, New Zealand, constrained by a microanalytical study of plagioclase and quartz. Journal of Petrology, 51(12), 2465–2488.

Saunders, K., Blundy, J., Dohmen, R., & Cashman, K. (2012). Linking Petrology and Seismology at an Active Volcano. Science, 336(6084), 1023–1027.

Scaillet, B. & Evans, W. E. (1999). The 15 June 1991 eruption of Mount Pinatubo. I. Phase equilibria and pre-eruption P-T-fO2-f H2O conditions of the dacite magma. Journal of Petrology 40, 381-411.

Schöpa, A., Annen, C. (2013). The effects of magma flux variations on the formation and lifetime of large silicic magma chambers. Journal of Geophysical Research: Solid Earth, 118(3), 926-942.

Scott,W. E., Hoblitt, R. P., Torres, R. C., Self, S., Martinez, M. L.&Nillos Jr, T. (1996) Pyroclastic flow deposits fromthe 15 June 1991 eruption ofMountPinatubo. In Fire and mud: eruptions and lahars of Mount Pinatubo, Philippines (ed. C. G. Newhall & R. S. Punongbayan), pp. 545–570. Quezon City; Seattle: Philippine Institute of Volcanology and Seismology; University of Washington Press.

Seitz, M. G. (1973). Uranium and thorium diffusion in diopside and fluorapatite. Year Book – Carnegie Institution Washington 72, 586-588.

Self, S. (2006). The effects and consequences of very large explosive volcanic eruptions. Philosophical Transactions of the Royal Society of London A: Mathematical, Physical and Engineering Sciences, 364(1845), 2073-2097.

Self, S., & Rampino, M. R. (1981). The 1883 eruption of Krakatau. Nature, 294, 699–704.

Self, S., Rampino, M. R., Newton, M. S., & Wolff, J. A. (1984). Volcanological study of the great Tambora eruption of 1815. Geology, 12(11), 659–663.

Self, S., Zhao, J.-X., Holasek, R.E., Torres, R.C., King, A.J. (1993). The Atmospheric Impact of the 1991 Mount Pinatubo Eruption, in: Fire and Mud: Eruptions and Lahars of Mount Pinatubo, Philippines. pp. 1089–1115.

Shane, P., Nairn, I. A., Smith, V. C., Darragh, M., Beggs, K., & Cole, J. W. (2008). Silicic recharge of multiple rhyolite magmas by basaltic intrusion during the 22.6 ka Okareka Eruption Episode, New Zealand. Lithos, 103(3–4), 527–549.

Shcherbakov, V. D., Plechov, P. Y., Izbekov, P. E., & Shipman, J. S. (2011). Plagioclase zoning as an indicator of magma processes at Bezymianny Volcano, Kamchatka. Contributions to Mineralogy and Petrology, 162(1), 83-99.

Shepherd, J.B., Lynch, L., Stasiuk, M. V., Latchman, J., Lindsay, J., Devine, J.D., Hoblitt, C., Miller, D., (2000). Shallow Magma Intrusion Generates Volcanic Earthquake Swarm Beneath Dominica, West Indies, September 1998 to July 2000., in: Conference Abstracts, IAVCEI General Assemby, Bali.

Sigurdsson, H., (1972). Partly-welded pyroclast flow deposits in Dominica, Lesser Antilles. Bulletin of Volcanology. 36, 148–163.

Sigurdsson, H., Carey, S.N., (1981). Marine Tephrochronology and Quaternary Explosive Volcanism in the Lesser Antilles Arc, in: Self, S., Sparks, R.S.J. (Eds.), Tephra Studies: Proceedings of the NATO Advanced Study Institute Tephra Studies as a Tool in Quaternary Research'', Held in Laugarvatn and Reykjavik, Iceland, June 18--29, 1980. Springer Netherlands, Dordrecht, pp. 255–280.

Sigurdsson, H., Carey, S., Alexandri, M., Vougioukalakis, G., Croff, K., Roman, C., & Goguo, A. (2006). Marine investigations of Greece's Santorini volcanic field. *EOS,* Transactions American Geophysical Union, 87(34), 337-342.

Sisson, T. W., & Layne, G. D. (1993). H2O in basalt and basaltic andesite glass inclusions from four subduction-related volcanoes. Earth and Planetary Science Letters, 117(3-4), 619-635.

Smith W.H.T. and Sandwell D.T., (1997) Global see floor topography from satellite altimetry and ship depth soundings. Science, 227, 1956-1962.

Smith, A.L., Roobol, M.J., Mattioli, G.S., Fryxell, J.E., Daly, G.E., Fernandez, L.A. (2013). The Volcanic Geology of the Mid-Arc Island of Dominica, Lesser Antilles—The Surface Expression of an Island-Arc Batholith, Geological Society of America Special Papers.

Sneeringer, M., & Hart, S. R. (1978). Sr diffusion in diopside. EOS Trans. Am. Geophys. Union 59, 402.

Sparks, R.S.J., (1976). Grain size variations in ignimbrites and implications for the transport of pyroclastic flows. Sedimentology 23, 147–188.

Sparks, R.S.J., Sigurdsson, H., Carey, S.N., (1980a). The entrance of pyroclastic flows into the sea I. oceanographic and geologic evidence from dominica, lesser antilles. Journal of Volcanology and Geothermal Research 7, 87–96.

Sparks, R.S.J., Sigurdsson, H., Carey, S.N., (1980b). The entrance of pyroclastic flows into the sea, II. theoretical considerations on subaqueous emplacement and welding. Journal of Volcanology and Geothermal Research 7, 97–105.

Sparks, R. S. J., Huppert, H. E., Turner, J. S., Sakuyama, M., & O'Hara, M. J. (1984). The fluid dynamics of evolving magma chambers [and discussion]. Philosophical Transactions of the Royal Society of London A: Mathematical, Physical and Engineering Sciences, 310(1514), 511-534.

Stanford, R. F., Huebner, J. S. (1979). Reexamination of diffusion processes in 77115 and 77215. Lunar Planet. Sci. X, 1052-1054.

Stasiuk, M. V., Shepherd, J.B., Latchman, J., Lindsay, J.M., (2002). Intrusion induced caldera fault slip imaged by shallow seismicity on Dominica , West Indies. Seismol. Res. Lett. 73, p. 242.

Stern, R. J. (2002). Subduction zones. Reviews of geophysics, 40(4).

Stewart, M. L., & Fowler, A. D. (2001). The nature and occurrence of discrete zoning in plagioclase from recently erupted andesitic volcanic rocks, Montserrat. Journal of Volcanology and Geothermal Research, 106(3), 243-253.

Stimpfl, M., Ganguly, J., & Molin, G. (2005). Kinetics of Fe2+-Mg order-disorder in orthopyroxene: Experimental studies and applications to cooling rates of rocks. Contributions to Mineralogy and Petrology, 150(3), 319–334.

Stormer, J. C., & Nicholls, J. (1978). XLFRAC: a program for the interactive testing of magmatic differentiation models. Computers & Geosciences, 4(2), 143-159.

Sykes, L. R., McCann, W. R., & Kafka, A. L. (1982). Motion of Caribbean plate during last 7 million years and implications for earlier Cenozoic movements. Journal of Geophysical Research: Solid Earth, 87(B13), 10656-10676.

Tatsumi, Y. (1989). Migration of fluid phases and genesis of basalt magmas in subduction zones. Journal of Geophysical Research: Solid Earth, 94(B4), 4697-4707.

Tatsumi, Y., & Eggins, S. (1995). Subduction zone magmatism (Vol. 1). Wiley.

Taylor, J. R., Wall, V. J., & Pownceby, M. I. (1992). The calibration and application of accurate redox sensors. American Mineralogist, 77(3–4), 284–295.

Tepley, F. J., Davidson, J. P., Tilling, R. I., & Arth, J. G. (2000). Magma mixing, recharge and eruption histories recorded in plagioclase phenocrysts from El Chichon Volcano, Mexico. Journal of Petrology, 41(9), 1397-1411.

Ter Heege, J. H., Dohmen, R., Becker, H., & Chakraborty, S. (2006, December). Experimental determination of Fe-Mg interdiffusion coefficients in orthopyroxene using pulsed laser ablation and nanoscale thin films. In AGU Fall Meeting Abstracts (Vol. 1, p. 0004).

Tomiya, A., & Takahashi, E. (2005). Evolution of the magma chamber beneath Usu Volcano since 1663: a natural laboratory for observing changing phenocryst compositions and textures. Journal of Petrology, 46(12), 2395-2426.

Tomiya, A., Miyagi, I., Saito, G., & Geshi, N. (2013). Short time scales of magma-mixing processes prior to the 2011 eruption of Shinmoedake volcano, Kirishima volcanic group, Japan. Bulletin of Volcanology, 75(10), 1–19. https://doi.org/10.1007/s00445-013-0750-1

Trial, A. F., Spera, F. J. (1994). Measuring the multicomponent diffusion matrix: experimental design and data analysis for silicate melts. Geochimica and Cosmochimica Acta 58, 3769-3783.

Trofimovs, J., Talling, P.J., Fisher, J.K., Sparks, R.S.J., Watt, S.F.L., Hart, M.B., Smart, C.W., Le Friant, A., Cassidy, M., Moreton, S.G., Leng, M.J., (2013). Timing, origin and emplacement dynamics of mass flows offshore of SE Montserrat in the last 110 ka: Implications for landslide and tsunami hazards, eruption history, and volcanic island evolution. Geochemistry, Geophysics, Geosystems 14, 385–406.

Turner, J. S., & Campbell, I. H. (1986). Convection and mixing in magma chambers. Earth-Science Reviews, 23(4), 255-352.

V-W-X-Y-Z

Van Orman, J. A., Cherniak, D. J., Kita, N. T. (2014). Magnesium diffusion in plagioclase: Dependence on composition, and implications for thermal resetting of the 26Al-26Mg early solar system chronometer. Earth and Planetary Science Letters 385, 79-88.

Van Orstrand, C. E. (1915). Preliminary report on the diffusion of solids. U. S. Geol. Survey Prof. Pap. 95-G, 83-96.

Vidal, C.M., Métrich, N., Komorowski, J.-C., Pratomo, I., Michel, A., Kartadinata, N., Robert, V., Lavigne, F. (2016). The 1257 Samalas eruption (Lombok, Indonesia): the single greatest stratospheric gas release of the Common Era. Sci. Rep. 6, 34868.

Wadge, G., (1984). Comparison of volcanic production rates and subduction rates in the Lesser Antilles and Central America. Geology 12, 555–558.

Wadge, G., (1985). Morne Patates volcano, southern Dominica, Lesser Antilles. Geol. Mag. 122, 253–260.

Wadge, G., (1986). The dykes and structural setting of the volcanic front in the Lesser Antilles island arc. Bulletin of Volcanology. 48, 349–372.

Wadge G. (1989). A Preliminary Analysis of Volcanic Hazards in Dominica. Seismic Research Unit: St. Augustine, Trinidad.

Wadge, G., Shepherd, J.B., (1984). Segmentation of the Lesser Antilles subduction zone. Earth and Planetary Science Letters 71, 297–304.

Wadge, G., Herd, R., Ryan, G., Calder, E.S., Komorowski, J.C. (2010). Lava production at Soufrière Hills Volcano, Montserrat: 1995-2009. Geophys. Res. Lett. 37.

Walker, G.P.L., 1983. Ignimbrite types and ignimbrite problems. Journal of Volcanology and Geothermal Research 17, 65–88.

Wallace, G. S., & Bergantz, G. W. (2002). Wavelet-based correlation (WBC) of zoned crystal populations and magma mixing. Earth and Planetary Science Letters, 202(1), 133-145.

Wallace, G. S., & Bergantz, G. W. (2004). Constraints on mingling of crystal populations from off-center zoning profiles: a statistical approach. American Mineralogist, 89(1), 64-73.

Wallace, G. S., & Bergantz, G. W. (2005). Reconciling heterogeneity in crystal zoning data: an application of shared characteristic diagrams at Chaos Crags, Lassen Volcanic Center, California. Contributions to Mineralogy and Petrology, 149(1), 98-112.

Ward, G.K., Wilson, S.R., 1978. Procedures for Comparing and Combining Radiocarbon Age Determinations: a Critique. Archaeometry 20, 19–31.

Wark, D. A., Hildreth, W., Spear, F. S., Cherniak, D. J., & Watson, E. B. (2007). Pre-eruption recharge of the Bishop magma system. Geology, 35(3), 235-238.

Waters, L. E., & Lange, R. A. (2015). An updated calibration of the plagioclase-liquid hygrometer-thermometer applicable to basalts through rhyolites. American Mineralogist, 100(10), 2172-2184.

Watt, E., 1880. Recent volcanic eruption in Dominica. Nature p .77.

Westercamp, D., 1988. Magma generation in the Lesser Antilles: geological constraints. Tectonophysics 149, 145–163.

Westercamp, D., Traineau, H., 1983. The past 5,000 years of volcanic activity at Mt. Pelee martinique (F.W.I.): Implications for assessment of volcanic hazards. Journal of Volcanology and Geothermal Research 17, 159–185.

Whitham, A. G. (1989). The behaviour of subaerially produced pyroclastic flows in a subaqueous environment: evidence from the Roseau eruption, Dominica, West Indies. Marine Geology, 86(1), 27-40.

Wills, K., 1974. The Geological History of Southern Dominica and Plutonic Nodules from the Lesser Antilles. University of Durham.

Wilson, C. J. N. (2001). The 26.5 ka Oruanui eruption, New Zealand: An introduction and overview. Journal of Volcanology and Geothermal Research (Vol. 112).

Wilson, C. J. (2008). Supereruptions and supervolcanoes: processes and products. Elements, 4(1), 29-34.

Wilson, C. J. N., Rogan, A. M., Smith, I. E. M., Northey, D. J., Nairn, I. A., & Houghton, B. F. (1984). Caldera volcanoes of the Taupo volcanic zone, New Zealand. Journal of Geophysical Research: Solid Earth, 89(B10), 8463-8484.

Wilson, C. J. N., Houghton, B. F., McWilliams, M. O., Lanphere, M. A., Weaver, S. D., & Briggs, R. M. (1995). Volcanic and structural evolution of Taupo Volcanic Zone, New-Zealand: a review. Journal of Volcanology and Geothermal Research, 68(1–3), 1–28.

Wilson, C. J., & Hildreth, W. (1997). The Bishop Tuff: new insights from eruptive stratigraphy. The Journal of Geology, 105(4), 407-440.

Wilson, C. J. N., Blake, S., Charlier, B. L. A., & Sutton, A. N. (2006). The 26· 5 ka Oruanui eruption, Taupo volcano, New Zealand: development, characteristics and evacuation of a large rhyolitic magma body. Journal of Petrology, 47(1), 35-69.

Wilson, C. J. N., & Charlier, B. L. A. (2009). Rapid rates of magma generation at contemporaneous magma systems, Taupo Volcano, New Zealand: insights from U–Th model-age spectra in zircons. Journal of Petrology, 50(5), 875-907.

Winchell, P. (1969). The compensation law for diffusion in silicates. High. Temp. Sci. 1, 200-215.

Winchell, P., & Norman, J. H. (1969). A study of the diffusion of radioactive nuclides in molten silicates at high temperatures. In: High Temp. Technol., 3rd Int. Symp. Asilomar, 1967, 479-492

Wolff, J. A., Balsley, S. D., Gregory, R. T. (2002). Oxygen isotope disequilibrium between quartz and sanidine from the Bandelier Tuff, New Mexico, consistent with a short residence time of phenocrysts in rhyolitic magma. Journal of Volcanology and Geothermal Research 116(1-2), 119-135.

Zellmer, G. F., Blake, S., Vance, D., Hawkesworth, C., & Turner, S. (1999). Plagioclase residence times at two island arc volcanoes (Kameni Islands, Santorini, and Soufriere, St. Vincent) determined by Sr diffusion systematics. Contributions to Mineralogy and Petrology, 136(4), 345-357.

Zellmer, G. F., Sparks, R. S. J., Hawkesworth, C. J., & Wiedenbeck, M. (2003). Magma Emplacement and Remobilization Timescales Beneath Montserrat: Insights from Sr and Ba Zonation in Plagioclase Phenocrysts. Journal of Petrology, 44(8), 1413–1431.

Zhang, Y. (2010). Diffusion in minerals and melts: theoretical background. Rev. Mineral. Geochem. 72, 5-59.

Zhao, Z. F., & Zheng, Y. F. (2007). Diffusion compensation for argon, hydrogen, lead, and strontium in minerals: Empirical relationships to crystal chemistry. American Mineralogist, 92(2-3), 289-308.

Zheng, Y. F., & Fu, B. (1998). Estimation of oxygen diffusivity from anion porosity in minerals. Geochemical Journal J. 32, 71-89.

UNIVERSITÉ SORBONNE PARIS CITÉ

Storage conditions and dynamics of magma reservoirs feeding the major pumiceous eruptions of Dominica (Lesser Antilles Arc)

Clara Solaro-Müller

Résumé

Nous présentons ici une étude pétrologique de trois éruptions ponceuses majeures (~10 km3) de la Dominique (Arc des Petites Antilles): Layou (~51kyrs cal BP), Roseau (~33kyrs cal BP) et Grand Fond (~24kyrs cal BP).
En combinant une étude de pétrologie naturelle et expérimentale, nous proposons un modèle complet des réservoirs à l'origine des trois éruptions. Les magmas sont des dacites à forte teneur en cristaux (~30%), comprenant plagioclases, orthopyroxènes, clinopyroxènes, amphiboles et oxides. Les expériences d'équilibre de phases sur ces dacites ont permis de contraindre les conditions de stockage à 850°C, 400-500 MPa (16-20 km), ~ΔNNO+1 et une teneur en eau pré-éruptive de ~7-8 wt % pour les trois éruptions. Les orthopyroxènes ont été utilisés pour étudier les dynamiques pré-éruptives du système magmatique en combinant : une analyse systématique de leur zonation, l'analyse de leurs inclusions vitreuses et la modélisation de l'interdiffusion Fe-Mg. Les résultats, couplées aux résultats d'équilibres de phases, nous permettent de définir le réservoir comme un environnement fortement cristallisé (~30%), modérément froid (~850°C) et fortement oxydé (~ΔNNO+1), possédant 80-85% de cristaux non-zonés, remobilisé par un réchauffement de 25°C produit par l'injection d'un magma plus chaud sous-jacent. La modélisation de l'interdiffusion Fe-Mg dans les orthopyroxènes indique que le réchauffement s'est produit ~10 ans avant chaque éruption. Ce processus crée la zonation inverse retrouvée dans 15-20% des orthopyroxènes et développe un panache thermique interne au réservoir qui est responsable de l'hétérogénéité cristalline retrouvée dans les échantillons.

Mots clefs : Dominique, Ignimbrite, orthopyroxène, Equilibres de phases, Crystal System Analysis, diffusion

Abstract

Here we present an integrated petrological study of the plinian fallout deposit of the latest three ignimbritic eruptions recognized on Dominica (Lesser Antilles arc): Layou (~51kyrs cal BP), Roseau (~33kyrs cal BP) and Grand Fond (~24kyrs cal BP). We combine natural and experimental petrology to investigate the prevailing storage conditions within the reservoir that fed each eruption. Whole rocks are all dacites with crystal contents of ~30%, comprising plagioclase, orthopyroxene, clinopyroxene, amphibole and Fe-Ti oxide. The residual melt is rhyolitic. Pre-eruptive storage conditions of 850 (±5) °C, 400-500 MPa (16-20 km depth), ~ΔNNO+1 and melt water content of ~7-8wt% were determined for all studied eruptions through phase equilibria experiments.
Orthopyroxenes were used to investigate the architecture and pre-eruptive dynamics of the plumbing system through crystal system analysis (CSA) combined to glass inclusions analysis and Fe-Mg diffusion modelling. Results enable to define the reservoir feeding each eruption as a highly crystalline (~30%), moderately cold (850°C) and highly oxidized (~ΔNNO+1) environment with 80-85% of unzoned orthopyroxenes, and 15-20% of zoned orthopyroxenes recording a heating process of 25°C, possibly produced by an underplating hotter magma that is responsible of the reservoir rejuvenation. Modelling of Fe-Mg interdiffusion suggests that this heating occurs in short timescales of ~10 years prior to each eruption. This heating process develops, over the considered eruptive time, a plume heating geometry able to bring together, on the scale of the hand sample, crystals of different sectors of the reservoir.

Keywords : Dominica, Ignimbrite, orthopyroxene, phase equilibria, Crystal System Analysis, diffusion